SUSTAINABLE DEVELOPMENT OF CRITICAL INFRASTRUCTURE

Edited by Xila Liu and A. H-S. Ang

ASCE

SUSTAINABLE DEVELOPMENT OF CRITICAL INFRASTRUCTURE

PROCEEDINGS OF THE 2014 INTERNATIONAL CONFERENCE ON
SUSTAINABLE DEVELOPMENT OF CRITICAL INFRASTRUCTURE

May 16-18, 2014
Shanghai, China

SPONSORED BY

The International Cooperation & Exchange Committee of the China Civil
Engineering Society (CCES)
The Council on Disaster Risk Management of the American Society of
Civil Engineers (ASCE)

EDITED BY
Xila Liu
A. H-S. Ang

ASCE Council on Disaster Risk Management
Monograph No. 8

ASCE AMERICAN SOCIETY
OF CIVIL ENGINEERS

Any statements expressed in these materials are those of the individual authors and do not necessarily represent the views of ASCE, which takes no responsibility for any statement made herein. No reference made in this publication to any specific method, product, process, or service constitutes or implies an endorsement, recommendation, or warranty thereof by ASCE. The materials are for general information only and do not represent a standard of ASCE, nor are they intended as a reference in purchase specifications, contracts, regulations, statutes, or any other legal document. ASCE makes no representation or warranty of any kind, whether express or implied, concerning the accuracy, completeness, suitability, or utility of any information, apparatus, product, or process discussed in this publication, and assumes no liability therefor. The information contained in these materials should not be used without first securing competent advice with respect to its suitability for any general or specific application. Anyone utilizing such information assumes all liability arising from such use, including but not limited to infringement of any patent or patents.

ASCE and American Society of Civil Engineers—Registered in U.S. Patent and Trademark Office.

Preface

This volume contains the selected papers presented during the International Conference on *Sustainable Development of Critical Infrastructure* (IC-SDCI2014) held in Shanghai, China on 16-18 May 2014. All the papers were reviewed and approved by at least two reviewers. The Conference is the first event jointly sponsored by the China Civil Engineering Society (CCES) and the American Society of Civil Engineers (ASCE).

The publication of the Proceedings Volume is intended to widely promote and review the technologies necessary to support the engineering development of sustainable infrastructure systems in China and elsewhere. The Volume consisted of four keynote papers and 51 contributed papers on various topics dealing with these technologies, including namely the fields of impacts and adaptation to a climate change, reliability engineering and risk management, life-cycle performance and cost, and new developments of traditional construction materials such as reinforced concrete and steel. Specific applications of sustainable engineering systems include buildings, bridges, transportation systems, electric power systems, and nuclear power plants.

The technical and scientific programs of the Conference were organized under the leadership of the respective committees of the two sponsoring societies – namely, the Committee for International Cooperation & Exchange of the CCES and the Council on Disaster Risk Management (CDRM) of the ASCE. The Technical Council on Life-Cycle Engineering (TCLC) of the Institute of Structural Engineering (SEI) and other groups of ASCE also contributed to the technical program of the conference.

Financial supports for the Conference were provided by the Shanghai Jiao-Tong University and the construction industry of Shanghai; these financial supports are highly appreciated and gratefully acknowledged. The efforts of the faculty and staff of the University were essential in managing the organization and operation of the Conference; many thanks are due to their tireless assistance.

Finally, the efforts of all the authors and presenters of papers at the Conference are acknowledged with thanks and appreciation; the success of the Conference is a credit to the contributions of each and every author.

Editors

Xila Liu,
Professor, Shanghai Jiao Tong University

and

A. H-S. Ang
Research Professor, University of California, Irvine

Conference Organization

Honorary Chairs:
Yun Chong Guo -- President, China Civil Engineering Society
Randy Over – President, American Society of Civil Engineers
Jie Zhang – President, Shanghai Jiao Tong University

Steering Committee

Conference Chairs
Xila Liu, Shanghai Jiao Tong University
Alfredo Ang (co-Chair), University of California, Irvine

Members
Erik Vanmarke – Princeton University
Dan Frangopol – Lehigh University
Bilal Ayyub -- University of Maryland
Geoffrey Mills -- Institution of Civil Engineers (UK)
Zhi Quan Jiang --Shanghai Construction Group
Wen Bo Zhou -- Shanghai Urban Construction Group
Hua Zhang -- Shanghai Xian Dai Architectural Design (Group) Co.，Ltd.
Jin Ke Sun -- Shanghai Research Institute of Building Sciences (Group) Co., Ltd
Shao Pei Lin -- Shanghai Jiao Tong University

International Scientific Committee

Alfredo Ang, Chair – University of California, Irvine
Xila Liu, co-Chair – Shanghai Jiao Tong University
Paul Chang -- Hong Kong University of Science and Technology
Hitoshi Furuta -- Kansai University, Japan
Yan Gang Zhao -- Kanagawa University�ⅽJapan
Sang-Hyo Kim -- Yonsei University, South Korea
Hasan Kamal -- Kuwait Institute of Scientific Research, Kuwait
Xilin Lv -- Tongji University
Dong Ping Fan -- Tsinghua University
Jia Ru Qian -- Tsinghua University
Jian John Lu -- Shanghai Jiao Tong University
Jin Cheng Zhao -- Shanghai Jiao Tong University
Gang Wu -- Southeast University
Chao Hui Chen -- Chongqing University
Yun Gui Li -- China State Construction Engineering Corporation Ltd.
Zhi Hua Shi -- China Academy of Building Research

Hen Shen Zhang -- China Society of Electric Engineering
Hong Hui Ge -- Shanghai Nuclear Engineering Research & Design Institute
Zong YuGao -- China Zhongtie -Major Bridge Reconnaissance & Design Institute
Co.

Local Organizing Committee

Hao Hu, Chair -- Shanghai Jiao Tong University
Shui Long Shen, Vice Chair -- Shanghai Jiao Tong University
Zhen Huang, Vice Chair -- Shanghai Jiao Tong University
Feng Xu -- Shanghai Jiao Tong University
Lulu Zhang -- Shanghai Jiao Tong University
Fan Wu -- Shanghai Jiao Tong University
Pei Yin Liu -- Shanghai Jiao Tong University Express
Guang Liang Li -- Shanghai Jiao Tong University Express
Ying Shi -- Shanghai Jiao Tong University
Xue Ping Wu -- Shanghai Jiao Tong University
Xiao Ning Zhao -- Tsinghua University

Co-Sponsors

The IC-SDCI2014 is also co-sponsored by a number of Chinese and international organizations, including the following:

> World Federation of Engineering Organizations (WFEO)
> Federation of Engineering Institutions of Asia and the Pacific (FEIAP)
> International Association for Bridge and Structural Engineering (IABSE)
> International Association for Structural Safety and Reliability (IASSAR)
> International Association for Bridge Maintenance and Safety (IABMAS)
> International Association for Life-Cycle Civil Engineering (IALCCE)
> China Association of Science and Technology (CAST)
> Chinese Academy of Engineering (CAE)
> American Association of Engineering Societies (AAES)
> American Concrete Institute (ACI)
> Institution of Civil Engineering (ICE)
> Institution of Structural Engineers (IStructE)
> Shanghai Construction Group (SCG)
> Shanghai Urban Construction Group (SUCG)
> Shanghai Xian Dai Architectural Design (Group) Co., Ltd.
> Shanghai Research Institute of Building Sciences (Group) Co., Ltd

Table of Contents

Keynote Papers

Workshop on Risk Management and Adaption to Climate Change

Workshop on Practical Applications of Life-Cycle Considerations

Construction Safety of Local and Overseas Projects

Collapse Control of Critical Infrastructure during Strong Natural Disasters

Robustness of Critical Infrastructure under Terror Attacks

Transportation Systems for Regional Sustainable Development

Life-Cycle Engineering of Nuclear Power Systems

Resilient Electrical Power Generation and Transmission Systems I

Resilient Electrical Power Generation and Transmission Systems II

Monitoring Systems of Long-Span Bridges

Disaster Prevention and Mitigation of Super-High Rise Buildings

Reliability-Based Design Criteria for Infrastructure Systems – *A New Look*

Alfredo H-S. Ang[*]

Abstract

The existing reliability-based codes for structural design must rely on "calibration" in specifying the required level of safety. This means that the safety level underlying a reliability-based design will be the same as that of the current traditional code-based design. In other words, reliability does not contribute to the decision on the required safety level for the design of structures or infrastructure systems. It relies on what is in existing codes of structural design.

Proposed is an alternative for the development of reliability-based design in which the decision on the required safety level does not depend on "calibration"; instead, it is based on acceptable risk or risk-averseness. For this purpose, uncertainties are divided into two broad types – namely, the aleatory and the epistemic types. The aleatory type is associated with the variability in the observed information (or data-based), whereas the epistemic type is associated with one's inability to accurately estimate or predict reality (i.e., knowledge-based).

   The two types of uncertainties, can and should be treated separately; in either case, the same probability principles are required and adopted. The effects of the aleatory type is represented in terms of a failure probability, whereas due to the effects of the epistemic type the relevant failure probability, or safety index, becomes a random variable. Values within this random variable correspond to different confidence levels. To ensure adequate safety level of structures, a high confidence level would be appropriate (e.g., the 90% or 95% confidence). Observe that the mean value of the safety index (obtained with the existing total uncertainty approach) is associated with a 50% confidence level which is obviously too low for ensuring safety of structures; thus, the need for calibration.

The proposed approach is illustrated with examples of the design of simple structural elements. Also the safety levels of major infrastructure systems are examined for the purpose of identifying the confidence levels underlying current engineering practice.

Introduction

The reliability-based criteria for codified design of structures have, thus far, provided

---

[*] Department of Civil Engineering, University of California, Irvine; ahang2@aol.com

a consistent basis for specifying safety among different materials of construction such as steel, concrete, wood, and masonry. However, the decision on the required level of safety is entirely based on "calibration" – this means that the value of the required safety index (β) is selected in order to obtain reliability-based designs that will ensure the same level of safety or performance as those obtained with existing traditional codes. This approach does not take full advantage of the virtue of the probability-based concept of safety or performance; it serves only to ensure that the safety of the reliability-based designs preserves that of traditional codes.

To take full advantage of the reliability approach, the decision on the safety level should be based on a tolerable risk, and not rely on "calibration". Proposed here is an alternative reliability-based approach without relying on "calibration". The value of the safety index (β) required to ensure the necessary level of safety is determined with a high confidence level that structural safety is sufficiently risk-averse or conservatively adequate.

This alternative approach is described for developing criteria for codified designs of infrastructure systems, and illustrated with practical examples of simple designs, as well as the evaluation of the safety levels of existing major structures. The latter serves to enlighten the degree of risk-averseness underlying existing engineering practice.

Types and Significance of Uncertainties
Uncertainties are always present in all engineering activities. In the case of structural design, uncertainties are unavoidable in predicting the lifetime maximum load that may be expected on a structure over its life, as well as the capacity of the structure (or structural element) with its potential deterioration over its useful life. There are also other major sources of uncertainty, including for example in the inaccuracy of modeling, as well as in the analysis, of a real structure.

Probability-based reliability engineering is the proper basis and tool for handling uncertainties; indeed, it is the main purpose of this technology.

For practical purposes, uncertainties may be classified into two broad types (Ang and Tang, 2007); namely, the *aleatory* and the *epistemic* types:
- the aleatory type is the variability in the observed data which is inherent in the randomness of the underlying phenomenon, and may be classified as "data-based"; whereas,
- the epistemic type is the uncertainty underlying one's inability to predict reality, and may be classified as "knowledge-based".

In either case, the analyses of their respective effects on the safety and performance of a structure require the tools of probability and statistics.

Assessment of Uncertainties
As a first step. each of the major sources of uncertainty must be systematically assessed. In this regard, the aleatory type should be assessed on the basis of available
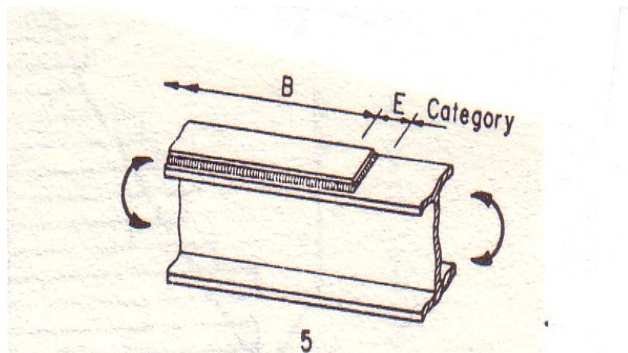
data, at least in terms of the mean and standard deviation (or coefficient of variation) from the observed data.

On the other hand, the epistemic type would pertain to the errors in the estimation or prediction; for practical purposes, these errors may be limited to those in the estimated mean or median values[†]. In this case, there would seldom be observed data to evaluate the degree of error or inaccuracy of an estimation or prediction. For this reason, assessment of the epistemic type may have to rely largely on judgment. A good way is to specify the possible range of error in the estimated mean or median value. A simple example relating to fatigue life of metallic structures is illustrated below.

Illustration -- The fatigue life of welded joints in steel structures are widely recognized to be highly variable; and there are extensive statistical data that have been observed and recorded for different weld configurations (see e.g., Ang and Munse, 1975).

Consider the wide-flange beam of A7 steel with a fillet-welded cover plate as shown below.

Test results of such beams under repeated constant-amplitude cyclic loadings show a scatter with a coefficient of variation (c.o.v.) of around 21%; this is the aleatory variability of the fatigue life of such beams with fillet-welded cover plates. In estimating the fatigue life of such a beam in a real structure, there are obviously other sources of uncertainty – most of which are of the epistemic type, specifically including the following (Ang and Munse, 1975), expressed as c.o.v.'s:

Error in the SN relation = 0.40;
Error in Miner's rule (for variable loadings) and effect of mean stress = 0.15;
Error in defining applied stress-ranges, including impact effect = 0.09.

Thus the total epistemic uncertainty becomes 0.44. These c.o.v.'s of the respective epistemic uncertainties were evaluated subjectively considering the possible ranges of errors in estimating the fatigue life, based largely on judgments.

Effects of Uncertainties
It is natural that the effect of the aleatory uncertainty (which is really variability in

---

[†] The most significant error would be that in the estimated mean or median value. Although there are also errors in the estimated higher moments (such as the variance), these errors are of secondary significance.

information) be expressed in terms of probability. Similarly, the effect of the epistemic uncertainty may also be expressed in the same terms; in fact for this purpose the two types of uncertainty may be combined and treated as the "total uncertainty".

However, treating the effect of both types of uncertainty in the same manner (as the total uncertainty) raises a question of consistency. When the two types of uncertainty are combined, this implies that the same probability distribution must necessarily be applied to both types of uncertainty. There is, however, no validity for this assumption. In other words, whereas the variability in information (i.e., the aleatory type) can and should properly be represented by an appropriate probability distribution (based on available data), this same distribution may not be proper for the epistemic type. As the epistemic type represents the error in estimation or prediction, the range of possible errors may have to be prescribed based often on subjective judgment, and if necessary with prescribed distribution within the range which may be different from that of the aleatory variability.

Properly, the two types of uncertainty and their respective effects ought to be treated separately; the effect of the aleatory variability should yield the probability of failure, or safety index, of a structure or structural element. On the other hand, as there is error in the estimated mean (or median) value underlying the variability of the pertinent phenomenon (epistemic uncertainty); this will lead to corresponding error in the calculated failure probability. By convolution of the aleatory variability with the prescribed distribution of the epistemic uncertainty, the correct failure probability will not be a single value but instead will result in a range of possible failure probabilities, or corresponding range of safety indices; i.e., become values of a random variable.

On Total Uncertainty
The aleatory and epistemic types may be combined to obtain the "total uncertainty". In this case, only the mean value of the failure probability, and its corresponding mean safety index, which are respectively single valued, would be obtained. Clearly, the mean value is associated with a "confidence level" of around 50%.

Example 1 (Fatigue of Metal Structures)
Consider the wide-flange beam (mentioned earlier) with a fillet-welded cover plate shown above.

In this case, the variability of fatigue life, in number of load cycles *n,* may be described with a Weibull distribution. Then the probability of no fatigue failure up to load cycle *n* is the reliability function (Ang, 1977),

$$L(n) = \exp\left\{-\left[\frac{n-\varepsilon}{\overline{n-\varepsilon}}\Gamma(1+\delta_n^{1.08})\right]^{\delta_n^{-1.08}}\right\} \qquad (1)$$

where: ε = minimum life, which may be conservatively assumed to be 0;

$\overline{n}$ = mean life to fatigue failure;

δ_n = c.o.v. of observed fatigue life, representing its aleatory variability; and

$\Gamma(x)$ = the gamma function.

The underlying fatigue life n has a Weibull distribution with $\overline{n} = 429,000$ and a c.o.v. of 0.21; the corresponding Weibull parameters are:

$w = 484,000$, the modal value;

$k = 2.20$, the shape parameter.

The corresponding probability of fatigue failure at load cycle n is

$$p_F(n) = 1 - L(n) \qquad (1a)$$

Clearly, from Eq. 1, the reliability to achieve a fatigue life of n cycles is a function of $\overline{n}$ (the mean life) and δ_n (the c.o.v. representing the observed variability of fatigue data) which is 0.21 for this example beam.

When subjected to constant-amplitude cyclic loading, s, the mean life $\overline{n}$ is generally determined by the empirical SN equation,

$$\overline{n} = \frac{c}{s^m} \qquad (2)$$

where c and m are, respectively, the intercept and (negative) slope of the regression of log n on log s of the available fatigue data. Whereas, for variable or random cyclic loadings, S, the mean life, $\overline{n}$, may be obtained (invoking the Miner's law) as follows,

$$\overline{n} = \frac{c}{E(S^m)} \qquad (3)$$

in which $E(S^m) = \int_0^\infty s^m f_S(s)ds$ is the mth moment of S, and therefore is a function of the probability distribution of the applied stress-range S.

For the example beam, $c = 3.98 \times 10^8$ and m 2.75. Therefore, when subjected to a constant-amplitude stress-range of 12 ksi the mean fatigue life for this beam would be

$$\overline{n} = \frac{3.98 \times 10^8}{12^{2.75}} = 429,000 \text{ cycles.}$$

Therefore, under the constant-amplitude stress-range of 12 ksi, the reliability for a fatigue life of 300,000 cycles would be

$$L(300,000) = \exp\left\{-\left[\frac{300000}{429000}\Gamma(1 + 0.21^{1.08})\right]^{0.21^{-1.08}}\right\}$$

$$= \exp[-(0.583 \times 0.921)^{5.40}] = 0.9113$$

The above reliability of around 91%, of course, assumes that there is no other uncertainty – in particular there is no epistemic type of uncertainty. However, there is significant epistemic uncertainty; as indicated earlier, for the fatigue life of this beam the epistemic uncertainty has a c.o.v. of 0.44. Combining this with the variability of 0.21, the total uncertainty will have a c.o.v. of

$$\Omega = \sqrt{(0.21)^2 + (0.44)^2} = 0.49$$

Then, according to Eq. 1, the mean reliability of the beam for a life of 300,000 cycles would be

$$L(300000) = \exp[-(\frac{300000}{429000} \times 0.8856)^{2.31}]$$

$$= 0.7185$$

The corresponding safety index would only be $\beta = 0.58$.

The actual mean life can vary over a wide range -- around 429,000 cycles with a c.o.v. of 44%. To include the effect of this epistemic uncertainty, a convolution integral is required. This integration can be performed with Monte Carlo simulations, yielding the histogram shown in Fig.1 of the reliability $L(n)$ of the beam for $n =$ 300,000 cycles under constant-amplitude loadings.

The two figures, Figs. 1 and 2, were generated with the following:

$$L(300,000) = \exp\left\{-(\frac{300000}{x} \times 0.921)^{5.40}\right\}$$

where $x = \overline{n}$ has a mean life of 429,000 cycles (median life = 394,000) and a c.o.v. of 0.44, and with a prescribed lognormal distribution. On this basis, the median reliability at 300,000 cycles is 0.87, whereas the 90% reliability is 0.99.

The histogram for the safety index, β, is shown in Fig. 1. This shows that the safety index, β, for a fatigue life of 300,000 cycles has a median value of 1.15; however, the
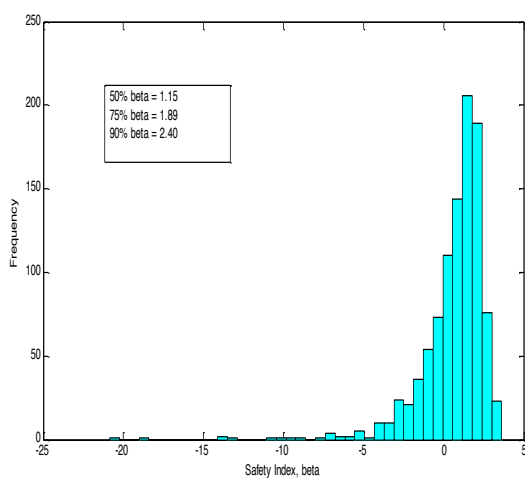
Figure 1: Histogram of β for 300,000 cys Figure 2:
(assuming lognormal mean life, x)
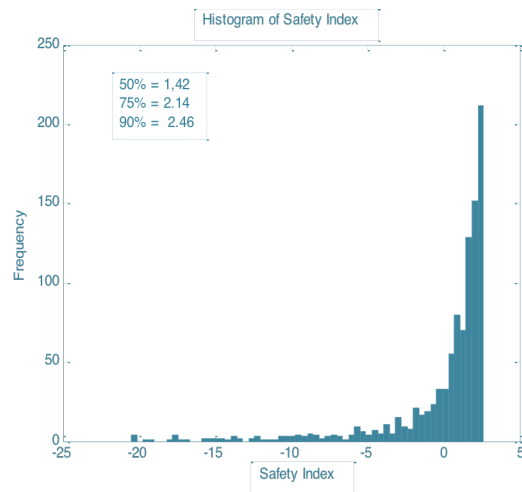
Figure 2: Histogram of β for 300,000 cys
(assuming uniform mean life, x)

actual value of β has a wide range of values as portrayed in Fig. 1; at a confidence level of 90%, β = 2.40. Of course, the median value of 1.15 would correspond to a confidence level of only 50%.

Figure 2 shows the same histogram of the safety index, β, assuming that the mean fatigue life, x, is uniformly distributed, whereas in Fig. 1 the mean fatigue life x is prescribe to be lognormal.

Appropriate Confidence Level -- For the design of structures, the appropriate confidence level will depend on the consequence of a failure (i.e., limit state). For example, in the case of fatigue failure involving the occurrence of an observable fatigue crack, a confidence level of 75% to 90% might be appropriate. Whereas, if the fatigue failure of the beam (e.g., total collapse) could lead to the partial collapse of the structure, a higher confidence might be required – around 90% to 95%.

Example 2 (*LRFD of R/C Structures*)
Current codes or standards for design of structures are widely based on the LRFD (load-and-resistance-factor design) format. A generic form of the LRFD may be stated as

$$\phi R \geq \sum_i \gamma_i Q_i \qquad (4)$$

where: R = the load-carrying capacity of a structural element;
    Q_i = the applied load i;
    ϕ = the resistance factor;
    γ_i = the load factor for load i.

For example, the ACI (American Concrete Institute) requirement for the design of R/C beams is

$$\mu_R \geq 1.56\mu_D + 1.72\mu_L \tag{5}$$

applicable to the respective mean capacity and mean loads.

If the aleatory c.o.v.'s of *R, D,* and *L* are respectively as follows:

$$\delta_R = 0.11$$
$$\delta_D = 0.10$$
$$\delta_L = 0.25$$

And assuming that the live load to dead load ratio is $\mu_L/\mu_D = 0.75$ we have; $\mu_R = 2.85\mu_D$; then the (mean) safety index of the beam would be,

$$\beta = \frac{2.85\mu_D - \mu_D - 0.75\mu_D}{\sqrt{(0.11\times2.85\mu_D)^2 + (0.10\mu_D)^2 + (0.25\times0.75\mu_D)^2}} = 2.904$$

This is the safety index due only to the aleatory variability; i.e., assumes no epistemic uncertainties. The estimated mean resistance $\overline{R}$ and the estimated mean loads $\overline{D}$ and $\overline{L}$ are invariably also subject to uncertainties (of epistemic type).

Suppose the correct mean-values may range, respectively, as follows:

$$\mu_R = \overline{R}\pm10\%; \quad \mu_D = \overline{D}\pm15\%; \quad \mu_L = \overline{L}\pm30\%$$

These ranges are epistemic uncertainties associated with imperfections in estimating the actual mean resistance and mean loads. The equivalent c.o.v.s of the respective estimates would be:

$$\Delta_{\overline{R}} = 0.06, \ \Delta_{\overline{D}} = 0.09, \ \Delta_{\overline{L}} = 0.17.$$

Assume uniform distribution (equally likely) of values within each range.

The effect of these epistemic uncertainties will lead to uncertainty in the calculated failure probability, p_F, and in the safety index, β. In this light, p_F and β become random variables. With the above ranges of possible mean values, (and the respective c.o.v.s) the histogram of the safety index β is shown in the following Fig. 3, obtained through Monte Carlo simulations (MCS) yielding a mean value of $\beta = 2.51$.
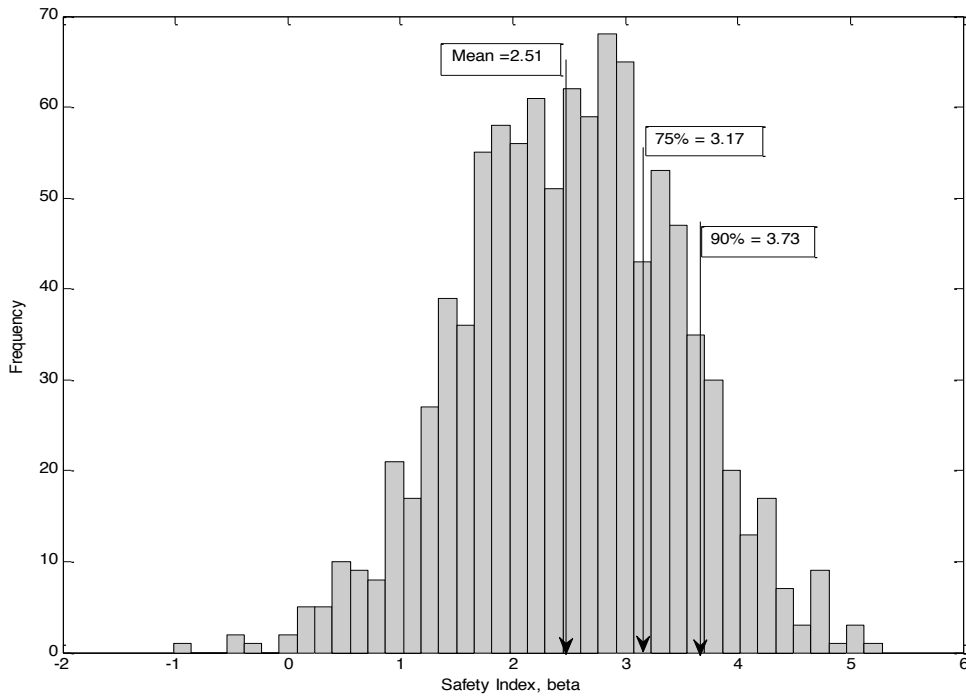
Figure 3: Histogram of Safety Index, β

Observe that if the above c.o.v.s of the aleatory variability and the epistemic uncertainties were combined, the respective total uncertainties would become as follows:

$$\Omega_R = \sqrt{(0.11)^2 + (0.06)^2} = 0.125;$$

$$\Omega_D = \sqrt{(0.10)^2 + (0.09)^2} = 0.134;$$

$$\Omega_L = \sqrt{(0.25)^2 + (0.17)^2} = 0.302.$$

Then, the safety index associated with these total uncertainties would be (by FORM),

$$\beta = \frac{2.85 - 1.0 - 0.75}{\sqrt{(0.125 \times 2.85)^2 + (0.134)^2 + (0.302 \times 0.75)}} = 2.48$$

which is close to the mean value of 2.51 of Fig. 3. This serves also to confirm that the with the total uncertainty, the resulting safety index is the mean value (a single value).

Remember that with the mean safety index, the confidence is around 50% in the design of the R/C beam. With the histogram of the safety index, as given in Fig. 3, the values of the safety index with higher levels of confidence are also

available; for example, for a confidence level of 90% the safety index would be $\beta = 3.73$ for the design of the beam.

The safety index obtained with FORM would be $\beta = 2.48$ which is close to the mean $\beta = 2.51$ of Fig. 3 obtained by MCS. (Incidentally, if the epistemic uncertainties in the estimated mean values were assumed to be normally distributed, instead of uniform, the mean value of β would be 2.48). This serves also to confirm that the result (such as the safety index) obtained with the total uncertainty is close to the mean value of the MCS results.

At a confidence level of 90%, the load and resistance factors for LRFD design would be obtained as follows.

$$\frac{\mu_R - \mu_D - 0.75\mu_D}{\sqrt{(0.125\mu_R)^2 + (0.134\mu_D)^2 + (0.302 \quad 0.75\mu_D)^2}} = 3.73$$

resulting in the quadratic equation,

$$\mu_R^2 - 4.47\mu_R\mu_D + 2.68\mu_D^2 = 0$$

The solution for μ_R is

$$\mu_R = 3.755\mu_D$$

With which the load and resistance factors for LRFD design of the beam, applicable to the mean design parameters are, therefore,

$$\overline{\phi} = 1 - 0.872 \times 3.73 \times 0.125 \quad 0.593$$
$$\overline{\gamma}_D = 1 + 0.249 \times 3.73 \times 0.134 \quad 1.124$$
$$\overline{\gamma}_L = 1 + 0.420 \times 3.73 \times 0.226 \quad 1.354$$

For comparison with Eq. 5, the above design factors can be transformed into the same terms as those of Eq.5; the corresponding design factors would become,

$$\overline{\phi} = 1.00, \quad \overline{\gamma}_D = 1.90, \quad \overline{\gamma}_L = 2.28$$

And the appropriate design equation would be

$$\mu_R \geq 1.90\mu_D + 2.28\mu_L \tag{6}$$

It is well to emphasize that the LRFD design of the R/C beam with Eq. 5 will

have an underlying confidence of around 50%, whereas its design with Eq. 6 will have a confidence level of 90%.

Acceptable Confidence Levels in Engineering Practice
For reference, it would be relevant and instructive to examine the confidence levels underlying the design and construction of major infrastructure systems. For this purpose, let us examine the designs of two a major infrastructure systems; a cable-stayed bridge shown in Fig. 4, and also an oil production offshore platform shown in Fig. 7.

A reliability analysis of the cable-stayed bridge was performed; also, its life-cycle cost was evaluated (Han and Ang, 2008). The results of these evaluations may then be compared with the actual design and construction of the bridge.

The major results are shown in Figs. 5 and 6. Fig. 5 shows the alternative designs of the bridge with the respective mean life-cycle costs E(LCC) and corresponding safety index underlying the various designs; whereas Fig. 6 portrays the histogram of the safety index β for the design with minimum life-cycle cost of the bridge.

A Cable-Stayed Bridge – Shown in Fig. 4 is the cable-stayed bridge in Jindo, Korea.
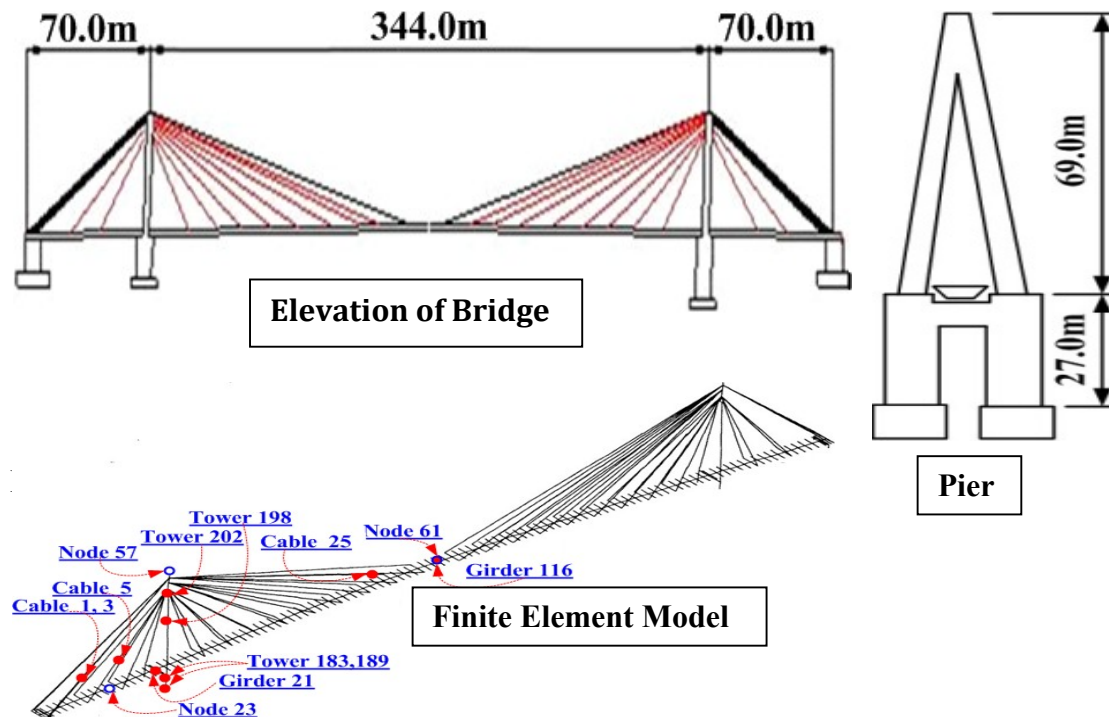
Figure 4: Cable-Stayed Bridge at Jindo, Korea ((c) 2008 Taylor & Francis Group, London, UK. Used with permission)
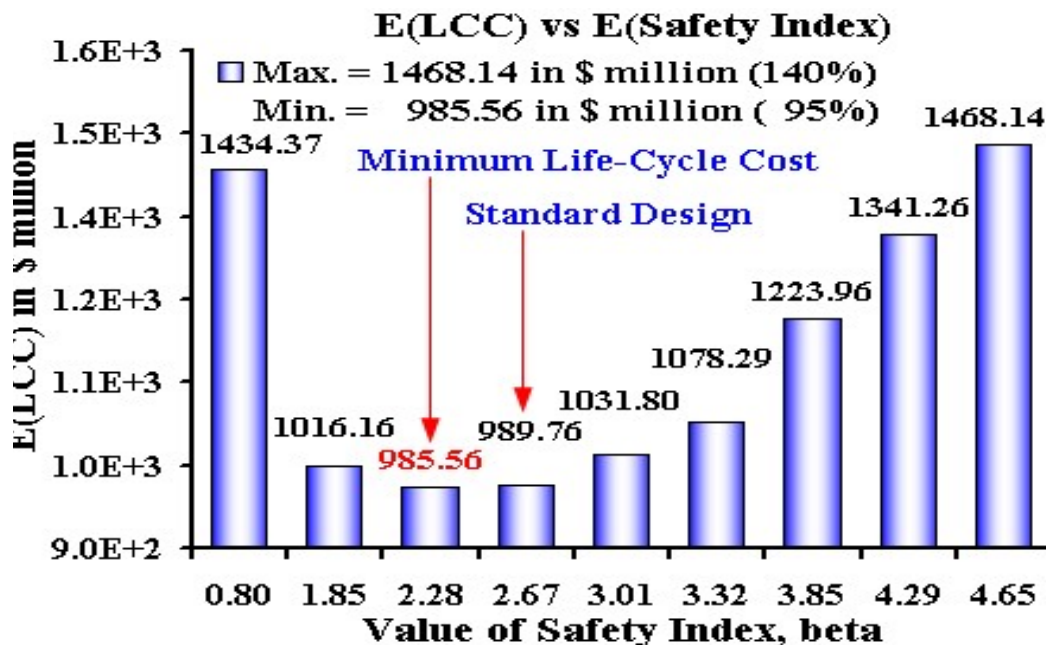
Figure 5: Life-Cycle Cost versus Mean Safety Index
Í "422: "Vc{ñqt"("Hcpeku'T tqwr ."Nqpfqp."W'M0'Wugf'y kj "rgtokuukqp

The actual design of the Jindo Bridge (as designed) is designated in Fig. 5 as the "standard design" with a mean safety index of 2.67.. Fig. 5 also shows that the standard design is close to the minimum life-cycle cost design.

In Fig. 6 is shown the histogram of the safety index of the minimum E(*LCC*) design of the Jindo Bridge, indicating its mean value is $\beta = 2.28$, whereas the 90% value is $\beta_{90} = 3.23$.
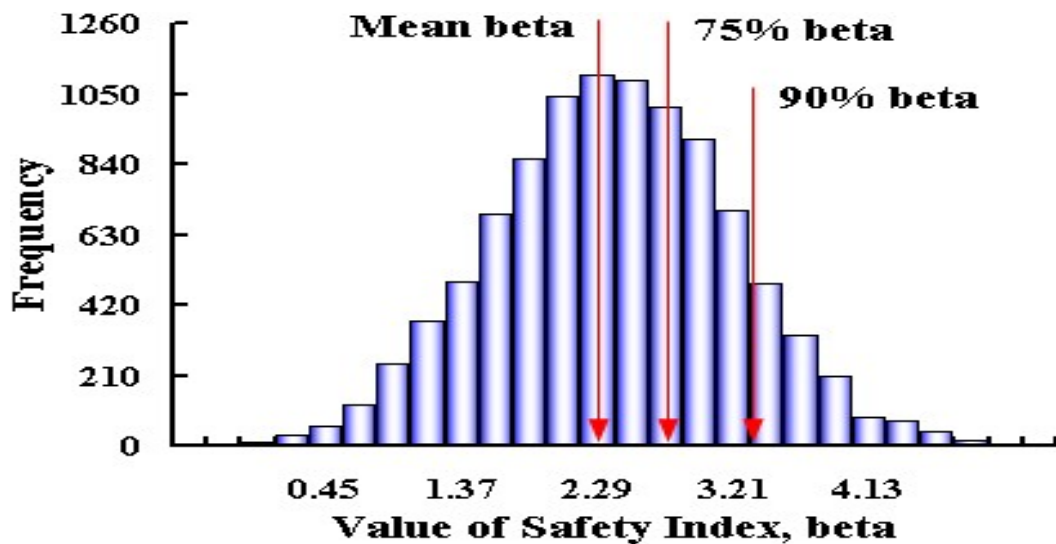
Figure 6: Histogram of Safety Index of the Minimum E(*LCC*) Design
© 2008 Taylor & Francis Group, London, UK. Used with permission

From Fig. 5, observe that the mean safety index of the standard design is 2.67, which means that it is slightly higher than that for the minimum E(LCC) design of mean β = 2.28. On this basis, it may be inferred that the safety index underlying the standard design would be higher than the 90% value of β = 3.23, perhaps closer to the 95% value.

An Offshore Oil Production Platform – Shown in Fig. 7 is a typical drilling platform for the production of oil in the Bay of Campeche, Mexico. It was designed based on the Mexican PEMEX (2000) Code for this type of structures in the Gulf of Mexico.

A reliability and associated life-cycle cost analyses of the platform were performed; the main results are summarized in Figs. 8 and 9. Fig. 8 shows the E(LCC) versus the 90% safety indices, β_{90}, of the respective designs, indicating that the design with the minimum E(LCC) would be obtained with a 90% safety index, β_{90}, of around 3.50.

Fig. 9 represents the complete histogram of the safety index for the design of the platform with minimum E(LCC).

The significant values of β for the platform, from Fig. 9, are the following:
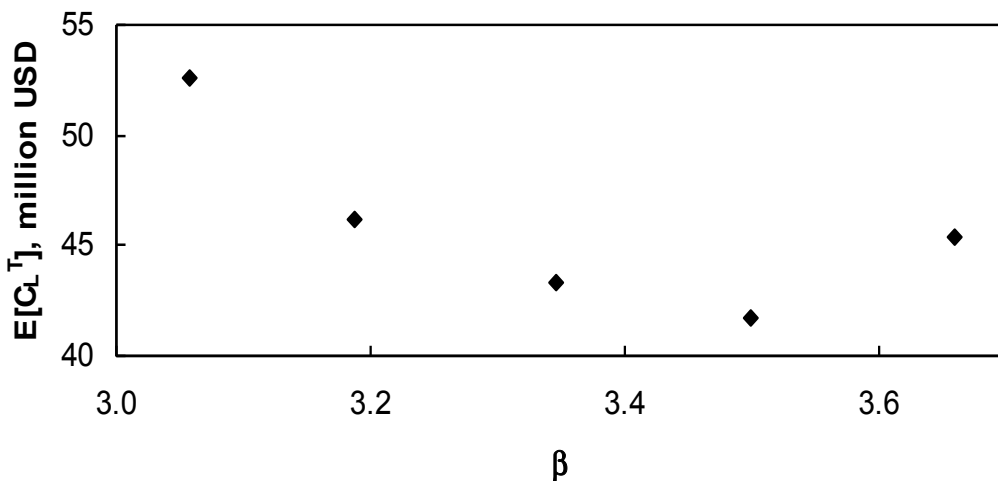
       90% safety index, β_{90} = 3.45;
       75% safety index, β_{75} = 3.21;
whereas the mean β = 2.96.
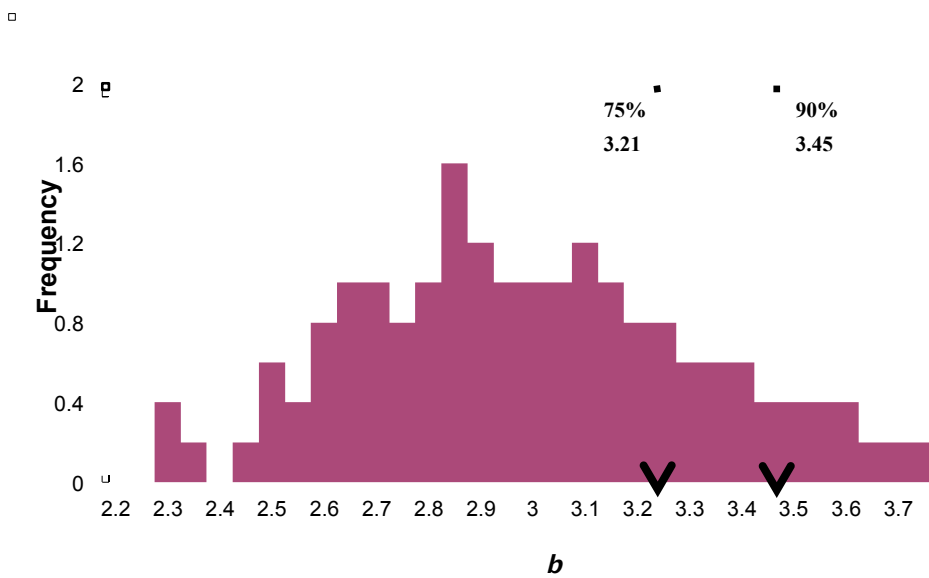
Figure 7: A Typical Offshore Oil Drilling Platform

Figure 8: E(*LCC*) versus β_{90} for Typical Offshore Platforms

For a typical offshore production platform, the current standards of the petroleum industry for important platforms require $\beta = 3.3 - 3.5$ (API, 1993; PEMEX, 2000). On this basis, therefore, the 90% safety index of 3.45 obtained above in Fig. 9 is consistent with the current standards for design of important oil drilling platforms.

Also, the above results indicate that current standards would yield designs that are close to the minimum E(*LCC*) designs.

Figure 9: Histogram of β of the Platform with Minimum E(*LCC*)

If the aleatory and epistemic uncertainties were combined, the optimal safety index for marine structures would be 2.96, the mean value. Clearly, this mean safety index is much lower than the requirement of the current design standards of API,1993 or of PEMEX, 2000.

In summary, on the basis of the two examples of major infrastructural systems as currently designed in practice, it is reasonable to infer that a confidence level of 90% to 95% is sufficiently adequate for the design of infrastructure systems.

Conclusions

The main conclusions are the following.

1. Thus far, reliability-based design is based and relies on "calibration" – meaning that the underlying level of safety is adjusted as to be consistent with that of traditional code-based designs.

    In this regard, therefore, the reliability approach does not contribute to the important decision – i.e., determining the appropriate safety level for structural design; in particular it does not address the question of "how safe is the design, from a risk standpoint?"

2. The "total uncertainty" approach, as referenced above, yields only the mean-value of the safety index which is inadequate for safety design of structures. And thus must be adjusted through "calibration" with existing traditional codes.

3. However, if the two broad types of uncertainty are treated separately, the issue of the required safety level for structural design can be based on a tolerable risk averseness, such as with a safety index associated with a high confidence level. This is possible because the safety index becomes a random variable (due to epistemic uncertainty) with higher values associated with increasing confidence levels.

4. Based on the examples of two major structural systems, it appears that the safety index (conversely, acceptable failure probability) corresponding to a confidence level of 90% to 95% would be sufficiently risk-averse to ensure adequate safety of major infrastructure systems.

5. Should higher level of safety be required, a confidence level >95% may be selected or specified.

Acknowledgement

References

Ang, A.H-S. (1977), "Bases for Reliability Approach to Structural Fatigue", *Proceedings, ICOSSAR'77*, Munich, Germany, Werner-Verlag

Ang, A. H-S. and Munse, W.H. (1975), "Practical Reliability Basis for Structural Fatigue:, Meeting Preprint 2494, ASCE National Structural Engineering Conf., New Orleans

Ang, A. H-S. and Tang, W.H. (2007), *Probability Concepts in Engineeging –* Emphasis on applications in civil end environmental engineering, J. Wiley & Sons, Inc., New York

Han, S.H. and Ang, A. H-S. (2008), "Optimal Design of Cable-Stayed Bridges Based on Minimum Life-Cycle Cost", *Proceedings. IABMAS'08,* Seoul, Korea

PEMEX, 2000 (see De Leon and Ang, 2008 for reference)

Practical Applications of Life-Cycle Considerations in Sustainable Development of Infrastructure

Dan M. Frangopol[1], Mohamed Soliman[2] and You Dong[3]

ABSTRACT

Infrastructure systems are subjected to progressive and/or sudden performance deterioration throughout their service life. This deterioration may start from the day the structure enters in service and, if not effectively managed, can cause a significant reduction in the structural functionality and safety. Over the last decades, research efforts have shown that life-cycle management techniques can be successfully used to manage such deteriorating systems. In these techniques, various modules are integrated to form a comprehensive framework responsible for the assessment of the life-cycle performance, analysis of system and component performance interaction, management activities (e.g., inspections, monitoring, and maintenance) optimization, and updating the life-cycle performance based on information obtained from structural health monitoring and/or controlled testing. Nowadays, aspects regarding the evaluation of the time-variant performance are gaining an increasing attention in the design, assessment, and management of infrastructure. A special consideration is given to performance measures which cover sustainability aspects. Accordingly, there exists a need for well-established methods which can quantify the metrics of sustainability and allow their integration into the life-cycle management process. The aim of this paper is to highlight the role of life-cycle management concepts and methodologies in the sustainable development of infrastructure systems. The goals and benefits of such management concepts are discussed and their recent applications to bridge structures are presented.

INTRODUCTION

Infrastructure systems play a key role in the Nation's social and economic development. On the other hand, they significantly contribute to the socio-economic

---

[1] Professor and the Fazlur R. Khan Endowed Chair of Structural Engineering and Architecture, Department of Civil and Environmental Engineering, ATLSS Engineering Research Center, Lehigh University, 117 ATLSS Drive, Bethlehem, PA 18015-4729, USA; email: dan.frangopol@lehigh.edu

[2] Graduate Research Assistant and P.C. Rossin Fellow, Department of Civil and Environmental Engineering, ATLSS Engineering Research Center, Lehigh University, 117 ATLSS Drive, Bethlehem, PA 18015-4729, USA; email: mos209@lehigh.edu

[3] Graduate Research Assistant, Department of Civil and Environmental Engineering, ATLSS Engineering Research Center, Lehigh University, 117 ATLSS Drive, Bethlehem, PA 18015-4729, USA; email: yod210@lehigh.edu

impact on the surrounding environment. Moreover, incidents involving the failure of a component of an infrastructure system may have severe social, economic, and/or environmental impact. An example of these events is the recent failure of a railway bridge near Paulsboro, New Jersey, USA, causing the derailing of a freight train and the release of hazardous gases to the surrounding environment (CNN 2012). Thus, efforts should be made throughout the life-cycle of an infrastructure system to minimize its environmental, social and economic footprint. These efforts should focus on the component level, system level, and system of systems level. Moreover, as indicated in the 2013 Report Card of America's Infrastructure (ASCE 2013), the Nation's infrastructure systems are highly deteriorating with an estimated investment of 3.6 trillion USD required to improve their condition within the next seven years. This implies that the construction of more structures may be required, in addition to the crucial need of maintaining and repairing the existing structures to meet the current and future social needs. However, these repair and maintenance actions may induce delays and pollution which can be adversely reflected on the society and the surrounding environment. For instance, a decision to replace an existing bridge subjected to corrosion may be the option to adopt instead of performing a repainting maintenance, since repainting may pollute the water stream below the bridge. This means that the life-cycle management of infrastructures should consider not only the economic aspects, but also the social and environmental ones. These three aspects (i.e., economic, social, and environmental), as indicated in Figure 1, constitute the three pillars of sustainability (Adams2006; Bocchini et al. 2013b; Dong et al. 2013a). In other words, the sustainability metrics should be included in the life-cycle management of infrastructure systems. In general, sustainability can be defined as the "*development that meets the needs of the present without compromising the ability of future generations to meet their own needs*" (Adams 2006).
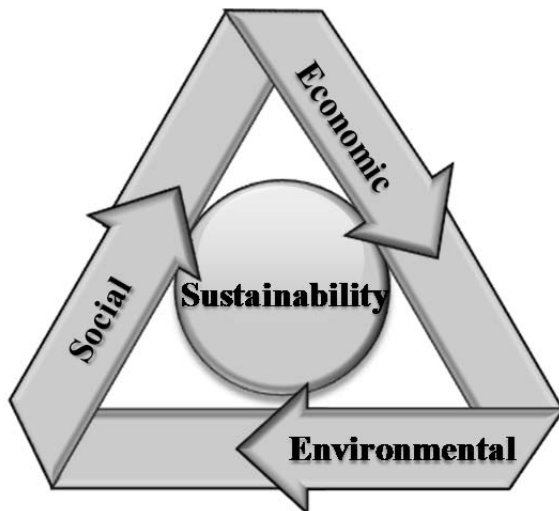
Figure 1. Three metrics of sustainability

Construction, inspection, and/or repair actions can impact the sustainability metrics. Therefore, if these actions can be coherently planned, the total down time,

delays, environmental impacts and life-cycle cost can be minimized. This requires (1) the deterioration of each structural system to be well understood and (2) the maintenance and repair actions to be pre-planned and updated along the life-cycle of the structure. These two aspects can be well covered through the concepts and techniques of the probabilistic life-cycle management process (Frangopol 2011). In this process, the structures under consideration are analyzed and their deterioration mechanisms are investigated. Next, the maintenance and management actions are scheduled to achieve the objectives of the management plans. For instance, an objective to minimize the downtime of the structure during maintenance actions can be considered, which in turn, will have social and environmental benefits. Additionally, since the structure will be out of service at pre-planned times, other maintenance actions can also be planned at the same time to prevent future delays. Moreover, competing objectives can be simultaneously considered to find the optimal trade-off between the life-cycle cost and the time-variant structural performance. This can be performed through an optimization process that integrates economic, social, and environmental metrics of the structural performance. Therefore, the life-cycle management provides rational methodologies to plan ahead for inspections, maintenance, and repair in order to achieve the management goals. Up to date, fewer sustainability assessment approaches are available for highway infrastructure systems compared to buildings (Bocchini et al. 2013b). Additionally, the available approaches are still not generalized and they deal with only one type of structures. Moreover, they may lack the comprehensive qualitative measures that enable the accurate assessment of different sustainable development aspects (Bocchini et al. 2013b). Therefore, there is still a need for more approaches that can quantitatively integrate the sustainability metrics within the general management scheme of infrastructures.

For the proper life-cycle management of infrastructure, reliability-based performance indicators can consider the uncertainties associated with the load and resistance but cannot account for the outcomes of a failure event. Risk-based performance measures, on the other hand, provide the means for combining the probability of structural system failure with the consequences associated with this event. The perception of risk is determined by the attitude of the decision maker and it is an essential component of risk and sustainability analysis, especially for low-probability high-consequence events (e.g., seismic events and floods). Based on the willingness of a decision maker, the attitudes can be classified as risk-averse, risk-neutral, or risk-taking. One of most popular decision theories is the expected utility theory (*UT*) (von Neumann and Morgenstern 1953). In this theory, the alternative with the highest utility value is always preferred. Other decision theories exist, such as the cumulative prospect theory (*CPT*) which is based on the notion of bounded rationality (Tversky and Kahneman 1992). Since the risk and sustainability assessment of a structure are highly dependent on the attitude of the decision maker, varying risk attitudes can yield different optimum management strategies for the same structure under consideration.

This paper presents an overview of the life-cycle management concepts and techniques under uncertainty and the application of such concepts in the sustainable development of infrastructures. Performance prediction under the effects of gradual deterioration (e.g., corrosion and fatigue) and sudden degradation (i.e., due to hazards

such as hurricanes and seismic events) is discussed. In particular, evaluating the social, economic, and ecological losses associated with multiple sources of hazards is discussed. Furthermore, various sources of uncertainty associated with the life-cycle management are presented. Additionally, methods for optimizing the total life-cycle cost and its associated scheduled maintenance, inspection and monitoring activities are presented. The effect of the attitude of the decision maker on the management strategies is briefly discussed.

LIFE-CYCLE MANAGEMENT UNDER UNCERTAINTY
Life-cycle management (LCM) of infrastructure systems is performed with multiple goals. These goals include maximizing the life-cycle structural performance and minimizing the total life-cycle cost (LCC) associated with interventions required to keep the system in its functional status, among others. Indeed, these tasks are, in many cases, not easy to fulfill due to the presence of multiple uncertainties associated with material properties, structural resistance quantification models, structural demand, and the effect of maintenance actions on the structural performance. Therefore, the proper LCM should include all these uncertainties as well as those associated with the cost of inspecting, maintaining, and monitoring the structure. Additionally, the LCM should be performed on an integrated platform where the mutual interactions between different tasks can be properly considered. For instance, calculating the life-cycle cost would require the results of the maintenance scheduling to be known a priori, which in turn requires information from the performance assessment process. Such an integrated framework was proposed in Frangopol (2011) for civil infrastructure systems and in Frangopol et al. (2012) for marine infrastructure systems. The proposed framework, shown in Figure 2, consists of several successive modules; each of which is responsible for a certain task. Modules for the (a) probabilistic performance assessment and prediction, (b) integration of information from inspection and structural health monitoring (SHM), and (c) multi-criteria optimization for the optimal scheduling of interventions under uncertainties, are included in the framework. Each of these modules can be executed individually or combined with other modules to perform an integral task.

        As shown in Figure 2, the framework starts with analyzing the structure to identify its deteriorating mechanisms. Next, the time-variant structural performance under uncertainty is predicted. Information from inspections or SHM, if available, is integrated to find updated performance profiles. This integration reduces epistemic uncertainties and improves the accuracy of the LCM. The next step, i.e., life-cycle optimization, provides the main outcomes of the LCM in which optimal management actions such as inspections, monitoring, and maintenance interventions can be established. As indicated in Figure 2, risk perception can be integrated into this framework, as a final step before establishing the optimal decisions, by analyzing the attitude of the decision maker. For the risk assessment, the attitude of the decision maker should be considered, especial for the low-probability high-consequence events (e.g., seismic events and floods) (Ellingwood 2007).
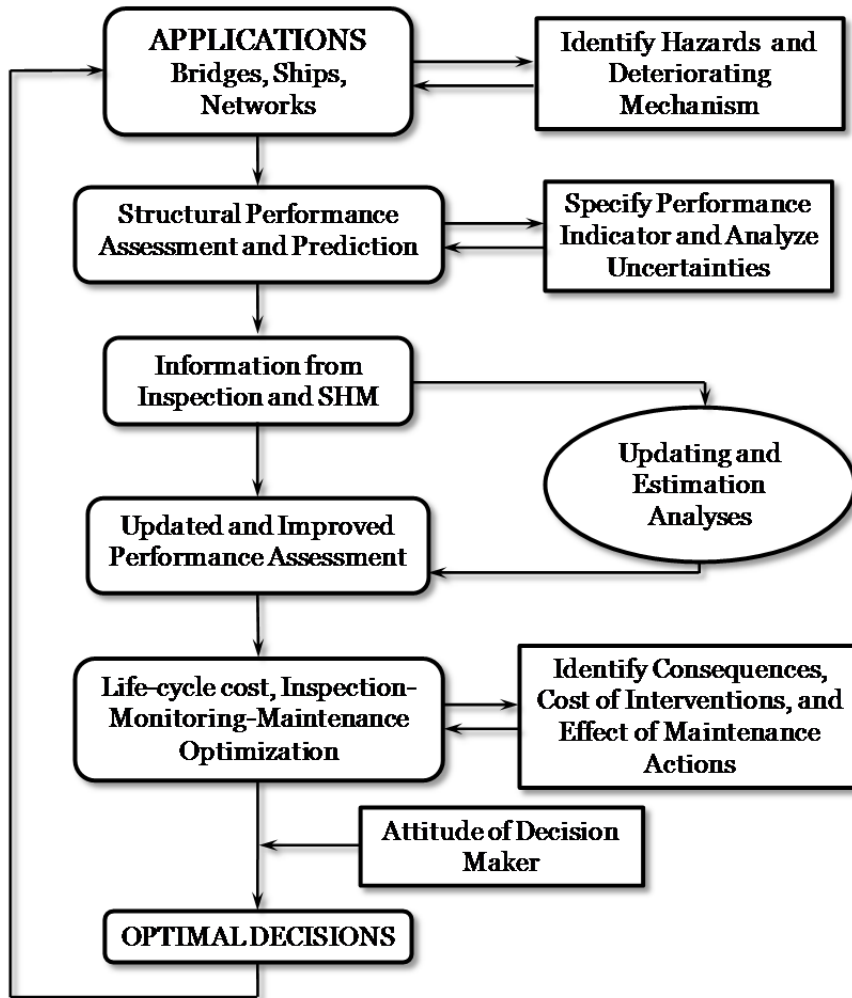
Figure 2. Integrated life-cycle framework

The implementation of such comprehensive framework was only possible through the formulation of a robust computational platform, as indicated in Figure 3. The platform consists of a structural analysis tool which is responsible to deliver the structural responses under a given condition. Reliability computational software uses structural responses and computes the reliability of a component or a system. The output of this module is also used in conjunction with consequences analyses to evaluate the risk within a risk analyses software. The software modules are connected to an updating algorithm that can update model parameters based on information from inspection actions or structural health monitoring (SHM). The information from these modules is used in the optimization algorithm to find the optimal life-cycle decisions. All these programs are connected within an interface algorithm which controls the data flow through all the modules. This computational platform was successfully used for the LCM of bridges (Akgül and Frangopol 2005a; Akgül and Frangopol 2005b; Frangopol et al. 2008a; Frangopol et al. 2008b; Kwon and Frangopol 2010; Okasha and Frangopol 2010b; Okasha and Frangopol 2010c; Kim and Frangopol 2011a; Kwon and Frangopol 2011; Okasha and Frangopol 2012; Barone and Frangopol

2013a; Barone and Frangopol 2013b; Barone et al. 2013; Soliman and Frangopol 2013; Soliman et al. 2013), bridge networks (Liu and Frangopol 2005; Liu and Frangopol 2006; Liu and Frangopol 2007; Bocchini and Frangopol 2011a; Bocchini and Frangopol 2011b; Bocchini and Frangopol 2011c; Bocchini and Frangopol 2013; Bocchini et al. 2013a; Dong et al. 2013b), and ships (Okasha et al. 2010; Okasha and Frangopol 2010a; Okasha et al. 2011; Kim and Frangopol 2011b; Frangopol et al. 2012; Kim et al. 2013).

PERFORMANCE ASSESSMENT
In this module of the LCM, the current condition and performance of the analyzed structure or system are investigated. It is determined whether the structure, in its current state, is suitable to remain in service or not. Next, the deteriorating mechanisms that may affect the structure are identified. These mechanisms can be gradual, such as corrosion, fatigue and scour, or sudden such as seismic events, floods, and explosions. Regardless of the deteriorating mechanism, uncertainties must be analyzed at this stage. Multiple sources of uncertainties are present at this stage. Part is associated with our imperfect modeling of the structural performance and the deteriorating phenomena (i.e., epistemic) and the other part is associated with randomness (i.e., aleatory). Therefore, it is necessary to use probabilistic performance indicators for this stage. Reliability, redundancy, robustness and risk, among others, are generally used in the LCM of deteriorating infrastructures (Saydam and Frangopol
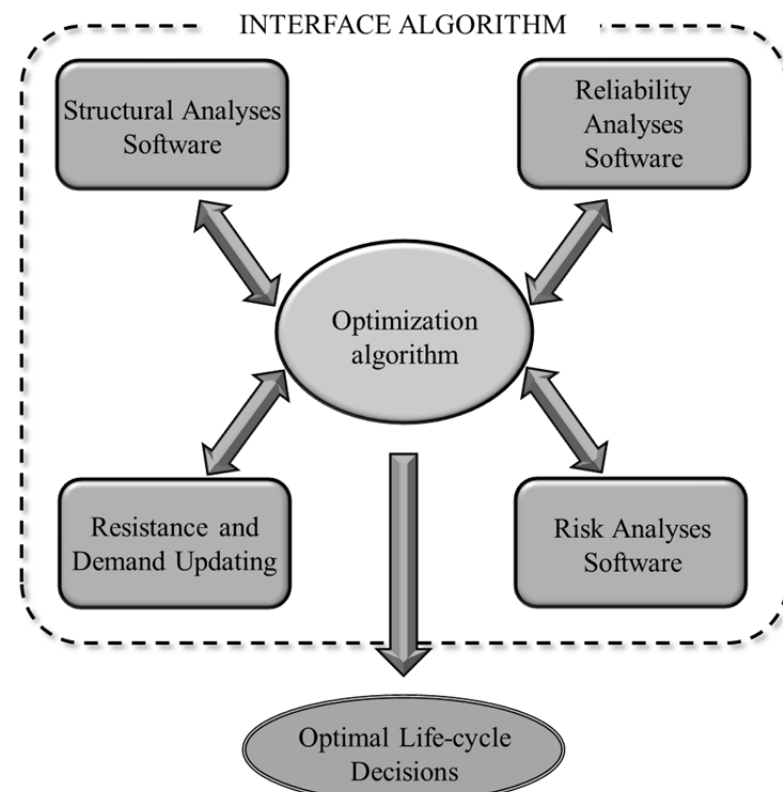
Figure 3. Computational platform for the integrated life-cycle management framework

2011; Zhu and Frangopol 2012). Resilience and sustainability are also used for the LCM, especially on the network level (Bocchini and Frangopol 2013; Bocchini et al. 2013b). Probability of failure and the reliability index are widely used performance indicators for the life-cycle assessment. The probability of failure of a system is defined as the probability of violating any of the limit states that define its failure modes. A limit-state consisting of the capacity and demand terms representing structural resistance, $R(t)$, and load effects, $S(t)$, respectively, is defined as:

$$g(t) = R(t) - S(t) = 0 \qquad (1)$$

where $R(t)$ and $S(t)$ are expressed in terms of the governing random variables (e.g., yield stress, modulus of elasticity, live load effects, and parameters of the deterioration model) at time t. Under the assumption that $R(t)$ and $S(t)$ are statistically independent random variables, the instantaneous structural probability of failure is (Melchers 1999)

$$P_f(t) = P(g(t) < 0) = \int_0^\infty F_R(x,t) f_S(x,t) dx \qquad (2)$$

where $F_R(x,t)$ is the instantaneous cumulative probability distribution function (CDF) of the resistance and $f_S(x,t)$ is the instantaneous PDF of the load effects. The corresponding reliability index $\beta(t)$ can be computed as

$$\beta(t) = \Phi^{-1}(1 - P_f(t)) \qquad (3)$$

in which $\Phi(\cdot)$ is the cumulative distribution function of standard normal distribution. The reliability index is generally decreasing due to various environmental and mechanical stressors. Figure 4 illustrates the effect of gradual and sudden deterioration on the time-variant reliability index profile.

Redundancy, as a performance indicator, measures the reserve capacity of the structure and gives an indication on the presence of alternative load paths within the structure. Most of the proposed redundancy measures attempt to quantify the amount of reliability available between the first component failure and the system failure (Frangopol and Nakib 1991; Okasha and Frangopol 2010d; Frangopol 2011; Decò et al. 2012). A system with high redundancy will not fail under the failure of one of its component and will give enough warning before the total structural collapse. Several redundancy indicators were proposed in literature, among those, the following indicator has been widely used in the time-variant redundancy evaluation.

$$RI(t) = \beta_f(t) - \beta_y(t) \qquad (4)$$

where $\beta_f(t)$ is the reliability index with respect to the system failure and $\beta_y(t)$ represent the reliability index with respect to the first failure (e.g., first yield). Although this definition is widely used for evaluating the redundancy, several other definitions can also be found (see for example Frangopol and Curley 1987; Frangopol

and Nakib 1991; Okasha and Frangopol 2009; Okasha and Frangopol 2010d; Decò et al. 2012; Frangopol et al. 2012; Zhu and Frangopol 2012).

Infrastructure systems and specifically bridges must be robust enough to resist collapse under the effect of prescribed hazards. For a structure with multiple failure modes, the probability of system failure under a given hazard is

$$P(F_t \mid H) = P\big([any\ g_i(t) < 0] \mid H\big),\ i = 1, 2, ..., n \tag{5}$$

in which $P\,[F_t \mid H]$ is the probability of failure under a given hazard H at time t and is calculated as the probability of violating any of the limit states, where $g_i(t) < 0$ is the failure event associated with the ith limit state at time t. Therefore, the probability of structural failure $P_f(t)$ is

$$P_f(t) = P(F_t \mid H) \cdot P(H) \tag{6}$$

where $P(H)$ is the probability of occurrence of the hazard.

The probability of failure can be mitigated through the development of timely and effective maintenance and management plans. This is directly addressed within the proposed life-cycle management framework.

Risk of structural failure under multiple hazards is evaluated on the basis of the probability of failure. The risk, as a performance indicator, provides more insight to the structural performance by integrating the consequences of failure into the performance index formulation. Accordingly, the risk of failure under a given hazard is expressed as (Zhu and Frangopol 2013; Saydam et al. 2013)

$$R(t) = P_f(t) \cdot C_f(t) \tag{7}$$
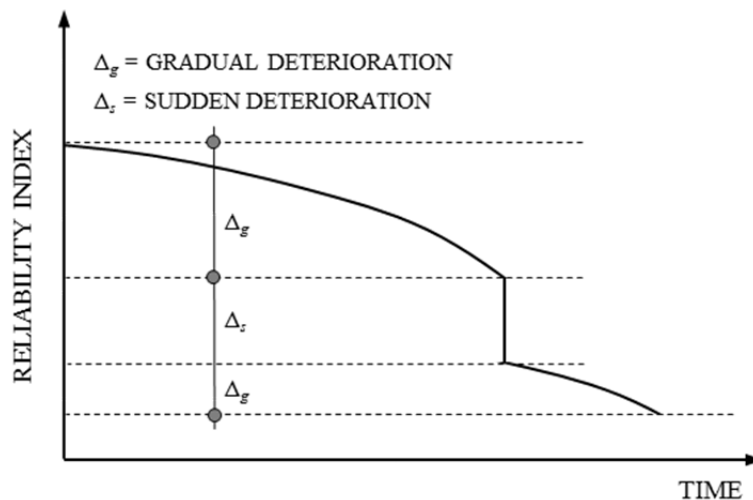
Figure 4. General time-variant reliability profile

where $C_f(t)$ represents the time-variant consequences associated with the failure of the structure. For the proper sustainability and risk analyses, these consequences should include the different economic, social and environmental losses, including rebuilding, running, time loss, and environmental costs, among others.

CONSEQUENCES ANALYSES

Sustainability is quantified in terms of social, environmental and economic metrics. A structure is more sustainable if the life-cycle cost (i.e., construction, maintenance, failure, and replacement costs) is low. Similarly, a structural system is more sustainable if the energy, carbon dioxide emissions and user delays arising from its repair are low. The social and environmental metrics of the sustainability can be expressed in monetary units if the consequences associated with these two metrics can be evaluated (Bocchini et al. 2013b; Dong et al. 2013a). Extensive research work has been done to evaluate the consequences associated with the sustainability metrics, especially for bridges and bridge networks. In these studies, the network is usually assumed to be composed of nodes and links, where a link is considered as an element connecting the nodes of the network (Shiraki et al. 2007; Dong et al. 2013b).

The consequences associated with the structural damage/failure under natural hazards (e.g., seismic event) include both direct and indirect consequences, and can be expressed in terms of social, environmental, and economic metrics. Earthquake can disrupt traffic flow and affect emergency responses and recovery operations which may yield much higher consequences than the repair or rebuilding costs of a damaged infrastructure system. Following a strong earthquake and its aftershocks, bridges and links can be damaged; this may cause human injuries, deaths, property loss, and traffic detours.

In this regards, the social metrics includes downtime, time loss, and fatalities. The downtime due to detour can be computed as

$$DT = d \cdot ADT \cdot \frac{D}{S} \tag{8}$$

where d is the duration of the detour (days); ADT is the average daily traffic to detour which is related to the damage states of the links; D is the detour length; and S is the detour speed (km/h).

As the links are damaged, the traffic carrying capacity and speed of the traffic on the damaged links are reduced, resulting in more travel time in the damaged links. The time loss associated with the damaged links can be computed as (Shiraki et al. 2007)

$$DE = d \cdot ADE \cdot [\frac{l}{S_D} - \frac{l}{S_0}] \tag{9}$$

where ADE is the average traffic remaining in the link; l is the length of the link; S_0 is the traffic speed on the intact link; and S_D is the traffic speed on the damaged link.

The time loss costs are associated with the downtime and time loss for the user and goods due to the partial functionality of the structural systems and can be computed using the following equation (Stein et al. 1999)

$$C_{TL} = \left[c_{AW} O_{car} (1 - \frac{T}{100}) + (c_{ATC} O_{truck} + c_{goods}) \frac{T}{100} \right] \cdot [DE + DT] \tag{10}$$

where c_{AW} is wage per hour (USD/h); c_{ATC} is total compensation per hour (USD/h); c_{goods} is time value of the goods transported in a cargo (USD/h); and O_{car} and O_{truck} are vehicle occupancies for cars and trucks.

The fatalities (FT) associated with the failure of a highway bridge can be related to the damage states of the bridges. A statistical analysis is required to evaluate the number of fatalities. The life loss costs associated with fatalities can be expressed as (Rackwitz 2002)

$$C_{SL} = FT \cdot ICAFB \tag{11}$$

where FT is the fatalities number and $ICAFB$ is the cost of a fatality.

The environmental metric includes the energy consumption, global warming potential, and air pollutant emission, among others. The commonly used environmental metrics including energy waste and carbon dioxide emissions are emphasized herein. The environmental metric associated with traffic detour is expressed as (Kendall et al. 2008)

$$EN_{DT} = ADT \cdot D \cdot d \cdot \left[Enp_{car} \cdot (1 - \frac{T}{100}) + Enp_{Truck} \cdot \frac{T}{100} \right] \tag{12}$$

where Enp_{car} and Enp_{Truck} are environmental metric per unit distance for cars and trucks (e.g., carbon dioxide kg/km); and T is daily truck traffic ratio.

The environmental metric associated with the repair action is computed as (Padgett et al. 2009)

$$EN_{RE} = (Enp_{Steel} \cdot V_{Steel} + Enp_{Conc} \cdot V_{Conc}) \cdot RCR \tag{13}$$

where Enp_{Steel} and Enp_{Conc} are environmental metric per unit volume for steel and concrete, respectively (e.g., carbon dioxide emissions kg/m^3); V_{Steel} and V_{Conc} are the volume of steel and concrete, respectively (m^3); and RCR is repair cost ratio for a bridge. The costs of carbon dioxide emission can be transferred into monetary value as indicated in the following equation (Kendall et al. 2008).

$$C_{EN} = [EN_{DT} + EN_{RE}] \cdot c_{Env} \tag{14}$$

where c_{Env} is cost value of environmental metric per unit (e.g., carbon dioxide USD/t).

For evaluating the economic loss, the loss associated with the repair of a damaged bridge can be expressed as (Stein et al. 1999)

$$C_{REP} = RCR \cdot c_{REB} \cdot W \cdot L \tag{15}$$

where W is bridge width (m) for bridge; L represents bridge length (m); and c_{REB} is rebuilding cost per square meter (USD/m^2).

After calculating the social, environmental and economic consequences, the performance of the structure or the network, in terms of sustainability or risk, can be analyzed. Dong et al. (2013b) presented an approach to find the time-variant sustainability metrics for bridge networks under seismic hazard. In their approach, the three metrics (i.e., social, environmental, and economic) of sustainability of a bridge network were evaluated for different earthquake scenarios. Seismic sustainability should be evaluated based on all possible earthquakes that can happen in a region. Social and environmental metrics were converted into economic metrics to evaluate their monetary value. The social considerations were converted to an economic measure by considering their appropriate monetary value. Moreover, carbon dioxide emissions, as an indication of environmental impact, were also included within the economic metric by considering the cost of the additional emissions of the vehicles in the presence of a detour. The total loss is the sum of losses associated with the possible seismic events, which is the sum of consequences weighted by the probabilities of occurrence of these consequences. Uncertainties exist in the hazard assessment and consequence evaluation. These uncertainties can be accounted for by using simulation methods (e.g., Latin Hypercube sampling).

The time-variant sustainability at both the component (i.e., single bridge) and system levels (i.e., network) was evaluated in Dong et al. (2013b). The contribution of each of these metrics to the total equivalent economic loss can be identified at any time. Additionally, the total economic loss and its probabilistic parameters can be determined. A typical outcome of such approach is shown in Figure 5. In general, the contribution of each of the sustainability metrics to the total loss depends on the type of the structure and its location. The approach proposed in Dong et al. (2013b) can also be used to plan for the life-cycle inspection and maintenance events based on the sustainability metrics.
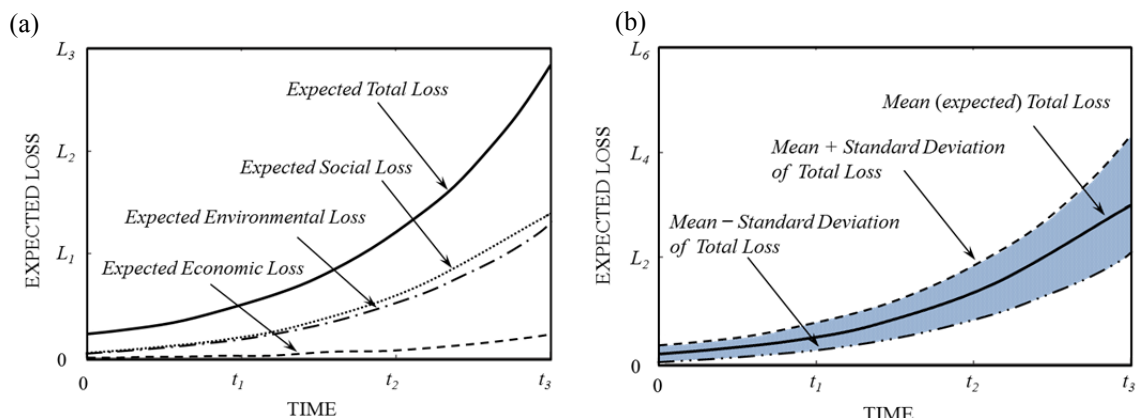
Figure 5. Time-variant expected loss for bridge network under seismic events: (a) contribution of various sustainability metrics, and (b) dispersion of the time-variant total loss

Zhu and Frangopol (2013) also introduced a system-based approach for quantifying the risk of a single bridge under multiple hazards, namely, traffic increase and seismic hazards. In their approach, the failure consequences included also social and economic metrics such as the rebuilding, running, time-loss, and fatalities costs. Their approach was applied to an existing bridge. The main advantage of their approach comes from the ability to identify the risk of failure arising from the different hazards individually or combined, as shown in Figure 6, allowing the proper allocation of maintenance and repair funding towards mitigating the effects of the most critical hazard. Figure 6 depicts the possibility of identifying the risk associated with different hazards; needless to say, the order of magnitude of each hazard depends significantly on the location of the bridge and the seismic activity.
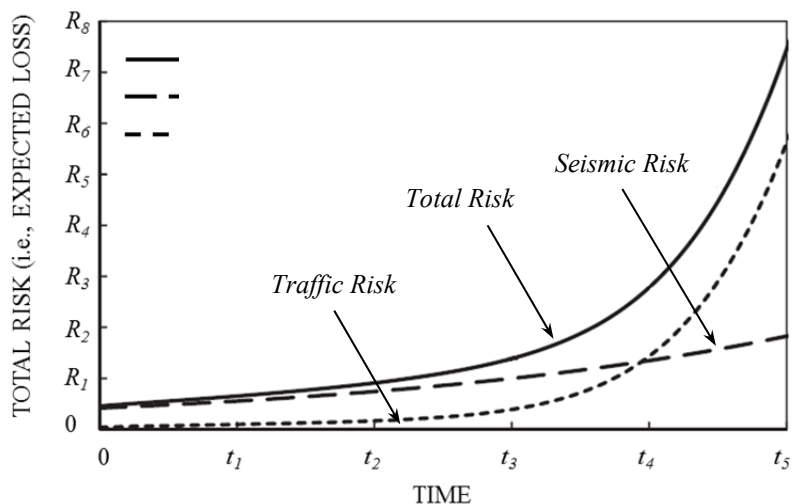
Figure 6. Risk profiles associated with live loads, seismic loads, and both (adapted from Zhu and Frangopol 2013)

LIFE-CYCLE OPTIMIZATION CONSIDERING RISK ATTITUDES

The life-cycle optimization is an essential task within the LCM framework. As shown in Figures 2 and 3, this process provides the final outcomes of the LCM framework. It also combines essential information regarding the structural performance with other data such as available budgets, performance thresholds, maintenance costs, and the effect of maintenance actions on the performance to find the optimal intervention options. In the proposed framework, this process is performed using a probabilistic platform considering various uncertainties associated with the LCM. Various goals for the life-cycle optimization can be taken into account, including minimizing the total life-cycle risk (Zhu and Frangopol 2013), minimizing the expected annual system failure rate (Barone et al. 2013), maximizing the expected service life (Kim et al. 2011; Kim et al. 2013), minimizing the damage detection delay (Kim and Frangopol 2011c; Kim and Frangopol 2011d; Kim and Frangopol 2012), maximizing the probability of damage detection (Soliman et al. 2013), and minimizing the life-cycle cost (Kim et al. 2013). Additionally, two or more conflicting objectives can be

considered simultaneously. Examples include minimizing the total life-cycle cost, which requires low number of maintenance actions to be performed, along with maximizing the expected service life, which, in contrast, will require additional inspections and maintenance actions.

The risk-based performance assessment approach presented in Zhu and Frangopol (2013) was also used to find the risk-based optimal preventive maintenance schedule which minimizes the life-cycle preventive maintenance cost and keeps the risk level below a given threshold. This methodology can be extended to include all the social, environmental, and economic metrics under consideration and to find the optimal preventive of essential maintenance schedule that minimizes the life-cycle cost and constrains the expected losses to certain maximum thresholds. Figure 7 shows a typical outcome of such an approach for bridges. In this approach, the optimization algorithm is capable of providing the optimal maintenance times for the various structural components within the system.
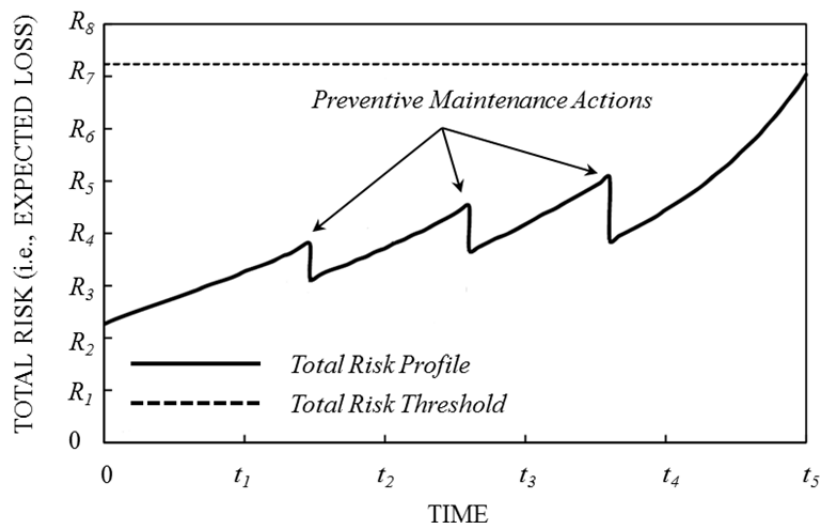
Figure 7. Risk profiles with optimal maintenance actions (adapted from Zhu and Frangopol (2013))

The attitude of the decision maker should be incorporated within the sustainability assessment and the life-cycle management process. The utility associated with sustainability metrics (e.g., total monetary loss) can be considered as a performance indicator which depends on the risk attitudes. Assessing the sustainability of infrastructure systems under gradual deterioration and sudden events (e.g., seismic hazards) considering risk attitudes is required in order to establish optimum management plans. The utility approach can be used to capture the decision maker's attitude under low-probability high-consequence events. The decision maker's utility $u_X(x)$ associated with a given value of gain or loss x can be expressed as (Howard and Matheson 1989; Beck et al. 2002)

$$u_X(x) = 1 - \exp(-\frac{x}{\rho}) \tag{16}$$

where X is the sustainability metric (e.g., total monetary loss) and ρ is the risk tolerance of the decision maker. For example, when the value of risk due to a certain hazard is significantly below ρ, the decision maker will act relatively risk-neutral. In other words, the value of ρ determines the corresponding value of risk that the decision maker can tolerate. The value of utility is negative when a loss occurs; while a positive value is associated with the occurrence of a gain. The utility values for the loss associated with $\rho = 10^6$, 2×10^6, and 3×10^6 USD are schematically shown in Figure 8.

The risk and sustainability can be evaluated in terms of utility while incorporating the attitude of the decision maker. As indicated in Eq. (16), large utility is associated with small loss; thus, a larger utility solution is preferred to a smaller utility one. This approach enables the integration of the attitude of the decision maker in the probabilistic evaluation of the loss, which in turn can be employed into the optimization module of the life-cycle management framework to provide optimal times and types of management actions (e.g., maintenance and repair). Conflicting objectives such as maximizing the minimum value of the expected utility and minimizing the total expected life-cycle cost can be considered simultaneously. In this
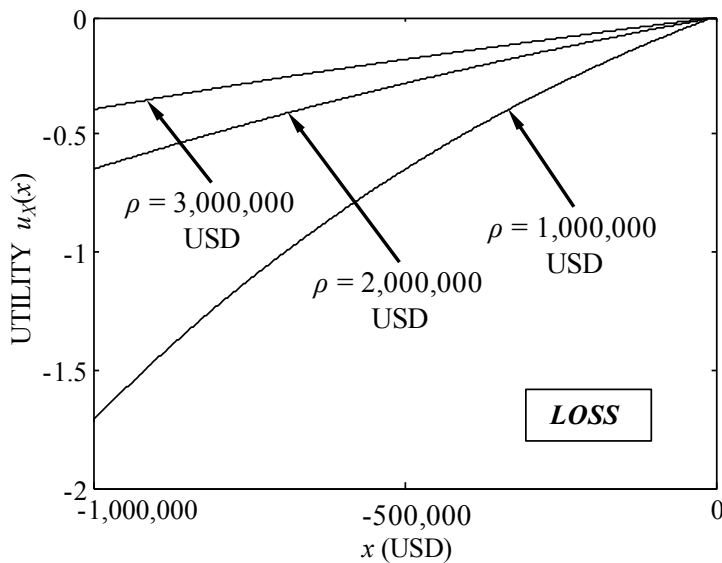
Figure 8 Utility function

case, the optimization module provides the Pareto optimum solutions which show the types and times of the management actions for the infrastructure systems under investigation. Figure 9 shows typical Pareto-optimal solution fronts resulting from this process.

Optimum solution fronts associated with different risk attitudes for an infrastructure system are qualitatively shown in Figure 9. The effect of the risk tolerance of the decision maker ρ is also indicated in this figure. As shown, the risk tolerance of a decision maker significantly affects the Pareto optimal solutions. The solutions corresponding to a decision maker with a relatively high ρ tend to result in larger expected utility, while optimal solutions associated with a decision maker with a relatively low ρ have smaller expected utility values. Ultimately, optimal solutions are

customized for each decision maker's risk tolerance and could greatly assist in the prioritization of management actions and their timing.
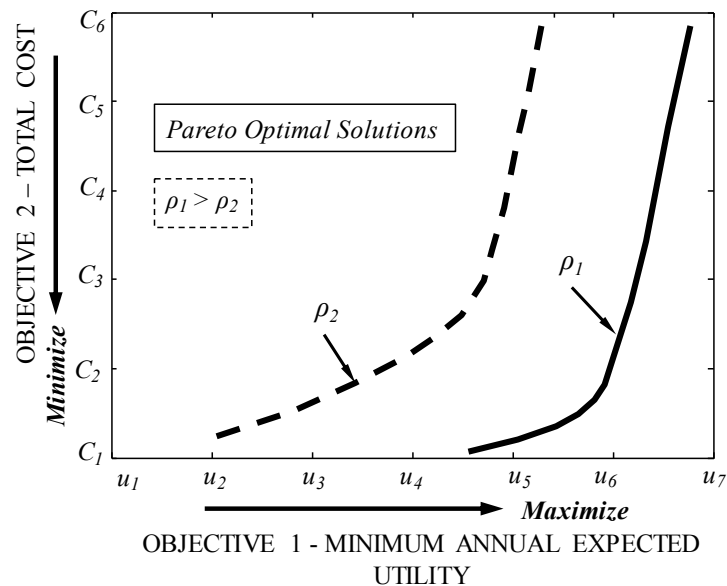
Figure 9. Optimal solutions associated with different risk tolerances ρ

CONCLUSIONS

This paper presented a brief overview on the integration of the sustainability measures into the life-cycle management framework. This framework covers predicting the time-variant structural performance and the future interventions scheduling, including inspections, monitoring, and/or maintenance and repairs actions, such that an optimal management solution which satisfies the goals and constraints (e.g., reliability levels and available budgets) is achieved. Various modules of the LCM framework are briefly explained with special attention to the performance assessment and the life-cycle optimization processes. The paper presented the available methodologies for quantifying the social, economic, and environmental metrics to evaluate the sustainability of bridges and bridge networks under seismic hazard. Sustainability can provide an in-depth understanding of the current and future risk associated with infrastructure systems. The sustainability metric utilized within this paper accounts for the impacts of structural failure on the society, environment, and the economy. It is shown that sustainability metrics, quantified in terms of their appropriate corresponding monetary value, can be generally integrated within the life-cycle management framework. This allows the efficient planning of interventions (e.g., inspection, monitoring, and repair) to maintain the total expected loss, as a measure of sustainability, below its prescribed threshold. The expected loss includes the rebuilding cost, cost of fatalities, carbon dioxide emissions, energy waste, time-loss and running costs. The risk tolerance of the decision maker has a significant impact on the resulting optimal strategies. The presented framework supports the sustainable

development of infrastructure systems and enables the rational and accurate decision making regarding the future interventions for the infrastructure systems under consideration.

REFERENCES
Adams, W.M. (2006). "The future of sustainability: re-thinking environment and development in the twenty-first century." *Report of the IUCN Renowned Thinkers Meeting*, 29–31.
Akgül, F. and Frangopol, D.M. (2005a). "Lifetime performance analysis of existing reinforced concrete bridges: I theory." *Journal of Infrastructure Systems*, 11(2), 122-128.
Akgül, F. and Frangopol, D.M. (2005b). "Lifetime performance analysis of existing reinforced concrete bridges: II application." *Journal of Infrastructure Systems*, 11(2), 129-141.
ASCE. (2013). *2013 Report Card for America's Infrastructure,* American Society of Civil Engineers, Reston, VA.
Barone, G., and Frangopol, D.M. (2013a). "Reliability, risk and lifetime distributions as performance indicators for life-cycle maintenance of deteriorating structures." *Reliability Engineering & System Safety,* doi:10.1016/j.ress.2013.09.013 (in press).
Barone, G., and Frangopol, D.M. (2013b). "Hazard-based optimum lifetime inspection/repair planning for deteriorating structures." *Journal of Structural Engineering*, doi: 10.1061/(ASCE)ST.1943-541X.0000810 (in press).
Barone, G., Frangopol, D.M. and Soliman, M. (2013). "Optimization of life-cycle maintenance of deteriorating bridges considering expected annual system failure rate and expected cumulative cost." *Journal of Structural Engineering,* doi:10.1061/(ASCE)ST.1943-541X.0000812 (in press).
Beck, J.L., Porter, K.A., Shaikhutdinov, R.V., Au, S.K., Moroi, T., Tsukada, Y., and Masuda, M. (2002). "Impact of seismic risk on lifetime property values." *Final Report CUREE-Kajima Joint Research Program, Phase IV*. Richmond, CA: Consortium of Universities for Research in Earthquake Engineering.
Bocchini, P., and Frangopol, D.M. (2011a). "A stochastic computational framework for the joint transportation network fragility analysis and traffic flow distribution under extreme events." *Probabilistic Engineering Mechanics,* 26(2), 182-193.

Bocchini, P., and Frangopol, D.M. (2011b). "Generalized bridge network performance analysis with correlation and time-variant reliability." *Structural Safety,* 33(2), 155-164.

Bocchini, P., and Frangopol, D.M. (2011c). "A probabilistic computational framework for bridge network optimal maintenance scheduling." *Reliability Engineering & System Safety,* 96(2), 332-349.

Bocchini, P., and Frangopol, D.M. (2013). "Connectivity-based optimal scheduling for maintenance of bridge networks." *Journal of Engineering Mechanics*, 139(6), 760-769.

Bocchini, P., Saydam, D. and Frangopol, D.M. (2013a). "Efficient, accurate, and simple Markov chain model for the life-cycle analysis of bridge groups." *Structural Safety,* 40, 51-64.

Bocchini, P., Frangopol, D.M., Ummenhofer, T. and Zinke, T. (2013b). "Resilience and sustainability of the civil infrastructure: Towards a unified approach." *Journal of Infrastructure Systems*, doi:10.1061/(ASCE)IS.1943-555X.0000177 (in press).

CNN, (2012). "Train cars with toxic cargo fall off New Jersey bridge." *Cable News Network*, http://www.cnn.com/2012/11/30/us/new-jersey-train-derail/index.html, accessed October 10, 2013.

Decò, A., Frangopol, D.M. and Zhu, B. (2012). "Reliability and redundancy assessment of ships under different operational conditions." *Engineering Structures,* 42(0), 457-471.

Dong, Y., Frangopol, D.M., and Saydam, D. (2013a). "Time-variant sustainability assessment of seismically vulnerable bridges subjected to multiple hazards." *Earthquake Engineering and Structural Dynamics*, doi:10.1002/eqe.2281 (in press).

Dong, Y., Frangopol, D.M. and Saydam, D. (2013b). "Sustainability of highway bridge networks under seismic hazard." *Journal of Earthquake Engineering*, doi:10.1080/13632469.2013. 841600 (in press).

Ellingwood, B.R. 2007. "Assessment and mitigation of risk from low-probability, high-consequence hazards." *International Forum on Engineering Decision Making*, Third IFED Forum, Shoal Bay, Australia

Frangopol, D.M. and Nakib, R. 1991. "Redundancy in Highway Bridges." *Engineering Journal*, American Institute of Steel Construction, 28(1), 45-50.

Frangopol, D.M. and Curley, J.P. (1987). "Effects of damage and redundancy on structural reliability." *Journal of Structural Engineering*, 113(7), 1533-1549.

Frangopol, D.M. and Nakib, R. (1991). "Redundancy in highway bridges." *Engineering Journal*, 28(1), 45-50.

Frangopol, D.M, Strauss, A. and Kim, S. (2008a). "Bridge reliability assessment based on monitoring." *Journal of Bridge Engineering,* 13(3), 258-270.

Frangopol, D.M., Strauss, A. and Kim, S. (2008b). "Use of monitoring extreme data for the performance prediction of structures: General approach." *Engineering Structures*, 30(12), 3644-3653.

Frangopol, D.M. (2011). "Life-cycle performance, management, and optimization of structural systems under uncertainty: Accomplishments and challenges." *Structure and Infrastructure Engineering,* 7(6), 389-413.

Frangopol, D.M., Bocchini, P., Decò, A., Kim, S., Kwon, K., Okasha, N.M. and Saydam, D. (2012). "Integrated life-cycle framework for maintenance, monitoring, and reliability of naval ship structures." *Naval Engineers Journal,* 124(1), 89-99.

Howard, R.A., and Matheson, J.E. (1989). *Readings on the principles and applications of decision analysis*, Menlo Park, CA, Strategic Decisions Group.

Kendall, A., Keoleian, G. and Helfand, G. (2008). "Integrated life-cycle assessment and life-cycle cost analysis model for concrete bridge deck applications." *Journal of Infrastructure Systems,* 14(3), 214-222.

Kim, S., and Frangopol, D.M. (2011a). "Cost-effective lifetime structural health monitoring based on availability." *Journal of Structural Engineering,* 137(1), 22-33.

Kim, S., and Frangopol, D.M. (2011b). "Cost-based optimum scheduling of inspection and monitoring for fatigue sensitive structures under uncertainty." *Journal of Structural Engineering,* 137(11), 1319-1331.

Kim, S., and Frangopol, D.M. (2011c). "Optimum inspection planning for minimizing fatigue damage detection delay of ship hull structures." *International Journal of Fatigue,* 33(3), 448-459.

Kim, S., and Frangopol, D.M. (2011d). "Inspection and monitoring planning for RC structures based on minimization of expected damage detection delay." *Probabilistic Engineering Mechanics,* 26(2), 308-320.

Kim, S., Frangopol, D.M. and Zhu, B. (2011). "Probabilistic optimum inspection/repair planning of deteriorating structures." *Journal of Performance of Constructed Facilities,* 25(6), 534-544.

Kim, S., and Frangopol, D.M. (2012). "Probabilistic bicriterion optimum inspection/monitoring planning: Application to naval ships and bridges under fatigue." *Structure and Infrastructure Engineering,* 8(10), 912-927.

Kim, S., Frangopol, D.M. and Soliman, M. (2013). "Generalized probabilistic framework for optimum inspection and maintenance planning." *Journal of Structural Engineering,* 139(3), 435-447.

Kwon, K., and Frangopol, D.M. (2010). "Bridge fatigue reliability assessment using probability density functions of equivalent stress range based on field monitoring data." *International Journal of Fatigue,* 32(8), 1221-1232.

Kwon, K., and Frangopol, D.M. (2011). "Bridge fatigue assessment and management using reliability-based crack growth and probability of detection models." *Probabilistic Engineering Mechanics,* 26(3), 471-480.

Liu, M. and Frangopol, D.M. (2005). "Balancing connectivity of deteriorating bridge networks and long-term maintenance cost through optimization." *Journal of Bridge Engineering*, 10(4), 468-481.

Liu, M. and Frangopol, D.M. (2006). "Optimizing bridge network maintenance management under uncertainty with conflicting criteria: life-cycle maintenance, failure, and user costs." *Journal of Structural Engineering*, 132(11), 1835-1845.

Liu, M. and Frangopol, D.M. (2007). "Bridge network maintenance optimization using stochastic dynamic programming." *Journal of Structural Engineering*, 133(12), 1772-1778.

Melchers, R. E. (1999). *Structural Reliability Analysis and Prediction,* 2nd Ed., John Wiley & Sons Ltd., Chichester, England.

Okasha, N.M., and Frangopol, D.M. (2010a). "Efficient method based on optimization and simulation for the probabilistic strength computation of the ship hull." *Journal of Ship Research,* 54(4), 244-256.

Okasha, N.M., and Frangopol, D.M. (2010b). "Advanced modeling for efficient computation of life-cycle performance prediction and service-life estimation of bridges." *Journal of Computing in Civil Engineering,* 24(6), 548-556.

Okasha, N.M., and Frangopol, D.M. (2010c). "Novel approach for multi-criteria optimization of life-cycle preventive and essential maintenance of deteriorating structures." *Journal of Structural Engineering,* 136(8), 1009-1022.

Okasha, N.M., and Frangopol, D.M. (2010d). "Redundancy of structural systems with and without maintenance: An approach based on lifetime functions." *Reliability Engineering & System Safety,* 95(5), 520-533.

Okasha, N.M., Frangopol, D.M. and Decò, A. (2010). "Integration of structural health monitoring in life-cycle performance assessment of ship structures under uncertainty." *Marine Structures,* 23(3), 303-321.

Okasha, N.M., and Frangopol, D.M. (2009). "Lifetime oriented multi-objective optimisation of structural maintenance considering system reliability, redundancy and life-cycle cost using GA." *Structural Safety,* 31(6), 460-474.

Okasha, N.M., and Frangopol, D.M. (2012). "Integration of structural health monitoring in a system performance based life-cycle bridge management framework." *Structure and Infrastructure Engineering,* 8(11), 999-1016.

Okasha, N.M., Frangopol, D.M., Saydam, D. and Salvino, L.W. (2011). "Reliability analysis and damage detection in high-speed naval craft based on structural health monitoring data." *Structural Health Monitoring,* 10(4), 361-379.

Padgett, J., Ghosh, J. and Dennemann, K. (2009). "Sustainable Infrastructure Subjected to Multiple Threats." *TCLEE 2009: Lifeline Earthquake Engineering in a Multi-hazard Environment,* American Society of Civil Engineers, 703-713.

Rackwitz, R. (2002). "Optimization and risk acceptability based on the life quality index." *Structural Safety,* 24(2–4), 297-331.

Saydam, D., and Frangopol, D.M. (2011). "Time-dependent performance indicators of damaged bridge superstructures." *Engineering Structures,* 33(9), 2458-2471.

Saydam, D., Frangopol, D.M., and Dong, Y. (2013). "Assessment of risk using bridge element condition ratings." *Journal of Infrastructure Systems*, 19(3), 252-265.

Shiraki, N., Shinozuka, M., Moore, J.E., Chang, S.E., Kameda, H., and Tanaka, S. (2007). "System risk curves: probabilistic performance scenarios for highway networks subject to earthquake damage." *Journal of Infrastructure Systems*, 213(1), 43–54.

Soliman, M., and Frangopol, D.M. (2013). "Life-cycle management of fatigue sensitive structures integrating inspection information." *Journal of Infrastructure Systems,* doi:10.1061/(ASCE)IS.1943-555X.0000169 (in press).

Soliman, M., Frangopol, D.M. and Kim, S. (2013). "Probabilistic optimum inspection planning of steel bridges with multiple fatigue sensitive details." *Engineering Structures,* 49, 996-1006.

Stein, S., Young, G., Trent, R. and Pearson, D. (1999). "Prioritizing scour vulnerable bridges using risk." *Journal of Infrastructure Systems,* 5(3), 95-101.

Tversky, A., and Kahneman, D. (1992). "Advances in prospect theory: Cumulative representation of uncertainty." *Journal of Risk Uncertainty*, 5(4), 297-323.

von Neumann, J. and Morgenstern, O. (1953). *Theory of games and economic behavior*, Princeton: Princeton University Press.

Whittemore, D. (2010). "Sustainable structures for the bridge engineer." *Structure*, Structural sustainability, discussion of sustainability and preservation as they pertain to structural engineering, National Council of Structural Engineers Associations (*NCSEA)*, Chicago, IL.

Zhu, B., and Frangopol, D.M. (2012). "Reliability, redundancy and risk as performance indicators of structural systems during their life-cycle." *Engineering Structures,* 41, 34-49.

Zhu, B., and Frangopol, D.M (2013). "Risk-based approach for optimum maintenance of bridges under traffic and earthquake loads." *Journal of Structural Engineering,* 139(3), 422-434.

Multi-hazard Risk Assessment of Civil Infrastructure Systems, with a Focus on Long Linear Structures such as Levees

Erik Vanmarcke

ABSTRACT

Multi-hazard risk assessment enables one to estimate the benefit of expenditures for risk mitigation – a reduction in potential future losses. This leads to improved decision-making in design, inspection and repair of all types of structures, new and existing. It is especially relevant and useful for complex spatially distributed systems such as levees, pipelines and railroads, when seeking to allocate limited resources to different 'segments' comprising a long linear 'lifeline' (or a network of such lifelines). To demonstrate an approach based on random field concepts (to characterize how loads and resistances vary in space and time), we assess the risk of sliding (limit-equilibrium failure) of long earth slopes, dams or levees. In this instance, the stochastic model indicates – fitting observations – that slope failure events involving very long or very short distances along the slope axis are highly improbable, and predicts the 'most likely width of the failure zone' for long earth slopes and embankments. It can also evaluate the mean rate of increase in the 'system failure' risk per unit length, a key controllable parameter in risk management of a system of long linear structures such as levees.

INTRODUCTION

Alternative methods of integrated risk assessment, in the context of engineering decision making for civil infrastructure systems, range from 'action-oriented' (requiring only minimal knowledge of probability and statistics) to 'analysis-oriented' (based on random field concepts to characterize how loads and resistances vary in space and time). To demonstrate the latter method

Department of Civil and Environmental Engineering, Princeton University, Princeton, NJ; Dist.M. ASCE; 1-609-751-0221; email: evm@princeton.edu

in sufficient and necessary detail, we take an in-depth look at how to assess the risk of sliding of long earth slopes, dams or levees,

Many studies aimed at determining the risk of slope failure – by Wu and Kraft (1970), Yucemen et al. (1973), Alonso (1976), Matsuo (1976), Hachich and Vanmarcke (1983), Christian et al. (1994), Li and Lumb (1987), Griffiths and Fenton (2004), Low et al. (1998 & 2007), among others — work within the framework of conventional plane strain analysis of slope stability. Based on classical limit-equilibrium stability analysis (e.g., Fellenius 1936; Bishop 1955), one considers a typical cross-section (in the present context, at any location x along the centerline of a long earthen slope or embankment or levee) and defines the (cross-sectional) safety factor F as the ratio of the resisting moment to the driving (or overturning) moment,

$$F = \frac{\text{Resisting Moment}}{\text{Driving Moment}} = \frac{M_R}{M_D}. \tag{1}$$

In a simple probabilistic treatment of the problem — easily extended, but without much altering this paper's main theses — the cross-sectional resisting moment M_R is treated as a random variable with mean $\overline{M}_R$, standard deviation $\widetilde{M}_R$, and coefficient of variation $V_{M_R} = \widetilde{M}_R/\overline{M}_R$. (Throughout the paper, $\overline{Z}$ and $\widetilde{Z}$ denote, respectively, the mean and the standard deviation of the random quantity Z). This requires consideration of the correlation structure of horizontal and vertical variation of shear strength within the cross-section. In static limit-equilibrium slope stability analysis, uncertainty about the driving moment is usually dwarfed by uncertainty about the resisting moment, rendering it reasonable, at first, to ignore the variability of M_D; hence, we assume $\widetilde{M}_D \approx 0$ in the probabilistic analysis presented below.

Mean and standard deviation of the safety factor. The mean of the (cross-sectional) safety factor F is then:

$$\overline{F} = \overline{M}_R/\overline{M}_D. \tag{2}$$

The standard deviation of of F equals the standard deviation of M_R times the reciprocal of the mean of M_D:

$$\widetilde{F} = \widetilde{M}_R/\overline{M}_D. \tag{3}$$

Note that the coefficient of variation $V_F = \widetilde{F}/\overline{F}$ is equal to $V_{M_R} = \widetilde{M}_R/\overline{M}_R$ if the driving moment is (or, as herein, is be assumed to be) deterministic.

Reliability Index and Probability of Failure. In the context of the 2-D stability analysis, the calculated probability of failure p_f corresponds to the area under the probability density function of the (cross-sectional) safety factor F at values less than one:

$$p_f = \text{Prob}[F < 1]. \tag{4}$$

An indicator of slope safety is the reliability index β, defined in terms of the mean and the standard deviation (or the coefficient of variation) of the factor of safety, as follows:

$$\beta = \frac{\overline{F} - 1}{\widetilde{F}} = \frac{1}{V_F} \frac{\overline{F} - 1}{\overline{F}}. \tag{5}$$

It measures the distance between the mean safety factor $\overline{F}$ and its failure threshold, $F = 1$, in units of standard deviation of the safety factor, $\widetilde{F}$.

The failure probability p_f may be expressed in terms of β as follows:

$$\begin{aligned} p_f &= P[F < 1] = P[(F - \overline{F})/\widetilde{F} < \beta] \\ &= P[U < -\beta] = F_U(-\beta), \end{aligned} \tag{6}$$

in which $F_U(\cdot)$ is the cumulative probability distribution of the standardized safety factor, $U = (F - \overline{F})/\widetilde{F}$, which has zero mean and unit standard deviation. Either the normal (Gaussian) or lognormal distribution is commonly adopted to evaluate this "notional" probability — "notional", because the event the probability refers to, $F < 1$, defined in the context of plane strain (2-D) analysis, is *not* a well-defined physically realizable event. This point is clarified in the next section, in which we explicitly consider the out-of-plane width of the soil mass involved in any real failure event.

The preceding analysis can be performed for any assumed circular or non-circular cross-sectional failure arc. One needs to search for the sliding-arc geometry, accounting for the material properties within the cross-section, that will yield the smallest value of the mean safety factor $\overline{F}$ or the reliability index β, or the largest value of failure probability p_f. (The reliability index β and failure probability p_f depend not only on $\overline{F}$, but also on the coefficient of variation and within-cross-section correlation structure of the shear strength. Owing to the nonlinearity between F and β, and between β and p_f, the various critical-arc geometries will likely differ, but not by much.

SIMPLIFIED 3-D SLOPE STABILITY: PROBABILISTIC TREATMENT

An analytically tractable and highly informative approach to probabilistic three-dimensional limit-equilibrium slope stability analysis rests on the assumption that the 3-D sliding mass has the same cross-sectional characteristics over a finite width b along the slope axis x, and has vertical cutoffs at both ends. If the cross-section through the finite-width sliding mass is a circular arc, the backside of 3-D failure surface will be cylindrical.

In the probabilistic treatment of the problem, the set of cross-sectional resisting moments $M_R(x)$ is seen as the realization of a weakly stationary one-dimensional random function of x, with mean $\overline{M}_R$, standard deviation $\widetilde{M}_R$, and a horizontal correlation structure that depends on separation distance (between pairs of cross-sections) measured along the slope axis. Specifically, the correlation structure of $M_R(x)$ can be described by a correlation function $\rho(\Delta x) \equiv \rho_{M_R}(\Delta x)$, where Δx measures the horizontal distance (along the slope axis) between two cross-sections, or by the reduction factor $\Gamma(b) \equiv \Gamma_{M_R}(b)$, which expresses how the standard deviation of $M_R(x)$ decreases under local averaging in function of the averaging-window size b. The scale of fluctuation of $M_R(x)$, the integral of $\rho(\Delta x)$ from $-\infty$ to $+\infty$, is denoted by $\delta \equiv \delta_{M_R}$. For common (single-scale) random process models, the reduction factor $\Gamma(b)$ will converge toward a simple asymptotic form as the ratio b/δ grows, namely $\Gamma(b) \approx (\delta/b)^{1/2}$, for $b \geq \delta$. This expression in fact provides an alternate definition for the scale of fluctuation (Vanmarcke 1977a & 1983). Also, to first approximation: $\Gamma(b) \approx 1$ for $0 \leq b \leq \delta$.

The function $\Gamma(b)$ is obtainable, in principle, from statistical analysis of weighted averages of shear strengths associated with individual cross-sections $M_R(x)$ at different locations x along the slope axis. A conceivable direct approach is to evaluate the actual cross-sectional resisting moments $M_R(x)$ from information (e.g., field and lab measurements) gathered at specific locations $(x_0, x_0 + \Delta x_0, x_0 + 2\Delta x_0,$ etc.). This would provide a set of values of $M_R(x)$ from which one could estimate the mean $\overline{M}_R$, the standard deviation $\widetilde{M}_R$, and characteristics of the (horizontal) correlation structure. An indirect approach, pursued in Vanmarcke (1980), is to derive these statistical parameters from data about the random variables (layer thicknesses, strength parameters, pore pressures) contributing to the uncertainty of $M_R(x)$.

Safety Factor in the 3-D Probabilistic Analysis. The factor of safety, in the three-dimensional formulation, now depends on the location of x of the center of the failure zone, and becomes itself a random function $F_b(x)$ whose marginal statistics — its mean $\overline{F_b}$ and its standard deviation $\widetilde{F}_b$ — depend on the failure-zone width b. For a sliding mass located between $(x_0 - b/2)$ and $(x_0 + b/2)$, the safety factor $F_b(x_0)$ may be expressed as follows:

$$F_b(x_0) = \frac{\text{Resisting Moment}}{\text{Driving Moment}} = \frac{M_{R,b}(x_0) + R_e}{M_{O,b}(x_0)}, \tag{7}$$

in which b = width of the failure zone; $M_{R,b}(x_0)$ = the integral of the resisting moments $M_R(x)$ for cross-sections on the backside of the potential sliding mass; $M_{D,b}(x_0)$ = the total driving moment, i.e., an integral of the cross-sectional driving moments within the failure zone; and R_e = the contribution of the end sections of the failure zone to the resisting moment. The quantity $M_{R,b}(x_0)$ is the integral of the resisting moments of cross-sections located between the limits $x_1 = (x_0 - b/2)$ and $x_2 = (x_0 + b/2)$:

$$M_{R,b}(x_0) = \int_{x_1}^{x_2} M_R(x)dx. \tag{8}$$

Keeping the interval $b = |x_2 - x_1|$ fixed and moving it along the slope axis gives rise to a derived random function, $M_{R,b}(x)$, which is a 'moving integral' of the random process $M_R(x)$. The means of $M_{R,b}(x)$ and $M_{D,b}(x)$ are:

$$\overline{M}_{R,b} = b\,\overline{M}_R \qquad \text{and} \qquad \overline{M}_{D,b} = b\,\overline{M}_D. \tag{9}$$

If the values of $M_R(x)$ corresponding to different locations x were perfectly correlated, the standard deviation of $M_{R,b}(x_0)$ would be equal to $b\,\widetilde{M}_R$. However, the integration operation (in Eq. 8) will mitigate the impact of large local deviations of $M_R(x)$ from its mean $\overline{M}_{R,}$. This effect can be quantified in terms of the dimensionless reduction factor $\Gamma(b) \equiv \Gamma_{M_R}(b)$, as follows:

$$\widetilde{M}_{R,b} = b\,\widetilde{M}_R\,\Gamma(b), \tag{10}$$

in which $\Gamma(b)$, already mentioned earlier, is by definition equal to the square root of the "variance function" (Vanmarcke, 1977a & 1983), which expresses the fractional reduction of the "point variance" (of stationary random processes) under local averaging, for different 'moving-window sizes' b.

The end-section contribution, R_e, to the resisting moment can be calculated, for a given sliding-surface-end-section geometry (not necessarily the straight vertical cutoff shown in Fig. 2), by integrating contributions to the resisting moment from all points within the two end-sections. We denote its mean by $\overline{R}_e$, and introduce the quantity $d = \overline{R}_e/\overline{M}_R$, with the dimension of length, obtainable from deterministic stability analysis. The mean of the total resisting moment can then be expressed as a sum of two components:

$$\overline{M}_{R,b} + \overline{R}_e = b\,\overline{M}_R + d\,\overline{M}_R = (b+d)\,\overline{M}_R. \tag{11}$$

The distance d also equals $2A/l$, where A = the area of cross-section above the (circular) failure arc, and l = the length of the arc. Since the shear strength throughout any cross-section is random, the resistance contribution R_e will also be random. However, the uncertainty in R_e has only a secondary effect on the results of the probabilistic stability analysis, especially at larger values of b of most practical interest in 3-D slope safety assessment, and it will not be explicitly treated (and accounted for) herein.

Mean and standard deviation of the factor of safety. Treating the driving moment as deterministic or prescribed — extensions are considered later — the mean of the safety factor $F_b(x_0)$ can be expressed as follows:

$$\overline{F}_b = \frac{\overline{M}_R\,b + \overline{R}_e}{\overline{M}_D\,b} = \frac{\overline{M}_R(b+d)}{\overline{M}_D\,b} = \overline{F}\left(1 + \frac{d}{b}\right), \tag{12}$$

where $\overline{F} = \overline{M}_R/\overline{M}_D$ is the 'plane strain' mean safety factor, obtainable either directly from Eq. 2 or by taking $\overline{F}_b$ in Eq. 12 to its asymptotic limit,

$$\lim_{b\to\infty} \overline{F}_b = \overline{F} = \frac{\overline{M}_R}{\overline{M}_D}. \tag{13}$$

The quantity $(b+d)$ may be thought of as the "effective width" of the failure zone (for the purpose of computing the mean resisting moment), while d/b measures the relative importance of the end effects. Actually, end-sections having more realistic shapes — different from the idealized vertical cutoffs — can also be represented by the distance $d = \overline{R}_e/\overline{M}_R$, now more generally interpreted (indeed, defined) as the value, $b \equiv d$, for which $\overline{F}_b \equiv \overline{F}_d = 2\,\overline{F}$.

The standard deviation of the safety factor $F_b(x_0)$ equals the standard deviation of $M_{R,b}$ times the reciprocal of the mean of $M_{D,b}$. We may write::

$$\widetilde{F}_b \simeq \frac{b\,\widetilde{M}_R\,\Gamma(b)}{b\,\overline{M}_D} = \Gamma(b)\,\widetilde{F}, \tag{14}$$

where $\widetilde{F} = \widetilde{M}_R/\overline{M}_D$ is the standard deviation of the (2-D) cross-sectional safety factor. Note that $\widetilde{F}$ is not equal to the asymptotic value of $\widetilde{F}_b$ when $b \to \infty$. Instead, $\widetilde{F}_b \to 0$, since $\Gamma(b) \to 0$, as $b \to \infty$ (*unless* the scale $\delta \equiv \delta_{M_R}$ of the one-dimensional random process $M_R(x)$ is itself infinite).

The mean and the standard deviation of $F_b(x_0)$ depend on: the mean plane strain safety factor $\overline{F}$; the coefficient of variation $V_F = V_{M_R}$ of the resistance mobilized along the 'failure arc' within each cross-section; the parameter d, accounting for end effects, obtainable from deterministic (for circular arcs, 2-D) stability analysis; and the correlation structure, represented by $\Gamma(b) \equiv \Gamma_{M_R}(b)$, of the cross-sectional resisting moments along the slope axis.

Reliability Index as a Function of the Failure-Zone Width. The reliability index can again be expressed in terms of the mean and standard deviation of the factor of safety, both now dependent on b, as follows:

$$\beta_b = \frac{\overline{F}_b - 1}{\widetilde{F}_b}. \tag{15}$$

It measures the distance between the mean safety factor, $\overline{F}_b$, and its failure threshold, $F_b = 1$, in units of standard deviation of the safety factor, $\widetilde{F}_b$. Inserting the expressions for $\overline{F}_b$ and $\widetilde{F}_b$, and dividing by the cross-sectional (2-D) reliability index β, yields the following expression for the ratio of the 3-D reliability index to the 2-D reliability index, for $b > 0$ and $\overline{F} > 1$:

$$\frac{\beta_b}{\beta} = \{1 + \frac{d}{b} \frac{\overline{F}}{\overline{F} - 1}\} \frac{1}{\Gamma(b)}. \tag{16}$$

This equation indicates that two factors, marked by opposing trends, control the behavior of the reliability index β_b as a function of the width b of the failure zone. As b increases, the first factor (dependent on d/b and $\overline{F}$) decreases from very high positive values when $b \to 0$ to unity as $b \to \infty$. The second factor, $[\Gamma(b)]^{-1}$, presuming the scale $\delta \equiv \delta_{M_R}$ is finite, grows from a unit value when $b \to 0$ to infinity as $b \to \infty$. Clearly, our interest focuses on the value $b_{critical} \equiv b_{cr}$ that minimizes the product of these two factors.

Before tackling the optimization problem, we can already draw some useful conclusions from Eq. 16, which expresses the ratio β_b/β of reliability indices (linked directly to the slope-failure probabilities) obtained by means of 3-D and 2-D analyses, respectively. The two factors on the right side of Eq. 16 are

both *no less than one* for all possible values of the failure-zone width b. This means, first, that the reliability index, and the corresponding failure risk, calculated based on 2-D stochastic stability analysis is *always conservative* relative to that obtained from 3-D analysis. (The limiting case, $\beta_b/\beta \to 1$, is associated with $\delta \to \infty$ and $b \to \infty$, an unrealistic situation). Second, as will be demonstrated below, for any realistic values of the parameters, the 2-D analysis yields *over-conservative* results, i.e., estimates for the probability of a (localized) slope-failure event that *may be orders of magnitude too high*. Such conservatism (in risk estimation) defeats the purpose of risk assessment and the goal and promise of risk-informed engineering decision-making.

Risk of Failure at any Specific Location. We now examine the probability of failure $p_f(b)$ involving a failure-zone segment of width b centered at any given location x along the slope (or embankment or levee) axis. Equal to the area under the probability density function of F_b for values below one, it can also be expressed in terms of the reliability index β_b, as follows:

$$
\begin{aligned}
p_f(b) \;&= P[F_b < 1] = P[(F_b - \overline{F}_b)/\widetilde{F}_b < \beta_b] \\
&= P[U < -\beta_b] = F_U(-\beta_b),
\end{aligned}
\tag{17}
$$

where, again, $F_U(\cdot)$ is the cumulative probability distribution of the standardized variable $U = (F_b - \overline{F}_b)/\widetilde{F}_b$ which has zero mean and unit standard deviation. It is reasonable to assume, in light of the Central Limit Theorem, that the spatially averaged resisting moments $M_{R,b}$ (and hence the safety factor F_b itself) obey a Gaussian distribution. Actually, for the same reason — averaging of random-strength values along the failure arc — it makes sense to use the Gaussian distribution when calculating p_f by means of Eq. 6.

Consider the two main statistics – mean and standard deviation – of the safety factor F_b as a function of b. The mean $\overline{F}_b$ drops down to its plane strain level, while the spread of the distribution of the safety factor, measured by $\widetilde{F}_b$, is roughly constant at small b-values and then steadily decreases once b exceeds the scale of fluctuation $\delta = \delta_{M_R}$ of the one-dimensional random process $M_R(x)$. At low b-values ("Case I") the failure probability is very small (relative to its maximum at some "critical value" b_{cr}, evaluated in the next subsection) due to the high mean values of the safety factor F_b. At large b-values ("Case II") the failure probability is also very small (relatively, of course) because the standard deviation of the safety factor F_b keeps decreasing as the mean approaches the asymptotic value $\overline{F}_{b\to\infty} \to \overline{F}$.

The following series approximation (Dwight 1961) for the Standard Gaussian cumulative distribution $F_U(\cdot)$ is useful at relatively large positive u-values:

$$F_U(-u) = (\sqrt{2\pi}u)^{-1}e^{-u^2/2}(1 - u^{-2} + 3u^{-4} - 16u^{-6} + ...). \qquad (18)$$

(The error in this series expansion is less than the last term used.) Combining Eqs. 17 and 18, we can express the failure-event probability $p_f(b)$ as follows:

$$p_f(b) = F_U(-\beta_b) = g(\beta_b)\, e^{-\beta_b^2/2}. \qquad (19)$$

The function $g(\beta_b)$ varies relatively slowly with β_b within the range of values of β_b likely to be of practical interest. For example, when $1.5 < \beta_b < 5$, the function $g(\beta_b)$ varies only by a factor of three, while the exponential factor changes by five orders of magnitude. For practical reliability calculations, it makes sense to use $g(\beta_b) \approx (\sqrt{2\pi}\beta_b)^{-1}$, thereby in effect ignoring all but the first term in the above series approximation. (It is straightforward, as well, to refine the approximation by including additional terms of the series.) We again use the above approximation in a subsequent section of the paper.

Critical Width of the Failure Zone. The minimum value of β_b can be found by setting the derivative of β_b/β (given by Eq. 16) with respect to b equal to zero, and solving for b. If and when the (standard-deviation-reduction) function $\Gamma(b)$ can be expressed as a power law, $\Gamma(b) \propto b^{-0.5}$, the b-value that minimizes β_b, denoted by b^*, can be expressed as follows:

$$b^* = \frac{\overline{F}\,d}{\overline{F} - 1}. \qquad (20)$$

Note that the major influence on b^* is the plane strain mean safety factor, $\overline{F}$. The smaller the *mean safety margin*, i.e., the difference between $\overline{F}$ and the unit failure threshold $F = 1$, the larger the ratio b^*/d.

The power law, $\Gamma(b) \propto b^{-0.5}$, does not apply when b is less than δ, however. Instead, $\Gamma(b) \approx 1$ when $b \leq \delta$. In case δ exceeds b^* (as given by Eq. 20), the critical failure-zone width b_{cr} will be roughly equal to δ. Hence,

$$b_{cr} \approx \text{Max}\,\{b^*, \delta\}. \qquad (21)$$

In words, the critical failure-zone width b_{cr}, defined as the value of b that minimizes β_b or maximizes $p_f(b)$, is expected to be the larger of two quantities, namely b^* (as expressed in Eq. 20) and the scale of fluctuation $\delta \equiv \delta_{M_R}$.

Minimum Value of the Reliability Index β_b. Substituting Eq. 20 into Eq. 16 yields the quotient of the minimum 3-D reliability index β_{b*} (applicable when $b^* \geq \delta$) and the 2-D reliability index β:

$$\frac{\beta_{b*}}{\beta} = \frac{2}{\Gamma(b^*)} \approx 2\,(b^*/\delta)^{0.5}\,. \tag{22}$$

When b^* is less than δ, we need to go back to Eq. 16 and set $b = \delta$ to evaluate the minimum ratio of 3-D to 2-D reliability indices. Inserting $\Gamma(\delta) \approx 1$ yields:

$$\frac{\beta_\delta}{\beta} \approx 1 + \frac{d}{\delta}\,\frac{\overline{F}}{\overline{F}-1}\,. \tag{23}$$

These two candidate expressions for the minimum ratio of reliability indices, Eqs. 22 and 23, give the same result, $\beta_b/\beta \approx 2$, when $b = b^* = \delta$, while for $\delta \geq b^*$, the minimum value of the ratio of reliability indices, given by Eq. 23, gradually decreases, from $\beta_\delta/\beta \approx 2$ (when $\delta \approx b^*$) to $\beta_\delta/\beta = 1$ as $\delta \to \infty$.

Multi-Scale and/or Self-Similar Correlation Structure. There is merit, in the context of modeling both short- and long-range patterns of spatial variation of cross-sectional resistances $M_R(x)$ at different locations x along the axis of long earth slopes, to consider a class of 'multi-scale' random processes that tend to exhibit self-similar behavior as observed in many natural phenomena, both temporal and spatial (Hurst 1951; Mandelbrot 1965).

In general, a stationary multi-scale random process, $Z(x)$, may be thought of as a sum of statistically independent component processes $Z_i(x)$, $i = 0, 1, ..., n$, each one characterized by its scale of fluctuation δ_i and its fractional contribution $\widetilde{Z}_i^2//\widetilde{Z}^2$ to the overall or composite variance $\widetilde{Z}^2$. Visualize the discrete *scale spectrum* (Vanmarcke 2010) of the composite process $Z(x)$, showing the component fractional contributions $\widetilde{Z}_i^2/\widetilde{Z}^2$, which sum to one, plotted against the component scales δ_i. The composite or overall scale of fluctuation of $Z(x)$ is then just a weighted combination of the component scales, the weights being the fractional contributions to the total variance.

Our interest focuses on composite random process models for $M_R(x)$ having a *wide scale spectrum*, i.e., for which the ratio δ_n/δ_0 is very large, which implies slow correlation decay and behavior indicative (by analogy to temporal variation) of 'long memory' and persistence of variability of local means, regardless of the averaging length. Instead of the power law $\Gamma(b) \propto b^{-1/2}$, for large values of b, one expects slower decay, characterized by $\Gamma(b) \propto b^{-\alpha}$,

where $0 < \alpha < 1/2$. Indeed, as mentioned in the preceding subsection, one expects (and observes) this kind of slow decay of $\Gamma(b)$ even for single-scale random processes, when b-values are less than the scale of fluctuation.

Note that the standard deviation of the *local integral*, instead of the local average, over a given distance b, will also follow a power law, but with co-efficient $\alpha + 0.5$. The latter is quite closely related to the (so-called) Hurst coefficient "H" used to characterize self-similar or fractal random variation. Note, however, that the 'Hurst effect' involves more than just the question of how local integration of a random process affects its 'point variance' — the original Hurst statistic (used to assess long-term storage capacity of the reservoir behind the Aswan Dam on the Nile River) is, by definition, the 'range' between minimum and maximum values of local integrals of a random process (observed for a long time or over a long distance). Hence, the coefficients "H" and "$1 + \alpha$", while related, are not directly comparable.

3-D Failure Risk Analysis in the Multi-Scale Case. We now examine the implications of the power-law behavior of the standard-deviation-reduction function, $\Gamma(b) \propto b^{-\alpha}$, with coefficient α in the range $0 < \alpha \le 0.5$, for the 3-D slope-failure-risk analysis. The upper-bound value $\alpha = 0.5$ implies "single-scale-process behavior" (i.e., no long-term persistence of correlation), while lesser (positive) values of α are indicative of multi-scale-process (and/or self-similar) behavior. The function $\Gamma(b)$ characterizing the cross-sectional resisting moments $M_R(x)$ may thus generally be expressed as

$$\Gamma(b) \equiv \Gamma_{M_R}(b) = (\delta_0/b)^\alpha, \quad b \ge \delta_0, \ \ 0 < \alpha \le 0.5, \tag{24}$$

in which $\delta_0 = \delta_{0,M_R}$ may be interpreted as the *smallest* scale of fluctuation of a presumed multi-scale random process model for $M_R(x)$. Also, we may assume $\Gamma(b) \approx 1$ when $0 \le b \le \delta_0$. No upper bound on b needs to be set when using the power law in Eq. 24, as there is presumably (for practical purposes) no limit on the largest scale of fluctuation δ_n of the underlying multi-scale random process. Note that in case $\alpha = 0.5$ the function $\Gamma(b) \equiv \Gamma_{M_R}(b)$ behaves as for a single-scale random process, with scale $\delta \equiv \delta_{M_R} = \delta_0$.

Inserting the power law for $\Gamma(b)$ into Eq. 16, again setting the derivative of the ratio β_b/β equal to zero, and solving for b, yields a result similar to Eq. 20 for the critical failure-zone width, expressed as a multiple of d:

$$\frac{b_{cr}}{d} = \frac{1-\alpha}{\alpha} \cdot \frac{\overline{F}}{\overline{F}-1}. \tag{25}$$

When $\alpha = 0.5$, and hence $[(1-\alpha)/\alpha] = 1$, Eq. 25 reduces to Eq. 20. However, in case $M_R(x)$ has a *wide scale spectrum* and/or exhibits self-similar behavior, the α-value might be, say, 0.25, corresponding to $[(1-\alpha)/\alpha] = 3$.

Finally, inserting the above expression for the ratio b_{cr}/d into Eq. 16 yields the quotient of the *minimum* 3-D (width-dependent) reliability index $\beta_{b_{cr}}$ and the 2-D (cross-sectional) reliability index β,

$$\frac{\beta_{b_{cr}}}{\beta} = \frac{1}{1-\alpha} \cdot \frac{1}{\Gamma(b_{cr})} \, , \qquad (26)$$

for values of the power-law coefficient α in the range $0 < \alpha \le 0.5$. Note that Eq. 26 reduces to Eq. 22 when $\alpha = 0.5$, in which case $(1-\alpha)^{-1} = 2$.

Comparing 2-D and 3-D Stochastic Slope Stability Analyses. Based on the results presented above — for different assumptions, expressed through the function $\Gamma(b)$, about the correlation structure of the cross-sectional resisting moments along the axis of a long slope or embankment — we conclude that one should expect the ratio of 3-D to 2-D reliability indices, β_b/β, for the critical value $b = b_{cr}$ of the failure-zone width, *to be close to two*. The reasons for this rather high value of the ratio $\beta_{b_{cr}}/\beta$ are: (1) the added resistance against sliding due to the (3-D) end effects, and (2) the variance reduction associated with *real* finite-width slope-sliding events. In light of the high sensitivity of the failure probability to the reliability index — note that the dominant factors in the expressions for $p_f(b)$ and p_f are, respectively, $\exp\{-\beta_b^2/2\}$ and $\exp\{-\beta^2/2\}$ — there is a clear message about the danger of doing stochastic slope stability analysis only within a 2-D framework, namely *over-conservatism* in the form of *gross over-estimation of the failure risk*.

RISK OF FAILURE OF LONG SLOPES

A most important 'system reliability' aspect of the slope stability problem is the dependence of risk of failure on the total length B of an earth slope, embankment or levee. Long 'linear' earth slopes associated with dams, dikes and highways should not fail anywhere along the axis, as any local failure may have severe 'system-wide' consequences. This aspect of 3-D probabilistic slope stability analysis differs greatly from that considered above. We now envision slope-failure events occurring at random, more or less frequently, along the axis of a long slope, and the focus is on trying to evaluate the mean rate of occurrence (per unit length along the slope axis) of such events — each

event is a 3-D slope failure characterized by a failure-zone width $b_{cr} \ll B$. For long slopes, the chance of one or more failures somewhere along the slope axis, and hence the probability of 'system failure', steadily increases with the overall length B of the slope. This 'systemic risk', $P_F(B)$, can easily exceed the probability p_f estimated based on 2-D (cross-sectional) stochastic slope stability analysis, even though the latter is prone to giving very conservative results compared to the 3-D local-failure-risk estimate $p_f(b)$.

An effective and elegant way to deal with this problem is by 'threshold-crossing analysis', in which the factor of safety $F_b(x)$ is viewed as a function of x, the position of the center of the failure zone along the embankment axis. We assume that the failure-zone width b is fixed, in particular, at the value $b = b_{cr}$ obtained in the preceding section. A slope failure will occur if the safety factor $F_b(x)$ crosses into the unsafe domain $F_b < 1$ at any location x between $b/2$ and $B - b/2$. The condition $F_b(x) \leq 1$ is equivalent to:

$$U_b(x) = \frac{F_b(x) - \overline{F}_b}{\widetilde{F}_b} < \frac{(1 - \overline{F}_b)}{\widetilde{F}_b} = -\beta_b. \tag{27}$$

For any given location x, the left side is a standardized random variable with zero mean and unit standard deviation. It may also be viewed as a random function, $U_b(x)$, characterizing the fluctuations of the cross-sectional resisting moments locally averaged over the failure-zone width b centered at different locations x. A slope-sliding event within the axial length interval b centered at x is equivalent to $U_b(x)$ being below the failure threshold $(-\beta_b)$.

The random function $U_b(x)$ will tend to be Gaussian (since the resisting moments $M_{R,b}$ are approximately Gaussian, in accordance with the Central Limit Theorem), and the slope reliability — or its 'survival' probability — will have the following approximate form (Vanmarcke 1975):

$$P_S(B) = \begin{cases} [1 - p_f(b)] \ \exp\{-(B - b) \ \nu(\beta_b)\}, & B \geq b, \\ 1 - p_f(B), & B \leq b, \end{cases} \tag{28}$$

in which $p_f(\cdot)$ is the probability of failure at any specific location (analyzed in the preceding section), and $\nu(\beta_b)$ is the rate of decay of the 'system reliability' per unit length along the slope axis. The probability of slope failure, $P_F(B) = 1 - P_S(B)$, can usually (in practice) be more simply expressed as follows:

$$P_F(B) \simeq \begin{cases} p_f(b) + (B - b) \ \nu(\beta_b), & B \geq b, \\ p_f(B), & B \leq b. \end{cases} \tag{29}$$

The above approximation, for $B \geq b$, is obtained by assuming $\nu(\beta_b) \ll 1$ and replacing the exponential form e^{-u} by $(1 - u)$ in Eq. 28. Of course, this works only if the resulting value for $P_F(B)$ remains well below one — otherwise, one must use the original expression, Eq. 28. The term linear in B, in Eq. 29, is expected to dominate the failure risk for long slopes:

$$P_F(B) \simeq B \, \nu(\beta_b), \tag{30}$$

in which $\nu(\beta_b)$ is the rate of increase of the system-failure risk per unit length of the slope. Again, the 'linear approximation' is suitable only if it yields (system-failure) probabilities well below one. Also, the idea, throughout this section, is that b is to be set equal to the critical failure-zone width b_{cr}.

Growth Rate of System Failure Risk per Unit Length.   From the theory of stationary Gaussian random processes, applied here to the normalized-safety-factor function $U_b(x)$, the mean rate $\nu(\beta_b)$ of down-crossings (per unit length) of the normalized failure threshold $(-\beta_b)$ can be expressed using the classical formula of S.O. Rice (1944):

$$\nu(\beta_b) = r_b \, \exp\{-\beta_b^2/2\}, \tag{31}$$

in which r_b denotes the mean *zero-crossing* rate, namely the value of $\nu(\beta_b)$ when $\beta_b = 0$. Eq. 31 indicates that the mean spatial rate of local-slope-failure events decreases rapidly as the reliability index β_b grows.

For any value $b > 0$, owing to the local averaging of cross-sectional resisting moments $M_{(}x)$, the derived one-dimensional random processes $M_{R_b}(x)$ and $F_b(x)$ (as well as the *normalized* safety-factor process $U_b(x)$) are sure to be "mean-square differentiable", that is, the variance of their derivative with respect to x is finite and can be reliably computed. An important related result is that the mean rate r_b can be expressed in terms of the correlation function $\rho(b)$ and the standard-deviation reduction factor $\Gamma(b)$ of the cross-sectional resisting moments $M_R(x)$, as follows (Vanmarcke 1983 & 2010):

$$r_b = \frac{1}{\pi\sqrt{2}} \frac{[1 - \rho(b)]^{1/2}}{b \, \Gamma(b)}. \tag{32}$$

Combining Eqs. 31 and 32, and assuming $[1 - \rho(b)] \approx 1$, amply justified in light of the fact that b is to be set equal to b_{cr}, yields

$$\nu(\beta_b) \approx [\pi\sqrt{2} \, b \, \Gamma(b)]^{-1} \, \exp\{-\beta_b^2/2\}. \tag{33}$$

We can now, in principle, evaluate $\nu(\beta_b)$ and $P_F(B)$ as a function of b for many different slip surfaces. A better choice is to adopt the "critical" cross-sectional failure arc (associated with $\overline{F}$ and found by deterministic analysis) and replace b by the "critical failure-zone width" b_{cr}. This leads to the following estimate for the failure risk of a slope of length B, for $B \geq b_{cr}$:

$$P_F(B) \simeq \frac{B}{b_{cr}} \, (\pi\sqrt{2})^{-1} \, [\Gamma(b_{cr})]^{-1} \exp(-\beta_{b_{cr}}^2/2), \qquad (34)$$

presuming $P_F(B) \ll 1$. The predicted mean rate of growth of the slope-failure risk per unit length (namely the multiplier of B on the right side of Eq. 34) depends — indirectly, through b_{cr}, $\beta_{b_{cr}}$ and $\Gamma(b_{cr})$ — on the following: (1) the mean plane strain safety factor $\overline{F}$, obtainable from 2-D deterministic slope stability analysis; (2) the distance d, also obtainable from the deterministic analysis; and (3) the parameters expressing the variability and spatial correlation structure of the random process $M_R(x)$ of cross-sectional resisting moments, namely the coefficient of variation V_{M_R}, the scale of fluctuation $\delta = \delta_{M_R}$ and/or the power-law coefficient α.

Risk Assessment and Management of Long Earth Slopes. A most important 'system reliability' aspect of slope stability is the dependence of the systemic risk on the length of the embankment or levee. The failure risk grows nearly linearly with B, provided the calculated risk is well below one. An argument can be made that the estimate for $P_F(B)$ thus obtained constitutes a close lower bound to the slope failure probability: slip surfaces different from the critical surface (as regards location, length or shape) are not explicitly accounted for, but elements favoring the closeness of the bound are: (1) the strong correlation among failure events associated with adjacent, partially overlapping failure surfaces (and masses of soil); and (2) the decay of the failure probability for failure surfaces different from the critical one.

The relationship between the slope failure risk $P_F(B)$ and the length B can be used in making risk-informed design decisions (or, for existing structures, decisions about maintenance and upgrading). Specifically, the methodology enables one to determine the required plane strain mean safety factor $\overline{F}$ to achieve a prescribed system-reliability criterion, e.g., $P_F(B) = 10^{-3}$. The required value of $\overline{F}$ will depend on the length of the slope and on the variability and correlation structure of the cross-sectional resisting moments.

FURTHER OBSERVATIONS

(1)   The probabilities $p_f(b)$ and $P_F(B)$ have been expressed in terms of the reliability index $\beta_b = (\overline{F_b} - 1)/\widetilde{F}_b$. Identical results are obtained when failure events are expressed in terms of the *safety margin*, namely the difference between the resisting moment and the driving moment, in case the latter is treated as deterministic, or is prescribed. Failure occurs if the safety margin $(M_R - M_D)$ turns negative or if the normalized safety margin becomes less than $(-\beta'_b)$, where β'_b is now defined as the quotient of the mean and the standard deviation of the safety margin. (The two reliability indices, β'_b and β_b, are identical if there is no uncertainty in the driving moment.)

(2)   For long slopes, if the cross-sections vary (systematically, predictably) as a function of the location x along the axis, and/or if either the soil layer depths or the soil properties have known trends or discontinuities, the decay rate $\nu(\beta_b)$ will likewise become dependent on x. Extension of the preceding analysis is straightforward if a slope can be divided into relatively long 'nominally homogeneous' segments with lengths B_1, B_2, etc. For each segment the critical values of b and $\nu(\beta_b)$ need to be determined and the segment-specific failure probabilities may be added, provided the sum of the probabilities involved is small, to obtain the "system" failure probability.

(3)   In the multi-scale model, the slow random fluctuations of local averages of the resisting moment $M_R(x)$ along the slope axis may be seen as a reducible source of uncertainty. By spacing boreholes (and determining the strength profile) along the embankment axis at intervals Δx smaller than the scale(s) of fluctuation of the more slowly varying components, one may succeed in significantly reducing the fraction of the variance in the safety factor F_b attributable to the more slowly varying components. This is an example of how formal risk analysis can be used to evaluate, in quantitative terms, the (risk-reduction) benefits of geotechnical data acquisition.

(4)   The probabilistic analysis has explicitly recognized only the true or inherent variability of the shear strength. The failure risk is expressed as a function of the reliability index, which in turn depends on the statistical parameters of the random variables contributing to the strength. The analysis assumes that these parameters are known, and essentially evaluates the *conditional* probability of failure given the parameter values. In reality, these values must be estimated on the basis of a limited geological information, im-

perfect field or laboratory strength measurements, and engineering judgment and experience. In principle, the procedure for incorporating such added uncertainty is straightforward: one obtains the value of $P_F(B)$ corresponding to each possible set of strength (or other stochastic-model) parameters, and then weighs these estimates according to their relative likelihood.

(5)   Random external loads may be treated in a similar way. These loads may be quite predictable (e.g., surcharges, hydrostatic loads) or highly unpredictable (e.g., earthquake loads). In either case, the analysis just presented may be used to obtain estimates of the *conditional* risk of slope failure given the external loading. These conditional probabilities must then be combined with the results of an assessment of the likelihood of occurrence of various load levels during the (intended) operational life of a (spatially extended) structure. Considering external loads such as floods and earthquakes will make the failure risk of slopes or levees dependent on both time and space. In the case of seismic loading, one needs to consider the likelihood of strong ground motion — dependent on the frequency of potentially damaging earthquakes in the region — as well as the characteristics of the ground motion, including its spatial variation, during an earthquake. Considering potential slope failures due to flooding caused by rainfall during tropical storms, different scenarios of potential global change (in tropical-storm frequency and intensity) will introduce long-term trends in slope failure risks.

CONCLUSIONS

To demonstrate the 'analysis-oriented' approach to assessing the failure risk of civil infrastructure systems, we investigated the classical limit equilibrium slope stability problem within a three-dimensional probabilistic framework. The methodology can be applied to safety assessment of slopes with rather general strength characteristics and drainage conditions, and can be adapted to any deterministic plane strain stability analysis method. Also, it can accommodate a wide range of models for the correlation structure of the cross-sectional sliding resistances along the slope axis, including those consistent with multi-scale and self-similar patterns of random variation.

The paper demonstrates the importance, in fact the necessity, of accounting for the three-dimensional nature of the problem in extending conventional stability analysis into the realm of quantitative risk assessment. For long embankments, failure events involving either very long or very short failure

zones are shown to be improbable. The existence of a most likely failure-zone width is revealed and a method to evaluate it is presented.

Based on a comparison of reliability indices — linked directly to calculated failure probabilities — obtained by means of 3-D and 2-D stochastic slope stability analysis, we reach these practically significant conclusions. First, the reliability index derived based on 2-D (plane strain) slope stability analysis is always conservative relative to that obtained from 3-D analysis. Second, for realistic parameter values the 2-D analysis yields over-conservative results, i.e., estimates for the probability of a (localized) slope-failure event that may be orders of magnitude too high. Such conservatism (in risk estimation) defeats the purpose of risk assessment and the promise of risk-informed decision-making (for this class of problems) in geotechnical engineering.

An estimate is obtained for the probability $P_F(B)$ that a failure, often with system-wide consequences, will occur anywhere along the axis of (long) slope of given total length B. In the basic analysis, the cross-sectional properties, nominally identical, are modeled as randomly varying along the axis of the slope. The dominant contribution to $P_F(B)$, provided $P_F(B) \ll 1$, is found to be a term linear in B, and we evaluate the mean rate of local-slope-failure events per unit of length (along the slope axis). Extension of this analysis is straightforward if a long slope can be divided into 'nominally homogeneous' segments with lengths B_1, B_2, etc. The segment-specific failure probabilities may then be added, provided the sum of probabilities involved is small, to obtain the "system" failure probability. These results have important implications in the design of cuts and slopes, and provides the basis for development of more rational reliability-based criteria for designing 'lifelines' such as highway or railway embankments, dams, dikes and levees.

The main source of uncertainty accounted for in the stochastic slope stability analysis is the spatial variation of cross-sectional resistances against sliding. If the results of the risk analysis are interpreted as conditional probabilities, however, the methodology provides the basis for more complete slope reliability assessment in which other (partially uncertain) information, mainly about loading and environmental conditions, can be incorporated.

ACKNOWLEDGMENT

Models, funded through the Cooperative Institute for Climate Science (CICS) by the National Oceanographic and Atmospheric Administration (NOAA).

REFERENCES

Alonso, E.E. (1976). "Risk analysis of slopes and its application to slopes in Canadian sensitive clays." *Geotechnique*, 26(3): 453-472.

Bishop, A.W. (1955). "The use of the slip circle in the stability analysis of slopes." *J. Geotechnique*, 5(1), 7-17.

Christian, J.T., Ladd, C.C. and Baecher, G.B. (1994). "Reliability applied to slope stability analysis." *J. Geotech. Eng. ASCE*, 120(12), 2180-2207.

Dwight, H.B. (1961) *Tables of Integrals and Other Mathematical Data*, 4th Edition, MacMillan, New York

Fellenius, W. (1936). "Calculation of the stability of earth dams." *Trans. Congr. Large Dams, 2nd*, Washington, 4: 445.

Griffiths, D.V. and Fenton, G.A. (2004). "Probabilistic slope stability analysis by finite elements." *J. Geotech. Geoenviron. Eng.*, ASCE, 130(5), 507-518.

Griffiths, D.V., Huang, J. and Fenton, G.A. (2009). "On the reliability of earth slopes in three dimensions." *Proceedings of the Royal Society A*, 465(2110), 3145–3164.

Hachich, W. and Vanmarcke, E. (1983). "Probabilistic updating of pore pressure fields." *J. Geot. Eng. Div.*, ASCE, vol. 109, 373-385.

Hurst, H.E. (1951). "Long-term storage capacity of reservoirs." *Trans. Am. Soc. Civil. Eng.* 116, 770-799.

Lacasse, E.E. (1994). "Reliability and probabilistic methods." *Proc. 6th Int. Conf. Appl. Stat. Problems in Civil Eng.*, 225-227.

Lacasse, E.E. and and Nadim, F. (1996). "Uncertainties in characterizing soil properties." *ASCE Uncertainties'96 Conf. Proc.*, 49-75.

Li, K.S. and Lumb, P. (1987). "Probabilistic design of slopes." *Can. Geotech. J.*, 24(4), 520-535.

Low, B.K., Gilbert, R.B. and Wright, S.G. (1998). "Slope reliability analysis using generalized method of slices." *J. Geotech. Geoenviron. Eng.*, ASCE, 124(4), 350-362.

Low, B.K. , Lacasse, S. and Nadim, F. (2007) ''Slope reliability analysis accounting for spatial variation." *Georisk*, 1(4), 177-189.

Mandelbrot, B.B. (1965). "Une classe de processus homothetiques a soi: Application a la loi climatologique de H.E. Hurst." *C.R. Acad. Sci.*, Paris, 260, 3274-3277.

Matsuo, M. (1976). "Reliability in embankment design." Mass. Inst. Tech., Dept. Civil Eng., Report R76-33.

Rice, S.O. (1944). "Mathematical analysis of random noise." *Bell System Technical J.*, 32, 282.

Vanmarcke, E. (1975). "On the distribution of the first-passage time for normal stationary random processes." *J. Appl. Mech.*, 42: 215-220.

Vanmarcke, E. (1977a). "Probabilistic modeling of soil profiles." *J. Geotech. Eng. Div.*, ASCE, 103 (GT11) 1227-1246.

Vanmarcke, E. (1977b). "Reliability of earth slopes." *J. Geotech. Eng. Div.*, ASCE, 103 (GT11) 1247-1265.

Vanmarcke, E. (1980). "Probabilistic stability analysis of earth slopes." *Eng. Geol.*, 16: 29-50.

Vanmarcke, E. (2010). *Random Fields: Analysis and Synthesis*, 2nd Edition, World Scientific Publishing Company; 1st Edition, M.I.T. Press, 1983.

Wu, T.H. and Kraft, L.M. (1970). "Safety analysis of slopes." *J. Soil Mech. Found. Div.*, 96, 609-630.

Yucemen, W.S., Tang, W.H., and Ang, A.H.S. (1973). "A Probabilistic Study of Safety and Design of Earth Slopes." University of Illinois Research Report.

Probabilistic Methodology for Quantifying Regional Risk Profiles from Sea Level Rise

Bilal M. Ayyub[1]

ABSTRACT

Global climate likely trends and the consequent global sea level rise, combined with potentially increased rates of extreme storms, necessitate the reconsideration of current planning, engineering and management practices of infrastructure. Recent storms, such as the 2012 Hurricane Sandy, resulted in inundation of coastal areas, flooding of tunnels and subway stations, power loss, shutdown of nuclear power plants, etc. Risks from such storms entail significant uncertainties. Increasing resilience to disasters requires bold decisions and actions that may pit short-term interests against longer-term goals. Quantitatively assessing these risks requires the development of spatial risk profiles based on hazard likelihood assessment, scenario identification, consequence and criticality assessment using inventories of assets along coastal areas particularly of population centers, vulnerability and inundation assessment, and benefit-cost analysis to manage risks and enhancing infrastructure and community resilience. The paper focuses on the Washington DC area; however the methodology can be used to examine other regions.

1. INTRODUCTION

According to the United Nations Office for Disaster Risk Reduction (UNISDR 2012), half of the world's inhabitants, expected by 2025 to increase to roughly two-thirds, and the vast majority of property and wealth are concentrated in urban centers situated in locations already prone to major disasters, such as earthquakes and severe droughts, and along flood-prone coastlines. It also reported that the 2011 natural disasters, including the earthquake and tsunami that struck Japan, resulted in $366 billion in direct damages and 29,782 fatalities worldwide. Storms and floods accounted for up to 70 percent of the 302 natural disasters worldwide in 2011, with earthquakes producing the greatest number of fatalities. It is anticipated that such disasters would occur in increasing trends of storm rates and disaster impacts due to a combined effect of climate change and increased coastal inventory of assets (Ayyub et al. 2012). Although no population center or a geographic area can ever be risk free from natural or human-causes hazards, communities should strive to enhance resilience to the destructive forces or the impacts of

---

[1] Director of the Center for Technology and Systems Management, Professor of Civil and Environmental Engineering, University of Maryland College Park, MD 20742, USA. ba@umd.edu

resulting events that may claim lives and damage property. Risk perceptions of the risk landscape as assessed at the 2011 World Economic Forum places storms and climate change at high levels as summarized in Figure 1. Gilbert (2010) provided population-and-wealth-adjusted loss and fatality count trends from 1960 to 2009 to demonstrate that both are about flat without significant slopes; however noted that the U. S. is becoming more vulnerable to disaster due to increased population concentration in areas prone to natural disasters (Burby 1998) and Berke et al. 2008) and persisting inadequate condition of infrastructure (ASCE 2009 Report Card of Infrastructure).

The impacts of super storms, such as the 2005 Hurricane Katrina and the 2012 Hurricane Sandy, are at levels unseen previously. These two hurricanes are comparatively summarized in Table 1 according to selected attributes. These levels have attracted the attention of policymakers and have spurred the reexamination of engineering, planning and mitigation practices.
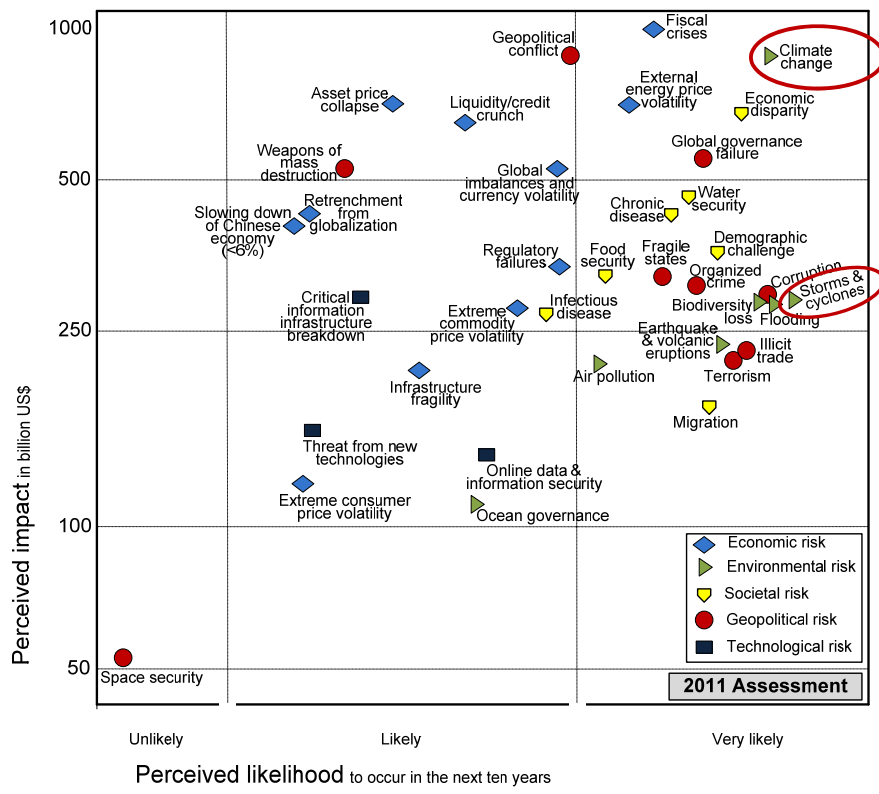
Figure 1. Perceived Risk Landscape in 2011

Table 1. Hurricanes Katrina and Sandy Compared

Attribute	Hurricane Katrina	Hurricane Sandy
Date	2005-10-25	2012-10-25
The Storm (Wikipedia)		
Fatalities	1,833	121
Property damage	$81b (2005 USD)	$72b NY & NJ (2012 USD)
Homes destroyed	214,700 in LA	305,000 in NY
Power outages	800,000	2.2 million
Businesses impacted	18,700	265,300

2. CARBON AND CLIMATE CHANGE

Carbon, as a primary element for all living systems, is present in *pools* (or *reservoirs*) in the Earth's atmosphere, soils, oceans and crust, and is in *flux* as it moves from one pool to another at different rates. The overall movement of the carbon can be described as a cycle. The Earth can be viewed as a whole with individual cycles linked to each on spatial and temporal scales to form an integrated global carbon cycle as shown schematically in Figure 2 that was constructed using values provided by the University of New Hampshire (2011). Pan et al. (2011) estimated a global carbon budget for two time periods of 1990-1999 and 2000-2007 of Figure 3 that clearly shows the increase of carbon under fossil fuel and cement over time. This increase goes unmatched in the carbon uptakes in efficiency with a potential for creating a prolonged time lag from emissions to uptakes. Such a time lag could drive other processes leading to global temperature increases and thereby contributing to sea level rise (SLR).

Global warming is generally considered a result of increasing atmospheric concentrations of greenhouse gasses, mainly due to human activity. Gillet et al. (2011) states that even if CO_2 (the major greenhouse gas) is no longer released into the environment, the effects of climate changes would continue as the West Antarctic ice sheet would still continue to melt. Global SLR could be 3 to 4 m by the year 3000 AD. Climate change due to CO_2 emissions is "irreversible". Antarctic temperature rise and rainfall are expected to get worse, even if all CO_2 emissions are stopped.

Fairbridge (1950, 1958, 1960 and 1961) documented that the ocean levels rose and fell over long time scales producing what has become known as the Fairbridge Curve of the Holocene Eustatic Fluctuations based on detailed observations off Western Australia and afterwards from elsewhere in the world. The oscillations include a relatively short periodicity component of relatively rapid rises and falls of up to four meters, although up to three meters is more common, taking place over periods of no more than 10 or 20 years. This short-periodicity component would now have catastrophic consequences for the world. Over the next 100 years and possibly within our lifetime such an occurrence is likely. The periodicities are revealed in a rich variety of sources, including: geology; geomorphology; glaciations; sediments; sand dunes; beach rock; the

circulation of the ocean; geomagnetic records; and the records of the isotopes of carbon, oxygen, beryllium, chlorine and hydrogen in tree rings, ice cores, biota, rocks, air and water (Mackey 2007; Finkl 1995, 2005).

Changes in the average sea level involve several global and regional factors along any particular coast. According to Cronin (2012), global processes include changes in ocean mass (glacio-eustasy from ice melt), ocean volume (steric effects), viscoelastic land movements (glacioisostatic adjustment GIA), and changes in terrestrial water storage. Moreover, regional processes, often connected to steric and glacial changes, include changes in ocean circulation (Meridional Overturning Circulation MOC), glacial melting, local GIA, regional subsidence and others. The factors, although interdependent with nonlinear associations, can be grouped as: (1) steric (volume) due to changes in temperature (thermosteric) and salinity (halosteric) levels of oceans; (2) worldwide carbon inventory; (3) the shape of the basins that contain the oceans; (4) the mass of water in these basins from melting of glaciers; and (5) local variations in land adjacent to the ocean basins. Most of the eastern and western United States coastlines are observing a steady rise. The Gulf Coast is observing a more concerning steady sea-level rise rate; whereas some locations in Alaska are actually observing a fall in sea level. This fall is due to uplifting of land due to coalitions between tectonic plates, i.e., the uplifting rate is greater than the sea level rise rate, making it appear as if sea levels were dropping when in fact land is moving more rapidly upwards. In addition to volumetric expansion of oceans and melting of ice sheets, ocean salinity can cause oceans to expand or contract, changing sea level both locally and globally. In simple terms, ocean salinity is primarily caused by the amount of carbon present in water. Carbon concentrations are greatest in the North Atlantic Ocean where industrialized nations are located (CCSP 2009; Dean 1987; IPCC 2007). These variables can form a basis for defining scenarios, termed storylines by IPCC (2007). Cronin (2012) reported that Paleoclimate, instrumental and modeling studies show that combinations of these factors can cause relatively rapid rates of sea-level rise exceeding 3 mm/yr over various timescales along particular coasts.

One of the most costly consequences of global warming is sea level rise (SLR), which is the result of thermal volumetric expansion of the oceans and the melting of global ice sheets (Grinsted et al. 2009). Northeastern coastal areas and coastal cities of the United States, such as Washington, DC are at a risk of inundation due to SLR. The short term effects of SLR are the flooding of low lying areas and the infiltration of salty water into fresh water sources. The long term effects include readjustment of coast lines due to land loss, and increase saltwater intrusion and erosion (Nicholls and Cazenave 2010). A study found that with the complete collapse of the West Antarctic Ice Sheet, Washington, DC could face up to 6.4 meters of flooding (Mitrovica et al. 2009).

Rising sea levels by the end of this century are estimated to impact at least 100 million people worldwide using the already recognized relatively conservative upper end of scenarios and assumptions (IPCC 2007). Among many climate scientists there exists considerable disquiet that this top end estimate could prove too low, as the contribution from polar ice melting still remains highly uncertain. The resulting impacts on global sea levels could be a rise on the order of 5.97 meters. An increase in the global trend is likely, and this increase can be on the order of two to two-and-a-half times what occurred in the 20th century, historically a period of the highest rate of sea level rise in the last thousand years (Kearney 2008).

One of the important economic consequences of sea level rise that merits immediate attention is the impact on ports, shipyards, naval installation, and coastal transportation arteries. As an example, in the Chesapeake Bay the Port of Baltimore services cargo, amounting to 32 million tons in 2004. The Port is directly responsible for 19,000 direct jobs ($2.4 billion in personal wages and salary), $2 billion in business revenue, and generates $278 million in state, county and municipal taxes (State of Maryland Governor's Office 2006). The total economic impact is well beyond these estimates. Comparable figures are available for the Port of Norfolk and Portsmouth in Virginia. This region includes also the United States' largest naval installation, having the added impact on national security and the ability to project national power to areas across the world. The impacts on other parts of the globe such as southern Asia can be total devastation for particular countries.

The challenge of such a sea level rise is indeed formidable, and requires immediate attention in order to examine associated risks and to assess the socioeconomic impacts for the purpose of developing appropriate long-term measures and mitigation strategies. SLR poses a major threat to people, property, and infrastructure. Risk studies (Ayyub 2003) are, therefore, essential for specific areas that are crucial but vulnerable. Understanding the risks and costs associated with SLR allows for the incorporation of counter measures to manage the risks of SLR. There are three possible ways of dealing with SLR: (1) protection of areas or cities by using flood walls and levees, (2) accommodating SLR yet maintaining infrastructure, (3) planned retreat from areas that are to be severely flooded. All of these options have risks, costs, as well as many social-economic implications and impacts that need to be considered for each affected area (Nicholls and Cazenave 2009). Size, importance, historical heritage, population density, infrastructural impact, and infrastructural planning of a region must be considered by lawmakers and city planners before deciding how to deal with SLR.

This paper investigates impacts of SLR and extreme storms by considering models of SLR, based on current sea level trends and prediction model of future SLR. A case study is presented using open-source information on the City of Washington, DC. An inventory of assets and infrastructure was created and damages were assessed using hypothetical SLR levels. Based on its results, ways in which damages due to SLR and extreme storms can be reduced are discussed.

Other impacts of a changing climate include the following: (1) urban heat, (2) extended hot weather, (3) extreme precipitation and flash flooding, (4) poor air quality, (5) salty water intrusion, (6) increase power consumption, etc. Adaptations to these changes are necessary.
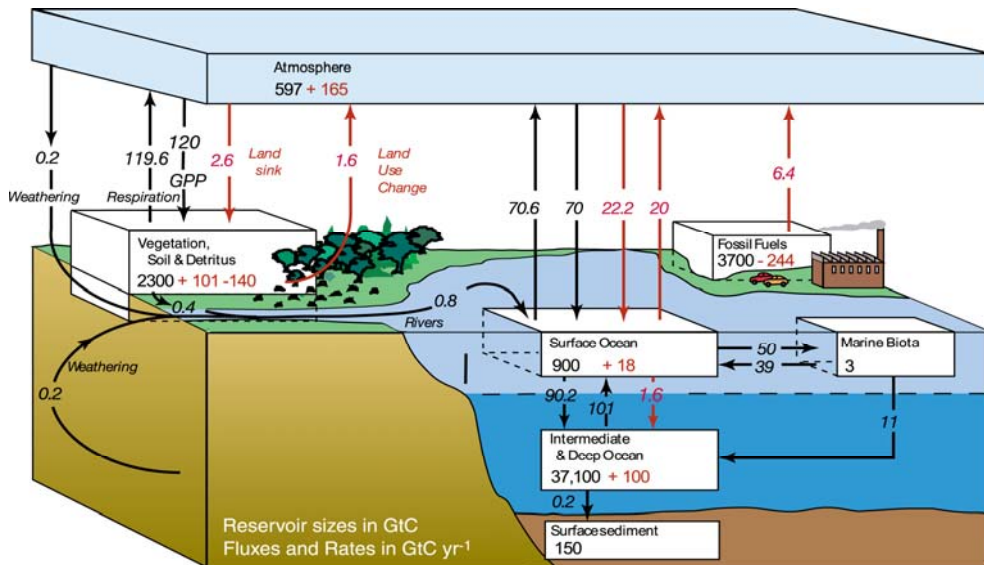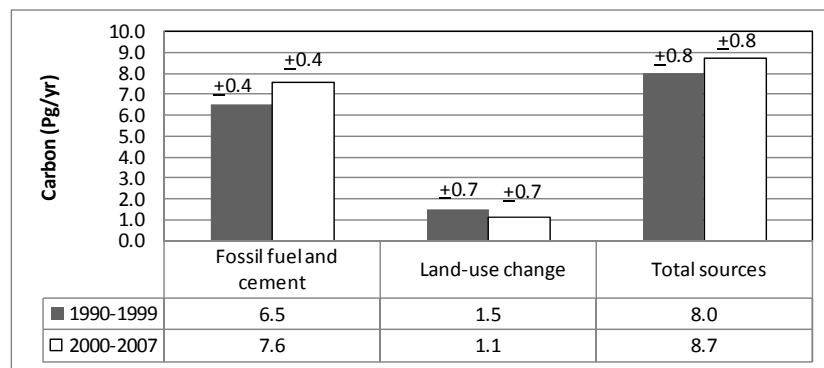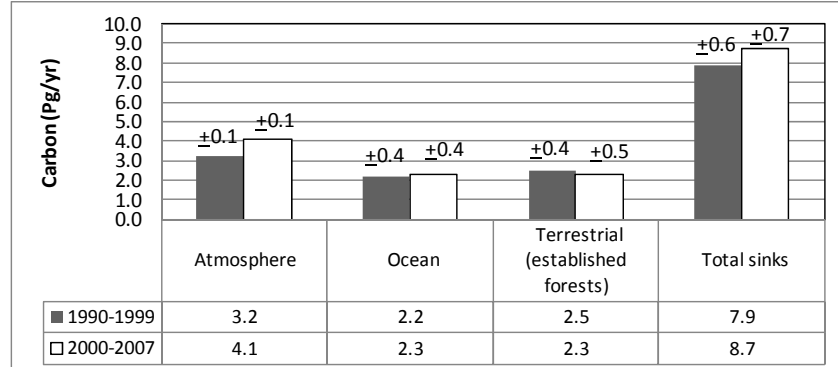
Figure 2. An Anthropogenic Carbon Cycle as Described in the 2007 IPCC WG1 (NOAA, GtC: gigatonnes of carbon; 1 GtC is equal to 10^9 tonnes of carbon or 10^{12} kg. 3.7 Gt carbon dioxide will give 1 GtC. To give you an idea how big this unit is: in 1997 the total supply of petroleum for the USA (including imports) was approximately 1 Gt per year.)

	Fossil fuel and cement	Land-use change	Total sources
1990-1999	6.5	1.5	8.0
2000-2007	7.6	1.1	8.7

(a) Sources (C Emissions)

	Atmosphere	Ocean	Terrestrial (established forests)	Total sinks
1990-1999	3.2	2.2	2.5	7.9
2000-2007	4.1	2.3	2.3	8.7

(b) Sinks (C Uptakes)
Figure 3. Carbon Budget for Two Time Periods

3. UNCERTAINTIES AND POTENTIAL ERRORS

The meteorological conditions, including temperature, precipitation and wind that characteristically prevail in a particular region are called collectively climate. The Intergovernmental Panel on Climate Change (IPCC 2007) defines climate as "the average weather, or more rigorously, as the statistical description in terms of the mean and variability of relevant quantities over a period of time ranging from months to thousands or millions of years." The period for averaging these variables has been classically taken as 30 years, as defined by the World Meteorological Organization. The IPCC (2007) also defines extreme weather events as being rare at a particular place and time of year; where rare means events falling outsides the bounds of the 10th and 90th percentiles of an observed probability density function. As for weather, the National Snow and Ice Data Center (NSIDC 2012) defines it as the "state of the atmosphere, mainly with respect to its effects upon life and human activities." The primary distinguishing feature from climate is that weather consists of the short-term, ranging from minutes to about 15 days, variations of the atmosphere state; whereas climate is characterized by a longer averaging period.

The ASCE Committee on Adaptation to a Changing Climate (CACC) is preparing a White Paper on bridging the gap between climate change science and the civil engineering practice (CACC 2013). The white paper summarizes global climate models and associated uncertainties, and defines for adaptation needs for the civil engineering practice. In this section, characteristics of global climate models and associated uncertainties are summarized.

Global climate models are available and used to examine trends and predictions based on four underlying components consisting of atmosphere, ocean, land surface, and sea ice. These global climate models solve the underlying equations of thermodynamics and fluid mechanics for key variables of interest that describe the atmospheric state. The variables are the temperature, pressure, humidity, winds, and water and ice condensate in clouds defined on a spatial grid of approximately 200 kilometers on each side (Randall et al 2007, Climate Change Science Program 2008). Some processes occur on a relatively small spatial or time scale. Such processes are included in the global model grid through parameterization, such as cloud formation and dissipation and convection; whereas topographic features are not well represented in these relatively large grid boxes. Global climate models can be used to show potentials for extreme events in rates and intensities. Extreme climate events also include persisting patterns of extreme weather events for some time, such as in a season in the case of drought or heavy rainfall over a season.

Many uncertainties are recognized in modeling global climate change, and scientists concern themselves with addressing and quantifying them. Uncertainty sources can be classified as (1) forcing uncertainty for future greenhouse gas emissions, (2) initial condition uncertainty, and (3) model imperfections associated with parameter values, such as for cloud formation and land cover effects (Stainforth et al 2007). Some of these uncertainties are expected to persist against scientific inquiry, for example, future greenhouse gas emissions depend on future government policies and future human behavior. This forcing uncertainty drives future emissions, and is modeled using different storylines by the IPCC (2007); however, recent evidence including the efforts at the 2012 Doha Climate Change Conference suggests that emissions may be above the ones indicated by the most extreme emission storylines. Another uncertainty example can be

described as model reliability where the global climate change models are better in simulating processes over large geographic areas and timescales than processes over smaller geographic areas and timescales. Similar in nature is that these models are better in simulating temperature than precipitation (Barsugli et al 2009). A global uncertainty source is the imperfect representation of the full complexity of the Earth system, such as temperatures at extreme ocean depths and gravitational forces, non-linear spatial and temporal feedbacks, and imperfect foresight of human behavior as described by Pielke (2004). Practicing engineers commonly are interested in local effects, and bringing results from these global climate change models to a local level is still associated with significant complexities and uncertainties (Barsugli et al 2009).

IPCC SREX (2012) provides an assessment of future changes in exposure, vulnerability, and climate extremes resulting from natural climate variability, anthropogenic climate change, and socioeconomic development. It also provides an assessment of the impacts of climate extremes on natural and human systems and the potential for disasters. Primary assessments that are relevant herein are:

- "Confidence in projecting changes in the direction and magnitude of climate extremes depends on many factors, including the type of extreme, the region and season, the amount and quality of observational data, the level of understanding of the underlying processes, and the reliability of their simulation in models."
- Models project substantial warming in temperature extremes by the end of the 21st century.
- It is likely that the frequency of heavy precipitation or the proportion of total rainfall from heavy falls will increase in the 21st century over many areas of the globe.
- The average tropical cyclone maximum wind speed is likely to increase, although increases may not occur in all ocean basins.
- It is likely that the global frequency of tropical cyclones will either decrease or remain essentially unchanged.
- There is medium confidence that there will be a reduction in the number of extratropical cyclones averaged over each hemisphere.
- There is medium confidence that droughts will intensify in the 21st century in some seasons and areas, due to reduced precipitation and/or increased evapotranspiration.
- Projected precipitation and temperature changes imply possible changes in floods, although overall there is low confidence in projections of changes in fluvial floods.
- It is very likely that mean sea level rise will contribute to upward trends in extreme coastal high water levels in the future.
- There is high confidence that changes in heat waves, glacial retreat, and/or permafrost degradation will affect high mountain phenomena such as slope instabilities, movements of mass, and glacial lake outburst floods."

Emanuel (2012), authoritatively expressing his perspective as a meteorologist, stated that "at its best, climate science deals in probabilities," and that scientists have inherent conservatism based on an asymmetric reward structure. According to this structure, "it is better to be a little late in what proves to be an important discovery than to publish too soon and be proved wrong. As a result, scientists often ignore apparent patterns in their data if there is as little as a 5 percent probability that they could have arisen by chance. But while this philosophy makes sense for science, it can be disastrous when applied to risk assessment." In risk assessment, engineers and

analysts consider many scenarios some of which are rare, i.e., with probabilities significantly smaller than the 5 percent, because of their significant potential impacts. Emanuel (2012) used the 2011 Fukushima Daiichi nuclear disaster as an example where the plant was built to withstand tsunamis triggered by offshore earthquakes up to magnitude 8.3 as the largest earthquake that scientists conservatively estimated might be possible. This *conservative* estimate for science, however, was anything but conservative in the arena of risk analysis. Risk analysis considers not only the probability but also the consequences, and in this case given the enormous potential downside, risk analysts would have increased safety margins in order to withstand larger magnitudes, such as the magnitude 9.0 quake, because of the associated consequences even though this quake magnitude would have been recognized in its design phase to be unlikely. The two probability types discussed herein are for two different respective purposes: (1) a science-related probability that is indicative of the knowledge reliability; (2) a risk-related probability that is for a scenario including rare ones. Someone would expect that the former to reach adequacy once the knowledge reliability exceeds 90% to 95%; whereas the adequacy of latter in terms of a truncation point for these probability values should be linked to the potential downside impacts.

Another important dimension is potential errors associated with engineering decisions in the design of civil or mechanical systems for a changing climate. Two error types can be defined in keep with statistical analysis and will be investigated in this study as follows:
- Error type I (alpha type). The decision to design for a changing climate and to eventually find out reliably through empirical evidence that climate does not change.
- Error type 2 (beta type). The decision to NOT design for a changing climate and to eventually find out reliably through empirical evidence that climate has changed.

These two error types have significant asymmetry in terms of their outcomes. These error types should be considered along with the most likely outcomes of the changing climate leading to serious but manageable consequences, and the somewhat less probable, but not impossible, benign outcomes. As a result, policymakers might differ on how far to go to manage these highly asymmetric risks; however, according to Emanuel (2012), "the argument that there is no risk or that we should do nothing is both scientifically and morally indefensible."

Link global or regional climate modeling and extreme environments, such as wind, is a primary scientific challenge as discussed in the 2012 National Academy of the Sciences (NAS) report on a national strategy for advancing climate modeling. It would be desirable to eventually develop such a capability of using climate models as a basis for weather models which in turn form the basis for some computational fluid dynamics (CFD) modeling of rain, wind, etc. with Monte Carlo techniques used to develop probability distribution functions. Such a concept was used in developing risk models for hurricane prone regions (Ayyub et al 2009a and 2009b). Such a major effort is beyond the scope of this paper and should be explored in future studies.

4. A RISK FRAMEWORK

This paper outlines a risk framework for SLR and extreme storms that includes quantifying the potential damages to a region's property inventory and infrastructure by using the City of Washington, DC as an example. IPCC SREX (2012) outlined the process as shown in Figure 4 to describe how disaster risk management and climate change adaptation can influence the degree

to which extreme events translate into impacts and disasters. A block diagram of a methodology to quantify potential damages is provided in Figure 5 by defining an inventory of assets for a particular region (Ayyub et al. 2012).
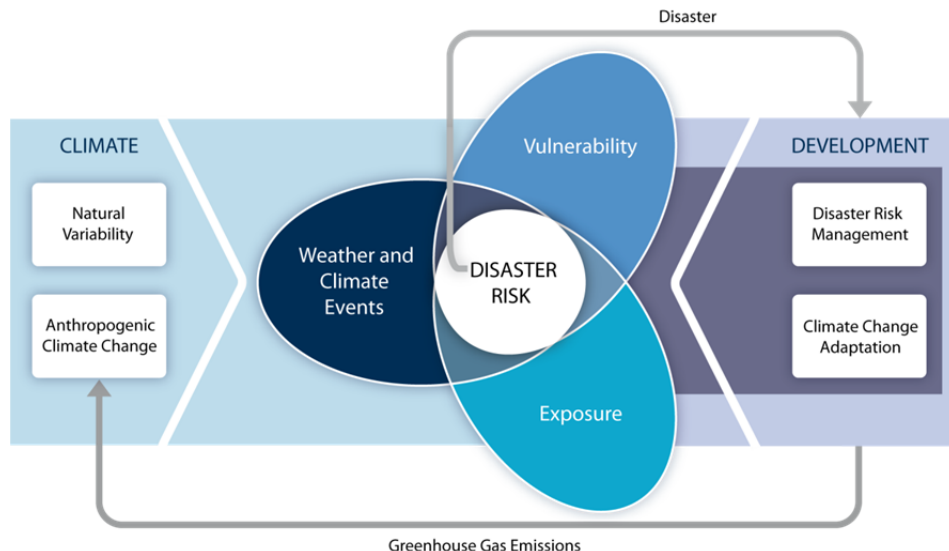
Figure 4. Disaster Risk Management and Climate Change Adaptation (IPCC SREX 2012)
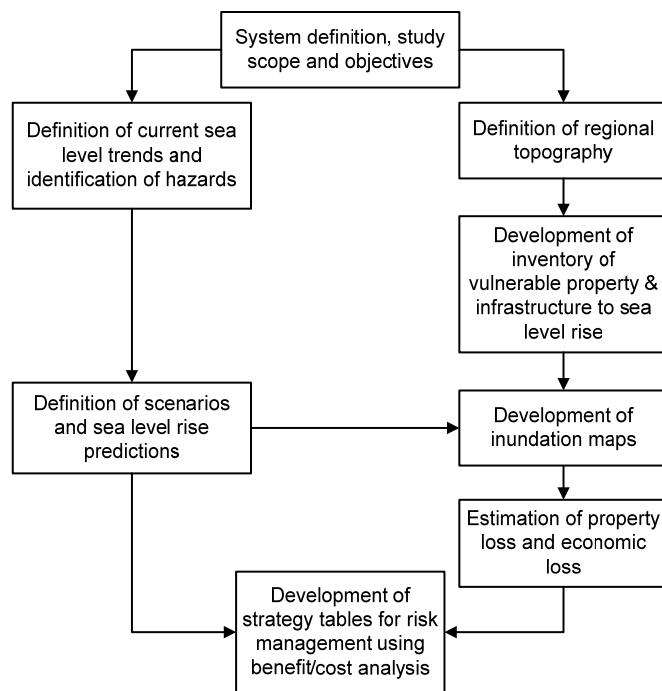
Figure 5. Definition of Vulnerable Asset Inventory to Sea Level Rise (after Ayyub et al. 2012)

4.1 *Risk Definition and Analysis*

Defining risk as the potential outcomes for a system resulting from an uncertain exposure to a hazard or generally as a result of an uncertain event (Ayyub 2003) offers a basis for risk quantification for identified risk events or event scenarios. This definition focuses on loss as the primary impact of interest, and on estimating associated rates, system vulnerabilities and

potential consequences. This definition offers a basis to quantify risk as the rate (measured in events per unit time, such as a year) or annual probability of lives, economic, environmental, and social/cultural losses occurring due to an event including the non-performance of an engineered system or component. Another common representation of risk is in the form of an exceedance rate (or exceedance probability) function of consequences. In a simplified notional (or Cartesian) product, it is commonly expressed as:

$$\text{Risk}=\text{Rate}\times\text{Vulnerability}\times\text{Consequence} \tag{1}$$

This equation not only defines risk but also offers strategies to control or manage risk: by making the system more reliable through vulnerability reduction, by reducing the potential losses resulting from a failure, or impacting event rates. As for SLR and extreme storms, the vulnerability part of the equation can be influenced by engineers by hardening existing systems or by adding additional protection to reduce fragilities; however the consequence part is highly dependent upon the actions and decisions made by populations at risk, government and local officials, including land-use changes, protection measures of coastal areas, response and population relocation plans and practices. Event rates can be impacted by policies relating to global warming and carbon reduction as examples. In densely populated areas, simply increasing the reliability of a protection system may not reduce risks to acceptable levels. Moreover, consequences could increase through continued development of flooding-prone areas offsetting any risk reductions.

Risk can be defined broadly to encompass impacts treated as departures from a stated objective where a departure can be either adverse or favorable relative to the objective. ISO (2009) provides such a broad definition as "the effect of uncertainty on objectives." In analyzing SLR and extreme storms, the focus herein is on the adverse departure from stated objectives, and hence the use of the traditional risk definition as previously stated is indeed consistent with the ISO definition.

Probabilistic risk analysis as described by Ayyub (2003) can be used to develop the overall risk analysis methodology suitable for quantifying and managing risks associated with SLR and extreme storms. Risk assessment is a systematic process for quantifying and describing the nature, likelihood and magnitude of risk associated with some substance, situation, action or event, including consideration of relevant uncertainties. Its objective is to provide, to the maximum extent practical, a scientific basis for answering the following questions: (1) What could happen? (2) How can it happen? (3) How likely is it to happen? (4) What are the consequences if it happens and associated uncertainties? (5) What can be done to reduce the risks in a cost effective manner? (6) What effects would these risk management decisions have on subsequent risks and options?

In an all-hazard context, risk analysis answers these questions by defining an exhaustive set of hazard or threat scenarios, assessing the likelihoods, vulnerabilities, and consequences reflecting existing threat or hazard reduction countermeasures, vulnerability reduction actions, and consequence mitigation actions. The combination of these three fundamental elements (hazard or threat, vulnerability, and consequence) gives the familiar expression for risk as provided in Eq. 1.

The process of risk management entails identifying actions, including countermeasures, planning options, land-use changes, consequence mitigation strategies, etc. aimed at reducing these risks

in an efficient and cost-effective manner with limited impact on future options. The selection of risk reduction alternatives depends on two factors: their relative cost effectiveness, any constraints including political and legal considerations. A common measure of cost-effectiveness for a given investment alternative is its benefit-to-cost ratio. In general, the computation of defensible benefit-to-cost ratios requires consideration of all aspects of risk, including consequence (economic loss, public health and safety, etc.), vulnerability (physical and otherwise), and threat likelihood within a unified probabilistic framework. The rationale behind this assertion is that a probabilistic paradigm permits rational and coherent comparisons among decision alternatives that affect multiple assets to determine the most cost-effective risk reduction strategies. Furthermore, quantification of risks under various investment alternatives facilitates a rational comparison with other societal risks (such as fire, earthquake, disease, flood and other natural hazards) to assist in establishing acceptable risk levels and achieve all-hazard risk reduction objectives (Ayyub et al. 2007, McGill et al. 2007).

4.2 *A Methodology for Risk Quantification*

Risk of SLR and extreme storms can be quantified using a regional surge level (S) probability distribution f_S at time t, scenarios of underlying variables (i) defining S and respective probabilities P_i, regional storm rate (λ) that is dependent on S and i, scenarios of underlying variables (j) defining λ_j and respective probabilities Q_j, and the conditional probability $P(C>c)$ with which a consequence valuation (C) exceeds a level (c) for i, j and coastal state at time t. A loss-exceedance probability at time t can be expressed as follows (Ayyub 2012):

$$P(C > c; t) = \sum_i P_i \left(\int_s f_S \left(\sum_j \lambda_{ij} Q_j P(C > c \,|\, i, j) \right) ds \right) \tag{2}$$

where f_S is probability density function of surge level (S) at time t; P_i is the probability of a scenario of underlying variables (i) defining S; λ is regional storm rate that is dependent on S and i; Q_j is the probability of a scenario of underlying variables (j) defining λ; and $P(C>c|i, j)$ is the probability that the consequence C exceeds c under a state defined by the pair (i, j) and the corresponding state of the coast at time t. Summations are over all scenario types i and j using a suitable discretization. The increased storm activities would include increased water depth, tidal effects, shoreline changes if any, and wave run-up. This model is consistent with recently developed and used risk model for natural hazards, such as the risk model for developing protection strategies of hurricane-prone regions (Ayyub et al. 2009a and 2009b).

Figure 6 provides the logic and computational flow diagram for the proposed risk methodology for SLR with extreme storms at a particular region starting with hazard identification and definition, followed by inventory definition to estimate losses based on inundation mapping, and finally constructing risk profiles and estimating associated uncertainty. This process requires the discretization of the underlying variables and system states according to Eq. 2 (Ayyub et al. 2012).
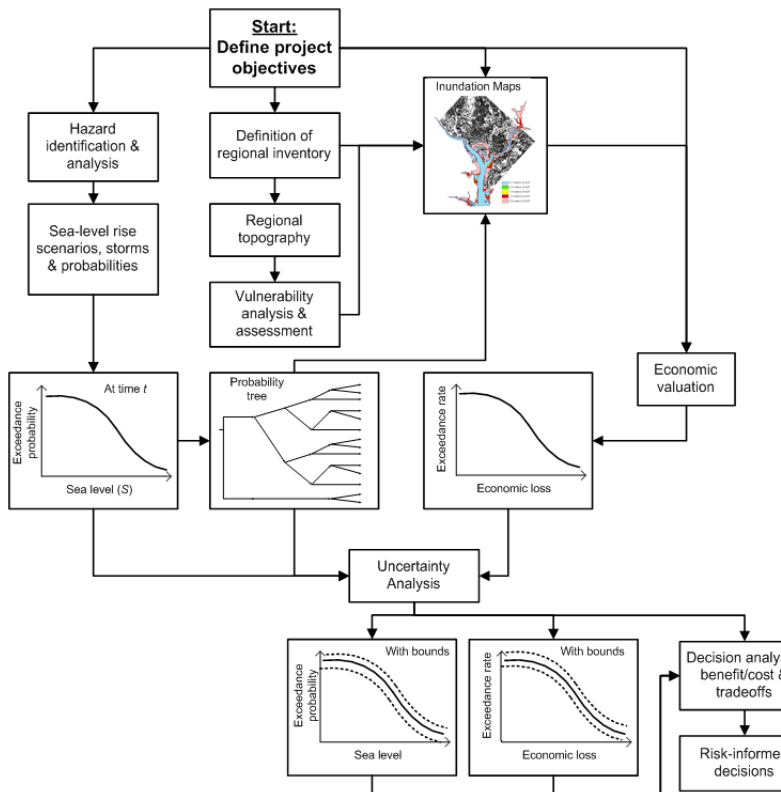
Figure 6. A Risk Methodology for Sea Level Rise and Extreme Storms at a Particular Region (Ayyub 2012)

4.3 *Uncertainties in Risk Quantification*

One of the objectives of risk analysis is to quantitatively assess the uncertainties associated with resulting risk profiles. A generalized treatment of uncertainty is available as provided by Ayyub and Klir (2006); however the methodology proposed in this paper utilizes a simplified treatment that is familiar to practitioners in which two fundamentally different sources of uncertainty affecting an estimated risk profile are considered. The first is attributed to the inherent randomness of events in nature. These events are predicted in terms of their likelihood of occurring (e.g., the chance of storm occurrence). This source of uncertainty is known as *aleatory uncertainty* and is, in principle, irreducible within present and foreseeable state of knowledge. The second source of uncertainty is attributed to our lack of knowledge or data. For example, the ability to determine the likelihood of an event (i.e., its rate of occurrence) requires that certain data be available. Depending on the volume of data that is available, the accuracy of the estimate of the rate of occurrence will vary. If limited data are available, the estimated rate may be quite uncertain (i.e., with a wide interval for a prescribed confidence level). A second type of knowledge uncertainty is attributed to our lack of understanding (e.g., knowledge) about the physical processes that must be modeled (e.g., the meteorological processes that generate hurricane events). Often scientists and engineers have interpretations of existing data and models of physical processes of interest that often competing in the sense they lead to different results, while at the same time are consistent with observations. In these instances expert evaluations are often required to assess the current state of knowledge and to quantitatively evaluate the level of uncertainty. These sources of uncertainty are referred to as *epistemic* (knowledge-based) *uncertainty*. The distinction between what is aleatory and what is epistemic uncertainty can often

seem arbitrary. For example, the distinction depends on the models that are used in a particular analysis. In addition, their estimates can change in time. Nonetheless, making a distinction between the sources of uncertainty in logical manner helps ensure that all uncertainties are quantified and those that can be reduced with additional data or knowledge identified. In principle, epistemic uncertainties are reducible with the collection of additional data or the use/development of improved models. However, in a given project, it is typically not possible to reduce these uncertainties. It should be noted that epistemic uncertainties in each part of the analysis lead to uncertainty in the final risk results. Propagating the uncertainties of the individual parts of the analysis through to the final result produces a probability distribution on the risk profile as provided in Figure 6.

4.4 *Risk Management*

The risk management phase assesses the cost-effectiveness of proposed countermeasures and consequence mitigation strategies for reducing the risk associated with an asset or portfolio of assets or a region. In the context of sea level rise and extreme storms, countermeasures aim to reduce vulnerabilities of coastal lines, property and asset exposure, impact on resources and populations, and land use changes. Consequence mitigation strategies aim to reduce the potential consequences given the occurrence of a successful scenario (Ayyub 2003). The probability of realizing a favorable benefit-to-cost ratio can be represented as follows:

$$P\left(\frac{\text{Benefit}}{\text{Cost}} \geq 1\right) = 1 - P\left(\text{Benefit} - \text{Cost} \leq 0\right) \tag{3}$$

where both benefit and cost in Eq. 3 are random variables. With knowledge of these distributions, the probability of realizing a favorable benefit-to-cost ratio can be computed using reliability assessment techniques including Monte Carlo simulation. It should be noted that the uncertainty associated with the benefit is typically greater than the uncertainty associated with the cost of the strategy.

5. PREDICTION OF SEA LEVEL RISE AND EXTREME STORMS

5.1 *Prediction Models*

The 2007 IPCC predicted an overall global SLR of 0.6 m by the year 2100; however, recent studies of the Antarctica ice sheet have increased the prediction to over 1 m. From the late 19th century, the rate of SLR has been estimated to be 1.7 ± 0.3 mm/year; however, in the 1990's and 2000's this rate increased to 3.3 ± 0.4 mm/year. The Antarctic coast is losing about 26 km[3] of ice per year, but about 150 km[3] of ice per year is melting from the West Antarctic. Over the next millennium, SLR could range approximately from 6 to 9 meters. The 2007 IPCC report used four storylines for sea level and temperature rise prediction to the year 2100, as listed in Figure 7. These four narratives, called also storylines, describe potential future conditions of the environment in the 21st century with regard to greenhouse gasses and aerosol precursor emissions (SRES scenarios 2011). The narrative provided in the figure can be used to generate a family of scenarios based on different social, economic, and scientific developments. The scenarios project the future defined by conflicting trends such as economic vs. environmental, and globalization vs. regionalization. These scenarios were used in integrated assessment models to predict sea level rise. Forty different scenarios were created, none of which was associated with an occurrence probability (SRES scenarios 2011).

The methodology proposed in this paper builds on trends and predictions of SLR. A number of different models are cited herein including the IPCC 2007 prediction models, the 2009 Vermeer and Rahmstorf model, and the 2009 Grinsted, Moore, and 2009 Jevrejeva model. These models are summarized in Figure 8 with the uncertainties associated with their predictions.

Data of SLR in the Washington, DC area was obtained from NOAA as presented in Figure 9. SLR rates for other cities are available as provided by Ayyub et al. (2012). Figure 9 shows the results from a linear model based on NOAA's station number 8594900. Based on the data, a rough timeline and a linear model of SLR were created. The record used in Figure 8 is relatively short and might not appropriately predict long term trends. Such predictions should be examined with other considerations and models of global sea level rise, climate change, and carbon budget lags. A geospatial and analytical model of the city was created and analyzed in conjunction with the SLR model. By defining the topography of the city and the location of infrastructure with respect to topography, inundation maps can be generated. Analysis of potential property and economic losses can be produced, along with countermeasures to reduce the damages.

Increasing economic emphasis ⟶

A1 storyline	**A2 storyline**
World: market-oriented Economy: fastest per capita growth Population: 2050 peak, then decline Governance: strong regional interactions; income convergence Technology: three scenario groups: • A1F: fossil intensive • A1T: non-fossil energy sources • A1B: balanced across all	World: differentiated Economy: regionally oriented; lowest per capita growth Population: continuously increasing Governance: self-reliance with preservation of local identities Technology: slowest and most fragmented development
B1 storyline	**B2 storyline**
World: convergent Economy: service and information based; lower growth than A1 Population: same as A1 Governance: global solutions to economic, social and environmental sustainability Technology: clean and resource-efficient	World: local solutions Economy: intermediate growth Population: continuously increasing at lower rate than A2 Governance: local and regional solutions to environmental protection and social equity Technology: more rapid than A2; less rapid, more diverse than A1/ B1

Increasing global integration ⟶ (left vertical axis)
Increasing regional emphasis ⟶ (right vertical axis)

⟵ Increasing environmental emphasis

Figure 7. The IPCC Storylines for Producing Scenarios (Adapted from IPCC 2007)
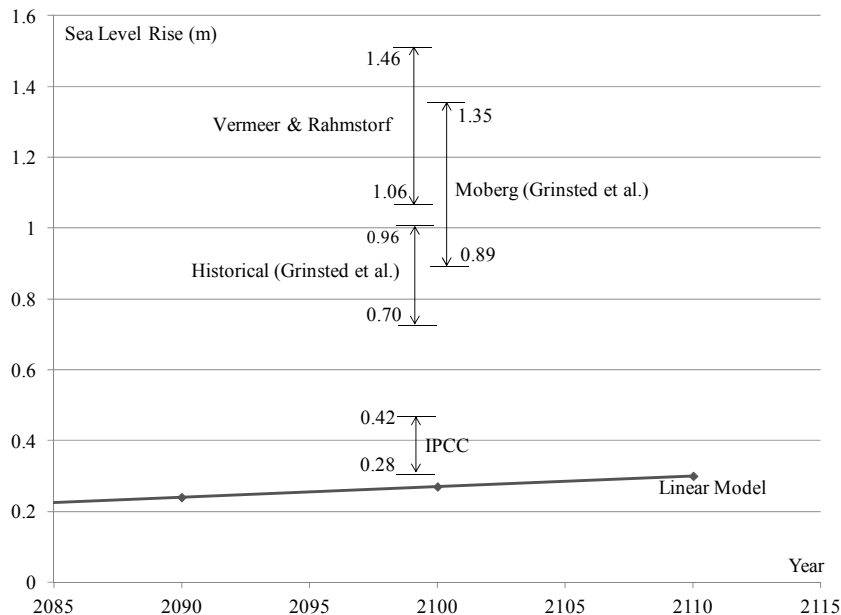
Figure 8. Predicted Sea Level Rise for 2100 using Several Models
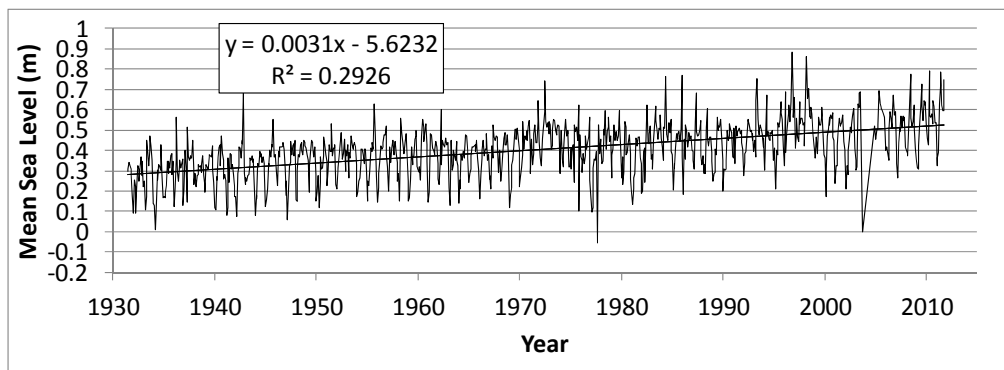
Figure 9. Linear Sea Level Rise for Washington, DC, from a NOAA Station from 1930 till 2010

5.2 *Prediction Uncertainties*

Several uncertainty sources need to be addressed to improve SLR prediction models that are under ongoing examinations and investigations. A primary source of uncertainty is the estimate of ice loss from the Greenland and Antarctic ice sheets as a result of rapid accelerations in ice flow. IPCC (2007) concluded that "understanding of these effects is too limited ... to provide a best estimate or an upper bound for sea level rise" in the twenty-first century; however excluding these effects limited SLR projections to the range 0.26 to 0.59 meters by the end of the century for their highest-emissions scenario. Observations from satellites reveal that Greenland and Antarctic ice sheets are losing mass overall at a faster rate that can be explained by melting and snowfall that can be explained perhaps by the speed-up of many outlet glaciers on Greenland and ice streams in the West Antarctic Ice Sheet discharging ice into the sea. Changes to this assumption could make the SRL as much as one to two meters (Lowe and Gregory 2010). The IPCC storylines of Figure 7 are uncertainty sources that cannot be resolved. The storylines impacts the carbon cycle among other factors that in turn affects the SLR through climate change and ocean capacity and condition changes relating to temperature, acidity, salinity, etc. At a

regional level, differentiating between SLR and subsidence of the ground, i.e., values obtained from NOAA (see Figure 8) represent only the net difference, not the global SLR values. The contribution of global SLR to the local SLR for a region is not fully coupled in prediction models. Other factors that could affect sea level are temperature variations along the full depth of oceans, changes in the shape of the oceanic basins and in land/sea distribution occurring over much longer geological timescales, and microbial carbon pumps in the oceans (Jiao et al. 2011). In order to enhance prediction, global SLR needs to be converted to local predictions and calibrated to local SLR measurements from NOAA stations and geological examinations.

Relating changes in rates and intensities of extreme storms to SLR is an important missing link that has been identified and is being examined by researchers; however practical and reliable models for these extreme storms are unavailable.

6. WASHINGTON DC AS AN EXAMPLE

Figure 10 shows inundation maps of Washington DC, as an example, using hypothetical SLR of 0.1 m, 0.4 m, 1.0 m, 2.5 m, and 5.0 m. Each image shows the clipped river shape and the streets data layer of Washington, DC (Ayyub et al. 2012). The Washington Post reproduced the results of Figure 10 as shown in Figure 11 (Washington Post Nov 4, 2012). The Washington Post interpreted the results as resulting from a powerful hurricane making landfall around Virginia Beach that would push loads of water into the Chesapeake Bay, causing a massive storm surge up the Potomac. Figure 12 shows the direct monetary losses of residential and some commercial properties that as reported in the city's databases as a function of SLR (Ayyub et al. 2012).
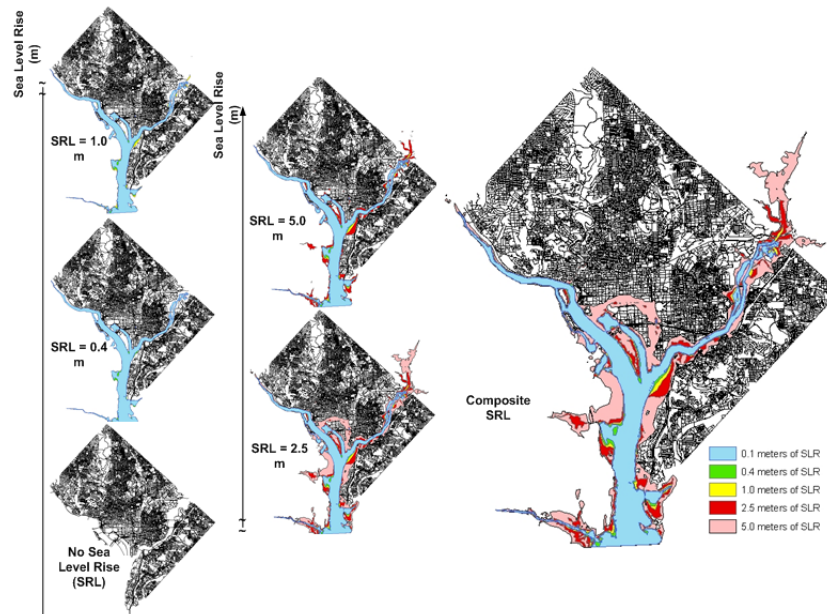
Figure 10. Impact of Sea Level Rise on Washington DC for 0.1m, 0.4m, 1m, 2.5m, and 5.0m (Ayyub et al. 2012)
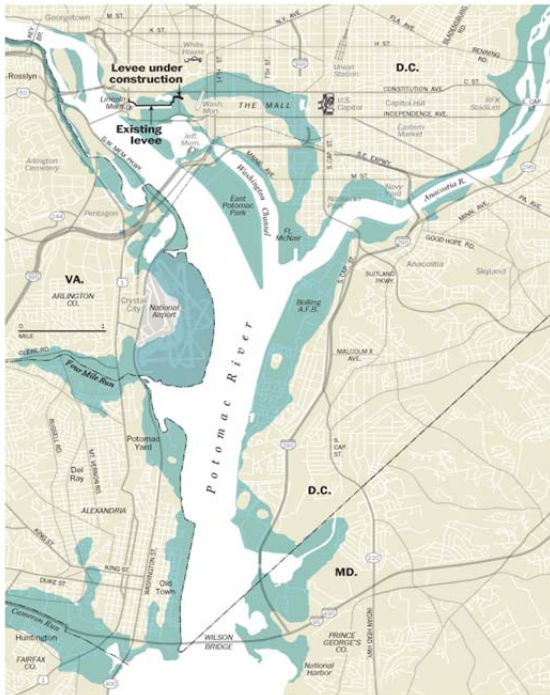
Figure 12. The Impact of a Powerful Hurricane Making Landfall around Virginia Beach, on Washington, DC (Washington Post 2012 based on Results by Ayyub et al. 2012)
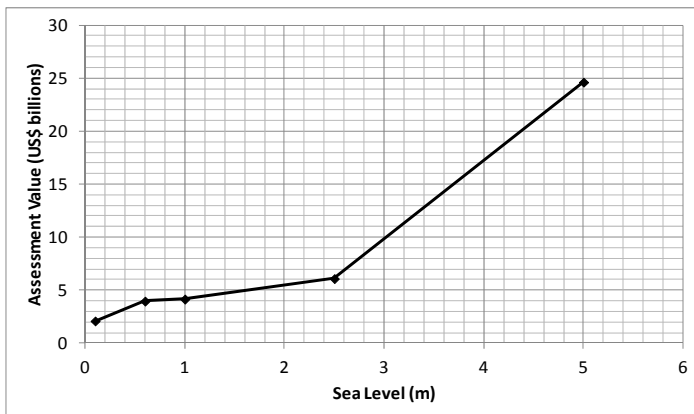
Figure 12. Assessment Value of Properties in DC vs. Sea Level Rise (Ayyub et al. 2012)

8. CONCLUSIONS

Models for global sea level rise indicate that a dramatic rise in the sea level trend is only a few decades away with potentially increasing extreme-storm rates and intensities. The threat posed by these changes to the world's coastal infrastructure is without historical parallels. Facing this challenge will require that engineers and scientists provide the necessary information on future coastal dynamics and risks affecting infrastructures and the social – economic and life – sustaining services they provide. However, uncertainty associated with our models should not forestall calls on the engineering community to provide adaptation solutions regardless of the lack of precedent or inadequate understanding.

Quantifying risk using a probabilistic framework produces hazard (elevation) and loss-exceedance probability curves based on a spectrum of SLR scenarios based on the mean sea

level as a function of time and increased storm rates with associated surges, waves and precipitation with uncertainty quantification. The methodology provided in this paper is a process for evaluating the loss potential for a region covering land-use changes, population affected, and property at risk by considering the topography and asset inventory for the region. The quantification of risk will enable decision makers to consider various alternatives to manage risk through setting appropriate policy relating to land use, land-use changes, infrastructure planning, building requirements and permits, water resource planning, and the enhancement of consequence mitigation measures.

The paper offers a preliminary, conceptual framework for quantifying SLR and extreme storm risks. The methodology requires refinement and additional development of computational details. Moreover the state of inventory of regions requires marked enhancements by focusing on coastal areas. The DC inventory used in this paper was based on open sources and is incomplete and/or inaccurate along the coastal lines. The increase in storm activity with wave run-up intensity escalation due to the rising sea level requires further investigation. The impacts of such increased activities at coastal lines would lead to interdependence with land-use and human-activity changes creating a need to examine SRL in socioeconomic system modeling.

BIBLIOGRAPHY AND REFERENCES

ASCE Committee on Adaptation to a Changing Climate (CACC), 2013. "Bridging the Gap between Climate Change Science and the Civil Engineering Practice," White Paper, T. Vinson (Committee Chair), Reston, VA.

ASCE Standard 7, Minimum Design Loads for Buildings and other Structures, Reston, VA.

ASCE, 2009. Report Card for America's Infrastructure, Reston, VA.

Ayyub, B. M., 2003. Risk Analysis in Engineering and Economics, Chapman and Hall/CRC Press, Boca Raton, FL.

Ayyub, B. M., 2013, "Systems Resilience for Multi-Hazard Environments: Definition, Metrics and Valuation for Decision Making," Working paper CTSM13-01, Center for Technology and Systems Management, University of Maryland, College Park, MD.

Ayyub, B. M., and Klir, G. J., 2006. Uncertainty Modeling and Analysis in Engineering and the Sciences, Chapman & Hall/CRC, Press Boca Raton, FL.

Ayyub, B. M., and McCuen, R. H., 2011. Probability, Statistics and Reliability for Engineers and Scientists, Chapman/Hall, Francis and Taylor, FL.

Ayyub, B. M., Braileanu, H. G., and Qureshi, N., 2012, "Prediction and Impact of Sea Level Rise on Properties and Infrastructure of Washington, DC," Risk Analysis Journal, Society for Risk Analysis, 32(11), 1901-1918.

Ayyub, B. M., Foster, J., McGill, W. L., 2009a, "Risk Analysis of a Protected Hurricane-Prone Region I: Model Development," ASCE Natural Hazards Review, May 2009, 38-53, DOI: 10.1061/(ASCE)1527-6988(2009)10:2(38).

Ayyub, B. M., Foster, J., McGill, W. L., 2009a. Risk Analysis of a Protected Hurricane-Prone Region I: Model Development, ASCE Natural Hazards Review, 10:2(38), 38-53.

Ayyub, B. M., McGill, W. L., Foster, J., Jones, H. W., 2009b, "Risk Analysis of a Protected Hurricane-Prone Region II: Computations and Illustrations," ASCE Natural Hazards Review, May 2009, 54-67, DOI: 10.1061/(ASCE)1527-6988(2009)10:2(38).

Ayyub, B. M., McGill, W. L., Foster, J., Jones, H. W., 2009b, Risk Analysis of a Protected Hurricane-Prone Region II: Computations and Illustrations, ASCE Natural Hazards Review, 10:2(38), 54-67.

Ayyub, B. M., McGill, W. L., Kaminskiy, M., 2007, Critical Asset and Portfolio Risk Analysis for Homeland Security: An All-Hazards Framework, Risk Analysis International Journal, Society for Risk Analysis, 27(3), 789-801.

Barsugli, J., Anderson, C., Smith, J. B., and Vogel, J. M., 2009. Options for Improving Climate Modeling to Assist Water Utility Planning for Climate Change. Water Utility Climate Alliance, http://www.wucaonline.org/assets/pdf/pubs_whitepaper_120909.pdf

Barth, J., 1984a, "The Literature of Replenishment: Postmodernist Fiction," The Friday Book: Essays and Other Non-Fiction, The Johns Hopkins University Press, Baltimore, MD.

Barth, J., 1984b, "The Literature of Exhaustion," The Friday Book: Essays and Other Non-Fiction, The Johns Hopkins University Press, Baltimore, MD.

Berke, P., Kartez, J., and Wenger, D., 2008, "Recovery after Disaster: Achieving Sustainable Development, Mitigation and Equity," Disasters, 17, 93-109.

Burby, R. (ed.), 1998. Cooperating with Nature: Confronting Natural Hazards and Land-use Planning for Sustainable Communities. Joseph Henry Press, Washington, DC.

CCSP, 2009. Coastal Sensitivity to Sea-Level Rise: A Focus on the Mid-Atlantic Region. A report by the U.S. Climate Change Science Program and the Subcommittee on Global Change Research, U.S. Environmental Protection Agency, Washington, DC.

Climate Change Science Program (CCSP), Bader, D.C., Covey, C., Gutowski Jr., W. J., Held, I. M., Kunkel, K. E., Miller, R. L., Tokmakian, R. T., and Zhang, M. H., (Authors), 2008. Climate Models: An Assessment of Strengths and Limitations. Department of Energy, Office of Biological and Environmental Research, Washington, D.C., USA.

Cronin, T. M., 2012, "Rapid Sea-level Rise," Invited Review, Quarterly Science Reviews, 56, 11-13.

Dean, R., 1987. Responding to Changes in Sea Level, National Academy Press, Washington, DC.

Ellingwood, B.R., & Mori, Y., 1993, "Probabilistic Methods for Condition Assessment and Life Prediction of Concrete Structures in Nuclear Plants," Nuclear Engineering and Design, Vol. 142, 155-166.

Emanuel, K., 2012, "Probable Cause: Are scientists too cautious to help us stop climate change? An article in Foreign Policy on November 9, 2012, http://www.foreignpolicy.com/articles/2012/11/09/probable_cause?page=0,1.

Fairbridge, R. W., 1950. The Geology and Geomorphology of Point Peron, Western Australia, Journal of the Royal Society of Western Australia, 33, 1-43.

Fairbridge, R. W., 1958. Dating the Latest Movements in the Quaternary Sea Level. New York Academy of science Transactions, 20 471-482.

Fairbridge, R. W., 1960. The Changing Level of the Sea, Scientific American, 202 (5), 70-79.

Fairbridge, R. W., 1961. Eustatic Changes in Sea-Level, in L. H. Ahrens, K. Rankama, F. Press and S. K. Runcorn (eds), Physics and Chemistry of the Earth, Vol. 4, London: Pergamon Press, 99-185.

Finkl, C W., Jr., (ed.), 2005. The Sun, Earth and Moon In Honor of Rhodes W. Fairbridge. J. of Coastal Research, Special Issue No. 42.

Finkl, C. W., Jr., (ed.), 1995. Holocene Cycles: Climate, Sea Levels, and Sedimentation. A Jubilee Volume in Celebration of the 80th Birthday of Rhodes W. Fairbridge. J. of Coastal Research, Special Issue No. 17.

Fox, D., "Could East Antarctica Be Headed for Big Melt?" *Science* 328.5986: 1630-631, 2010.

Gilbert, S. W., 2010. Disaster Resilience: A Guide to the Literature. NIST Special Publication 1117, Office of Applied Economics, Engineering Laboratory, National Institute of Standards and Technology, Gaithersburg, MD.

Gillet, N.P., Arora, V.K., Zickfeld, K., Marshall, S.J., and Merryfield, W.J. "Ongoing Climate Change following a Complete Cessation of Carbon Dioxide Emissions." *Nature Geoscience* 4.2 (2011). *Nature Geoscience*. 11 Jan. 2011. Web. 15 Jan. 2011. http://www.nature.com.proxy-um.researchport.umd.edu/ngeo/journal/vaop/ncurrent/full/ngeo1047.html, 2011.

Grinsted, A., Moore, J., and Jevrejeva, S., "Reconstructing Sea Level from Paleo and Projected Temperatures 200 to 2100AD." *IOP Conference Series: Earth and Environmental Science* 6.1:012001, 2009.

Intergovernmental Panel of Climate Change (IPCC), 2007, Solomon, S., Qin, D., Manning, M., Chen, Z., Marquis, M., Averyt, K. B., Tignor, M., and Miller, H. L. (eds.), Climate Change 2007: The Physical Science Basis. Contribution of Working Group I to the Fourth Assessment Report of the Intergovernmental Panel on Climate Change. Cambridge University Press, Cambridge, United Kingdom and New York, NY, USA.

Intergovernmental Panel of Climate Change (IPCC), 2012, Special Report on Managing the Risks of Extreme Events and Disasters to Advance Climate Change Adaptation (SREX), http://ipcc-wg2.gov/SREX/report/, Cambridge University Press, Cambridge, United Kingdom and New York, NY, USA.

IPCC SRES Scenarios." *Socioeconomic Data and Applications Center*. IPCC Data Distribution Centre. Web. 04 Mar. 2011. <http://sedac.ciesin.columbia.edu/ddc/sres/>.

IPCC, 2007: Summary for Policymakers. In: *Climate Change 2007: The Physical Science Basis. Contribution of Working Group I to the Fourth Assessment Report of the Intergovernmental Panel on Climate Change* [Solomon, S, Qin, D, Manning, M, Chen, Z, Marquis, M, Averyt, KB, Tignor, M, and Miller, HL (eds.)]. Cambridge University Press, Cambridge, United Kingdom and New York, NY, USA.

Jiao, N., Azam, F., Sanders, S., 2011, Microbial Carbon Pumps in the Oceans, Supplement to Science, 13 May 2011.

Kearney, M. S. 2008. The potential for significant impacts on Chesapeake Bay: Sea Level Impacts and Ecology. In M. McCracken (ed.), The Likelihood and Character of Large and Disruptive Climate Change. London: EarthScan, 85-100.

Lowe, J. A., and Gregory, J. M., 2010, A sea of Uncertainty, Nature, Published online: 6 April 2010, doi:10.1038/climate.2010.30.

Mackey, R., 2007. Rhodes Fairbridge and the Idea that the solar System Regulates the Earth's Climate, J. of Coastal Research, Special Issue No. 50.

McGill, W. L., Ayyub, B. M., Kaminskiy, M., 2007, A Quantitative Asset-Level Risk Assessment and Management Framework for Critical Asset Protection, Risk Analysis International Journal, Society for Risk Analysis, 27(5), 2007.

Mitrovica, J.X., Gomez, N., and Clark, P.U., 2009, "The Sea-Level Fingerprint of West Antarctic Collapse." *Science*, 323.5915, 753.

National Academy of the Sciences (NAS), 2012. A National Strategy for Advancing Climate Modeling, http://dels.nas.edu/Report/National-Strategy-Advancing-Climate/13430

National Research Council (NRC), 2012. Disaster Resilience: A National Imperative. The National Academies Press, Washington, DC.

National Snow and Ice Data Center (NSIDC), 2012, Arctic Climatology and Meteorology Glossary (http://nsidc.org/arcticmet/glossary/weather.html.

Nicholls, R.J., and Cazenave, A., "Sea-Level Rise and Its Impact on Coastal Zones." *Science* 328.5985, 1517-519, 2010.

Pan, Y., Birdsey, R. A., Fang, J., Houghton, R., Kauppi, P. E., Kurz, W. A., Phillips, O. L., Shvidenko, A., Lewis, S. L., Canadell, J. G., Ciais, P., Jackson, R. B., Pacala, S. W., McGuire, A. D., Piao, S., Rautiainen, A., Sitch, S., and Hayes, D., "A Large and Persistent Carbon Sink in the World's Forests," Science 133, 19 August, 2011, 988-993.

Randall, D.A., R.A. Wood, S. Bony, R. Colman, T. Fichefet, J. Fyfe, V. Kattsov, A. Pitman, J. Shukla, J. Srinivasan, R.J. Stouffer, A. Sumi and K.E. Taylor, 2007. Climate Models and Their Evaluation. In: Climate Change 2007: The Physical Science Basis. Contribution of Working Group I to the Fourth Assessment Report of the Intergovernmental Panel on Climate Change [Solomon, S., D. Qin, M. Manning, Z. Chen, M. Marquis, K.B. Averyt, M. Tignor and H.L. Miller (eds.)]. Cambridge University Press, Cambridge, United Kingdom and New York, NY, USA.

Stainforth, D.A., Allen, M. R., Trdger, E. R., and Smith, L. A., 2007. "Confidence, Uncertainty and Decision Support Relevance in Climate Predictions." Philosophical Transactions of the Royal Society, No. A 365: 2145-2161.

UNISDR, 2012, Making Cities Resilient: My city is getting ready! A global snapshot of how local governments reduce disaster risk, United Nations Office for Disaster Risk Reduction Report, Geneva, Switzerland, www.unisdr.org/campaign

University of New Hampshire, 2011, Global Carbon Cycle, accessed on October 15, 2011, http://globecarboncycle.unh.edu/CarbonCycleBackground.pdf   based   on http://globe.gov/science/topics/carbon-cycle#Overview

Vermeer, M., and Rahmstorf, S. 2011, "Global Sea Level Linked to Global Temperature." *PNAS* 106.51 (2009): 21527-1532. *PNAS*. 22 Dec. 2009. Web. 16 Jan. 2011. http://www.pnas.org.proxy-um.researchport.umd.edu/content/106/51/21527.full?sid=c6b72f05-ebfb-41dc-96d3-625f49553e1b.

Washington Post, Nov 4, 2012, Worst-Case Scenario, http://wapo.st/SF1ta7.

World Economic Forum, 2011. Global Risks, Sixth Edition, World Economic Forum, in collaboration with: Marsh & McLennan Companies, Swiss Reinsurance Company, Wharton Center for Risk Management,, University of Pennsylvania, and Zurich Financial Services, Geneva, Switzerland.

SUSTAINABILITY OF CIVIL INFRASTRUCTURE SYSTEMS: THE PAST, THE PRESENT AND THE WAY FORWARD

Leslie Odartey Mills[1] and Nii Attoh-Okine[2]

ABSTRACT

With the turn of the last two decades, sustainability has become a watch word taking on global dimensions and significance. The concept of sustainability, which calls for a paradigm shift in the status quo of development, has grown to influence core human values, encompassing significant attributes such as the physical, economic and social survival of the human race. Civil infrastructure systems are not left out in this evolution, and stakeholders have drawn attention to the need to design, construct and manage infrastructure efficiently so as to obtain maximum return on investment in light of increasing demand, dwindling resources and continued infrastructure deterioration. As a result, different stakeholders have instituted their own ideas about sustainability and how it can be realized for civil infrastructure. In as much as this has helped broaden the concept of sustainability it has also created a very fragmented field. This article examines the progression of various sustainable actions and initiatives in the field of highway infrastructure and how these individual entities could be synchronized to standardize developments in the provision of sustainable highway infrastructure.

[1] Leslie Mills, Regional Manager for Africa, International Road Federation, Alexandria, Virginia, USA

[2] Nii Attoh-Okine, Professor, Civil and Environmental Engineering , University of Delaware, Newark, Delaware, USA

INTRODUCTION

Sustainability is a descriptive term synonymous with a state whose being can be upheld or prolonged for a defined period of time with no setbacks to the state. For the specific case of sustainability and development, Ramani et al. (2011) recounted that the term "sustainable development" is made up of two distinct yet related concerns: sustainability and development. However through its widespread use, the concept of sustainable development is usually identified with the practical notion of sustainability and both are often time used interchangeably. As noted by Fischer and Amekudzi (2011) sustainability can be viewed as a state where the key goals of sustainable development are satisfied, a high quality of life is achievable by all and the environment is preserved.

In the face of a growing concern about accelerated deterioration of the human environment and natural resources, the report of the World Commission on Environment and Development (WCED) drew the world's attention to the need for future development to proceed in a sustainable manner. WCED (1987) defined sustainable development as "development that meets the needs of the present without compromising the ability of future generations to meet their own needs." Ever since, sustainability has evolved to become a concept attaining global appeal that has expanded to include added elements and attributes as knowledge of it becomes widespread.

One challenge though is that in civil engineering and other related disciplines, a present precise definition of sustainability has often proven to be elusive (Foxon et. al 2002; Sahely et al. 2005). Loucks (1999) detailed this elusiveness associated with a precise definition to stem from questions such as:

- Should the welfare of future generations be enhanced by preserving the current state of natural environmental resources and ecological systems? If so over what spatial scales?
- How should trade-offs among current immediate "needs" and those of future generations be made? Can a standard economic approach such as discounting of future benefits, costs and losses be equally applied to environmental resources?

Questions such as those posed above comprise some of the challenges faced in precisely defining the principle of sustainability

Sustainability "Defined" For Civil Infrastructure

To overcome this hurdle of precision and elusiveness, different organizations tend to construct unique "definitions" that suit their specific needs at a given period in time. Most "definitions" are however consistent with the WCED concept of sustainability. A common approach used by stakeholders in a particular field is to adopt and adapt that of WCED to their field. For example stakeholders in transportation engineering will define sustainability as the ability to meet the needs of the present generation in providing for the movement of people and goods from one location to another without compromising on the ability of future generations to meet their own needs. Other varied definitions given in the field of civil engineering include:

- A set of environmental, economic and social conditions in which all of society has the capacity and opportunity to maintain and improve its quality of life indefinitely without degrading the quantity, quality or availability of natural, economic and social resources. (Caldwell 2011).

- A continuum of decisions, actions and practices encompassing all aspects of transportation – from project planning to operations and on to infrastructure replacement. The goal of sustainable transportation is to protect the environment and conserve natural resources while taking into consideration societal needs as well as costs and benefits (Helmer and Gough, 2010).
- Further insight from Transportation Research Board: "… sustainability is not about threat analysis; sustainability is about systems analysis. Specifically, it is about how environmental, economic, and social systems interact to their mutual advantage or disadvantage at various space-based scales of operation." (TRB 1997)

For all these definitions, overarching themes that cut across most of them are (i) proper assessment of relevant environmental, economic and social factors, (ii) consideration of expanded temporal and spatial horizons (iii) intergenerational equity and (iv) the need for multi-disciplinary considerations (Foxon et al. 2002; Rijsberman and van de Ven 2000). A physical representation of the first overarching theme showing the relationship between economic, social and environmental factors as three rings is given in Figure 1.
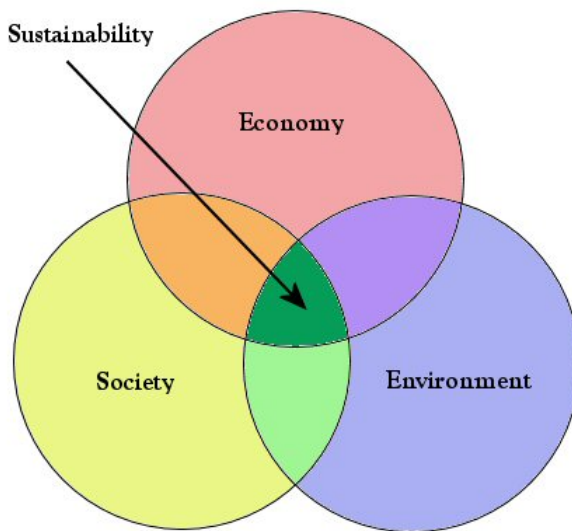
Figure 1 Three rings illustrating sustainability

Sustainability in this way is depicted as a balance of the three factors and is represented by the intersection of the three rings. Litman and Burwell (2006) emphasize that although Figure 1 implies each issue fits into a specific category, in practice they often overlap. The authors cite pollution as an example that has not only environmental impacts but health (social) and economic impacts too. As such an integrated analytical approach must be used to account for interaction between impacts.

Table 1 sheds more light on what each dimension: social scope, economic development and environmental stewardship generally entails.

Table 1 Sample description of sustainability dimensions

Sustainability Dimension	Description of Sustainability Dimensions
Social scope	• A provided safe and secure environment. • Includes issues such human interaction, health, education and quality of life.
Economic development	• Financial and economic needs of current and future generations need to be met. • Includes issues such as business activity, employment, productivity, tax issues and trades.
Environmental stewardship	• Clean environment for present and future generations. • Tackles issues like pollution prevention, climate protection, habitat preservation, aesthetics.

OBJECTIVE

To enhance knowledge and advance the current state of practice, this research examines the challenges listed above and proposes strategies to address them. Knowledge as expressed above is encapsulated by work undertaken thus far by researchers on the influence of sustainability in infrastructure decision-making. For example in an effort to examine the flow and application of knowledge on sustainability to infrastructure development, Yuan and Yang (2008) summarized existing knowledge on sustainability into four groups: assessment tools, government polices and guidelines, company procedures, and project experiences. This article uses assessment as its main focal point while the other groups are briefly espoused.

ASSESSING SUSTAINABILITY

Defining infrastructure sustainability is a critical element in the development of indicators and metrics to assess sustainability in civil infrastructure systems (Gudmundsson 2003, Jeon and Amekudzi 2005). A practical interpretation of this definition calls for a framework which first recognizes the feature of sustainability being assessed, a local measure of individual entities involved with that feature of sustainability and a global assessment of the contribution of these entities towards the overall sustainability of a given infrastructure. Ramani et al. (2011) viewed such a framework as a formalized system of goals, objectives and performance measures applied to sustainability.

Attributes of a robust sustainability performance measurement framework were explored in work by Pei et al. (2010). Some of these common must-have attributes of frameworks for agencies include:

- A comprehensive and holistic approach that encompasses a balanced view of sustainability
- A connection to agency goals and objectives that represent causal relationships between agency action and desired outcomes
- An allowance for vertical and horizontal integration of agency actions
- A capability to capture the effects of interactions amongst variables
- A reflection of stakeholder perspectives

- An ability to consider agency as well as stakeholder capabilities and constraints
- Flexibility and self-learning features

An example of a general framework for assessing sustainability for civil infrastructure systems is shown in Figure 2. The framework contains some of the attributes recommended by Pei et al. (2010) especially in presenting a holistic approach and capturing the effects amongst the various entities. In the framework, the authors identified three key components required for a performance measurement based implementation of sustainability. These are fundamental components, overarching components and auxiliary components.
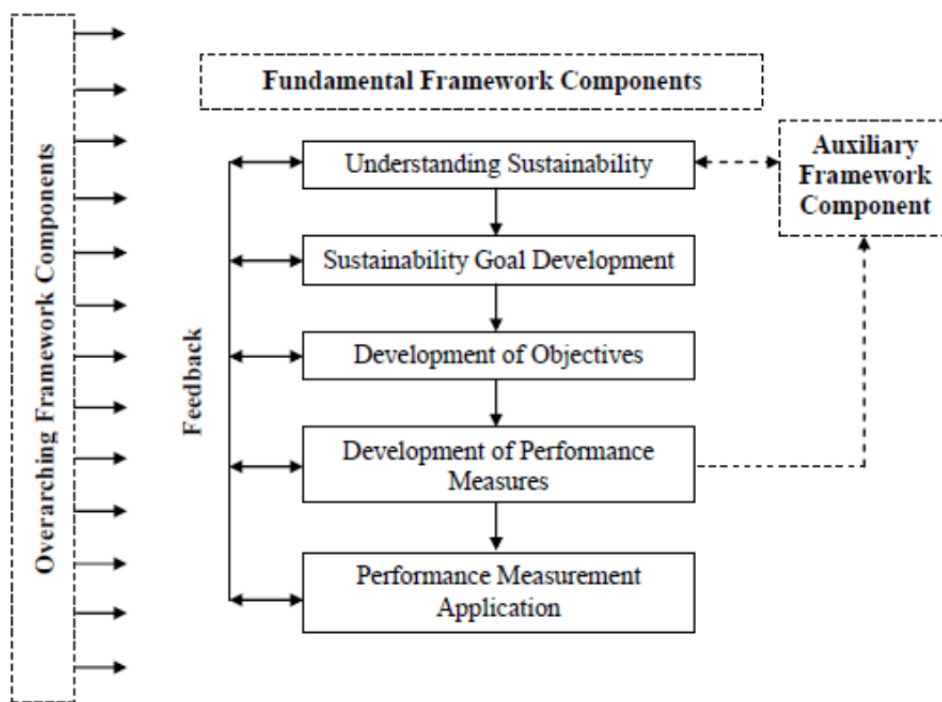
Figure 2 Sustainability Framework Diagram (Ramani et. al 2011).

Fundamental components, which form the basis of the framework, are sequential and iterative and encompass the process of understanding sustainability through to applying it in performance measurement. Overarching components are required throughout the entire application framework process and include elements like stakeholder engagement and participation and coordination with external agencies. Auxiliary components are optional components that supplement the framework application process. They include organizational sustainability initiatives and performance measures not related to an agency's core functions. Information obtained through feedback as per whether decisions are leading to desired or intended outcomes is an essential part of the process. It leads to refinements being made to the framework to ensure continual improvement.

Generally, the quest to construct frameworks for sustainability assessment is in itself cumbersome; however work by Jeon and Amekudzi (2005) in reviewing the structure of frameworks across different countries and agencies identified three categories of frameworks:

linkages-based frameworks, impact-based frameworks and influence -oriented frameworks. They defined linkages-based frameworks as those that capture relationships between the causal factors, impacts and corrective actions related to achieving sustainability. Impacts-based frameworks focus on the nature and extent of various kinds of impacts (e.g. economic, environmental, and social) that collectively determine the sustainability of a system (without necessarily capturing causal factors and corrective actions). The term "influence-oriented" is used to capture frameworks that are developed bearing in mind the relative levels of influence that the responsible agency or organization has on various actions and/or activities that influence progress toward sustainability.

An example of an impacts-based framework for assessing sustainability as a system-based approach is shown in Figure 3. In the framework, Sahely et al. (2005) proposed the following criteria for infrastructure systems: environmental, economic, engineering and social. Environmental criteria examined optimal resource utilization and minimal waste production; economic criteria looked at traditional costs like capital costs, operation and maintenance costs in addition to new items like investments in innovation and level of reserve funds needed for effective asset management and timely infrastructure renewal.
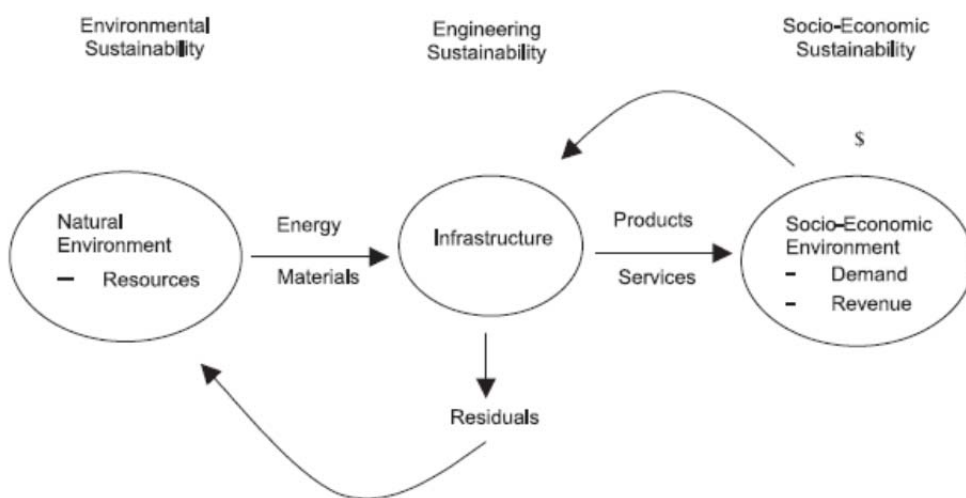
Figure 3 Framework for assessing infrastructure systems (Sahely et al. 2005).

Engineering criteria assess infrastructure performance using measures such as reliability, resiliency and vulnerability whilst social criteria investigate issues such as health and safety, accessibility and acceptability of the infrastructure. The feedback mechanisms inherent in the framework also possess significant sustainability implications: for example: revenue from operation of the system can be used to promote more "sustainable" infrastructure and residuals from construction of infrastructure can be used to promote a more "sustainable" environment.

Incorporating sustainability into any decision support process requires an assessment of the social, environmental and economic consequences of potential options. Assessment provides an avenue where progress can be objectively measured using a set of agreed-upon tools. Different measurement approaches for measuring sustainability are suggested in literature, examples of which are presented in this section.

McLaren and Simonovic (1999) proposed two metrics by which sustainability could be measured: indicators and criteria. In their definition, indicators are useful in monitoring and

measuring the state of the environment using a manageable number of variables or characteristics and criteria are yardsticks against which sustainability indicators are measured.

Other authors (Foxon et al. 2002) have used a three-pronged approach by aptly distinguishing between sustainability principles, criteria and indicators. According to them, principles are constant, normative definitions or goals for sustainability; criteria are the set of factors used in making judgments about relative sustainability for a given set of options; and indicators measure the past and current values of specific criteria. Whereas principles remain constant over time, the choice of criteria and indicators may change with the advancement of knowledge. In other cases, literature does not always distinguish between criteria and indicators and these terms have sometimes been used interchangeably (Sahely et al. 2005).

Guidelines for Sustainability Indicators

The Danish National Strategy for Sustainable Development defines an indicator as a parameter that can show development in some condition compared with important goals or initiatives (Danish Government 2002). They are constructed variables that can either be qualitative or quantitative, are able to describe a situation or time trend and can contribute particular information about a criterion that is being measured (Gudmundsson 2003).

A consensus agreed on by authors is the likelihood for indicators and criteria to evolve over time prompting the need for them to be monitored regularly while engineers and decision-makers make changes to infrastructure systems. In selecting indicators, Foxon et al. (2002) recommend five guiding principles: comprehensiveness, applicability, tractability, transparency and practicability. Bossel (1999) and Levett (1998) also suggested representative indicators be as small as possible, but as large as essential. Both authors recommend that indicators must be clearly defined, reproducible, resonant and measurable to determine appropriate levels of indicators. Additionally indicators must be relevant, understandable and usable by stakeholders. They must be project-specific and be targeted to a particular user community.

Indicators are value-laden (Levett, 1998), often driven by the background, knowledge and experience of the investigators. In addition Levett establishes that they are inputs to policy as well as consequences of it and as such developing indicators for sustainability is a dialectical rather than deductive process defined by the process of inventing, trying, criticizing, discarding and refining possible indicators till a clear meaning of sustainability with regards to a given system is obtained. Review of literature lays emphasis on the need for balance when choosing indicators. They must clearly portray the dynamics of the system being explored without diminishing the effect of influential variables on the total output of the system.

The above mentioned characteristics for indicators fit into work by Foxon et al. (2002) in defining measurable entities for water service provision as shown in Table 3.3. By clearly defining criteria relevant to the assessment of sustainability in water provision, the stage is then set for the development of indicators associated with the set criteria. For example, with environmental criteria, indicators must measure optimal resource utilization (e.g. use of water, nutrients, energy and land) and minimal waste production (e.g. gaseous emissions, waste water effluent and solid waste). In the case of economic criteria, indicators look at cost analysis and performance targets and include capital costs and operation and maintenance costs. Measure of investment in research and development (innovation) can also be considered. The categories and criteria proposed in this decision-making context and listed in Table 2 can be broadly applied to other civil infrastructure systems.

Table 2 Set of primary criteria for water service infrastructure (Foxon et al. 2002)

Category	Primary Criterion
Economic	Life Cycle Costs
	Willingness to pay
	Affordability
	Financial risk exposure
Environmental	Resource utilization
	Service provision
	Environmental impact
Social	Impact on risks to human health
	Acceptability to stakeholders
	Participation and responsibility
	Public awareness and understanding
	Social inclusion
Technical	Performance of the system
	Reliability
	Durability
	Flexibility and adaptability

Sustainability for Transportation Infrastructure
The drive to achieve sustainability within the field of transportation infrastructure permeates all aspects and levels associated with planning, concept development and implementation. Specifically, providing sustainable transportation infrastructure encompasses different attributes such as efficient land use planning, innovative designs that improve the welfare of intended users and the incorporation of recycled and reused materials in construction. This section explores some of the more prominent sustainability programs used in assessing sustainable transportation infrastructure. They are CEEQUAL, Greenroads and Green LITES. These three systems are referenced by Hardy (2011) in his study.

CEEQUAL
CEEQUAL is defined as an evidence-based assessment and awards scheme for improving sustainability in civil engineering (CEEQUAL, 2012). Aimed at improving project specification, design and construction of civil engineering works, CEEQUAL is a rating system that equips clients, designers and contractors with the ability to assess the environmental and social performance of their systems. These systems include transportation infrastructure like highways and railways. Launched in 2003, CEEQUAL is a collaborative effort between agencies and institutions, notable amongst which are the Institution of Civil Engineers, the Crane Environmental Ltd and the Construction Industry Research and Information Association.

It works by means of rigorous evidence-based self-assessment criteria followed by external verification of results obtained. A CEEQUAL score shows how far a project is between minimum legal compliance and pinnacle best practice. An example of scoring used in CEEQUAL Version 4 is as follows: Project Management (10.9%), land use (7.9%), landscape (7.4%), ecology and biodiversity (8.8%), historic environment (6.7%), water resources and water

environment (8.5%), energy and carbon (9.5%), material use (9.4%), waste management (8.4%), transport (8.1%), effects on neighbors (7%) and relations with local community and other stakeholders (7.4%).

The latest version of CEEQUAL, Version 5, reduced the number of benchmarks in Version 4 and uses the following in assessing sustainability: project strategy, project management, people and communities, land use and landscape, the historic environment, ecology and biodiversity, water environment, physical resource use and management and transport. Awards are given based on the maximum possible score for a project and the thresholds used are as follow: more than 25% - pass; more than 40% - good; more than 60% - very good and more than 75% - excellent. According to CEEQUAL, it is not possible to achieve a 100% score because of conflicting issues in assessment.

Greenroads

A third-party points-based system, the Greenroads Rating System was developed to aid road and bridge design and construction experts certify the sustainability of transportation infrastructure projects. This rating system was developed by the University of Washington and CH2M Hill but is presently reviewed and updated by the Greenroads Foundation. It is applicable to all types and sizes of bridges and roadway projects including new, reconstruction and rehabilitation projects.

Greenroads works via a collection of sustainable roadway design and construction best practices called "credits" that encompass water, environment, access, community impact, construction practices and materials. By achieving credits, projects earn points and attain a total score which serves as an indicator of how sustainable the projects are. For a bridge or road project to be considered a Greenroad, it must first meet minimum criteria called Project Requirements. Some of the criteria listed under Project Requirements include an environmental review process, a life-cycle cost analysis, a waste management plan, a site maintenance plan and some form of educational outreach. Meeting Project Requirements is a baseline expectation when using Greenroads and no points are attached accordingly to achieving them.

The second layer above Project Requirements is Voluntary Credits. Voluntary Credits range from access and equity to pavement technologies and materials. Points are awarded when projects clock up Voluntary Credits. A maximum score of 118 is available as Voluntary Credit points and "achievement" levels are accorded to projects based on the number of points attained. The levels are as follows: certified (all project requirements + 32-42 voluntary points); silver (all project requirements + 43-53 voluntary points); gold (all project requirements + 54-63 voluntary points) and evergreen (all project requirements + 64 or more voluntary points).

GreenLITES

GreenLITES (**Green Leadership In Transportation and Environmental Sustainability**) is primarily an internal management program for the NewYork State Department of Transportation (NYSDOT) to establish independent measurement criteria for planning, project design and operations. It is a self-certification program that uses a suite of tools: sustainability rating systems, spreadsheets and other metrics to distinguish transportation projects based on the extent to which they incorporate sustainable design choices. Modeled after the Leadership in Energy and Environmental Design (LEED[TM]) and Greenroads systems, GreenLITES assigns credits to project designs to ascertain a corresponding certification level for the project. Certification categories used in assessment are sustainable sites, water quality, materials and resources, energy and atmosphere and innovation. Credits accumulated from these categories translate into the

following certification levels: certified, silver, gold and evergreen. Using a score card in assigning credits, certified is assigned 15 – 29 points; silver 30 – 44 points; gold 45 – 59 points and evergreen is above 60.

GreenLITES assists NYSDOT attain its aim of aligning transportation with the needs of a sustainable society. As such GreenLITES is structured along the triple bottom line of society: economy, society and environment in its quest to improve transportation infrastructure sustainability. It achieves this by contributing to a vibrant economy and improving quality of life while minimizing adverse impacts to the environment.

DISCUSSION

The mention of sustainability in transportation usually draws attention to the hurdle faced by this sector in bringing down green-house gas emissions and shrinking any associated carbon foot-print. However, one feature that is often time forgotten is that transportation by itself is a system, and its challenges including that of meeting sustainable requirements are "multi-sectoral, multi-disciplinary and multi-problemed" (Manheim, 1976). Particular elements of the transportation system can be analyzed individually, but the ultimate aim in analysis should be to look at the contributions of individual elements and synthesize them to form a global assessment of the system under study. This is especially critical since the converse creates a problem of fragmentation, stove-pipe solutions and uncoordinated responses from stakeholders and jurisdictions as a result of a lack of simultaneous considerations of the transportation system.

Sustainable interventions in transportation cut across a wide array of sectors including but not limited to land use planning, design, construction, operations and maintenance. Other sectors include the coupling of climate change and fiscal factors with growing congestion and ageing infrastructure. All these exhibit a complex set of interrelated issues that must be addressed by policymakers and professionals. It must however be stated that strides have been made by transportation stakeholders to make the industry more sustainable. Today's road builders are adding recycled rubber to asphalt mix to improve riding quality and reduce waste; fly-ash or slag is being used instead of cement for rigid pavements; warm mix asphalt technology with its merits is attracting a significant proportion of the market share previously held by hot-mix asphalt; new and energy efficient lighting are being introduced along highways; urban design initiatives are leading to more sustainable communities; vehicles with lower emission rates are being manufactured; research into alternative fuel technologies is gaining root; governments world-wide are exploring viable, sustainable investment options such as funding for highways and transit and congestion-pricing alternatives that have a socio-economic equity construct to them. All these initiatives demonstrate positive feats; but compared to the building industry there still remains more to be done.

Moves by the building industry geared towards sustainability present a host of opportunities that can be duly emulated by the transportation sector. The building industry has a focused effort to overhaul design standards, construction methods, selection of materials and operating systems and has achieved relative success in doing this by using the Leadership in Energy and Environmental Design (LEED) rating system. Developed by the US Green Building Council, LEED provides a best practice method through which building designers, local officials and building owners can create benchmarks and certification methods for high-performance green buildings. LEED assesses building features like lighting, heating and cooling systems and examines operating, maintenance and replacement alternatives to rate and certify the levels of sustainability and preservation of resources inherently involved in these systems and processes.

The awareness of sustainability requirements has significantly changed the design and construction of buildings, their internal operating systems and their orientation to the surrounding environment.

Following in the steps of the building industry, stakeholders in the transportation sector have developed rating systems and certification procedures that use LEED as a template. There is an increasing demand by transportation infrastructure stakeholders for a holistic investment decision-making framework which brings all social, environmental, economic and political factors to bear in a logical and systematic way. In as much as developing ratings shows progress in sensitizing transportation stakeholders on sustainability assessment, more work has to be done to shift from a largely based subjective assessment to one that is complemented by a well-structured quantitative framework. Sahely et al (2005) attested to the fact that though sustainability's universality as a unifying and holistic paradigm appeals to many, the main obstacle remains the transformation of its principles into operational models. In particular, the authors mention the development of practical tools to measure and enhance urban sustainability as the major challenge facing the civil engineer. Similar to many other systems, hurdles faced in promoting sustainability for civil infrastructure hinges on factors related to determining meaningful indicators and reference values for desirable or undesirable states and developing analytical tools and models for sustainability data assessment.

The support of a quantitative framework assessment to the already established subjective system will aid decision-makers in their desire to acquire analytical tools that make sustainability assessments more tangible and more reliant on a consistent procedure than one dependent on subjective analysis. The transportation rating systems discussed earlier are by far based on the principle of subjective assessment, raising the potential for the issue of complicity during assessment. Solving this problem would require ratings that can be translated into input for mathematical models to streamline the process of holistically assessing sustainability. Ratings should correspondingly be founded on performance indicators that act effectively to assess sustainability.

REFERENCES

1. Bossel H. (1999): "Indicators for Sustainable Development: Theory, Method and Applications." International Institute for Sustainable Development, Winnipeg, Manitoba.
2. Caldwell K. (2011): "Sustainability in the 21st Century." President's Note, Civil Engineering. February, 2011.
3. CEEQUAL (2012): Website: www.ceequal.com. Accessed February 5th 2012.
4. DANISH GOVERNMENT (2002): Danmarks nationale strategi for bæredygtig udvikling Foelles fremtid – udvikling i balance. Forslag til Indikatorsæt. Copenhagen: Regeringen
5. Fischer J. and Amekudzi A. (2011): "Quality of Life, Sustainable Infrastructure and Sustainable Development: Strategically expanding choice." Journal of Urban Planning and Development; Vol. 137; No. 1; pp. 39-48
6. Foxon T., McIlkenny G., Gilmour D., Oltean-Dumbrava C., Souter N., Ashley R., Butler D., Pearson P., Jowitt P. and Moir J. (2002): "Sustainability Criteria for Decision Support in the UK Water Industry." Journal of Environmental Planning and Management, Vol.45; No.2; pp. 285-301

7. Gudmundsson H. (2003): "Making Concepts Matter: Sustainable Mobility and Indicator Systems in Transport Policy." International Social Sciences Journal, Vol. 176, pp. 199-217.

8. Hardy D. (2011): "Sustainability 101: A Primer for ITE Members." ITE Journal, April 2011, pp. 28 – 34.

9. Helmer J. and Gough J. (2010): "Best Practices in Sustainable Transportation." ITE Journal, March 2010, pp. 20 – 24.

10. Jeon C. and Amekudzi A. (2005): "Addressing Sustainability in Transportation Systems: Definitions, Indicators and Metrics." Journal of Infrastructure Systems; Vol. 11; No. 1; pp. 31 – 50.

11. Levett R. (1998): "Sustainability Indicators – Integrating Quality of Life and Environmental Protection." Journal of Royal Statistical Society, Series A. (Statistics in Society); Vol. 161; No. 3; pp. 291 – 302

12. Litman T. and Burwell D. (2006): "Issues in Sustainable Transportation", International Journal of Global Environmental Issues; Vol.6; No.4; pp.331–347.

13. McLaren, R. and Simonovic, S. (1999): "Evaluating Sustainability Criteria for Water Resource Decision Making: Assiniboine Delta Aquifer Case Study." Canadian Water Resources Journal; 24 (2), pp. 147-163

14. Manheim M. (1976): "Fundamentals of Transportation Systems Analysis." Vol. 1; MIT Press.

15. Pei Y., Amekudzi A. Meyer M., Barrella E. and Ross C. (2010): "Performance Measurement Frameworks and the Development of Effective Sustainable Transport Strategies and Indicators." Presentation at 89th Annual Meeting of the Transportation Research Board.

16. Ramani T., Ziestman J., Gudmundsson H., Hall R. and Marsden G. (2011): "A Generally Applicable Sustainability Assessment Framework for Transportation Agencies." Transportation Research Record: Journal of the Transportation Research Board, No. 2242, Figure 1, Page 13.

17. Rijsberman M. and van de Ven F. (2000): "Different Approaches to Assessment of Design and Management of Sustainable Urban Water Systems." Environmental Impact Assessment Review; Vol. 20; pp. 333-345.

18. Sahely H., Kennedy C. and Adams B. (2005): "Developing Sustainability Criteria for Urban Infrastructure Systems." Canadian Journal of Civil Engineering Vol. 32; No.1; pp. 72-85.

19. Transportation Research Board (1997) Toward a Sustainable Future, Special Report 251, Washington DC.

20. World Commission on Environment and Development. (1987): "Our Common Future." Oxford University Press, Oxford, England.

21. Yuan M. and Yang J. (2008). "The Promotion of Sustainability Agenda for Infrastructure Development through Knowledge Management." In Naaranoja, M., Otter, A., Prins, M., Karvonen, A. and Raasakka, V., Eds. Proceedings Joint CIB 2008 Conference for Performance and Knowledge Management; pp. 167-178, Helsinki, Finland.

Quantification and Valuations of Resilience for Emergency Management

Bilal M. Ayyub[1]

ABSTRACT

The United Nations Office for Disaster Risk Reduction reported that the 2011 natural disasters, including the earthquake and tsunami that struck Japan, resulted in $366 billion in direct damages and 29,782 fatalities worldwide. Storms and floods accounted for up to 70 percent of the 302 natural disasters worldwide in 2011, with earthquakes producing the greatest number of fatalities. Average annual losses in the US amount to about $55 billion. Enhancing community and system resilience could lead to massive savings through risk reduction and expeditious recovery. The rational management of such reduction and recovery is facilitated by an appropriate definition of resilience and associated metrics. In this paper, a resilience definition is provided that meets a set of requirements with clear relationships to the metrics of the relevant abstract notions of reliability and risk. Those metrics also meet logically consistent requirements drawn from measure theory, and provide a sound basis for the development of effective decision-making tools for multi-hazard environments. Improving the resiliency of a system to meet target levels requires the examination of system enhancement alternatives in economic terms, within a decision-making framework. Relevant decision analysis methods would typically require the examination of resilience based on its valuation by society at large. Methods for valuation and benefit-cost analysis based on concepts from risk analysis and management are introduced.

1. Background

The United Nations Office for Disaster Risk Reduction (UNISDR 2012) reported that the 2011 natural disasters, including the earthquake and tsunami that struck Japan, resulted in $366 billion in direct damages and 29,782 fatalities worldwide. It is anticipated that such disasters would occur in increasing trends of storm rates and disaster impacts due to a combined effect of climate change and increased coastal inventory of assets (Ayyub et al 2012). Although no population center or a geographic area can ever be risk free from natural or human-causes hazards, communities should strive to enhance resilience to the destructive forces or the impacts of resulting events that may claim lives and damage property.

---

[1] Director of the Center for Technology and Systems Management, Professor of Civil and Environmental Engineering, University of Maryland College Park, MD 20742, USA. ba@umd.edu

Enhancing system resilience at the structure, network, community, etc. levels could lead to massive savings through risk reduction and expeditious recovery. The rational management of such reduction and recovery is facilitated by an appropriate definition of resilience and associated metrics.

2. Resilience Defined

The concept of resilience appears in different domains ranging from ecology to child psychology and psychiatry to infrastructure systems. It was formally introduced in ecology, defined as the persistence of relationships within a system (Holling 1973), and measured by the system's ability to absorb change-state variables, driving variables and parameters and still persist. Several reputable entities defined resilience in their high-impact documents, most notably in the Presidential Policy Directive (PPD-21, 2013) on Critical Infrastructure Security and Resilience where the "term *resilience* means the ability to prepare for and adapt to changing conditions and withstand and recover rapidly from disruptions. Resilience includes the ability to withstand and recover from deliberate attacks, accidents, or naturally occurring threats or incidents." Ayyub (2013) provides a comprehensive coverage of definitions and its requirements, and proposed resilience definition based on PPD-21 (2013) that lends itself for measurement and meets the above requirements was provided by Ayyub (2013) as follows:

> *Resilience notionally means the ability to prepare for and adapt to changing conditions and withstand and recover rapidly from disruptions. Resilience includes the ability to withstand and recover from disturbances of the deliberate attack types, accidents, or naturally occurring threats or incidents. System resilience for a particular function can be measured based on the persistence under uncertainty of a corresponding system's performance in the face of disturbances.*

This definition is consistent with the ISO (2009) risk definition of the "effect of uncertainty on objectives." The proposed measure includes three key words that offer a basis for quantification. These words are listed in a suggested order for their analysis as follows:

- System's performance defined in terms of requirements or objectives, and examined in the form of output, throughput, structural integrity, lifecycle cost, etc.;
- Uncertainty relating to events such as storms, disturbance, conditions, system states, etc.;
- Persistence examined in terms of enduring the events, recovery, continuance and/or resumption of performance.

Subsequent sections of this paper provide metrics based on this definition that meet logically consistent requirements drawn partly from measure theory, and provide a sound basis for the development of effective decision-making tools for multi-hazard environments.

3. Resilience Measurement and Metrics

Ayyub (2013) used Figure 1 as a schematic representation of a system performance (Q) with aging effects and an incident occurrence with a rate (λ) according to Poisson process at time t_i leading to a failure event with a duration ΔT_f. The failure event concludes at time t_f. The failure event is followed by a recovery event with a duration ΔT_r. The recovery event concludes at time t_r. The total disruption (D) has a duration of $\Delta T_d = \Delta T_f + \Delta T_r$. The figure shows for illustration purposes three failure events: brittle ($f1$), ductile ($f2$) and graceful ($f3$), and six recovery events: expeditious recovery to better than new ($r1$), expeditious recovery to as good as new ($r2$),

expeditious recovery to better than old ($r3$), expeditious recovery to as good as new ($r4$), recovery to as good as old ($r5$) and recovery to worse than old ($r6$). These events define various rates of change of performance of the system. The figure also shows the aging performance trajectory and the estimated trajectory after recovery. The proposed model to measure resilience is

$$\text{Resilience}\,(R_e) = \frac{T_i + F\Delta T_f + R\Delta T_r}{T_i + \Delta T_f + \Delta T_r} \tag{1}$$

where for any failure event (f) as illustrated in Figure 1, the corresponding *failure profile F* is measured as follows:

$$\text{Failure}(F) = \frac{\int_{t_i}^{t_f} f\,dt}{\int_{t_i}^{t_f} Q\,dt} \tag{2}$$

Similarly for any recover event (r) as illustrated in Figure 1, the corresponding *recovery profile R* is measured as follows:

$$\text{Recovery}(R) = \frac{\int_{t_f}^{t_r} r\,dt}{\int_{t_f}^{t_r} Q\,dt} \tag{3}$$

The failure-profile value (F) can be considered as a measure of robustness and redundancy; whereas the recovery-profile value (R) can be considered as a measure of resourcefulness and rapidity. The time to failure (T_f) can be characterized by its probability density function computed as follows:

$$-\frac{d}{dt}\int_{c=0}^{\infty} \exp\left[-\lambda t\left(1 - \frac{1}{t}\int_{\tau=0}^{t} F_L(\alpha(\tau)s)d\tau\right)\right] f_{S_0}(s)ds \tag{4}$$

where Q is defined as the system's performance in terms of its strength (S) minus the corresponding load effect (L) in consistent units, i.e., $Q = S\text{-}L$. Both L and S are treated as random variables, with F_L = the cumulative probability distribution function of L, and f_S = the probability density function of S. The aging effects are considered in this model by the term $\alpha(t)$ representing a degradation mechanism as a function of time t. It should be noted that the term $\alpha(t)$ can also represent improvement to the system. Equation 4 is based on a Poisson process with an incident occurrence, such as loading, rate of λ, and is based on Ellingwood and Mori (1993). The probability density function of T_f as shown in Eq. 4 is the negative of the derivative of the reliability function.

The times T_i, T_f and T_r are random variables as shown in Figure 1, and are related to durations as follows:

$$\Delta T_f = T_f - T_i \tag{5}$$

$$\Delta T_r = T_r - T_f \tag{6}$$

The disruption duration is given by

$$\Delta T_D = \Delta T_f + \Delta T_r \tag{7}$$

The resilience model of Eq. 1 can be used for systems, such as buildings, other structures, facilities, infrastructure, networks and communities. The primary basis for evaluating Eq. 1 is the definition of performance (Q) at the system level with meaningful and appropriate units, followed by the development of an appropriate breakdown for this performance, using what is termed herein as performance segregation. The performance segregation should be based on some system-level logic that relates the components of the performance breakdown to the overall performance at the system level as the basis for a system model. This model can be used to aggregate the performance of components to the assess system-level performance. Such performance segregation and aggregation analysis is essential for examining the resilience of systems for buildings, other structures, facilities, infrastructure, networks and communities. The uncertainties associated with the performance components can be modeled as random variables with any necessary performance events in order to use Boolean algebra and the mathematics of probability to characterize the performance Q in Eq. 1.

MCEER (2010) proposed the use of resilience index (R_i) in the range [0,1] for each (the ith) quality of service, and an aggregation model for these resilience indices using an independence assumption. For examples in the case of two indices, the aggregated index is as follows:

$$\text{Resilience}(R_{12}) = \frac{R_1.R_2}{R_1 + R_2 - R_1.R_2} \tag{8}$$

Figure 2 shown a plot of Eq. 8 for the case of two identical indices, i.e., resilience components, for the entire range of values of R_i (Ayyub 2013). The figure also shows the effect of increasing the number of components is increased from one to ten. The downward intensification is attributed to the independence assumptions.

The development of such a system-level model relating components' performances to a system performance is beyond the scope of this paper. Such a model is domain specific; however future studies should set meta-methodological requirements for the development of such models.

The units of performance at the system level vary depending on the system type and the objectives of the analysis. Table 1 shows examples of performance types and units of measurement for selected systems for demonstration purposes.
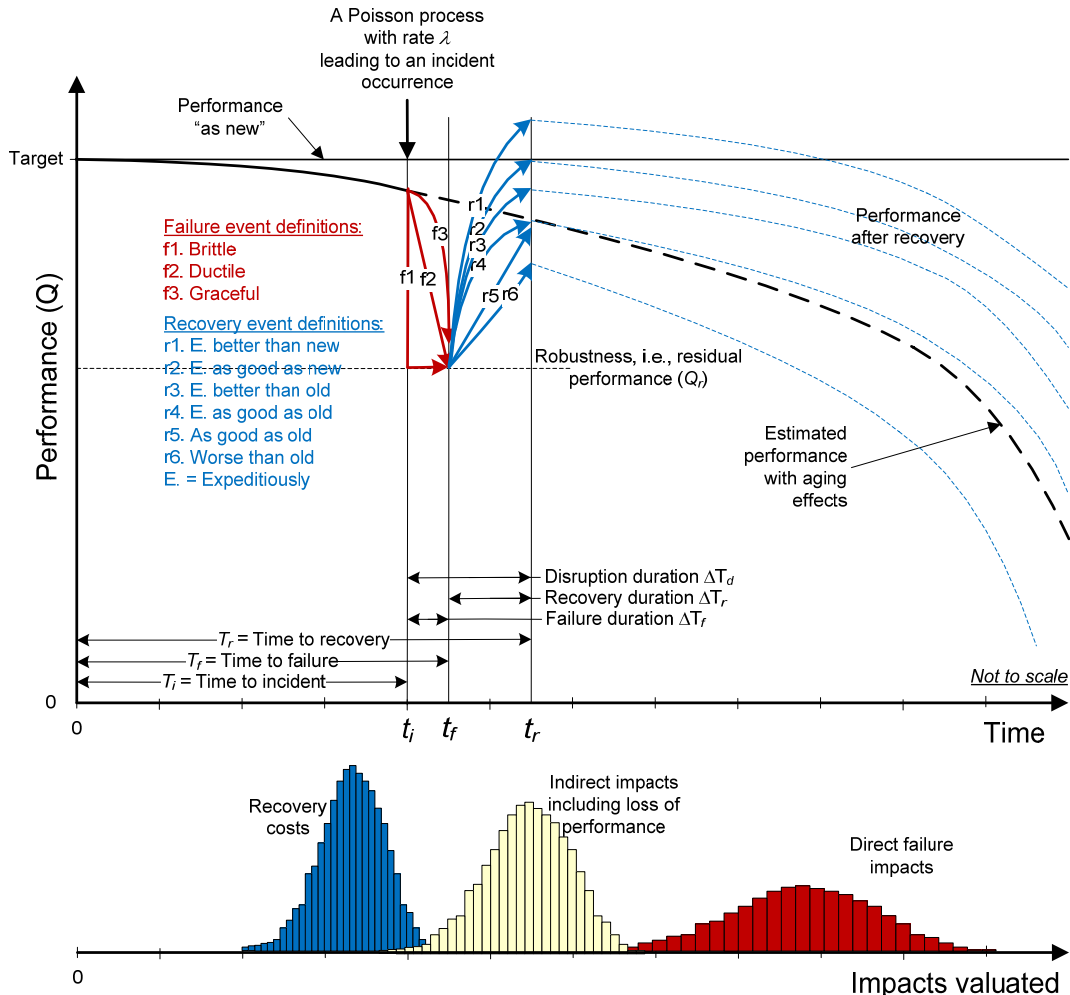
Figure 1. Proposed Definitions of Resilience Metrics (Ayyub 2013)

Table 1. Systems and Performance Measurements

Systems	Performance	Units
Buildings	Space availability	Area per day
Other structures: Highway bridges	Throughput traffic	Count per day
Facilities: Water treatment plants	Water production capacity	Volume per day
Infrastructure: Water delivery	Water available for consumption	Volume
Network: Electric power distribution	Power delivered	Power per day
Communities	Economic output Quality of life (consumption)	Dollars Dollars
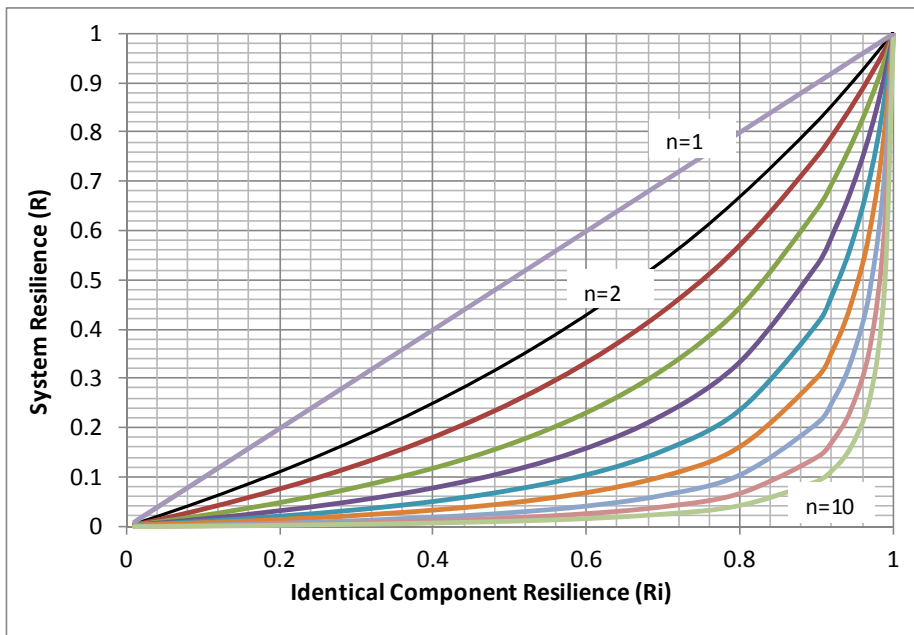
Figure 2. System Resilience Aggregate based on Two Identical Resilience Components (Ayyub 2013)

5. Economic Valuation and Benefit-Cost Analysis

Improving the resiliency of a system to meet target levels requires the examination of system enhancement alternatives in economic terms, within a decision-making framework. Relevant decision analysis methods would typically require the examination of resilience based on its valuation by society at large. Methods for the total economic valuation of resilience are needed, and should satisfy the essential requirement of consistency with respect to the definition and metrics of resilience. Concepts from risk analysis and management can be used for this purpose (Ayyub 2003).

Valuation can be approached broadly from philosophy and particularly from ethics in order to make distinctions among values such as: (1) instrumental and intrinsic values, (2) anthropocentric and biocentric (or ecocentric) values, (3) existence value, and (4) utilitarian and deontological values (Callicott 2004, NRC 2004). The focus of this section is on economic valuation; however it is necessary to introduce and discuss these distinctions. An ecosystem is used as an example to discuss these distinctions.

An anthropocentric value system considers humankind as the central focus or final goal of the universe, human beings as the only thing with intrinsic value, and the instrumental value of everything else is derived from its usefulness in meeting human goals. On the other hand, biocentric value system, i.e., non-anthropocentric, assigns intrinsic value to all individual living systems, including but not limited to humans, and assumes that all living systems have value even it its usefulness to human beings cannot be determined or can be harmful to human beings. In this paper, the use of a valuation approach with the following characteristics is proposed:
- Anthropocentric in nature based on utilitarian principles
- Consideration of all instrumental values, including existence value

- Its utilitarian basis to permit the potential for substitution among different sources of value that contribute to human welfare
- Individual's preferences or marginal willingness to trade one good or service for another that can be influenced by culture, income level and information making it time- and context-specific
- Societal values as the aggregation of individual values

This approach is consistent with NRC (2004) and does not capture non-anthropocentric values, e.g., biocentric values and intrinsic values as it related to rights. In some decisions including environmental policy and law, biocentric intrinsic values should be included in agreement with previous practices, e.g., the Endangered Species Act of 1973.

A total economic value (TEV) framework can be constructed based on the above characteristics and using individual preferences and values. The TEV framework is necessary to ensure that all components of value are recognized and included while avoiding double counting of values (Bishop et al. 1987, Randall 1991).

An economic measure of the value of a good or the benefit from a service can be defined as the maximum amount a person is willing to pay for this good or service. The concept of willingness to pay (WTP) is central to economic valuation. An alternate measure is the willingness to accept (WTA) of an amount by the person to forgo taking possession of the good or receiving the service. WTP and WTA produce amounts that are expected to be close; however generally WTA generated amounts are greater than WTP generated amounts due primarily to income levels and affordability factors.

The valuation of resilience can be based on the savings in potential direct and indirect losses, and cost of recovery as illustrated in Figure 1. Alternatives for enhancing resilience that can reduce these potential losses can be analyzed using models for benefit–cost analysis, where the benefit (B) is the potential savings in losses and recovery costs due to the implementation of an alternative and the cost (C) is the cost of the alternative. The benefit and costs are treated as random variables (Ayyub 2003). Assuming B and C to be normally distributed, a benefit–cost index ($\beta_{B/C}$) can be defined as follows:

$$\beta_{B/C} = \frac{\mu_B - \mu_C}{\sqrt{\sigma_B^2 + \sigma_C^2}} \tag{9}$$

where μ and σ are the mean and standard deviation. The probability of cost exceeding benefit can be computed as:

$$P_{f,B/C} = P(C > B) = 1 - \Phi(\beta) \tag{10}$$

where Φ is the standard normal cumulative distribution function. In the case of lognormally distributed B and C, the benefit–cost index ($\beta_{B/C}$) can be computed as:

$$\beta_{B/C} = \frac{\ln\left[\frac{B}{C}\sqrt{\frac{\sigma_C^2 + 1}{\sigma_B^2 + 1}}\right]}{\sqrt{\ln[(\sigma_B^2 + 1)(\sigma_C^2 + 1)]}} \tag{11}$$

where δ is the coefficient of variation. In the case of mixed distributions or cases involving basic random variables of *B* and *C*, other reliability methods can be used as described by Ayyub (2003).

6. Conclusions

Enhancing the resilience of a system, including buildings, infrastructure, network and communities, could lead to massive savings through risk reduction and expeditious recovery. In this paper, a resilience definition is provided that meets a set of requirements with clear relationships to metrics of the relevant abstract notions of reliability and risk. Those metrics also meet logically consistent requirements drawn from measure theory, and provide a sound basis for the development of effective decision-making tools for multi-hazard environments. The proposed metrics provide a strong basis for the rational management of such reduction and recovery facilitated by an appropriate definition of resilience and associated metrics. Also, the paper provides a framework for the valuation of resilience by society at large, methods for benefit-cost analysis based on concepts from risk analysis and management. Although resilience valuation is in its infancy and additional work is necessary along with case studies, this paper offers a basis for such efforts.

References

Ayyub, B. M., Braileanu, H. G., and Qureshi, N., 2012, "Prediction and Impact of Sea Level Rise on Properties and Infrastructure of Washington, DC," Risk Analysis Journal, 32(11), 1901-1918.

Ayyub, B. M., 2013, "Systems Resilience for Multi-Hazard Environments: Definition, Metrics and Valuation for Decision Making," Risk Analysis J., DOI: 10.1111/risa.12093.

Ayyub, B. M., 2003. Risk Analysis in Engineering and Economics, Chapman & Hall/CRC, Taylor & Francis Group, Boca Raton, NY.

Bishop, R.C., Boyle, K. J., and Welsh, M. P. 1987, "Toward Total Economic Value of Great Lakes Fishery Resources," Transactions of the American Fisheries Society, 116 (3), 339-345.

Callicott, J.B. 2004. Explicit and Implicit Values in the ESA. In The Endangered Species Act at Thirty: Retrospect and Prospects, Davies, Goble, Heal, and Scott (eds.), Island Press, Washington, DC.

Ellingwood, B.R., & Mori, Y., 1993, "Probabilistic Methods for Condition Assessment and Life Prediction of Concrete Structures in Nuclear Plants," Nuclear Engineering and Design, 142, 155-166.

Holling, C. S., 1973, "Resilience and Stability of Ecological Systems," Annual Review of Ecology and Systematics, vol. 4, pp. 1–23, 1973.

International Organization of Standardizations (ISO), 2009, Risk Management – Risk assessment techniques, ISO Standard IEC/FDIS 31010, iso.org, Geneva, Switzerland.

MCEER, 2010. "PEOPLES: A Framework for Defining and Measuring Disaster Resilience." Working Paper, Multidisciplinary Center for Earthquake Engineering Research (MCEER) of the State University of New York at Buffalo.

National Research Council, 2004. Valuing Ecosystem Services: Toward Better Environmental Decision-Making, The national Academies Press, Washington, DC.

Presidential Policy Directive (PPD), Critical Infrastructure Security and Resilience. PPD-21, Released February 12, 2013, http://www.whitehouse.gov/the-press-office/2013/02/12/presidential-policy-directive-critical-infrastructure-security-and-resil

Randall, A. 1991. Chapter 10 Total and Nonuse Values in Measuring the Demand for Environmental Quality, Braden, J.B., and C.D. Kolstad (eds.). North Holland, Amsterdam.

UNISDR, 2012, Making Cities Resilient: My city is getting ready! A global snapshot of how local governments reduce disaster risk, United Nations Office for Disaster Risk Reduction Report, Geneva, Switzerland, www.unisdr.org/campaign

The Risk Analysis of Long-distance Pipeline System in Mountain Area Subjected to Multi-hazard (I): Risk of Rain-Caused Landslide

Jinghua Huang[1], Zhaohui Chen[2], Peng Zhang[3] and Wenliang Fan[4]

ABSTRACT

This is the first one of a succession paper of the risk analysis of pipeline due to multi-hazard in mountain area. The present paper is focused on the risk of rain-caused landslide which would induce the damage of the pipeline. Considering the spatial variations of soil hydraulic properties, such as permeability and pore size distributions, the random field model for unsaturated seepage is present by the application of stochastic finite element method. A 3D probability based slope stability analysis model due to the rainfall by the application of limit equilibrium method is applied. The spatial variation of soil hydraulic properties is analyzed.

KEY WORDS

Rain caused landslide, Slope stability, Pipeline system, Soil hydraulic property

INTRODUCTION

The pipeline system is an important infrastructure for collection and transmission subjects for long distance, such as the drainage or sewage pipeline system and gasoline pipeline system in urban. Once damaged, it would result in tremendous economic losses and/or environmental effects. With the process of global warming and urbanization, the extreme value of rainfall and the ratio of impervious surface in urban is growing greatly which would increase the risk of landslide and flooding in mountain area. In mountain area, the elevated pipe and buried pipe are the two common used pipe types. The buried pipe is prone to the risk of landslide in continuous rain, while the elevated pipe crossing gully or river is fragile to the attack of rain-induced floods (Chen et.al. 2011). By now, the mechanism-based theoretical model for the slope stability analysis due to the rainfall is still in requirement. Most of the rain-induced slope stability analysis models are based on the data statistics and empirical arguments (Dai & Lee 2001; Zhang 2005; Zhang et al. 2007). It has been

---

[1] Faculty of Civil Engineering, Chongqing University, Chongqing 400045, China. Email: hjh.524@163.com.
[2] Faculty of Civil Engineering, Key Laboratory of New Technology for Construction of Cities in Mountain Area, Chongqing University, Chongqing 400045, China.
[3] Guizhou Electric Power Design Institute, NO. 56 Zunyi Road, Guiyang 550002, China.
[4] Faculty of Civil Engineering, Key Laboratory of New Technology for Construction of Cities in Mountain Area, Chongqing University, Chongqing 400045, China.

commonly recognized that the negative pore water pressure, also referred to be matrix suction, contributes to the decrease of shear strength and thus deduce the slope stability. With the water infiltrating into the soil, the pore water pressure turns to be positive from negative which would result in the instability of slope. Ng (Ng 1998) investigated the physical processes of slope instability caused by rainfall infiltration and proposed a landslide prediction model taken into account of the change of soil properties due to rainfall infiltration. This model provides an explanation for the mechanism of rain-induced landslide. However, the temporal and spatial variations of the soil properties during the rain process are ignored for the simplification purpose in this model which would cause inappropriate assessment of the probability of rain-caused slope stability (Guo et al. 2007).

Considering the uncertainties of the factors influencing the safety of pipeline system, the probability based analysis method might be an appropriate method (Bryan et al. 2001). Taken into account of the spatial variations of soil hydraulic properties, such as permeability and pore size distributions, the random field model for unsaturated seepage is present in this paper. A 3D probability based slope stability analysis model considering the degradation of the shear strength of soil and increasing of pore water pressure due to the rainfall by applying the limit equilibrium method is provided. The application of the present model is shown in the succession paper.

THE RISK ANALYSIS OF SLOP STABILITY DUE TO RAINFALL

The slope instability due to the rain in mountain area is, in great degree, related to rainfall infiltration. During the process of raining, the soil moisture content increases and the matrix suction decreases with the rainfall infiltration, resulting in the degradation of soil shear strength that would cause landslide (Fredlund 1993). Because of the un-uniform of the mineral composition, deposition conditions, stress history, weathering and other geological effects from point to point, the soil parameters such as soil shear strength, compressibility, soil permeability and so on, are spatial variation. In addition, due to the time variant raining process, the rain-induced slope stability is also time-dependent. Based on the traditional deterministic assessment approach of the slope stability, the space-time variation is simplified as random variables, or uniform characteristics. In order to take into account of the spatial variations of shear strength in a specific slope due to the extreme rain, a stochastic simulation model is proposed. Based on the present random field of the permeability and shear strength of soil in slope, a three dimensional slope stability analysis model originated by Vanmarcke(Vanmarcke 1977) is applied for the probability assessment of the rain-caused slope stability.

The random field model of soil shear strength under drainage.
According to Darcy's law and mass conservation law, the governing differential equation of porous media seepage in the condition of rainfall infiltration can be obtained as (Liu 2006):

$$\frac{\partial}{\partial x}\left[K_x(\theta)\frac{\partial H}{\partial x}\right] + \frac{\partial}{\partial y}\left[K_y(\theta)\frac{\partial H}{\partial y}\right] + \frac{\partial}{\partial z}\left[K_z(\theta)\frac{\partial H}{\partial z}\right] = m_w \gamma_w \frac{\partial H}{\partial t} \tag{1}$$

where $K_x(\theta)$, $K_y(\theta)$ and $K_z(\theta)$ are the coefficients of permeability in the directions of x, y, and z respectively; H is the space-dependent head which equals to the sum of position head h_z and pore water pressure head h_w, $h_w = u_w/\gamma_w$, u_w is the pore water pressure, γ_w is the weight of water per unit volume; t is the time. m_w, the so called soil water capacity, is the slope of the curve of volumetric water content to the matrix suction head. Because of the common adaptation of van-Genuchten-Mualem model (VGM) (Van Genuchten 1979)) to most of the soil hydraulic characteristics as shown in Eq.(3), it is chosen for the simulation of the soil-water relationship.

$$\theta(h) = \begin{cases} \theta_r + \dfrac{\theta_s - \theta_r}{[1+|\alpha h|^n]^m} & h < 0 \\ \theta_s & h > 0 \end{cases} \tag{2}$$

where $m = 1-1/n$，$n > 1$; h and θ are matrix suction head and volumetric moisture content respectively varied with space; θ_s and θ_r are the saturated-and-residual volumetric water content respectively; α and n are shape parameters. Then the unsaturated permeability due to rainfall can be simulated as:

$$K(\theta) = K_s \left(\frac{\theta-\theta_r}{\theta_s-\theta_r}\right)^{\frac{1}{2}} \left\{1 - \left[1 - \left(\frac{\theta-\theta_r}{\theta_s-\theta_r}\right)^{\frac{1}{m}}\right]^m\right\}^2 \tag{3}$$

where K_s is the coefficient of saturated permeability which could be separated into different directions as in Eq.(1), being assumed rationally as a lognormal random field in a specific slope. The rainfall is introduced by the given flow boundary condition. When the rainfall intensity is greater than the mean value of coefficient of permeability, the constant head boundary condition is used; otherwise, the constant flow boundary condition is used. The pore water pressure field varied linearly with depth could be used as the initial condition. By the combination of Expression (1)-(3), based on the random filed models of coefficients such as θ_s, θ_r ans K_s, the random field of the pore water pressure can be obtained by the stochastic finite element method.

A numerical simulation example of a typical slope with silt soil is given as follows. The parameters for VGM model are shown in Table 1. Figure.1 gives the rainfall in 30 days according to the rain record in Chongqing. The atmospheric boundary condition and deep drainage boundary condition are applied at the surface and bottom of the slope respectively, while the two lateral boundaries are assumed as no-flow boundaries. During the numerical simulation, the pore-air pressure is ignored, so the matrix suction head equals to the negative pore water pressure head, $-h_w$. The simulated random distributed permeability and pore-water pressure with various correlation lengths of the coefficient of saturated permeability K_s in horizontal and vertical space, δ_h and δ_v respectively, are shown in Figure 2 and Figure 3.

According to Figure 2 and Figure 3, as the ratio of the δ_h/δ_v increases, the saturated permeability exhibited in the layer characteristic more and more obviously. As the correlation length of the coefficient of saturated permeability K_s in space increases, the spatial variation of the saturated permeability and the fluctuation of the pore water pressure at the same level decrease.

Fredlund et al.(Fredlund et al. 1993) proposed the simulating method of shear strength s of unsaturated soil, based on Mohr–Coulomb criterion, in which the matrix suction and the net normal stress at the failure surface of slope is taken into account.

$$s = c' + (\sigma - u_a)_f \tan\varphi' + (u_a - u_w)_f \tan\varphi^b \tag{4}$$

where c' is effective cohesion; u_a and u_w are the pore-air and pore-water pressure on the failure surface respectively, (u_a-u_w) is the matrix suction; φ' is the angle of internal friction to the net normal stress $(\sigma-u_a)$, while σ is the total normal strength on the failure surface. φ^b is the angle of internal friction indicating the ration between shear strength and the matrix suction. According to D.V. Griffiths (Griffiths 2011), the parameters c', φ', φ^b are all spatial variation and could be treated as lognormal random fields. Assuming the net normal stress $(\sigma-u_a)$ as a lognormal random field, the random field of the soil shear strength could be simulated by the application of Motel-Carlo method using the for-mentioned pore-water random field model in the condition of specific rainfall.

Table. 1 The parameters of soil water characteristic of VGM model

Parameters	θ_r/(cm^3/cm^3)	θ_s/(cm^3/cm^3)	α	N	K_s/(mm/d)	L
Values	0.067	0.45	0.02	1.41	10.8	0.5
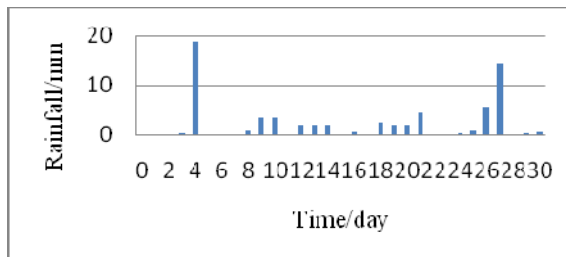
Figure 1. Rainfall record in October 2009 in Chongqing

| (a) | (b) | (c) |
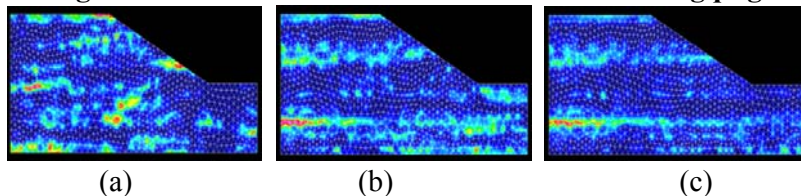
Figure 2. Typical random field realizations of saturated permeability with various correlation lengths: (a) δ_h=10m, δ_v=1m ; (b) δ_h=30, δ_v=1m; (c) δ_h=50m, δ_v=1m.

| (a) | (b) | (c) |
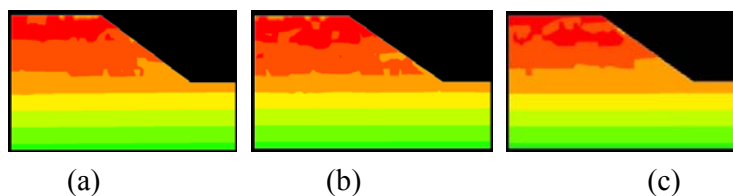
Figure 3. Typical random field realizations of pore water pressure with various correlation lengths: (a) δ_h=10m, δ_v=1m; (b) δ_h=30, δ_v=1m; (c) δ_h=50m, δ_v=1m.

The risk assessment of three-dimensional slope stability due to rainfall.
The limit equilibrium method of rigid body, such as Bishop method, Janbu method, Spencer method and so on, is one of the common used methods of slope stability analysis (Duncan 2005). These methods are all limited within the framework of conventional plane force-displacement analysis of slope stability. In fact, the (2-D) slope analysis defined in the context plane strain, is not a well-defined physically realizable event. Vanmarcke (Vanmarcke 1977; 1980) proposed a basic three-dimensional (3-D) slope stability approach in probabilistic framework in a simple and practical way. The procedure used is basically an extension of the circular arc method by regarding the sliding mass as a portion of a cylinder with finite length bounded by vertical soil end sections. The model is described in Figure 4. In the present paper, we extension the 3-D method provided by Vanmarcke into the situation of rain-caused slope stability analysis by taken into account of the soil strength characteristics under drainage.
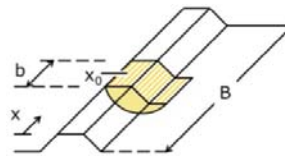
Figure 4. The three-dimensional sliding mass model

The safety factor of 3-D slope stability can be expressed as follows:

$$F_b(x_0) = \frac{M_{R,b}(x_0) + R_e}{M_{D,b}(x_0)} = \frac{s_b L r b + R_e}{W a b} \tag{5}$$

where s_b is the mean shear strength on the slip surface of length b, L is the length of the slip arc; r is the radius of circular slip arc which can be determined by the plane slope stability analysis method; W is the soil mass of per unit width over the sliding surface; a is the horizontal distance from the center of rotation to the center of gravity of the slope; R_e is the contribution of the both end sections to the resistance moment.

For the purpose of simplification, the soil shear strength can be assumed as stationary random field along the slope axis x. So the mean value of soil shear strength is uniform over the length b. In general, the coefficient value of the correlation decreases with the distance between two vertical sections, as well as between two points at the slip arc. Let the standard deviation of soil shear strength along the axis x for unit length is $\tilde{s}_1$, so the standard deviation within the length of b can be expressed as $\tilde{s}_b = \Gamma(b)\tilde{s}_1$, where $\Gamma(b)$ is the reduction factor of correlation within b. The reduction factor can be expressed approximately as the follows,

$$\Gamma(b) = \begin{cases} 1; & b \leq \delta \\ \left(\frac{\delta}{b}\right)^{\frac{1}{2}}; & b \geq \delta \end{cases} \tag{6}$$

where δ is correlation length of the soil shear strength within the length b. The mean of safety factor of 3-D slope stability is:

$$\overline{F_b} = \frac{\overline{s_2} L r b + R_e}{W a b} \tag{7}$$

where R_e the contribution of the both end sections to the resistance moment is calculated as $R_e \approx \overline{R_e} = 2Ar'\bar{s}$, A is the cross section area, r' is effective rotation arm for the end sections and approximately equals to r for simplification. The variance of the safety factor of slope stability is $\widetilde{F_b} = \Gamma(b)\tilde{F}$. $\tilde{F}$ is the standard deviation of the 2-D cross-sectional safety factor. Then the reliability index of the slope stability can be expressed in terms of the mean and standard deviation of the factor of safety as follows:

$$\beta_b = \frac{\overline{F_b}-1}{\widetilde{F_b}} \tag{8}$$

Assume the safety factor F_b follow a Gaussian probability distribution, the failure probability within the length of b is given in Eq.(9):

$$P_f(b) = P(F_b \leq 1) = P\left(\frac{F_b-\overline{F_b}}{\widetilde{F_b}} \leq -\beta_b\right) \tag{9}$$

For a certain slope segment B, it is unrealistic that the slope failures either in a very small width or in a very large width. It is reasonable to infer that there is a range of most likely width of the failure zone. Varmarcke (Varmarcke 1980) also provided the approximation of the so called critical width b_{cr} for the most likely failure zone in slope segment B, on which the minimum reliability index $\beta_{b_{cr}}$ or the maximum failure probability is dependent. Based on $\beta_{b_{cr}}$ and the related reduction factor $\Gamma(b_{cr})$, the threshold crossing analysis method is used to get the system failure probability of a slope segment $P_F(B)$, by assuming that a slope failure will occur if the safety factor crosses into the unsafe domain $F_{bcr} < 1$ at any location x.

$$P_F(B) \cong \frac{B}{b_{cr}}\left(\pi\sqrt{2}\right)^{-1}[\Gamma(b_{cr})]^{-1}exp\left(-\beta_{b_{cr}}^2/2\right) \tag{10}$$

The risk of the slope stability due to the rain is a conditional probability dependent on the event of the rain which is spatial-time variant. As given in Eq.(11), the risk of the slope stability within the length b could be assessed on the condition of given extreme value of rainfall in specific recurrence period, such as 1 year, 10 years et al..

$$
\begin{aligned}
P_{risk\ of\ slope\ stability}\left(B\right) &= P_{risk\ of\ slope\ stability}\left(b^{*}\right) = P\left(F_{b^{*},rain} \leq 1 \middle| \text{given rainfall}\right) \\
&= P_{f}\left(F_{b^{*},rain} \leq 1\right) P\left(\text{rainfall in specific recurrence period}\right)
\end{aligned}
\tag{11}
$$

CONCLUSION

The slope instability due to the rain in mountain area is related to rainfall infiltration. During the process of raining, the soil moisture content increases and the matrix suction decreases with the rainfall infiltration, resulting in the degradation of soil shear strength that would cause landslide. It is shown that the parameters c', φ', φ^{b} are all spatial and temporal variations which could be treated as lognormal random fields. Considering the spatial variations of soil hydraulic properties, such as permeability and pore size distributions, the random field model for unsaturated seepage is present by the application of stochastic finite element method. The common used (2-D) slope analysis defined in the context plane strain, is not a well-defined physically realizable event. A 3D probability based slope stability analysis model due to the rainfall by the application of limit equilibrium method is applied. The procedure used is an extension of the circular arc method by regarding the sliding mass as a portion of a cylinder with finite length bounded by vertical soil end sections. The risk of the slop stability within the finite length is assessed on the condition of given extreme values of rainfall in specific recurrence period.

REFERENCES

Bryan A., Rade H., & Eugen B. (2001). "Comparison of hazard scenarios using probabilistic methods." *Safety, Risk Reliability-Trends in Engineering*. Malta: IABSE.

Chen Z. H., & Huang J. H. (2013). "The risk assessment of the sewage pipeline system in the urban area of Chongqing." *Proceedings of the 11th International Probabilistic Workshop*, Brno 2013, 127-134.

Griffiths D.V., Jinsong H., & Gordon A. F. (2011). "Probabilistic infinite slope analysis." *J. Computers and Geotechnics*, 38, 577-584.

Dai F. C., Lee C. F. (2001). "Frequency-volume relation and prediction of rainfall-induced landslides." *J. Engineering Geology*, 59: 253-266.

Fredlund D. G., Rahardjo H. (1993). *Soil mechanics for unsaturated soils*. New York: John Wiley & Sons.

Guo C. B., Zhang Y. S., et.al. (2007). "Monte-Carlo reliability analysis of landslide based on numerical solution of Sweden slice method." *J. Hydrogeology & Engineering Geology*, 4: 18-21.

Duncan J. M., Wright S. G. (2005). *Soil strength and slope stability*. New York: John Wiley & Sons.

Liu J. L., et al. (2006). "Seepage and stability analysis of saturated- unsaturated soil slope under rainfall infiltration." *J. Rock and Soil Mechanics*, 27(Supp): 103-107.

Ng C. W., Shi Q. (1998) "A numerical investigation of the stability of unsaturated soil slopes subjected to transient seepage." *J. Computers and Geotechnics*, 22(1)：1-28.

Van Genuchten M. (1979). "A closed form equation for prediction the hydraulic conductivity of unsaturated soils." *J. Soil Science Society of America Journal*, 44(5): 892-898.

Vanmarcke E. (1977) "Reliability of earth slopes." *J. Journal of the Geotechnical Engineering Division*, ASCE, , 103(GT11): 1247-1265.

Vanmarcke E. (1980). "Probability stability analysis of earth slopes", *Engineering Geology,* 16:29-50.

Vanmarcke E. (2010). *Random fields: Analysis and Synthesis*. 2nd Edition. World Scientific Publishing Company: 1st Edition, M.I.T. Press.1983.

Vanmarcke E. (2011) "Risk of limit-equilibrium failure of long earth slopes: how it depends on length." GeoRisk 2011: Geotechnical Risk Assessment and Management-Proceedings of the GeoRisk 2011, n224 GSP, 1-24.

Zhang Y. Y., Hu Y. W., & Zhu H. Y. (2007). "Prospect of research on relationship between landslide and rain fall." *J. Journal of Natural Disasters*, 1: 104-108.

Zhang Z., Li S. H., & Ma L. (2005). "Probability analysis of relationship between landslide and rainfall in Chongqing area." *J. Chinese Journal of Rock Mechanics and Engineering*, 24(17): 3185-3191.

The Risk Analysis of Long-distance Pipeline System in Mountain Area Subjected to Multi-hazard (II): the Application

Zhaohui Chen[1], **Jinghua Huang**[2], **Peng Zhang**[3] and **Wenliang Fan**[4]

ABSTRACT

In mountain area, the pipeline system is friable to multi-hazards, such as the rainfall induced flood and landslide, the deterioration of the pipe materials due to the erosive effects of soil, gas, waste water inside or outside of the pipe, and improper municipal construction, et al.. In the second one of a serial of papers of the risk analysis of pipeline in mountain area, the risk analysis models of rain-caused landslide and rain-induced flood are applied to evaluate the safety grade of the pipeline system. The extreme value distribution functions of the rain-induced flooding in different rainfall recurrence intervals are modeled by taking into account of the terrain feature and surface runoff of specific gully, and also the statistics of the rainfall records in recent 30 years in Chongqing. A comprehensive hierarchical model for the risk assessment of the pipeline, by taking into account of the multi damage modes of the pipe under multi hazards, is proposed. The application of the present model in Chongqing is given in the end to approve its practicability.

KEY WORDS

Risk analysis, Rain caused flood, Pipeline system, Mountain area, Hierarchical model

INTRODUCTION

This is the second one of a succession paper, which discusses the risk of long-distance pipeline system in mountain area. As mentioned in the first paper, the pipeline system is an important infrastructure for collection and transmission subjects for long distance, such as the drainage or sewage pipeline system and gasoline pipeline system in urban. In mountain area, the elevated pipe and buried pipe are the two common used pipe types. The buried pipe is prone to the risk of landslide, while the elevated pipe crossing gully or river is fragile to the attack of rain-induced floods (Chen et.al. 2011). In addition, the deterioration of the pipe materials due to the erosive effects of soil, gas, waste water inside or outside of the pipe, and improper municipal construction and other factors would result in the degradation of structural performance, and reduce the safety of pipeline system (Chen, et al.,2003). Therefore,

[1] Faculty of Civil Engineering, Key Laboratory of New Technology for Construction of Cities in Mountain Area, Chongqing University, Chongqing 400045, China.
[2] Faculty of Civil Engineering, Chongqing University, Chongqing 400045, China. Email: hjh.524@163.com.
[3] Guizhou Electric Power Design Institute, NO. 56 Zunyi Road, Guiyang 550002, China.
[4] Faculty of Civil Engineering, Key Laboratory of New Technology for Construction of Cities in Mountain Area, Chongqing University, Chongqing 400045, China.

it is necessary for the risk analysis of the long-distance pipeline system in mountain area subjected to multi-hazard.

In the first paper, a 3D probability based slope stability analysis model due to the rainfall by the application of limit equilibrium method is present. However, the damage of the gully or river crossing bridges and pipelines, caused by the impact of flood is another worldwide problem in mountain area. Most of the research efforts are concentrated on the risk assessment of river crossing bridge while the risk analysis of the river crossing pipeline to flood is lack. Considering the risks due to flood impulse and other damage factors, Elias (Elias 1994) provided a risk assessment model based on the database of the bridges in US, that was developed by Gardner et al. (Gardner et al. 1999). Bryan (Bryan 2001) defined the limit states of bridge subjected to flood impulse and analyzed the failure probability of bridge respect to different limit states. The research on the spatial variations of flood, esp. on the non-uniform and uncertainty distributions of flood impact force to the river or gully crossing structures are still deficiency.

Considering the uncertainties of the factors influencing the safety of pipeline system, the probability based analysis method might be an appropriate method. However, most of the probability based risk analysis models of pipeline systems are simplified the uncertainties into random variables (Bao and Mays 1990; Tang et al. 1991), by ignoring the temporal and spatial variations of rainfall and of the soil properties and topographies of river bed or gully. Therefore, the slop stability model and the flood risk analysis model are applied for the damage risk assessment of the pipeline. The 3D probability based slope stability analysis model, present in the first paper, considers the degradation of the shear strength of soil and the increasing of pore water pressure due to the rainfall by applying the limit equilibrium method. In addition, the extreme value distribution functions of the rain-induced flooding in different rainfall recurrence intervals are modeled by taking into account of the terrain feature and surface runoff of specific gully, and also the statistics of the rainfall records in recent 30 years in Chongqing. Based on these rain-caused natural hazard risk analysis models, a comprehensive hierarchical model for the risk assessment of the pipeline, by taking into account of the multi damage modes of the pipe under multi hazards, is proposed.

THE RISK ANALYSIS OF FLOOD DUE TO RAINFALL

The rainfall-induced flood in a gully is a convergence process, dependent on the temporal and spatial variation of rainfall process, the time of flow convergence which depends on watershed runoff, the geological characteristics, hydraulic and characteristics of soil. For a specific gully, according to local rainfall records and geological characteristics, the convergence time of flow in the gully can be calculated based on hydrology theory. Zhang and Chen (Zhang 2013) provide an extreme value of flood flow assessment method based on the geological and topographical information in a specific gully and the rainfall data in Chongqing. In the present method, based on 30 years rainfall records from 1980 to 2009 in Chongqing, and the geological and topographical information, the convergence time of flood flow in the

specific gully located at the Yangtze River estuary is determined which is less than one hour. According to the records of rainfall in 30 years, the runoff parameters and statistics of the effects of geological and topographical of the gully, the distributions of the flood flow extreme value different recurrence intervals is obtained which obeys the Pearson-III type distribution function. The flood flow extreme value in different recurrence period in Chongqing for a specific gully is shown in Table 1. There might be several failure modes of the gully-crossing pipe subjected to the flood force, such as the yield of the reinforcement, the cracking of the concrete, and the large lateral shift of the pipe which could result in the pipe turning over. The critical flood flow Q_{mi} corresponding to different failure modes can be ascertained by the numerical simulation of the pipes under the load case of flood. Therefore, the failure risk of the pipeline subjected to the flood force caused by rainfall in different recurrence periods can be expressed as the likelihood that the flood flow in a particular periods exceeds the critical flow as in Eq.(1). In Table 2, an example of a particular pipe segment in Line A, one of the primary sewage pipeline in Chongqing, is given with the probability of critical flood flow and flood level to different failure mode of the specific gully-crossing elevated culvert. The recurrence period of the rainfall considered in Table 2 is 30 year and the data is based on the record of Chongqing.

$$P_{\text{risk due to flood}} = P_f \left\{ \bigcup_i Q_m > [Q_{mi}] \right\} \tag{1}$$

Table 1. The flood flow extreme value in different recurrence period for a specific gully in Chongqing

Recurrence period T	50	20	10	5	3	2	1
flood flow extreme value Q_m	2563	2201	1911	1590	1107	849	699

Table 2. The probability of critical flood flow and flood level to a pacific pipe in 30 years according to the rainfall record of Chongqing

Failure mode of pipe	Flood level (%)	Critical flood flow (m³/s)	Probability (%)
reinforcement yield of top board	38	1953.20	9.3
concrete cracking	43	2023.40	8.1
pipe over turning	49	2107.63	6.6
reinforcement yield of lateral board	66	2348.72	3.8
Load capacity loss	78	2531.45	2.3

THE RISK ANALYSIS OF PIPELINE SYSTEM IN MOUNTAIN AREA

As mentioned above, the pipeline system in mountain area is subjected to various natural hazards. By applying the hierarchical analysis methodology (Prasanta 2003), a

synthesis risk assessment model considering effects of multi-hazard for long-linear pipeline system by combining the qualitative judgment and quantitative evaluation is proposed below.

The proposed hierarchical analysis model for the risk assessment of the pipeline system in mountain area is shown in Figure 1. At the bottom layer of the model, they are the failure factors of the pipeline which could be the natural hazard or human errors. For the simplification, it is sound to ignore the interaction and the concurrence opportunities of several hazard events. At the second layer, they are the damage modes caused by the natural hazard or human errors. In the present model, the considered damage modes of pipeline include the load capacity failure mode and durability damage mode. The durability damage mode refers to the erosion of concrete and the corrosion of steel bar. The load capacity failure mode are such as the yield of the reinforcement, the over-large deformation of the pipe, the cracking of concrete et al., caused by the internal over-pressure in the rain-storm, the rainfall-induced landslide, the flood, the explosion of gas inside the pipe and other random events such as improper construction by human error termed as third-part damage.

The third layer of the model is the numbered pipeline section, and the forth layer, is the category of pipe. According to the types of the pipe, elevated pipe or buried pipe, and the geological condition, the pipeline is divided into several categories, such as the elevated pipes crossing gully which is subjected to flood, the elevated pipes over plain which is prone to the over-internal-water-pressure due to the rain-storm, the buried pipes subjected to the over-soil-pressure due to the rain-induced landslide, or construction of new buildings on the site of the pipe, et al.. For different categories, the different failure mode to different hazard is taken into account respectively. By now, it is difficult to predict the exact soil pressure to the pipe due to the landslide, so it is practical and reasonable to simplify the risk assessment of the buried pipes due to the landslide as the stability risk analysis of the slope aside the pipe.
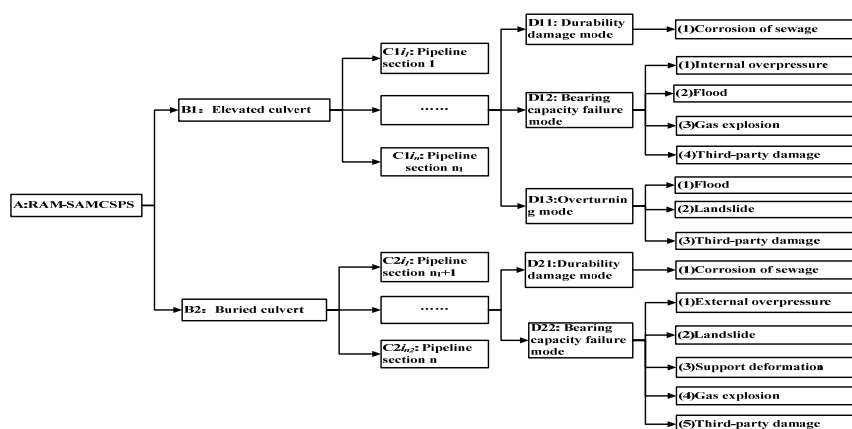
Figure 1. The hierarchical analysis model for the safety assessment of pipeline system in mountain area

For simplification, a discrete safety or damage grade criteria, instead of the continuity reliability index or failure probability, is introduce. Totally four grades are present, which are Grade 1, related to the pipe in good working condition, no obvious crack observed; Grade 2, to the working situation of pipe that small cracks at the concrete cover observed, the reinforcement and stirrups in elastic state; Grade 3, to the working condition of pipe that the stirrups yield, the longitudinal reinforcement in elastic state, and cracks being obvious in the tension area; Grade 4, refers to the situation that the longitudinal reinforcement yield, the load capacity and stiffness of the culvert being deduced severely. More details of the criteria is given by Chen (Chen 2011; Chen 2013).

The risk of one failure mode for a specific pipe subjected to several load cases could be evaluated as follows.

$$\alpha_{i,j} = max_k\{\alpha_{k,i,j}\} + \begin{cases} 1, & \alpha_{k,i,j} \geq max_k\{\alpha_{k,i,j}\} - 1 > 1 \\ 0, & otherwise \end{cases} \tag{2}$$

in which, $\alpha_{i,j}$ is the grade of failure mode i for pipe section j, $\alpha_{k,i,j}$ is the grade of the failure mode i subjected to load case k. The method described in Eq. (2) shows that the grade of pipe section j subjected to several load is obtained by adding the maximum grade of this pipe section subjected to specific load. It is reasonable to take into account of the effects of critical load case and the coupled effect of other load cases to pipe.

However, the consequences of different failure modes, such as the load capacity failure mode, the overturning of pipe and the durability damage mode, are quite different. The weighted parameters of different failure modes for different category of pipes are introduced, based on the judgment matrix and the expert's idea (Table 3 and Table 4), for the synthetic risk assessment of pipeline system subjected to multi-hazards. Based on the matrix, the weighted parameters of different failure modes for elevated culverts are (0.163, 0.297, 0.540) , and those for buried culverts are (0.333, 0.667) (Chen 2013).

Table 3. The important factor matrix for elevated culvert

	Durability mode	Load capacity mode	Overturning mode
Durability mode	1	½	1/3
Load capacity mode	2	1	½
Overturning mode	3	2	1

Table 4. The important factor matrix for buried culvert

	Durability mode	bearing capacity mode
Durability mode	1	2
Load capacity mode	½	1

APPLICATION IN CHONGQING

The application of the present risk assessment model for the pipeline system subjected to multi-hazard in mountain area is given below. Line A of the primary sewage pipeline in Chongqing, which is longest sewage pipeline with the length of 23km, setting along the North Shore of Jialing River and collects the sewage water of Jiangbei District of Chongqing, in a comprehensive working conditions with several types of pipes such as elevated pipe, gully-crossing pipe and buried pipe and so on, is selected to be analyzed. The failure due to the risk of rain-caused landslide, flood impact, the internal over-pressure and the corrosion effects of the sewage water are taken into account. The analysing results are shown in Figure 2. It is shown that, most of the pipeline sections are in good working condition with Grade 1 colored in green. The pipe sections, numbered as 120# to 124#, are gulch-crossing culverts subjected to the risk of rain-caused flood, the grade of this section is 2 colored in yellow. The pipeline sections with the number of 38# to 43# and 70# to 80#, are located at the region of high-risk of landslide, are in the grade of 3 en-coloured in orange.
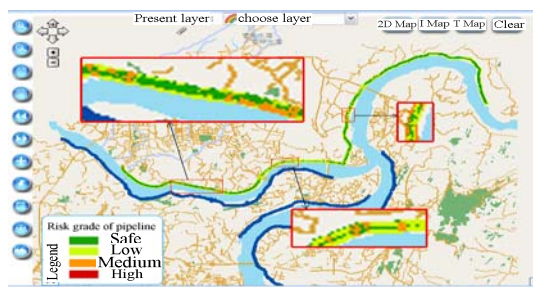
Figure 2. The risk assessment of Line A of the primary sewage pipeline system in Chongqing

CONCLUSION

Because of the particularity of geological and terrain features, and weather conditions, the long-distance tranforming pipeline in mountain area is prone to multi natural hazards, ie. rain-induced landslide and flood, and also to the enviromental corrosion effects. In the present two succession papers, by considering the spatial variations of soil hydraulic properties, such as permeability and pore size distributions, the random field model for unsaturated seepage is present by the application of stochastic finite element method. A 3D probability based slope stability analysis model due to the rainfall by the application of limit equilibrium method is applied. In addition, the extreme value distribution functions of the rain-induced flooding in different rainfall recurrence intervals are modeled by taking into account of the terrain feature and surface runoff of specific gully, and also the statistics of the rainfall records in recent 30 years in Chongqing. By introducing the safety grade criteria, the present hierarchical analysis model can deal with the multi hazard induced damage risk assessment isssue of the long-linear sewage pipeline in moutain area practiclly and effectively. In future, the interaction of load-errosion effects of the pipe, the temporal-spatial variations of the rain fall flood and landslide, the stochastic analysis of the soil properties are needed to be further researched.

REFERENCES
Bao Y. X., Mays L W. (1990). "Model for water distribution system reliability." *J. Journal of Hydraulic Engineering*, ASCE, 116(9): 1119-1137.

Bryan A., Rade H., Eugen B. (2001). "Comparison of hazard scenarios using probabilistic methods." *Safety, Risk Reliability-Trends in Engineering*. Malta: IABSE.

Chen Z.H., He Q., Yan W.T. (2003) Research on the Corrosion of Sewer System Pipelines from Domestic Wastewater. Proceedings of the ASCE International Conference on Pipeline Engineering and Construction: New Pipeline Technologies, Security, and Safety, No.1:524-529.

Chen Z. H., Huang J. H. (2013). "The risk assessment of the sewage pipeline system in the urban area of Chongqing." *Proceedings of the 11th International Probabilistic Workshop*, Brno 2013, 127-134.

Chen Z. H., He Q., Wang G. L., et.al. (2011). "Structural safety analysis of sewage pipeline of typical mountain city in Three Gorges reservoir region." *J. China Water & Wastewater*, 27(8): 22-26.

Chongqing University. (2011). *The Major Projects on Control and Rectification of Water Body Pollution, the inspection report of sub-topics: the structural safety monitoring system research and demonstration of sewage pipeline in mountain city. Chongqing, China.*

Elias V. (1994). *Strategies for managing unknown bridge foundations*. FHWA- RD-92-030.

Prasanta K. D. (2003). "Analytic Hierarchy Process Analyzes Risk of Operating Cross-Country Petroleum Pipelines in India." *J. Natural Hazards Review*, 4(4), , 213-221.

Tang W. H., Yen B. C. (1991). "Dam safety inspection scheduling." *J. Journal of Hydraulic Engineering*, ASCE, 117(2): 214-229.

Van Genuchten M. (1979). "A closed form equation for prediction the hydraulic conductivity of unsaturated soils." *J. Soil Science Society of America Journal*, 44(5): 892-898.

Gardner W. R., James R. S., Stephen R. N. (1999). *Kentucky bridge scour program*. WRPMD.

Zhang P. (2013). *Risk analysis of failure of drainage box culvert built on stilts under heavy rain caused flood in mountain city*. Chongqing: Chongqing University(supervised by Chen Z.H.)

Reliability Assessment of RC Structures Subjected to Carbonation by Incorporating Spatial Variations

T. Hagino[1], M. Akiyama, Aff.M.ASCE[2] and Dan M. Frangopol, Dist.M.ASCE[3]

Abstract: When carbonation reaches the depth of the rebar embedded into the concrete, the high alkalinity of the concrete pore solution is neutralised and hydration products are dissolved. As carbonation progresses, the corrosion could extend enough to deteriorate the structural performance. In this paper, a time-dependent structural reliability analysis method taking the carbonation into consideration is proposed. To predict the corrosion process of reinforced concrete (RC) structures, spatial variability of corrosion has to be considered. A computational procedure to integrate the spatial variability of corrosion due to carbonation into life-cycle reliability assessment of existing RC structures is established. An illustrative example of a RC structure subjected to carbonation is presented. The emphasis is placed on investigating the effects of the spatial variation of inspected carbonation depths on the reliability estimates of RC structures.

Introduction

Carbonation can be defined as the chemical reaction between carbon dioxide present in the air and cement hydration products resulting in the formation of calcium carbonate (Ann et al. 2010). The risk of carbonation is severe in urban or/and industrial area. Carbonation of concrete itself does not do harm to the performance of structure; in fact a marginal enhancement of the compressive strength was observed (Khemm and Berger 1972). However, when carbonation penetration reaches the depth of the steel, the high alkalinity of the concrete pore solution is neutralized and hydration products are dissolved (Sung et al. 2010). Carbonation destroys the passivation film on the steel surface in concrete. Corrosion initiation could lead to cracking due to corrosion products and concrete cover spalling. Cracking and/or spalling accelerate the corrosion rate and finally lead to serviceability failure and a deterioration of long-term structural performance. Such deterioration will reduce the service life of structures and increase the life-cycle cost of maintenance interventions.

It is well recognized that the material properties of a concrete structure and structural dimensions are random due to the spatial variability associated with workmanship and other factors. This randomness cause spatially distributed corrosion damages. Research on reliability assessment has included the spatial variability in RC and PC deterioration process. For example, Engelund and Sørensen (1998) considered spatial variation of the variables associated with the critical

---
[1]Department of Civil and Environmental Engineering, Waseda University, Okubo 3-8, Shinjuku-Ku, Tokyo 169-8555, JAPAN; PH +81-3-5286-2694; FAX +81-3-5286- 3485; e-mail: lili@akane.waseda.jp
[2]Department of Civil and Environmental Engineering, Waseda University, Okubo 3-8, Shinjuku-Ku, Tokyo 169-8555, JAPAN; PH +81-3-5286-2694; FAX +81-3-5286- 3485; e-mail: akiyama617@waseda.jp
[3]Department of Civil and Environmental Engineering, ATLSS Engineering Research Center, Lehigh University, 117 ATLSS Drive, Bethlehem, PA 18015-4729, USA; PH (610) 758-6103; FAX (610) 758-4115; e-mail: dan.frangopol@lehigh.edu

threshold for initiation of corrosion of rebar, coefficient of diffusion of chloride, and surface chloride concentration. They estimated the distribution of the time of initiation of corrosion based on FORM/SORM-analysis. Stewart (2004) considered the spatial variability of pitting corrosion in RC beams. These beams were discretized into a series of elements as one-dimension (1D) random field and maximum pit depths were generated for each reinforcing steel bar in each element. Stewart and Suo (2009) also used a 1D random field to predict the likelihood and extent of corrosion-induced cracking of RC beams. A spatial time-dependent reliability estimation has been established for RC components modeled as two-dimension (2D) random field that considers the effect of pitting corrosion on shear and flexural probabilities of failure (Stewart 2009), and effect of corrosion on cover cracking (Vu and Stewart 2005, Stewart and Mullard 2007). Marsh and Frangopol (2008) presented a novel reliability model for RC bridge deck incorporating both spatial and temporal variations of probabilistic corrosion rate sensor data. The corrosion rate readings from hypothetical sensors were interpolated spatially between sensor locations, and temporally between annual sensor readings.

A procedure to obtain the failure probability of RC structures in a marine environment updated by the Sequential Monte Carlo Simulation (SMCS) was presented in Akiyama et al. (2010), and Akiyama et al. (2012). Using SMCS, multiple random variables related to observational information such as corrosion crack width can be updated simultaneously, even if the relationships between observational information and related random variables are nonlinear and non-Gaussian variables are involved. However, in this procedure, the spatial corrosion distribution was ignored and each reinforcing bar was assumed to have the same steel weight loss over the entire structure analyzed.

In this paper, life-cycle reliability analysis of RC structures subjected to the carbonation by incorporating spatial variations is conducted. Failure probability is estimated by the limit state associated with comparing the carbonation depth with concrete cover. To improve the accuracy in the life-cycle reliability assessment of RC structures, multiple random variables related to the inspected carbonation depth are updated using SMCS. The effect of the spatial variability of inspected carbonation depth on the updated estimates of reliability associated with the occurrence of steel corrosion is discussed in the illustrative example.

Deterioration of concrete subjected to carbonation

Many researchers suggested that the carbonation of RC structures could be divided into four stages (Sung et al., 2010). In the first stage (i.e., the incubation stage) the carbonation depth of concrete has not yet reached a critical threshold. The rebars do not begin to corrode, so that the degradation of structural performance is not significant. As carbonation propagate (i.e., the propagation stage), the corroded rebars tend to grow in volume and generate a dilative pressure towards the surrounding concrete. At the same time, the effective cross-sectional area of the

corroded rebars has been reduced. At the end of the propagation stage, the corrosive speed of rebars reaches a threshold value, resulting in the cracking of the cover concrete.

If carbonation continues, the structure will further deteriorate due to the widening cracks, as depicted by the acceleration stage. Finally, severe degradation of structural performance will occur in the deterioration stage due to intensive cracks in the concrete and severe corrosion of the rebars. For each carbonation stage, if concrete properties, corrosion depths of rebars and the varied strength of rebars can be determined quantitatively, time-dependent structural capacity can be calculated. However, it is very difficult to evaluate the steel weight loss and its spatial variation over the concrete structures subjected to the carbonation. In this study, reliability analysis for concrete structures in the incubation stage is conducted. Failure probability is estimated using the performance function g comparing the carbonation depth with concrete cover. That is

$$g = x_1 \cdot C_v - x_2 \cdot X \tag{1}$$

where $X = \alpha \cdot \kappa \cdot \gamma \cdot \sqrt{t}$ (2)

$$\gamma = (x_3 \cdot WC - 0.25)/\sqrt{0.3(1.15 + 3 \cdot x_3 \cdot WC)} \tag{3}$$

Table 1. Parameters of random variables

Variables	Distribution	Median	COV[a]
x_1	Lognormal	1.0	30.0 %
x_2	Lognormal	1.0	40.0 %
x_3	Lognormal	1.0	20.0 %

[a]Coefficient of variation

where C_v is the concrete cover specified in the design, x_1 is the construction error associated with concrete cover, x_2 is the random variable representing model uncertainty. X is the depth of carbonation (Izumi, 1988, Nakayama and Matsubara, 1992, and Chien et al., 2008), α is the environment coefficient, κ is the material coefficient, γ is the coefficient associated with water to cement ratio, WC is water to cement ratio, and x_3 is the construction error associated WC. In the illustrative example, α and κ are assumed to be 1.0. Table 1 shows assumed parameters and probabilistic distribution of random variables x_1 to x_3.

Procedure for estimating the life-cycle reliability of existing concrete structure subjected to carbonation by incorporating spatial variations

Even though aleatory uncertainty cannot be reduced, improvement in our knowledge or in the accuracy of predictive models will reduce the epistemic uncertainty (Ang and De Leon, 2005). This means that for existing structures, the uncertainties associated with predictions can be reduced by the effective use of information obtained from visual inspections, field test data regarding structural performance,

and/or monitoring. In this study, SMCS is applied to the updating of random variables. Figure 1 shows the flowchart of reliability estimation using SMCS.
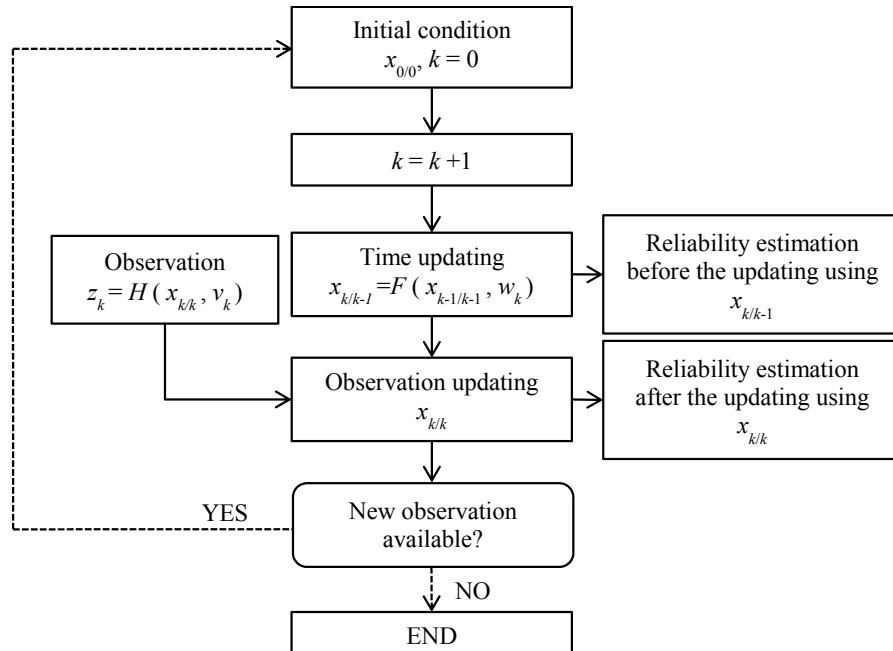
Figure 1. Flowchart of reliability estimation using SMCS

When depth of carbonation by the phenolphthalein test is given, the observation equation based on the observation data (i.e., carbonation depth) is provided by Equations 1 to 3.

$$z = x_2 \cdot \alpha \cdot \kappa \cdot \frac{x_3 \cdot WC - 0.25}{\sqrt{0.3(1.15 + 3 \cdot x_3 \cdot WC)}} \cdot \sqrt{t} + v \tag{4}$$

where z is the observed depth of carbonation from the concrete surface, and v is the observation noise. v is assumed to have a standard normal distribution.
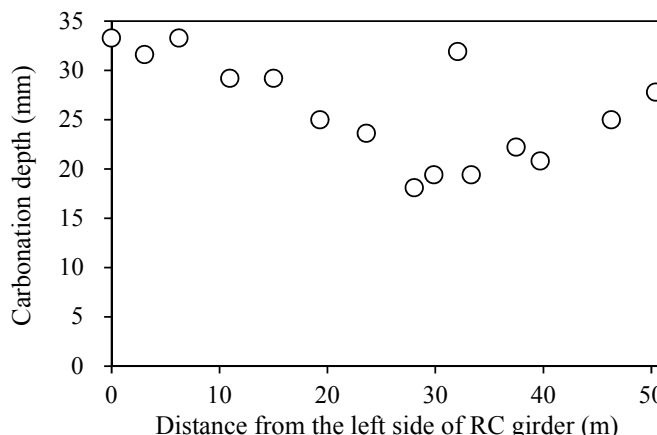
Figure 2. Measured carbonation depth used to determine the parameters for Kriging
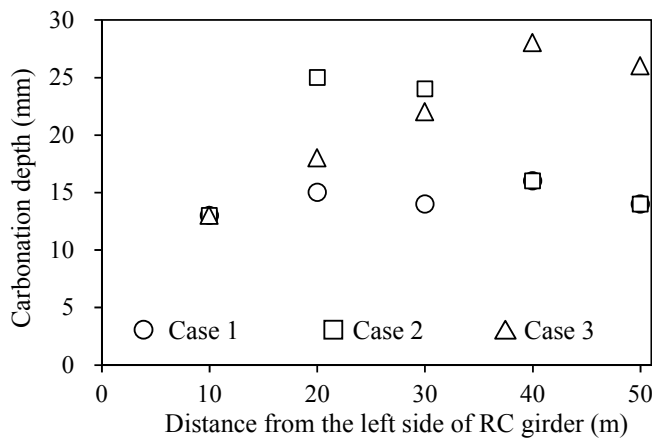
Figure 3. Assumed carbonation depth

It is assumed that spatial variability over longitudinal concrete structure is represented by the use of 1D random field. The spatially distributed variable for concrete structure analyzed is represented by the inspection results of carbonation depth given by the phenolphthalein test. When several inspection results of carbonation depth are provided over concrete structure, Kriging is used to build an approximation of a function from a set of evaluations of the function as a finite set of points (Matheron 1973). Based on the approximated carbonation depth at each location, random variables x_1, x_2 and x_3 are updated using SMCS. As a result, these three random variables are spatially distributed after updating.

Illustrative example
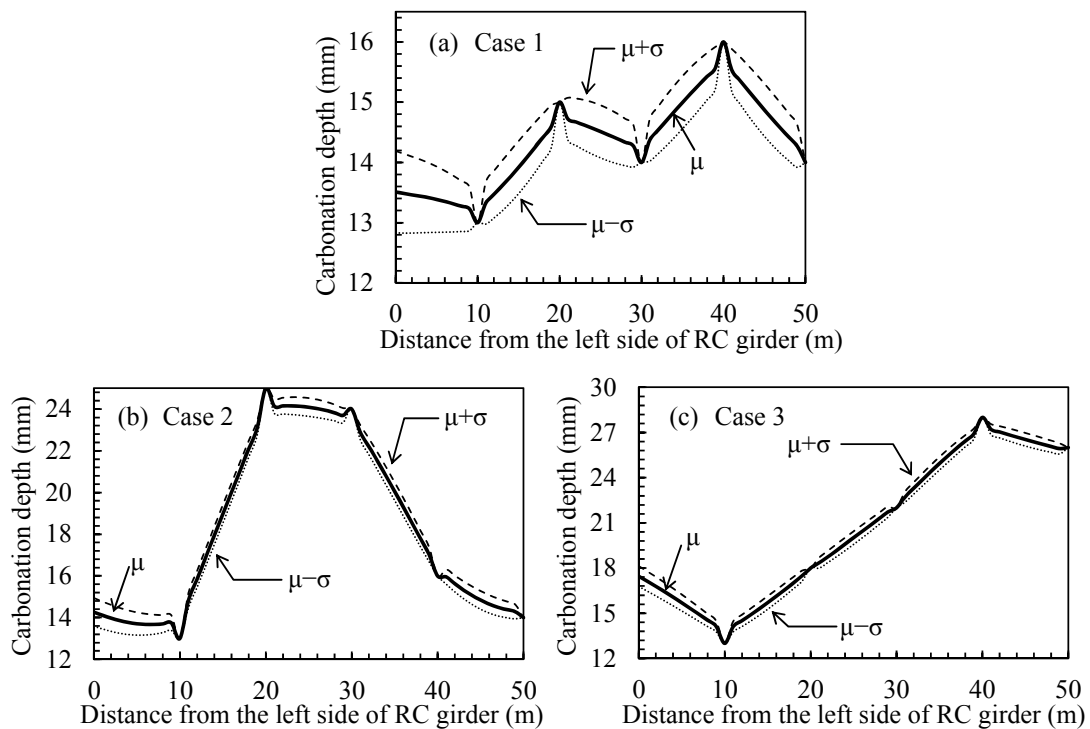
Figure 4. Carbonation depth interpolated by Kriging with confidence intervals

Figure 2 shows the measured carbonation depths along a longitudinal reinforced concrete girder with the span of 50m. They are used to determine the parameters for Kriging. In the illustrative example, Cases 1 to 3 with different variation in carbonation depths are considered as shown in Figure 3 assuming that they are provided at 30 years after construction. Five measured carbonation depths by the phenolphthalein test are provided for each case. Figure 4 shows the approximation of carbonation depths interpolated by Kriging with confidence intervals.
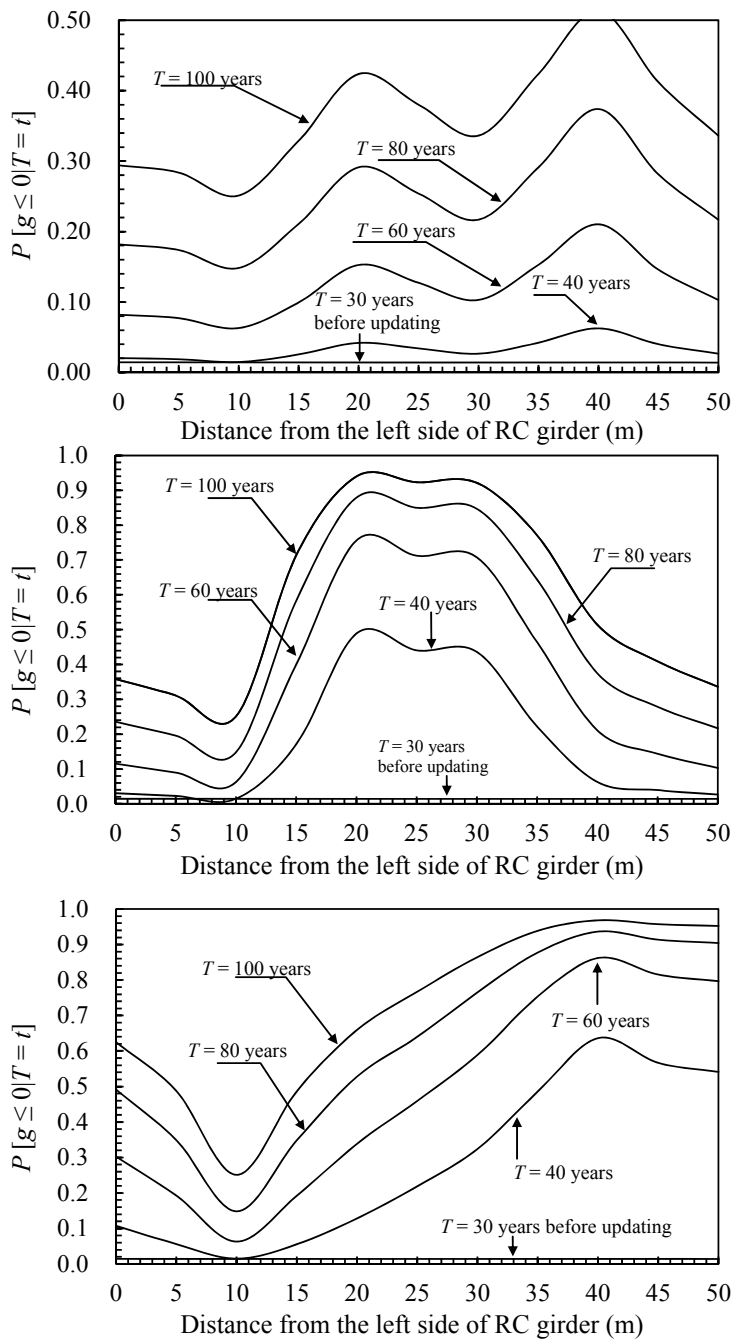
Figure 5. Time-variant failure probability with updating

Computational results given by SMCS are almost the same for all cases if the number of samples is more than 500,000. Therefore, the number of samples is set to 500,000. Figure 5 shows the relationship between the failure probabilities associated with the occurrence of rebar corrosion due to the carbonation, time after construction and the location. Failure probability at 30 years (i.e. just before the updating by SMCS) is independent of the location as shown in Figure 5. After updating, the distributions of failure probabilities over concrete structure for all cases are consistent with the inspection results shown in Figure 4. Correlations among random variables before and after updating are shown in Figure 6. As these random variables are updated using the same inspection results, it is confirmed in Fig. 6 that they have to be correlated after updating.

(a) before updating   (b) after updating
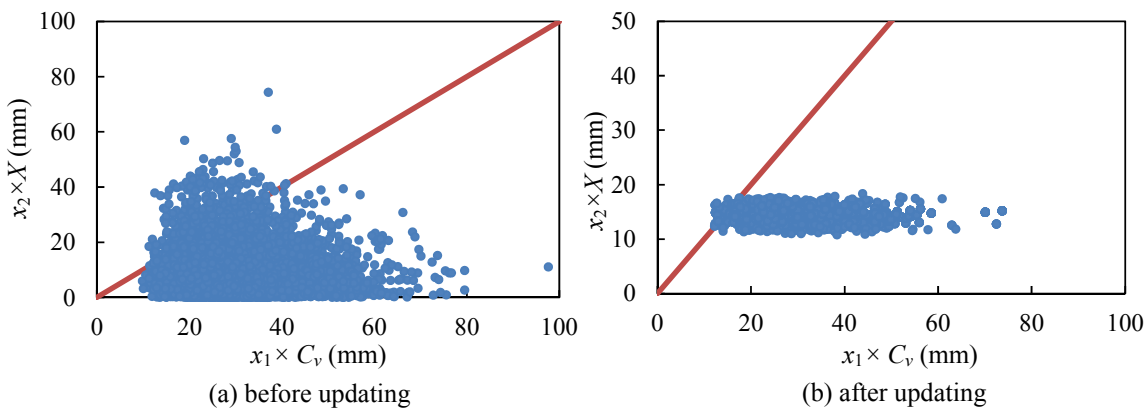
Figure 6. Samples before and after updating using SMCS

Concluding remarks

The procedure to obtain the failure probabilities of concrete structures subjected to carbonation by incorporating spatial variations was presented in the present paper. Using SMCS, the failure probabilities were updated to be consistent with observational data of the carbonation depth provided by the phenolphthalein test. The effects of the spatial variation of inspected carbonation depths on the reliability estimates were investigated in an illustrative example.

References

Akiyama M., Frangopol D.M., and Yoshida I. (2010). "Time-dependent reliability analysis of existing RC structures in a marine environment using hazard associated with airborne chlorides." *Engineering Structures*, 32(11), 3768-3779.

Akiyama, M., Frangopol, D. M., and Suzuki, M. (2012). "Integration of the effects of airborne chlorides into reliability-based durability design of R/C structures in a marine environment." *Structure and Infrastructure Engineering*, 8(2), 125-134.

Ang, A. H.-S., and De Leon, D. (2005). "Modeling and analysis of uncertainties for risk-informed decisions in infrastructures engineering." *Structure and Infrastructure Engineering*, 1(1), 19-21.

Ann, K.Y., Pack, S.-W, Hwang, J.-P., Song, H.-W., and Kim, S.-H. (2010). "Service life prediction of a concrete bridge structure subjected to carbonation." *Construction and Building Materials*, 24, 1494-1501.

Chien, K., Noguchi, T., and Kanematsu, M. (2008). "Optimal Maintenance Plan of an Reinforced Concrete Member by Minimizing." *Advanced Concrete Technology*, 6(3), 469-480.

Engelund, S., and Sørensen J.D. (1998). "A probabilistic model for chloride-ingress and initiation of corrosion in reinforced concrete structures." *Structural Safety*, 20, 69-89.

Izumi, I. (1988). "A reliability design method of cover thickness for reinforcement in concrete structures." Concrete Journal, 26(11), 38-43. (in Japanese)

Klemm, W.A., and Berger, R.L. (1972). "Accelerated curing of cementitious systems by carbon dioxide: part I. Portland cement." *Cement and Concrete Research*, 2(5), 567–576.

Marsh, P.S., and Frangopol, D.M. (2008). "Reinforced concrete bridge deck reliability model incorporating temporal and spatial variations of probabilistic corrosion rate sensor data." *Reliability Engineering & System Safety*, 93, 394-409.

Matheron, G. (1973). "The intrinsic random functions and their applications." Advances in Applied Probability, 5, 439-468.

Nakayama, T., and Matsubara, K. (1992). "Deteriorate of appropriate cover of reinforced concrete structures based on reliability-based design" *Journal of Structural Engineering*, 38, 509-516. (in Japanese)

Stewart, M.G. (2004). "Spatial variability of pitting corrosion and its influence on structural fragility and reliability of RC beams in flexure." *Structural Safety*, 26, 453-470.

Stewart, M.G., and Mullard, J.A. (2007). "Spatial time-dependent reliability analysis of corrosion damage and the timing of first repair for RC structures." *Engineering Structures*, 29(7), 1457-1464.

Stewart M.G. (2009). "Mechanical behavior of pitting corrosion of flexural and shear reinforcement and its effect on structural reliability of corroding RC beams." *Structural Safety*, 31, 19-30.

Stewart, M.G., and Suo, Q. (2009). "Extent of spatially variable corrosion damage as an indicator of strength and time-dependent reliability of RC beams." *Engineering Structures*, 31(1), 198-207.

Sung, Y.C., Huang, C.H., Liu, K.Y., Wang, C.H., Su, C.K., and Chang, K.C. (2010). "Life-cycle evaluation of deteriorated structural performance of neutralized reinforced concrete bridges." *Structure and Infrastructure Engineering*, 6(6), 741-751.

Vu, K.A.T., and Stewart M.G. (2005). "Predicting the likelihood and extent of reinforced concrete corrosion-induced cracking." *Journal of Structural Engineering*, 131(11), 1681-1689.

Structural Upgrade Selection via Shortest-Path Algorithm Based on Life-Cycle Sustainability Metrics

Citlali Tapia[1] and Jamie E. Padgett[2]

ABSTRACT

This paper poses the minimization of sustainability impacts from structural upgrades and repairs as a shortest path problem solved by Dijkstra's algorithm. A case study is presented that evaluates the impact of retrofit and repair options in terms of sustainability metrics and "full-cost price". Alternative bridge seismic retrofits and repairs minimizing negative impacts to the environment, economy, and society are found using the proposed algorithm. The sustainability metrics considered are: carbon dioxide emissions, embodied energy, downtime, and monetary costs. In addition to seeking the minimum expected value, the associated variance as well as shortest path for the uncertainty of each of these measures is found. Results highlight impacts of traditional engineering decisions on the environment and society and displays uncertainty variations associated with sustainability metrics. This framework is anticipated to help guide the selection of sustainable structural upgrades and in the future facilitate accommodation of stakeholder preferences regarding target sustainability measures.

1.   INTRODUCTION

In addition to having economic costs, structural upgrades and repairs following natural hazards also have environmental and social "costs" associated with them which are measured through sustainability metrics such as carbon dioxide emissions and waste. However, environmental and social costs are in general not considered for common engineering decisions such as selecting designs, upgrades, or rehabilitation methods. To progress towards more sustainable decisions and structures, alternatives should be evaluated based on the impacts these options have on the three pillars of sustainability– the economy, society, and environment.

Studies have progressed in considering sustainability metrics for multiple life phases, such as construction, maintenance, and hazard exposure, of structures exposed to threats in their analyses. These studies have found that consequences from hazard exposure contribute significantly to lifetime sustainability metric totals but by improved hazard protection can decrease negative impacts to sustainability components

[1]Graduate Research Assistant, Department of Civil and Environmental Engineering, Rice University, 6100 Main Street, MS-318, Houston, TX USA 77005 (cittapia@gmail.com)
[2]Assistant Professor, Department of Civil and Environmental Engineering, Rice University, 6100 Main Street, MS-318, Houston, TX USA 77005 (jamie.padgett@rice.edu)

(Bastidas-Arteaga et al. 2010; Collings 2006; Dong et al. 2013b; Itoh et al. 2005; Padgett and Tapia 2013). Recent research has begun exploring the selection of structural upgrades that simultaneously minimize select sustainability metrics through multi-objective optimization by genetic algorithm (Dong et al. 2013a; Tapia and Padgett 2013). These studies provide valuable insight to the selection of sustainable alternatives, however are not easy to visualize. Additionally most former studies optimize structural upgrades based on expected sustainability value metrics. Using different methods such as shortest-path algorithms can facilitate helpful visualization and conceptualization of such problems. This paper poses the selection of structural upgrades minimizing sustainability measures as a shortest-path problem. Variances associated with the measures are quantified to also seek paths that offer minimal uncertainty. The focus of this paper will be on contributions from retrofit construction and hazard exposure phases. Dijkstra's algorithm is used to find which retrofit and repair combinations lead to minimal carbon dioxide (CO_2) emissions, embodied energy (EE) expenditure, driver downtime (D), monetary cost (C), and full-cost price (FCP) for a bridge column subject to a seismic hazard. FCP is a quantity that reflects not only monetary cost associated with an activity/procedure, but also the dollar costs estimated to be associated with resulting environmental and social impacts. Results highlight advantages of representing selection of structural retrofits and repairs as a shortest-path problem to enable helpful conceptualization of the problem and the value of quantifying uncertainty of sustainability metrics to identify least variant alternatives.

2.   HAZARD RELATED SUSTAINABILITY ANALYSIS AND SHORTEST PATH ALGORITH

2.1   *Quantification of Sustainability Metrics and their Uncertainty*

Life-cycle phases of a structure in general consist of construction, operation, maintenance, retrofit construction, hazard exposure, and demolition phases. The complete process and development for quantifying lifetime indicators of sustainability at each structure phase can be found in Padgett and Tapia (2013). Since the focus of this paper is limited to the retrofit construction and hazard exposure phases, only a general overview will be given for the derivation of indicators associated with these phases.

Retrofit construction phase refers to the upfront investment required for a structural retrofit or risk mitigation upgrade option to be implemented. Sustainability costs related to this phase account for material and equipment related costs. Therefore the expected sustainability costs of retrofit construction (S_c) can be calculated as:

$$E[S_c] = (V_M \cdot C_M) + (NE \cdot ND \cdot C_E) \tag{1}$$

where V_M and C_M are volume and sustainability metric coefficients associated with material required for a given retrofit option. Sustainability metric coefficients are defined by the U.S. Energy Information Administration as values a standard rate of metric per unit of activity such as CO_2 per unit volume or EE per machine. *NE* and *ND* are the number of machines and number of days needed to perform a retrofit action respectively. C_E is the sustainability metric coefficient of equipment per day. The hazard exposure phase relies on natural hazard risk information. Procedures assumed to take place in this phase are repairs performed after a natural hazard event to restore functionality of the structure. In this study, the natural hazard is assumed to be an earthquake event. Structures incur different levels of damage upon exposure to the hazard and a different repair option may be necessary to restore the structure to its pre-disaster state. Therefore,

hazard exposure phase sustainability costs ($E[S_h]$), are given by summing repair related sustainability costs at each year t during the total remaining service life, T, of the structure, for each n potential levels of damage to the structure. Assuming hazard damage follows a non-homogenous Poisson process to reflect the occurrence of hazard events as well as time-dependent vulnerability, expected sustainability costs from the hazard phase are given by:

$$E[S_h] = \sum_{n=1}^{N} \sum_{t=1}^{T} \lambda_n(t) exp\left(-\sum_{t=1}^{T} \lambda_n(t)\right) I_{n,j} \tag{2}$$

where $\lambda_n(t)$ is the mean annual rate of damage level n occurrence due to natural hazard exposure, and together with the exponential term reflects the distribution of time between the beginning of exposure of a deteriorating structure to natural hazard and the occurrence of first failure. $I_{n,j}$ is the expected sustainability cost associated with a particular repair j—which is predetermined and subject to change depending on the level of damage. $I_{n,j}$ repair related sustainability costs are calculated similar to S_c but instead summing the costs of material and equipment used in repairs:

$$E[I_{n,j}] = (V_{Mj} \cdot C_{Mj}) + (NE_j \cdot ND_j \cdot C_{Ej}) \tag{3}$$

where the variables defined similar to those for Equation1 but for repair procedures—hence the added subscript j. Total expected lifetime sustainability cost ($E[LSC]$) for the structure, using only life phases considered in this study, is then given by the summation of $E[S_c]$ and $E[S_h]$. Further details regarding the specific steps towards formulating Equation 2 or sustainability metric costs for other phases of a structures life can be found in Padgett and Tapia (2013).

The dollar values associated with EE expenditure and CO_2 emissions are assumed to be $0.167 per mega-joules (MJ) of EE (Camill 2002) and $0.036 per kilograms (kg) of CO_2 emissions (U.S. Government 2013). Since dollar costs due to downtime are already considered in C, cost of downtime is not included in FCP to prevent double counting. To compute FCP, total $E[LSC]$ values must first be calculated for C, EE, and CO_2 costs, and then converted into dollar values using the conversion factors given. $E[LSC]$ dollar values from EE, CO_2 and C can then be summed to get total FCP value.

Uncertainty of S_h and S_c values is assumed to stem from sustainability metric coefficients and given in terms of the variance (Var). Sustainability metric coefficients, C_M, C_E, C_{Mj}, and C_{Ej}, are assumed to be normally distributed random variables with coefficients of variation (CV) of 0.2 based on Dong et al. (2013a). Letting C_s stand for all sustainability metric coefficients and using basic concepts of probability and statistics (Ang and Tang 1975) the variance of sustainability metric coefficients ($Var(C_s)$) is calculated as $Var(C_S) = (CV \cdot \mu_s) = (0.2 \cdot C_s)$ where μ_s is the mean of sustainability metric coefficients equal to C_s values assumed in Equations 1 and 3. Using this with Equation 1, the variance of retrofit construction sustainability costs ($Var(S_c)$) is calculated as follows:

$$Var(S_c) = (V_M)^2 Var(C_M) + (NE \cdot ND)^2 Var(C_E) \tag{4}$$

where the variables are as previously defined in Equation 1. The uncertainty of hazard exposure sustainability costs is evaluated by first calculating variance of repair sustainability costs ($Var(I_{n,j})$) using Equations 3 and $Var(C_s)$:

$$Var(I_{n,j}) = (V_{Mj})^2 Var(C_{Mj}) + (NE_j \cdot ND_j)^2 Var(C_{Ej}) \tag{5}$$

Equation 5 can then be used in combination with Equation 2 to calculate the variance of hazard exposure phase costs ($Var(S_h)$) as follows:

$$\text{Var}(S_h) = \sum_{n=1}^{N} \left[\sum_{t=1}^{T} \left(\lambda_n(t) exp\left(-\sum_{t=1}^{T} \lambda_n(t) \right) \right)^2 Var(I_{n,j}) \right] \quad \quad (6)$$

where variables shown are defined as stated in Equation 2. Total LSC variance, Var(*LSC*), is then equal to the sum of Var(S_c) and Var(S_h) quantities. In order to calculate FCP variances, Equations 4 and 6are converted into monetary values by multiplying by the appropriate conversion factor squared.

2.2   *Shortest Path Problem: Dijkstra's Algorithm*

The objective of a shortest-path problem is to find the shortest path from an origin node to a destination node such that the total cost associated with the sum of the arcs along the path is minimized. Shortest-Path problems are represented by a set of nodes (*N*) connected by a set of arcs (*A*) that each have an associated "weight" or cost. Common methods for solving such problems include: Dijkstra's algorithm, Bellman-Ford Algorithm, and Johnson's algorithm, to name a few. More information regarding alternative algorithms and shortest-path problems can be found in Cherkassky et al. (1996). To construct the selection of retrofit and repairs for structures as a shortest path problem, nodes are defined as repair and retrofit options available while lengths of arcs correspond to expected sustainability costs, E[S_c] and E[S_h], or variances, Var(S_c) and Var(S_h), associated with the connected node. The number of nodes and arcs will depend on the number of retrofit and repair options available to choose from. For the problem at hand, the number of arcs (*A*) is significantly greater than the number of nodes (*N*) and no negative lengths (i.e. costs) are associated with any arcs. Given these conditions, an efficient algorithm for solving the proposed problem is Dijkstra's algorithm. The complexity of Dijkstra's algorithm is $O(N^2)$ where *N* is the number of nodes. For such a problem where *A>N*, the complexity is reduced through Dijkstra's algorithm.

3.   CASE STUDY: RESULTS AND DISCUSSION

3.1   *Bridge Column and Node-Arc Details*

The proposed methodology is demonstrated for the retrofit and repair of a bridge column from a multi-span continuous (MSC) steel girder bridge exposed to a seismic hazard. The geometry of the column is shown in Figure 1 and is assumed to have 50 years of remaining life assuming the seismic retrofit is applied at the present date. The E[S_c] and $I_{n,j}$ values for retrofit and repair options considered in this study are tabulated in Table 1 in terms of CO_2, EE, C, D, and FCP costs. Var(S_c) and Var($I_{n,j}$) values for retrofit and repairs are shown in parenthesis in terms of each sustainability metric. The arc lengths for the shortest-path graph are E[S_h] and Var(S_h) values which are found using quantities given in Table 1. Each node is numbered as shown in Table 2.
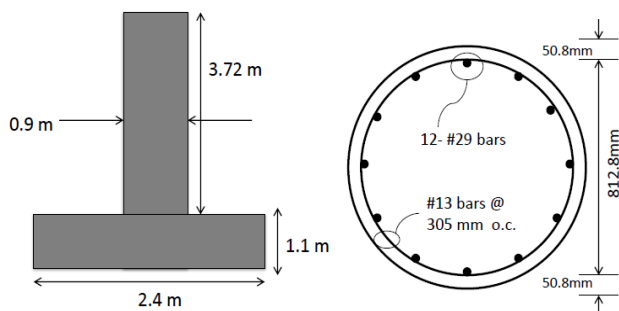

Figure 1: Case Study MSC Steel Bridge Column Geometry

Values of $E[S_c]$ change when different retrofit options are implemented on a bridge. Repair options available at each level of damage remain the same regardless of the retrofit adopted.　However, implementation of different retrofits do change the vulnerability of bridge components to seismic damage; therefore values of $E[S_h]$ must be re-evaluated each time a different retrofit option is adopted.　Since repairs available are the same for all retrofits, repairs are only labeled for the first retrofit in Table 2.　Ranges of the node number designations are tabulated for the rest of the retrofits. There are 138 nodes, therefore a total of 138*138= 19,044 arcs.　Beginning at the start node (N1), arcs connect N1 to retrofit nodes N2 to N9.　Next arcs connect nodes N2 to N9 with corresponding "slight" repairs shown in column 2 of Table 2.　Arcs then connect "slight" repair nodes to corresponding "moderate" repair nodes, followed by connections to "extensive" and then "complete" repair nodes.

3.2　Shortest-Path: Sustainability Metric Totals and Uncertainties

Using Dijkstra's algorithm to solve for retrofit and repair combinations which minimize expected LSC values in terms of CO_2, EE, D, C, and FCP, the resulting shortest path solutions are presented and compared in Table 3along with their associated Var(LSC) values. Additionally shortest paths based on minimizing uncertainty of sustainability metric totals are also given in Table 3 for comparison purposes to acknowledge that minimizing the variance may also be of mutual interest to stakeholders.

Results in Table 3 show that the retrofit options minimizing total LSC values of sustainability metrics considered are: steel jackets, elastomeric isolation bearings, and restrainer cables.　Although steel jackets and elastomeric isolation bearings have the highest upfront costs ($E[S_c]$), they reduce the vulnerability of bridge columns to seismic events the most therefore reducing $E[S_h]$ related costs.　Restrainer cables may not be as effective in mitigating seismic damage to bridge columns, but they do have the lowest $E[S_c]$ cost.　In all cases, the repairs which minimize total LSC values at each of the four levels of damage are epoxy injection at slight damage, epoxy injection at moderate damage, column replacement at extensive damage, and demolish and replace bridge at complete damage.　Since demolishing and replacing the bridge is the only option available when the column incurs complete damage, it is expected to be the only solution for all cases.　Among the repair options available, epoxy injection has the lowest repair sustainability cost, $I_{n,j}$, of options at the slight and moderate levels of damage, while column replacement has the lowest $I_{n,j}$ of options at extensive levels of damage.　Repairs are assumed to restore the structure to its prior state before damage; therefore it is reasonable that the least costly repairs will reduce total LSC values for all metrics.

Table 1: Sustainability Metric Costs and Variances Associated with Retrofit and Repairs Considered

Retrofit Action	CO$_2$ in kg	EE in MJ	C in $	D in days	FCP in $
As-Built	0 (0)	0 (0)	0 (0)	0 (0)	0 (0)
Steel Jacket	9,668 $(3.74*10^6)$	243,711 $(2.38*10^9)$	36,000 $(51.84*10^6)$	0 (0)	77,000 $(1.18*10^8)$
Restrainer	958	24,148	8,460	0 (0)	12,500

Cables	$(36.7*10^3)$	$(23.33*10^6)$	$(2.86*10^6)$		$(3.51*10^6)$
Seat Extenders	6,862 $(1.88*10^6)$	172,984 $(1.2*10^9)$	9,000 $(3.24*10^6)$	0 (0)	38,000 $(3.65*10^7)$
Shear Keys	5,623 $(1.25*10^6)$	41,478 $(67.54*10^6)$	15,000 $(9*10^6)$	0 (0)	22,100 $(1.09*10^7)$
Restrainer Cables & Shear Keys	6,580 $(1.29*10^6)$	65,626 $(90.87*10^6)$	23,460 $(11.86*10^6)$	0 (0)	34,600 $(1.44*10^7)$
Seat Extenders & Shear Keys	12,485 $(3.14*10^6)$	214,462 $(1.26*10^9)$	24,000 $(12.24*10^6)$	0 (0)	60,100 $(4.74*10^7)$
Elastomeric Isolation Bearings	27,587 $(13.11*10^6)$	177,134 $(192.81*10^6)$	37,237 $(55.46*10^6)$	0 (0)	67,800 $(6.08*10^7)$
Repair Action					
Epoxy Injection	934 $(35*10^3)$	13,842 $(7.66*10^6)$	1,059 $(38*10^3)$	0.046 $(8*10^{-5})$	20,508 $(1.50*10^6)$
Concrete Patch	7,285 $(2.12*10^6)$	107,871 $(465*10^6)$	15,265 $(4.66*10^6)$	0.355 $(5.1*10^{-3})$	201,895 $(1.055*10^8)$
Grouting	14,596 $(8.47*10^6)$	215,920 $(1.86*10^9)$	15,122 $(9.11*10^6)$	0.711 $(20.2*10^{-3})$	311,521 $(3.65*10^8)$
Concrete Lining	7,285 $(2.12*10^6)$	107,871 $(464.93*10^6)$	7,637 $(2.28*10^6)$	0.355 $(5.1*10^{-3})$	156,124 $(9.12*10^7)$
Wrap	46,477 $(85.89*10^6)$	713,607 $(18.85*10^9)$	50,300 $(92.5*10^6)$	2.263 $(2.1*10^{-1})$	1,030,916 $(3.7*10^9)$
Reinforce Column	4,057 $(352*10^3)$	56,753 $(69.71*10^6)$	6,473 $(591*10^3)$	0.138 $(8*10^{-4})$	96,797 $(1.56*10^7)$
Reinforce and Recast Column	8,167 $(2.15*10^6)$	114,356 $(464.93*10^6)$	11,252 $(2.53*10^6)$	0.355 $(5.1*10^{-3})$	184,492 $(9.3*10^7)$
Demolish and Replace Bridge	4,092,952 $(356*10^9)$	63,777,691 $(72.7*10^{12})$	3,788,096 $(366*10^9)$	141 $(7.9*10^2)$	1,4621,704 $(2.69*10^{12})$

Note: Values within parentheses indicate $Var(S_c)$ and $Var(I_{n,j})$ values

Table 2: Node Designation and Order of Connectivity

Retrofit	Slight	Moderate	Extensive	Complete
N2- As-Built	N10- Epoxy Injection N11- Concrete Patch N12- Grouting N13- Concrete Lining N14- Wrap N15- Replace Column	N16- Epoxy Injection N17- Concrete Patch N18- Concrete Lining N19- Wrap N20- Replace Column N21- Reinforce and Recast	N22- Replace Column N23- Reinforce and Recast N24- Demolish and Replace Bridge	N25- Demolish and Replace Bridge
N3- Steel Jacket	N26 - N31	N32- N37	N38- N40	N41
N4- Restrainer Cables	N42-N47	N48- N53	N54- N56	N57
N5- Seat Extenders	N58- N63	N64- N69	N70- N72	N73
N6- Shear Keys	N74- N79	N80- N85	N86- N88	N89
N7- Restrainer Cables & Shear Keys	N90- N95	N96- N101	N102- N104	N105
N8- Seat Extenders & Shear Keys	N106- N111	N112- N117	N118- N120	N121
N9- Elastomeric Isolation Bearings	N122-N127	N128- N133	N134- N136	N137

Table 3: Case Study Shortest Path Solutions

		Shortest Paths					
Metric	Retrofit	Slight	Moderate	Extensive	Complete	E[LSC]	Var(LSC)
E[CO_2]	Steel Jacket	N26	N32	N38	N41	$9.9*10^3$	$3.7*10^6$
Var[CO_2]	Restrainer Cables	N42	N48	N54	N57	$2.1*10^4$	$1.9*10^5$
EE	Elastomeric Isolation Bearings	N122	N128	N134	N137	$2.5*10^5$	$1.9*10^8$
Var(EE)	Restrainer Cables	N42	N48	N54	N57	$3.3*10^5$	$6*10^7$
C	Restrainer Cables	N42	N48	N54	N57	$2.7*10^4$	$3*10^6$
Var(C)	Restrainer Cables	N42	N48	N54	N57	$2.7*10^4$	$3*10^6$
D	Steel Jacket	N26	N32	N38	N41	$1.0*10^{-2}$	$1*10^{-5}$
Var(D)	Steel Jacket	N26	N32	N38	N41	$1.0*10^{-2}$	$1*10^{-5}$
FCP	Steel Jacket	N26	N32	N38	N41	$7.8*10^4$	$1.2*10^8$
Var(FCP)	Restrainer Cables	N42	N48	N54	N57	$8.3*10^4$	$4.7*10^6$

Comparing solutions for CO_2, EE, D, and C sustainability metrics, the shortest paths of each metric total are different except for those of CO_2 emissions and D. Shortest paths for the LSC of these two metrics are the same. This can be due to the relative costs in terms of D and CO_2 emissions following a similar pattern. Retrofits and repairs with

high CO_2 impacts also have high levels of D, which makes sense since vehicles are one of the largest source of carbon dioxide emissions in the U.S. (U.S. Department of Energy 2011) and as downtime increases, the amount of time vehicles are on the road also increases. Finding shortest paths for individual sustainability metric costs is a useful strategy when the retrofit/repair options are known to be within a specific metric limit. For example, if decision makers want to minimize carbon dioxide emissions from structural upgrades by using a set of repair options known to be within given monetary constraints, a shortest-path based on CO_2 emission totals can be used.

Results show that the shortest path for FCP is the same as shortest paths for CO_2 emissions and D, but different from shortest paths for EE and C. Additionally, FCP is about 65% larger than total LSC value for the C metric shortest path. From the difference in shortest paths and the significant increase in total dollar costs (comparing C and FCP), the importance of accounting for impacts to society and the environment is highlighted. Although FCP offers an effective manner of representing all pillars of sustainability in a single value, in some cases it may be best to keep sustainability measures in their respective units. A few examples of these cases include the fact that not all sustainability metrics have an easily quantified monetary value associated with it (e.g. happiness) and that the magnitudes of social and environmental impacts incurred are lost in the conversion to monetary terms. Furthermore, additional uncertainty is introduced when converting all measures to monetary values due to uncertainty in the conversion factors adopted—something to be explored in future work. However FCP is a convenient and efficient technique to quickly find a holistic measure of sustainability.

4.   CONCLUSIONS

A framework for selecting structural retrofit and repair actions that result in minimal E[*LSC*] and Var[*LSC*] is presented and posed as a shortest-path problem solved by Dijkstra's algorithm. Case study results underline the need to consider measures beyond monetary costs in engineering decisions and to use metrics which reflect impacts not only to the economy, but the society and environment as well. Shortest-path solutions based on Var[*LSC*] values highlight the difference of minimizing measures of uncertainty versus expected LSC values. Future work should focus on performing a detailed study on uncertainties related to sustainability coefficients as well as developing the proposed framework to explicitly take into account the preferences of decision makers within the framework.

5.   ACKNOWLEDGEMENTS

6.   REFERENCES

Ang, A. H.-S., and Tang, W. H. (1975). *Probability Concepts in Engineering Planning and Design, Vol. 1: Basic Principles*, John Wiley & Sons, New York.

Bastidas-Arteaga, E., Chateauneuf, A., Sanchez-Silva, M., and Capra, B. (2010). "Probabilistic Evaluation of the Sustainability of Maintenance Strategies for RC Structures Exposed to Chloride Ingress." *International Journal of Engineering Under Uncertainty: Hazards, Assessment and Mitigation*, 2(1-2), 61-74.

Camill, P. (2002). "Watch Your Step: Understanding the Impact of Your Personal Consumption on the Environment."

Cherkassky, B., Goldberg, A., and Radzik, T. (1996). "Shortest paths algorithms: Theory and experimental evaluation." *Mathematical Programming*, 73(2), 129-174.

Collings, D. (2006). "An Environmental Comparison of Bridge Forms." *Proceedings of the Institution of Civil Engineers-- Bridge Engineering*, 159(4), 163- 168.

Dong, Y., Frangopol, D. M., and Saydam, D. (2013a). "Sustainability of Highway Bridge Networks Under Seismic Hazard." *Journal of Earthquake Engineering*, In Press.

Dong, Y., Frangopol, D. M., and Saydam, D. (2013b). "Time Variant Sustainability Assessment of Seismically Vulnerable Bridges Subject to Multiple Hazards." *Earthquake Engineering & Structural Dynamics*, 42, 1451-1467.

Itoh, Y., Wada, M., and Liu, C. (2005). "Lifecycle Environmental Impact and Cost Analyses of Steel Bridge Piers with Seismic Risk." 9th International Conference on Structural Safety and Reliability, Millpress, Rome, Italy, 1581-1588.

Padgett, J. E., and Tapia, C. (2013). "Sustainability of Natural Hazard Risk Mitigation: A Life-Cycle Analysis of Environmental Indicators for Bridge Infrastructure." *Journal of Infrastructure Systems*, In Press.

Tapia, C., and Padgett, J. E. (2013). "Life-Cycle Optimization of Structural Retrofit and Repair Based on Sustainability Criteria." 11th International Conference on Structural Safety & Reliability, New York, NY.

U.S. Department of Energy. (2011). "Emissions of Greenhouse Gases in the United States 2009." Washington, D.C.

U.S. Government. (2013). "Technical Support Document: Technical Update of the Social Cost of Carbon for Regulatory Impact Analysis Under Executive Order 12866."

Concepts of developing traffic load model for multi-span cable supported bridges

Xin Ruan[1] , Junyong Zhou[1] and Zhiyi Yin[1,2]

Abstract: Traffic load effects of multi-span cable supported bridges are significantly different from those of small and medium span bridges. However the current traffic load codes are generally specified for small and medium span bridges, which are extremely conservative for the design of multi-span cable supported bridges. A profound and comprehensive review on existing research of traffic load models for large span bridges is presented, providing theoretical foundation for the concepts of performance based traffic load models. Different structure performance levels, design states and parameters are discussed under varied traffic load service levels. Novel techniques in related traffic load research field are introduced to explore the possible performance based design methodology and process. Application of the traffic load effect analysis is stated by two practical examples. According to the results, it is indicated that concepts of performance based design are more accurate and efficient for the traffic load effect, and provides the structure optimization with favorable conditions.

Key words: traffic load model, performance based design, multi-span cable supported bridges, structure optimization

Introduction

Multi-span cable supported bridges with large spans have significant advantages in crossing ability, aesthetic value and economic performance and are getting more and more practical applications in large span bridge construction field. During the development of multi-span cable supported bridges(Virlogeux, 2001), one of the most important constraints to enlarging spans is the determination of traffic load. It is recognized that when unbalanced traffic load is considered, the structure will show obvious deflection, which will put the whole bridge in a most unfavorable deformation and mechanic state. To avoid this situation, structure stiffness is greatly emphasized in current design, based on which approaches such as improving stiffness of middle pylon and introducing stiffening cables between pylons are proposed in practice(Virlogeux, 2001).

It is realized now that research on estimating the precise practical effect of multi-span cable supported bridges to traffic load can be another effective solution to the existing problem. In the current bridge design codes, most traffic load is suitable for bridges with small or medium spans. Very few codes have particular regulations

[1] Department of Bridge Engineering, Tongji University, 1239 Siping Road, Shanghai, P.R.C.; PH: (86)13917829960; email: ruanxin@tongji.edu.cn
[2]Center for Advanced Technology for Large Structural Systems (ATLSS Center), Lehigh University, 117 ATLSS Drive, Imbt Laboratories, Bethlehem, PA 18015 USA

on selection of traffic load models for large span bridges. The EUROCODE(EN, 1991) specifies that its traffic load model is not suitable for the design of bridges with a load length more than 200m. Traffic load model for bridge design in China is determined by "General Code for Design of Highway Bridges and Culverts" (JTG D60-2004)(Ministry of Communications, 2004), in which the traffic load model is presented with a combination of both uniform load and concentrated load. The traffic load is supplied in the most unfavorable arrangement based on the influence surface. However, this traffic load model is developed by referring to research results based on bridges with small and medium spans (Yang,YH et al,1997). For the large span bridges, the applicability of longitudinal reduction index remains further research.

With the rapid evolution in measuring techniques, it becomes more and more convenient to obtain the bridge traffic load data in practical operation stage, by precise measurement of vehicle flow and traffic load data, many statistic characteristic parameters can be acquired and adopted for a better and more accurate simulation on traffic load. The simulation can comprehensively provide the researchers with the variation laws of long term vehicle flow and its load, establishing extensive data foundation for traffic load research. With these newly developed techniques, related research aspects such as traffic load simulation, load effect extrapolation and assessment are now getting more and more attention(Caprani and OBrien, 2010; Cremona, 2001; Getachew, 2003; Ruan, Zhou and Shi, 2013; Ruan,Zhou and Guo,2012). To develop a reliable load model, extreme value extrapolation of traffic load effect is of essential value. In the early development, Nowark(Nowak and Hong, 1991; Nowak, Nassif and DeFrain, 1993) collected the vehicle weight and axle load of trucks on typical roads, based on which extreme values in design reference period were obtained by adopting normal distribution linear extrapolation method. Cremona(Cremona, 2001) deducted extreme value of load effect in 1000-year recurrence period by Rice extrapolation method. Fu(Fu and You, 2009) obtained extreme value of load effect in 100-year recurrence period by maximum extrapolation method. Based on the mentioned fundamental theories and methodologies, scholars in related field developed extensive research on traffic load model at particular locations(O'Connor and Eichinger, 2007). Field measurements were introduced to acquire practical traffic data. By introducing load simulation, extreme value extrapolation and reliability theory, service states and levels of bridge structures regarding traffic load condition were extensively assessed and studied.

Although fundamental techniques in traffic load model research have been provided, there remains great difficulty in the unification of load effect and load models because of the huge uncertainties in traffic load and structure effect. Yet there is not much research regarding this matter. Load effects of large span bridges, especially multi-span cable supported bridges, are of noteworthy difference to those of small and medium span bridges. By referring to the provided research method, establishment of traffic load model for multi-span cable supported bridges is an

essential attempt for the state-of-the-art of bridge engineering. In this way, practical load effect characteristics of multi-span cable supported bridges can be obtained for a more efficient and economic design process.

1. Traffic load effect characteristics

The most significant differences between traffic load effect characteristics of multi-span cable supported bridges and small span bridges can be reflected in three major aspects, the loading length, the type amount and the complexity of influence surface distribution of load effects individually.

When the loading length is comparatively short, vehicles that can be arranged in the possible influence surface range at the same time are quite limited. The load effect value usually depends on single heavy vehicle. When the loading length is comparatively long, more vehicles can be arranged in the possible influence surface range at the same time. At this moment, the load effect is determined by the vehicle queue on the whole. Effects caused by time and space headway and vehicle queue features should be considered.

There are many structure component types of multi-span cable supported bridges, load effects of which are relatively complicated and large in amount. During the design process, it is important to pick out the most representative effect types, i.e. featured effects, for analysis purpose. In the overall design of small and medium bridges, the amount of featured effects is quite limited. The most decisive effects in structural design only exist in the key sections of main girder at the support or the mid span. While, multi-span cable supported bridges are statically indeterminate structures with complicated components, in different structural states, locations of key component in which exist the featured effects are quite uncertain.

Load effect influence surfaces of small and medium span bridges are usually distinctly distributed. Variation of the surfaces can be distinguished by the spans. As is illustrated in Figure 1, in the middle span of a continuous girder bridge, the moment influence line of mid-span section remains positive in the entire span. Also the variations are told distinctively according to different spans. Figure 2 indicates the moment influence line of bottom section of the middle pylon in a three-pylon cable stayed bridge. The influence line is distributed in the whole four spans. Also the sign of the influence line in the same span changes repeatedly. Therefore the arrangement approach of load model for multi-span cable supported bridges should consider most distribution characteristics of influence surfaces of load effects.

In the current bridge design codes, definition and determination approach of traffic load can hardly cover all the mentioned load effect characteristics of multi-span cable supported bridges. In the Chinese bridge design code(Ministry of Communications, 2004), the traffic load values reduce with the increase of bridge span. However, the span reduction is not significant enough to reflect the variation characteristics of average vehicle weight in the whole loading range. At the same time, the loads are arranged in the determinative loading range based on influence

surfaces, without any consideration to the characteristics of influence surface of different effects. It is too conservative to apply the traffic load model in the current codes to multi-span cable supported bridges, giving that only the extreme situation of traffic load is considered in the load valuation and arrangement.

Figure 1.   Moment influence line of mid-span section of a continuous girder bridge
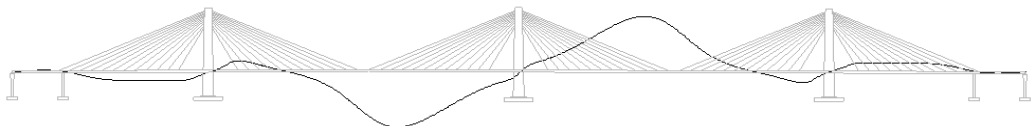
Figure 2.   Moment influence line of bottom section of the middle pylon in a three-pylon cable stayed bridge
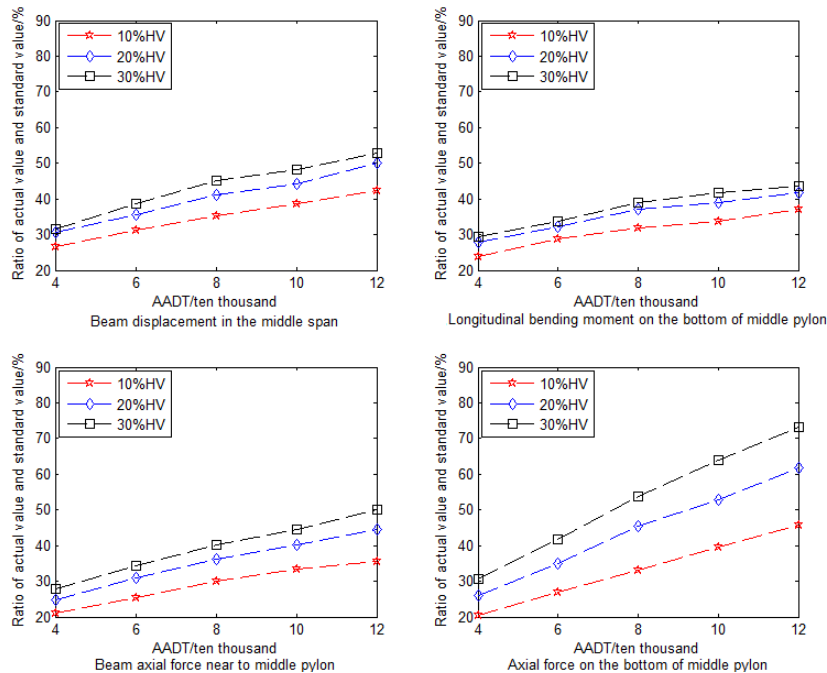
Figure 3.   Overall traffic load effects on normal operation condition

Figure 3 shows different featured effects of a typical three-pylon cable stayed bridge under the influence of traffic characteristics. Abscissas in the figures represents the annual average daily traffic volume (AADT) standardized by bidirectional traffic volume of four lanes. Ordinate in the figures represents the ratio of actual value and standard value. Different line types in the figures show the influence of heavy vehicle (HV) proportion. According Figure 3, in the regular operation state, the actual extreme values of traffic load effects are only 20 percent to 50 percent of the standard calculation values. The load effects increase with the

augment of heavy vehicle proportion and AADT in an approximately linear way. Even when random vehicle flow is only arranged in the influence line range with same sign, the actual extreme values of traffic load effects are still only 20 percent to 80 percent of the standard calculation values with consideration to extreme operation state. The results indicate that it is necessary to adjust not only the load value but also the load arrangement approach in the current bridge design codes when it comes to the traffic load model for multi-span cable supported bridges.

2. Traffic load design method

Traffic load effects are influenced by multiple factors and hence posses a significant characteristic of randomness, which resembles the seismic load in a way. In the structural seismic design field, performance based designed conception is widely accepted and applied. Similarly traffic load model can be developed by performance based method at the same time.

Performance based design intensively concerns both structural capacity and performance requirements. As is illustrated in Figure 4, performance index is adopted to symbolize some structural requirement. Effect levels of structural performance indices under external load can be represented by performance requirements. The process can be described by load design states. The essential significance of performance levels is the classification of performance targets. The performance based design is a verification process of design expressions under various performance levels by adopting different design methods and approaches.
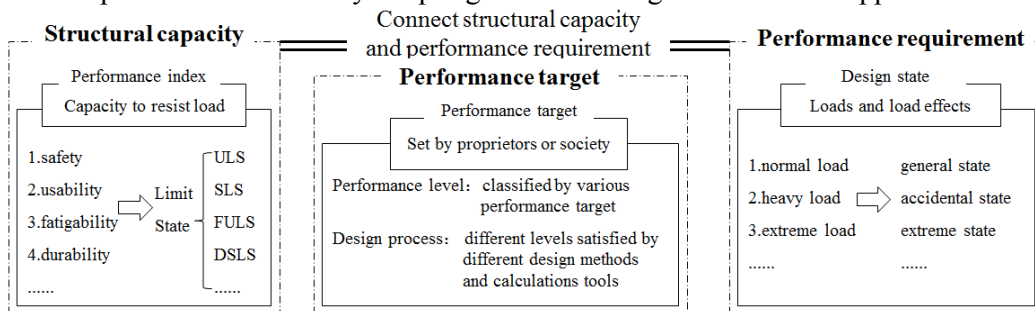
Figure 4.   Framework of performance based design

There are basically three operation states of vehicle flow with long loading length, individually regular state, accident state and extreme state. Basic characteristics of different operation states of vehicle flow with long loading length are consistent, so a traffic load model with both uniform load and concentrated load can be recommended. In performance based design, design grades are determined by performance design levels, so practical performance based design framework can be provided as in Table 1. For performance design level 1, only the feasibility design of the structure is in concern, during which only the extreme state of vehicle flow is considered. Under this circumstance, structure safety for the structure performance index is solely needed to be verified. For level 2, structural serviceability under regular state and load capacity safety under extreme state should be analyzed. The

corresponding load model can be used for the construction drawings design. On level 3, structure serviceability is analyzed exquisitely. All the operation states of vehicle flow, as well as all the performance indices, should be considered. Load models adopted in this level are applied directly for structure state assessment, so as to assess the residual life time of the structure in consideration.

Table 1.   Performance based traffic load design

Performance Design Level		Level 1	Level 2	Level 3
Applicable Design Stage		Primary	Construction	Maintenance
Load Design State	Regular		√	√
	Accident			√
	Extreme	√	√	√
Structure Performance Index	Safety	√	√	√
	Serviceability		√	√
	Fatigability			√
	Durability			√

According to the structure performance based design level requirements, traffic load model can be derived by adopting approaches such as load simulation, extreme value extrapolation and statistic regulation on load feature value. The derivation process of traffic load model should be integrated with due consideration to the corresponding vehicle service state. The proposed traffic load model can be further applied in the integral structure design or component design controlled by traffic load effect. Practical structure or component design methodology can be developed for a more accurate and efficient assessment on structure state.

3.   Case study

3.1 *Performance based anti-sliding design of middle pylon saddle of a three-pylon suspension bridge*

Taizhou Yangtze River Bridge is a three-pylon suspension bridge with two symmetric spans of 1080m. One of the most essential problems is anti-sliding of the middle pylon saddle, as it would become extremely unfavorable for structure design if the traffic load model for structure effect calculation is adopted under the guidance of current Chinese bridge design codes.

According to the issue, Random vehicle flow simulation is introduced to calculate different reliability indices under different given conditions, results show that reliability indices are generally bigger than 4.75 under the random vehicle (Ruan, Ruan and Chen, 2012), which is larger than the safety margin calculated by current codes. Based on the calculation results, performance based design can be introduced for the traffic load model establishment under different performance levels as is detailed in Table 2. According to the component design requirements in different

design stages, traffic load models with varied degrees of application difficulty are presented correspondingly. This approach solves the key component design problem brought by over conservative traffic load models in current codes.

Table 2.   Performance design levels of middle pylon saddle

	Level I	Level II	Level III
Accuracy	High	Medium	Low
Applicability	Assessment	Construction drawing design	Initial design
Failure Probability	1×10^{-6}	1×10^{-8}	2×10^{-19}

3.2 *Traffic load model for integral design of multi-span cable stayed bridge*

Jiashao Bridge is a six-pylon cable stayed bridge with five 428-meter main spans and bidirectional eight lanes. One of most concerned design problems of this bridge is that under the influence of the traffic load model provided by current Chinese design code, deflection of the middle span is too significant to design, which endangers the structure stress state and traffic safety.

Table 3.   Comparison of load combination effects between traffic load models in this paper and in current design code

Structure Effects	Dead Load Effect	Traffic Load Effects		Design Values of Load Effect S_d	
		this paper	current code	this paper	current code
Girder deflection/RS	0	63.662	177.755	101.859	177.755
Girder axial force/ES	6.90E+06	1.09E+06	3.89E+06	9.77E+06	1.43E+07
Pylon longitude moment/ES	6.61E+08	2.32E+08	4.09E+08	1.26E+09	1.50E+09

Based on the vehicle load field data, practical traffic load effects of the integral bridge under different traffic state, including regular and extreme states (RS and ES), are calculated. Based on the traffic load models, traffic load effects can be obtained and then combined with structure deadweight effects for structure design. Table 3 presents a comprehensive comparison of the traffic load models proposed in this paper and in the current Chinese bridge design code. It is realized that traffic load effects, as well as the load combination effects, based on the model in this paper are much smaller than those based on the current code. This result suggests that the deflection of middle span and other effects under the actual traffic is less significant than the values derived from Chinese code.

4.   Conclusion

Traffic load for large span cable supported bridges is elaborated in this paper. Characteristic differences of traffic load effects in large span cable supported bridges and medium and small span bridges are analyzed in detail. Conception of performance based design is introduced for the approach establishment of the traffic load model design for multi-cable cable supported bridges. Two typical projects are

illustrated to apply this approach. According to research results, significance of performance based design is thoroughly realized in the establishment of traffic load model for multi-span cable supported bridges.

5. Acknowledgement

References

Caprani, C. C., and OBrien, E. J. (2010). "The Use of Predictive Likelihood to Estimate the Distribution of Extreme Bridge Traffic Load Effect." *Structural Safety,* 32(2), 138-44.

Cremona, C. (2001). "Optimal Extrapolation of Traffic Load Effects." *Structural Safety,* 23(1), 31-46.

EN, B. "Eurocode 1: Actions on Structures." NA to BS EN, 1991. Print.

Fu, G., and You, J. (2009). "Truck Loads and Bridge Capacity Evaluation in China." *Journal of Bridge Engineering,* 14(5), 327-35.

Getachew, A. (2003). "Traffic Load Effects on Bridges, Statistical Analysis of Collected and Monte Carlo Simulated Vehicle Data." KTH Royal Institute of Technology.

Ministry of Communications, P. R. C. "General Code for Design of Highway Bridges and Culverts (Jtg D60-2004)." Beijing: China Communications Press, 2004. Print.

Nowak, A. S., and Hong, Y.-K. (1991). "Bridge Live-Load Models." *Journal of Structural Engineering,* 117(9), 2757-67.

Nowak, A. S., Nassif, H., and DeFrain, L. (1993). "Effect of Truck Loads on Bridges." *Journal of transportation engineering,* 119(6), 853-67.

O'Connor, A., and Eichinger, E. M. (2007). "Site-Specific Traffic Load Modelling for Bridge Assessment." *Proceedings of the ICE-Bridge Engineering,* 160(4), 185-94.

Ruan, X., Zhou, J., and Shi, X. (2013). "Comparison on Highway Traffic Flow and Load Properties of China and France." *Journal of Tongji University,* 41(9), 1392-1397.

Ruan, X., Ruan, J., and Chen, A. (2012). "Anti-sliding safety assessment for main saddle on middle tower of Taizhou Bridge." *Engineering Science,* 14(5), 71-74.

Ruan, X.,Zhou, X.,and Guo J.(2012)."Extreme Value Extrapolation for Bridge Vehicle Load Effect Based on Synthetic Vehicle Flow".*Journal 0f Tongji University*,40(10),1458-1462

Virlogeux, M. (2001). "Bridges with Multiple Cable-Stayed Spans." *Structural Engineering International,* 11(1), 61-82.

Yang,Y.,BAO,W.,GUO,X.et al(1997). "Structural Reliability and Probability Limit State Design for Highway Bridge Structure." *China Communications Press, Beijing*.

Incorporation of Concrete Rehabilitation Measures into Life-Cycle Maintenance

Harald Budelmann, Anne Wachsmann, Alexander Holst [1]

Abstract

Key components of life cycle analysis of concrete structures are models for the assessment of the actual condition and for the prediction of its further development. Durability models have to consider the different influencing effects and degradation processes throughout the entire life cycle of a structure taking into account mutual dependences, interactions, scattering and uncertainties. If reinforced concrete structures have been repaired during life time also aging and deterioration of maintenance measures like surface coating or concrete cover replacement must be taken into account. Degradation mechanisms of repair measures are different and they are going to be crucial for the durability of the repair measure. Prediction models taking into account the important parameters like bond properties between concrete and repair mortar under thermal gradients or of the adhesion influencing parameters of surface coatings are needed. In this contribution first ideas are presented, how the complex dependencies of the functionality and durability of repair measures may be recorded.

Introduction

It is a frequent practice nowadays to establish the durability of concrete structures by help of service life design approaches, fib (2006). Such approaches are based on quantifiable models on the load side (e.g. environmental actions) as well as on the resistance side (e.g. concrete resistance against environmental actions). Rehabilitation measures of reinforced concrete structures like surface coating or concrete cover replacement resp. improvement by repair mortar must be integrated into durability assessment of structures. While reliable durability related degradation prediction models for concrete structures are available and have been established in durability design practice, prediction models of repair measures are still not very developed.

In case of repaired or additionally protected concrete surface areas different degradation mechanisms are going to be crucial for the durability of the repair measure. Prediction models taking into account the important parameters like bond properties between concrete and repair mortar under thermal gradients or of the

1) iBMB, Department of Civil Engineering, University of Braunschweig, Braunschweig, Germany, Beethovenstr. 52, D-38106 Braunschweig, PH +49 (531) 3915405, FAX +49 (531) 3915900, e-mail: h.budelmann@tu-bs.de

adhesion influencing parameters of surface coatings are needed. In this contribution first conceptual deliberations are presented, how the complex dependencies of the functionality and durability of repair measures can be recorded in terms of engineering models applicable to structures under use.

Durability aspects of reinforced concrete structures

It is the general purpose of concrete structures to carry loads and to endure different exposures, both resulting from ambient conditions and from using conditions and both primarily being responsible actions for the structure's durability and service life. The exposures of concrete structures differ broadly; therefore also their predominant deterioration mechanisms are different. Figure 1 gives an overview on the predominant deterioration mechanisms for different types of structures, Buenfeld et al. (2008).

Type of structure	Corrosion			Freeze / thaw	Alkali aggregate reaction	Sulphate attack	Leaching	Abrasion	Acid attack
	Cloride-induced	CO₂-induced	Biological activity						
Above ground building	light grey	dark grey			light grey				
Bridges	dark grey	light grey		light grey	light grey				
Foundations			light grey		light grey	light grey			
Marine structures	dark grey					light grey	light grey	light grey	
Dams				light grey	light grey		light grey		
Tunnels	dark grey	light grey	light grey		light grey	light grey			
Tanks and pipes	light grey	light grey	light grey		light grey	light grey			light grey
Industrial floors		light grey						dark grey	light grey

Shading: commonly affected (dark grey), sometimes affected (light grey), uncommon (no shading)

Figure 1. Deterioration mechanisms of concrete structures, Buenfeld et al. (2008).

Durability evaluation needs the comparison of relevant attacks and resistances. The most relevant impact parameters are types, concentrations and intensities of substances or actions. The resistance primarily depends from concrete composition, concrete cover of reinforcement, porosity, permeability and transport parameters. For most reinforced concrete structures of infrastructure or industry the relevant damage mechanisms may be summarized and systematized into those affecting the durability of the reinforcement and those affecting the durability of the concrete. Electrochemical attacks are targeted at the reinforcement, chemical and physical attacks at the concrete, cp. Figure 2.
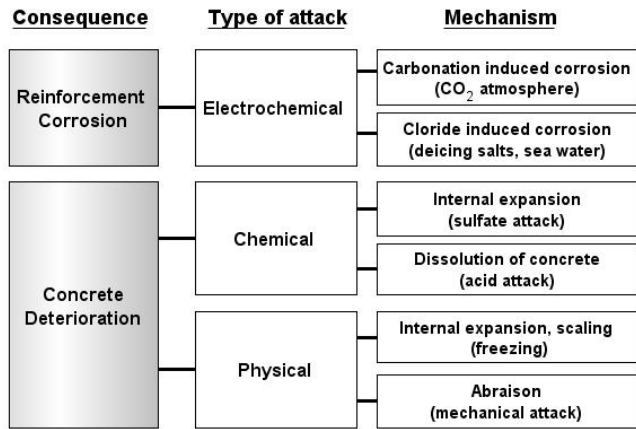
Figure 2. Classification system of deterioration mechanisms of reinforced concrete, fib (2006).

Durability prediction models for life cycle assessment

The aim of durability related life cycle assessment is the provision of information on the nature, cause, extent, location and time development of any deterioration process. The inventory of life cycle assessment tools consists of as-built-information (birth certificate), current condition information (inspection, monitoring, condition assessment), prognosis (deterioration model) and intervention (limit states, measures) as illustrated in Figure 3.
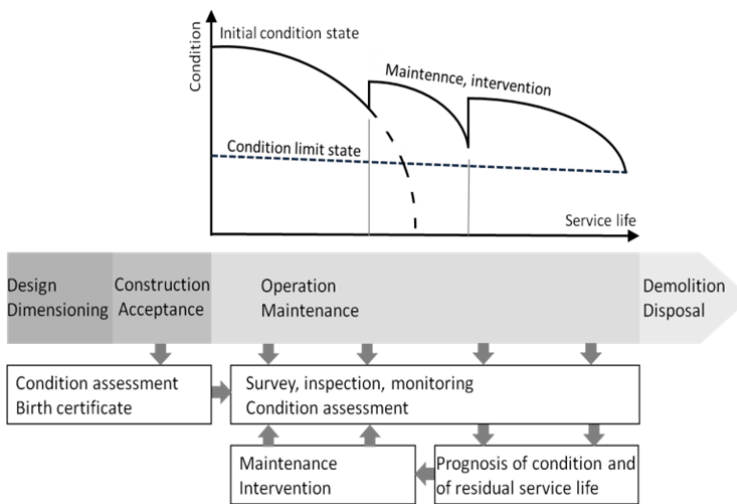
Figure 3. Inventory of life cycle assessment.

Deterioration models are key components of life cycle assessment. They should predict the durability affecting deterioration processes sufficiently accurate, physically and chemically correct, as simple as possible and based on information that is available from the structure.

Reinforcement corrosion, the most frequently observed deterioration cause of RC structures, can be regarded as a two periods process, consisting of an initiation period and a propagation period. The first stage means the time of ingress of harmful substances like carbon dioxide or chloride ions, the second phase is concerned with the steel corrosion itself, the loss of cross section, the cracking and spalling off of the concrete cover, cp. Figure 4.
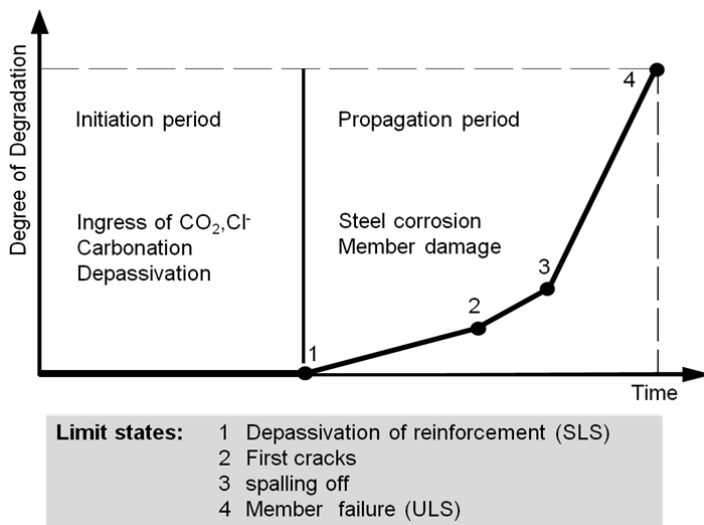
Figure 4. Deterioration periods of RC structures due to reinforcement corrosion.

Compared to reinforcement corrosion models the description of deterioration processes of the concrete itself is less developed. This is primarily attributed to the complexity of chemical and physical processes like acid attack, sulphate attack, freeze-thaw attack and alkali-aggregate reaction, in which multiple processes are interacting which could not yet be described by simple engineering models with respect to well defined limit states, suited for monitoring. Table 1 gives an overview on the deterioration processes and on common serviceability and ultimate limit states.

Generally, three different approach levels of models may be distinguished; cp. Strauss et al. (2009): macro-level models ('deemed-to-satisfy' approach), simplified models (mostly semi-empirical, verified by comparison of results of lab tests with on-site conditions, probabilistic approach with statistic and probabilistic time dependent parameters), micro level models (complex models based upon physical and constitutive laws of mechanics).

Today, most commonly used models for prediction of durability related degradation are either semi-empirical engineering models or analytical models. The first are understood as simple equations, usually derived from experimental results or from on-site observation (e.g. by monitoring) by regression. By help of them results from the past at a certain spot can be extrapolated to the future in order to estimate the future development from those of the past, without regarding changing attacks or

resistance of the structure. Combined with a threshold monitoring they may be a workable solution for certain tasks, especially if a comprehensible prognosis is not needed or not possible.

Table 1. Overview on deterioration processes and limit states, Buenfeld et al. (2008).

Deterioration process	Serviceability limit state	Ultimate limit state
Reinforcement corrosion	Corrosion initiation	Flexual failure
	Cover cracking	Shear failure
	Spalling	Anchorage failure
	Excessive crack widths	
	Excessive deflections	
alkali aggregate reaction	Cover cracking	Degradation of mechanical properties
	Spalling	
Sulphate attack	Cover cracking	Degradation of mechanical properties
	Spalling	
Freeze-thaw attack	Cover cracking	Degradation of mechanical properties
	Spalling	
Leaching	Loss of alkalinity at depth of rebar	Degradation of mechanical properties
Acid attack	Loss of alkalinity at depth of rebar	Degradation of mechanical properties
Abrasion	Loss of cover	

Shading: Models widely available (dark grey), limited modeling (light grey), no models available (no shading)

Analytical models describe more or less realistically and based on the relevant physical or chemical mechanisms a degradation process by solving the appropriate differential equations, Li & Melchers (2006). Of course, material properties and environmental attacks can only be considered in a simplified manner. Usually the input parameters of the models are determined from laboratory or field tests. For the description of transport controlled processes like carbonation of concrete or chloride ions ingress (initiation period) such models have been developed to an applicable performance, cp. fib (2011). Limitation of accuracy is given by several simplifications like one-dimensional perspective, considering only one mechanism (e.g. diffusion), constant transport- and concentration parameters, neglecting mutual influences and interactions of different effects. A significant advantage of such analytical models is that the stochastic nature of all parameters of the model as far as they are known either from the structure regarded or from experience, can directly be considered in a full probabilistic approach.

Generally, for any life time assessment the end of service life has to be specified in terms of limit states. For the ultimate limit state (ULS) of concrete structures there are acknowledged rules and associated levels of reliability defined by codes. But for the service limit state (SLS) there are only rigid criteria. Individual ideas of the appearance of a structure or of certain usability criteria may influence the specification. Commonly used condition related limit states are shown in Figure 4 and in Table 1. From the view of practical handling a plausible condition state is the time of depassivation of reinforcement, expressed by the carbonation of concrete or a critical chloride content at the depth of reinforcement, Zhang et al. (2009). This definition of SLS of RC structures has already long been established; Hansson et al. (2004). An optimal point for intervention limit state can only be defined in

combination with a strategic approach on the economic management of a structure and has to be integrated into a decision making process. A defined performance limit state is useful if the development of the reliability of a structure is calculated within a probabilistic approach.

Integration of rehabilitation measures into durability prediction
The most commonly used rehabilitation measures of concrete structures are the application of repair mortar and / or of surface coating (surface protection systems) as indicated in Figure 5.
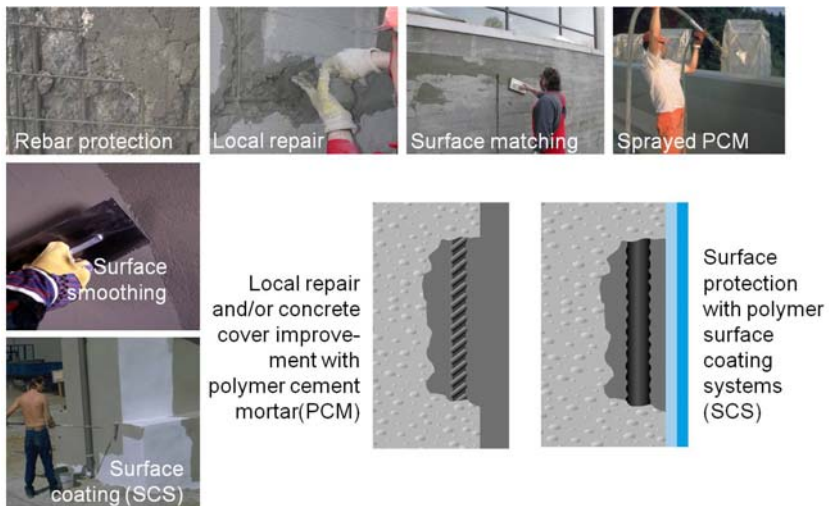
Figure 5. Illustration of concrete repair measures.

To protect concrete members from the ingress of harmful substances, such as carbon dioxide or chloride ions, surface coating is an established measure. The material composition and the thickness of the coating layer are chosen according to the exposure and to the protection objective. Important requirements are e.g. resistance against mechanical abrasion or chemical attack. The interaction between concrete and surface coating is ensured by the bond due to mechanical adhesion.

For reprofiling of damaged concrete surface near areas repair mortar is used. Repair mortar normally is a polymer modified mortar in which the hydraulic binder component is partly replaced by polymers. As in the case of coating, the bond between the repair system and the concrete underneath is encompassed by adhesion. The bond interaction between the old and the rehabilitated areas must resist against shear stresses at the interface between old concrete and rehabilitation mortar for the whole lifetime period of the measure. Both introduced repair measures are often combined with each other.

As indicated in Figure 6, repair layers offer for a certain lifetime an improved reliability, which needs to be quantified in terms of reliability and service life. But unlike to existing prediction models for the durability of concrete today, there are no models for the behavior of those maintenance measures available.
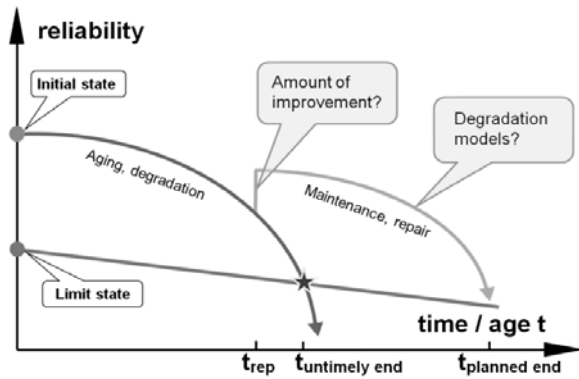
Figure 6. Principal influence of concrete repair measures on service life.

As a first approach repair measures may be regarded as additional barriers, which eliminate harmful ingress into the concrete underneath. So for the first time there is no further degradation of the concrete member. With increasing aging of the rehabilitation materials or in case of other damages the protection decreases and the original deterioration processes accelerate again.
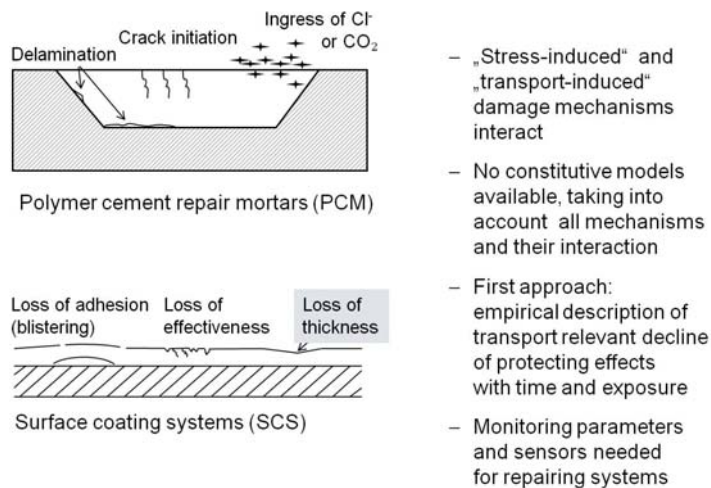
Figure 7. Failure mechanisms of surface coating and repair mortar for concrete.

In order to describe the time and condition dependent protection degradation of the repair materials more realistically, material models are needed which take into consideration the specific degradation phenomena of the repair materials and their bond behavior to the substrate, cp. Figure 7. In Budelmann et al. (2010) a first approach is described assuming that the individual damage processes occur independently of each other. For degradation due to transport processes, the well known models for the carbonation process of concrete and of chloride ingress can be applied, described as a 2-layer-system, regarding the repair mortar and the concrete beneath each in one layer. More details and calibration tests of the models are published in Wachsmann & Budelmann (2012).

Conclusions

An overview of existing durability models for concrete is given and first attempts of recording the durability of concrete repair systems by help of models are made. Two rehabilitation methods, surface coating and repair mortar were examined. It comes clear that due to the diversity of impacts a failure cannot be described in one model. First deliberations for the description of the mechanisms were made.

Acknowledgement

References

Budelmann, H.; Starck, T.; Wachsmann, A. (2010). „Approaches for durability prediction of concrete rehabilitation measures". *Proc. 2nd Int. Symposium on Life-Cycle Civil Engineering (IALCCE 2010)* Taipei: National Taiwan University of Science and Technology (Taiwan Tech.), 2010, 165-175.

Budelmann, H.; Holst, A.; Wachsmann, A. (2012). „Durability related Life-Cycle Assessment of Concrete Structures – Mechanisms, Models, Implementation". *IALCCE 2012.* In: *Proc. 3rd Int. Symposium on Life-Cycle Civil Engineering (IALCCE 2012)*. 3-6 October 2012, Vienna. 2012, 47-54.

Buenfeld, N.R., Davies, R.D.; Karimi, A.; Gilbertson, A.L. (2008). „*Intelligent monitoring of concrete"*. London: CIRIA

fib bulletin 34. (2006). "*Model code for service life design"*. International Federation for Structural Concrete (fib), Lausanne.

fib bulletin 59. (2011). "*Condition control and assessment of reinforced concrete structures"*. International Federation for Structural Concrete (fib), Lausanne.

Li, C.Q. & Melchers, R.E. (2006). „Time-dependent serviceability of corrosion-affected concrete structures". *Magazine of Concrete Research*. 58 (9): 567-574.

Strauss, A., Bergmeister, K., Wendner, R. & Hoffmann, S. (2009). „System- und Schadensidentifikation von Betontragstrukturen". In: *BetonKalender 2009*: 53-134. Berlin: Beuth-Verlag (in German).

Wachsmann, A. & Budelmann, H. (2012). "Life time prediction for concrete repair measures". In: *Proc. 3rd Int. Symposium on Life-Cycle Civil Engineering (IALCCE 2012)*. 3-6 October 2012, Vienna, 209-216.

Zhang, R., Castel, A. and Francois, R. (2009). "Serviceability limit state criteria based on steel-concrete bond loss for corrodes reinforced concrete in chloride environment". *Materials and Structures,* 42: 1407-1421.

Model of compressive strength degradation of concrete under both freeze thaw cycles and compressive loads

Sijia Chen[1], Xiaobing Song[2], and Xila Liu[3]

Abstract：The frost resistance and compressive strength degradation of concrete under the simultaneous action of compressive load and freeze-thaw cycles are experimentally investigated in this paper. In order to track the strength degradation process, the nondestructive tests are carried out after each freeze-thaw cycle to get the residual strength for each specimen. Based on the experimental data, a variable *Kss* is proposed to describe the damage velocity and a prediction model of compressive strength degradation of concrete under freeze thaw cycles and external load is established. By comparing with other researchers' indoor experiment data and outdoor inspection data, the model is proved to be reliable to predict the compressive strength degradation of concrete in cold region.

Keywords: compressive strength degradation, external load, freeze-thaw cycles, prediction model, model verification

1 Introduction

In cold regions, frost resistance is the most important parameter to define the durability of reinforced concrete (RC) structures, and many researches have been conducted on frost resistance of concrete in recent years (Alan et al. 2011; Alexander and Magee 1999; Graybeal and Tanesi 2007; Hahn et al. 2010; Pospichal et al. 2010). However, there are still some limitations of most existing researches.

Firstly, most researchers focused on the freeze-thaw durability of concrete without external loads, while in practice, most concrete structures in cold regions are subjected to both external loads and freezing-thawing. Secondly, with regard to the influence of the external loads, only the frost resistance of flexural loaded mortar or plain concrete was discussed in a few papers (Mu et al. 2002; Sun et al. 1999; Zhou et al. 1994). However, for most RC members, concrete resists compressive stresses whilst reinforcement resists the tensile stresses. Comparing with flexural load, it

[1] PhD Candidate at Shanghai Jiao Tong University, China; E-mail:csj5719@163.com
[2] Associate Professor, Department of Civil Engineering at Shanghai Jiao Tong University, China; E-mail: xbsong@sjtu.edu.cn
[3] Professor, Department of Civil Engineering at Shanghai Jiao Tong University, China; E-mail: xilaliu@tsinghua.edu.cn

seems that the research on frost resistance of concrete under compression is more attractive in engineering community. Thirdly, the dynamic modulus of elasticity and weight loss were the main focuses for almost all previous researches. However, civil engineers are mainly concerned with the residual strength of concrete after freeze-thaw cycles.

So, in the present paper, the frost resistance and the compressive strength degradation of compressively preloaded concrete will be researched by experiment. Based on the experimental results, the model of compressive strength degradation will be established. At last, by comparing with others' indoor experiment data and outdoor inspection data, the validity of the degradation model will be verified.

2   Experiment

2.1   Sample preparation

The proportions of the various concrete mixes and the major parameters are listed in Table 1. Some concrete prisms with 40mm×40mm×160mm were made.

Table 1. Mix proportions and major parameters of concrete

Series	Cement (kg/m³)	Water (kg/m³)	w/c ratio	Sand (kg/m³)	Coarse aggregate (kg/m³)	Air-entraining agent (kg/m³)	Compressive strength at 28 days(MPa)
E-0.67	297	199	0.67	749	1125	0	27.1
E-0.59	320	189	0.59	749	1125	0	29.5
E-0.47	338	159	0.47	749	1125	0	32.1
E-0.47A	338	159	0.47	749	1125	1.01	30.1

2.2   Preloading details

Before freeze-thaw testing, the concrete prisms were compressively preloaded, and the maximum load applied to each prism was adjusted to generate a maximum compressive stress of 0, 30, 50, and 80 percent (*i.e.*, the stress ratios are 0, 0.3, 0.5 and 0.8) of the compressive strength of the same prism. Preloading was generated through a specially designed apparatus, as shown in Figure 1.

Figure 1.   Specially designed apparatus for preloading

2.3   Freeze-thaw test

At the age of 28 days, tests of the concrete specimens were carried out for suffering of the freeze-thaw cycles and external loads according to ASTM C666.

2.4 Ultrasonic method and preliminary test

The residual compressive strength of each specimen after every freeze-thaw cycle was obtained by ultrasonic method(Popovics 2007; Prassianakis and Prassianakis 2004). In order to accurately evaluate the concrete compressive strength with this method, individual relationship between concrete strength and ultrasonic velocity for each type of concrete is obtained by preliminary tests, as shown in Table 2.

Table 2. Relationships between concrete compressive strength in MPa (C) and ultrasonic pulse velocity in km/s (V)

Series	Equation	R^2
E-0.47	$C=0.0007*9.66^V$	0.94
E-0.59	$C=0.057*3.72^V$	0.91
E-0.67	$C=0.45*2.28^V$	0.92
E-0.47A	$C=0.002*7.98^V$	0.93

3 Model building of compressive strength degradation of concrete under freeze thaw cycles and external load

3.1 Definition of damage velocity

In order to understand the relationship between preloading level and damage velocity, the residual compressive strength (RCS) after each freeze-thaw cycle was recorded by ultrasonic impulse method with the formulas in Table 2. The relative residual compressive strength (RRCS) is the ratio of the RCS value measured after each freeze-thaw cycle to that before the freeze-thaw cycling, as shown in Figure 2.
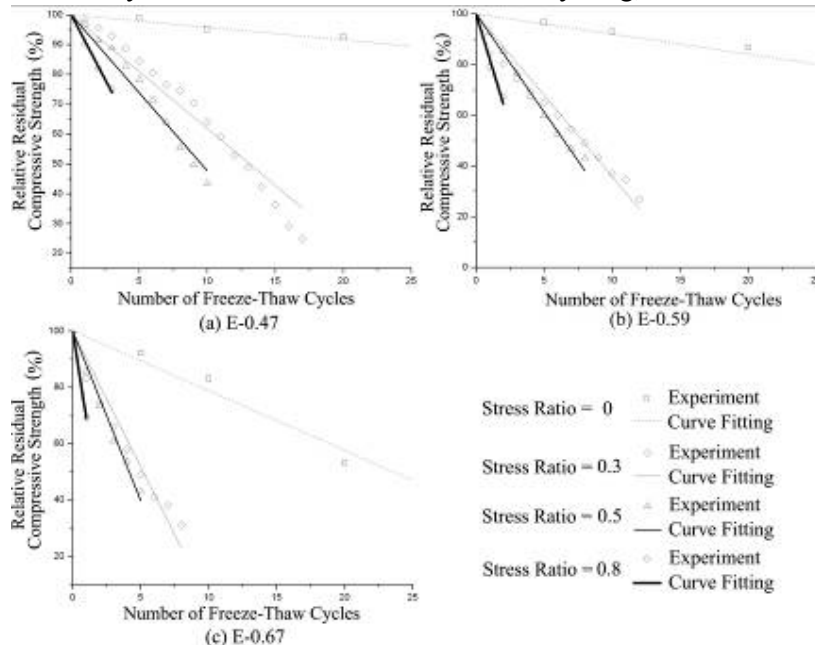
Figure 2.   RRCS versus number of freeze-thaw cycles

The RRCS loss in one freeze-thaw cycle (designated K_{ss}) can be defined as the damage velocity, which is the slope in the coordinate system. So, K_{ss} can be obtained through the equation as follows:

$$K_{ss(N)} = \frac{(f_{(N+1)} - f_{(N)})}{f_{(0)}} \tag{1}$$

where, $K_{ss(N)}$ is damage velocity after a certain number (N) of freeze-thaw cycles; $f_{(N)}$ is RCS after a certain number (N) of freeze-thaw cycles; and $f_{(0)}$ is initial compressive strength.

From formula(1), we can easily obtain the following equation by mathematical transformation:

$$f_{(N+1)} = f_{(0)}(1 + \sum_{0}^{N} K_{ss(i)}) \tag{2}$$

Formula (2) is the compressive strength degradation model of compressively preloaded concrete under freeze thaw cycles.

If damage velocity ($K_{ss(N)}$) was obtained, the RCS after each freeze-thaw cycle can be derived from formula(1), in other words, the degradation model of compressive strength can be derived. So, damage velocity is the key factor to obtain the degradation model of compressive strength.

3.2 Compressive strength degradation model of concrete under freeze thaw cycles and external load

The experimental results reported above (Figure 2) demonstrate that damage velocity changes with the increase of freeze-thaw cycles. From some researches(Guangpu 2006; Shang et al. 2005), it appears that the compressive strength could decline approximately linearly with the increase of freeze-thaw cycles. And from comparison of the experimental results and regression analysis in Figure 2, it appears that the concept of average damage velocity gives a sufficiently accurate description of the damage velocity of concrete under freeze thaw cycles and external load. In other words, it is sufficiently accurate for practical engineering application that damage velocity is replaced by average damage velocity to predict the strength degradation. The linear regression analysis results for average damage velocity are shown in Table 3.

Table 3. Linear regression analysis results for K_{ass}

		Stress ratio 0	Stress ratio 0.3	Stress ratio 0.5	Stress ratio 0.8
w/c ratio	0.47	-0.0042	-0.0382	-0.0523	-0.0870
w/c ratio	0.59	-0.0080	-0.0641	-0.0773	-0.1770
w/c ratio	0.67	-0.0212	-0.0964	-0.1204	-0.3090

So, with the average damage velocity instead of damage velocity in formula(2), the following equation can be easily derived:

$$f_{(N)} = f_{(0)}(1 + Kass \times N) \tag{3}$$

Where, $f_{(N)}$ is RCS after a certain number (N) of freeze-thaw cycles; $f_{(0)}$ is initial compressive strength; and *Kass* is average damage velocity of concrete under freeze thaw cycles and external loads.

4 Verification of the compressive strength degradation model

4.1 Prediction results compared with laboratory experiment results

In this paper, some experimental results (Li 2004; Shang et al. 2005; Yang 2010) of strength degradation without external load are used to compare with the model prediction results. For different experiment, the different strength degradation model should be obtained with different $f_{(0)}$ and *Kass*. The initial compressive strength of concrete ($f_{(0)}$) can be found in the original data of experiment. The average damage velocity of concrete (*Kass*) can be directly found in Table 3 with w/c ratio, or can be obtained by linear interpolation. Predicted results compared with experimental results are shown in Figure 3.

The predicted model for Yang's, Shang's and Li's experiments are:

$$f_{(N)} = f_{(0)}(1 + (-0.0044) \times N)$$
$$f_{(N)} = f_{(0)}(1 + (-0.0056) \times N)$$
$$f_{(N)} = f_{(0)}(1 + (-0.02) \times N)$$

respectively.
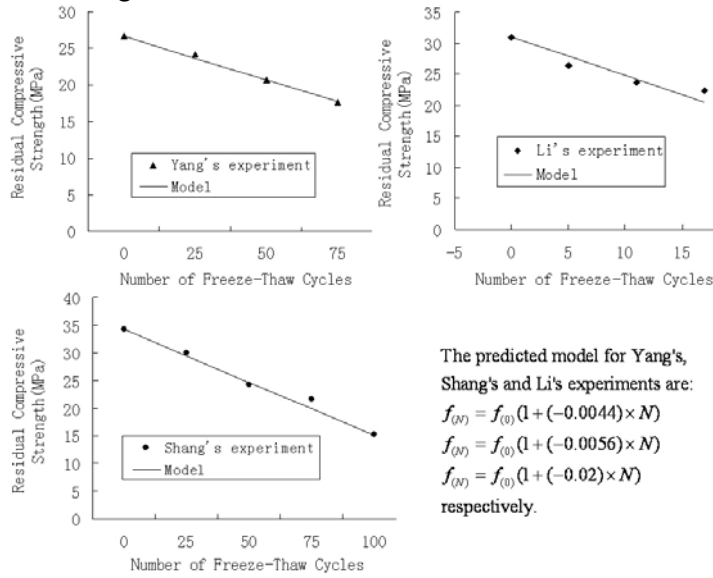
Figure 3.   Laboratory experiment verification of the prediction model

From the comparison in Figure 3, it can be seen that the agreement between experimental results and predicted results is good. No matter the w/c ratio of experiment is low or not, the experimental results are very close to the predicted ones. Although there are errors between predicted results and experimental results, the errors are comparatively small (<10%) and within the engineering allowance.

4.2 Prediction results compared with inspection results from a seaport wharf

The inspection data of a seaport wharf had worked for 26 years before inspection at Qingdao in China is used(Gao 2011) , as shown in Figure 4. In this paper, the actual amount of RCS of three T-shaped beams (designated as beam A, B and C respectively) is used to verify the predicted model.
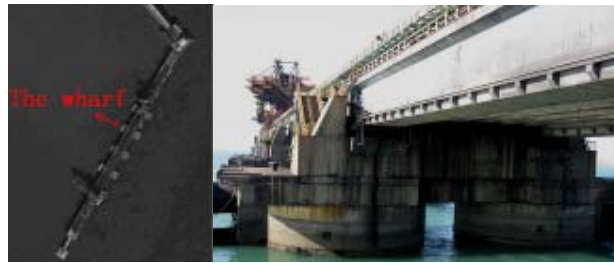
Figure 4.   The figure of a seaport wharf(Gao 2011)

From the compressive strength degradation model (formula(3)) established above, it is apparent that $f_{(0)}$, N and $Kass$ are the key factors. $f_{(0)}$ is initial compressive strength, which can be found in the original data of the inspection report.

N is the number of rapid freeze thaw cycles in laboratory. While formula (3) is used to predict the strength of concrete in practical engineering, the number of natural freeze thaw cycles should be equivalently transformed to the number of rapid freeze thaw cycles in laboratory first. From Lin's research results(Lin et al. 1999), it can be found that the number of natural freeze thaw cycles for a year in Qingdao is 47. And from Li's research results(Li et al. 2000), it can be found that the indoor-to-outdoor ratio of freeze thaw cycles for the wharf is 1:15. So, the equivalent number of rapid freeze thaw cycles for the seaport wharf in 26 year is $N = 47 \div 15 \times 26 \square 81$.

Such as noted above, $Kass$ can be directly found in Table 3 with w/c ratio and stress ratio, or can be obtained by linear interpolation or parabola interpolation. The w/c ratio of beam A, B and C is 0.45. The stress ratio can be obtained by calculation, and some information about the T-shaped beam is listed in Figure 5.
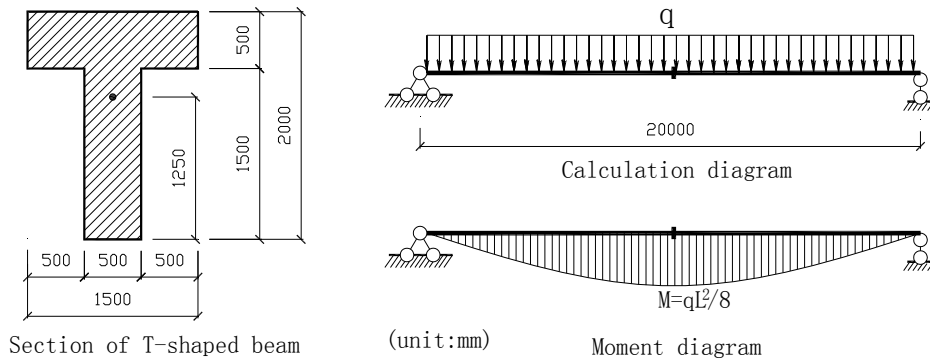
Figure 5.   The calculating sketch of T-shaped beam

From Figure 5, the compressive stress of the top line of the T-shaped section can be derived, and with the initial compressive strength, the stress ratio of beam A, B and C can be derived too. Together with the w/c ratio (0.45), $Kass$ (designated as $KassA$, $KassB$ and $KassC$ for beam A, B and C respectively) can be obtained as: $KassA = -0.00559, KassB = -0.00547, KassC = -0.00547$.

From above all, with the key factors ($f_{(0)}$, N and $Kass$) and the compressive strength degradation model (formula(3)), the predicted RCS can be calculated, as

shown in Figure 6. For comparison, the predicted RCS without external load (stress ratio=0) was also be calculated, as shown in Figure 6.
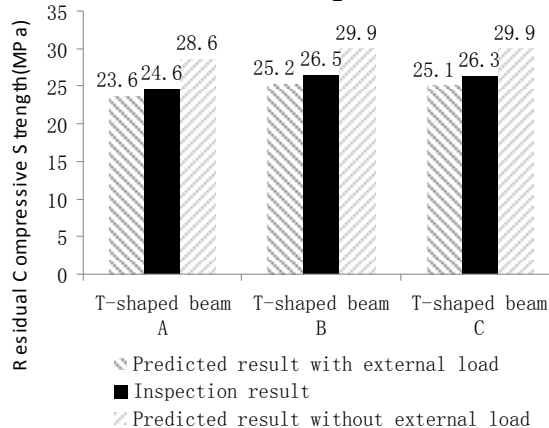
Figure 6.   The comparison between predicted result and actual residual strength

From the comparison in Figure 6, the predicted results are very close to actual ones, which confirm that the degradation model obtained in this paper is reliable to predict the compressive strength degradation under freeze thaw cycles and external load.

5   Conclusions

Based on the experimental investigation, it is apparent that the loss of compressive strength of concrete under the simultaneous actions of load and freeze-thaw cycles was more severe than that under the single frost action. External load can reduce the frost resistance of concrete significantly. Based on the concept of damage velocity and the experimental results, the model of compressive strength degradation under freeze thaw cycles and external load was established. By comparison between model predicted results and experimental or inspection results, the validity of the degradation model is verified.

References

Alan, R., Kathryn, C., and Jennifer, B. (2011). "Freeze/thaw durability of concrete with recycled demolition aggregate compared to virgin aggregate concrete." *Journal of Cleaner Production*, 19(2-3), 272-277.

Alexander, M. G., and Magee, B. J. (1999). "Durability performance of concrete containing condensed silica fume." *Cement and Concrete Research*, 29(6), 917-922.

Gao, X. (2011). "Area of a seaport terminal oceanic and atmospheric assess the durability of reinforced concrete structures and repair(in Chinese)", Qingdao Technological University, Qingdao, China.

Graybeal, B., and Tanesi, J. (2007). "Durability of an ultrahigh-performance concrete." *Journal of Materials in Civil Engineering*, 19(Compendex), 848-854.

Tang, G,. (2006). "Research on Durability Evalution Methods of Concrete Structures under Freeze-thaw Conditions(in Chinese)," Tsinghua University, China.

Hahn, A., Shamloo, M. A., Hurlburt, G., and Alam, M. S. (2010). "Freeze-thaw durability flow chart model for concrete infrastructure in Canada." *Annual Conference of the Canadian Society for Civil Engineering 2010, CSCE 2010, June 9, 2010 - June 12, 2010*, Winnipeg, MB, Canada, 1598-1606.

Li, J. (2004). "durability design and construction of concrete under freeze thaw cycles(in Chinese)." *International Conference Hydropower 2004*, Yichang, China, 9.

Li, J., Pen, X., and Deng, Z. (2000). "Quantitative design of frost resistance of concrete(in Chinese)", *5th Academic communication on concrete durability*.

Lin, B., Cai, Y., and Shan, G. (1999). "research on measures to improve structural durability of marine concrete." *Science and technology of cementitious composite*, Beijing, China, 16-23.

Mu, R., Miao, C., Luo, X., and Sun, W. (2002). "Interaction between loading, freeze-thaw cycles, and chloride salt attack of concrete with and without steel fiber reinforcement." *Cement and Concrete Research*, 32(Compendex), 1061-1066.

Popovics, S. (2007). "Analysis of the Concrete Strength Versus Ultrasonic Pulse Velocity Relationship." American Society for Nondestructive Testing.

Pospichal, Kucharczykova, Misak, and Vymazal. (2010). "Freeze-Thaw Resistance of Concrete with Porous Aggregate." *10th International Fatigue Congress, FATIGUE 2010, June 6, 2010 - June 11, 2010*, Prague, Czech republic, 521-529.

Prassianakis, I. N., and Prassianakis, N. I. (2004). "Ultrasonic testing of non-metallic materials: concrete and marble." *Theoretical and Applied Fracture Mechanics*, 42(2), 191-198.

Shang, H., Song, Y., and Qin, L. (2005). "Experimental Study on Properties of Concrete after Freezing and Thawing Cycles." *Concrete and Cement Products*(02), 9-11.

Sun, W., Zhang, Y. M., Yan, H. D., and Mu, R. (1999). "Damage and damage resistance of high strength concrete under the action of load and freeze-thaw cycles." *Cement and Concrete Research*, 29(Compendex), 1519-1523.

Yang, Z. (2010). "Reaserch about uniaxial compression performance of concrete under freeze-thaw cycles(in Chinese) ", Yangzhou University, China.

Zhou, Y., Cohen, M. D., and Dolch, W. L. (1994). "Effect of external loads on the frost-resistant properties of mortar with and without silica fume." *ACI Materials Journal*, 91(Compendex), 591-601.

Reliability Assessment of Bolting Systems for Steel Frame Connected to Reinforced Concrete Structure

Hasan Kamal[1], Jafarali Parol[1], Thamer Al-Yaqoub[1], Zafer Sakka[1], Ahmad Yousif[1]

Abstract

For improving the performance and safety, retrofitting/strengthening or repairing of existing reinforced concrete structures is an important issue in structural engineering. Attaching steel bracing system is one of the common solutions for retrofitting or repairing of damaged structures. An efficient load transfer between existing structural members and attached retrofit system is significant to such repairs. For steel bracing systems, the load transfer between the steel system and existing concrete structures are achieved through proper anchorage between them. A typical steel-to-concrete connection includes: a steel attachment consisting of a baseplate welded to the attached member and the anchors that actually connect the steel to concrete as bolting system. In the present paper, reliability method is used to assess the safety of the steel bolting system that is used to connect steel frame systems to existing reinforced concrete columns. Herein, the steel frame systems are used to retrofit/strengthen existing reinforced concrete corbel beams as structural supporting system. The effect of applied loadings, bolts geometry, bolts spacing variation and concrete quality on the concrete breakout strength are examined for the current problem. Reliability is assessed by estimating the failure probability of the single bolt failure and system bolt failure. The results are used to determine the parameters affecting safety of the connection system and to improve the performance and the technique of strengthening/repairing of the steel supporting frame systems.

Keywords: *concrete bolt connection, retrofitting/strengthening, reliability analysis, steel frame*

[1]Infrastructure Risk and Reliability Program, Energy and Building Research Center, Kuwait Institute for Scientific Research, PO Box 24885 Safat, 13109 Kuwait, Tel: +965 2498-9261, Fax: +965 2498-9099, *hkamal@kisr.edu.kw;jparol@kisr.edu.kw*

Introduction

Strengthening of existing reinforced concrete buildings is becoming an important research subject in civil engineering. This is because a large number of existing structures need rehabilitation or strengthening due to aging or deterioration due to extreme environmental conditions or due to combinations of many factors (American Concrete Institute (2008); Wiener (1985)). Retrofitting / strengthening techniques depend upon the type of damage that exists in the structure. Strengthening using carbon fiber reinforcement or attaching a steel frame to the existing structural member are few of the commonly used techniques. In the case of carbon fiber reinforcement, it is important that the new added carbon fiber should properly bond with the existing structural member. On the other hand, in the case of steel frame attachment, proper connection should be ensured between the existing structural member and the newly added steel frame. Load transfer between the existing concrete structural members and newly added steel frame is ensured through the connection between them. One common type of connection between concrete to steel is implemented using steel bolts. There are several design guidelines available for the design of such connections (American Concrete Institute, 2008).

Wiener (1985) studied the cyclic behavior of steel to concrete connections using epoxy-grouted bolts. In his experiments, various parameters were considered such as number of fasteners, use epoxy at the steel-concrete interface, etc. Wiener had shown that, epoxy coated bolts improved the elastic capacity by a factor two and reduced by the amount of slip. He had shown that a greater amount of non-uniformity in load distribution among bolts without epoxy coating and he attributed this to the greater amount slip between steel and concrete. Effect of oversize holes has been examined by several investigators (Allen and Fisher, (1968)). Effect of plate flexibility has been examined by Cannon *et al.* (1981).

In the practical cases of post bolt installation, it is very unlikely that all the anchors will be installed perpendicular to concrete surfaces. According to Blickford (1981), if the bolts are inclined, it may take greater amount of tension to generate the necessary clamping force between joint elements, and as a result relaxation will most likely be worse. It has been shown that minor differences in connection geometry can result in more substantial differences in the state of the stress in the bolt.

It can be seen that most of the research in this subject are based on the experimental study with single bolt. So far in literatures, no definitive work on the group bolt has been presented. It is possible in steel to concrete anchor connections that, any change in the design parameters from the nominal design can cause major changes in the actual capability of such connection. As an example, edge distance and embedment depth of the bolt are few of the design parameters that majorly affect many failure modes (American Concrete Institute (2008)). So, it is very important to arrive at the tolerance

range that is allowed for each design variable. Not many research papers are available in the literature based on the probabilistic analysis of steel to concrete bolt connection.

In the current paper, reliability analysis of the steel frame connection to the existing concrete column using steel bolts is presented. In this case, the steel frame is attached to the concrete column to carry part of the load from an existing damaged cantilever beam. Effect of various design parameters such as embedment depth of bolts, edge distance, spacing etc on concrete break out failure mode is examined. The geometric dimensions and load values presented here are normalized values and hence the probability of failure thus presented are not the actual values but again normalized.

Brief Description of Steel to Concrete Connection Failure Modes
Detailed design procedure and various failure modes have been explained in detail in ACI design guidelines. It can be seen that unlike steel to steel anchor connections, there are unique failure modes that is experienced only in steel to concrete bolt connections such as concrete breakout failure in tension and shear. The following section will briefly discuss these two failure modes. Further detail can be found in reference (American Concrete Institute (2008)).

Concrete Breakout Failure in Tension

According to the appendix D of ACI 318M-08, the nominal concrete breakout strength of a single anchor N_{cb} or group of anchors N_{cbg} in tension shall not exceed:

$$N_{cb} = \frac{A_{Nc}}{A_{Nco}} \Psi_{ed} \Psi_c \Psi_{cp} N_b \qquad (1)$$

Here, A_{Nc} is the projected concrete failure of a single or group of anchors as illustrated in reference in appendix D of ACI 318M-08. It can be seen that edge distance is an important parameter for calculating the projected area. A_{Nco} is the maximum projected concrete failure area which is equal to $9h_{ef}^2$, where h_{ef} is the effective embedment depth of bolt. Here Ψ_{ed}, Ψ_c, and Ψ_{cp} are modification factors based on proximity of the edges of concrete member, presence of crack in concrete etc.
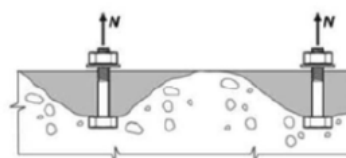
Figure 1: Concrete breakout failure in tension

The basic concrete breakout strength of concrete of a single anchor in tension is defined as, $N_b = k_c \lambda \sqrt{f'_c} h_{ef}$, where, k_c is the coefficient for basic concrete breakout strength in tension and λ is the modification factor reflecting the reduced mechanical properties of lightweight concrete. Similarly for a group of anchors, the concrete breakout strength is given by,

$$N_{cbg} = \frac{A_{Nc}}{A_{Nco}} \Psi_{ec} \Psi_{ed} \Psi_c \Psi_{cp} N_b \qquad (2)$$

Where Ψ_{ec} is the factor used to modify tensile strength of anchors based on eccentricity of applied load and the expression is given as per reference ACI Code (American Concrete Institute (2008)).

Concrete Breakout Failure in Shear

Concrete shear breakout failure mode is graphically depicted in Figure 2. According to the ACI, the nominal concrete breakout strength of a single anchor V_{cb} or group of anchors V_{cbg} in shear shall not exceed:

$$V_{cb} = \frac{A_{Vc}}{A_{Vco}} \Psi_{ed} \Psi_c \Psi_h V_b \qquad (3)$$

Here, A_{vc} is the projected concrete failure area of a single anchor or group of anchors, for calculation of strength in shear and A_{vco} is projected concrete failure area of a single anchor, for calculation of strength in shear, if not limited by corner influences spacing, or member thickness. Basic concrete breakout strength in shear of a single anchor in cracked concrete, V_b is given by

$$V_b = 0.6 \left(\frac{l_e}{d_a}\right)^{0.2} \sqrt{d_a} \, \lambda \, \sqrt{f'_c} (C_{a1})^{1.5} \qquad (4)$$

Where l_e is the load bearing length of anchor for shear (American Concrete Institute (2008)). Similarly, for group of anchors, the expression is given by

$$N_{cbg} = \frac{A_{Vc}}{A_{Vco}} \Psi_{ec} \Psi_{ed} \Psi_c \Psi_h V_b \qquad (5)$$

(iii) Concrete breakout
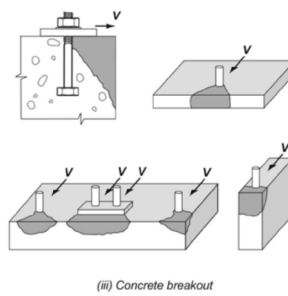
Figure 2: Concrete breakout failure mode in shear
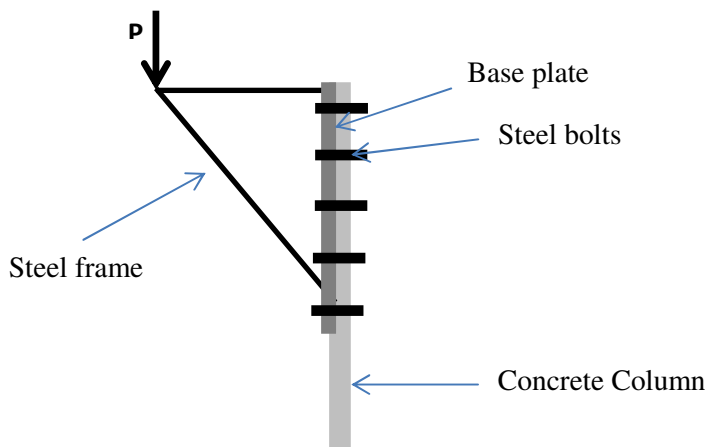
Figure 3: Steel frame connected to the concrete column through bolts

It can be seen that steel to concrete bolt connections are associated with unique brittle failure modes such as breakout failure modes in tension and shear.

Analysis, Results and Discussion

In this paper, steel bolt connection that is used to connect a steel frame attached to a concrete column to strengthen the existing reinforced concrete cantilever beam as shown in Figure 3. Bolt configuration is shown in Figure 4. There are twelve bolts present in this connection. This is a case study problem that is taken from the analysis of a recently completed project within the team. The steel frame is used to carry a portion of the load from the existing reinforced concrete cantilever beam. For the purpose of analysis, the loads and other dimensions shown are not the exact values that are used for the actual analysis of the structure, but are normalized values only. The main purpose of this work is to investigate the relative importance of each design parameters of a steel to concrete bolt connections. The concrete cantilever beam is subjected to a tip load at the free end. The tip load is the reaction from one end of a continuous beam where it is supported at the free end of this cantilever beam. Hence the steel bolts are subjected to tension and shear loads. The tension loads on each bolt is different, where the top row of bolts are subjected to maximum load and are linearly reduced towards bottom row, and the bottom most row of bolts are subjected to the least tension load.

In order to understand, the current steel bolt connections, an in-house excel spread sheet has been developed to calculate the probability of failure (P_f) and the safety index (β) for each single bolt and group of bolts under tension and shear loads. Several iterations were done by varying the values of the effective bolt depth (h_{ef}), distance from the center of a bolt to the edge of concrete (C_{a1}), distance from center of bolt to the edge of concrete in the direction perpendicular to C_{a1} (C_{a2}), specified compressive strength of concrete (f'_c), tension force acting on an anchor or group of anchors (T_s), and the shear force acting on an anchor or group of anchors (V). For the purpose of analysis, value of each parameter under investigation is varied within the range of ±10%, while the other parameters were

fixed to observe the effectiveness of each parameter compared to the P_f value. It may be noted that the actual tolerance range that is allowed in the actual design is different from this value.

Based on experience and for the purpose of analysis the COV for the random variables are assumed as given below;

$$h_{ef} = 0.2; \ C_{a1} = 0.2; \ C_{a2} = 0.3; \ f'_c = 0.2; \ T_s = 0.1; \ and \ V=0.1$$

These parameters random variables are assumed to be normally distributed. In this study only two failure modes are considered, that is concrete breakout failure in tension and shear. Accordingly the performance function that is used in the current analysis is given below.

$$Z= R\text{-}L \qquad\qquad (6)$$

where, R is given by Eq. 1, 2, 3 and 5 respectively for breakout failure of a single anchor in tension and shear for single and group of anchors. Here L is the tension or shear load on each bolt or group of bolts. For the purpose of analysis Monte Carlo simulation is used with number of cycles, N, is limited to 1000. The probability of failure is therefore calculated using the following equation:

$$P_f = \frac{No.of \ Failures}{N} \qquad\qquad (7)$$

Analysis has been performed for all the bolts as the bolt loads and few other design parameters are different for each bolt. As expected the probability of failure varies for each bolts and the maximum probability of failure for the case study example was observed for the corner bolt number 7 and 8 (Figure 4). These two bolts are subjected to maximum tensile load and least edge distance. For the purpose of evaluating the effect of different parameters, only normalized values are presented. The probability values are normalized in such a way that, the maximum probability of failure obtained in the actual case is normalized to 1. Figure 5 presents analysis results for breakout failure in tension. It is clear from the graph that the distance from the center of bolt to the edge of concrete in one direction (C_{a1}) was the most dominant parameter.

As the tension load increases the probability of failure increases. Alignment and number of bolts affects the load on each bolt. By increasing the number anchors tension load acting on each anchor will be reduced. It is observed from the analysis that as the edge distance decreases the probability of failure increases. Therefore the designers should consider these parameters while designing and arranging the location of the steel bolt connections. The second most effective factor was the tension force acting on an anchor or group of anchors (T_s,).
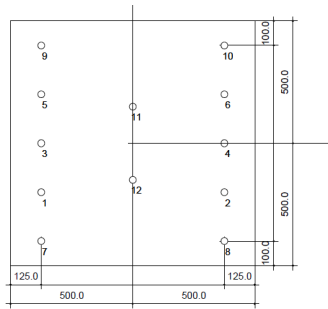
Figure 4: Geometric alignment of the bolt connections

Another important parameter is the effective bolt depth (h_{ef}). Similarly, for the group of bolts, breakout failure in tension, it has been observed that, eccentricity of loads is the only major additional parameter that is present in the case of group of bolts compared to the single bolt case. Otherwise the effect different parameters are similar to what was seen in the case of single bolt case. In the case of breakout failure due to shear, shear the most dominant factor is the distance from the center of a bolt to the edge of concrete (C_{a1}). Other parameters that influence the failure mode are the shear force acting on an bolt or group of bolts (V), and the distance from center of bolt to the edge of concrete in the direction perpendicular to C_{a1} (C_{a2}). Analysis results are graphically depicted in Figure 6.
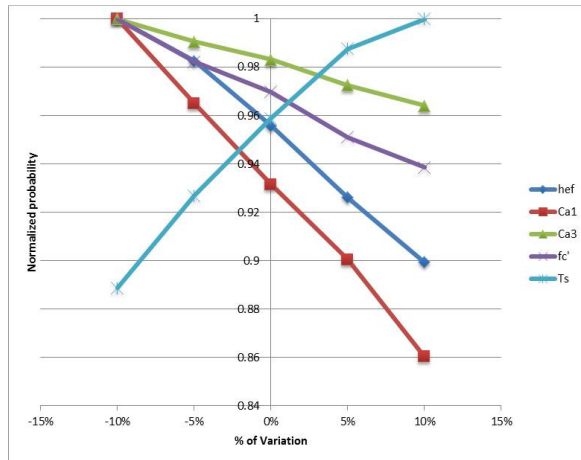
Figure 5: Effect of different parameters on probability of failure for breakout failure of single bolt
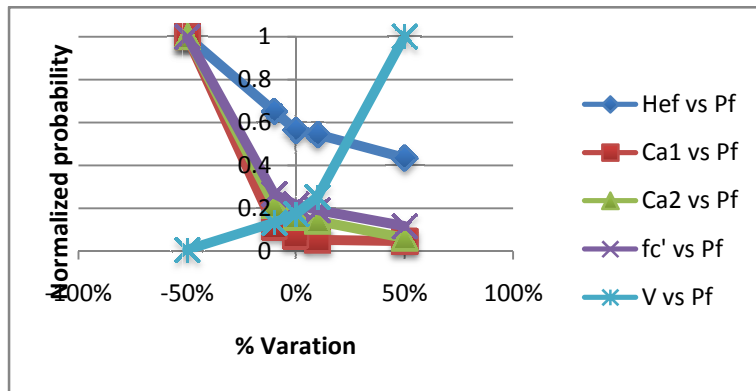
Figure 6: Effect of different parameters on probability of failure for breakout failure of single bolt

Conclusion

In the present work an attempt has been made to examine the effect of various parameter on the probability of failure in steel to concrete bolt connections. Concrete breakout failure in tension and shear failure modes are considered for the present study. It is observed from the analysis that edge distance and embedment depth of bolts are two major parameters that affect the reliability index for the concrete breakout failure in tension. Similarly, edge distance is a major factor that affects the breakout failure mode in shear the major factor that affect is the edge distance. Hence the tolerance range for these two parameters needs to be carefully arrived and controlled while implementing a steel to concrete bolt connection. A case study example from an ongoing project has been presented with normalized load values. Further work need to be done in order to understand the effect of inclination of bolts on the probability of failure.

Acknowledgement

Authors of this paper would like to thank the project team members and the management of Kuwait Institute for Scientific Research for their continuous support.

References

1. *American Concrete Institute*. (2008). Appendix D,"*Building Code Requirements for Structural Concrete and Commentary*"(Publication No. ACI 318M-08).
2. Allen, R.N. and Fisher, J.W. (1968), "Bolted joints with oversize or slotted holes", *Journal of the Structural Division*, Vol 94.
3. Blickford, J.H (1981), "*An introduction to the design and behavior of bolted joints*", Marcel Dekker, Inc,.
4. Cannon, R.W., Godfrey, D.A. and Moreadith, F.M, (1981), "Guide to design of anchor bolts", *Concrete International*, pp.28-41.
5. Wiener, D.F. (1985), "*Behavior of steel to concrete connections used to strengthen existing structures*", Master's Thesis, University of Texas at Austin.

Risk Management in China: Applying International Best Practice to Foreign-Invested Projects

Geoffrey Mills[1]

Abstract

Chinese contractors operating overseas have experienced difficulties in adjusting to the international environment. This in fact mirrors earlier international experience of western firms entering new markets – so, as with much in life, the main lessons have already been learned by our predecessors and the challenge is to pass them on to the next generation. One of the key differences in moving from a relatively mature and well regulated construction environment, as China is, to a range of different and largely immature markets is the need to become much more aware of risks that in the home market to a large degree are covered by an established legal, regulatory and operating environment.

To understand the differences it is first necessary to understand the characteristics of the home market and in China there are many features of the system that effectively provide a safety net to contractors who fail to perform.

This paper describes how the operating environment in China in many respects provides a poor grounding for Chinese contractors moving overseas and hence how important it is for such firms to adopt a rigorous approach to risk management as will be covered by other papers.

Text

I am writing this from the perspective of a consulting engineer and with a lifetime in consulting engineering.

Thucydides, in his History of the Peloponnesian War, had lived through a period of some decades of turmoil when the fledging Greek states were trying to find a peaceful solution to their coexistence. Every attempt at a peaceful solution failed and he concluded that it was in our nature that the future of mankind would be

---

[1] BSC MBA DIC CEng FICE, FIStructE, MCIWM, MCIQA
China Representative, the Institution of Civil Engineers

warfare. The quest for a risk free construction environment may be similarly challenging but that does not, of course, mean that we should not continue to strive for improvement.

Thucydides further realised that in his short but nonetheless eventful life he had seen more than he could assimilate and so he felt that his history needed to be not just (and indeed not even) an assessment of the turmoil that he had witnessed but a factual record of events which might allow some future historians to make more sense of it.

Having passed normal retirement age just before writing this paper I feel that my more effective contribution is not to repeat the good advice that we have all heard so many times in the past and that is now enshrined in eminent publications and even (from 2009) an ISO Standard but to share my own experience of mistakes – my own and those of which I have had first-hand experience.

I will loosely collect them together under some common headings which I note conveniently gives me a Ten Commandments of circumstances to avoid, or more likely to watch for as they inevitably occur again in the future. Unfortunately libel laws and common courtesy mean that a number of my best examples have had to be left out to. So in no particular order:

1. Innovation

There is so much published on this crucial topic but to the best of my knowledge there is still no agreed definition. My own preference is "anything that the team involved has not done before." Given that as a safe rule "every innovation fails" and that as a construction industry we cannot build prototypes without great risk, then attempting something new should be generally be avoided. In many cases, strengthening the team can solve the problem but if the team is new to a task it will probably fail.

Let me take, for example, some very large dockside cranes. Costs were trimmed as part of an overall "value engineering" exercise and one saving was associated with an automatic anchoring system, which would be used in storm conditions. This was replaced with a manually operated pin system involving a steel dowel that could be twisted to release and then lowered into one of a number of a restraint holes in the jetty deck. This assumed that the meteorological warning of a storm would be sufficient to allow the crane driver time to move the crane to one of the anchor locations and then exit the cab to drop the anchor into position. In the event, that assumption was false – and two cranes ended up in the river!

Sometimes it is possible to construct a prototype and this was the case for a specially designed fleet of rough terrain tipping vehicles. The risk of falling over

sideways was identified and so a bespoke, extra-long axles set was specified. To test this, the prototype was taken to an established vehicle test centre. The prototype passed the test. A field trial was then run with the prototype, fortunately, where it was found that it was quite stable laterally but the entire vehicle tipped over backwards when the tipping mechanism was operate.

Over the past 20 years, many of China's teams of engineers have been responsible for significant projects on which they had no prior direct experience. We should recognise their achievement.

2. Unrealistic Programme

There is a saying in Quality Assurance: "there is never enough time to get it right first time but always time to do it again when it fails." Too frequently, investors do not want to put in the time at the outset to ensure that the job is likely to go smoothly.

An extreme case – ignoring good advice, an investor commenced work on a development in China without the necessary permissions in order to save time. A year later the company was made to dig up what it had started and to reapply for a license. The China board was sacked.

More commonly, an investor will underestimate the time needed to complete all the pre-contract activities, including his own review and development tasks, and so either the contract proceeds with the risk of avoidable later variations and extensions of time, or the contract start is postponed for a longer period than would have been needed if adequate time had been planned in from the outset.

It needs a very persuasive consultant to convince an investor that he should probably slow down, or take alternative action to achieve the programme more reliably if time really is "of the essence." In any case, whose place is it to determine the correct business decision?

To have an educated discussion on that subject requires the investor to value the benefit of time. This is required not in the somewhat cruder way normally used to assess the limits of delay damages but a real assessment of the value (or cost) to the business of beating, meeting or failing to meet the programme. In most cases, that time will vary depending on when any delay might be known, since contingency options close down the closer one gets to completion.

Some investors, in my experience, will fail to make that assessment but still exert strong – albeit uninformed – pressure to finish on time. In the event of a possible delay, the informed investor will be ready to discuss acceleration and know what it might be worth spending to achieve that. The lesser informed will threaten

action and may have the apparent contract powers to do so, but will nevertheless suffer the delay and so any redress becomes a financial one which is rarely adequate compensation – although without knowing the value of time, how can that be assessed?

3. Unrealistic Budget

It was reported that when Churchill and Eisenhower first asked the head of the Royal Engineers when he expected to complete construction of the Mulberry Harbours (for the Allied invasion of France), he responded "By 1953, or thereabouts."

When they explained their need to have it in place by 1944 – some nine years sooner than he anticipated – he reportedly retorted, "You can have it cheap, quick or clever – any two, but not all three."

It may be an exaggeration to say "there are no technical problems on projects, only financial ones" but it contains more than a germ of truth.

Assuming a reasonable degree of design and procurement competence, then the final balance of quality, price and programme represents a block of rubber in which two sides can be squeezed at the expense of the other but to reduce the total volume is a much greater challenge.

Budgets should – like cigarettes – be presented in packets with a health warning, since until the project is quite well advanced there needs to be significant contingencies, well beyond the level that most investors will want to hear.

4. Failure of Legal Remedy

This is a significant problem in China and in many other parts of the world. Indeed my neighbour in Oxford runs a group in one of the Oxford colleges researching how countries work where the law does not.   The law in England is imperfect and the law in China is imperfect – but each has their own imperfect characteristics.

A recent out-of-court settlement in the UK, which was close to the insured limit of the (large) consulting firm concerned, was totally used to pay legal fees with no damages being awarded to either side.   The law had completely failed as a remedy and both parties decided to wrap matters up as they were merely feeding the major law firms.   The total legal fees of the two parties were greatly in excess of the settlement.

China has some problems with the legal system that I cannot write about, but some of the problems I have experienced (and can write about) are:

- In over 300 contracts not one of our clients (western investors) has ever tested the courts or an arbitral tribunal – although one is about to as I write. Western investors, as a breed, settle. That means that in so many areas there are no clear legal precedents. My company has initiated some court/arbitral actions and been generally satisfied with the process (even where we lost!) and we have been involved as expert witnesses but recourse to the law is very much the exception even though the costs of an action in China are low in comparison to western jurisdictions.
- Defaulting contractors in China cannot be removed from a project and a replacement brought in without a formal judgement, which generally takes more time than is available and hence leads to negotiation.
- Local provincial authorities often act outside of the national laws but given that there is no available enforcement mechanism, investors just have to live with those aberrations.
- The application of the law favours the labour force and that can be manipulated to the disadvantage of the investors – by (for example) the courts requiring the investor to pay workers directly who have not been paid by their contractor or sub-contractor employers.

5. Overstretch

This can apply nationally, corporately and individually although individual overwork is a symptom of a corporate failure.

Nationally, I recall the struggle in the early days of our motorway programme, in my first holiday job working on one of Britain's new motorways. The team I was assigned to had a bridge collapse during construction with some fatalities. From no experience of motorway building at all, the UK construction industry had to mobilise to build a network and in the first decade in particular there was a national skills shortage. The leadership of that programme included engineers who had been responsible for the Mulberry Harbours and they resorted to widespread standardisation which allowed the programme to continue with reduced risk but of course stifled innovation.

That is indeed a challenge for the next generation – building safely and sustainably requires a solution to the innovation challenge. I saw evidence of a similar challenge faced by the Chinese government in a national schools building programme following the end of the Cultural Revolution where many schools were built but not to consistent standards. One collapsed in the Sichuan Earthquake in 2008 for which there was much criticism of shoddy workmanship –

but the message was lost that even in the most remote regions, China had been investing in new schools with a programme of a scale that experience would have shown would lead to some risk.

6. Fraud

The old cartographers had a nice convention for illustrating areas that were either uncharted or known to be dangerous and illustrated their maps with sea monsters and other supernatural hazards where the simple advice was just to "beware entering here."   We have no such convention but this is a most challenging area. I have a colleague, an expatriate Christian, who is married to a Chinese wife and who wanted his son to go first to Chinese school to learn Chinese language and culture and then for secondary education to move to an expatriate school of his father's nationality.   A couple of years before it was time to switch he said that he was making the transition and I asked why.   He said that his son was unhappy as his culture and beliefs were so different to his young friends.   My colleague told me "Of course I know that Chinese parents love their children as much as any other parent so I was interested to find why they were teaching a different set of attitudes, so I spoke to some of them."   He learned that his son's friend's parents believed that their children would be growing up in a very difficult world and in order to survive they had to have the tools to deal with all forms of behaviour. Hence better to ground them in the teachings (for example) of Sun Tzu and his "Rules of War" than leave them without the capability to deal with the challenges that they would have to face in the future, whether they wished to or not.   My friend moved his son and continued to reinforce his Christian beliefs.

7. Culture

Some aspects of this are covered in the discussion on fraud but the cultural issues are much deeper and affect every aspect of professional life.   To a very large degree my own professional career has been based on a long established British indentureship system.

Following the Cultural Revolution, China lost sight of much of its cultural heritage so the current generation of engineers is having to find its own cultural foundation. The Western model has, understandably, lost much of its earlier credibility in recent years.   China's current President is so concerned about the need to re-establish China's traditional culture and values that he has made that endeavour a hallmark of his Presidency with the support, for example, of the Qunshu 360 (www.mchunghua.org).

For all the mistakes that I have made and seen I was brought up in an environment in which safety (in the broadest sense) was given the highest priority and the

British consulting firms produced engineers who were dedicated to looking after their clients and the public.   There were exceptions of course but they were exceptions.

Since the Cultural Revolution, China has had a tremendous challenge in rebuilding its economy and developing a reliable construction industry both nationally and, latterly, internationally.

Emphasis has been given to initiative and the rewards available for success have exceeded the sanctions for failure.   The spirit has been "he who makes no mistakes makes nothing" and indeed amongst the outstanding successes evident to any China visitor there have been a few spectacular failures.

China's own construction profession recognises the need to mature and hence the international risk assessment programme that was initiated in 2010 jointly by the Chinese construction industry and the Institution of Civil Engineers and that (at the time of writing) is due to be concluded early in 2014.

One of the important aspects of culture in relation to risk is what society judges to be acceptable, since a level of risk control that stifles development is likely to be considered counterproductive.

8.   Genuine Undiscovered Mistake

People are fallible and will remain so.   I have been reasonably successful through my career but I think of myself as a "70% man."   I realised at university that from an early age, through school and latterly at university, I averaged around 70%.   Indeed I graduated with upper second class honours, so maintaining my 70% consistency.   It was at university that I first asked myself how, in professional practise, I could regularly and reliably achieve 100%, which surely I would need to do if the projects on which I worked were not to fail.

I subsequently learned of safety factors, of layer of protection analysis (LOPA) and of the legal and commercial foundation of the profession being based on not being negligent.   The law does not expect me to be superior to my peers and recognises the inevitability of error.   The law, in that respect, recognises reality. No business will succeed if the business plan involves no taking of risk and no structure will ever be built that is risk free.

I strongly believe that the best foundation for society for the future will be to continue to develop professions in which the commercial risk is at the negligent level, since we need to work constructively with our clients to help them achieve

their business objectives, we need to innovate to a much greater degree and must balance those objectives with the obligation to protect the third parties who will use the facilities we design.

9. Act of God

I was amused that the cause of failure of one of my buildings that collapsed in China was ascribed by the Chinese authorities to an "Act of God" which made it an insured event and had the (I'm sure unintentional) consequence of deflecting criticism from the Chinese contractor, design and supervisor. The underwriter agreed. I would love to say more but cannot.

Most Force Majeure events are in fact predictable but the profession needs the protection of national/international agreement on the acceptable level of risk to be taken in design. A standard cannot be "negligent" since by definition it represents an agreed view. So design for a one in X year flood event will certainly leave the risk of a "Force Majeure" flood inundation but as a society we need the national and international standards structures to define X rather than leave it to individual engineers or firms.

A situation where X (as in China's snow loading) is found by more recent events to have been too low leads to a challenge for society in respect of how to deal with pre-existing structures.

I recall earlier in my career being involved in the structural assessment of buildings (and indeed a tunnel) with High Alumina Cement, where there was a real risk of a large number of British structures being condemned. One of the professional institutions formed a panel to define the assessment criteria which took the problem away from the individual firm and engineer and again circumvented the negligence risk. Economically for the country it was a good solution but in fact left many structures with likely residual safety factors below the designed requirement. To the best of my knowledge, subsequent performance of these structures justified the panel's recommendations.

10. Failure of Leadership

That leaves the last of my Ten Commandments, the failure of leadership. Ultimately any and all failures are a failure of leadership. "A good craftsman does not blame his tools." The future of the profession within and outside of China has been and will continue to be in the hands of relatively few people who have great responsibility to secure our future infrastructure needs and balance the competing pressures of progress, reliability, resource shortages, economic limitations and the essentially flawed characteristics of the tools available to them to do so.

A challenge indeed and I wish the next generation of leaders well.

The fate of a state lies in the hands of the generals, and so kings in the past placed utmost importance on the selection of generals and commanders.
Scroll 31: Liu Tao

Quantitative Solution of Overseas Project Risk Management by Knowledge Engineering

Xu Feng,[1] Lin Shaopei,[1] Hu Hao[1] and Zhu Wei[1]

Abstract: In this paper, the Project risk management is studied through the fuzzy quantitative evaluation of risks and the counter-measures of its mitigation. Based on knowledge engineering, we established the so-called "Risk-Knowledge Framework" model as the basis of building knowledge base, which serves as the skeleton of system procedure for the problem solving. The fuzzy mathematical model is established for quantitative analysis of different risks through fuzzy reasoning. Correspondingly, a prototype software KB-FDSS recognized as Knowledge-Based Fuzzy Decision Supporting System, is developed for verifying the solution. Testify of the risks by KB-FDSS through practical project were carried out and favorable results were achieved.

Risks in International Engineering Market

Construction overseas engineering projects are facing high risk, as these risks exist in every stage of the project implementation, any negligence would bring serious economic losses. The risks of overseas projects in different stages of its implementation include Political Risks, Legal Risks, Economic Risks, Natural Risks, Social Risks, Contract Risks, Technical Risks, Implementing Risks, Financing Risks and Operational Risks (Zhang 2012).

It is obvious that most of these risks are accompanied by improper or wrong decision-making and inadequate of early investigation work in project early stage of the project. Therefore, in order to make correct decision, we should understand and study the corresponding measure against the risks of overseas projects, which involve the contents of Political, legal, social, economic, financial, marketable and technical aspects, etc (Zhang 2012).

Risk Knowledge Framework for Project Risk Management

The qualitative recognition, classification and building the frame modeling of project risks are a sophisticated intellectual activities based on the experience of human being. The corresponding measure against specific risk is the decision making from their knowledge, which is initiated as an intuitive and heuristic manner.

In the era of knowledge economy, the losses of experience and knowledge wealth are a serious issue that cannot be negligible for a modern enterprise, the only way out is to take the advantage of artificial intelligence technology relied on knowledge engineering to accumulate significant knowledge system persistently.

---

[1] School of Naval Architecture, Ocean and Civil Engineering, Shanghai Jiao Tong University, 1954 Huashan Road, Shanghai, PRC, 200030; PH (86) 21-62933091; FAX (86) 21-62933163; e-mail: F.Xu@sjtu.edu.cn

Knowledge-based Model under Risk Knowledge Framework

There are various risks that can be composed as a system of main risks with its subordinates hierarchically; correspondingly, the countermeasure for mitigating the specific risk could form a system too. These two systems link by "connecting line" to build a logic network system with the "risk" at one end and "countermeasure" at the other. The physical meaning of "connecting line" represents how effective the measure (it is knowledge itself) to be taken could mitigate the risk. The essence of "Risk-Knowledge Framework"（RKF） is a *Game relationship* between risk and countermeasure (knowledge) characterized of "this grows with that vanishes" and "this vanishes with that grows". Math-physically, it is a highly non-linear multi-layer network between risk and knowledge. The Risk-Knowledge Framework symbol description is introduced as following: Construction Risk (CR), Knowledge Base (KB), Risk Point Framework (RF), Knowledge Point Framework (KF), Risk-Knowledge Framework (RKF), Construction Risk Point Framework (CRF) and Construction Risk Knowledge Framework (CRKF).

A knowledge based decision supporting system for project risk management is developed and its framework is RKF (Risk Knowledge Framework), concretely, it is Construction Risk Knowledge Framework (CRKF) for contractors. Figure 1 illustrates the logical structure of CRKF, which is essentially a complex nonlinear network with the functions.

Even extremely complicated relationships in risk evaluation can be simplified to a series of choice among the fuzzy vectors reflecting the one-to-one links in "RKF" Model; Moreover, it is more simple that only a choice of number among 1, 2, 3 and 4. is needed, for the choice reflects the evaluator's experience and knowledge. Nevertheless, the logical structure of RKF is a complex nonlinear network with relationships characterized in "one-to-one", "one-to-multiple" and "multiple -to-multiple" which composes the basic structure of knowledge base.

Risk-Knowledge Framework Model

A knowledge based decision supporting system for project risk management is expected to be developed and its framework is RKF (Risk Knowledge Framework). Concretely, it is Construction Risk Knowledge Framework (CRKF) for contractors. Its functions include:

(1) Based on different cases, Risk Knowledge Framework establishes the relation of risk set and knowledge set (for risk prevention or mitigation) accordingly as a link and reflects the corresponding relation. The relationship reflected by the link can be "one-to one", "one-to many" or "many-to-many".

(2) Experts' knowledge and experience is reflected by the effectiveness of the knowledge based measures in risk control, since the completeness of RKF will provide a platform on which the functions of risk evaluation experts can be adequately developed.

(3) The evaluation process given by experts is actually to assess every single risk and knowledge. The effectiveness of knowledge in risk control can be measured through fuzzy membership vector (Lin 2008) and that means to make a choice among four kinds of fuzzy membership. We define: Classified fuzzy vector 1 is very effective (VE) for risk control; Classified fuzzy vector 2 is rather effective (RE) for risk control; Classified fuzzy vector 3 is slightly effective (SL) for risk control; Classified fuzzy vector 4 is negligibly effective (NG) for risk control. On the basis of getting fuzzy vectors through linking risk and knowledge, quantifying the risk based on fuzzy inference, the quantitative evaluation of each risk of the project can be obtained.

(4) Through "Risk-Knowledge Framework" Model, even the extremely complicated relationships in risk evaluation can be simplified to a series of choice among the fuzzy vectors reflecting the one-to-one links between risk and knowledge. And now it is more simplified to be a choice of number among 1, 2, 3 and 4 and the choice reflects the evaluator's experience and knowledge. Based on this, the risk state of a project can be reflected in a simple and operational way. In spite of this, the physical essence of the issue is to reveal the *game relationship* of the multi-layered nonlinear networks between the risks and corresponding measures while its mathematically structured solutions are still hard to find.

(5) The "linked" fuzzy vectors are composed of four areas representing the corresponding fuzzy membership grades of the four "effectiveness degree" (Lin 2012a). The fuzzy vectors in correspondence of the four kinds of "effectiveness degree" can be given in the software program (Lin 2012b). Based on the inference character of fuzzy sets, a slight change of the fuzzy membership grades of the fuzzy vectors would not so sensitive as influence to the final result of the fuzzy inference. That is to say the final result, just as proved by vast practical projects, is insensitive to the variation of fuzzy membership (Sharma 2011).

Know Based Fuzzy Decision Supporting System KB-FDSS

The expression of risk through fuzzy set

The essence of mathematical model is to quantify the fuzzy information of the knowledge among project risks and measures. Through fuzzy inference, verification and human's induction and deduction, the updated information and conceptions of project risks can be obtained.

The definition of fuzzy subsets is: Define a fuzzy subset A in the domain U, for any element $u \in U$ there is a $u_A（u）\in [0,1]$, as the membership of u to A and regard u_A the membership function of A, where fuzzy subset A can be described by its membership function, which represents the degree of belonging and membership of elements to the set rather than the probability of the element to the set. For common set, we have: If $u_A（u）\in U$, then $u_A = 1$. If $u_A（u）\notin U$, then $u_A = 0$. For fuzzy set, u_A can be taken continuous value between domain $[0,1]$, where we called u_A

=*[0,1]* the multi-value logic. Define a fuzzy subset R is a subset of $U \times V$, a fuzzy relation from U to V. We write $U \xrightarrow{R} V$ a fuzzy relation, while *[R]* is described by its membership function u_R.

Fuzzy Assessment and Quantification of Risks

The information of fuzzy vectors is utilized to get the effectiveness of the measures (knowledge), so as to build the relation between the risk and knowledge. In project risk management, for making risk management decision, it is necessary to quantize the risk level by following fuzzy mathematical model.

Define: risk factor set $U=$ {Political Risk, Economic Risk, Legal Risk, Social Environment Risk, Security Risk (assault, slaughter), Technical Risk, Management Risk, etc.} ; Then define V is the effectiveness of knowledge in reducing risks, V can be expressed by four grades: Very Effective (*VE*), Rather Effective (*RE*), Slight Effective (*SE*) and Negligible (*NG*). Thus, $V=$ *{VE、 RE、 SE、 NG}* .

Introduce fuzzy sets to describe degrees of the problems, then the fuzzy relation R between U and V can be described as: $R_i = r_{ij}$ *(i=1,2,3,4,...,7），(j=1,2,3,4)*.

r_{ij}: membership of the i-th risk in U to the j-th domain of V. Fixing i, then we have：$R_i = \{r_{i1}, r_{i2}, r_{i3}, r_{i4}\}$. It is membership of the i-th risk in U to the four domains of V. When *i=1,3*, the risks can be effectively reduced, and the fuzzy risk matrix of the project R (Lin 2011) should be:

$$R = \left[r_{ij} \right] = \begin{bmatrix} 0.85 & 0.1 & 0.05 & 0 \\ 0 & 0.2 & 0.7 & 0.1 \\ 0.85 & 0.1 & 0.05 & 0 \\ 0 & 0.05 & 0.1 & 0.85 \\ 0 & 0.05 & 0.1 & 0.85 \\ 0 & 0.2 & 0.7 & 0.1 \\ 0 & 0.2 & 0.7 & 0.1 \end{bmatrix} \tag{1}$$

Introduce the Risk weight matrix of each functional system:

$$P=[P_i] \qquad (i=1,2,...,7) \tag{2}$$

Considering the political risk, economic risk and social security risk of the local region are most influential to the safety of the project, these risks should be considered in priority. Then, $P=$ {0.25,0.20,0.10,0.10,0.25,0.05,0.05} . Where, P is a risk weight matrix revealing the influences of the risks, then the vector quantity E as

the comprehensive fuzzy risk assessment matrix should be *E=P ×R={0.1275,0.0745,0.2525,0.3275}*. After nominalization, *E={0.163,0.095,0.322, 0.419}*.

According to the principle of maximization the membership function, the domain where maximum membership of E is located reflects the effectiveness of risk reduction. The physical meaning can be summarized as: If it is in domain VE, that means the risks are negligible and can be very effectively reduced; If RE, that means the risks are slight and can be effectively reduced; If SE, that means the risks are comparatively serious which can be just slightly reduced; Finally if NE, that means the risks are extremely serious which can barely be reduced.

In this project, *Max (E) =0.419* when *V* is in the fourth *NG* region, thus the risks are barely reduced. Since it is evaluated that the measures are negligibly effective for both social environment risks and security risks, the project should be denied or reconsidered.

KB-FDSS and Its System Function

Software system KB-FDSS (Knowledge-Based Fuzzy Decision Supporting System) is developed for quantitative assessment of project risks by fuzzy decision making approach. Following function modules should be contained in the system:

(1) Data and Knowledge Module: The main task of which is as the supporting module to gather and to generate data and knowledge that feed to the decision-making software.

(2) Object Decision-Making Module: Its primary task is to provide multiple decisions for project risk management, including: the evaluation of specific risks, decision-making for bidding, decision-making for investment, decision optimization in project risk management, which can be performed in every stage of the project implementation, etc.

(3) Input-Output Module: The primary missions of which include treating the data and knowledge needed for input, dealing with the output information (data and knowledge) prepared by the customers. For above reasons, this module is equipped with pre-processors and post- processors.

Example Verification of Risk Evaluation

A China contractor is contracted to build a railway project in Africa with the main track around 350 kilometers. The project is tested and verified for the risks by means of the software prototype KB-FDSS (Knowledge-Based Fuzzy Decision Supporting System). Sequentially input the rank of fuzzy membership vectors (very efficient, rather efficient, slightly efficient and negligible) of the measures to be taken for constraining the sub-risks to the main risks (political, economic, policy & legislation, environmental, implementation and technical risks), which represent the effectiveness of control to these risks, the software could automatically calculate and output the fuzzy risk membership vector of each main risk, as well as the "zone" where the maximum membership of the vector is located. The state of this "zone"

represents the risk state of the project after those measures have been taken place. The results of fuzzy risk assessment of the project by KB-FDSS are shown in Figure 2.

The example shown in Figure 2 illustrates the distribution map of the fuzzy assessment vectors are listed in Table 2; among them, the blue one show the maximum membership of the entire project as 0.365 which means the risk is "rather effectively" controlled, and thus the project is in the domain of "Slight Risk". The distribution of project fuzzy risk membership vector of main risks and sub-risks of the project is shown in Table 1.

Table1 Distribution of fuzzy risk membership vector of the railway project in Africa

Kind of risk	Weight	NG Zone	SE Zone	RE Zone	VE Zone	Assessment
Overall risk	1.0	0.266	0.146	0.365	0.223	SL Risk
Political	0.168	0.103	0.123	0.330	0.443	NG Risk
Economic	0.237	0.500	0.132	0.275	0.042	VS Risk
Policy & legislation	0.132	0.442	0.100	0.158	0.300	VS Risk
Environmental	0.177	0.237	0.160	0.423	0.180	SL Risk
Implement	0.191	0.203	0.170	0.468	0.160	SL Risk
Technical	0.095	0.122	0.143	0.393	0.343	SL Risk

Here the fuzzy membership vector is distributed among the main risks of the project. We recognize: (1) For *political* risk, the maximum fuzzy membership is located in VE zone, that means the measures taken for its mitigation is very efficient, so this risk should be evaluated as negligible (*NG*). (2) For *Economic* risk, Max (*E*) is located in *NG* zone, so this risk could be evaluated as very severe (*VS*). (3) For *policy and legislation* risk, Max (*E*) is located in *NG* zone, so it could be evaluated as very severe (*VS*). (4) For *environmental* risk, Max (*E*) is located in *RE* zone, the risk is evaluated as slight risk (*SL*). (5) For *implemental* risk, the maximum fuzzy membership is located in *RE* zone, it shows the risk as slight risk (*SL*). (6) For *technical* risk, Max (*E*) is located in *NG* zone, it implies the risk is very severe (*VS*).

For the project itself, the maximum fuzzy membership is located in *RE* zone that means the global measures taken for its mitigation is rather efficient, so it should be evaluated as "slight risk (*SL*) and easy to control". This conclusion is coincident with the past empirical evaluation of the project in its feasibility studies as "The project risks are controllable".

Conclusive Remarks

Every project is processed under uncertain environment. Since the project environment itself is full of uncertainty, yet the only certainty for the project is its uncertainty. Unfortunately, uncertainty is just the source of risk, thus inevitably the risk will associate with the project. The control of risk will determine the success or

failure of the project, especially for those complex projects, due to seriously increasing the uncertainties, causing tremendous consequence of risk emergence for the project.

As the risk emerged, one needs to take corresponding countermeasures, thus there will be a complicated relationship between risk and it countermeasure (knowledge), which is a game of counter partnership of "this grows with that vanishes" and "this vanishes with that grows". The composition of risk is so complicated that it comprised of hierarchical and subordinate relations. Consequently, the corresponding countermeasures (knowledge) would be engaged in these relation and make Risk-Knowledge Framework (RKF) to be a sophisticated non-linear network. Such situation is more challengeable for those complicated projects since it is impossible to realize an overall comprehensive maneuver of those severe and hostile project risks just by empirical and heuristic knowledge of the project decision maker. Under such case, how to relying on computer aided decision making for quantitative project risk management seems inevitable.

Another problem is how computer helps people to evaluate risk degree for decision making? There is another uncertain problem of how the countermeasure (knowledge) could work in constraining the risk? The uncertain mathematics should be used for the solution by introducing the concept of fuzzy sets and fuzzy membership vector to modify the "effectiveness of knowledge constraining the risk". Moreover, through fuzzy inference we may determine the level of each particular risk in the RKF network quantitatively, thus provide the fuzzy decision support for the risk management under complex project environment.

The theory and practice presented in this paper are devoted to solve risks under high complexity of project environment. By applying knowledge engineering methodology, one may avoid the subjective interferes to the final solution and may properly treat the complexity of the project risk and gear it up into the regular and reasonable track of formulated solution. It is our understanding that this is a valuable experiment for promoting the progress in quantitative management and decision science for its upgrading from qualitative to quantitative.

Push forward the method in this paper for solving project risk management is a kicking off test of practicing "quantitative management" theory, more theoretical and practical works are needed in the future, such as the RKF network optimization problem and the system error estimation of solution by means of fuzzy membership vector   need to be further investigated.

References：

Lin, S.P. (2008). "Fuzzy-AI Model for Managerial Science." *Plenary Session Speech and Proceedings of PMI Research Conference*, 13-16 July, Warsaw, Poland.

Lin, S.P., Zhang, W.Y. (2011). "Decision Traps and Fuzzy Quantitative Risk Management of Overseas Projects." *Civil Engineering Innovation*, 5(1), 29-40.

Lin, S.P., Yang, D., Zheng, H. et al. (2012a). "On Optimization of Subway Vehicle Maintenance based on 'FMEA-Fuzzy' Model (I) ---- Theoretical Studies." *Journal of Optimization in Infrastructure Management*, 24(2), 22-28 (in Chinese).

Lin, S.P., Yang, D., Zheng, H. et al. (2012b). "On Optimization of Subway Vehicle Maintenance based on 'FMEA-Fuzzy' Model (II) ---- Software Implementation." *Journal of Optimization in Infrastructure Management*, 24(3), 14-19 (in Chinese).

Sharma, A., Yadava, G.S. and Deshmukh, S.G (2011). "A Literature Review and Future Perspectives on Maintenance Optimization." *Journal of Quality in Maintenance Engineering*, 17(1), 5-25.

Zhang, W.Y., Lin, S.P. (2012). "The Factor Analyses of Risk Decision Traps for Overseas Projects." *Journal of Optimization in Infrastructure Management*, 24(1), 8-13 (in Chinese).
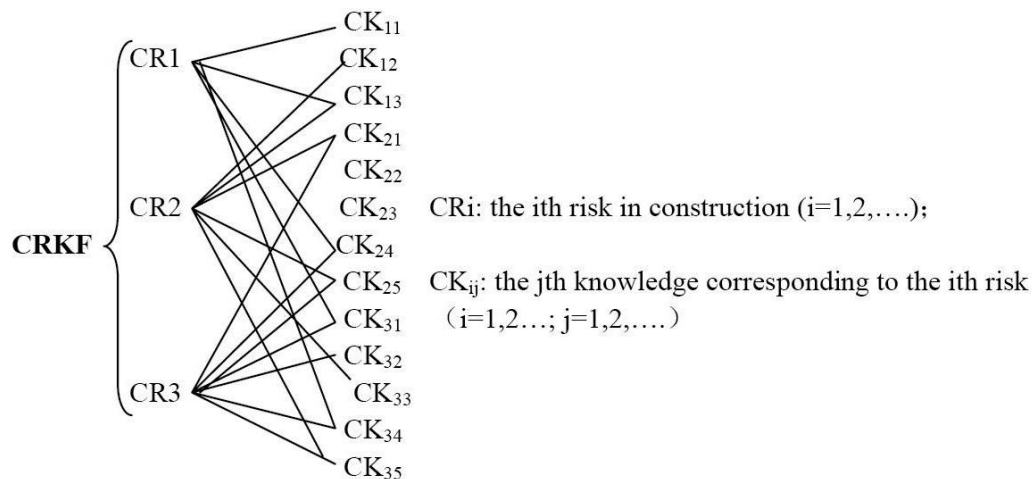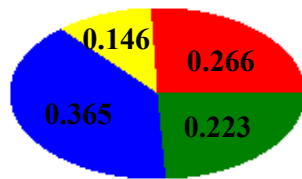

Figure 1 Construction Risk Knowledge Framework
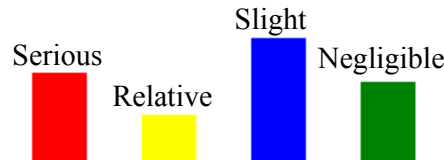


Figure 2 Fuzzy assessment result of the railway project in Africa

Software Integration of Safety Analysis of Reinforced Concrete Structure Considering Temperature During Construction

Kefeng Huang[1], Xila Liu

Abstract: The reinforced concrete structure during construction is a time-dependent structure consisting of a partly completed structure and a formwork shore system. During construction the time-dependent structure may be under the most vulnerable stress state and accidents may occur. For safety control, new structural models and analysis methods are proposed to simulate load transfer and demonstrate the influence of daily temperature variation, and a new software named Safety Analysis during Construction considering Temperature (SACT) is developed. SACT is suitable for analyzing reinforced concrete frames, slab-column systems, and shear wall structures.

SACT is developed using modular techniques and object-oriented techniques. Since each module is object oriented designed in C++ language, the system development is much less complicated. After comparing with field test data, a good agreement has been observed. The proposed software SACT can provide accurate simulation of reinforced structures during construction under various circumstances, and it is also a convenient software for construction safety control in practice.

Keywords: Reinforced concrete structure, shore system, safety analysis, construction, temperature variation, SACT

1. Introduction

The reinforced concrete structure during construction is a time-dependent structure which consists of a partly completed structure and a formwork-shore system (Liu 1997). The strength of concrete slabs increases over time and formwork-shore system keeps shoring and re-shoring along with construction process. It is clear that, during the process, the configuration, material properties and carried loads of the

---

[1] Department of Civil Engineering, Shanghai Jiaotong University, Shanghai, China

time-dependent structure all vary with time. Some effects on the uncompleted structure connected with the formwork-shore system, such as construction loads and ambient temperature, may not be neglected.

During these decades, many researches have been carried out on the load transfer during construction (Calderón 2011, Chen 1991, Grundy 1963, Li 2000, Liu 1986, and Zhang 2012). Characteristics of materials have been studied, static loads and dynamic loads have been discussed separately, but effects of ambient temperature have not been fully understood. In order to thoroughly understand the load transfer during construction, the influence of ambient temperature has to be considered.

In the present paper a simple and unified software (SACT) is programmed for reinforced concrete frames, slab-column systems, and shear wall structures. By integrating the model for calculating effects of temperature into the safety analysis, the "time-dependent" structure can be analyzed more thoroughly. The program is validated by the valuable measurements from on-site experiment at the Law building of Tsinghua University (Fang 2001).

2. Calculation model

2.1 Basic assumptions

The paper attempts to present a simple and direct method to determine safety risks quickly during construction, and the following assumptions are made:

1) The temporary structure during construction is two dimensional. The materials of structure and shores are linear elastic;

2) main loads are weights of slabs and transferred weights;

3) the stiffness of the ground floor is infinite relative to the others;

4) temperature field is uniform in space but changes with time;

5) only steel pipe shore system is considered.

2.2 Structure calculation model

Three models are established (Fang 2000) according to different reinforced concrete structure types based on different failure mechanisms respectively:

1) Slab-column structure
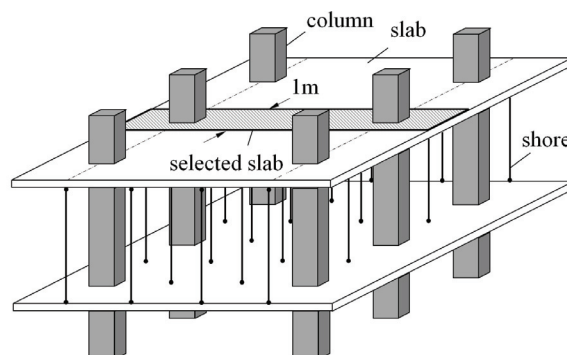
Figure 1. Computational model of slab-column structure

The failure of slab-column structure is primarily the punching failure of the concrete at joints of columns and slabs. As shown in Figure 1, the calculation model of slab-column structure is a single-span or multiple-span 2-dimensional time-dependent structure in which one span structure consists of two columns at both ends, a 1m wide slab band through these two columns, and the shore system connected to the slab band.

2）Frame structure

The failure of frame structure is mainly the bending failure of slabs. As shown in Figure 2, the calculation model of frame structure is a single-span or multiple-span 2-dimensional time-dependent structure consisting of a 1m wide slab band along the line through each mid-span point of beams and shores connected to the slab band.
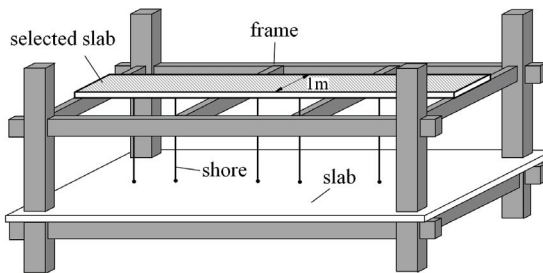
Figure 2. Computational model of frame structure

3）Shear wall structure
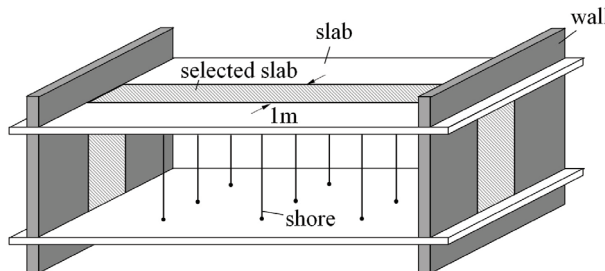
Figure 3. Computational model of shear wall structure

The failure of shear wall structure is mainly the bending failure of slabs. As shown in Figure 3, the calculation model of shear wall structure is a single-span or multiple-span 2-dimensional time-dependent structure consisting of a 1m wide slab band along the line through each middle point of shear walls, a 1m wide shear wall band at the center of the entire wall, and shores connected to the slab band.

Three types of structures can be expressed in a general 2-dimensional structural model, which includes the selected 1m wide slab band regarded as a beam, shores below the slab, and supports at both ends. Depending on construction conditions, different stories and spans are considered. Internal forces and node displacements then can be solved by structural mechanics.

3 Temperature model

The response of steel pipes to temperature change is very fast because of their small

volume and high thermal conductivity. So the temperature of pipes is considered as the same as the ambient temperature, while the temperature of concrete columns lags behind due to large volume and low conductivity. Evidently the temperature difference between steel pipes and columns (ΔT_{cs}) is smaller than the ambient temperature variation between day and night (ΔT_a). Since the thermal conduction resistance of concrete is smaller than the surface thermal resistance, the temperature distribution inside a concrete column is considered uniform, and the lumped parameter method is adopted to determine the temperature difference between pipes and columns.

According to meteorological data, the cyclic change of ambient temperature repeats in every 24 hours. Therefore, in the proposed analysis, the lowest ambient temperature (T_L) can be taken as the ambient temperature at the initial moment; at the same time ΔT_{cs} is very little and the temperature of concrete columns can be treated as T_L. After 12 hours, the ambient temperature reaches a highest value (T_H), the temperature of columns also reaches its highest value, but it should be lower than T_H. During the past 12 hours, the analyzed temperature variation between day and night is: $\Delta T_a=T_H-T_L$, and the difference between the ambient temperature and the temperature of columns is also the largest when they both reach their highest values. Since the temperature of steel pipes is synchronized with the ambient temperature, the analyzed temperature difference between steel pipes and columns (ΔT_{cs}) can be treated as the maximum temperature difference between environment and columns in the past 12 hours.

According to the lumped parameter method, the thermal differential equation describing the heat transfer is as (1), where T_c is the temperature of concrete column ($^\circ$C) and it is changing with time t (h), ρ is the density of concrete (kg/m^3), c is the specific heat of concrete (kJ/($^\circ$C•kg)), V is the volume of a concrete column (m^3), A_{ca} is the contact area between concrete column and atmosphere (m^2), and h is the heat transfer coefficient between concrete and air (kJ/($^\circ$C•m^2•h)).

$$\rho c V \frac{dT_c}{dt} = -A_{ca}h\left(T_c - T_H\right) \tag{1}$$

As explained previously, when t=0, the ambient temperature is the lowest value (T_L), then it can be obtained that, the surplus temperature of concrete (T_θ) is the temperature difference between the highest ambient temperature and the temperature of concrete columns, which is $T_\theta=T_c-T_H$, and the initial surplus temperature (T_{θ_0}) is $T_{\theta_0}= T_L-T_H$.

By introducing the surplus temperature of concrete, (1) becomes (2).

$$\rho c V \frac{dT_\theta}{dt} = -A_{ca}hT_\theta \tag{2}$$

After integrating (2) from 0 to t (3) can be achieved. (3) can also be written as (4).

$$\ln\frac{T_\theta}{T_{\theta_0}} = -\frac{hA_{ca}}{\rho c V}t \tag{3}$$

$$\frac{T_\theta}{T_{\theta_0}} = \frac{T_c - T_H}{T_L - T_H} = \frac{T_c - T_H}{-\Delta T_a} = \exp\left(-\frac{hA_{ca}}{\rho c V}t\right) \tag{4}$$

As explained previously, the analyzed temperature difference between steel pipes and concrete columns (ΔT_{cs}) can be taken as the temperature difference between the environment and concrete columns in the past 12 hours, thus it can be calculated in (5).

$$\Delta T_{cs} = \Delta T_a \cdot \exp\left(-12\frac{hA_{ca}}{\rho c V}\right) \tag{5}$$

The variation of shore length caused by the temperature variation between steel pipes and concrete columns (Δt) can be expressed as (6) (Li 2000), where α is the coefficient of thermal expansion of steel material, and L is the original length of shore.

$$\Delta L = \alpha \cdot \Delta t \cdot L \tag{6}$$

Therefore, the axial force (P) in steel pipe shore caused by temperature variation can be calculated as (7), in which EA is the stiffness of a steel shore.

$$P = EA\frac{\Delta L}{L} = EA\alpha\Delta t = EA\alpha\Delta T \cdot \exp\left(-\frac{hA}{\rho c V}\tau\right) \tag{7}$$
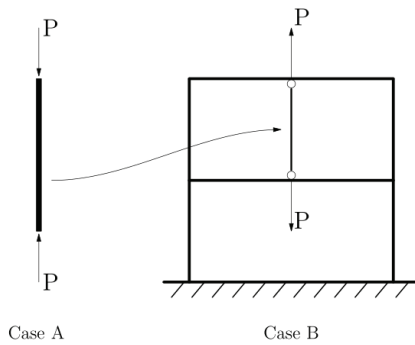
Figure 4. Effects of temperature variations

During analysis, the axial force P caused by the temperature variation can be applied to the structure by three steps as follows: first, for the temperature rise, an unconstrained steel pipe shore, which is named case A, is assumed to be compressed at two ends with a force P. Then, a complete structure without any temperature variation is applied a tensile force P at the two slab-shore connections and is named case B. At last, the final structure under the effects of temperature variations can be deduced by combining cases A and B as shown in Figure 4.

4. Computer realization

A new software named Safety Analysis during Construction considering Temperature (SACT) is developed based on proposed models. SACT can run under systems such as Windows-7 and Windows XP, and SACT also runs fast with a

small-footprint. As shown in Figure 5, after each construction step, stress distributions in structure elements and steel shores under the influence of temperature can be analyzed by SACT with the input of real-time temperature.
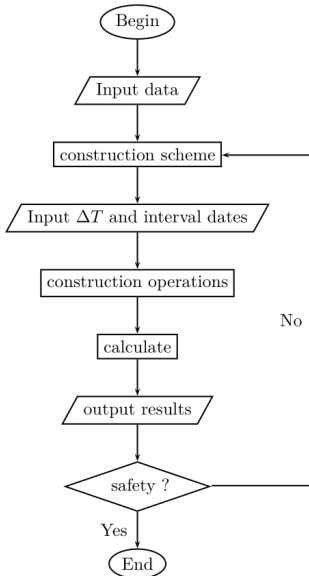
Figure 5. Process flow chart of SACT

SACT is also a well programmed software. SACT consists of interface codes and business codes, and both of them are simply programmed and easy to understand.

Interface codes implement human-computer interactions, such as the main frame of SACT, title bars, menu bars, tool bars, status bars and dialog boxes. These functions are implemented by classes derived from parent classes in MFC (Microsoft Foundation Class). As an important code reuse technique, derivation makes the development of SACT fast and dependable.

Business codes consist of four modules: Data input, data output, construction simulation and calculation. Each module is programmed using the object-oriented programming technique, and data structures and operands are all defined using classes in C++. Therefore, the system development is much simpler, inheritance and security can be found in each module, and future improvement would cost the least modification. A few system interfaces are also preserved for future development.

5. Case Analysis

5.1 Description of the Law building at Tsinghua University

The Law building at Tsinghua University (Fang 2001) is taken as an example in the present paper for validation. The Law building is a frame structure with three spans, each of which is 3.6m wide. The structure was constructed with two stories of steel pipe shores. There were 3 steel pipe shores in each span, and the spacing between two shores in the same span was 0.9m. The slab weighs 2.64kN/m^2, the framework weighs

$0.2kN/m^2$ and each steel pipe shore weighs 0.2kN. Resistance strain gauges of length 5mm were installed on all the shores in the test area to continuously measure the vertical load and its change using the 7V07 data acquisition system.

Since this experiment was carried out between April and June, according to weather data the average ΔT can be taken as 12.7℃.

5.2 Analysis of SACT calculated results and on-site measurements

After each construction step, distributions of internal forces are analyzed by SACT. In the present paper, the load transfer coefficient (κ) is introduced to demonstrate variations of load transfer. The coefficient κ is the ratio between the load carried by an arbitrary floor (F) and the weight of this floor (D) as shown in (8).

$$\kappa = \frac{F}{D} \tag{8}$$
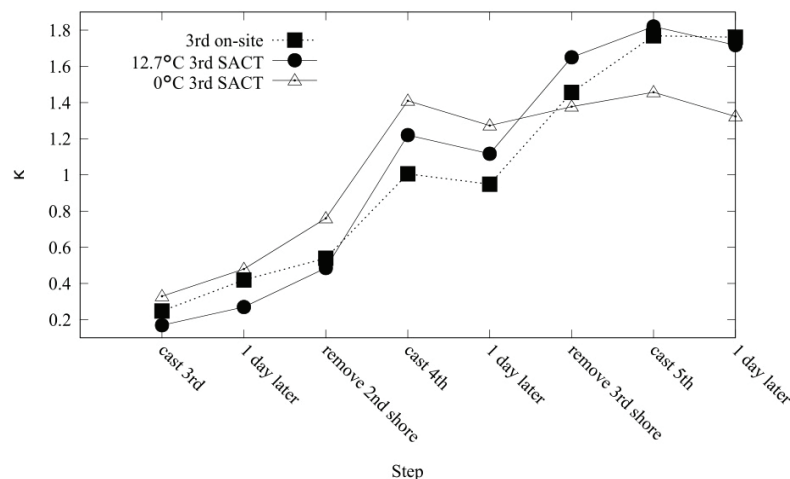
Figure 6 The comparison of SACT and on-site measurements (3rd floor)

As an example, the relationship between κ of 3rd floor and construction procedures is as shown in Figure. 6, and obviously the results considering effects of temperature is in better agreement with on-site measurements. Since the structure is more vulnerable when κ is larger, the prediction of the most vulnerable state ignoring effects of temperature would be wrong.

During the comparison, several important patterns of load transfer during the construction process have been observed as follows:

(1) the largest κ would found in the 3rd floor when casting the 5th floor, at which time the 3rd floor is the lowest story connected by steel shores. Therefore, the whole structure is in the most dangerous state for shores when one new floor is being cast;

(2) load transfer coefficients of the floors that remain connected by shores would suddenly change after the removal of one layer of shores;

(3) if structure profile remains the same, the load transfer coefficients of the bottom floor connected by shores decreases with time.

Patterns of load transfer do not change with the ambient temperature, however, effects of temperature variations can not be ignored in order to achieve more accurate internal forces of shores and slabs.

6. Conclusions

In the present paper, a new software named Safety Analysis during Construction considering Temperature (SACT) is developed to analyze load transfer in reinforced concrete structures considering effects of temperature during constructions.

By adopting modular techniques and object-oriented techniques, the complexity of programming can be reduced, and the software is easy to understand and debug.

After comparing with on-site measurements, SACT is proved to be accurate. It has been observed that the comparison between SACT results and measurements also shows that the effects of temperature variations are significant and can not be ignored. However, with the daily temperature change taken into account, SACT can provide convenient and accurate safety control service for on-site engineers.

References

Calderón, P. A., Alvarado Y. A., and Adam J. M. (2011). "A New Simplified Procedure to Estimate Loads on Slabs and Shoring during the Construction of Multistorey Buildings." *Engineering Structures*, 33(5), 1565-1575.

Chen W. F., and Mosallam K. (1991) "Concrete Buildings Analysis for Safe Construction", CRC Inc, Honolulu, 35-65.

Fang D. P., Geng C. D., Zhu H. Y., and Liu X. L. (2000). "Analysis of Reinforced Concrete Structures during Construction." *China Civil Engineering Journal*, 33(6), 57–62.

Fang D. P., Geng C. D., Zhu H. Y.，and Liu X. L. (2001) "On-site Measurements of Characteristics of Reinforced Concrete Structure." *China Civil Engineering Journal*, 34(2), 7–10.

Grundy P., and Kabaila A. (1963). "Construction loads on slabs with shored formwork in multistory building." *J. ACI*, 60(12), 1729-1738.

Li Y. (2000). "Improvement Analysis of Reinforced Concrete Structures During Construction. Master Dissertation of Shanghai Jiao Tong University." *Shanghai Jiao Tong University*, 25-37.

Liu X. L., Chen W. F., and Browman M. D. (1986). "Construction load analysis for concrete structures." *J. ACI*, 112(3), 227-244.

Liu X. L. (1997). "The Status and Prospects of Structural Engineering. China Communications Press." Beijing, 52-59.

Zhang H., Rasmussen K. J., and Ellingwood B. R. (2012). "Reliability assessment of steel scaffold shoring structures for concrete formwork". *Engineering Structures,* 36, 81-89

Study on the Key Technology of Membrane Structure Design in Shanghai Norwegian Pavilion

Hao Song[1] and Zefeng Bi[2]

ABSTRACT

Norway pavilion is a complex membrane structure in 2010 Shanghai World Expo. The study was made on the key technical problems of the structure design. Regarding that it is the first application of TENARA membrane and polyester belt is used instead of edge cables of membrane structures for the first time, the tensile test studies on the tension performance of TENARA membrane and polyester belt. The reasonable compensation value of TENARA membranes is put forward to provide reliable data for design on the membrane structure. The study on form-finding analysis of membrane structure and node design is made to ensure the safety of the structure. Further, the global stability of cable-membrane is analyzed by the scale model test. Based on the above study, the mechanical properties of the material are determined and the key technical problems are solved, so the safety and stability of the structure is ensured.

KEYWORDS

Membrane Structure; Polyester Belt; Form-Finding Analysis; Scale Model Test

INTRODUCTION

The key technology of the design process includes overall design, form-finding analysis, load analysis as well as cutting analysis. Some achievements have been made on the domestic research about the key issues of cable membrane structure design. Qian analyzed the force density method, dynamic relaxation method and nonlinear finite element method for optimization (Qian & Song 2002). Wei proposed the ideas and algorithms of tensioned optimization design of membrane structure on the basis of the genetic algorithm (Wei & Shen 2004). Lin introduced the dynamic relaxation method and studie the initial morphological analysis and static load analysis about cable-membrane structure (Lin & Chen 2006). Li constructed the strategy of coupled equation's iterative

---

[1] Senior Engineer, Shanghai Taiyo Kogyo CO.,LTD; No.2200, Kaixuan Road, shanghai 200030; Email: songhao@taiyokogyo.com.cn

[2] Shool of civil and environment Engineering, University of Science and Technology Beijing; No.25, Xueyuan Road, Beijing 100083; Email: bizefeng163@163.com

solution and carries on the numerical simulation, analysis and comparison about the structure surface wind pressure distribution and the structural wind-induced response (Li et al. 2009). Zhang studied the dynamic characteristics of the cable-membrane structure under fluctuating wind and obtains structure time history response curve (Zhang & Dan 2004). Yang chose the layout of cutting line according to the curvature change of different parts on the surface (Yang & Li 2004). Xiang made the geodesic on the curved surface of the membrane structure, and calculated cutting line to generate cutting figure (Xiang & Shen 1999). Based on the new characteristics of the tensioned membrane structure, the key technology of form-finding analysis, node design and so on is studied in this paper.

PROJECT OVERVIEW

The Norway Pavilion's body structure is composed of 15 prefabricated assembly trees. The roof is constituted of a four-pivot support sails membrane. The area of membrane surface is about 2800 square meters. The roof membrane structure is composed of three parts: the unit main membrane, the cover membrane between unit seams, and downward flanging membrane. TENARA membrane is selected as the engineering membranes and membrane edge cable. It has some advantages, such as excellent flame retardant properties, good sewing performance, and so on. The main performance parameters of TENARA membrane is shown in Table 1. Polyester belt is processed by chemical fiber industrial wire with high strength. It has the advantages of high tensile strength, good impact resistance, lightweight and flexible. It is shown in Table 2 about the elasticity modulus of the membrane and the polyester tape.

Table 1. The membrane material properties

Width (m)	Weight (g/m^2)	Thickness (mm)	Tensile strength at warp/weft direction (N/5cm)	Tear strength at warp/weft direction (N)	Light transmittance (%)	Fire rating
1.57	1080	0.55	4000/4000	798/752	19	ASTM E84-ClassA

Table 2. Elastic modulus value table of membrane material and polyester belt

Elastic modulus of membrane at warp direction(MPa)	Elastic modulus of membrane at weft direction (MPa)	The poisson's ratio of membrane at warp/weft direction	The polyester elastic modulus (MPa)	Elastic Modulus of steel cable (MPa)
239	324	0.834/0.6	$8.6×10^2$	$1.9×10^6$

RESEARCH ON THE EXPERIMENT OF THE MECHANICAL PROPERTIES OF TENARA MEMBRANES AND POLYESTER TAPE

TENARA membrane material is a kind of composite materials. Its mechanical property is very different at warp/weft direction. The membrane may occur creep and stress relaxation. This can lead to the reducing of stiffness and structural failure. The amount of displacement for secondary import tension can be concluded by biaxial stress relaxation test and biaxial creep test. Through setting reasonable compensation value by the data, it can be ultimately determined on the membrane stress state, and the performance of long-term use and safety performance. In addition, the study on tensile strength and elasticity modulus of polyester belt can be made for guaranteeing the safety of cable-membrane structure about by tensile test.

In order to ensure the compensation value and stress state, the study on the mechanical property is made. Cross cutting seam sample is adopted, which is shown in Fig.3. Samples should be obtained in symmetric way, and the arm width of the sample core region and cantilever arm length shall not be less than 16 cm. Kerf handling is done uniformly, what is interval of 3-5cm along the cantilever direction. The length of Sample transition arc radius is about 0.5~1.5 cm. Each test shall include 3 pieces of samples at least. In accordance with the load ratio of 1:1, the load is applied in the sample at warp and weft directions. The load and strain must be measured in time. The maximum tensile load is 1000kgf / m.

By TENARA membrane's biaxial test, the stress strain curve of membrane material is obtained, as shown in Fig.4, in which W is the abbreviation of the Warp and F is the abbreviation of the Fill. Because of different compilation methods, the radial deformation of TENARA membrane material is greater than the latitudinal, in contrast with PTFE membrane material's. It is predicted on long-term relaxation modulus of the TENARA membrane material and creep compliance at warp/weft direction. Some conclusions are made in order to avoid the reducing of use performance and safety performance. At first, the compensation value of membrane 100 kg/m pretension is 2.5% of the warp and 1.2% of the weft. Secondly, it is adopted to cut membrane materials in the way of diagonal arrangement in order to keep the compensation value (1.8%) of each boundary.

The tensile rate is 50 mm/min and the test temperature is 27 . The elastic modulus of Polyester belt is obtained by the following method to calculate. It is selected on the stable slope of force-displacement curve, and the slope is calculated by the least square method. The size is 4.5 mm in thickness and 100 mm in width for the single-layer polyester belt. It should be paid attention to the interface shape of tensile fixtures and polyester belt. Generally, the semicircle is used as well as the way of wrapping material on the surface of the contact in order to improve the breaking force of polyester belt. The test results of tensile strength about Polyester belt are shown in Table 3.

Table 3. Tensile strength test results of polyester belt

Specimen	Tensile strength (*kN*)	Modulus of elasticity(MPa)
1	223.9	868
2	216.5	863
3	215.6	826
Mean	218.7	852

RESEARCH ON THE KEY TECHNICAL PROBLEMS ON THE DESIGN OF THE CABLE-MEMBRANE STRUCTURE

In the design of the Norway pavilion, because of its novel design concept and the application of the new material, the higher request is put forward on the Form-finding Analysis and overall stability of cable membrane structure. It is necessary to solve the key technical problems and put forward the processing method.

The initial shape and prestressing force of structure are interactional, the Form-finding Analysis is needed. The membrane can obtain the ideal shape by setting the prestressing force of polyester belt and membrane reasonably. The prestressing force of four wing membranes, which are connected to the main structure, is 1kN/m. The prestressing force of eye membrane, which is connected by polyester belt and four wing membranes, is 0.5kN/m. The prestressing force of Barrier membrane, which is connected by polyester belt and four wing membranes, is 0.5kN/m. According to the principle of design of surface tension, the pretension of polyester belt is determined by Eq.1.

$$T=qR \tag{1}$$

In the formula, T represents polyester belt pretension, q represents the membrane pretension, and R represents curved radius of polyester belt. In addition, tension size of each area of polyester belt is shown in Table 4. The pretension distribution of polyester belt is shown in Fig.7.

Table 4. Pretension of the polyester belt

Relations of pretension between middle and outer	Relations of pretension on the edge with flanging membrane	Relations of pretension on the edge without flanging membrane
T1=(1-0.5)×16=8*kN*	T2=(1+0.5)×16=24*kN*	T3=1×16=16*kN*

The polyester belt sewing with 0.45 cm thick is used to meet the tensile requirement of polyester belt. In order to avoid exposed, the polyester belt end is outsourced by membrane. The PTFE with the ability of anti-aging and resistance to ultraviolet ray can be used for sewing membrane material and polyester belt. The polyester belt end without the membrane material processing is shown in Fig.8. The polyester belt end with the membrane material processing is shown in Fig.9.

The study on the joint way of membrane material and polyester belt is made in order to guarantee the whole stability of the structure. Combining with the characteristics of the project, there are some following processing methods to improve the joint of TENARA membrane material and polyester belt:

(1) The PTFE membrane is used to sew the connected nodes of polyester band and membrane material. The $\phi 35$ foam pipe is used to drain the rain water to sink at both ends or one end in border.

(2) Considering of the stress compensation of the membrane material, the compensation value of polyester belt must be determined in order to ensure membrane material and polyester belt to work together. It is used to do tension experiment with the proportion of 1:1 for determining compensation value of polyester belt. The weld distribution form of the membrane material is oblique and the compensation value of membrane material is about 1.8%. Therefore, the compensation values of polyester belt at warp/weft direction are both 1.2%. In the actual machining process, according to the size of spacing which is the multiplication result of 20 cm and compensation value, it is adopted to mark points in membrane and polyester belt, do sewing processing for joint and compound together through the tension.

(3) In order to ensure the safety performance of the structure, the scale model test is carried out. The rationality of processing method is determined for global stability of the structure. Whether the work characteristics can meet the requirements of structure is also validated. With the proportion of 1:3, the model is made of four ontology membrane and four eye membrane. It is covered by the membrane material with an area of 100 square meters. Scale model is as shown in Fig.10.

CONCLUSION

Based on the research of the key technology about Membrane Structure Design of the Norwegian Pavilion, it can be concluded that:

(1) By biaxial tensile test, the biaxial tensile curve and the compensation value of the membrane can be obtained. A solid foundation is made for the application of this kind of membrane material in our country. By uniaxial tensile test to determine the elastic modulus and tensile strength, the analysis on tensile property of polyester is obtained. It provides the reliable basis for design work.

(2) By the Form-finding Analysis of the structure, the prestressing figure of polyester is obtained. In order to ensure the stability of connected nodes of polyester belt end and the frame structure, the membrane material is outsourced at polyester belt end.

(3) By the cutting analysis, considering of the release stress and compensation value, the special processing is used at the joint for ensuring the mechanical performance and durability of membrane materials and polyester. By the scale model test, the overall stability analysis of membrane structure is obtained for ensuring the safety of the structure.

REFERENCES

Qian, J.H., and Song T. (2002). "The Form finding and the Shape stress Optimization of Membrane Structures." *Journal of Building Structures*, 06(2002), 84-88.

Wei D., and Shen Sh.Zh. (2004). "Shape-state optimization design of Tensional Membrane Structure." *China Civil Engineering Journal*, 02(2004), 12-18.

Lin W.J, and Chen Sh.H. (2006). "Static Analysis of Cable-Membrane Structures." *Acta Scientiarum Naturalium Universitatis Sunyatseni*, 03(2006), 4-8.

Li H.F., Zhou L., and Zhou D. (2009). "Wind Pressures and Wind-Induced Dynamic Response of Tension Structure Subjected to Fluid-Structure Interaction." *Journal of Shanghai Jiaotong University*, 06(2009), 967-971.

Zhuang H., and Dan J. (2004). "Research on buffeting dynamic properties of Membrane Structures." *Engineering Mechanics*, 06(2004), 61-65.

Yang W.G., and Li M.G. (2004). "Research on the Cutting Pattern Method for Membrane Structure Based on Element Division." *Building Structure*, 02(2004), 47-49.

Xiang Y., and Shen Sh.Zh. (1999). "A practical cutting design method of Membrane Structures." *Spatial Structures*, 06(1999), 46-50.

Figure 1. The membrane roof structure   **Figure 2. The wooden support**
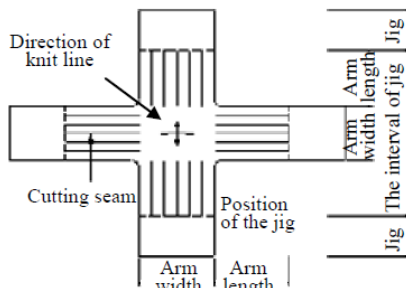
**Figure 3. The sample with
the shape of a cross**
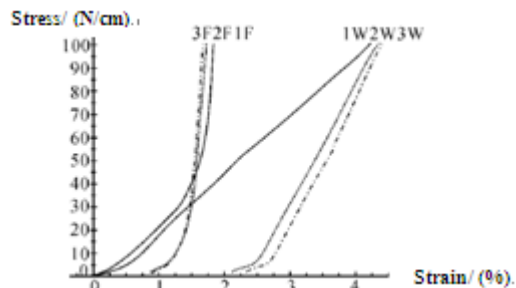
**Figure 4. Stress strain curve
of TENARA membrane material**

**Figure 5. Test Photos
of polyester belt**

**Figure 6. Failure pattern
of polyester belt**
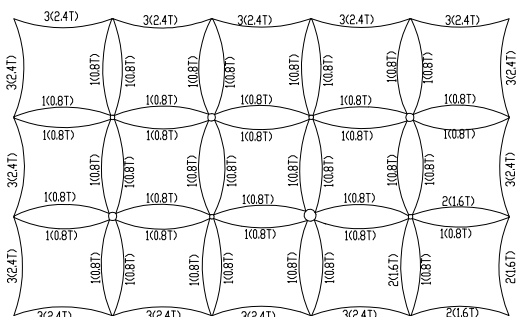
**Figure 7. Prestressing
distribution of polyester belt**

Figure.8 Polyester belt end with the membrane material processing

Figure.9 Polyester belt end without the membrane material processing

Figure.10 Scale test model

Quantitative evaluation on building collapse induced human casualty for performance-based earthquake engineering

Shuang Li[1], Yanjuan Zhang[2], Zhitao Du[3], Changhai Zhai[4], and Lili Xie[5]

ABSTRACT

This research aims to propose an effective method which simulates the evacuation process and evaluates the human casualty during the building collapse for a structure. The explicit nonlinear dynamic time-history method is used to analyze the collapse process of a three-story steel frame structure under earthquakes. Combining the cellular automata (CA) based evacuation simulation with the results of the nonlinear dynamic time-history analysis, it shows that the occupant flows in the building are mainly distributed in stairs and corridors, and when collapse occurs, the main positions of casualty is the corridor in the first story. The method quantitatively assesses seismic casualties, which has a positive effect on the structural design to resist building collapse, the building layout design to speed up evacuation, and the determination of guideline for post-disaster rescue.

---

[1]Key Lab of Structures Dynamic and Control (Harbin Institute of Technology), Ministry of Education, Harbin 150090, China; School of Civil Engineering, Harbin Institute of Technology, Harbin 150090, China; e-mail: shuangli@hit.edu.cn

[2]School of Civil Engineering, Harbin Institute of Technology, Harbin 150090, China; e-mail: yjzhang1101@163.com

[3]School of Civil Engineering, Harbin Institute of Technology, Harbin 150090, China; e-mail: dzt_hit@163.com

[4]School of Civil Engineering, Harbin Institute of Technology, Harbin 150090, China; e-mail: zch-hit@hit.edu.cn

[5]School of Civil Engineering, Harbin Institute of Technology, Harbin 150090, China; Institute of Engineering Mechanics, China Earthquake Administration, Harbin 150080, China; e-mail: xiell@cae.cn

INTRODUCTION
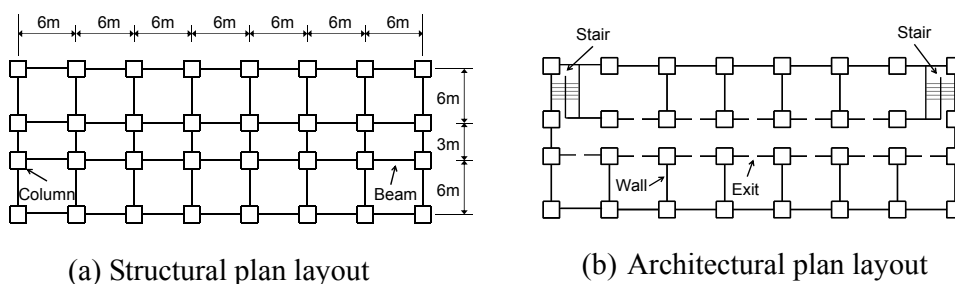
Estimates of seismic casualties due to building collapse are generally based on the statistical methods (Samardjieva and Badal, 2002, Tantala et al., 2008), and the fortification criteria of casualties is not presented quantitatively in seismic design codes. Because of the limited sources of historical earthquake data and the rarely shared conditions of evaluation object and data source, this method has a low degree of accuracy. Recently, collapses of adobe structures are simulated to assess casualties using the 3D distinct element method (Furukawa et al., 2010). By investigating relationships between the earthquake intensity, the structural damage, the interior-space damage, and the casualties, it is found that the casualties have a strong positive correlation with the interior-space damage the casualty fragility functions are proposed. However, in the casualty assessment of structures, indoor people's distribution is generally not uniform, nor unchanged. The dynamic evacuation process should be considered when estimating seismic casualties.
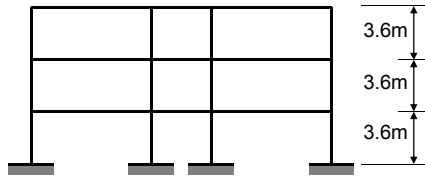
In the study, cellular automata based dynamic evacuation processes are simulated under earthquakes in a three-story steel frame structure, which shows the distribution positions of casualties and stranded occupants. Combining the results with the nonlinear dynamic time-history analysis, building collapse-induced human casualty can be evaluated quantitatively. This study considers structure response, evacuation and casualty criteria comprehensively, and gives the expected casualty distribution and numbers.

MODEL DESCRIPTION

Structural Modeling

The structure model is a three-story steel frame school building with reinforced concrete floor slabs and stair treads. The layout of the structure studied is shown in Figure 1. Evacuation simulation is carried out with these parameters: corridor width C=2.5 m, stair width of each run S=1.0 m, main exit in the middle of first floor with width D=3.5 m, population density ρ=0.3. The column section is □300×300×6 mm and beam section is H300×150×7×9 mm.

(a) Structural plan layout   (b) Architectural plan layout
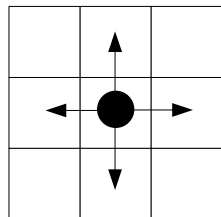
(c) Structural elevation

Figure 1. Layout of structure

Evacuation Model

The floor slab space is discretized into square cells of size $0.5\text{m} \times 0.5\text{m}$ which can either be empty or occupied by one occupant at any time step. Each person can move to one of the unoccupied neighbor cells (i, j) or stay at the present cell at each time step $t \to t+1$ according to certain transition probabilities p_{ij} (shown in Figure 2) as below:

Figure 2. Von Neumann neighborhood and transition probability, $\sum_j p_{i,j} = 1$

Transition probability is given by the following equation:

$$p_{i,j} = N \exp(k_s S_{i,j})(k_D D_{i,j})(1 - n_{ij})\xi_{ij} \tag{1}$$

where $S_{i,i}$ and $D_{i,i}$ denote the static exit attraction and the dynamic crowd attraction, respectively; k_S and k_D denote the weight coefficients of $S_{i,i}$ and $D_{i,i}$, respectively; n_{ii} is the cell state, with $n_{ii} = 0$ for an empty cell and $n_{ii} = 1$ for an occupied cell; ξ_{ii} denotes whether a cell is occupied by walls, with $\xi_{ii} = 0$ for an occupied cell and $\xi_{ii} = 1$ for an unoccupied one; N is the normalization coefficient:

$$N = \left[\sum_{(i,j)} \exp(k_s S_{ij})(k_D D_{ij})(1 - n_{ij})\xi_{ij} \right]^{-1} \tag{2}$$

where $S_{i,i}$ depends on the distance from a cell to the exit and is unchangeable. Generally, a cell nearer to the exit is with a larger $S_{i,i}$. $S_{i,i}$ can be calculated by:

$$S_{i,j} = \min_{(i_e, j_e)} \left\{ \max_{(i_l, j_l)} \left\{ \sqrt{(i_e - i_l)^2 + (j_e - j_l)^2} \right\} - \sqrt{(i_e - i)^2 + (j_e - j)^2} \right\} \qquad (3)$$

where $D_{i,i}$ depends on a person's judgment of the surroundings with the properties of diffusion and decay. $D_{i,i}$ can be calculated by counting the total passing times of cell (i, j) by occupants.

There will be conflicts when two or more occupants attempt to enter a same target cell at the same time. It assumes that each occupant has the randomly opportunity to enter the target cell. To better solve this problem, we use a coefficient μ which represents the intensity of confliction, the stay or move, and which occupant moves into the target cell are all randomly. The parameter set with $k_S = 1.0$ and $k_D = 1.0$ and $\mu = 0.5$ is used.

Casualty Criteria
If the vertical displacement of two adjacent floor slab is less than 1.65 m and there exists occupant in the corresponding cellular space at this time step, casualty occurs. Assumption is made for infill walls which will collapse in out-of-plane when peak acceleration of the wall center reaches 1.0 g, and collapse direction is randomly.

ANALYSIS
Casualty Distribution
The earthquake input of TCU065-N from 1999 Chi-Chi, Taiwan earthquake, as shown in Figure 3, is used. Structural collapse-induced casualty is computed under the earthquake excitation. The relationship between the number of stranded occupants under earthquake and time is as follows. As time goes on, occupants in the third floor evacuate to the second floor and the number of occupants decreases gradually; the number of occupants in the second floor also decreases before structural collapse, but with the first floor collapse, occupants in the second floor are stayed and occupants in the third floor swarm continually, which results in an increase in the number of occupants in the second floor; occupants in the first floor evacuate out through exits. When the building collapses, stranded occupant casualties occurred.

Occupant distributions of stranded occupants and casualties are shown in Figure 4. The Figure 4(a) shows the initial distribution of occupants; after the earthquake, occupants are mainly distributed in stairs and corridors as can be seen in Figure 4(b) and collapse of the structure causes a large number of casualties. Until the end of the ground motion, the number of the stranded, casualties and escapees are 792, 421 and 164, respectively. The escapees are all the occupants in the first floor. Gray dot denotes stranded occupants and red dot denotes casualty. Based on the analysis above,

it's apparently that when collapse happens, high-incidence position of casualties focuses on the first floor, especially in corridors. Consequently, when encountering earthquakes, occupants in some buildings shouldn't just run to the stairs or corridors to escape out because there will be a mass of casualty if these parts collapse. If there isn't enough evacuation time, it's an effective means of protecting oneself to choose a relatively safe place for emergency shelter.
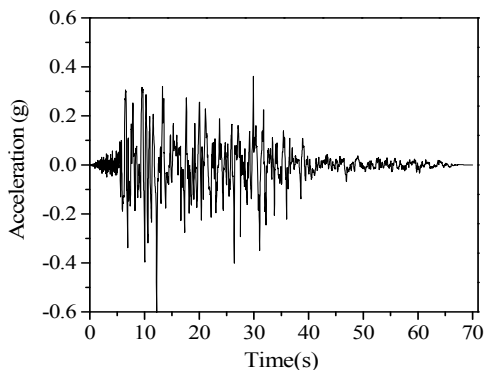
Figure 3. Acceleration time history of TCU065-N

(a) The initial distribution   (b) After earthquake
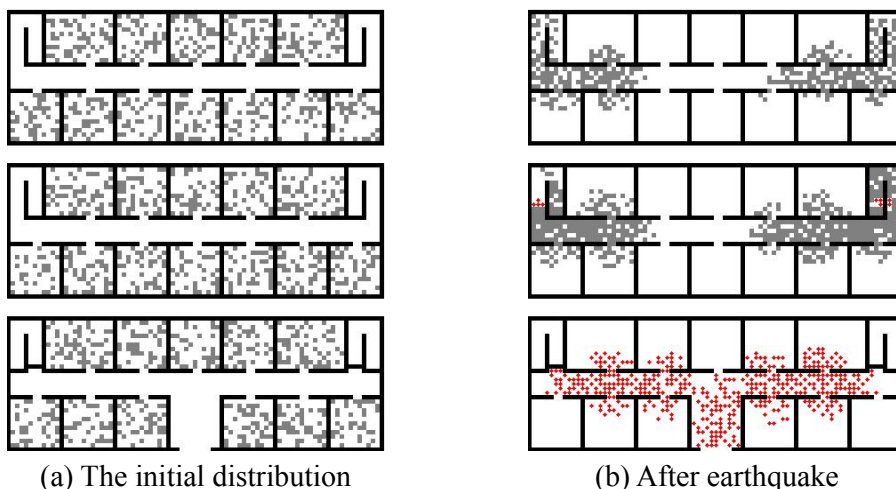
Figure 4. Distributions of stranded occupants and casualties

Casualty Evaluation

For a given ground motion intensity, fragility function represents the probability of reaching or exceeding the specific damage status under the intensity. Here, casualty fragility function is derived by adopting the probabilistic seismic demand model (Baker and Cornell, 2006; Zhang and Huo, 2009). The method assumes that the ground motion intensity and the median of number of casualties obey the lognormal distribution. The relationship between *EDP* and *IM* is:

$$\ln(EDP) = \ln(a) + b\ln(IM) \tag{1}$$

where *a* and *b* are regression parameters. It is shown that for a given *IM*, the variability of *EDP* is relatively constant (Luco and Cornell, 2007) and its standard deviation is:

$$\xi_{EDP|IM} = \sqrt{\frac{\sum_{i=1}^{n}\left[\ln(EDP_i) - (\ln a + b\ln IM_i)\right]^2}{n-2}} \tag{2}$$

For a given *IM*, the exceeding probability of specific damage state *LS* is:

$$P[DI \geq LS \mid IM] = 1 - \Phi\left(\frac{\ln(LS) - \ln(a \times IM^b)}{\xi_{EDP|IM}}\right) \tag{3}$$

The fragility of casualty can be gained by the above equation for different *IM*. Then we can obtain the expected number of casualties under a given ground motion intensity according to probability theory:

$$\mu_{ID} \mid IM = \sum_{i=1}^{N} i \cdot P(x = i \mid IM) \tag{4}$$

where $P(x=i|IM)$ is the probability when the number of casualties is *i* under *IM*. It can be calculated as:

$$P(x = i \mid IM) = \begin{cases} G(x_i \mid IM) - G(x_{i+1} \mid IM) & i \neq N \\ G(x_i \mid IM) & i = N \end{cases} \tag{5}$$

where $G(x_i|IM)$ is the exceeding probability when the number of casualties is x_i under *IM*. *N* is the total number of occupants.
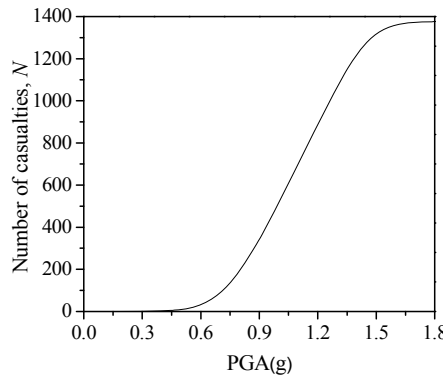
Figure 5. Relationship between the expected number of casualties and PGA

A total of 114 ground motion samples are used as earthquake inputs. The fragility curve can be obtained by using of Eq. (3). Then, the expected number for various *IM*,

i.e., the vulnerability, can be obtained. Figure 5 shows the relationship between the expected number of casualties and PGA. It can be imaged that when the ground motion intensity is smaller, it approaches to non-structural damage induced casualty curve; when the ground motion intensity is bigger, it approaches to structural damage induced casualty curve.

CONCLUSIONS

The casualty estimation contains many uncertainties and needs more quantitative methodology. In this study, cellular automata evacuation model has been applied to evaluate seismic casualties in a structure. In the simulation, stranded occupant distribution of each floor and the number of casualties are presented. Then, the fragility analysis method is used to calculate the expected number of casualties. The presented methodology is more quantitative than the traditional experiential methods, which is useful in the implementation of performance-based earthquake engineering.

REFERENCES

Baker, J. W. and Cornell, C. A. (2006). "Vector-valued ground motion intensity measures for probabilistic seismic demand analysis." *PEER Report 2006/08*.

Furukawa, A., Spence, R., and Ohta, Y. (2010). "Analytical study on vulnerability functions for casualty estimation in the collapse of adobe buildings induced by earthquake." *Bulletin of Earthquake Engineering*, 8(2), 451-479.

Luco, N., and Cornell, C. A. (2007). "Structure-specific scalar intensity measures for near-source and ordinary earthquake ground motions." *Earthquake Spectra*, 23(2), 357-392.

Samardjieva, E., and Badal, J. (2002). "Estimation of the expected number of casualties caused by strong earthquakes." *Bulletin of the Seismological Society of America*, 92(6), 2310-2322.

Tantala, M. W., Nordenson, G. J. P., Deodatis, G., and Jacob, K. (2008). "Earthquake loss estimation for the New York City metropolitan region." *Soil Dynamic and Earthquake Engineering*, 28(10-11), 812-835.

Zhang, J. and Huo, Y. L. (2009). "Evaluating effectiveness and optimum design of isolation devices for highway bridges using the fragility function method." *Engineering Structures*, 31(8), 1648-1660.

An Unified Model of Ultimate Capacity of RC Members with Rectangular Section under Combined Actions

Pu Wang[1], Zhen Huang[2], Liang Sun[3]

ABSTRACT

Reinforced concrete elements with a rectangular section are commonly used in frame structural buildings and bridges. Such reinforced concrete structures failed often with the force combination of axial load, bending, shear and torsion caused by wind and earthquake.

However, there are few researches on four loading combination of tension/compression, bending, shear and torsion, especially for the axial force effects on the failure mechanism and bearing capacity of reinforced concrete members.

In this paper, a theoretical study and deduction of the unified failure model on the reinforced concrete members with rectangular section under combined axial force, bending, shear and torsion were carried out with the ultimate equilibrium theory.

The results of a theoretical analysis were compared with the experimental results of RC members under combined loading actions. Both of the theoretical results and test results showed a good correlation.

KEYWORDS: Unified model; Ultimate capacity; Combined loading actions; Rectangular section; Building frames; Bridges.

INTRODUCTION

In the frame structures and bridges, rectangular RC members are widely used. Under the complex horizontal and vertical loads, such as wind loads, earthquake loads, dead loads and live loads, temperature loads etc., reinforced concrete members are under combined loading actions of tensile/compressive axial force, bending, shear and torsion. Such reinforced concrete structures and members fail often with the force combination of axial force, bending, shear and torsion. It is very important to find out the failure mechanism and give a unified failure expression of RC members under combined actions of axial forces, bending, shear and torsion.

However, because the behavior of reinforced concrete at the ultimate limit state is extremely complex, there are few researches on four loading combination of tensile/compressive axial forces, bending, shear and torsion, especially for the axial force effects on the failure mechanism and bearing capacity of reinforced concrete members under combined loading actions.

The existed failure theories of RC members under combined loads can be generally sorted into two categories. One is the spatial truss theory, and the other one is the ultimate equilibrium theory on failure surface. Rausch puts forward the spatial truss theory in unified ultimate capacity of RC members, which is already widely

---

[1] School of Naval Architecture, Ocean and Civil Engineering, Shanghai Jiaotong University, Shanghai, 200240, P.R. China, Email: wangpu@sjtu.edu.cn
[2] School of Naval Architecture, Ocean and Civil Engineering, Shanghai Jiaotong University, Shanghai, 200240, P.R. China, Email: zhenhang@sjtu.edu.cn
[3] School of Naval Architecture, Ocean and Civil Engineering, Shanghai Jiaotong University, Shanghai, 200240, P.R. China, Email: sunliang@sjtu.edu.cn
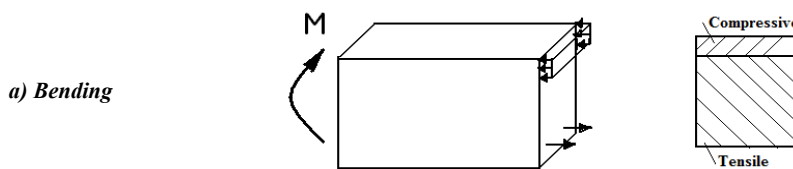
applied on the research (Thomas T.C.Hsu 2001&2003). However, when it is applied to RC members with a low ratio of torque to bending moment or to shear force, the spatial truss theory differs much from the practical as cracks only appear on three of the four sides of the RC members. Gvozdev (Gvozdev et al. 2005)presented the limiting equilibrium theory of failure surface, which is successfully applied on the ultimate capacity expression of RC members under bending and shear and is widely used worldwide(Vecchio 2001;Vecchio et al 2001; Huang 2006; Greene2009) Nielson(Nielson 2000) puts forward failure criterion for RC plates with evenly distributed reinforcement. Applying Nielson criterion, unified model for evenly distributed reinforced RC members is established (Huang 2007). The ultimate equilibrium theory is developed by introducing compatibility conditions. But the introduction of compatibility conditions in combination of axial force, bending, shear and torsion may cause a complicated calculation, which usually need help of computers and makes the application inconvenient.

This paper focuses on the axial force effects on unified ultimate capacity expression of RC members under combined loading actions. The twist failure surface angles are different as the change of the axial force. Considering the variation of the twist failure surface angles and using the three dimensional ultimate equilibrium theory, an unified failure model for RC structural members under combined loadings is deduced. Finally the results of the theoretical analysis will be compared with the experimental results of RC members under combined loading actions.

AXIAL FORCE EFFECT

Axial force influences much on the geometrical shape of failure surface of RC member under different loading combination. Fig 1a) shows the failure surface of RC member under bending without other loadings, the failure angle is nearly 90 degree. Fig. 1b) shows the failure surface of RC member under bending and shear, the failure angle is nearly 45 degree. Fig.1c) shows the failure surface of RC member under combined bending, shear and torsion, the twist failure angle is nearly 45 degree. Fig. 1d) shows the failure surface of RC member under combined compressive axial force, bending, shear and torsion, the twist failure angle is small than 45 degree. Fig. 1e) shows the failure surface of RC member under combined tensile axial force, bending, shear and torsion, the twist failure angle is larger than 45 degree. In extreme situation with large compressive axial force combined with bending, shear and torsion, the twist failure angle in Fig. 1d) could be near 0 degree, the RC member will fail with ductile failure like normal compressive failure of RC members. In extreme situation with large tensile axial force combined with bending, shear and torsion, the twist failure angle in Fig. 1e) could be nearly 90 degree, the RC member will fail with brittle failure like normal tensile failure of RC members.

a) Bending

b) Bending and Shear

c) Bending, Shear and Torsion

d) Compressive Axial Force, Bending, Shear and Torsion

e) Tensile Axial Force, Bending, Shear and Torsion
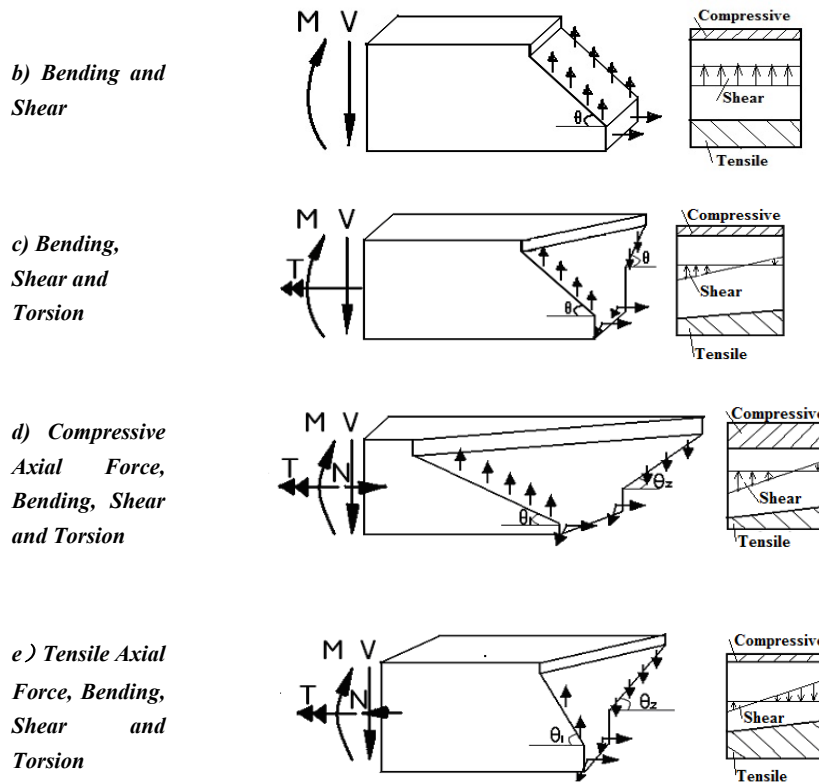
Fig. 1 The axial force effects on failure surfaces of RC members under combined loadings

Therefore the twist failure surface angle θ changes with the variation of axial force. Axial compressive force decreases the twist failure surface angle, and makes it more apt to produce ductile compressive failure mode. Axial tensile force increases the twist failure surface angle, and makes it more apt to produce brittle tensile failure mode.

The key to establish unified failure model is studying the influence of axial force to the twist failure surface angles, failure mode and ultimate bearing capacity. Through the equilibrium equation of angle- variable twist failure surface, the unified ultimate capacity of RC members under combined loads could be deduced as follows.

MODEL EXPRESSION

Basic assumption. To simplify the unified ultimate capacity expression of RC member under combined loadings, the basic assumptions are adopted in this paper as the bellowing.

1. The rectangular section of reinforced concrete members can be divided into the external RC box section and the concrete core area (see Fig. 2). The bending moment and torque are completely resisted by the external RC box section. Axial force and shear force are resisted by the external RC box section and the concrete core area together.

2. The longitudinal reinforcements and stirrups across the failure surface are assumed to achieve their yield strength. The concrete in compressive failure area is assumed to achieve its compressive strength. The dowel action of rebar is ignored to simplify the expressions.

The external forces resisted by the external RC box section are axial force $N_{ext}=\alpha_N N$, bending moment M, shear force $V_{ext}=\alpha_V V$ and torque T. The external forces resisted by the concrete core area are axial force $(1-\alpha_N)N$ and shear force $(1-\alpha_V)V$. The coefficient α_N and α_V are

$$A_N = 1 - \frac{A_{int}}{A} = 1 - \frac{(b-2t)(h-2t)}{bh} \qquad (1)$$

$$\alpha_V = \frac{2t}{b} \qquad (2)$$

While

A is the total rectangular section area of members;

b is the width of rectangular section;

h is the height of rectangular section;

A_{int} is the concrete core area;

t is the effective thickness of RC box section's side walls.
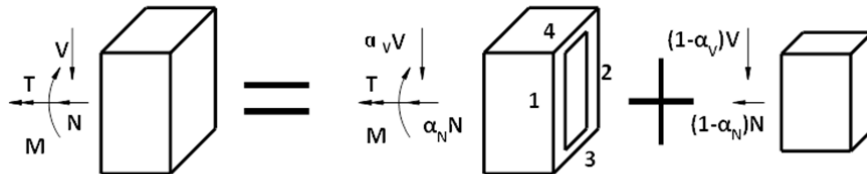
Fig.2 The rectangular cross section is divided as external RC box section and concrete core section

Concrete failure criterion.Fig3 shows Tasuji-Slate-Nilson criterion. Through this criterion, the concrete ultimate limit shear stress under a certain normal stress can be deduced. A factor γ can be adopted to consider shear strength deduction after concrete cracking.

$$\tau_c = \frac{1}{11}\gamma\sqrt{f_c^2 - 9f_c\sigma - 10\sigma^2} \qquad (3)$$
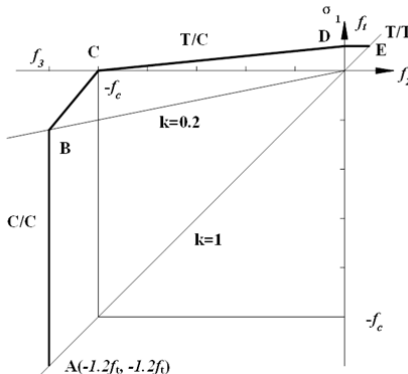
Fig.3 Tasuji-Slate-Nilson criterion

Shear stress. The four hollow webs are numbered in Fig.2.The shear stress on the four hollow webs can be expressed by equations

$$\tau_1 = \frac{T}{2b_{cor}h_{cor}} + \frac{V}{bh}$$

$$\tau_2 = \frac{T}{2b_{cor}h_{cor}} - \frac{V}{bh}$$

$$\tau_3 = \tau_4 = \frac{T}{2b_{cor}h_{cor}} \tag{6}$$

On the isolated segment 1,the force in the vertical direction is resisted by concrete and stirrups,which can be expressed by

$$\left(\frac{T}{2b_{cor}h_{cor}} + \frac{V}{bh}\right) h_{cor}t = \tau_C h_{cor}t + n_1 f_{sv}A_{sv} \tag{7}$$

Fig.4 shows the twist failure surface and failure surface angle θ.Stirrup quantities n_i across the failure surface can be expressed by

$$n_1 = \frac{h_{cor}cot\theta_1}{s} \tag{8}$$
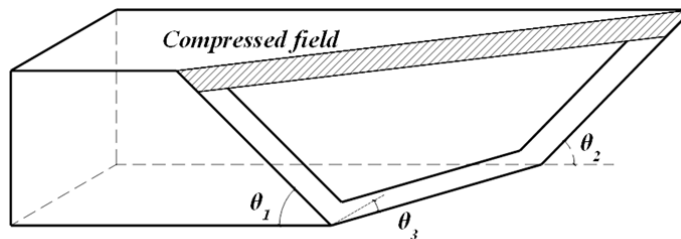
Fig.4 Twist failure surface and failure surface angle θ

From equation (6), equation (7) and equation (8),the cotangent of failure surface angle can be expressed by

$$cot\theta_1 = \left(\frac{T}{2b_{cor}h_{cor}t} + \frac{V}{bh} - \tau_C\right)\frac{t}{A_{sv}f_{yv}s} \tag{9}$$

Similarly,

$$cot\theta_2 = \left(\frac{T}{2b_{cor}h_{cor}t} - \frac{V}{bh} - \tau_C\right)\frac{t}{A_{sv}f_{yv}s}$$

$$cot\theta_3 = \left(\frac{T}{2b_{cor}h_{cor}t} - \tau_C\right)\frac{t}{A_{sv}f_{yv}s} \tag{10}$$

With different ratios of reinforcements, the compression zone of concrete may occur at the top, the left or the right of the section. Defining the compression zone of concrete occur at the top, equilibrium equation could be deduced with the ultimate equilibrium state of the concrete of compression zone and longitudinal reinforcement of tensile zone.

The equilibrium equation could be established according to the bending equilibrium of the compression zone's center, which is

$$M + N_{ext}\frac{h_{cor}}{2} = f_yA_sh_{cor} - n_1A_{sv}f_{yv}\left(\frac{h_{cor}\cot\theta_1}{2} + \frac{b_{cor}\cot\theta_3}{2}\right) - n_2A_{sv}f_{yv}\left(\frac{h_{cor}\cot\theta_2}{2} + \frac{b_{cor}\cot\theta_3}{2}\right) \tag{11}$$

While

A_s is the area of longitudinal reinforcement in the tensile zone;

f_y is the yield strength of longitudinal reinforcement in the tensile zone.

Substituting equation (9), equation (10) into equation (11),the result is

$$\frac{\alpha_N N}{2f_y A_s} + \frac{M}{f_y A_s h_{cor}} + \frac{st^2 V^2 h_{cor}}{f_y A_s b^2 h^2 A_{sv} f_{yv}} + \frac{s(b_{cor}+h_{cor})(T-T')^2}{4f_y A_s b_{cor}^2 h_{cor}^2 A_{sv} f_{yv}} = 1 \quad (12)$$

The equation can be also expressed as follow

$$\frac{N}{N_0} + \frac{M}{M_0} + \frac{V^2}{V_0^2} + \frac{T''^2}{T_0^2} = 1 \quad (13)$$

Defining

$N_0 = \frac{2f_y A_s}{\alpha_N}$, $M_0 = f_y A_s h_{cor}$, $V_0^2 = \frac{f_y A_s b^2 h^2 A_{sv} f_{yv}}{st^2 h_{cor}}$,

$T_0^2 = \frac{4f_y A_s b_{cor}^2 h_{cor}^2 A_{sv} f_{yv}}{s(b_{cor}+h_{cor})}$, $T'' = T-T'$, $T' = 2b_{cor}h_{cor}t\,\tau_C$.

EXPERIMENTAL VALIDATION

In order to check the validation of theoretical model under combined actions, comparisons with experimental data are necessary.This paper refers to test results of RC members under combined loads by Jiming Liu(Jiming Liu 2004)and Jiakang Zhao(Jiakang Zhao 1993).Taking t=0.17h (Yongmei Lin 1996)and γ=0.35,the comparison is shown in Table 1. The table shows the average values are 1.119 and 0.889, and the variation coefficients are 0.136 and 0.090.The theoretical results coincided well with the test results.

Table 1. Comparison between Theoretical model and Test results

Reference	Specimen Name	Test results				Theoretical results	Comparision
		N_{test} (kN)	M_{test} (kN·m)	V_{test} (kN)	T_{test} (kN·m)	T_{model} (kN·m)	T_{test}/T_{model}
Jiming Liu(2004)	H2-2	-481.3	19.7	32.8	42.81	43.45	0.99
	H2-3	-481.3	29.5	49.2	41.04	39.86	1.03
	H2-4	-481.3	39.4	65.6	40.5	35.83	1.13
	H3-2	-660	27	45	44.81	44.36	1.01
	H3-3	-660	40.5	67.5	47.25	39.46	1.20
	H3-4	-660	54	90	44.41	33.75	1.32
	H4-2	-880	54	90	48.36	39.14	1.24
	H4-3	-880	72	120	46	31.14	1.48
	H3-2-2	-607.5	21.6	36	44.23	45.01	0.98
	H3-2-3	-607.5	32.4	54	42.32	41.23	1.03
	H3-2-4	-607.5	43.2	72	39.6	37.02	1.07
	H16	-607.5	28.2	36	40.35	34.85	1.16
	H18	-607.5	28.2	36	34.6	39.61	0.87
	H22	-607.5	28.2	36	52.1	44.74	1.16
Jiakang Zhao(1993)	MV 4-3-2	-457.5	33.1	60.11	22.84	25.34	0.90
	MV 5-3-2	-571.88	31.67	57.93	23.75	27.28	0.87
	MV 6-3-1	-686.25	43.64	80	24	25.94	0.93
	MV3-3-2b	-343.13	23.23	42.4	16.96	16.29	1.04
	MV 3-3-2	-481.88	32.33	59	23.6	26.74	0.88
	MV 3-2-2	-481.88	25.99	47.3	23.65	28.27	0.84
	MV 4-2-2	-627.5	29.23	53.2	26.6	29.43	0.90
	MV 3-5-1	-481.88	55.91	102.5	18.45	23.57	0.78
	MV3-2-2b	-481.88	24.77	45.19	25.76	28.55	0.90
	MV 4-2-3	-627.5	21.22	38.5	26.95	31.15	0.87
	MV 3-2-3	-481.88	18.21	33	26.4	30.01	0.88
	MV 4-2-ul	-627.5	24.78	0	28	30.46	0.92
	MV4-3-2m	-505	36.65	49.48	19.79	25.42	0.78
	MV 5-4-2	-631.25	51.78	66.76	25.37	23.32	1.09

CONCLUSIONS

From the theoretical and experimental study carried out in this paper, the following are the main conclusions for the unified ultimate capacity of RC members under combined actions.

1. Axial forces have much influence on the shear strengthen. This paper suggests biaxial failure criterion of concrete to consider this effect.

2. Axial force influences much on the geometrical shape of twist failure surface. The twist failure surface angle θ changes with the variation of axial force. Axial pressure force decreases the twist failure surface angle, and makes it more apt occur ductile compression failure. Axial tension force increases the twist failure surface angle, and makes it more apt occur brittle tensile failure.

3. This paper suggests a new unified model of RC members under combined loads of axial force, bend, shear and torque based on the modified ultimate equilibrium theory.

The theoretical model coincides well with test data. The model could be used as references for concrete failure theory.

REFERENCES
Gvozdev A.A., Lessig N.N., Ruulle L.K. (1968), "Research on Reinforced Concrete Beams under Combined Bending and Torsion in Soviet Union", [J]ACI SP-18, Detroit, 1968:307-336.
Greene, G., Belarbi,A. (2009), "Model for Reinforced Concrete Members under Torsion, Bending and Shear. I: Theory." [J]ASCE Journal of Engineering Mechanics, Sep.2009:961-969.
Greene, G., Belarbi,A. (2009), "Model for Reinforced Concrete Members under Torsion, Bending and Shear. II: Model Application and Validation." [J]ASCE Journal of Engineering Mechanics,Sep.2009:970-977.
Huang Zhen, Liu Xila(2007), "Unified approach for analysis of box-section members under combined actions." [J]ASCE Journal of Bridge Engineering，2007,Vol.12, No.4:494-499.
Huang Zhen, Liu Xila(2006), "Modified Skew Bending Model for Segmental Bridge with Unbonded Tendons, " [J]ASCE Journal of Bridge Eng. Jan.2006, Vol.11,No.1:59-63.
Jiming Liu(2004). "The study on tensional behaviors and design method of reinforced concrete under combined force." Dissertation Submitted to Academic Committee of Xi'an University of Architecture and Technology,(2004) (In Chinese)
Jiakang Zhao, Liande Zhang, Yunting Wei(1993), "Torsional strength of RC members subjected to compression,bending,shear and torsion." China Civil Engineering Journal,Vol.26,No.1(1993) (In Chinese)
Nielson M.P.(2000), "Limit Analysis And Concrete Plasticity," RENTICE-HALL, INC., Englewood Cliffs, N.J.07632, 2000:15-72.
Thomas T.C.Hsu(2003), "Toward a unified nomenclature for reinforced-concrete theory. " [J]ASCE Journal of Structural Engineering, 2003: 275-283.
Thomas T.C.Hsu(2001), "Unified approach to shear analysis and design", [J]ACI Structural Journal, 2001: 2781-2791.
Vecchio F J(2001)."Disturbed stress field model for reinforced concrete: implementation "[J]. Journal of Structural Engineering 2001, 127 (1): 12-20.
Vecchio F J,Lai D,Shim W, et al(2001). :Disturbed stress field model for reinforced concrete: validation" [J]. Journal of Structural Engineering 2001, 127 (4): 350-358.

Yongmei Lin, Xiaozhen Zhou, Liande Zhang, Yunting Wei(1996). "Study on tensional behavior of RC members subjected to biaxial eccentric compression, biaxial shear and monotonic torsion." [J]Journal of Building Structures,Vol.17,No.1(1996) (In Chinese)

Unified Failure Model of Reinforced Concrete Members Subjected to Hazard Loads I: Ductile Failure Analysis

Xi Chen[1], Xila Liu[2]

Abstract: A simple and unified failure model is proposed for rectangular reinforced concrete (RC) members subjected to axial loads, bending, shear force and torsion. As observed in experiments, there are two distinct types of failure mechanisms, ductile failure and brittle failure. They are analyzed separately and different analyses are proposed respectively only using failure criteria and equilibrium conditions.

In the present paper, a lower-bound limit analysis of ductile failure is proposed. At first, the warped 3-dimensional failure surface is demonstrated, then stress distributions on the failure surface can be described, and finally equilibrium conditions would lead to the interaction relationship among external loads.

Keywords: Reinforced concrete members; unified theory; rectangular members; axial loads, bending, shear, and torsion; ductile failure; warped failure surface

0. Introduction:

Failures of reinforced concrete structures in hazards are mainly caused by different combinations of axial loads, bending, shear force and torsion, and failure mechanisms are very complex(Liu 2003). For decades, researchers have been working on a unified theory using compatibility conditions, equilibrium conditions, and constitutive laws(Vecchio 1986, Gregori 2007, Hsu 2010). Currently, only this approach is capable of analyzing structures subjected to complex loads at any loading stage and give out accurate results, but in practice it seems very necessary to be expressed in a simpler way. A mature theory should be rigorous and unified in theory, and also simple in expression (Liu 2003).

A simple and unified model is proposed in the present paper for widely used rectangular reinforced concrete elements subjected to axial loads, bending, shear

---

[1] Department of Solid Mechanics, Shanghai Jiaotong University, Shanghai 200240, China,
E-mail: cx541026@hotmail.com
[2] Department of Civil Engineering, Shanghai Jiaotong University, Shanghai 200240, China

force and torsion. As observed in experiments, there are two types of failure mechanisms, ductile failure and brittle failure. In the present paper, a lower-bound limit analysis of ductile failure is proposed based on the failure mechanism.

If the applied axial compression is relatively small, after the appearing of cracks, part of concrete can not contribute any more, reinforcing steels and the remaining concrete continue to carry more external loads until failure occurs, and the failure mechanism is called ductile failure. Inspired by previous theories based on the limit equilibrium method, the presented limit analysis of ductile failure will be established as follows: the 3-dimensional warped failure surface needs to be described at first, then stress distributions of concrete and steel bars at failure should be estimated, and finally the interaction equation can be derived from equilibrium equations.

Ductile failure analysis proposed in this paper is suitable for concrete members with rectangular sections reinforced with appropriate amount of stirrups and longitudinal steel bars, and longitudinal bars should be placed at each corner. Performances of high strength concrete and high strength steel are not considered.

1. Failure Criterion

In this proposed lower-bound limit analysis, reinforcing steel is considered as one-dimensional material. The failure of concrete under 3-dimensional stresses is dominated by the Mohr-Coulomb model with tension cut-off(Li 1992, Chen 2004). The theory developed by Hong Li and Xila Liu(Li 1992) is adopted to calculate c (the cohesion) and φ (the angle of internal friction). In their theory, at the transition state principal stresses are $\sigma_1 = f_{ct}$ and $\sigma_3 = -0.5 f_c$, and the Mohr-Coulomb criterion on the σ_z-τ_{zx} plane can be written as Eq. (1).

$$\sqrt{\sigma_z^2 + 4\tau_{zx}^2} \left(f_c + 2f_{ct}\right) + \sigma_z \left(f_c - 2f_{ct}\right) = 4 f_c f_{ct} \tag{1}$$

2 Geometric Description of failure surface
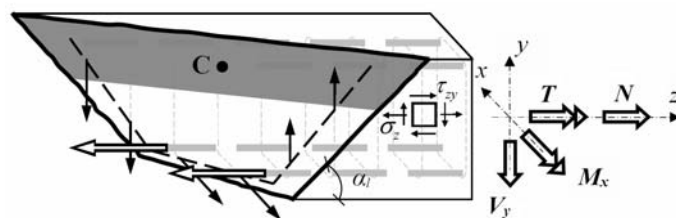
Figure 1. Ductile failure mechanism (compression zone along the top)

In order to describe the warped failure surface of an RC member subjected to axial load, bending, shear, and torsion, a method to predict the angle of significant inclined crack in each side is primarily required. Taking Figure 1 as an example, if compression zone is in the top, then inclined cracks in the other three sides can be estimated by the dominant mechanism of concrete, and the direction of each crack is presumed to coincide with the direction of principal compressive stress.

Based on observations and experiments, stress distributions at the verge of cracking are assumed as follows. For a solid rectangular member, normal stress is mainly caused by axial load and bending. The normal stress distribution caused by bending is assumed to be the distribution graphic of members only subjected to bending as shown in Fig. 2(a) (Baikov 1981) developed by researchers in former Soviet Union(Baikov 1981). Therefore, the tensile stress caused by bending is: $\sigma_M=24M_{cr}/(7BH^2)$, where H is the height of normal-section, B is the width, and M_{cr} is the bending moment acting on RC member at cracking. The normal stress caused by axial load is evenly distributed on the normal section, and it (σ_N) can be calculated as: $\sigma_N=N_{cr}/(BH)$, where N_{cr} is the axial load acting on RC member at cracking.
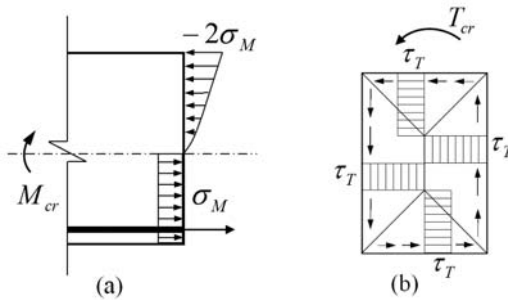
Figure 2. (a) Normal stress caused by bending(Baikov 1981); (b) Shear stress caused by torsion(Nádai 1950)

Shear stress is caused by torsion and shear force. The shear stress distribution caused by torsion is the plastic stress distribution developed by Nádai(Nádai 1950) as shown in Figure 2(b), and the shear stress (τ_T) caused by torsion can be written as: $\tau_T =6T_{cr}/(B^2(3H-B))$, where T_{cr} is the torque acting on RC member at cracking. The shear stress caused by shear force is like evenly distributed in most area at cracking, except for top and bottom edges where there is no shear stress due to boundary conditions. The shear stress (τ_V) can be written as: $\tau_V =V_{cr}/(BH)$, where V_{cr} is the shear force acting on RC member at cracking.

When the stress of concrete reaches the failure criterion, which is the Mohr-Coulomb model with tension cut-off, crack starts to develop. The stress state at failure is used to calculate the crack angle (α) by geometry conditions as Eq. (2), in which σ_z is the normal stress and τ_{zx} and τ_{zy} are shear stresses at cracking.

$$\cot\alpha = \frac{2\tau_{zy}}{\sqrt{\sigma_z^2 + 4\tau_{zy}^2} + \sigma_z} \quad \text{or} \quad \cot\alpha = \frac{2\tau_{zx}}{\sqrt{\sigma_z^2 + 4\tau_{zx}^2} + \sigma_z} \tag{2}$$

After cracks in tension zone are obtained, on the fourth side of the warped failure surface, ends of cracks are joined by a compression zone as shown in Fig. 1. With the present simplified method, the warped failure surface can be easily found by using the most important affecting factor which is the load proportion.

3 Assumptions on stress distribution at failure

During the examination of equilibrium conditions of ductile failure, on the warped failure surface, the bond between steel and concrete is neglected.

3.1 Stresses of reinforcement bars at failure

In equilibrium equations of ductile failure, all longitudinal bars and stirrup bars exposed on the failure surface are considered yield to balance external loads.

However, when RC members are subjected to shear and flexure longitudinal steel may not yield. In the present paper, longitudinal steel tension will be calculated under Bernoulli hypothesis in equilibrium equations.

For a simply supported reinforced concrete member as shown in Figure 3(a), in Bernoulli beam theory, the axial compression stress acts at longitudinal concrete strut in the top of member. Therefore, bottom bars exposed on failure surface are not yield, and the stress depends on the location of section B (Figure 3(a)). Since tensile steels at section C are yield as shown in Figure 3(b)(Kim 2008), the moment carried by longitudinal bars (M_{sB}) under Bernoulli hypothesis can be estimated without calculating the stress of bottom bars expressed as $M_{sB}=A_s f_y h_{C-B}-Va$. where h_{C-B} is the vertical distance between concrete strut and longitudinal steel bars in the bottom, A_s is the total cross-sectional area of tensile steels, f_y is the yield strength of tensile steels, V is shear force, and a is the longitudinal distance between the center of concrete strut (point C) and the center of bottom bars (point B).
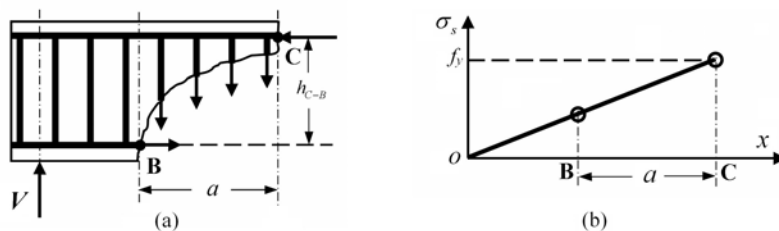
Figure 3. (a) Failure mechanism for combined shear and flexure; (b) Steel tension in Bernoulli hypothesis(Kim 2008)

Studies show that, longitudinal steel bars and stirrups should have a proper ratio so that they would all yield at failure(Hsu 1984). Generally more longitudinal steel is reinforced in the bottom (A_b is the area of a steel bar in the bottom and f_b is its yield strength) than steel reinforced in the top (A_t is the area of a steel bar in the top and f_t is its yield strength). Since the failure is dominated by the weaker steel bars, the ratio of longitudinal steel to stirrups has to satisfy Eq. (3)(China 2010), where A_w is the area of a stirrup bar, f_w is the yield strength of stirrups, s is the stirrup spacing, b_1 is the transverse distance between stirrup bars in the left and bars in the right, and h_1 is the vertical distance between stirrup bars in the top and bars in the bottom.

$$0.6 \leq \frac{2A_t f_t s}{A_w f_w (b_1 + h_1)} \leq 1.7 \tag{3}$$

3.2 Stress distribution of concrete at failure

At failure the normal-section of concrete will be divided into two parts, a tension zone and a compression zone. Contributions of these two parts of concrete in equilibrium equations are analyzed separately as follows.

Concrete in tension zone cracks first during loading, and still contributes after cracking because of aggregates' interlock(Reinhardt 1982, Gambarova 1987). According to previous studies on the mechanism of aggregates' interlock and the transfer of tensile forces across cracks, the restraining force is a major influencing factor(Reinhardt 1982, Gambarova 1987). Instead of involving compatibility conditions, a ductile reduction coefficient k_T is introduced to demonstrate the effect of crack opening. Since restraining force is the most important influencing factor, the value of k_T is only decided by axial load.

If there is no axial compressive load or the axial load is tensile, crack opening is considered too large to transfer any shear or tensile force and k_T is equal to zero.

If stress states at cracking not only satisfies the Rankine model but also satisfies the Mohr-Coulomb model, concrete would be crushed and RC members would fail at the same time as cracking happens, transfers of shear and tensile forces are presumed not to be weakened by crack opening. According to studies of Hong Li and Xila Liu(Li 1992), at the transition state, principal stresses are: $\sigma_1 = f_{ct}$ and $\sigma_3 = -0.5f_c$. Therefore, if the axial compression satisfies: $N = (f_{ct} - 0.5f_c)BH$, k_T is equal to one.

And if the applied axial compression (N) is in between $0 \sim (f_{ct} - 0.5f_c)BH$, the value of k_T linearly increases with the compressive force as Eq. (4).

$$k_T = \frac{N}{BH\left(f_{ct} - f_c/2\right)} \tag{4}$$

At cracking, the first principal stress (σ_1) and the crack angle (α) as shown in Figure 4(a) can be calculated as Eq. (2), which can also be written as Eq. (5).

$$\cot\alpha = \frac{2\tau_{zy}}{\sqrt{\sigma_z^2 + 4\tau_{zv}^2} + \sigma_z} = \frac{\tau_{zy}}{\sigma_1} \tag{5}$$
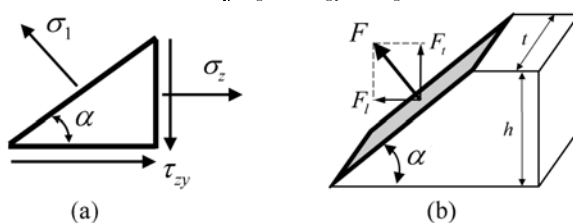
Figure 4. (a) Stress state at cracking; (b) Contribution of σ_1

While analyzing a block of concrete near the crack with a thickness of t and a height of h as shown in Figure 4(b), the tensile force (F) acting on failure surface is valued as: $F = \sigma_1 th/\sin\alpha$. The horizontal component (F_l) of the tensile force (F), which is in the longitudinal direction, is valued as: $F_l = F\sin\alpha = \sigma_1 th$. The vertical component

(F_t), which is in the transverse direction, is valued as: $F_t=F\cos\alpha=\sigma_1 th\cot\alpha=\tau_{zy}th$.

When analyzing equilibrium conditions, in order to calculate the contribution of concrete in tension zone, the deducted F is considered to be transferred across cracks and can be divided into a horizontal component (k_TF_l) and a vertical component (k_TF_t). Therefore, the contribution of tension zone is made up by two parts: the contribution of deducted normal stress and the contribution of deducted shear stress.

In compression zone, since the priority for concrete is to balance axial compression, the value of shear stress is considered as the same as the shear stress in tension zone. At the limit state, the normal stress in compression zone and the deducted shear stress together reach the Mohr-Coulomb criterion for concrete.
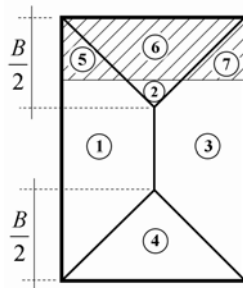
Figure 5. Stress distribution on normal-section at failure

Therefore, stress distribution is as shown in Figure 5 if compression zone is in the top. Region 1 is in tension zone. The normal stress in this region is $k_T\sigma_{t-l}$ (σ_{t-l} is the first principal stress in the left at cracking), the shear stress is $k_T\tau_l$ (τ_l is the shear stress in the left at cracking), and the area of region 1 is A_{t-l}. Region 2 is in tension zone. The normal stress in this region is $k_T\sigma_{t-t}$ (σ_{t-t} is the first principal stress in the top at cracking), the shear stress is $k_T\tau_t$ (τ_t is the shear stress in the top at cracking), and the area of region 2 is A_{t-t}. Region 3 is in tension zone. The normal stress in this region is $k_T\sigma_{t-r}$ (σ_{t-r} is the first principal stress in the right at cracking), the shear stress is $k_T\tau_r$ (τ_r is the shear stress in the right at cracking), and the area of region 3 is A_{t-r}. Region 4 is in tension zone. The normal stress in this region is $k_T\sigma_{t-b}$ (σ_{t-b} is the first principal stress in the bottom at cracking), the shear stress is $k_T\tau_b$ (τ_b is the shear stress in the bottom at cracking), and the area of region 1 is A_{t-b}. Region 5 is in compression zone. The normal stress in this region is σ_{c-l} (σ_{c-l} is the normal stress in the left at failure), the shear stress is $k_T\tau_l$ (τ_l is the shear stress in the left at cracking), and the area of region 1 is A_{c-l}. Region 6 is in compression zone. The normal stress in this region is σ_{c-t} (σ_{c-t} is the normal stress in the top at failure), the shear stress is $k_T\tau_t$ (τ_t is the shear stress in the top at cracking), and the area of region 1 is A_{c-t}. Region 7 is in compression zone. The normal stress in this region is σ_{c-r} (σ_{c-r} is the normal stress in the right at failure), the shear stress is $k_T\tau_r$ (τ_r is the shear stress in the right at cracking), and the area of region 1 is A_{c-r}.

4 Equilibrium conditions

There are three failure modes distinguished by the location of compression zone on failure surface. Compression zone can form along the top, along the bottom, or along one of the flank sides of the member. The location is decided by loading proportion and sectional properties (Figure 6), and corresponding bearing capacities are the smallest among results of all possible failure modes.
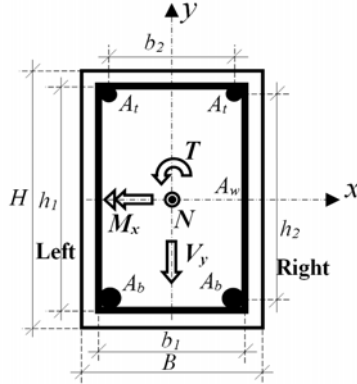
Figure 6. Normal-section properties

4.1 Compression zone along the top

At first, by analyzing the equivalence of internal forces along the longitudinal axis as Eq. (6), the position of the neutral axis can be determined. After the neutral axis is determined, coordinates of the center of compression zone (point C) can be obtained $(0, y_c)$. The axial contribution of concrete in tension zone can be considered as a concentrated axial force $(\sigma_{ct} A_{ct})$ acting at the centroid of tension zone, σ_{ct} is the area-weighted average tensile stress of tension zone, and A_{ct} is the area.

$$
\begin{aligned}
N = 2A_b f_b - 2A_t f_t + \sigma_{c-l} A_{c-l} + \sigma_{c-t} A_{c-t} + \sigma_{c-r} A_{c-r} \\
+ k_T \left(\sigma_{t-l} A_{t-l} + \sigma_{t-t} A_{t-t} + \sigma_{t-r} A_{t-r} + \sigma_{t-b} A_{t-b} \right)
\end{aligned}
\tag{6}
$$

The equivalance of shear force is calculated as Eq. (7), in which α_l is the crack angle in the left and α_r is the crack angle in the right.

$$
V = A_w f_w h_1 \left(\cot \alpha_l - \cot \alpha_r \right) / s + \left(\tau_l - \tau_r \right) k_T B (2H - B) / 4
\tag{7}
$$

Torsion is calculated about point C as Eq. (8). α_b is the angle in the bottom.

$$
\begin{aligned}
T = A_w f_w h_1 b_1 \left(\cot \alpha_b + \cot \alpha_l / 2 + \cot \alpha_r / 2 \right) / s \\
+ k_T B^2 (3H - B) \left(\tau_t + \tau_b + \tau_r + \tau_l \right) / 24 + B^2 k_T y_c \left(\tau_b - \tau_t \right) / 4
\end{aligned}
\tag{8}
$$

Bending moment about x-axis can be calculated about point C as Eq. (9).

$$
\begin{aligned}
M + N y_c = {} & 2A_b f_b \left(h_b + y_c \right) + 2A_t f_t \left(h_t - y_c \right) + A_{ct} \sigma_{ct} H / 2 - V \left(h_b + y_c \right) \left(\cot \alpha_l - \cot \alpha_r \right) / 2 \\
& + A_w f_w h_1 y_c \left(\cot \alpha_l - \cot \alpha_r \right)^2 + k_T y_C B (2H - B) \left(\cot \alpha_l - \cot \alpha_r \right) \left(\tau_l - \tau_r \right) / 8 \\
& - A_w f_w h_1 b_1 \left(\cot \alpha_r + \cot \alpha_l \right) \left[2 \cot \alpha_b + H \left(\cot \alpha_r + \cot \alpha_l \right) / B \right] / (4s) \\
& - k_T B (3H - B) \left(2B \cot \alpha_b + H \cot \alpha_r + H \cot \alpha_l \right) \left(\tau_l + \tau_r \right) / 48
\end{aligned}
\tag{9}
$$

Then interaction equations can be obtained:

$$\frac{N}{N_0} + \frac{M}{M_0} + \frac{V^2}{V_0^2} + \frac{T^2}{T_0^2} = 1 \tag{10}$$

$$N_0 = \left(2A_b f_b \left(h_b + y_c\right) + 2A_t f_t \left(h_t - y_c\right) + A_{ct}\sigma_{ct} H / 2\right)/ y_c \tag{11}$$

$$M_0 = 2A_b f_b \left(h_b + y_c\right) + 2A_t f_t \left(h_t - y_c\right) + A_{ct}\sigma_{ct} H / 2 \tag{12}$$

$$V_0^2 = \frac{\left[2A_b f_b \left(h_b + y_c\right) + 2A_t f_t \left(h_t - y_c\right) + A_t \sigma_t H / 2\right]}{h_2 \left(\cot \alpha_l - \cot \alpha_r\right)} \tag{13}$$
$$\times \left[4A_w f_w h_1 \left(\cot \alpha_l - \cot \alpha_r\right)/ s + \left(\tau_l - \tau_r\right)k_T \left(2H - B\right)B\right]$$

$$T_0^2 = \frac{4B\left[2A_b f_b \left(h_b + y_c\right) + 2A_t f_t \left(h_t - y_c\right) + A_{ct}\sigma_{ct} H / 2\right]}{\left[H\left(\cot \alpha_l + \cot \alpha_r\right) + 2B \cot \alpha_b\right]}$$
$$\times \frac{\left[\begin{array}{l} A_w f_w b_1 h_1 \left(2\cot \alpha_b + \cot \alpha_l + \cot \alpha_r\right)/\left(2s\right) \\ +k_T B^2 \left(3H - B\right)\left(\tau_l + \tau_r + \tau_t + \tau_b\right)/ 24 + k_T B^2 y_c \left(\tau_b - \tau_t\right)/ 4 \end{array}\right]^2}{\left[A_w f_w b_1 h_1 \left(\cot \alpha_l + \cot \alpha_r\right)/ s + k_T \left(\tau_l + \tau_r\right)B^2 \left(3H - B\right)/12\right]} \tag{14}$$

In the equilibrium equation for bending moment (Eq. (9)), the crack angle not only affects the number of stirrups exposed on failure surface but also affects distances. However, torsion and shear only have a linear relationship with the crack angle (Eqs. (7) and (8)). These are reflected in interaction equations (Eqs. (10)~(14)).

4.2 Compression zone along the bottom

If compression zone forms along the bottom as shown in Figure 7, interaction equations (15) ~ (19) can be derived using the same method. α_t is the angle in the top.
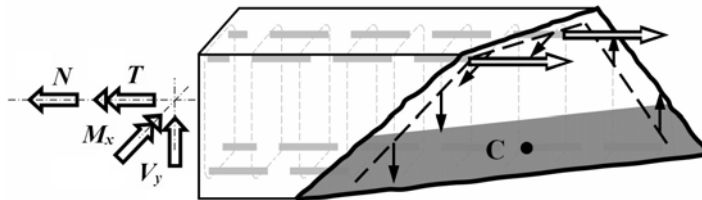
Figure 7. Ductile failure mechanism (compression zone along the bottom)

$$\frac{N}{N_0} + \frac{M}{M_0} + \frac{V^2}{V_0^2} + \frac{T^2}{T_0^2} = 1 \tag{15}$$

$$N_0 = -\left[2A_b f_b \left(h_b + y_c\right) + 2A_t f_t \left(h_t - y_c\right) + A_{ct}\sigma_{ct} H / 2\right]/ y_c \tag{16}$$

$$M_{x0} = -\left[2A_b f_b \left(h_b + y_c\right) + 2A_t f_t \left(h_t - y_c\right) + A_{ct}\sigma_{ct} H / 2\right] \tag{17}$$

$$V_0^2 = \frac{\left[2A_b f_b \left(h_b + y_c\right) + 2A_t f_t \left(h_t - y_c\right) + A_t \sigma_t H / 2\right]}{h_2 \left(\cot \alpha_l - \cot \alpha_r\right)} \tag{18}$$
$$\times \left[4A_w f_w h_1 \left(\cot \alpha_l - \cot \alpha_r\right)/ s + \left(\tau_l - \tau_r\right)k_T \left(2H - B\right)B\right]$$

$$T_0^2 = \frac{4B\left[2A_b f_b\left(h_b + y_c\right) + 2A_t f_t\left(h_t - y_c\right) + A_{ct}\sigma_{ct}H/2\right]}{\left[H\left(\cot\alpha_l + \cot\alpha_r\right) + 2B\cot\alpha_t\right]}$$

$$\times \frac{\left[\begin{array}{l}A_w f_w b_1 h_1\left(2\cot\alpha_t + \cot\alpha_l + \cot\alpha_r\right)/(2s)\\ +k_T B^2\left(3H - B\right)\left(\tau_l + \tau_r + \tau_t + \tau_b\right)/24 + k_T B^2 y_c\left(\tau_b - \tau_t\right)/4\end{array}\right]^2}{\left[A_w f_w b_1 h_1\left(\cot\alpha_l + \cot\alpha_r\right)/s + k_T\left(\tau_l + \tau_r\right)B^2\left(3H - B\right)/12\right]} \quad (19)$$

4.3 Compression zone along one of flank sides

If compression zone forms along one of flank sides of the member, the failure mechanism (Figure 8) is the same as the mechanism when compression zone is in the top if the member in Figure 1 rotates 90 degrees about axis z. Therefore, interaction equations $(20) \sim (22)$ can be derived, in which b_2 is the horizontal distance between longitudinal bars in the left and bars in the right.

$$\frac{N}{N_0} + \frac{\left(T + V\left(B - A_c/H\right)/2\right)^2}{T_{C0}^2} = 1 \quad (20)$$

$$N_0 = \left(A_t f_t b_2 + A_b f_b b_2 + A_{ct}\sigma_{ct}B/2\right)/x_c \quad (21)$$

$$T_{C0}^2 = \frac{4H\left[A_t f_t b_2 + A_b f_b b_2 + A_{ct}\sigma_{ct}B/4\right]}{\left[B\left(\cot\alpha_t + \cot\alpha_b\right) + 2H\cot\alpha_l\right]}$$

$$\times \frac{\left[\begin{array}{l}A_w f_w b_1 h_1\left(2\cot\alpha_l + \cot\alpha_t + \cot\alpha_b\right)/(2s)\\ +k_T B^2\left(3H - B\right)\left(\tau_r + \tau_l + \tau_t + \tau_b\right)/24 + k_T B\left(2H - B\right)x_c\left(\tau_l - \tau_r\right)/4\end{array}\right]^2}{\left[A_w f_w b_1 h_1\left(\cot\alpha_t + \cot\alpha_b\right)/s + k_T\left(\tau_t + \tau_b\right)B^2\left(3H - B\right)/12\right]}$$

$$(22)$$
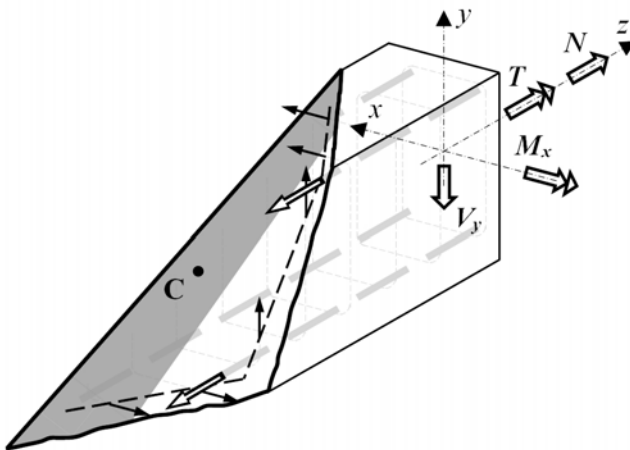
Figure 8. Ductile failure mechanism (compression zone along a flank side)

With interaction equations of all ductile failure modes, the interaction surface of ductile failure for axial load, bending, shear, and torsion can be determined.

5. Conclusion

This paper presents a new lower-bound limit analysis of ductile failure when RC members subjected to axial load, bending, shear, and torsion.

In the ductile failure analysis, a new method is proposed to describe the warped failure surface. After quantifying aggregates' interlock capacity, this limit analysis is capable of predicting the contribution of concrete in tension zone. Combined with the contribution of concrete subjected to normal and shear stresses in compression zone, concrete contributions are thoroughly considered. By analyzing equilibrium equations the interaction relationship between axial load and torsion can be achieved.

References

Baikov V. and Sigalov E. (1981). *Reinforced Concrete Structures*. Moscow, Mir Publishers

Chen W. F. and Saleeb A. F. (2004). *Elasticity and Plasticity*, China Architecture & Building Press.

China. (2010). "GB50010-2010 Code for Design of Concrete Structures." Beijing, Ministry of Construction of the People's Republic of China.

Gambarova P. G. (1987). Modelling of Interface Problems in Reinforced Concrete. *Computational Mechanics of Concrete Structures - Advances and Applications*. Delft, IABSE. 54**:** 1-16.

Gregori J. N., Sosa P. M., Prada M. A. F. and Filippou F. C. (2007). "A 3D numerical model for reinforced and prestressed concrete elements subjected to combined axial, bending, shear and torsion loading." *Engineering Structures* 29(Compendex): 3404-3419.

Hsu T. T. C. (1984). *Torsion of Reinforced Concrete* Van Nostrand Reinhold.

Hsu T. T. C. and Mo Y. L. (2010). *Unified Theory of Concrete Structures*. Chichester, West Sussex, U.K. , John Wiley and Sons.

Kim W. and Kim D.-J. (2008). "Analytical model to predict the influence of shear on longitudinal steel tension in reinforced concrete beams." *Advances in Structural Engineering* 11(Compendex): 135-150.

Li H. and Liu X. (1992). "The critical tensile-shear failure and shear strength of concrete." *Engineering Mechanics* 9(4): 1-9.

Liu X. (2003). *Going to mature:the theoretical development of reinforced concrete structures*. International Conference on Advances in Concrete and Structures (ICACS), Xuzhou, China, RILEM Publications.

Nádai Á. (1950). *Theory of Flow and Fracture of Solids*, McGraw-Hill (New York).

Reinhardt H. W. and Walraven J. C. (1982). "Cracks in Concrete Subject to Shear." *Journal of the Structural Division, Proceedings of ASCE* 108(ST1): 207-224.

Vecchio F. J. and Collins M. P. (1986). "The modified compression field theory for reinforced concrete elements subjected to shear." *ACI Journal* 83(2): 219-231.

Unified Failure Model of Reinforced Concrete Members Subjected to Hazard Loads II: Brittle Failure Analysis

Xi Chen[1], Xila Liu[2]

Abstract: A simple and unified failure model is proposed for rectangular reinforced concrete (RC) members subjected to axial loads, bending, shear force and torsion. There are two distinct types of failure mechanisms, ductile failure and brittle failure. In the present paper, a lower-bound limit analysis of brittle failure is proposed. The normal-section at failure is considered intact and stress distributions at failure can be presumed. Then the interaction relationship can be deducted when stress distributions reach the failure criterion of concrete and RC members fails at the same time.

Combined with the ductile failure analysis proposed in part I, a unified failure model is obtained and it is in good agreement with experimental results. This unified failure model not only can explicitly explain failure mechanisms, ultimate bearing capacities can be easily calculated and the failure mechanism can be quickly determined. Overall, this model is significative for the analyses of reinforced concrete structures in engineering.

Keywords: Reinforced concrete members; unified theory; rectangular members; axial loads, bending, shear, and torsion; brittle failure;

0. Introduction:

A simple and unified model is proposed for the widely used rectangular reinforced concrete elements subjected to axial loads, bending, shear force and torsion. As observed in experiments, there are two types of failure mechanisms, i.e. ductile failure and brittle failure. In the present paper, a lower-bound limit analysis of brittle failure is proposed based on the failure mechanism.

---

[1] Department of Solid Mechanics, Shanghai Jiaotong University, Shanghai 200240, China,
E-mail: cx541026@hotmail.com
[2] Department of Civil Engineering, Shanghai Jiaotong University, Shanghai 200240, China

When brittle failure occurs, concrete would be crushed first, the RC member fails at the same time and not all longitudinal steel bars yield at failure. Since the stress state of concrete decides the condition of member, stress distributions at failure should be presumed. When stresses of concrete reach the 3-dimensional failure criterion, failure occurs, and the interaction relationship can be expressed.

During analysis, two different brittle failure mechanisms have been identified. Depending on axial compression, RC member could fail before or after cracks appear. Failure equations of both failure mechanisms will be developed and the axial compression range of each failure mechanism will be determined.

The ductile failure analysis proposed in part I and the brittle failure analysis proposed in this paper together can provide rather accurate results comparing with experimental results. The proposed failure analyses is suitable for concrete members with rectangular sections reinforced with appropriate amount of stirrups and longitudinal steel bars, and longitudinal bars should be placed at each corner. Performances of high strength concrete and high strength steel are not considered.

1. Failure Criterion

In this proposed lower-bound limit analysis, reinforcing steel is considered as one-dimensional material. The failure of concrete under 3-dimensional stresses is dominated by the Mohr-Coulomb model with tension cut-off(Li 1992, Chen 2004). The theory developed by Hong Li and Xila Liu(Li 1992) is adopted to calculate c (the cohesion) and φ (the angle of internal friction). In their theory, at the transition state principal stresses are $\sigma_1 = f_{ct}$ and $\sigma_3 = -0.5 f_c$, f_c is the compressive strength of concrete, f_{ct} is the tensile strength of concrete, and the Mohr-Coulomb criterion on the σ_z-τ_{zx} plane can be written as Eq. (1).

$$\sqrt{\sigma_z^2 + 4\tau_{zx}^2}\left(f_c + 2f_{ct}\right) + \sigma_z\left(f_c - 2f_{ct}\right) = 4 f_c f_{ct} \tag{1}$$

2. Stress distributions at failure

During brittle failure analysis, all stirrup bars are presumed yield at limit state, and longitudinal steel bars are replaced by equivalent concrete in calculation.

Stress distributions on the normal-section at failure are assumed as follows. Normal stress is caused by axial load and bending. The normal stress caused by axial load is evenly distributed and it can be calculated as Eq. (2), in which $A_t f_t / f_c$ represents the equivalent area of concrete for a longitudinal bar in the top and $A_b f_b / f_c$ represents the equivalent area of concrete for a bar in the bottom. B is the width of the normal-section and H is the height. A_b is the area of a steel bar in the bottom and f_b is its yield strength; A_t is the area of a bar in the top and f_t is its yield strength.

$$\sigma_N = \frac{N}{BH + 2\dfrac{A_t f_t}{f_c} + 2\dfrac{A_b f_b}{f_c}} \tag{2}$$

The normal stress distribution caused by bending is in coincidence with Bernoulli hypothesis. After replacing longitudinal steels with equivalent concrete, coordinates of the centroid $(0, y_N)$ and the moment of inertia (I_N) of the equivalent normal-section need to be calculated, then the normal stress at any coordinate (x, y) can be calculated as Eq. (3).

$$\sigma_M = -\frac{M(y - y_N)}{I_N} \tag{3}$$

Shear stress is caused by shear force and torsion. The shear stress caused by shear force is evenly distributed in most area except for top and bottom edges where there is no shear stress due to boundary conditions, and it can be calculated as Eq. (4), in which $2A_w f_w h_1/s$ is the contribution of stirrups. A_w is the cross-sectional area of a stirrup bar, f_w is the yield strength of stirrups, s is the stirrup spacing, and h_1 is the vertical distance between stirrup bars in the top and stirrup bars in the bottom.

$$\tau_V = \frac{V - \dfrac{2A_w f_w h_1}{s}}{BH} \tag{4}$$

The shear stress distribution caused by torsion is the plastic stress distribution developed by Nadai(Nádai 1950) and can be calculated as Eq. (5), in which $2A_w f_w b_1 h_1/s$ is the contribution of stirrups and $B^2(3H-B)/6$ is the section modulus. b_1 is the transverse distance between stirrup bars in the left and stirrup bars in the right.

$$\tau_T = 6\frac{T - \dfrac{2A_w f_w b_1 h_1}{s}}{B^2(3H - B)} \tag{5}$$

3. Brittle failure equation one

If axial compression is rather large, concrete would be crushed before cracks appear. Therefore, stresses of concrete reach the Mohr-Coulomb criterion first. With the obtained stress distributions bearing capacities can be calculated using Eq. (1).

This approach is valid only if stresses of concrete reach the Mohr-Coulomb criterion first instead of the Rankine criterion. In the adopted theory developed by Hong Li and Xila Liu(Li 1992), at the transition state between the Mohr-Coulomb criterion and the Rankine criterion principal stresses would be: $\sigma_1 = f_{ct}$ and $\sigma_3 = -0.5f_c$.

Therefore, if axial compression satisfies Eq. (6), this approach is suitable to calculate loading capacities and the interaction curve. The starting point of this curve is when axial compression is equal to $N_1 = (BH + 2A_t f_t/f_c + 2A_b f_b/f_c)(f_{ct} - f_c/2)$.

$$N \le \left(f_{ct} - \frac{f_c}{2} \right) \left(BH + 2\frac{A_t f_t}{f_c} + 2\frac{A_b f_b}{f_c} \right) \tag{6}$$

4. Brittle failure equation two

If axial compression does not satisfy Eq. (6), brittle failure could still happen. In this case, stresses of concrete reach the Rankine criterion first and cracks appear. However, before longitudinal steel bars reach yield, redistributed stresses of concrete reach the Mohr-Coulomb criterion first and the RC member fails. In this case, both ductile failure analysis and brittle failure equation one are not suitable to calculate loading capacities, and a simplified solution is proposed to approximately describe the failure mechanism and calculate loading capacities.

Since the RC member would fail quickly after cracks appear, external loads at cracking are close to loading capacities. Therefore, when stresses of concrete reach the revised Rankine criterion (Eq. (7)), the RC member is assumed failed. The revised Rankine criterion (Eq. (7)) is proposed to approximately describe the redistributed stress state at failure, and the brittle reduction coefficient k_T' is introduced to represent the effect of cracking. With the obtained stress distributions caused by external loads, bearing capacities can be calculated using Eq. (7).

$$\sigma_1 = \frac{\sigma_z}{2} + \sqrt{\frac{\sigma_z^2}{4} + \tau_{zx}^2} = k_T' f_{ct} \tag{7}$$

Similar to the ductile reduction coefficient k_T, the brittle reduction coefficient k_T' is introduced to demonstrate the effect of crack opening. As introduced in ductile failure analysis, restraining force is the most important factor and the value of k_T' is only decided by axial load. If loading proportions between bending, shear, and torsion remain the same, the interaction curve of ductile failure and the interaction curve of brittle failure case one can be obtained as shown in Figure 1.
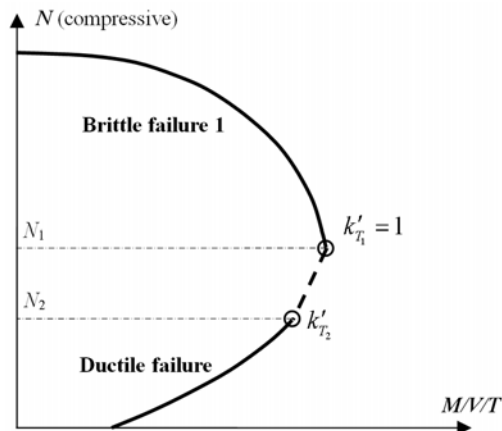
Figure 1. The relationship between k_T' and axial compression (N)

When stresses at failure are at the transition state between the Mohr-Coulomb criterion and the Rankine criterion concrete would be crushed and RC members would fail at the same time as crack appears. Therefore, if axial compression is equal to N_1, the brittle reduction coefficient is k_{T1}' and the value is one.

A line crossing the point of $N=N_1$ on the interaction curve of brittle failure can be found tangent to the interaction curve of ductile failure as shown in Figure 1. The point of tangency on the curve of ductile failure is considered as the transition point between ductile failure and brittle failure and the starting point of the interaction curve of brittle failure. Therefore, loading capacities of the point of tangency also satisfy Eq. (7), and the axial compression at this point is called N_2. After substituting loading capacities of the point of tangency into Eq. (7), the brittle reduction coefficient at this point (k_{T2}') can be obtained.

If axial compression is in between N_1 and N_2, the value of k_T' linearly increases with the compressive force as Eq. (8).

$$k_T' = \left(k_{T1}' - k_{T2}'\right)\frac{\left(N - N_2\right)}{\left(N_1 - N_2\right)} + k_{T2}' \tag{8}$$

Therefore, when axial compression satisfies $N_2 \leq N \leq N_1$, this approach is suitable to calculate loading capacities and the interaction curve.

Brittle failure equation one and brittle failure equation two together compose the limit analysis of brittle failure, and a complete convex interaction curve for combined axial load, bending, shear, and torsion can be obtained by combining the curve of ductile failure and two curves of brittle failure.

5. Comparison of experimental and theoretical results

Twelve specimens(Zhao 1993) are used to evaluate the ability of the proposed failure model. All specimens had a cross section of 250mm×250mm, and were all reinforced longitudinally with four 10mm diameter steel bars placed at corners and

laterally by closed stirrups with a diameter of 6.5mm. The stirrup spacing of the specimen MV3-3-2b was 200mm, and the stirrup spacing of other specimens was 70mm. The predetermined axial compression was applied first, followed by proportional loads to destruction. Loading proportions are listed in Table 1.

Ultimate loads are calculated as shown in Table 1, in which λ is the shear span ratio, T_{exp} is the experimental torsion capacity, and T_{th} is the theoretical torsion capacity. Values in Table 1 show that a good agreement has been observed.

Table 1 Comparisons between test and theoretical results

No.	$N/A/f_c$	λ	T/M	T_{exp}(kNm)	T_{th} (kNm)	T_{exp}/T_{th}
MV6-3-2	-0.6	2.5	0.75	23.75	22.23	1.07
MV6-3-1	-0.6	2.6	0.55	24	18.77	1.28
MV5-4-2M	-0.5	3.6	0.49	25.37	20.5	1.24
MV4-2-2	-0.4	2.5	0.91	26.6	28.62	0.93
MV4-2-3	-0.4	2.5	1.27	26.95	31.61	0.85
MV4-3-2	-0.4	2.5	0.69	22.84	22.1	1.03
MV4-3-2M	-0.4	3.3	0.54	19.79	21.16	0.94
MV4-2-VL	-0.4	∞	1.13	28	30.98	0.90
MV3-2-2	-0.3	2.5	0.91	23.65	26.11	0.91
MV3-2-3	-0.3	2.5	1.46	26.4	29.74	0.89
MV3-3-2	-0.3	2.5	0.73	23.6	24.3	0.97
MV3-3-2b	-0.3	2.5	0.73	16.96	17.78	0.95
MV3-2-2B	-0.3	2.6	1.04	25.76	27.69	0.93
					Average	0.99
					Standard Deviation	13.18%

6. Conclusion

This paper presents a new lower-bound solution in limit analysis for RC members subjected to axial load, bending, shear, and torsion, and it is the first time that ductile failure and brittle failure are analyzed separately according to their failure mechanisms and separate limit analyses are developed only using equilibrium conditions and failure criteria.

In the proposed brittle failure analysis, concrete would be crushed first and the RC member fails at the same time. Stress distributions at failure can be presumed, and then the interaction relationship can be expressed using the failure criterion for concrete. Two different brittle failure mechanisms have been identified. Failure equations of both failure mechanisms are developed respectively and the axial compression range of each failure mechanism is determined.

The ductile failure analysis proposed in part I and the brittle failure analysis proposed in this paper compose the proposed unified failure model. After comparing the lower-bound solution in the present paper with experimental results, ultimate loads are rather accurate. The proposed unified model not only can explicitly explain failure mechanisms, ultimate bearing capacities can be easily calculated and the failure mode can be quickly determined. Overall, this model is significative for the analysis of reinforced concrete structures in engineering.

References

Chen W. F. and Saleeb A. F. (2004). *Elasticity and Plasticity*, China Architecture & Building Press.

Li H. and Liu X. (1992). "The critical tensile-shear failure and shear strength of concrete." *Engineering Mechanics* 9(4): 1-9.

Nádai Á. (1950). *Theory of Flow and Fracture of Solids*, McGraw-Hill (New York).

Zhao J., Zhang L. and Wei Y. (1993). "Torsional Strength of RC Members Subjected to Compression, Bending, Shear and Torsion." *China Civil Engineering Journal* 26(1): 20-30.

Seismic Damage Assessment of

Masonry Infilled Reinforced Concrete Structures

Jia-Chao Zhang[1], Lei-Ming Zhang[2], Xi-La Liu[3] and Si-Jia Chen[4]

Abstract: In this study a new damage assessment procedure is proposed to make assessment of structural damage for masonry infilled reinforced concrete (R/C) structures subject to earthquakes. The structural damage index is defined as a weighted combination of damage indices of each component in the structure. The weight factor for each component is determined by considering the effects of the component failure on the structural failure. Then the state of the structure is classified according to the structural damage index. In the end a three-story building is analyzed to demonstrate the feasibility of the presented procedure in practice.
CE Database subject headings: Seismic damage assessment; Masonry infilled R/C structures; Structural damage index; Damage index of structural component.

Introduction

Most building codes for seismic design have specific requirements on performance of earthquake resistant structures. In China, the criterion of *no collapse under severe earthquake* has been made as early as in the first design code, "*Code for seismic design of buildings* (GBJ 11-89)" after the 1976 Great Tangshan Earthquake. Traditionally the damage in building structures is assessed by a ductility factor μ usually defined as

$$\mu = \frac{\Delta_m}{\Delta_y} \tag{1}$$

where Δ_m is structural peak displacement during designed ground shaking; and Δ_y is idealized elasto-plastic yield displacement. According to (Chai et al. 1995), however, the damage assessed by Eq. 1 is rather inadequate, since it is implicitly assumed that the structural damage occurs only due to maximum displacement, and

[1]Shanghai Shenzhou Electric Power Co., Ltd, No.1 Building, 412 Guilin Road, Xuhui District, Shanghai 200233, P.R. China (corresponding author). E-mail: jczhang07@yahoo.com
[2]Dept. of Civil Engineering, Shanghai Jiaotong Univ., No. 800 Dongchuan Rd., Shanghai 200240, P.R. China. E-mail: lmzhang@sjtu.edu.cn
[3]Dept. of Civil Engineering, Shanghai Jiaotong Univ., No. 800 Dongchuan Rd., Shanghai 200240, P.R. China. E-mail: xilaliu@tsinghua.edu.cn
[4]Dept. of Civil Engineering, Shanghai Jiaotong Univ., No. 800 Dongchuan Rd., Shanghai 200240, P.R. China. E-mail: csj5719@163.com

is therefore independent of the loading path or the plastic strain energy dissipated in the structure. Besides, the current performance criteria are based on the analysis of structural frame model in which slabs and walls are not included. In the present paper, the building function state is assessed by a structural damage index from the structural initial damage to its collapse quantitatively, and the structural damage index is defined as a weighted combination of damage indexes of all components in the structure including walls and slabs. The weight factor is determined by considering the effect of the component failure on the structural failure. In this study it is focused mainly on reinforced concrete building structures.

Importance of Structural Components

It is obvious that different components have different influences on overall structural responses. It is recognized that a component is significant in a structure if its failure would lead to large area of failure in the overall structure (Liu et al. 2001; Liu et al. 2005; Gao et al. 2008). Those significant components are usually treated as *important components* and their existence may reduce the structural robustness. Therefore, it is necessary to take into account the component importance in evaluating structural potential damage.

As an integrated system, the structural properties of geometry, material and loads should be taken into consideration synthetically. (Zhang et al. 2007) defined the importance of components as a function of the strain energy, i.e.

$$\gamma = \frac{U^{(i)}}{U} \tag{2}$$

Where U is total strain energy of the original structure; and $U^{(i)}$ is strain energy of the remain structure with the removal of component i. It can be seen that the larger the total strain energy of remaining structure after the component removed, the more important of the removed component. The concept and calculation of this method is simple for practicing. However, the numerical domain of the importance index calculated by Eq. 2 is [1, +∞], which is not convenient in calculation. It is modified by (Ye et al. 2007) as

$$\gamma = \left| 1 - \frac{U}{U^{(i)}} \right| \tag{3}$$

which is adopted in this study.

Seismic Damage Assessment for Reinforced Concrete Buildings

Structural damage index

Failure of important components may result in disproportionate progressive collapse of the entire structure. It is reasonable to quantify the overall structural damage based on the component damage assessment with component importance. In

the present paper, the structural damage index is defined as weighted combination of damage indexes of components, which is expressed as

$$D = \sum_{i=1}^{n} w(\gamma_i) d_i \tag{4}$$

where n is the number of components in the structure; D is the structural damage index; d_i is the damage index of ith component which will be described in more detail in the following sections; and $w(\gamma_i)$ is weight factor of ith component, which is determined as

$$w(\gamma_i) = \frac{\gamma_i}{\sum_{i=1}^{n} \gamma_i} \tag{5}$$

where γ_i is the importance index for i^{th} component and is obtained from Eq. 3.

Classification of building function state

For building structures the function state may be classified by different damage levels. Each level is associated with the damage index. According to (Park et al. 1985), four classes of function state are defined as in Table1.

Damage indexes of components

The damage index proposed by Park & Ang (Park et al. 1985) is employed to calculate damage in a structural component. It is defined as the linear combination of deformation and strain energy which is expressed as

$$d_i = \frac{\delta_m}{\delta_u} + \mu_s \frac{E_i}{\delta_u P_y} \tag{6}$$

where δ_m is the maximum response deformation under an earthquake; δ_u is the ultimate deformation capacity of a component under monotonic loading; P_y is the yield strength of the component; E_i is the hysteretic energy absorbed by the component during the response history; and μ_s is a model constant parameter, a value of 0.1 has been suggested by (Park et al. 1985) for ordinary reinforced concrete structures. The component fails when the damage index is bigger than 1.0.

Masonry infill wall elements

The ultimate strength V_m is determined as (Tomazevic et al. 1997)

$$V_m = \frac{L_{in} t_w f_{tp}}{C_1} \left(1 + \sqrt{C_1^2 \left(1 + \frac{N}{f_{tp} A_w} \right) + 1} \right) \tag{7}$$

where $C_1 = 1.925 L_{in} / H_{in}$, L_{in} is width of infill wall; H_{in} is height of infill wall; t_w is thickness of infill wall; A_w is area of cross section; and f_{tp} is tension strength of masonry material. The yield strength is determined as $V_y = 0.8 V_m$.

According to (Tomazevic et al. 1997), the ultimate shear deformation can be determined using the secant modulus when the shear force is $0.3 V_m$, and the corresponding secant modulus is expressed as follows.

$$K_y = K_0 - \sqrt{a \cdot d_m - b} \tag{8}$$

$$K_0 = \left(\frac{H_{in}^3}{12 E_w I_w} + \frac{1.2 H_{in}}{G_w A_w} \right)^{-1} \tag{9}$$

where $a = 1.281 K_0^2$; $b = 0.320 K_0^2$; d_m is damage coefficient, at the limit state, $d_m = 1$; K_0 is elastic shear stiffness of infill wall; E_m and G_m are the Young's modulus and shear modulus of masonry respectively; I_w is moment of inertia of the masonry infill wall element.

Slab elements

According to the plastic hinge theory, the ultimate carrying capacity is determined as follows (Shen et al. 1993).

$$q_u = \frac{24 k \left(1 + \beta_2 \right) m_1}{\xi^2 l_1^2} \tag{10}$$

where l_1 is length of slab along short edge; and k、ξ、β_2、m_1 are the parameters determined by ultimate moments of slab.

The ultimate deflection of slab can be calculated as follows (Cheng et al. 2005).

$$f = \alpha \frac{q_u l_1^4}{B_c} \tag{11}$$

$$B_c = \frac{E t^3}{12 \left(1 - \upsilon^2 \right)} \tag{12}$$

where α is deflection coefficient; t is thickness of slab; E and υ are the Young's modulus and Poisson ratio of concrete respectively.

Experimental Case Study

To demonstrate the reasonability and feasibility of the proposed procedure, a reinforced concrete structure with slabs and walls under strong earthquake is analyzed and compared with test results from (Hashemi, 2007). The failure evolution

of the structure is studied by elasto-plastic time history analysis and structural damage is assessed quantitatively.

Mechanical model

The tested specimen is a one-floor reinforced concrete structure with geometry outline shown in Figure 1. The structure was tested on a shake table and subjected to the ground motion input along the X direction.

The mechanical model is shown in Figure 2, where columns and beams are modeled with two-node spatial beam element, slabs and masonry walls are modeled with BAC macro model (Zhang et al. 2012). The smeared cracking model (HKS, 2005; Chen et al. 2005) is used to describe the behavior of concrete and masonry. The linear kinematic hardening model is applied to represent the behavior of reinforcement.

The input acceleration record is processed based on the ground motion of Düzce earthquake occurred in Turkey, 1999. The input acceleration record is shown in Figure 3 with PGA of 1.52g.

Structural failure and damage assessment

The numerical results indicate that concrete cracks in two bare frames in X direction, and the reinforcements have not reach the yield strength yet. The main damage region occurred in the middle frame infilled with masonry wall.

Figure 4 shows the calculated failure evolution of the middle frame infilled with masonry wall. The damage first appears at the connection between infill wall and beam. In the end reinforcements in columns and beams yield and the connection between infill wall and confined frame fails. The main failure mode of the masonry infill wall is characterized as horizontal cracks combined with diagonal cracks at corners, as shown in Figure 4a. It matches very well with the test failure mode shown in Figure 4b schematically.

Meanwhile, component damage indexes shown in Table 2 basically reflect the damage extent in each component. For instance, the damage indexes of the structural components of two bare frames in X direction are around 0.5; whereas the damage index of column CI is bigger than 1.0, and damage indexes of column DJ and wall CIDJ are about 0.8, which indicate severe damage happened in the frame infilled with masonry wall. Correspondingly the overall structural damage index is 0.514, the building function state is irreparable, reasonable assessment is performed on the damage in the structure since the middle frame has suffered severe damage.

Conclusion

A new procedure is presented to quantitatively evaluate the seismic damage in reinforced concrete buildings considering component importance including slabs and walls on the overall structural response. An example structure is analyzed and comparison with experimental results indicates that the structural damage index proposed provides a reasonable damage assessment of structures subjected to earthquake excitation.

References

Chai, Y.H., Romstad, K.M., and Bird, S.M. (1995). "Energy Based Linear Damage Model for High-intensity Seismic Loading." *Journal of Structural Engineering*, ASCE, **121** (5): 857-864.

Liu, X.L., and Liu, C. (2001). "A practical method for safety classification of structural systems." *Journal of Building Structures*, **22**(1):42-47. (in Chinese)

Liu, C.M., and Liu, X.L. (2005). "Stiffness-based evaluation of component importance and its relationship with redundancy." *Journal of Shanghai Jiaotong University*, **39**(5):746-750. (in Chinese)

Gao, Y., and Liu, X.L. (2008). "Importance coefficients of components in evaluation of structure robustness." *Chinese Journal of Rock Mechanics and Engineering*, **27**(12):2575-2584. (in Chinese)

Zhang, L.M., and Liu, X.L. (2007). "Network of energy transfer in frame structures and its preliminary application." *China Civil Engineering Journal*, **40**(3):45-49. (in Chinese)

Ye, L.P., Lin, X.C., and Qu Z., et al. (2010). "Evaluating method of element importance of structural system based on generalized structural stiffness." *Journal of Architecture and Civil Engineering*, **27**(1): 1-7. (in Chinese)

Park, Y.J., and Ang, A.H.S. (1985). "Mechanistic Seismic Damage Model for Reinforced Concrete." *Journal of Structural Engineering*, ASCE, **111** (4): 722-739.

Park, R., and Paulay, T. (1975) "Reinforced concrete structures." New York: John Wiley and Sons.

Tomazevic, M., and Klemenc, I. (1997). "Seismic behavior of confined masonry walls." *Earthquake Engineering and Engineering Vibration*, **26**: 1059-1071.

Shen, J.M., Wang, C.Z., and Jiang J.J. (1993). "Finite element method of reinforced concrete and limit analysis of plates and shells." Beijing: Press of Tsinghua University.(in Chinese)

Cheng, W.R., Yan, D.H., and Tang, G.Y. (2005). "Concrete structures." Beijing: China Architecture & Building Press. (in Chinese)

Hashemi, S.A.(2007). "Seismic evaluation of reinforced concrete buildings including effects of masonry infill walls." University of California, Berkeley.

Zhang, J.C., Zhang, L.M., and Liu X.L.(2012). "A beam-and-column bassed macro model for walls and slabs." *China Civil Engineering Journal*, **45**(6): 1-12. (in Chinese)

Abaqus analysis user's manual. Version 6.6 [M]. pawtucket: Hibbit, Karlsson & Sorensen, Inc., 2005.

Chen, W.F., and Saleeb A.F. (2005). "Constitutive equations for concrete and soil." Beijing: China Architecture & Building Press.

List of captions of all figures
Figure 1 Reinforced concrete frame with masonry infill wall
Figure 2 Computational model of reinforced concrete frame with masonry infill wall
Figure 3 The acceleration of Düzce earthquake
Figure 4 Failure evolution of middle frame infilled with masonry wall
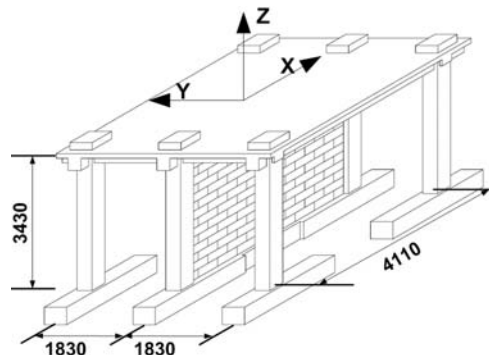
**Figure 1.**Reinforced concrete frame with masonry infill wall (Unit of dimensions: mm)
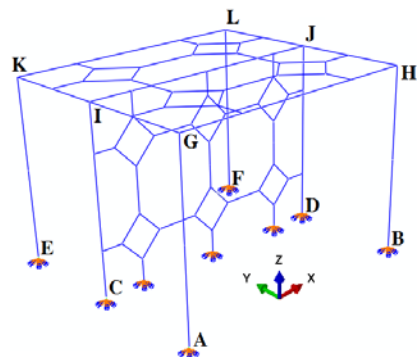
Figure 2. Computational model of reinforced concrete frame with masonry infill wall
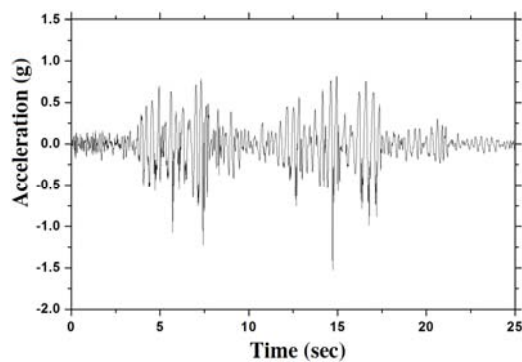
Figure 3. The acceleration of Düzce earthquake
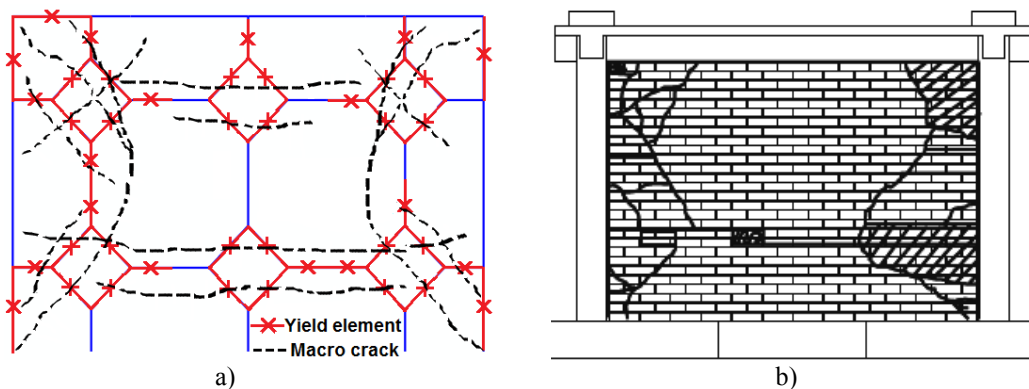
Figure 4. Failure pattern of middle frame infilled with masonry wall: (a) numerical result; (b) test result (Hashemi S.A, 2007)

List of captions of all tables

Table 1 Classification of building function state and the corresponding damage index

Damage Index	Physical Appearance	Degree of Damage	Function State
$D \geq 0.8$	Partial or total collapse of building	Collapse	Loss of function
$0.4 \leq D < 0.8$	Extensive crushing of concrete and masonry, yield of reinforcement	Severe	Irreparable, endanger life
$0.25 \leq D < 0.4$	Large macro cracks in concrete and masonry	Moderate	Repairable
$D < 0.25$	Minor cracks	Minor	Normal

Table 2 Damage indexes of each component and the overall structure

Component Number	Column -AG	Column -BH	Column -CI	Column -DJ	Column -EK	Column -FL	Slab -GIJH	Slab -IKLJ
Component Damage Index	0.577	0.533	1.14	0.838	0.577	0.533	0.325	0.325
Component Number	Beam -GH	Beam -IJ	Beam -KL	Beam -GI	Beam -IK	Beam -HJ	Beam -JL	Wall -CIDJ
Component Damage Index	0.530	0.727	0.530	0.0653	0.0653	0.127	0.127	0.792
Overall Damage Index	0.514							

Numerical Analysis on Nonlinear Behavior of the Superimposed Wall under Quasi-Static Reversed Cyclic Loading

Xun Chong[1] , **Junqi Huang**[2] , **Xianguo Ye**[3]

ABSTRACT：To evaluate seismic performance of superimposed reinforced concrete (RC) walls, six full-scale cantilever units, four representing the superimposed RC walls and two representing the cast-in-place RC walls, were tested under quasi-static reversed cyclic loading. The hysteresis property, deformation capacity and failure patterns of the superimposed walls were studied. Based on the test, micro model finite element analysis (FEA) of the six units was conducted using ANSYS, and the numerical results were compared with the test ones to validate the finite element model. The results indicate that the failure modes, hysteretic loops and envelop curves obtained by the numerical analysis agree well with the test results. The finite element model considering the concrete interface by using "contact element" can be used to simulate the behavior of horizontal joint of the superimposed RC walls. The model and parameters adopted are reasonable in analyzing the seismic behavior of superimposed RC wall.

KEYWORDS：superimposed reinforced concrete wall, seismic performance, quasi-static reversed cyclic loading test, nonlinear finite element analysis

INTRODUCTION

Structural walls are a common and cost-effective way of providing lateral force resistance to buildings in seismic areas of the world, and buildings constructed incorporating structural walls showed excellent performance during the past several earthquakes (Wood et al.1987; Fintel 1995; Holden et al. 2003; Sezen et al. 2003). In China, cast-in-place reinforced concrete (RC) has been the most commonly used method of construction for structural wall systems. More recently, there has been an increase in the research and use of precast concrete walls for its obvious advantages

---

[1] Associate Professor, School of Civil Engineering, Hefei University of Technology; 193 Tunxi Road, Hefei 230009; e-mail:chongxun_sun@163.com

[2] Graduate student, School of Civil Engineering, Hefei University of Technology; 193 Tunxi Road, Hefei 230009; e-mail:junqihuang001@163.com

[3] Professor, School of Civil Engineering, Hefei University of Technology; 193 Tunxi Road, Hefei 230009; e-mail: yexg428@aliyun.com

of providing high-quality structural members, high speed of construction and saving the cost of investment, and so on (e.g., Restrepo et al. 2007; Pavese et al. 2011).

The superimposed reinforced concrete (RC) wall studied in the paper is a kind of semi-precast RC wall which is composed of two precast panels and the cast-in-place core concrete. The truss bars which are made up of one upper chord bar, two lower chord bars and the continuous inclined web bars are prefabricated with the two precast panels, aiming to connect the precast and cast-in-place concrete together, and enhance shear resistance at the connection interface. Figure 1 depicts the detail of the superimposed RC wall and foundation.

To evaluate the seismic performance of this kind of walls, six full-scale cantilever units, four representing the superimposed RC walls and two representing the cast-in-place RC walls, were tested under quasi-static reversed cyclic loading.

Numerical analysis is another method to study the inelastic behavior of the structures. For the superimposed RC walls, horizontal joint between the wall panel and the foundation is the main region where inelastic deformation would occur, which is quite different from the cast-in-place RC walls. The micro model finite element analysis (FEA) of the six test specimens was conducted using ANSYS 12.0. For the four superimposed RC walls, contact between the interface of the new and old cast concrete was considered to simulate the behavior of the walls accurately. The numerical analysis results were compared with the test ones to investigate the validity of the numerical analysis model, which would be used for further study.
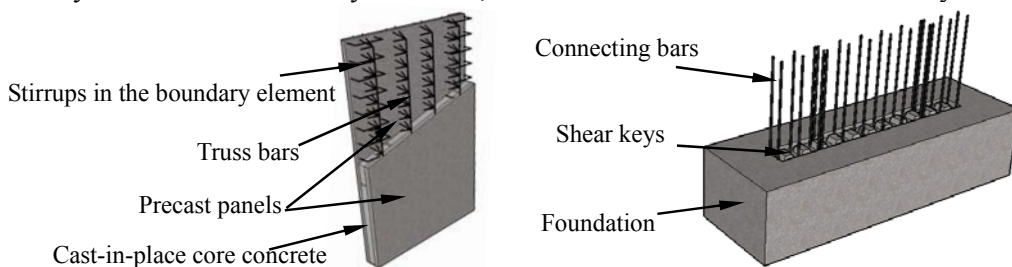

Figure 1. Detail of superimposed RC wall and foundation

EXPERIMENT DISCRIPTION

Test specimens

Six full-scale units, four representing the superimposed RC walls (W-2, W-3, W-5, W-6) and two representing the cast-in-place ones (W-1, W-4), were tested under quasi-static reversed cyclic loading. The geometry of each unit was identical, with the wall panels being 3.1m high by 1.8m long by 200mm wide. The aspect ratio of the wall panels, measured from the base to the point of application of the horizontal force was 1.67; the height-to-width ratio was 15.

As for the construction progress of the four superimposed RC walls, the foundation beams with connecting reinforcing bars were produced first, and then the precast panels were erected and placed on the beams with connecting bars sticking into the hollow core of the panels. Some rubber blocks were put under the panels to adjust the horizontality and form a gap of about 40mm height between panels and foundation beams meanwhile. The panels and foundation beams were connected together finally through pouring fine aggregate concrete in the hollow core of the

panels and the gaps between panels and foundations. Furthermore, some shear keys were prefabricated on the surface of the foundation beams to enhance the shear slip resistance ability.

Two kinds of boundary elements were adopted in the four superimposed RC walls. For W2 and W5, the whole boundary elements were cast-in-place RC members, while for W3 and W6, the boundary elements were prefabricated in the walls. Stirrups or truss rebars are arranged in both kinds of boundary elements to confine the concrete, aiming to increase the ductility of the walls.

The measured cubic compressive strength for units W1 and W4 is 30.3Mpa, while that for the other four units is 28.8Mpa. Deformed longitudinal and transverse reinforcement was incorporated in all units (see Figure 2), and the mechanical properties are summarized in Table 1.

Table 1. Mean values of mechanical properties of the reinforcement

Specimen	d(mm)	f_y (MPa)	f_u (MPa)	f_u/f_y
W-1&W-4	10	479.6	633.2	1.32
	12	503.8	614.9	1.22
W-2, W-3,	8	589.2	638.9	1.08
W-5, W-6	10	560.5	603.8	1.08

d: diameter; f_y: yield strength; f_u: ultimate strength.

Test setup and procedure

The schematic of the test setup is shown in Figure 3. The lateral load was applied to the specimens through the 1000kN servo-controlled hydraulic actuator. For W1~W3, an external downward axial load of about 740kN was applied at the centerline of the wall at the top, while for the other three units, no axial load was applied. Reversed cyclic quasi-static lateral loading was applied in load control first, and after yielding of the units, displacement control method was adopted. The test terminated when the lateral load dropped to about 85% of the maximum strength.

The lateral displacement was measured by linear voltage differential transducers (LVDTs) at the same height of the loading point as well as the displacement transducers inside the hydraulic actuator. A computer aided data acquisition system was utilized to record the data from strain gauges and LVDTs.

(a) W-1 and W-4   (b) W-2 and W-5

(c) W-3 and W-6   (d) 1-1 section   (e) 2-2 section
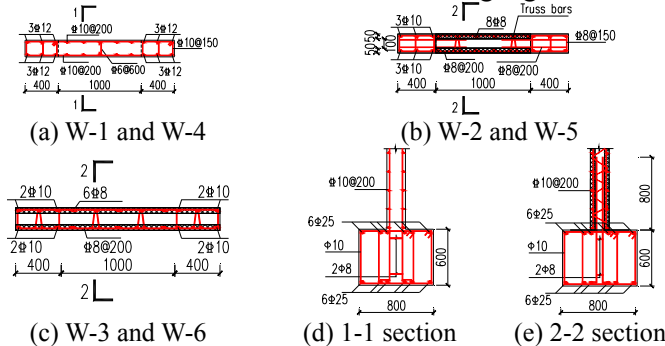
Figure 2. Reinforcement of test specimens

Figure 3. Schematic of the test setup

Test results

Behavior of the four superimposed RC walls during the test was quite different with that of the two cast-in-place ones. The cast-in-place concrete specimens

performed as the usual ductile elements, several major cracks scattered evenly at the bottom part of the wall under the application of lateral loads into inelastic range, and the walls was damaged severely at the end of the test. While for the superimposed walls, the primary mode of displacement occurred through gap opening at the horizontal joint between the panel and the foundation, allowing the wall to undergo large lateral displacements with little damage. Since the inelastic deformation focused at the horizontal joint, the reinforcing bars across the joint endured large elongation, inducing decrease of the ductility for the superimposed walls.

The superimposed RC walls with different kinds of edge components behaved quite similarly, except that much less cracks appeared on the surface of the wall with superimposed boundary elements, since the strength of the precast concrete is higher and the quality is better. Until broken of the units, none vertical crack appeared along the interface of precast and cast-in-place concrete, and the lateral bending cracks extended from the boundary elements to the precast panels smoothly, indicating that the old and new concrete could work well together. Moreover, owing to the bolting effect of the longitudinal reinforcements, friction of the concrete and extrusion of the shear keys, no obvious shear slip appeared at the horizontal joints. Figure 4 depicts the failure modes of the specimens. Figure 5 shows the damage of the wall toes on W-1, W-2, W-3 respectively.
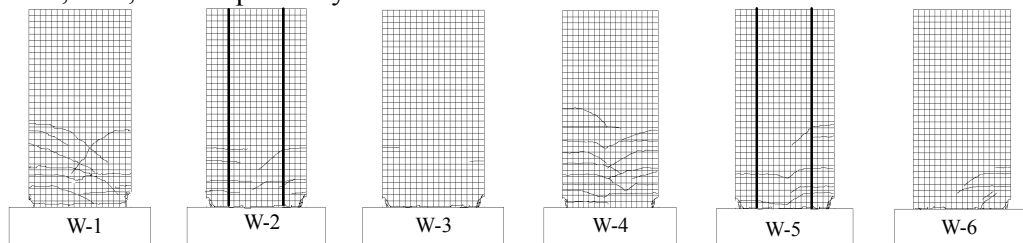

Figure 4. Failure mode of test specimens

Figure 5. Damage of the wall toes on W-1, W-2 and W-3

NUMERICAL SIMULATION

Numerical models of the designed walls was established using nonlinear finite element analysis program ANSYS. In this work, the following issues were considered:

1. The cracked concrete was defined by a smeared crack model.

2. Full bond was assumed between the concrete and reinforcements.

3. The superimposed wall was assumed to be an integrated unit, and contact effect between the precast panel and the cast-in-place concrete core was not considered.

Material constitutive models

The 3D solid element (SOLID65) was adopted for concrete elements in the study. ANSYS provides a number of kinematic and isotropic hardening plasticity options that can be used to model the compression behavior. A multi-linear isotropic

(MISO) compressive stress-strain curve for concrete combined with the tensile failure criteria of William-Warnke (William et al. 1975) formulation (CONC) was used to define the plastic behavior of concrete. The uniaxial stress-strain relationship is obtained using the Hongnestad model, the relationship between the stress (f_c) and strain (ε_c) of concrete in compression is assumed to be a parabolic curve for the strain under ε'_c and constant afterwards, as follows:

$$f_c = f'_c \left[2\left(\frac{\varepsilon_c}{\varepsilon'_c}\right) - \left(\frac{\varepsilon_c}{\varepsilon'_c}\right)^2 \right]; \quad \varepsilon_c \leq \varepsilon'_c \tag{1a}$$

$$f_c = f'_c; \qquad \varepsilon'_c \leq \varepsilon_c \tag{1b}$$

Where f_c and ε_c are the compressive stress and strain of concrete, f'_c and ε'_c are the compressive strength of concrete and the corresponding strain.

Additional concrete material data, such as the shear transfer coefficient β_t for open cracks and β_c for closed cracks are also needed for the concrete constitutive material data table. Typical shear transfer coefficients range from 0.0 to 1.0, with 0.0 representing complete loss of shear transfer and 1.0 representing no loss of shear transfer. A value of 0.3 and 0.8 was used in the model for β_t and β_c, respectively.

Steel bar is an isotropic and homogeneous material which shows similar behavior under tension and compression. The 3D spar element (LINK8) was adopted for reinforcements in the study, for which a multi-linear kinematic hardening model and the Von Mises yield criterion were adopted. The 3D solid element (SOLID45) was utilized for the loading pad at the top of the walls.

Contact element used in the superimposed wall

For the superimposed walls, the horizontal joint between the wall and the foundation was simulated through contact element. The 3-D surface-to-surface contact element (CONTA174) and 3-D target element (TARGE170) were used for the contact and target surfaces respectively since the contact is between two different surfaces. Surfaces at the bottom of the wall were designated as contact surfaces while surfaces at the top of the foundation beam were considered target surfaces. Since no obvious shear slip occurred at the horizontal joint, horizontal degree of freedom in superposition nodes on the interface was coupled.

For this model, additional contact data, such as the contact algorithm, normal penalty stiffness factor (FKN) and penetration tolerance factor (FTOLN) were needed for the contact data table. Typical normal penalty stiffness factor range from 0.01to 10 and higher stiffness values decrease the amount of penetration. Penetration tolerance factor is a tolerance factor to be applied in the direction of the surface normal (ANSYS user's manual). Inappropriate value of FKN and FTOLN will cause convergence problem. For FKN, a value of 1 can help in achieving a quicker convergence, and the default value of 0.1 was adopted for FTOLN.

Meshing, loading and boundary condition

Taking the superimposed unit W-3 for example, Figure 6 illuminates the finite element model, including the reinforcement and contact elements, and the meshing and boundary condition.

The model should be meshed carefully for achieving convergence. A value of 150mm in meshing size was adopted for achieving a quicker convergence and a precise result.

Nodes at the bottom and edge of the beam foundation are restrained in all translational degrees of freedom. The horizontal degrees of freedom of the nodes on the loading pad at the top of the wall panel are coupled to ensure all the nodes associated with this area move together. Constraint equations (CEINTF) were adopted to constrain the rebar with the concrete.

The applied cyclic displacements were divided into a series of increments called load steps and load substeps. At the end of each incremental solution, ANSYS adjusts the stiffness of the model before proceeding to the next incremental load step in order to reflect the nonlinear changes in the stiffness of the model. To control load step size increments, the automatic time stepping option (AUTOTS) is turned on in this study. The model stiffness is updated in ANSYS by Newton-Raphson equilibrium iterations with the maximum number of 50.

The loading in the test was applied as follows:

1. For W-1 W-2 W-3, an axial pressure of 2MPa was applied to the loading pad to develop an axial load ratio of 0.1.

2. Cyclic loading was applied to the master coupled node at the top surface of loading pad through displacement loading.


(a) Meshing of model   (b) contact element and reinforcement   (c) Boundary conditions
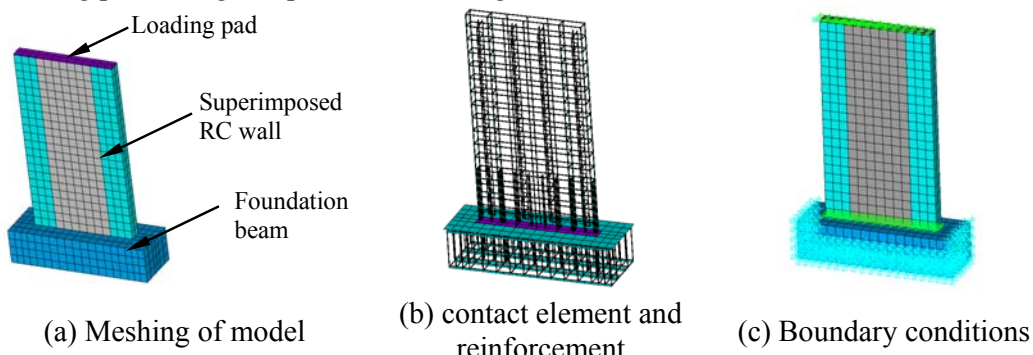
Figure 6. Finite element model of the unit W-3

Comparison between the test and analysis results

The load-displacement hysteretic curves and envelope curves of the specimens obtained from the test and the analysis are plotted in Figure 7, 8 respectively. It is shown that the shape of the hysteresis loops obtained from the numerical analysis agrees well with the test results, except that more residual deformation was attained at large displacement for the unit W-2 and W-3 with contact elements. For unit W-4~W-6, both the numerical and test hysteresis loops present pinching effects, since no axial loads was applied to the two units, and the shear deformation took a higher proportion. For W-1 and W-4, the analyzed peak loads are greater than those of the test results (within 20%) in the last stages of the cyclic loading, and for W-2, the analyzed peak loads are greater than those of the test results (within 10%) in the middle stages but almost the same in the last stages of loading cycles. The difference between the analysis and test results at different stages of loading could be attributed to the mesh refinement, idealized boundary conditions in the finite element model, and material nonlinearity.

Taking unit W-1~W-3 for example, the comparison of failure patterns between the test and numerical analysis results is presented in Figure 9. For the analysis results, crushing trend can be observed at the wall base from the 3rd principal plastic strain contour plot. It could be found that the failure pattern achieved by the finite element analysis is quite similar to that observed in the test. For the cast-in-place RC walls, range of concrete with large strain is relative wide. While for the superimposed RC walls, the panels rocked around the horizontal gaps during inelastic loading stage, and crushing of concrete was restricted to the bottom corners of the wall.
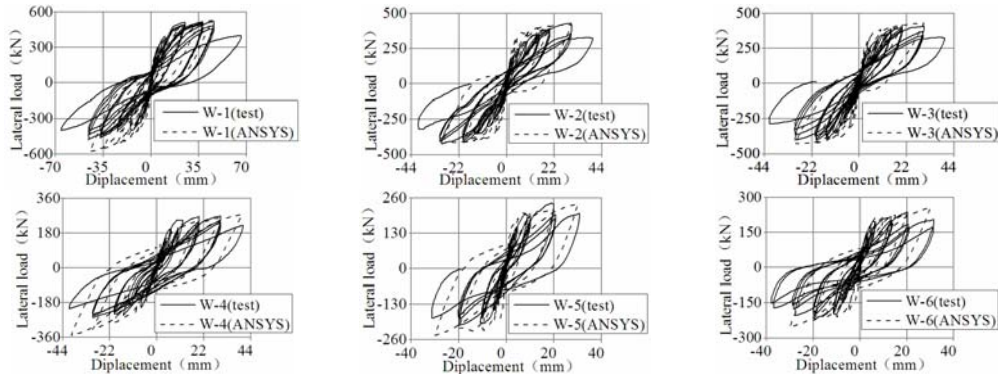

Figure 7. Comparison of hysteretic curves
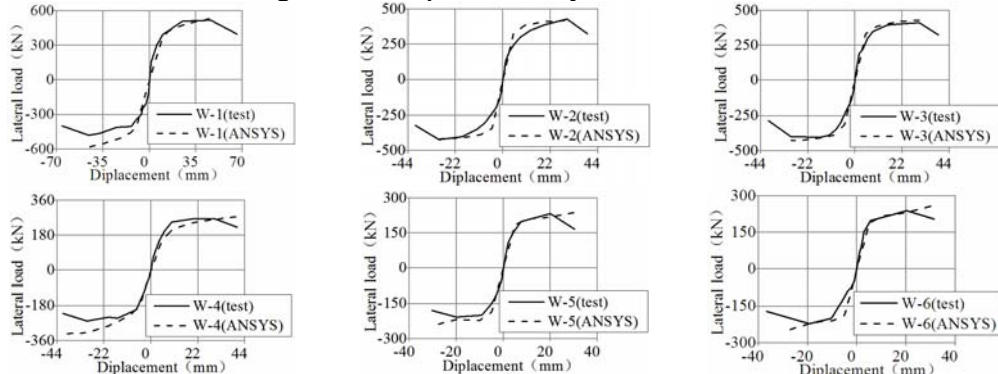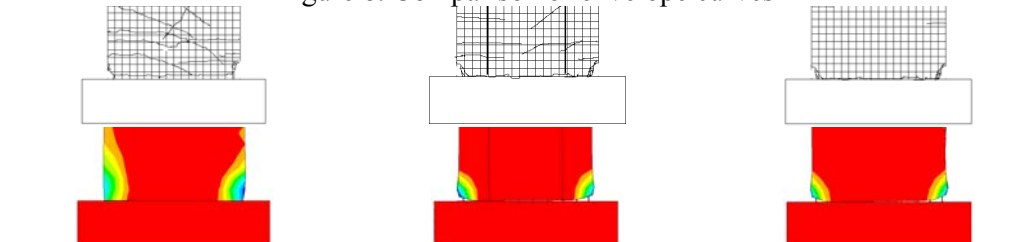
Figure 8. Comparison of envelope curves

(a) Failure pattern of W-1   (b) Failure pattern of W-2   (c) Failure pattern of W-3
Figure 9. Comparison of failure patterns between test and analysis results

CONCLUSION

Four superimposed RC walls and two cast-in-place RC walls were tested under quasi-static reversed cyclic loading, and then inelastic numerical analysis of the six test specimens was conducted using ANSYS. The results and discussions presented in this paper allow the following conclusion to be drawn:

(1) For the superimposed RC walls, the primary mode of displacement occurred through gap opening at the horizontal joint between the panel and the foundation, which is quite different with the conventional cast-in-place RC walls.

(2) Since the inelastic deformation of the superimposed walls focused at the horizontal joint, the reinforcing bars across the joint endured large elongation, inducing decrease of the ductility for the superimposed walls.

(3) The behavior of the superimposed RC walls with different kinds of edge components had no obvious difference during the test.

(4) The failure mode, hysteretic loops and envelop curves obtained by the numerical analysis agree well with the test results, indicating that the finite element model with consideration of the concrete interface by using "contact element" are capable of simulating the behavior of horizontal joint of the superimposed RC walls.

(5) The model and parameters adopted are reasonable for analyzing the seismic behavior of superimposed RC wall, and could be used in further study.

ACKNOWLEDGEMENT

REFERENCES

ANSYS Version 12.0, User's and Theory Reference Manual, 2009.

Fintel, M. (1995). "Performance of buildings with shear walls in earthquakes of the last thirty years." *PCI J.,* 40(3), 62-80.

Holden, T., Restrepo, J., and Mander, J. B. (2003). "Seismic Performance of Precast Reinforced and Prestressed Concrete Walls." *Journal of Structure Engineering*, 129(3), 286-296.

Pavese, A., Bournas, D. A. (2011). "Experimental assessment of the seismic performance of a prefabricated concrete structural wall system." *Engineering Structures,* 33(6), 2049-2062.

Restrepo, J. I., and Rahman, A. (2007). "Seismic performance of self-centering structural walls incorporating energy dissipators." *Journal of Structural Engineering,* 133(11), 1560-1570.

Sezen, H., Whittaker, A. S., Elwood, K. J., and Mosalam, K. M. (2003). "Performance of reinforced concrete buildings during the August 17, 1999 Kocaeli, Turkey earthquake, and seismic design and construction practise in Turkey." *Engineering Structures,* 25(1), 103-114.

Willam, K. J., Warnke, E. D. (1975). "Constitutive model for the triaxial behavior of concrete.", *Proc., Int. Association for Bridge and Structural Engineering,* ISMES, Bergamo, Vol. 19, 1-30.

Wood, S. L., Wight, J. K., and Moehle, J. P. (1987). "The 1985 Chile earthquake, observations on earthquake-resistant construction in Vina del Mar." *Civil Engineering Studies, Structural Research Series No. 532,* Univ. of Illinois, Urbana, Illinois.

The rationality of the geometric topology of cable dorms

Danbing Long[1], Qin Zhang[2], Xila Liu[3]

Abstract: To discuss the robustness of a structure in terms of the rationality of its geometric topology, the relative importance for components is considered as the key. Firstly in this paper, the sphere of the influence that caused by the local damage on one component is analyzed, as well the influence distribution map of the local damage is plotted. And then, the quantity of the sphere of influence is proposed and defined as the relative importance for the component. Based on the obtained influence distribution map and the quantitated relative importance, the optimization of the geometric topology of a cable dome to improve its robustness can be further considered. Finally, as an example, the analysis of a Geiger cable dorm is implemented to prove the effectiveness of the presented method, meanwhile the roles of the influence distribution map and the quantitated relative importance in optimizing the system are shown.

Keyword: robustness; topology; cable dome; quantitates analysis; optimization

1. Introduction

The cable dome is known as a very efficient flexible structure for its low redundancy. However, the most remarkable advantage also make it vulnerable. Lots of efforts have been done on optimizing the classical cable dome to make it robust, and a lot of new types have emerged (Xue et al. 2011). While, it is believed that robustness assessment in terms of the rationality of its geometric topology was missing in the designs. Consequently, some of the optimizations made themself less competitive because of that the redundancy was increased largely and the domes became just less vulnerable slightly.

The robustness of a structure is generally defined as the property of system to maintain its function in risk event. 'In a robust structure, no damage disproportionate to the initial failure will occur (Baker et al. 2008). Literally, the components of a robust structure should be arranged in a topologically rational way to avoid the aggressive damage. The cable dome is no exception.

In this work, the relative importance of the most important component was considered as the key to index the rational topology. Firstly, by introducing a local damage to one component, the influence distribution map of the damage was plotted and the relative importance of the component defined by the quantity of the sphere of the influence was proposed. Naturally, the most important component was detected. And then a topological optimization for decreasing its relative importance in terms of geometry was presented. Finally, a Geiger-type cable dome was analysis and optimized to illustrate the purposeful optimization under the instruction of the proposed method.

---

[1] Lecture, Dept. of Civil Engineering, Southwest Jiaotong Univ. (corresponding author). E-mail: lornalong@163.com

[2] Engineer assistant, Chengdu JZFZ architectural design CO.LTD. E-mail: zhangqin05@163.com

[3] Professor, Dept. of Civil Engineering, Shanghai Jiaotong Univ. E-mail: xilaliu@tinghua.edu.cn

2. The topological analysis
2.1 The influence

It has to point out that the cable dome is quite different from the so-called rigid system. Because that when a cable totally slacks, the part of the system or even the whole system will encounter a failure, the method which removes a component conceptionally for analyzing the rigid structures is invalid (Gao and Liu 2012; Gao and Liu 2013). Therefore, the local damage sketched in fig. 1, in this work, is introduced and defined as the loss of the section area, and 'local' implies a very short section.

A rate of the area loss denoted by β is recommended by

$$\beta_{\text{rec}} = \frac{A_{\text{damaged}}}{A} \leq \frac{\sigma_0}{[\sigma]} \qquad (1)$$

Where, A notes the area of the section, σ_0 denotes the responding stress of the original component which is to-be damaged, $[\sigma]$ denotes the yielding stress of the same component. And the reason of recommending Eq. 1 is that when the plastic deformation grows, the influence of the damage becomes prominent.

Now that the local damage is factitiously introduced, to characterize the influence of the local damage, the change of the strain energy of each component (with the damaged section excluded) is taken in this paper, for its ability to represent the retributions of the inner forces and the deformations. Therefore, the influence on the component i caused by the local damage on the component k is defined as

$$\zeta_i^k = \left(1 - \frac{U_i^k}{U_i}\right) \times 100\% \qquad (2)$$

Where, U_i is the strain energy of the component i in the undamaged system, U_i^k is the strain energy of the component i which has changed for the damage on the component k. The cable is nearly slack when ζ_i^k is close to 100%, moreover when the inner force increases in the cable, ζ_i^k is negative, the limitation of which is defined as

$$\left(\zeta_i^k\right)_{\min} = \left(1 - \frac{\left(U_i^k\right)_{\text{Yield}}}{U_i}\right) \times 100\% \qquad (3)$$

Where denotes the strain energy of the component i when itself yields. Apparently, ζ_i^k should be a number between $(\zeta_i^k)_{\min}$ and 100%. It should be noted that the bars under pressure will not be discussed in this paper.

In the case that the relative importance is targeted, it is not necessary to over fractionize the influence with 1% as the smallest unit. Thus, the grading rule is employed as table 1. From table 1, it is obvious that when

$$G_i^k \geq G_k^k \qquad (4)$$

Where G_k^k is the grade of the influence to the component k itself and G_i^k is the grade of the influence to the component i, there is a trend that the component i will be no longer in force following the failure of the component k. To make it simple and clear, the component i that satisfying Eq. 4 is called 'the slacking component' in this paper.

2.2 The influence distribution map

Based on the grades of the influence, the distribution map could be plotted as the one sketched in fig. 2. With the numbers and the colors representing the grades, the sphere of the influence could be understood simply and visually.

It suggests that the distribution map must be applied relative to the functional requirements of the cable dorm when contemplating the robustness.

2.3 Quantitated the sphere of the influence

To represent the influence of the local damage to the system in its entirety, as well as to quantitate the sphere of the influence, the quantitative indicators indicated by *R* is proposed and defined as

$$R_k = \sum_{G=0}^{10} \left(G \times n_G^k \right) \qquad (5)$$

Where, R_k denotes the quantitative indicators of the influence of the local damage to component *k*, *G* is the grade of the influence, and n_G^k denotes the number of the components of which the grades are assessed at *G* when the local damage occurs to the component *k*. Comparing the *R* values of all the cables, the partial damaged component with the largest *R* value is considered to have the most severe influence to the whole system. In another word, the component with the largest *R* value is the most important one in the system. Consequently, in this work, the relative importance of the component is represented by the quantitative indicators *R*.

As a conclusion, the most important thing now in the optimization of the cable dome becomes decreasing the largest *R* value to achieve that there are no fatal cables who are relatively over-important.

3. Example

The well-researched and widely used Geiger's cable dome is analyzed and optimized in terms of its topology in this section. A small-scale Geiger's cable dome with the geometry and the dimensions shown as fig. 3, which is subjected to the equivalent loading also depicted in fig. 3 as well, is designed according to Technical specification for cable structures (J1402-2012, Industry standard of PRC). The elastic-perfectly plastic material of the cable with elastic parameters $E = 1.8e5MPa$ and $v = 0.3$ as well as yield stress $\sigma = 1636MPa$ is assumed.

3.1 Analysis

Because of the symmetries both in geometry and the loading, only 5 cables with the circled number from 1 to 5 shown in fig. 3a , which are called interior rigid cable, interior diagonal cable, hoop cable, outer rigid cable and outer diagonal cable respectively, are factitiously partially damaged, and the 5 models with different local damages are numerically analyzed. The strain energy of all the cables in all the models are also calculated automatically. According to Eq. 2 and table 1, the grades of the influence from the damage on each cable are obtained and recorded in table 2. The *R* values are also computed according to Eq. 5 after that the grades of the influence are determined, and noted both in table 2 and fig. 4. From the histograms in fig. 4, it is obvious that the cable ③ and the cable ⑤ which are the hoop cable and the outer diagonal cable, are relatively much more important than others.

By plotting the influence distribution map based on the data, the sphere and the extent of the influence from the local damage can be observed. For the hoop cable

and the outer diagonal cable are endowed the relatively larger R values, there are two distribution maps of them are displayed in fig. 5a and fig. 5b respectively to investigate the rationality of their topologies. Meanwhile, a distribution map for the outer rigid cable is also plotted as a comparison in fig. 5c.

From fig. 5a, one can find that all the cables become the slacking cables, in another word, the whole system is going to collapse after that the hoop cable is broken. Moreover, fig. 5b shows that the failure of the outer diagonal cable has the great opportunity to lead to the breakdown of the top of the entire system. While, fig. 5c illustrates that only four cables along the arrow slack as a result of cutting off the outer rigid cable.

Incorporating the function of the cable dome into the analysis above, it can conclude that the topology of the outer rigid cable is acceptable, while the topologies of the hoop cable and the outer diagonal cable must be optimized.

3.2 The topological optimization

The common way to improve the system is to increase a bunch of cables to play the roles of the hypothetically damaged ones. In this work, it will be done purposefully. Now that the fatal cables in this example are identified, then the next questions are clear to be how many cables must be increased as well as how to arrange them. Firstly, the alternates of the hoop cables must be introduced. To play the role of hoop cable 1 shown in fig. 6a, the increased alternate must be settled in the shadow (1) composed by slashes as sketched in fig. 6a.The same rule is employed in introducing alternates for the rest hoop cables. Besides, the introduced cable should be able to take the place of the outer diagonal cable, thus the scope for the layout of it is narrowed down to the shadow (2) sketched in fig. 6a composed by dots.

With a view to the symmetries, cable 1 and cable 2 as shown in fig. 6b are chosen to be the alternates of the hoop cable 1, the hoop cable 2 as well as the outer diagonal cable 1. To make it concise, the increased cables are better to joint together as the same as cable 1 and cable 3 do in fig. 6b, meanwhile, the original outer diagonal cables are all removed in the final decision.

Going through all the improvements, the optimized Geiger Cable Dome is proposed and illustrated in fig. 7. There is no denying that the redundancy of the cable dome is increased, yet it is not increased too much.

3.3 The analysis of optimized system

Based on the numerical results, the bar graphs of the R values of all cables in the optimized dome are depicted in fig. 8. It shows that the R values of the cable ② to ⑤ are on the whole the same, namely, there no longer exists a cable which is relatively over important in the optimized cable dome.

The influence distribution maps of the cable ③ to ⑤ represented the hoop cable, the outer rigid cable and the new outer diagonal cable respectively, are plotted in fig. 9. From the figures, the limitations of the sphere of the influence from different local damages are observed. Thus from the topological point of view, the optimized system is much more rational than the original one, and its robustness is greatly improved by just increasing 6 cables.

4. Conclusions

In this work, a concept in terms of the rationality of its geometric topology which

named the sphere of the influence of the local damage to a cable was proposed and the influence distribution map based on the concept was also presented. Meanwhile, its quantitation which called the *R* value was proposed as well to index the relative importance of the cables and to further instruct the robustness optimization of the system.

In the analysis of the original system, the effectiveness of the *R* values and the influence distribution maps were proved. On the basis of the numerical results, the optimization of the system was done purposefully in terms of the geometry and topology. By analyzing the optimized system, it concluded that the robustness of the system was dramatically improved and the improving method was efficient.

References

Baker, W.J., Schubert, M., and Faber, H.M. (2008). "On the assessment of robustness." *Struct. Safe.*, 30, 253-267.

Gao, Y. and Liu X.L. (2013). "Weighted graph form of structures and its application in robustness analysis." *J. Shanghai Jiaotong Univ. (Science)*, 18(2), 216-223.

Gao, Y. and Liu, X.L. (2012). "Quantitative robustness analysis of reinforced concrete frames." *Selected Peer Reviewed Papers from 2012 2nd Int. Con. Civil Eng. Build. Mater.*, *CEBM*, HK, 787-793.

Xue, S.D., Gao, Z.Y., and Li, X.Y. (2011). "Research Status and Prospects of Cable Domes." *Appl. Mech. Mater.*, 94-96, 1424-1432.

The list of figures:
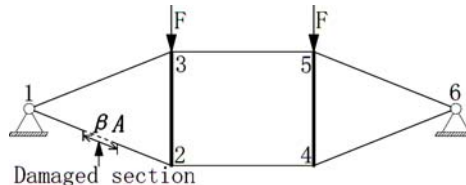
Figure 1 the schematic diagram of the local damage factitiously introduced to a cable
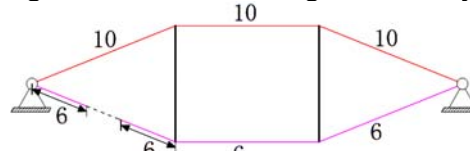
Figure 2 the schematic diagram of the influence distribution map

(a) Front view   (b) Perspective view
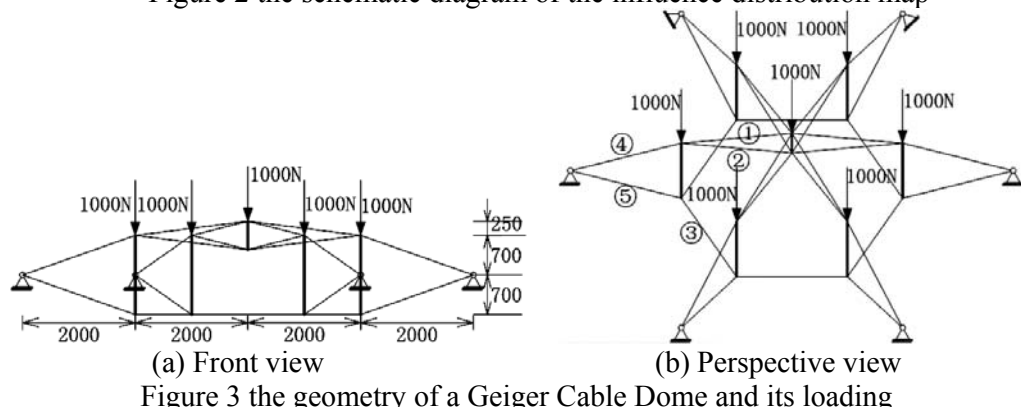
Figure 3 the geometry of a Geiger Cable Dome and its loading
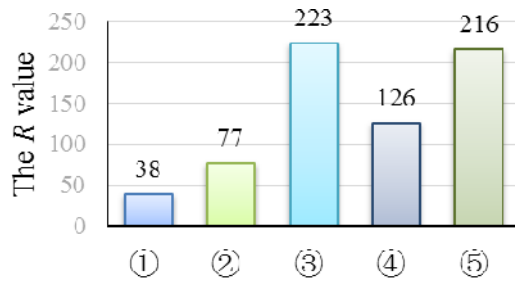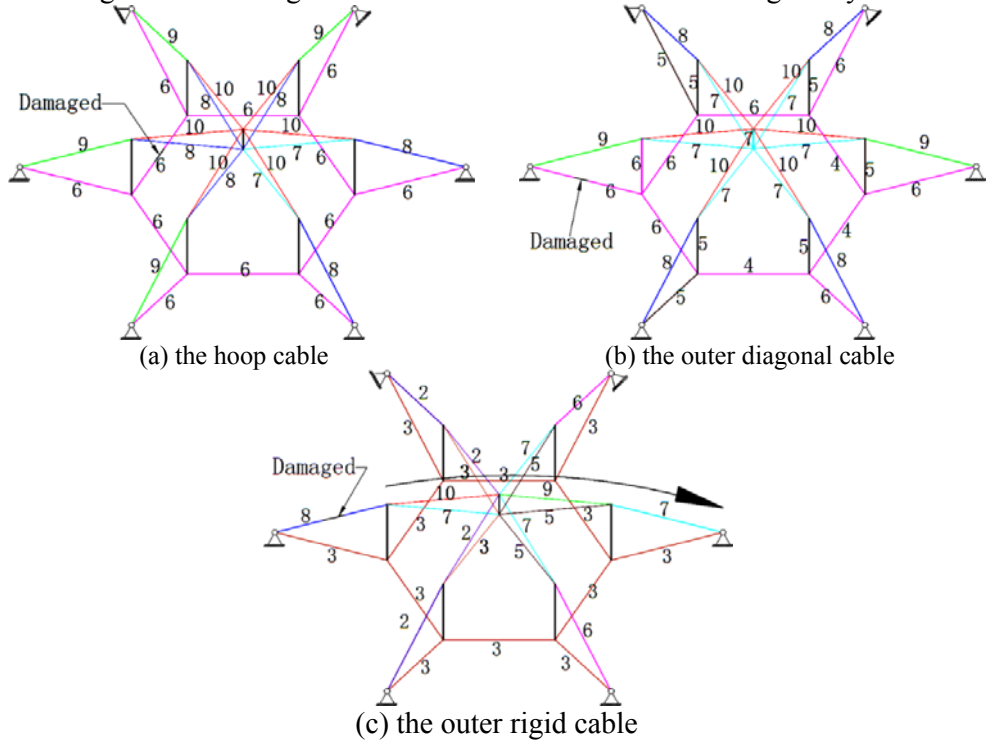
Figure 4 the histogram of the R values of cables in the original system

(a) the hoop cable   (b) the outer diagonal cable

(c) the outer rigid cable

Figure 5 the influence distribution maps of the cables in the original system

(a) the analysis   (b) the final decision
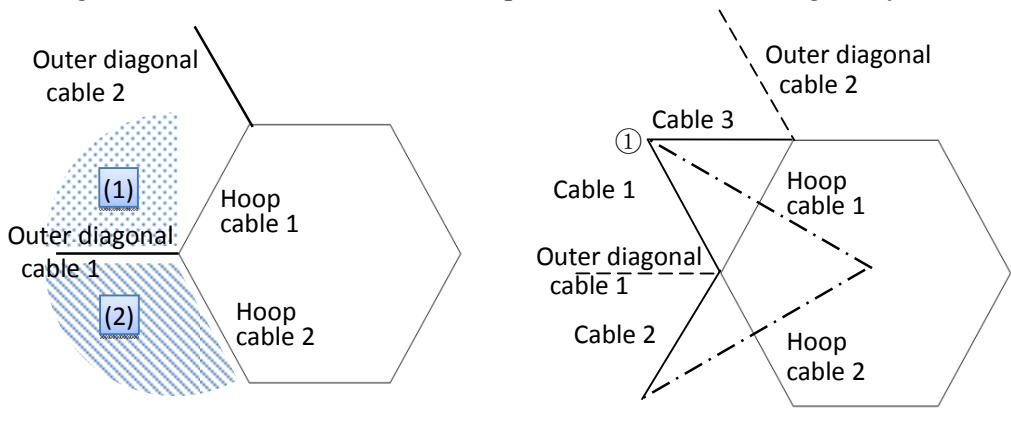
Figure 6 Fig.4-3 Improvements for the hoop cable and the outer diagonal cable

(a) Front view   (b) Perspective view
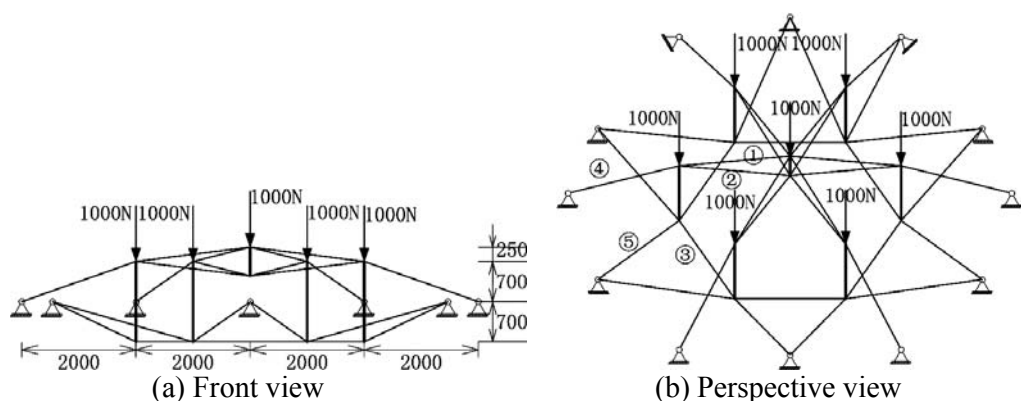
Figure 7 the geometry of the optimized Geiger Cable Dome and its loading
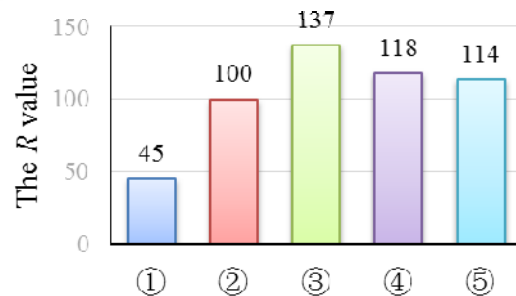
Figure 8 the histogram of the R values of cables in the optimized system

(a) the hoop cable   (b) the outer rigid cable

(c) the new outer diagonal cable
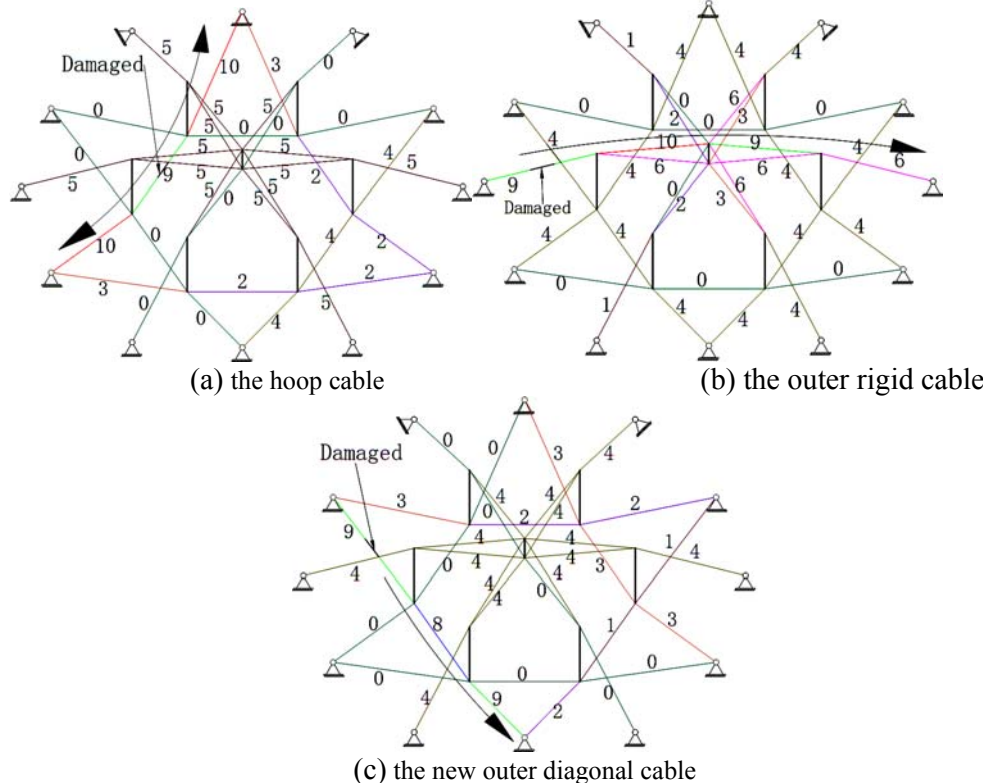
Figure 9 the influence distribution maps of the cables in the optimized system

The list of tables:

Table 1 grades of the influence denoted by G based on ζ_i^k

G	10	9	8	7	6	5
ζ_i^k （%）	90-100	80-90	70-80	60-70	50-60	40-50

G	4	3	2	1	0
ζ_i^k （%）	30-40	20-30	10-20	0-10	$(\zeta_i^k)_{\min} \leq \zeta_i^k \leq 100\%$

Table 2 the grades G and the R values of the analyzed cables

Partial damaged cable	The grades of the influence G											R
	10	9	8	7	6	5	4	3	2	1	0	
① interior rigid cable	0	0	0	0	1	0	1	2	3	16	6	38
② interior diagonal cable	2	1	2	0	0	0	2	1	5	11	5	77
③ hoop cable	6	4	5	3	11	0	0	0	0	0	0	223
④ outer rigid cable	1	1	0	4	2	3	1	14	3	0	0	126
⑤ outer diagonal cable	6	2	4	6	9	2	0	0	0	0	0	216

Topology-based Quantitative Analysis of Structural Robustness

Yang Gao [1] and **Xi-La Liu**,[2]

Abstract: Robustness has been recognized as the ability of a structure to maintain stable functioning in the face of local damages. The purpose of the robustness analysis is to quantify such an overall performance and to identify the defect of the structural topology. This paper presents a methodology to quantitatively analyze the structural robustness from the topological point of view. In the proposed method, the structural failure is viewed as a transformation and feedback process between the damage input and the failure output. By using the uncertain disturbance and the topological change of the structure to respectively measure such two quantities, the transfer matrix is established not only to describe the structural topology, but also to determine the operation of the closed-loop system. By studying the related properties of the transfer matrix, the importance of each loading path, the robustness of the entire structure, as well as the most vulnerable part of the system can be found concisely.

Key words: Structural robustness; Structural topology; Closed-loop system; Transfer matrix.

Introduction

Structural robustness is the ability of a structure to avoid a disproportional collapse under sudden events (Liu 1997). It has been concerned as an important complement of the traditional cognition of the structural safety (Liu 2001). In most of the existing design codes, the analysis of the structural safety which eventually comes down to the calculation of the specific member of the structure does not truly reflect the safety of the overall system. And such flaw has become one of the key reasons of several high profile system failures, such as the world trade center in 2001. In order to promote the structural analysis from the member level to the system level, the structural topology is necessary to be studied.

Most of the existing research of structural robustness is aimed at the sensitivity of the

[1] Doctoral student, Dept. of Civil Engineering, Shanghai Jiaotong Univ., No.800 Dongchuan Rd., Shanghai 200240, P.R. China (corresponding author). E-mail: gaoy-02@163.com

[2] Professor, Dept. of Civil Engineering, Shanghai Jiaotong Univ., No. 800 Dongchuan Rd., Shanghai 200240, P.R. China. E-mail: xilaliu@tinghua.edu.cn

structural performance to local damages. With different emphasis, the structural performance can be chosen as the failure probability (Lind 1995), the formedness (Pinto et al 2002), the energy transferring (Zhang et al 2001) or others. Through the sensitivity analysis, the importance of a specific part of the structure can be observed directly. And it effectively solves the problem about the coupling of random variables of the load effect and structural resistance. However, in the previous research, the modes of initial damage and structure unzipping were mostly chosen artificially. In addition to be greatly different from the reality, these treatments were based on the simple collection of the member importance. The corresponding robustness analysis has not been up to the system level, yet.

In the present paper, the structural collapse is viewed as a transformation and feedback process between the damage input and failure output. The most important factor to promote the operation of the closed-loop is thought as the rationality of the structural topology. And it is described by the transfer matrix between the uncertain disturbance and the topological change. By studying the related properties of the transfer matrix, the relation and difference between the member importance and structural robustness are discovered.

Structural Topological Relationship and Feedback Model

Topology is a major area of mathematics concerned with the most basic properties of space, such as connectedness, continuity and boundary (Wilson 1985). This concept is also available in the structural analysis. Let the joints and members of the structure be the corresponding vertexes and edges of the graph, and let the member mechanical characteristic be the weight of the edge. The structural system can be described by a weighted graph.

Under sudden events, the weight of each edge inside the structural graph is not a constant. It changes by the inner fore redistribution which is the consequence of the structural degradation. It causes the damage spread, indicates the interconnectedness of the members and shows the structural ability of the inner force redistribution. This means that the failure process is mainly determined by the rationality of the structural topology, although the structure collapse is affected by many uncertainties which come from the material failure mechanism, the structure dynamic conditions and the block impact effect.

In any moment of the failure process, there is an intermediate state consisting of the current structure, the damage and the dynamic condition. This state can be viewed as is formed by applying a specific damage on the original structure. Due to the inner force redistribution, new breaking occurs inside the structure to form a failure output. The failure output records the total destruction and the structural response of the current state, and becomes the damage input of the original structure in the following state (see Fig.1).
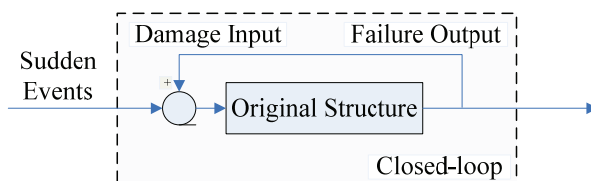
Fig.1 Feedback form of structure collapse

Furthermore, the nominal state of static equilibrium is defined as is achieved by the damaged structure to statically resist the external loading in the linear stage with no subsequent failures. By comparing the nominal equilibrium state of the damaged structure and the real equilibrium state of the original structure, the topological difference indicates the change of the working condition and interaction of each member. It indirectly measures the failure output in the current state. In a similar way, the uncertain disturbance which is the reason of the topological change can be used to measure the damage input. Thus, the transformation in the dashed line in Fig.1 can be transferred to a closed-loop (see Fig.2(a)).

If the structural topology is unreasonable, a small uncertain disturbance may cause a disproportional topological change and a probably large failure output. The damage input and the uncertain disturbance of the following state will be most likely to increase. As the consequence of the feedback process, the damage spreads and the structure collapses. On the contrary, if the structural topology is insensitive to the uncertainty, the progressive collapse will be avoided. In this way, the closed-loop can be simplified as Fig.2(b) to highlight the core effect of the structural topology and also to draw the essence of the structural robustness from the complicated collapse process. The quantitative analysis of the structural robustness can then be achieved by studying the sensitivity of the topology to the uncertainty.
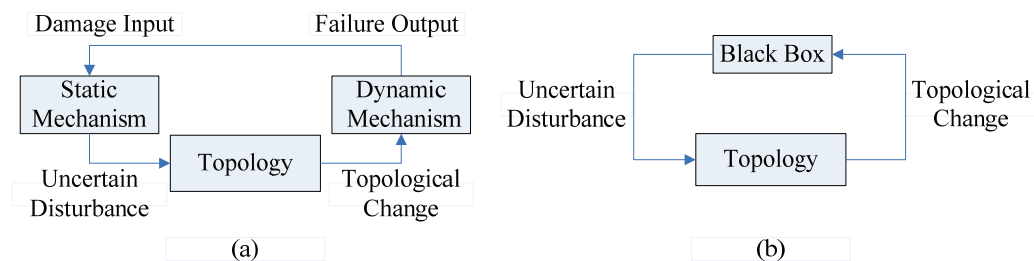
Fig.2 (a) Transferred closed-loop; (b) Integration of complex information

Structural Robustness Theory
Uncertainty of the system

In a particular moment of the failure process, the real equilibrium state of the original structure and the nominal equilibrium state of the damaged structure are shown below.

$$\begin{cases} \mathbf{KV} = \mathbf{R} \\ (\mathbf{K} - \delta\mathbf{K})(\mathbf{V} + \delta\mathbf{V}) = \mathbf{R} - \delta\mathbf{R} \end{cases} \tag{1}$$

where $\mathbf{K}$ = the structural stiffness matrix; $\mathbf{V}$ = the nodal displacement vector; $\mathbf{R}$ = the external loading vector; δ stands for the change of each physical quantity. Furthermore, $\delta\mathbf{V}$ can be solved from Eq.(1) as shown in Eq.(2).

$$\delta\mathbf{V} = (\mathbf{K} - \delta\mathbf{K})^{-1}(\delta\mathbf{KV} - \delta\mathbf{R}) = (\mathbf{K} - \delta\mathbf{K})^{-1}\mathbf{a}\delta\mathbf{P} = \mathbf{K}^{-1}(\mathbf{I} - \delta\mathbf{KK}^{-1})^{-1}\mathbf{a}\delta\mathbf{P} \tag{2}$$

where $\mathbf{a}$ = the transfer matrix between the inner force $\mathbf{P}$ and the external loading $\mathbf{R}$;

$\delta\mathbf{P}$ = the changes of the inner forces caused by the variations of the structural stiffness and the external loading. If the matrix $\mathbf{I} - \delta\mathbf{K}\mathbf{K}^{-1}$ is singular, it can be changed into a block matrix $\mathbf{E}\begin{bmatrix} \mathbf{0} & \mathbf{0} \\ \mathbf{0} & \mathbf{A} \end{bmatrix}\mathbf{E}^{\mathrm{T}}$ and its approximate inverse is then expressed as $\mathbf{E}^{-\mathrm{T}}\begin{bmatrix} \mathbf{M} & \mathbf{0} \\ \mathbf{0} & \mathbf{A}^{-1} \end{bmatrix}\mathbf{E}^{-1}$, where $\mathbf{E}$ is an elementary transformation matrix; $\mathbf{A}$ is an invertible matrix; $\mathbf{M}$ is a matrix formed by large numbers as its elements. Due to the linear independence of the rows of $\mathbf{a}$, there is always a solution $\tilde{\mathbf{P}}\delta\mathbf{x}$ to satisfy the function (3).

$$\mathbf{a}\left(\tilde{\mathbf{P}}\delta\mathbf{x}\right) = \left(\mathbf{I} - \delta\mathbf{K}\mathbf{K}^{-1}\right)^{-1}\mathbf{a}\delta\mathbf{P} \tag{3}$$

where $\tilde{\mathbf{P}}$ = the matrix formed by putting the vector $\mathbf{P}$ on its main diagonal; $\mathbf{x}$ = the dimensionless form of the inner force of each loading path; $\delta\mathbf{x}$, defined as $\delta x_i = \delta P_i / P_i$, describes the size of the perturbation of the corresponding inner force.

Hence, Eq.(2) can be changed into another form.

$$\delta\mathbf{V} = \mathbf{K}^{-1}\mathbf{a}\tilde{\mathbf{P}}\delta\mathbf{x} \tag{4}$$

It means that the change of the nodal displacement in Eq.(1) can also be obtained by applying a proper inner force perturbation on the original structure. This equivalency between the damage input and the inner force perturbation is also available with respect to the change of the structural topology, if the topological form can be expressed as the linear transformation of the nodal displacement. For this reason, the size of the inner force perturbation $\delta\mathbf{x}$ is treated as the uncertainty of the system.

Change of Structural Topology

From the topological point of view, the two joints at the end of each member inside the structure are viewed as being connected by three loading paths, transferring the axial force, shear force and bending moment respectively. And the weight is chosen as the ratio of the inner force and the strength of each loading path (see Eq.(5)). When the weights change to constitute some certain combination, the corresponding member breaks in accordance with its failure criteria and leads to the change of the connectedness. The analysis of the topology is therefore focused on the weight of each loading path.

$$w_i = \frac{P_i}{P_{0,i}^{-1}}, \quad \left(i = 1, 2, \cdots n\right) \tag{5}$$

where P_i = the ith inner force component which is defined as the axial force N_i, shear force

V_i or the bending moment M_i at the midpoint section of the member; $P_{0,i}$ = the strength level of ith loading path which is represented by Eq.(6).

$$P_{0,i} = \sqrt{\frac{1}{2}\left[\left(P_{0,i}^+\right)^2 + \left(P_{0,i}^-\right)^2\right]}, \ (P = N, V, M) \tag{6}$$

where $P_{0,i}^\pm$ = the uni-axial strength, pure shear strength or pure bending strength of the member; the superscript $+$ and $-$ denotes the two opposite directions of each kind of strength. The structural topology is then expressed as shown in Eq.(7).

$$\mathbf{w} = \left(w_1, w_2, \cdots w_n\right)^{\mathrm{T}} = \mathbf{NP} \tag{7}$$

where $\mathbf{N} = \mathrm{diag}\left(\begin{bmatrix} P_{0,1}^{-1} & P_{0,2}^{-1} & \cdots & P_{0,n}^{-1} \end{bmatrix}^{\mathrm{T}}\right)$ and $\mathrm{diag}(\cdot)$ = the operator to form a matrix by putting the corresponding vector on its main diagonal.

The change of the structural is shown as follows.

$$\delta\mathbf{w} = \mathbf{N}\delta\mathbf{P} \tag{8}$$

The transformations from the nodal displacement $\mathbf{V}$ to the inner force $\mathbf{P}$ and from the inner force $\mathbf{P}$ to the structural topology $\mathbf{w}$ are both linear. According to the conclusion mentioned previously, it indicates that the change of the structural topology caused by the damage input can be achieved by applying an appropriate inner force perturbation.

Index of Structural Robustness

The inner force is redistributed once the uncertain disturbance works on the structure. And the inner force change of each loading path can be derived according to Eq.(4).

$$\delta\mathbf{P} = \mathbf{K}''\mathbf{a}^{\mathrm{T}}\delta\mathbf{V} = \mathbf{K}''\mathbf{a}^{\mathrm{T}}\mathbf{K}^{-1}\mathbf{a}\tilde{\mathbf{P}}\delta\mathbf{x} \tag{9}$$

According to Eq.(9), the relation between $\delta\mathbf{w}$ and $\delta\mathbf{x}$ can be established.

$$\delta\mathbf{w} = \mathbf{NK}''\mathbf{a}^{\mathrm{T}}\mathbf{K}^{-1}\mathbf{a}\tilde{\mathbf{P}}\delta\mathbf{x} = \mathbf{H}\delta\mathbf{x} \tag{10}$$

where $\mathbf{H}$ = the transfer matrix defined as $\mathbf{NK}''\mathbf{a}^{\mathrm{T}}\mathbf{K}^{-1}\mathbf{a}\tilde{\mathbf{P}}$.

The element H_{ij} means the change of the weight of the ith loading path due to the unit inner force perturbation of the jth loading path, and it shows the influence of the jth loading

path and the sensitivity of the ith loading path. Likewise, H_{ji} has the conjugate physical meaning. They both measure the relationship between the two corresponding loading paths.

The column vector $\mathbf{H}_i$ is the change of structural topology due to the unit inner force perturbation of the ith loading path. The 2-norm of the vector $\|\mathbf{H}_i\|_2$ actually quantifies the importance of the ith loading path to the whole system. Furthermore, the change of the topology under a specific disturbance can be shown by the linear combination of the corresponding column vectors. Just like the acknowledgement that the overall properties of the matrix can not be described by the simple combination of column vectors, the structural robustness is not the simple collection of the member importance.

The matrix $\mathbf{H}$ is the arrangement of the interaction of loading paths. At different intermediate states, the inner force perturbations and the changes of structural topology are different, but the transfer matrix between them remains unchanged. If the norm of the vector is viewed as some kind of energy, the compatible matrix norm $\|\mathbf{H}\|_2$ indicates the amplification of the energy of the disturbance $\|\delta\mathbf{x}\|_2$ (See Eq.(11)).

$$\|\mathbf{H}\|_2 = \max_{\delta\mathbf{x}\neq\mathbf{0}} \frac{\|\mathbf{H}\delta\mathbf{x}\|_2}{\|\delta\mathbf{x}\|_2} = \max_{\delta\mathbf{x}\neq\mathbf{0}} \frac{\|\delta\mathbf{w}\|_2}{\|\delta\mathbf{x}\|_2} \tag{11}$$

With the consideration of the original state of the structure, the indexes of structural vulnerability and structural robustness can be defined as follows.

$$\begin{cases} \text{V.I.} = \dfrac{\|\mathbf{H}\|_2 \|\mathbf{x}\|_2}{\|\mathbf{w}\|_2} = \max_{\delta\mathbf{x}\neq\mathbf{0}} \dfrac{\|\delta\mathbf{w}\|_2/\|\mathbf{w}\|_2}{\|\delta\mathbf{x}\|_2/\|\mathbf{x}\|_2} \\[4mm] \text{R.I.} = \dfrac{1}{\text{V.I.}} = \dfrac{\|\mathbf{w}\|_2}{\|\mathbf{H}\|_2 \|\mathbf{x}\|_2} \end{cases} \tag{12}$$

where the particular disturbance $\delta\mathbf{x}$ to cause the maximum amplification of the uncertainty is the eigenvector corresponding to the spectral radius of the matrix $\mathbf{H}^{\mathrm{T}}\mathbf{H}$. It actually shows the most vulnerable part of the system. Each component δx_i of the vector $\delta\mathbf{x}$ indicates the participation of each loading path in the inner force perturbation. To each loading path, the participation may not be in line with its importance. In another word, the uncertainty, which makes the structure most dangerous, may not come from the inner force perturbation of the most important loading path.

Example

A frame with 4 spans and 3 stories is analyzed as an example. The layout and the load case are shown in Fig.3. The properties of the members are presented in Table1. When the member No. is i, the loading paths which transfer the axial force, the shear force and the bending moment are marked as $3i$-2, $3i$-1 and $3i$, respectively.


(a)   (b)
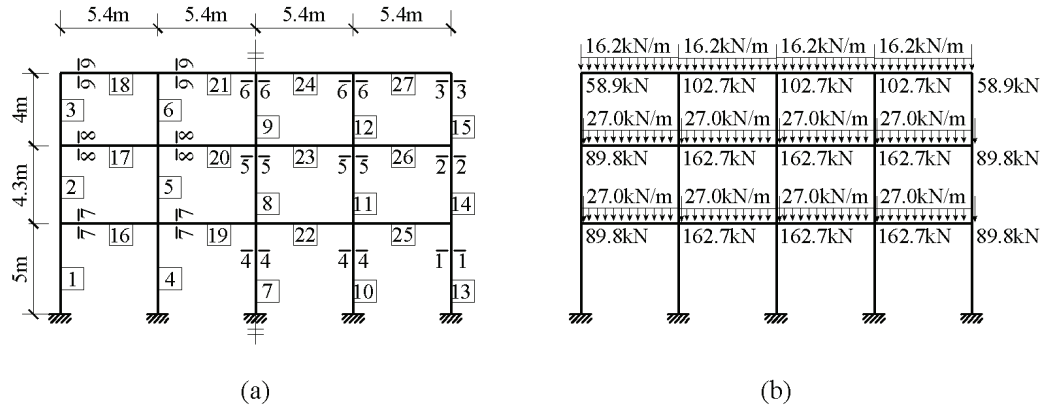
Fig.3 (a) Layout of the example; (b) Load case of the example

Table 1 Properties of the members

Section	1	2	3	4	5	6	7	8	9
Area (10^5mm^2)	1.8	1.8	1.8	1.6	1.6	1.6	1.5	1.5	1.35
Moment of inertia (10^9mm^4)	3.04	3.04	3.04	2.13	2.13	2.13	3.13	3.13	2.28
Axial strength*(10^3kN)	2.58	2.28	2.15	2.23	2.09	1.86	2.14	2.00	1.71
Shear strength*(10^2kN)	2.91	2.91	2.91	2.59	2.59	2.59	2.78	2.78	2.08
Bending strength*(10^2kN.m)	1.97	1.32	1.04	1.47	1.17	0.71	1.81	1.46	0.99

* The strength is deduced by Eq.(6).

The transfer matrix **H** (81×81 in size) is calculated by Eq.(10). Only the related properties are analyzed as follows. The importance of each loading path is shown in Fig.4.
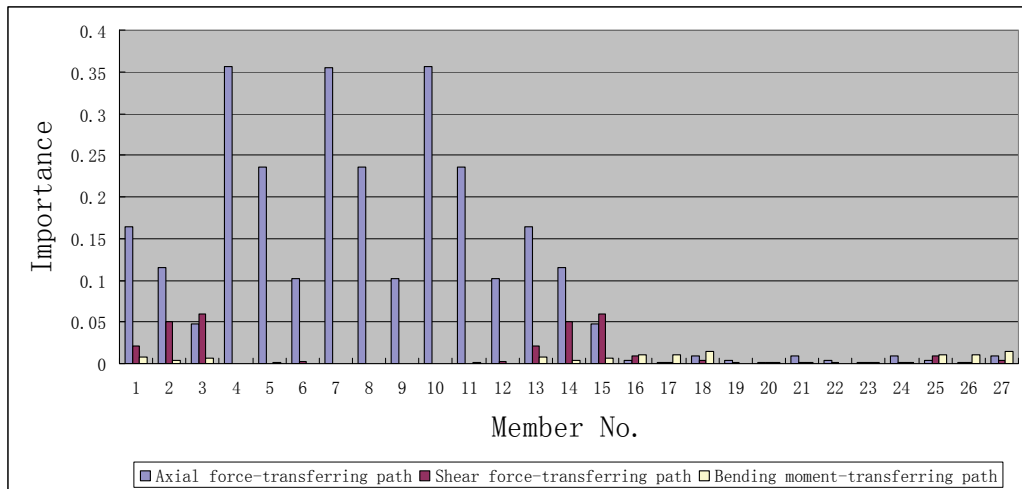
Fig.4. Importance of each loading path

In this system, the importance of the loading paths is symmetrically distributed in accordance with the structural configuration and loading formation. The paths of the columns are more important than the ones of the beams. And inside the column, the paths transferring the axial force are more important than the others. It matches the mechanical performance of the frame under the vertical loading.

It can be obtained from Eqs.(11)~(12) that $\|\mathbf{H}\|_2$ is 0.361, the system size $\|\mathbf{x}\|_2$ is 9, the initial state $\|\mathbf{w}\|_2$ is 0.878. The vulnerability index V.I. is 3.87 and the robustness index R.I. is 0.258. The maximum components of the most adverse uncertainty $\delta\mathbf{x}$ are δx_{10} (-0.497 in number), δx_{19} (-0.711 in number) and δx_{28} (-0.497 in number). They are the axial force-transferring paths of members 4, 7 and 10, respectively. From the perspective of the member level (see Fig.4), the paths 10, 19 and 28 are the most and almost the same important. However, from the perspective of the system level, the participation of these three paths varies widely. It indicates the difference between the member importance and the structural robustness.

Conclusions

In this paper, a methodology of topology-based analysis of structural robustness is proposed. In this method, a feedback system is used to describe the process of the structural collapse. The uncertain disturbance and the topology change are used to measure the damage input and the failure output, respectively. In this way, the transfer matrix between the two measurers, which indicates the rationality of the topology, determines the operation the closed-loop. The 2-norm of each column of the matrix shows the influence of the corresponding loading path on the whole system. And the 2-norm of the matrix itself indicates the maximum amplification of the uncertainty. On this basis, the importance of each loading path, the robustness of the whole structure, as well as the most vulnerable part of the system can be found concisely.

References
Liu, X.L. (1997). "The development and prospects of structural engineering (in Chinese)." *China Communications Press, Beijing*.

Liu, X.L. (2001). "Building science：rethinking after the collapse of the Twin Towers (in Chinese)．" *Newton Science World*, 10, 62-67.

Lind, N.C. (1995). "A measure of vulnerability and damage tolerance." *Reliability Engineering & System Safety*, 48(1), 1–6.

Pinto, J.T., Blockley, D.I. and Woodman, N.J. (2002). "The risk of vulnerable failure." *Structural Safety*, 24(2-4), 107-122.

Zhang, L.M. and Liu, X.L. (2001). "Some issues in the collapse analysis of frame structures (in Chinese)." *Journal of Shanghai Jiaotong University*, 35(10), 1578-1582.

Topology-based Robust Design of Structures

Yang Gao [1] and **Xi-La Liu** [2]

Abstract: Local damages to a structure will cause disproportional collapse if the system is lack of robustness. The engineering significance of robust design is to provide a relatively rational structural form in the conceptual design, in order to meet the function of the building and to reduce the impact of the incidents. From the topological point of view, this paper presents a robust design methodology of structures. It includes a detailed discussion on how to describe the structural quality and how to account for the design uncertainty. In the design process, the section parameter of each member in the ground structure is chosen as the design variable. The minimum of the structural vulnerability, which is subject to the constraint conditions like construction measures and capacity requirements, is treated as the objective function. The results of the examples show not only the difference between the traditional optimization and the robust design, but also the conformity with the qualitative experiences.
Key words: Structural robustness; Structural topology; Robust design; Ground structure.

Introduction

The engineering design is actually an optimization process to obtain the expected quality of the product. For engineering structures, such quality is commonly focused on the safety. In the traditional design, except for the management and supervision in the construction stage, the structural safety is realized mainly by increasing the safety margin of the members (Liu 2007). This cognition of structural safety has been recognized to be seriously defective as a result of several high profile system failures, such as the Ronan Point Apartment Building in 1968, where the consequences were deemed unacceptable relative to the initiating damage. It indicates that some special uncertainties can make the "nominal" optimal solution heavily infeasible and practically meaningless (Ben-Tal et al 1998). It is therefore necessary to introduce the robust design method to the structural design.

[1]　Doctoral student, Dept. of Civil Engineering, Shanghai Jiaotong Univ., No.800 Dongchuan Rd., Shanghai 200240, P.R. China (corresponding author). E-mail: gaoy-02@163.com

[2]　Professor, Dept. of Civil Engineering, Shanghai Jiaotong Univ., No. 800 Dongchuan Rd., Shanghai 200240, P.R. China. E-mail: xilaliu@tinghua.edu.cn

The robust design approach was firstly proposed by Taguchi (Taguchi 1989). It pointed out that the product was expected to improve its quality by minimizing the influence of the unavoidable cause. On this basis, Otto (Otto et al 1993), Ramakrishnan (Ramakrishnan et al 1994) and Chen (Chen et al 1996) improved this method on the applicability and feasibility, respectively. Although Taguchi's method performs quite well in the designs of wings, spacecrafts and solar systems, there are still many controversial debates on it due to the efficiency considerations of the calculation and the disputable definition of some quantities. To engineering structures, in the authors' opinion, the basic conception of Taguchi's method can be used as the guidance of the robust design, while the specific probability-based means are not available. The reason is that the probability of the sudden events is too low to determine the probability density function or membership function of such kind of uncertainty.

In the present paper, the well-known ground structure method is used. The layout of a structure is found by allowing a certain set of connections between a fixed set of nodal points. In the robust design, the section parameter is chosen as the design variable; the topological relationship is used to describe the structural quality; and the intended structural function under normal condition is defined as the quality requirement. A series of structures which satisfy the quality requirement can then be obtained by optimizing the design variable. In face of potential local damages, a further choice should be sought inside the series. The objective structure is asked for the minimum vulnerability to ensure the insensitivity of the structural quality to the uncertainties.

Structural Robust Design

Taguchi envisioned a three-stage design methodology comprising system design, parameter design and tolerance design (Beyer et al 2007).According to these three steps, the robust design of engineer structures is discussed as follows.

System design

In reality, sudden events, especially the malevolent attacks normally do not take place simultaneously with the extreme natural disasters, such as hurricanes and earthquakes. It indicates that the most common loading condition of the structure can be used in the robust design. At the same time, the layout of the structural nodal points can be determined according to the initial architectural planning. The purpose of the system design is to find a preliminary structural configuration to meet requirements under the given nodal points and loading case.

Strictly speaking, the connections should be represented by the logic variables (exit or not exit). However, it will make the analytical model much more complex. To deal with this problem, Dorn proposed the ground structure method which converts the structural topology design to the member section optimization. The layout of a structure is found by allowing a certain set of connections between a fixed set of nodal points as potential structural or vanishing members. In the present paper, with the consideration of the engineering application, the connections are required to satisfy the construction conditions and function requirements of the structure. The joints of the connections are uniformly rigid except for the ones of the truss structure.

In order to check whether the quality meets the requirements in the parameter design stage and to inspect the quality change caused by the uncertainties in the tolerance design stage, it is necessary to make a description of the structural quality. In normal conditions, the structure resists the external loading and realizes the expected function mainly relying on the force-transferring mechanism between the nodes and the bearing capacity of the members. Under sudden events, the inner force is disturbed by the change of the structure and its loading. The influence of local damages further depends on the ability of each connection to redistribute this perturbation. Such adjacency of the nodes and property of each connection are exactly the structural topology. And the topological relationship can be used to describe the structural quality, accordingly.

On this basis, in the system design stage, the general structure is determined as the ground structure. And the structural topology is chosen as the basic performance parameter.

Parameter design

The structure is designed to function as intended in normal conditions. And the so-called quality requirement is the selection criteria of structural topology to satisfy the bearing capacity of the structure and the strength redundancy of the members.

The graph theory is used to quantify the structural topology. Each member is viewed as three loading paths, transferring the axial force, shear force and bending moment respectively. Let the joints and members of the structure be the corresponding vertexes and edges of the graph, and let the ratio of the inner force and strength of each path be the weight of each edge (See Eq.(1)). The structural can be described by a weighted graph.

$$w_i = P_i P_{0,i}^{-1}, \quad \left(i = 1, 2, \cdots n \right) \tag{1}$$

where w_i = the weight of the ith loading path; P_i = the ith component of inner force vector

$\mathbf{P}$; $\mathbf{P} = \mathbf{K}'' \mathbf{a}^{\mathrm{T}} \mathbf{K}^{-1} \mathbf{R}$, in which $\mathbf{K}$ and $\mathbf{K}''$ are the matrices assembled by the member

stiffness in the global coordinate and in the basic coordinate, respectively, $\mathbf{R}$ is the external

loading vector, $\mathbf{a}^{\mathrm{T}}$ is the transfer matrix between the nodal displacement and the member

deformation; $P_{0,i}$ = the strength level of ith loading path and is expressed as

$\sqrt{\left[\left(P_{0,i}^+ \right)^2 + \left(P_{0,i}^- \right)^2 \right] \Big/ 2}$; $P_{0,i}^{\pm}$ = the uni-axial strength, pure shear strength or pure bending

strength of the member; the superscript $+$ and $-$ denotes the two opposite directions of each kind of strength; n = the number of inner forces.

In this way, the structural topology can be expressed as Eq.(2).

$$\mathbf{w} = \left(w_1, w_2, \cdots w_n \right)^{\mathrm{T}} = \mathbf{NP} = \mathbf{NK}''\mathbf{a}^{\mathrm{T}}\mathbf{K}^{-1}\mathbf{R} \tag{2}$$

where $\mathbf{N} = \mathrm{diag}\left(\left[P_{0,1}^{-1}, P_{0,2}^{-1}, \cdots P_{0,n}^{-1} \right]^{\mathrm{T}} \right)$ and $\mathrm{diag}(\bullet)$ = the operator to form a matrix by putting the corresponding vector on its main diagonal.

In conceptual design, some parameters are supposed to be estimated to simplify the calculation. To the reinforced concrete member, for example, the ratio between the rectangular section height and the member length, the symmetrical longitudinal reinforcement ratio and the stirrup reinforcement ratio can be preset. With this settlement, the inner force of the structure is decided by the width of each member. And the strength of each loading path is, more ideally, proportional to the width of the corresponding member. This conclusion is also available to the steel member, if the actual section is equivalent to the calculated one in the area and moment of inertia. Thus, the structural topology $\mathbf{w}$ becomes the function of the member section width $\mathbf{b}$.

Different structures can be obtained by changing the section width of the members. Only the ones who meet the quality requirements are wanted in this stage. To any of the members, there is a strength criterion expressed by the inner forces (see Eq.(3)).

$$f_j \left(N_{\mathrm{cr},j}, V_{\mathrm{cr},j}, M_{\mathrm{cr},j}, N_{0,j}, V_{0,j}, M_{0,j} \right) \leq 1, \quad \left(j = 1, 2, \cdots n/3 \right) \tag{3}$$

where $n/3$ is the number of the members; $\left(N_{\mathrm{cr}}, V_{\mathrm{cr}}, M_{\mathrm{cr}} \right)$ = the inner force state of the critical section. According to the inner force transformation from the critical section to the midpoint section, the strength criterion with respect to the weights can be achieved as below.

$$\tilde{f}_j \left(w_{3j-2}, w_{3j-1}, w_{3j}, N_{0,j}, V_{0,j}, M_{0,j} \right) \leq 1, \quad \left(j = 1, 2, \cdots n/3 \right) \tag{4}$$

In this way, in the parameter design stage, the design variable $\mathbf{b}$ is optimized to meet the quality requirement as shown in Eq.(4).

Tolerance design

On the basis of the second design stage, a further choice should be sought to control the range of the quality fluctuation caused by the uncertainties. The resulting structure tends to increase the cost as a consequence. The purpose of the tolerance design is just to find the balance between the tolerance and the cost. Being different from the whole process of product design mentioned in Taguchi's method, it is hard to make a good estimate of the structure cost in the conceptual design. And it is more unrealistic to establish the relation between the tolerance and the cost. Thus, in the present paper, the structure which is least affected by the uncertainty is preferred. In the further design, the engineer can appropriately relax the tolerance in accordance with the specific condition to reduce the cost.

The consequence of the structure caused by local damage is not only the change of the stiffness, the mass and the external loading but also a certain dynamic effect. It is led to, equivalently, by applying a proper external loading perturbation or inner force perturbation on the original structure. In accordance with the expression of the structural topology, the size of the inner force perturbation $\delta \mathbf{x}$ is treated as the system uncertainty in the robust design.

$$\delta \mathbf{P} = \mathrm{diag}(\mathbf{P}) \delta \mathbf{x} \tag{5}$$

The relation between the uncertainty and the change of the quality can then be established.

$$\delta \mathbf{w} = \mathbf{N} \mathbf{K}'' \mathbf{a}^{\mathrm{T}} \mathbf{K}^{-1} \delta \mathbf{R} = \mathbf{N} \mathbf{K}'' \mathbf{a}^{\mathrm{T}} \mathbf{K}^{-1} \mathbf{a} \delta \mathbf{P} = \mathbf{N} \mathbf{K}'' \mathbf{a}^{\mathrm{T}} \mathbf{K}^{-1} \mathbf{a} \, \mathrm{diag}(\mathbf{P}) \delta \mathbf{x} = \mathbf{H} \delta \mathbf{x} \tag{6}$$

If the norm of the vector is viewed as some kind of energy, the compatible norm $\|\mathbf{H}\|_2$ indicates the maximum amplification of the energy of the disturbance $\|\delta \mathbf{x}\|_2$ (See Eq.(7)).

$$\|\mathbf{H}\|_2 = \max_{\delta \mathbf{x} \neq 0} \frac{\|\mathbf{H} \delta \mathbf{x}\|_2}{\|\delta \mathbf{x}\|_2} = \max_{\delta \mathbf{x} \neq 0} \frac{\|\delta \mathbf{w}\|_2}{\|\delta \mathbf{x}\|_2} \tag{7}$$

With the consideration of the original state of the structure, the indexes of structural vulnerability (defined as Eq.(8)) can be used to describe the extent of the structural quality affected by the uncertainty.

$$\mathrm{V.I.} = \frac{\|\mathbf{H}\|_2 \|\mathbf{x}\|_2}{\|\mathbf{w}\|_2} = \max_{\delta \mathbf{x} \neq 0} \frac{\|\delta \mathbf{w}\|_2 / \|\mathbf{w}\|_2}{\|\delta \mathbf{x}\|_2 / \|\mathbf{x}\|_2} \tag{8}$$

In this way, the objective of the robust design is quantified by bringing in the vulnerability index. In the tolerance design stage, the design parameter $\mathbf{b}$ obtained in the second stage is fine-tuned to desensitize the structural quality $\mathbf{w}$ to the uncertainty $\delta \mathbf{x}$, or in another word, to minimize the structural vulnerability.

Optimization function of robust design

The robust optimization task in this paper can be stated as.

$$\left. \begin{aligned} \min: \ \max_{\mathbf{b}} \ & \frac{\|\delta \mathbf{w}(\mathbf{b})\|_2 / \|\mathbf{w}(\mathbf{b})\|_2}{\|\delta \mathbf{x}\|_2 / \|\mathbf{x}\|_2} \\ \mathrm{s.t.:} \ \ & \mathbf{b} \in \left\{ \mathbf{w}(\mathbf{b}) \middle| \tilde{f}_j \left(w_{3j-2}, w_{3j-1}, w_{3j}, N_{0j}, V_{0j}, M_{0j} \right) \leq 1, j = 1, 2, \cdots, n/3 \right\} \\ & \forall \delta \mathbf{x} \neq \mathbf{0} \end{aligned} \right\} \tag{9}$$

Two facts are noted here. First, to any given structure, the strength requirement of each member can be satisfied by changing the section width in a unified proportion. Second, with this proportion, the inner force of each loading path remains unchanged and its strength changes in a same multiple. It makes the vulnerability index (defined in Eq.(8)) invariable. On this basis, the optimization function adopted in the practical calculation is shown below.

$$
\left.
\begin{array}{l}
\min: \ \max_{\mathbf{b}} \ \dfrac{\left\| \delta\mathbf{w}\left(\mathbf{b}\right)\right\|_{2} \big/ \left\|\mathbf{w}\left(\mathbf{b}\right)\right\|_{2}}{\left\|\delta\mathbf{x}\right\|_{2} \big/ \left\|\mathbf{x}\right\|_{2}} \\[2em]
\text{s.t.:} \ \ \forall \delta\mathbf{x} \neq \mathbf{0}
\end{array}
\right\}
\tag{10}
$$

It can be solved by the genetic algorithms. The solution $\mathbf{b}$ is multiplied by a scale λ to meet the quality requirements.

$$
\lambda\mathbf{b} \in \left\{ \mathbf{w}\left(\lambda\mathbf{b}\right) \middle| \tilde{f}_{j}\left(w_{3j-2}, w_{3j-1}, w_{3j}, N_{0,j}, V_{0,j}, M_{0,j} \right) \leq 1, j=1,2,\cdots,n/3 \right\}
\tag{11}
$$

As is mentioned above, the result $\lambda\mathbf{b}$ also satisfies the function(10). And it is exactly the solution of the robust design. By this means, the complex calculation of verifying the member capacity is independent of the optimization process. It fits more closely with the requirements of the structural conceptual design.

Example
Example 1

The ground structure of a truss is shown in Fig.1(a). Each bar has the same Young's modulus. The uni-axial strength is 300Mpa with the safety factor 1 (without considering stability). The concentrated load R is 1000kN. The robust design result is shown in Fig.1(b). As a contrast, the traditional optimization solution, which requires for the minimum volume of the members, is shown in Fig.1(c). The detailed data of the structural vulnerability and the member section area are listed in Table 1.
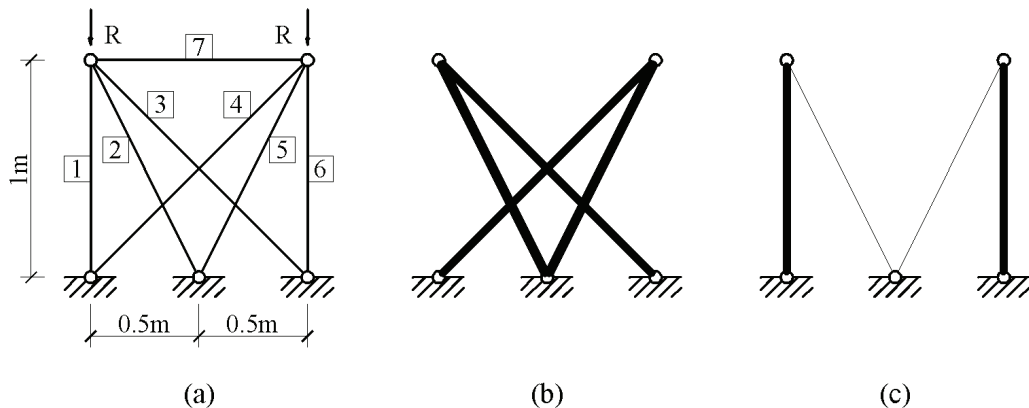
Fig.1 (a) Ground structure of example 1; (b) Robust design result; (c) Traditional optimization result
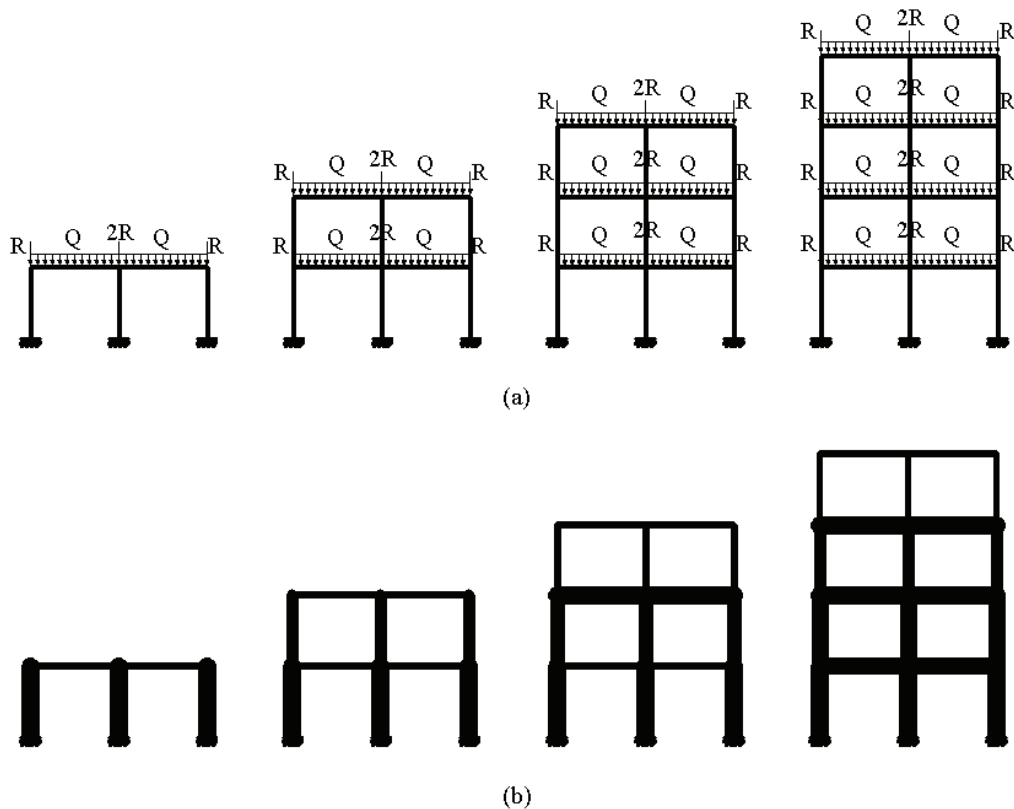
Table 1 Structural vulnerability and member section area of example1

Structure	Section area (10^{-4}m^2)							Vulnerability	Volume (10^{-3}m^3)
	1	2	3	4	5	6	7		
b	0	74.6	47.2	47.2	74.6	0	0	1.73	30.03
c	33.3	0.1	0	0	0.1	33.3	0	2.46	6.68

The comparison between the traditional optimization solution and the robust design result indicates that it tends to increase the cost to improve the structural robustness. What's more, the essential difference between the two kinds of design cognition is shown typically. In the former design the most concise way of force transmission is required, while in the latter one the effective alternative loading paths are considered.

Example 2

A group of ground structures of buildings are shown in Fig.2(a). Only the columns and the beams are permitted to set. Each span of the frame is 5m. The storey height is 4m. The concentrated load R is 50kN and the distributed load Q is 20kN/m. Each member has the same Young's modulus. The section height is preset as the 1/10 of the member length. The section width is required to be less than 0.5m and more than 1/3 height. To the $b \times h$ section, the path strength is 1.167×10^7N, $2.25 \times 10^6 bh$N, and $1.44 \times 10^6 bh^2$Nm, respectively.

(a)

(b)

Fig.2 (a) Ground structures of example 2; (b) Robust design results

For the convenience of the practical engineering, the columns and the beams of each floor are, respectively, chosen to be the same wide. The results of the robust design are shown in Fig.2(b) and Table 2 without checking the bearing capacity of each member.

Table 2 Structural vulnerability and member section width of example2

Structure	Section width (m)								V.I.
	1st floor		2nd floor		3rd floor		4th floor		
	column	beam	column	beam	column	beam	column	beam	
1-floor	0.5	0.167							2.03
2-floor	0.5	0.167	0.254	0.167					2.78
3-floor	0.5	0.167	0.336	0.5	0.171	0.167			2.95
4-floor	0.5	0.443	0.379	0.5	0.252	0.5	0.133	0.167	3.03

The research data shows that the higher the building is, the more vulnerable the system is. Such safety defect is the natural topological disadvantage of the high-rise building which can not be eliminated by the robust optimization design.

Conclusions

In this paper, a methodology of topology-based robust design is proposed. In this method, the section parameter of each member in the ground structure is chosen as the design variable; the inner force perturbation is taken as the uncertainty; and the minimum of the structural vulnerability is treated as the objective function. Through the robust design, a certain set of connection between the fixed nodal points are found to form the objective structure which satisfies the quality requirement and the insensitivity of the quality to the uncertainty.

References

Liu, X.L. (2007). "The development and prospect of structural engineering (in Chinese)." *China Architecture & Building Press*, Beijing.

Ben-Tal, A. and Nemirovski, A. (1998). "Robust convex optimization." *Math. Oper. Res.*, 23(4), 769-805.

Taguchi, G. (1989). "Introduction to quality engineering." *American Supplier Institute*.

Otto, K.N. and Antonsson, E.K. (1993). "Extensions to the taguchi methods of product design." *Journal of Mechanical Design*, 115(3), 5-13.

Ramakrishnan, B. and Rao, S.S. (1994). "An efficient strategy for the robust optimization of large scale nonlinear design problems." *Proceeding 20th ASME Design Automation Conf.*, Minneapolis, MN.

Chen, W., Allen, J.K. and Mistree, F. (1996). "System configuration: concurrent subsystem embodiment and system synthesis." *Journal of Mechanical Design*, 118(2), 165-170.

Beyer, H.G. and Sendhoff, B. (2007). "Robust optimization – A comprehensive survey." *Comput. Methods Appl. Mech. Engrg.*, 196, 3190-3218.

Flow Potential in Structures and Application in Analysis of Structural Vulnerability

Ning Xu[1] and Lei-Ming Zhang[2]

Abstract: Structural vulnerability has been a main focus in structural community for decades since the collapse of Ronan Point Tower in 1968. Its quantitative evaluation, however, is still a problem today. In this paper a new concept of flow potential in structures is brought forward based on which a procedure to evaluate structural vulnerability is presented. Two example structures are given to demonstrate the calculation of flow potential in structures and the feasibility of the proposed index of structural vulnerability.

Keywords: Energy flow; Flow potential; Structural vulnerability; Quantitative evaluation

Introduction

It has been recognized that collapses of civil structures are main sources for significant property and life losses. In 1968, a small gas explosion initiated the collapse of one entire corner of the Ronan Point apartment tower in London, with four killed and 17 injured (Griffiths et al 1968). It was the first collapse incidence that led to major modifications in building regulations. The shocking event of September 11, 2001 prompted another major reassessment of the current practices in structural engineering (Bazant et al 2002). Thereafter the safety requirements on structures especially high-rise buildings are much more highlighted. Structural vulnerability is actually one way to deal with it. It was first addressed by the Standing Committee on Structural Safety (SCOSS) in 1994. From then structural vulnerability is widely studied, where, however, no widely accepted procedure has been accomplished.

In this study, flow potential field is first established based on the energy flow occurred in structures subjected to external loads. Then the index of structural vulnerability is constructed. Several example structures are given to demonstrate the calculation of flow potential in structures as well as the feasibility of the presented index of structural vulnerability. This study is currently limited to: linear elastic material; small displacement with small strain; no structural failure during loading.

Flow Potential in Structures

Energy flow in a structure subjected to loads can be termed as a field denoted by $\mathbf{E}$. By analogy to electric potential in electric field, there is also flow potential in structures accordingly, which is denoted by P. According to field theory (Truesdell et

---

[1]Graduate student, Dept. of Civil Engineering, Shanghai Jiaotong Univ., No. 800 Dongchuan Rd., Shanghai 200240, P.R. China. E-mail: xuning1989520@126.com
[2]Assoc. professor, Dept. of Civil Engineering, Shanghai Jiaotong Univ., No.800 Dongchuan Rd., Shanghai 200240, P.R. China (corresponding author). E-mail: lmzhang@sjtu.edu.cn

al), the general relations between the flow potential and the energy flow field in three-dimensional (3D) case can be expressed as

$$\mathbf{E} = E_x\mathbf{i} + E_y\mathbf{j} + E_z\mathbf{k} = -\nabla P \tag{1}$$

where E_x, E_y, E_z are the energy flow density in three directions, respectively.

For simplicity, only flow potential in two-dimensional (2D) case and member structures are discussed in this paper.

Flow Potential in 2D Cases

For an infinitesimal plane element shown in Fig.1, the energy balance can be expressed as

$$E_x dy + E_y dx + W_{ext} dxdy = Wdxdy + \left(E_y + dE_y\right)dx + \left(E_x + dE_x\right)dy \tag{2}$$

where E_x and E_y are the energy flow density in x-, y-direction respectively; W is the strain energy density; and W_{ext} is the work density done by external load.

(a) General energy flow in 2D case   (b) Energy balance of an infinitesimal element
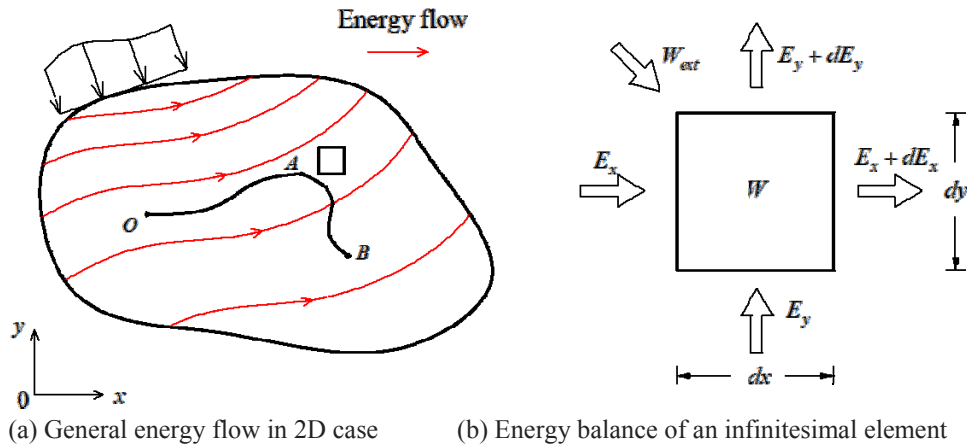
Figure 1. Energy flow in 2D case

Eq.2 can be rewritten as

$$W = -\left(\frac{dE_x}{dx} + \frac{dE_y}{dy}\right) + W_{ext} \tag{3}$$

which is actually the relation among energy flow, strain energy and external work. The energy flow in a structure can be easily obtained with structural analysis, which then can be verified by Eq.3.

By appointing a zero-point O of flow potential in the field, the flow potential at any point A can be obtained by line integral of Eq.1 along any path between O and A (see Fig.1a), which is

$$P_A = -\int_{OA} \mathbf{E} \cdot d\mathbf{l} = -\int_O^A (E_x dx + E_y dy) \qquad (4)$$

Obviously the flow potential difference between two points A and B can be expressed as (see Fig.1a)

$$\Delta P = P_B - P_A = \int_{AB} \mathbf{E} \cdot d\mathbf{l} = -\int_A^B (E_x dx + E_y dy) \qquad (5)$$

As an example the schematic flow potential and energy flow in a cantilever beam is shown in Fig.2.
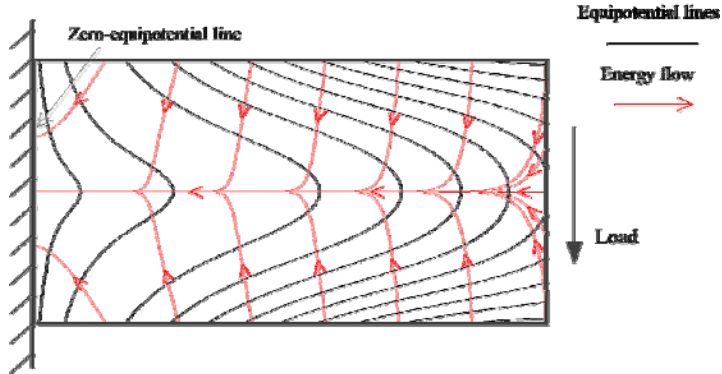

Figure 2. Schematic flow potential and energy flow in cantilever beam

(a) Schematic of a member   (b) Energy balance of member segment
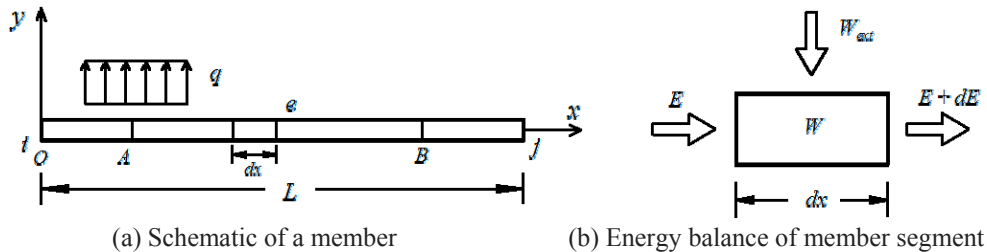
Figure 3. Flow potential in member

Flow Potential in Members

For an infinitesimal member segment as shown in Fig.3, the energy balance equation is

$$E(x) + W_{ext} dx = W dx + E(x) + dE(x) \qquad (6)$$

where $E(x)$ is energy flow in member through the section at x.
Eq.6 may be re-written as

$$W = -\frac{dE(x)}{dx} + W_{ext} \qquad (7)$$

which, again, is the relation among energy flow, strain energy and external work. Similarly, the energy flow in a member can be easily obtained and verified by Eq.7 after structural analysis.

By appointing a zero-section of flow potential in the member (such as the origin in Fig.3a), the flow potential at any section can be obtained by integral of Eq.1 along the member, which is

$$P(x) = -\int_o^x E(x)\,dx \tag{8}$$

Again, the flow potential difference between section A and B can be expressed as (see Fig.3a)

$$\Delta P = P_B - P_A = -\int_A^B E(x)\,dx \tag{9}$$

Flow Potential in Frame Structures
First the basic equation for flow potential in a typical member is obtained. By constructing flow rules in frame structures, solution for the flow potential can be transformed into linear programming problem which can be readily solved.

Flow Potential in Frame Member
For a typical plane member e as shown in Fig.3a with transverse load only, the strain energy density can be expressed as

$$W(x) = \frac{1}{2} EI(v'')^2 + \frac{1}{2} EA(u')^2 \tag{10}$$

where v is transverse displacement, u is longitudinal displacement, EI is flexural rigidity and EA is axial rigidity.
From Eq.7, the energy flow in the member can be obtained as

$$E(x) = -\frac{1}{2}\int_0^x \Big[EI(v'')^2 + EA(u')^2 - qv \Big]dx + E_i^e \tag{11}$$

where q is transverse uniform load, E_i^e and E_j^e are energy flow at two member ends of member e, which can easily be obtained from member-end forces and member-end displacements. From Eq.11 one has

$$E_j^e = -\frac{1}{2}\int_0^L \Big[EI(v'')^2 + EA(u')^2 - qv \Big]dx + E_i^e \tag{12}$$

From Eq.8 the flow potential in the member is

$$P(x) = \frac{1}{2}\int_0^x \left\{ \int_0^x \left[EI(v'')^2 + EA(u')^2 - qv \right] dx \right\} dx - E_i^e x + P_i^e \tag{13}$$

where P_i^e is flow potential at member-end i of member e.

Denote the flow potential at member-end j of member e as P_j^e, it is obvious from Eq.13 that

$$P_j^e = \frac{1}{2}\int_0^L \left\{ \int_0^x \left[EI(v'')^2 + EA(u')^2 - qv \right] dx \right\} dx - E_i^e L + P_i^e \tag{14}$$

Then the flow potential difference between two member-ends is

$$\Delta P^e = P_j^e - P_i^e = \frac{1}{2}\int_0^L \left\{ \int_0^x \left[EI(v'')^2 + EA(u')^2 - qv \right] dx \right\} dx - E_i^e L \tag{15}$$

After the internal forces and deflections of the member are obtained, the energy flow can be obtained from Eqs.11~12. From Eq.13 and Eq.15, the flow potential in the member can be uniquely determined when the flow potential at one member-end is obtained. Eq.15 is actually the basic equation for flow potential at member ends.
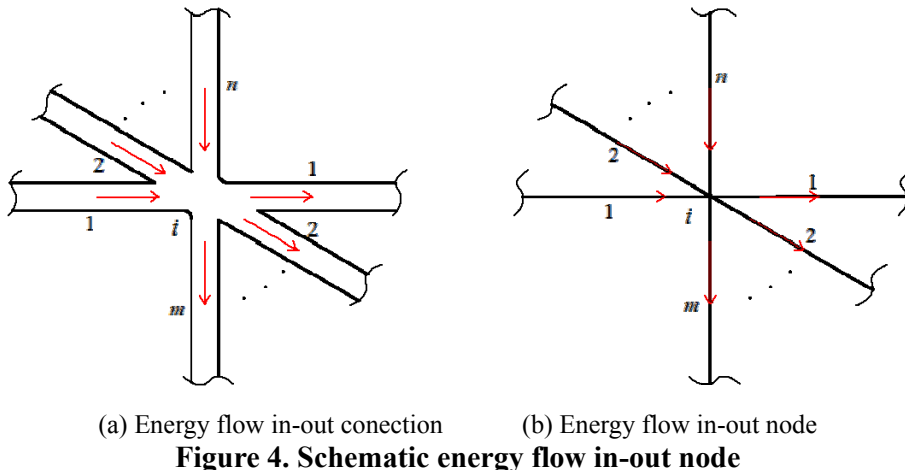
(a) Energy flow in-out conection   (b) Energy flow in-out node
Figure 4. Schematic energy flow in-out node

Flow Rules to Determine Flow Potential in Frame Structures
As shown Fig.4, the energy flow as well as the distribution of flow potential at a real connection among members might be very complicated. In structural modeling the connection is modeled as a node. Thus the flow potential of members connected at the same node should satisfy certain rules which can be drawn from a primary fact: energy always flows from high potential areas to low potential areas.
Assuming there are $(m+n)$ members connected at node i (see Fig.4) with m is the number of members with energy flowing out from the node and n is the number of members with energy flowing in through the node, the nodes can be classified into two types and the flow rules are constructed as follows:

For simple node, i.e. the node where $m < 2$ or $n < 2$:

$$\begin{cases} P_i^{e_{in}} - P_i^{e_{out}} \geq 0 & e_{in} = 1,...n; e_{out} = 1,...m \\ P_i^{e_{out}} = const. & e_{out} = 1,...m \end{cases} \qquad (16)$$

For complex node, i.e. the node where $m \geq 2$ and $n \geq 2$:

$$\begin{cases} \max_{e_{in}=1,n}(P_i^{e_{in}}) - \max_{e_{out}=1,m}(P_i^{e_{out}}) \geq 0 \\ \min_{e_{in}=1,n}(P_i^{e_{in}}) - \min_{e_{out}=1,m}(P_i^{e_{out}}) \geq 0 \end{cases} \qquad (17)$$

Solution for Flow Potential in Frame Structures

There is also a basic fact that a system always tends to the lowest potential. Thus for a structure with M members and N nodes, the solution for flow potential can be termed as an optimism problem which can be express as

$$\min : F = \sum_{e=1}^{M} \left(P_i^e + P_j^e \right)$$

$$\text{satisfying: \quad for all members, Eq.15}$$
$$\text{for all nodes, Eq.16 or 17}$$

where the equations will not be repeated. It is obvious that the optimism problem can be transformed into linear programming problems, which can be easily solved by the simplex method. These will not be discussed further in this paper.

Index of Structural Vulnerability

The index of structural vulnerability for a structure with M members is proposed as

$$\gamma^S = \sum_{e=1}^{M} \int_0^{L_e} P(x) \cdot W(x) dx \qquad (18)$$

where L_e is length of member e ; $P(x)$ is flow potential and $W(x)$ is strain energy density in the member, as described before.

Example Structures

Example 1

A typical statically determinate truss shown in Fig.5 is analyzed with $EA = 1 \times 10^9 N$ for all members. For the purpose of comparison, a vertical concentrated force $F = 10kN$ is applied at nodes 2, 4 and 5 respectively.

The indexes of structural vulnerability for different load condition cases are given in Table1. It is obvious that when the load is applied at node 4, its energy flow path to the pinned support at node 1 is the shortest, while the energy flow path for loading at node

2 is the longest. The vulnerability index ranks exhibits that the longer path of energy flow, the greater the index and thus more vulnerable of the structure accordingly.
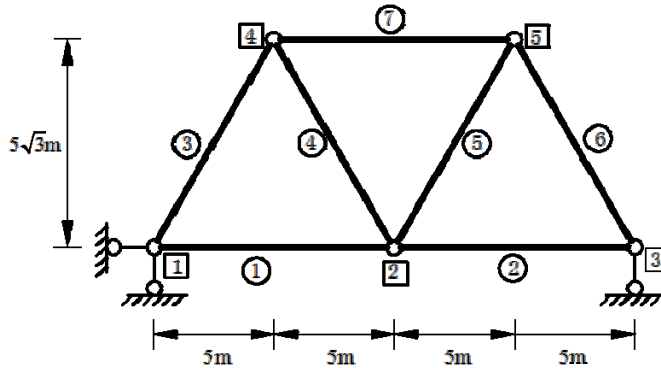

Figure 5. Typical statically determinate truss

Table 1. Index of structural vulnerability under different load condition

| Loading at	Node 4	Node 5	Node 2
Energy flow			
γ^S ($N^2 \cdot m^3$)	1.87	2.01	2.81
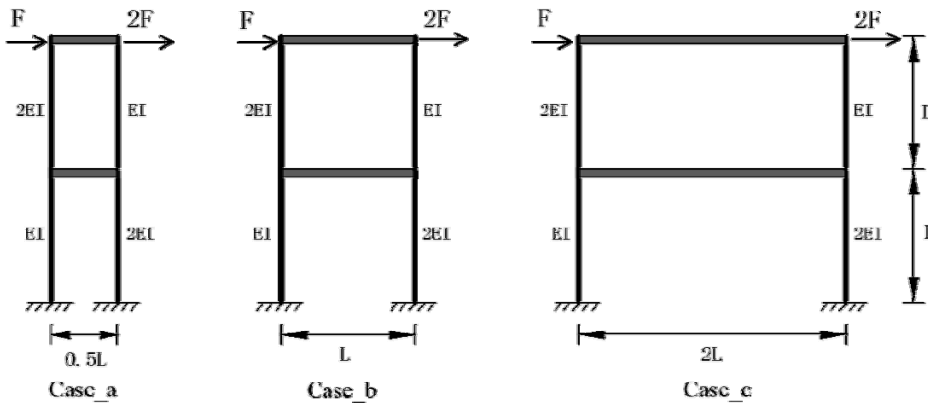
Figure 6. Typical two-story shear frame

Example 2

A typical shear frame with different span shown in Fig.6 is analyzed.

The energy flow as well as the distribution of flow potential is shown in Fig. 7. The indexes of structural vulnerability are given in Table2. Although the span of the shear frame has no effects on the internal forces or the displacements, it should be noted that the flow potential distribution changes significantly for different spans. Thus the span

also changes the vulnerability of the frame: the longer the span, the more vulnerable of the frame. It seems reasonable since longer span means more possibility of suffering attack and failure.
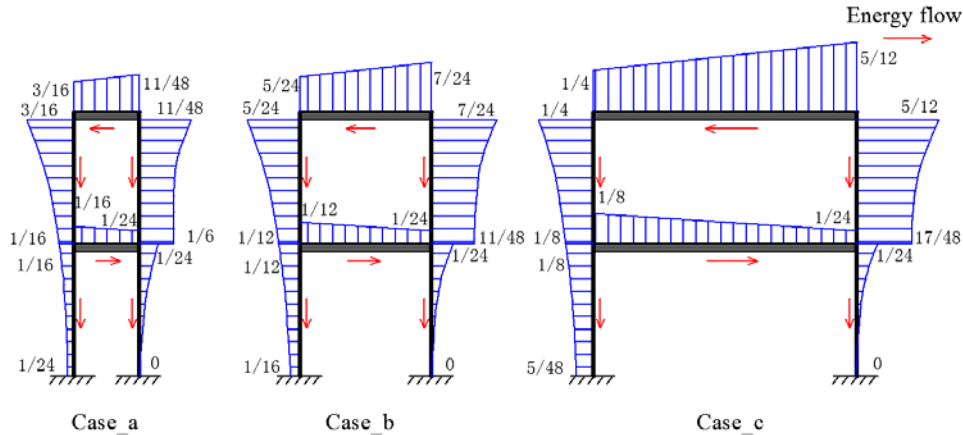
Figure 7. Flow potential distribution of shear frames ($\times F^2 L^4 / EI$)

Table 2. Index of structural vulnerability of different arrangement

	Case_a	Case_b	Case_c
$\gamma^S \, (\times \dfrac{F^4 L^7}{E^2 I^2})$	$\dfrac{319}{8064}$	$\dfrac{375}{8064}$	$\dfrac{795}{8064}$

Conclusions

There is energy flow in structures subject to loads. By analogy to electric potential in electric field, flow potential in structures are brought forward and the relations among the flow potential, energy flow and external work are established for both 2D cases and members. For framed structures, by setting appropriate flow rules at nodes the solution for flow potential can be transformed into linear programming problem which can then be readily solved. The index of structural vulnerability is proposed based on the flow potential and energy flow in the structure.

Two example structures are analyzed to demonstrate the reasonability and feasibility of the proposed procedure. It is shown that the proposed index can properly represent the vulnerability of structures.

References

Bazant, Z.P., and Zhou, Y. (2002). "Why did the world trade center collapse? - Simple analysis." *Journal of Engineering Mechanics*, 128(1): 2-6.

Griffiths, H., Pugsley A., and Saunders, O. A. (1968). Report of the inquiry into the collapse of flats at Ronan Point, Canning Town: presented to the Minister of Housing and Local Government. London: HMSO.

Truesdell, C., and Toupin, R. (1960). "The classical field theories". Springer.

The Standing Committee on Structural Safety (SCOSS). (1994). *10th Report of SCOSS.* , London: SETO Ltd

Robustness Analysis and Key Element Determination of Framed Structures

Nan Xiao[1], Hai-Lei Zhan[2], and Hua-Peng Chen[3*]

Abstract: A new method is proposed to determine key elements in framed structures, where the relative condition number of the global stiffness matrix is chosen as the quantitative indicator of structural robustness. By comparing the mathematical meaning of the relative condition number with the physical meaning of the structural robustness, the structural robustness can be evaluated from the relative condition number between the modified system and the original structure. A simple statically determinate truss was used to verify the applicability of the proposed approach. A more complex Kiewitt single layer shell was further adopted to show the effectiveness of the proposed method. The numerical results indicate that the proposed structural robustness indicator can not only clearly reflect the characteristics of framed structures, but also effectively predict the influence of individual structural members on the behaviour of the structural system.

Keywords: Structural robustness; stiffness matrix; condition number; key element; framed structure.

1. Introduction

Research on structural robustness was mainly started in 1968 due to the progressive collapse of Ronan Point Apartment in London. Since then, a number of investigations have been carried out to analyse robustness and vulnerability, to study reliability and integrity, and to investigate progressive collapse of building structures (Izzuddin et al. 2008). On the basis of these investigations, the techniques for preventing progressive failure and increasing structural integrity were proposed and adopted in design standards and guidance. Recently, structural robustness and progressive failure analyses have attracted greater attentions, in particular since the September 11 attacks in New York, USA.

   The robustness and reliability of a structure is considered as the performance of the structure during its designed service life. Structural reliability depends on many factors, including the cause and mode of structural failure, possible consequences of

---

[1] College of Civil Engineering and Architecture, Zhejiang University, Hangzhou 310058, China.
    Email: sholran@zju.edu.cn
[2] College of Civil Engineering and Architecture, Zhejiang University, Hangzhou 310058, China.
    Email:zhanhailei@gmail.com
[3] School of Engineering, University of Greenwich, Chatham Maritime, Kent, ME4 4TB, UK.
* Corresponding Author. Tel.:++441634883031. Fax:++44 1634 883153. E-mail: h.chen@gre.ac.uk

structural failure, costs for reducing the risk of failure, and social and environmental impact of structural failure. Structural reliability can be evaluated from the probability of failure by probabilistic analyses (Chen and Alani 2013). Ellingwood and Dusenberry (2005) suggested that the probability of a progressive collapse $P(F)$ caused by an abnormal event could be represented as a chain of partial probabilities:

$$P(F) = P(F|DH) \cdot P(D|H) \cdot P(H) \tag{1}$$

where $P(H)$ denotes the probabilities of an abnormal event H; $P(D|H)$ is the probability of local damage D due to the event H; and $P(F|DH)$ represents the probability of failure F of the structure as a result of local damage D by event H. Further investigations on structural robustness and reliability due to an accidental action have been carried out in many studies including Starossek (2006).

In order to analyse structural robustness and evaluate the preventative strategy for progressive collapse of framed structures, it is essential to determine the key elements in the structural systems during structural design and construction stages. The identification of key elements in framed structures is useful to structural maintenance as well to avoid any unexpected structural failure during the service life. Many methods have been proposed for determining key elements such as in the studies by Agarwal et al. (2003), Frangopol and Curley (1987), Sørensen (2011) and Starossek and Haberland (2011), as summarised in Table 1.

Table 1 Summary of methods for identifying key elements

Method type		Theoretical background
Structural properties		System stiffness
		Structural topology
Structural behaviour	Deterministic methods	Extent of damage development
		System load-carrying capacity
		Strain energy
		Displacement
		Structural sensitivity
	Probabilistic methods	Probability of failure
		Number of plastic hinge and probability
		Response spectrum and probability
		Strength and number of plastic hinge
		Information theory
		Risk analysis

In this paper, on the basis of the perturbation theory in matrix error analysis, the definition of structural robustness is introduced to determine key elements in framed structures. The global stiffness matrix of framed structures is generated and analysed by adopting matrix computation methods. The relative condition number of the global stiffness matrix is chosen as the quantitative indicator of structural robustness. Finally, two numerical examples are used to demonstrate the applicability of the proposed method for determining key elements in framed structures.

2. Key element indicator

Framed structures are geometrically stable systems consisting of a number of structural members, such as continuous beams, trusses, rigid frames, arches and grid

structures. Finite element numerical methods are usually adopted to analyse the framed structures subjected to loads acting on the structures. The governing equation for the finite element analyses is expressed here as

$$\mathbf{Ku=p} \tag{2}$$

where $\mathbf{K}$ is the global stiffness matrix of the framed structure concerned, $\mathbf{u}$ and $\mathbf{p}$ are the global nodal displacement vector and load vector, respectively. From the governing equation, the displacements at nodes are determined when the loads acting on the framed structure are known. Consequently, the stresses in structural members are calculated from the obtained displacements, which can be utilised for the design of the framed structure. In numerical analyses with elastic material properties and small geometrical deformation, framed structures are often assumed to behave linearly. The characteristics of the global stiffness matrix $\mathbf{K}$ in linear stage is useful to predict the structural behaviour. This assumption however may not be appropriate when structural collapse occurs.

In the case when the global stiffness matrix $\mathbf{K}$ is singular, the displacements in Eq. (2) can not be found while $\mathbf{p} \neq 0$, which indicates that the system is geometrically unstable. In the case when $\mathbf{K}$ is an ill-conditioned matrix, the governing equation in Eq. (2) becomes an ill-posed problem. There are three methods to determine whether $\mathbf{K}$ is ill-conditioned, i.e. very small values appear in the diagonal entry after $\mathbf{K}$ is decomposed by a triangular decomposition method, the determinant of $\mathbf{K}$ approaches zero, and the condition number of $\mathbf{K}$ approaches infinite. However, due to the complexity and large dimensions of the global stiffness matrix in the finite element analysis of framed structures, it may be difficult in undertaking the triangular decomposition and in computing the determinant of the global stiffness matrix due to the restrains of computational efforts. From the theory of inverse problems, if the condition number of the global stiffness matrix is large enough, any small perturbation of $\mathbf{K}$ or $\mathbf{p}$ will lead to significant change in the displacement vector $\mathbf{u}$. The physical interpretation is that if the global stiffness matrix is ill-conditioned, the small perturbation of physical properties (such as material and geometry properties) or of loads acting on the structure will lead to significant change in nodal displacements.

In order to assess the influence of the perturbations of load or stiffness on the displacement, the mathematical background of the matrix computations and inverse problems is described in Golub and Van Loan (1996) and Tikhonov and Arsenin (1977) and summarised below. When a perturbation $\delta\mathbf{p}$ exists in the right-hand side of Eq (2), its solution will be $\mathbf{u+\delta u}$, expressed here as

$$\mathbf{K(u+\delta u)=p+\delta p} \tag{3}$$

Substituting Eq. (2) into Eq. (3), leading to

$$\delta\mathbf{u=K^{-1}\delta p} \tag{4}$$

From the properties of matrix norm, the norm of the perturbation of $\mathbf{u}$ and the load vector $\mathbf{p}$ can be written as

$$\| \delta\mathbf{u} \| \leq \| \mathbf{K}^{-1} \| \cdot \| \delta\mathbf{p} \| \tag{5}$$

$$\| \mathbf{p} \| \leq \| \mathbf{K} \| \cdot \| \mathbf{u} \| \tag{6}$$

where $\| \bullet \|$ denotes a norm. From Eq. (5) and (6), giving

$$\|\delta \mathbf{u}\|/\|\mathbf{u}\| \le \|\mathbf{K}\| \cdot \|\mathbf{K}^{-1}\| \cdot \|\delta \mathbf{p}\|/\|\mathbf{p}\| \tag{7}$$

in which $\|\mathbf{K}\| \cdot \|\mathbf{K}^{-1}\|$ is defined as the condition number of the matrix $\mathbf{K}$, denoted here in the format of norm as

$$Cond(\mathbf{K}) = \|\mathbf{K}\| \cdot \|\mathbf{K}^{-1}\| \tag{8}$$

Equation (8) shows the upper bound of the relative error of $\mathbf{u}$ when a perturbation of $\mathbf{p}$ exists in Eq. (2). Extensive numerical investigations indicate that the solution of $\mathbf{u}$ disturbs greatly when the upper bound is large.

In the case when a perturbation $\delta \mathbf{K}$ presents in the left-hand side of Eq. (2), its solution assumed to be $\mathbf{u}+\delta \mathbf{u}$, namely

$$(\mathbf{K}+\delta \mathbf{K}) \cdot (\mathbf{u}+\delta \mathbf{u}) = \mathbf{p} \tag{9}$$

By using Eq. (2), the above equation is rewritten as

$$\delta \mathbf{u} = -(\mathbf{I}+\mathbf{K}^{-1}\delta \mathbf{K}) \cdot \mathbf{K}^{-1} \cdot \delta \mathbf{K} \cdot \mathbf{u} \tag{10}$$

From the properties of matrix norm, leading to

$$\|\delta \mathbf{u}\| \le \|\mathbf{I}+\mathbf{K}^{-1}\delta \mathbf{K}\|^{-1} \cdot \|\mathbf{K}^{-1}\delta \mathbf{K}\| \cdot \|\mathbf{u}\| \tag{11}$$

As the perturbation $\delta \mathbf{A}$ is small, it is reasonable to assume that

$$\|\mathbf{K}^{-1}\| \cdot \|\delta \mathbf{K}\| < 1 \tag{12}$$

By introducing the Banach lemma

$$\|\mathbf{I}+\mathbf{K}^{-1}\delta \mathbf{K}\|^{-1} \le 1/(1-\|\mathbf{K}^{-1}\delta \mathbf{K}\|) \tag{13}$$

The relative error of the solution can be expressed as

$$\|\delta \mathbf{u}\|/\|\mathbf{u}\| \le \|\mathbf{K}^{-1}\delta \mathbf{K}\|/(1-\|\mathbf{K}^{-1}\delta \mathbf{K}\|) \tag{14}$$

therefore

$$\frac{\|\delta \mathbf{u}\|}{\|\mathbf{u}\|} \le \frac{\|\mathbf{K}^{-1}\delta \mathbf{K}\|}{1-\|\mathbf{K}^{-1}\delta \mathbf{K}\|} = \frac{\left(\|\mathbf{K}^{-1}\| \cdot \|\mathbf{K}\|\right)\left(\|\delta \mathbf{K}\|/\|\mathbf{K}\|\right)}{1-\left(\|\mathbf{K}^{-1}\| \cdot \|\mathbf{K}\|\right)\left(\|\delta \mathbf{K}\|/\|\mathbf{K}\|\right)} \tag{15}$$

By using the condition number defined in Eq. (8), the above equation is rewritten as

$$\frac{\|\delta \mathbf{u}\|}{\|\mathbf{u}\|} \le \frac{Cond(\mathbf{K})\left(\|\delta \mathbf{K}\|/\|\mathbf{K}\|\right)}{1-Cond(\mathbf{K})\left(\|\delta \mathbf{K}\|/\|\mathbf{K}\|\right)} \tag{16}$$

From the relative errors in Eqs. (7) and (16), the condition number can be used as an indicator to determine the ill-posed problem described in Eq. (2). In order to simplify calculations, the norm in the condition number Eq. (8) is determined by

$$\|\mathbf{K}\|_{\infty} = \max_{1 \le i \le m} \sum_{j=1}^{n} |a_{ij}| \tag{17}$$

Thus, Equation (9) is rewritten as

$$Cond(\mathbf{K})_{\infty} = \|\mathbf{K}\|_{\infty} \cdot \|\mathbf{K}^{-1}\|_{\infty} \tag{18}$$

When structural damage occurs in the elements of the structure, structural stiffness may change, and then the global stiffness matrix may be modified. The relative condition number associated with the original and modified structural systems is defined as

$$R(\mathbf{K}) = Cond(\mathbf{K}_{new})/Cond(\mathbf{K}_{orig}) \tag{19}$$

where $\mathbf{K}_{orig}$ is the global stiffness matrix for the original structure, and $\mathbf{K}_{new}$ is the global stiffness matrix for the modified structure. When $R(\mathbf{K})$ increases due to structural damage, the damaged structure becomes less robust, and the member associated with the structural damage is considered as more critical. On the basis of this concept, key elements is determined and structural behaviour can be predicted.

3. Verification of the concept

In order to verify the proposed concept, a simple plane truss is chosen for analysing the condition number of the global stiffness matrix, as shown in Fig. 1. The plane truss has cross-sectional area of 0.01 m² for horizontal members, 0.005 m² for vertical members and diagonal members in the middle, and 0.0125 m² for diagonal members on both sides. The elastic modulus of materials is taken as 210 GPa.
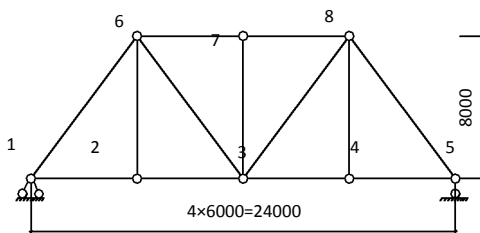

Fig. 1 Plane truss (units: mm)

Since the plane truss is statically determinate, removal of any bar in the structure will make the structure geometrically unstable, and the global stiffness matrix will be singular. Here, it is assumed that the structural numbers 3-7 and 3-8 are removed, respectively. The results for the condition number of the original and modified structures and the relative condition number between them are summarised in the following Table 2.

Table 2 Relative condition number of the global stiffness matrix

	$Cond(\mathbf{K})$	$R(\mathbf{K})$
Original structure	132.16	1.00
Modified structure by removing member 3-7	∞	∞
Modified structure by removing member 3-8	4.2E+17	3.2E+15

A Matlab programme was performed to obtain the results for the conditional number of the global stiffness matrix. In the case with removal of member 3-7 infinitive values were obtained for the $Cond(\mathbf{K})$ and $R(\mathbf{K})$, while in the case with removal of 3-8 a significantly large value was obtained. Thus, in these two modified cases the global stiffness matrix becomes singular. The same conclusion can be drawn when any member is removed from the structure.
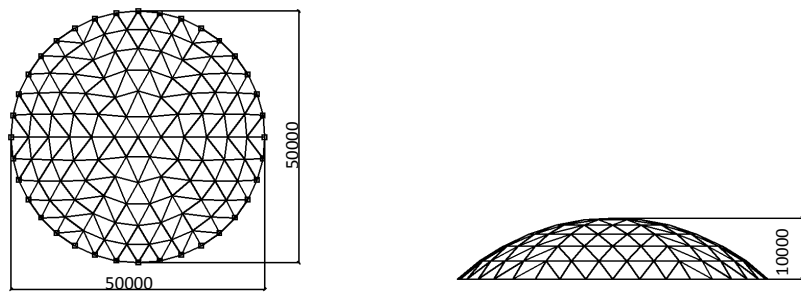
The global stiffness matrix becomes singular, if any member is removed from the statically determinate plane truss structure. It is obvious that the structure becomes a mechanism by taking away any member. Therefore, any member in the truss is a key element. From this simple numerical example, it is concluded that the relative

conditional number can indicate the behaviour of the structure and can be used for determining the key elements in the structure.

4. Case study

In order to further investigate the applicability of the relative conditional number in predicting structural behaviour, the proposed method is now applied to a more complex problem and compared with the strain energy based approach. A structure will deform and strain energy will be generated in the members while loads act on the structure. Strain energy is closely related to the geometrical and material properties of the structure, and could be reprehensive for structural behaviour as an indicator.

 A Kiewitt single layer shell is now used for numerical investigations, as shown in Fig. 2, where the nodes in outer ring are restrained in three directions. The members of the shell have cross-sectional area of 140×4 mm, elastic modulus of 206 GPa and density of 7850 kg/m^3. The members are modelled as 3D-beam-colume elements and connected by rigid joints. Due to its symmetry, only the 1/12 of the shell is taken for analysis and the structural members are numbered, as shown in Fig. 3. A total number of 33 cases for the modified structure are generated by removing an individual member at each time in the structure.

(a) Plan of the shell (units: mm)   (b) Elevation of the shell (units: mm)

Fig. 2 The Kiewitt single-layer shell
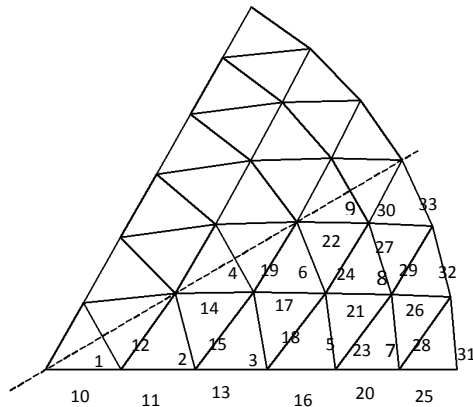
Fig. 3 Element numbering of the Kiewitt shell

As discussed in Zhang and Liu (2007), the structural strain energy can be used to assess the importance of members by introducing the ration of the modified strain energy to the original strain energy, namely

$$\gamma = U^{(e)}/U \tag{20}$$

where $U^{(e)}$ is the modified strain energy after removing the member e and U is the stain energy of the original structure. The structural strain energy for both $U^{(e)}$ and U typically consists of two components, i.e. the strain energy U_F generated by non-nodal loads and the strain energy U_N caused by nodal displacements.

For a beam fixed at both ends under the uniformly distributed load q, the component U_F^e for the modified structure can be calculated as follows

$$U_F^e = q^2 L^5/(1440EI) + q^2 L^2/(24EA) \tag{21}$$

where EI is the flexural stiffness, EA is the axial stiffness and L is the length of the beam. The component U_N^e for the modified structure can be calculated from

$$U_N^e = \mathbf{u}_e^T \mathbf{K}_e \mathbf{u}_e \tag{22}$$

where $\mathbf{u}_e$ and $\mathbf{K}_e$ are the nodal displacement vector and global stiffness matrix of the modified structure, respectively. The structural strain energy increases as loads increase. Further increase in loads may cause structural failure due to excessive strain energy stored in the structure.

When the shell is subjected to the gravitational body forces, i.e. $g=9.8$ m/s^2, the structure should behave linearly under this loading. In order to compare the results from two different methods, the results for both the relative conditional number $R(\mathbf{K})$ and the strain energy ratio γ are shown in Figs. 4(a) and 4(b), respectively.

(a) Relative condition number   (b) Strain energy ratio
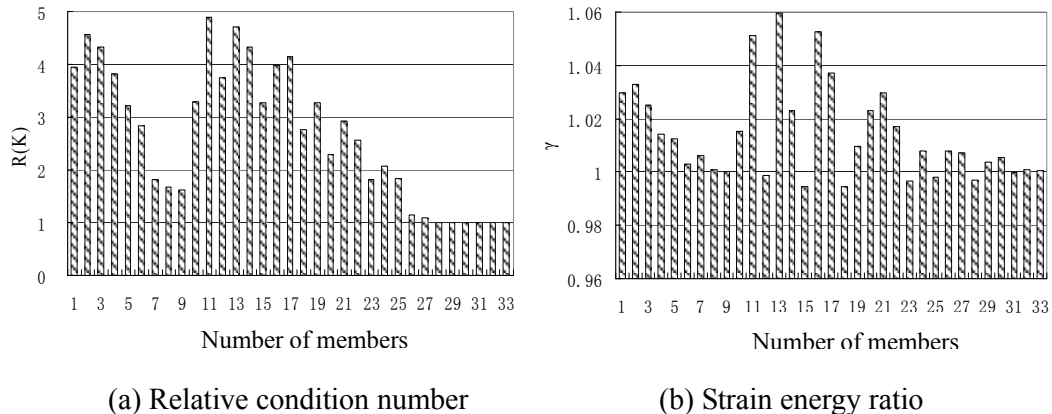
Fig. 4 Identification of key elements in the Kiewitt shell from different methods.

From the results indicated in Fig. 4, the results for the relative condition number obtained by the proposed method agree well with the results for the strain energy ratio. From the computed indicators, the inner members are more important than outer members. Members numbered from 31 to 33 are bars of zero forces, thus they have no contributions to the global stiffness matrix and strain energy.

Furthermore, the relative conditional number can reflect the characteristics of the structure. There are three types of members in the Kiewitt single layer shell, i.e. radial members, hoop members and diagonal members. In general, the radial members carry direct compress, while the hoop members take direct tension and the diagonal members mainly contribute to structural stability. Therefore, the radial members play more critical roles than the hoop members and diagonal members. The importance of the diagonal members increases if they are connected with critical radial and hoop members. From the results, radial members numbered 11 and 13 are the most critical members. The hoop member numbered 2 ranks the third important member, and the diagonal member 14 connected to the hoop member 2 is the fourth important member. The results in this case study show that the relative conditional number can not only predict the structural behaviour, but also reflect the structural characteristics.

5. Conclusions

A new indicator for determining the key elements in framed structures is proposed on the basis of relative conditional number for the original and modified global stiffness matrices. The proposed method can correctly predict the critical elements in the structure, which agrees well with the results from strain energy based method. From the results obtained for numerical investigations, following conclusions can be drawn: 1) The relative condition number of the global stiffness matrices is a useful indicator for determining key elements in framed structures; 2) The proposed relative condition number can be easily computed, since it only depends on the global stiffness matrix, without requiring information on loads and displacements; 3) The proposed method can give the rank of importance for members in framed structures by using the quantitative indicator of relative condition number; 4) The proposed indicator is able to predict structural behaviour and reflect structural characteristics.

References

Agarwal, J., Blockley, D., and Woodman, N. J. (2003). "Vulnerability of structural systems." *Structural Safety*，25(3), 263- 286．

Chen, H. P., and Alani, A. M. (2013). "Optimized maintenance strategey for concrete structures affected by cracking due to reinforcement corrosion." *ACI Structural Journal*, 110(2), 229-238.

Ellingwood, B. R., and Dusenberry D. O. (2005). "Building design for abnormal loads and progressive collapse." *Computer-Aided Civil and Infrastructure Engineering*, 20(3), 194-205.

Frangopol, D. M., and Curley, J. P. (1987). "Effects of damage and redundancy on structural reliability." *Journal of Structural Engineering*, *ASCE*, 113(7), 1533-1549.

Golub, G. H., and Van Loan, C. F. (1996). "*Matrix computations*." 4th Edition, JHU Press, USA.

Izzuddin, B. A., Vlassis, A. G., and Elghazouli, A., Y. (2008). "Progressive collapse of multi-storey buildings due to sudden column loss—Part I: Simplified assessment framework." *Engineering Structures*, 30(5), 1308-1318.

Sørensen, J. D. (2011). "Framework for robustness assessment of timber structures." *Engineering Structures*, 33(11), 3087-3092.

Starossek, U. (2006). "Progressive collapse of structures: Nomenclature and procedures." *Structural Engineering International*, 16(2), 113-117.

Starossek, U., and Haberland, M. (2011). "Approaches to measures of structural robustness." *Structure and Infrastructure Engineering*, 7(7-8), 625-631.

Tikhonov, A. N., and Arsenin, V. Y. (1977). "*Solutions of Ill-Posed Problems*." Wiley, New Yark.

Zhang, L., and Liu, X. (2007). "Network of energy transfer in frame structures and its preliminary application." *China Civil Engineering Journal*, 40(3),45-49 (in Chinese).

Numerical Simulations of Dynamic Responses of High-Speed Trains

to Random Track Irregularities

Mengyi Zhu[1], Xiaohui Cheng[2], Lixin Miao[1]

Abstract

High-speed railway is one of the most important critical infrastructure projects in China and develops rapidly in recent years. Its operational safety and comfortableness level draws great attention from the society. The random track irregularities may cause unacceptable dynamic responses of high speed trains and degrade the operational safety and passengers' comfortableness. In current Chinese safety control practices, comprehensive track inspection cars are used to record track irregularity data and corresponding vibration data of inspection cars at a regular frequency. In this paper, the track irregularities data recorded from Beijing-Guangzhou High-Speed Railway are studied following an advanced stochastic modeling approach. A simplified train-track interaction model is created using SIMPACK, which allows for the numerical analysis of the dynamic responses of high speed trains to random track irregularities. On basis of the simulation results of this simplified model, dynamic response for the train under different traveling velocity is analyzed.

Key Words

Comprehensive Inspection Train (CIT), Rail Track Irregularity, Random Process, SIMPACK Simulation, Dynamic Response

Introduction

High-speed railway constructions and operation have developed rapidly in China. The safety of such a long linear infrastructure also becomes a widely discussed topic. The challenge of reducing the malfunctioning and catastrophic derailment risks draws great attention to management department and civil engineers. As a basic but important interference source of railway train vibration, track irregularity influences train safety and comfort of passengers significantly. Though rail track irregularity is frequently observed, the accurate condition assessment of rail track system remains a challenge.

In China's current management, comprehensive inspection trains (CIT) are used to acquire data of track condition. But only time history analysis of this mega test data is performed for the performance evaluation of track system. The track maintenance scheme is advised on basis of the data analysis. (Chen 2006)Only the statistics of mean value, a threshold value and the standard deviation a reused to characterize the condition of track irregularity. The utilization of this mega data is

[1]Department of Industrial Engineering, Tsinghua University, Beijing, China
[2]Department of Civil Engineering, Tsinghua University, Beijing, China

inefficient. Since the current data analysis methods seldom discuss the frequency domain properties, the periodical components are ignored.

Therefore, a more efficient data analysis approach is required. To quantify the frequency domain properties of track irregularity, the power spectrum density (PSD) method is widely used. Corbin and Kaufman (Corbin 1983) calculated the PSD of track irregularity data obtained from American railways, and the periodic components in the PSD were studied as a tool to evaluate track conditions. Lyengar and Jaiswal (Lyengar 1995) established a Gaussian random field model for vertical irregularity data obtained from Indian railways. Random field theory (Vanmarcke 2010) was adopted in this research. The model can also predict the values of peak amplitudes in a given track length. Mohammadzadeh (Mohammadzadeh 2011) analyzed the track geometric irregularities using reliability techniques to study railway derailment probability. Jin (Jin 2009) carried out the PSD analysis of track irregularity on Beijing-Tianjin Inter-City Railway, discussed the properties of different wavelength components and compared the results with PSD of German railway.

Moreover, the dynamic response of a traveling train is a good approach to analyze the effect of track irregularity. This requires a complete train-track model and an accurate description of track irregularity. Studies have focused on the experimental or simulation methods. Kassa (Kassa 2009) established a train-track interaction model, in which the train was modeled as a multi-body component, and the track and switch were modeled as finite element model to analyze the high-frequency properties. Galvin (Galvin 2010) modeled the train as a three-degree-of-freedom body, but the track as a boundary element to analyze the dynamic response of high-speed trains. Wang (Wang 2011) applied the coupling dynamics theory to study the stability of trains on elastic tracks.

This Paper focuses on frequency spectrum analysis of the test data of CIT for Beijing-Guangzhou high-speed railway line, and establishes a train-track interaction model to study the dynamic response of different components under changing traveling velocities to random track irregularities.

Data

The track irregularity data analyzed in this paper was recorded by a comprehensive inspection train (CIT) in Jun. 2013, on Beijing-Guangzhou high-speed railway in China, where the maximum operation speed is 300km/h. Data from a 10-kilometer section of the track is studied, whose parameters are shown in Table 1. The CIT recorded 7 different parameters of irregularity, which includes vertical profile (left, right), alignment (left, right), lateral profile, gauge and twist of track. In practice, the vertical and alignment irregularities are used and studied extensively. The four samples of data used in this paper are shown in Figure 1.

| Section Mileage(km)	90-100
Test Train Velocity(km/h)	180
Sampling Interval(m)	0.25

Table 1 CIT Test Condition
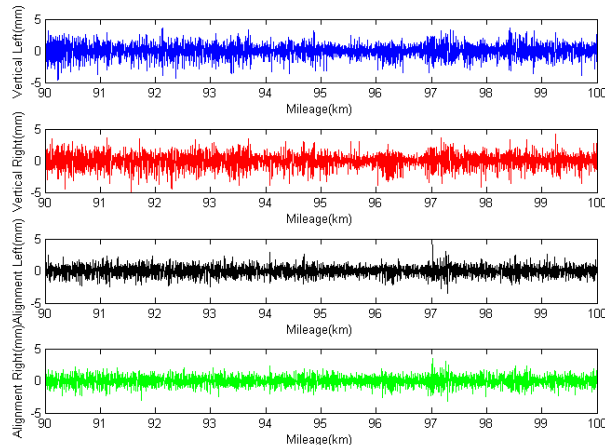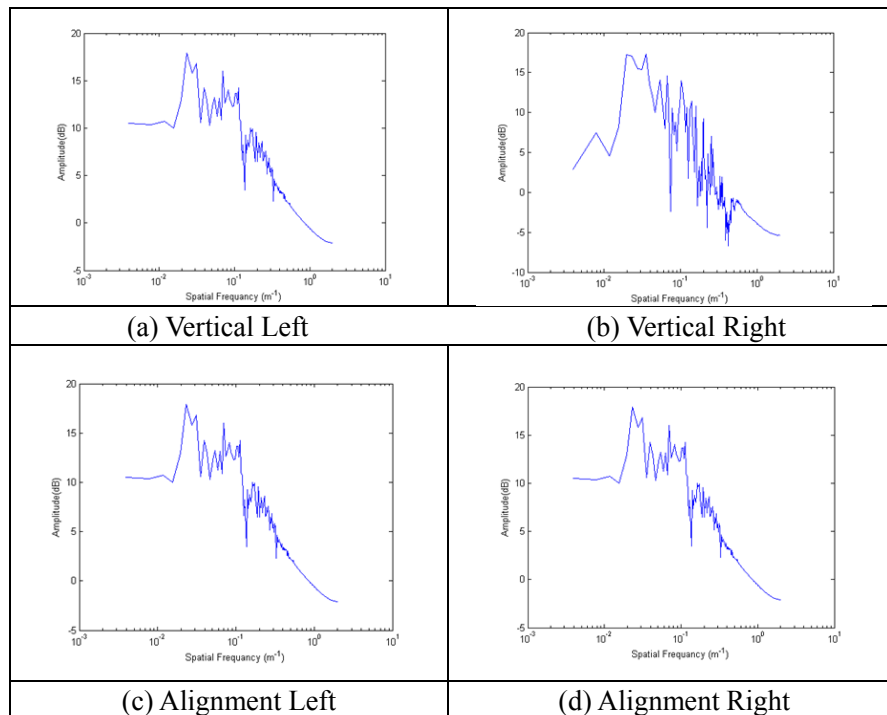
Figure 1 Data from the Selected Section

PSD Calculation

PSD function is a basic description of stochastic process in frequency domain. There are varies of algorithms to calculate the PSD function. In this paper, Periodogram method is applied. Results of PSD function of the four samples are shown in Figure 2. It can be observed that components whose spatial frequencies are between 10^{-2}-10^{-1} m^{-1} are most significant for all samples.

(a) Vertical Left	(b) Vertical Right
(c) Alignment Left	(d) Alignment Right

Figure 2 Result of PSD Calculation

Fitting of PSD Functions

In order to describe the PSD function as inputs for dynamic response simulation, analytic expressions are demanded. Several existing studies have presented different PSD fitting models. Chen (Chen 2011) gave PSD models for vertical and alignment track irregularity for railways in China. For vertical track irregularity PSD, the model is:

$$S_v(f) = \frac{A \cdot B^2}{f^2(f^2 + B^2)}$$

And the model for alignment track irregularity is:

$$S_v(f) = \frac{A \cdot B^2}{(f^2 + B^2)(f^2 + C^2)}$$

Where $S(f)$ is track irregularity PSD, f is spatial frequency; A, B and C are regression coefficient. Based on the data acquired from the section, the results are shown in Table 2.

Parameter	A	B	C
Left Vertical	0.8901	0.4519	-
Right Vertical	0.7726	0.3710	-
Left Alignment	1.3214	0.1826	0.0977
Right Alignment	1.5508	0.2217	0.0824

Table 2 Results of Regression Coefficient

Dynamic Model

A simplified multi-body model of train is established, as shown in Figure 3. The simulation of dynamic response for high-speed train is studied using SIMPACK software, as shown in Figure 4. And some critical parameters for train model are shown in Table 3.
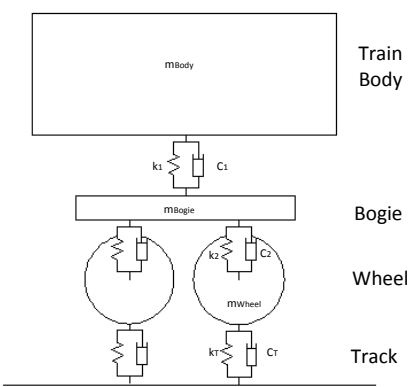
Figure 3 Dynamic Model
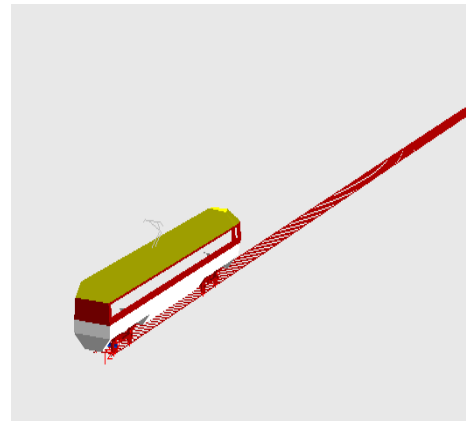
Figure 4 SIMPACK Model

Parameter	Value	Unit
Mass of Train Body	23825	kg
I_{yy} of Train Body	528	t·m2
I_{zz} of Train Body	506	t·m2
I_{xx} of Train Body	339	t·m2
Mass of Bogie	3970	kg
I_{yy} of Bogie	2936	kg·m2
I_{zz} of Bogie	4716	kg·m2
I_{xx} of Bogie	2058	kg·m2
Mass of Wheelset	1654	kg
I_{yy} of Wheelset	100	kg·m2
I_{zz} of Wheelset	726	kg·m2
I_{xx} of Wheelset	726	kg·m2
Diameter of Wheel	890	mm
Gauge	1493	mm
Bogie Wheelbase	2700	mm
Length between Bogie Pivot Centers	19000	mm

Table 3 Train Parameters

Input to Simulation

As mentioned above, the calculated PSD functions for track irregularities are applied as the inputs to the simulation.

Simulation Results

Velocity (km/h)	Location	Direction	Average Amplitude (m/s^2)	Standard Deviation (m/s^2)
100	Train Body	Vertical	0.1371	0.1728
		Lateral	0.0954	0.1180
	Bogie	Vertical	0.2984	0.3785
		Lateral	0.1446	0.1966
	Wheel	Vertical	7.1772	8.9360
		Lateral	0.1570	0.2568
180	Train Body	Vertical	0.1542	0.1731
		Lateral	0.1749	0.2192
	Bogie	Vertical	0.5145	0.6716
		Lateral	0.4866	0.6167
	Wheel	Vertical	18.4846	22.6746
		Lateral	0.6241	0.8562
300	Train Body	Vertical	0.4783	0.5553
		Lateral	0.4844	0.6189
	Bogie	Vertical	1.6782	2.2034
		Lateral	7.8413	10.5693
	Wheel	Vertical	49.8523	60.8961
		Lateral	18.3347	33.7415

Table 4 Results of Dynamic Response

Discussion

The simulation results under the same traveling velocity as the CIT test are compared with the test data in Table 5, which shows the average and maximum acceleration amplitudes are similar. This similarity verifies the effectiveness of the dynamic model used in this paper. Checked with the maintenance level of the current management method, neither of the CIT data nor the simulation data shows any results beyond level I, which suggests the track condition of this section is extremely good.
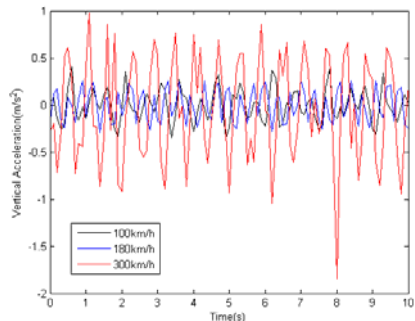
Item	Source	Average Amplitude (m/s^2)	Number of Result over Level I	Maximum Amplitude (m/s^2)
Vertical Acceleration of Train Body (m/s^2)	CIT Test	0.0814	0	0.4513
	Simulation	0.1542	0	0.2915
Lateral Acceleration of Train Body (m/s^2)	CIT Test	0.0691	0	0.2060
	Simulation	0.1749	0	0.5512

Table 5 Comparison of CIT Test Data and Simulation Results
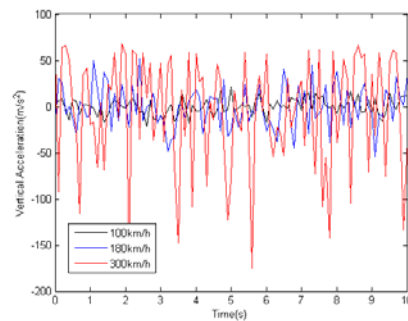
Item	Maintenance Level			
	I	II	III	IV
Vertical Acceleration of Train Body (m/s^2)	1.0	1.5	2.0	2.5
Lateral Acceleration of Train Body (m/s^2)	0.6	0.9	1.5	2.0

Table 6 Standard of Maintenance Level

Results under different traveling velocity of the same components are compared, as shown in Table 4 and Figure 5. It can be observed that the amplitude of acceleration increases significantly as the velocity ascends. This result indicates that higher speed makes larger dynamic response.

(a)Vertical Acceleration of Train Body   (b)Vertical Acceleration of Wheel

Figure 5 Acceleration under Different Traveling Speed

Results of different components under the same traveling velocity are compared, as shown in Table 4 and Figure 6.It can be observed that the acceleration amplitudes of the wheel are significantly larger than those of the bogie. And the acceleration amplitudes of the bogie are larger than those of the train body. This result can be explained by the existence of the two-level suspension system. It also indicates that the observations of the dynamic response of wheels rather than train body are easier to be analyzed and compared.

| (a) Vertical Acceleration at 100km/h | (b) Vertical Acceleration at 180km/h |
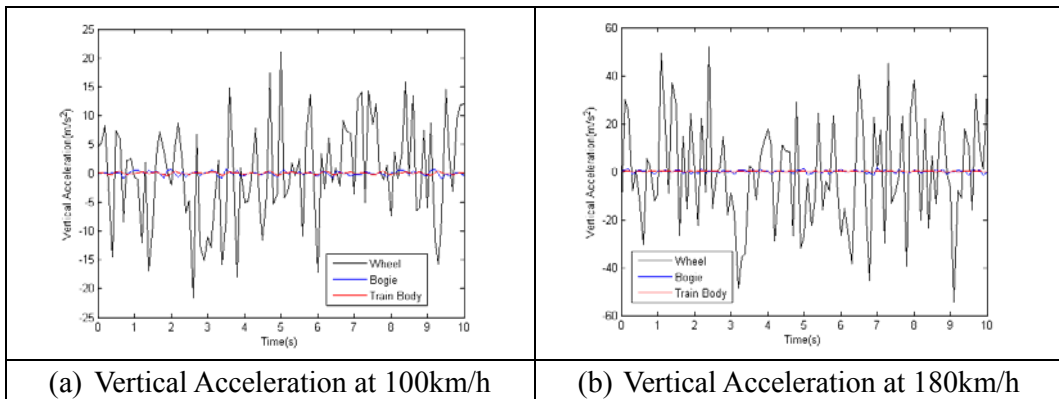
Figure6 Acceleration of Different Train Components

Conclusions

Random process modeling in time domain and frequency domain is extensively studied in engineering, which could become an important tool for evaluating the effects of track irregularity on railway operation and maintenance. Since the current track management methods involve little consideration of frequency domain properties, methods such as PSD analysis could be used to implement the current evaluation method of track conditions.

In this paper, track irregularities, which include data of vertical and alignment profile, are modeled as random processes. PSD of related irregularities are calculated and fitted into typical PSD functions as well. After establishing a multi-body train-track model in SIMPACK, the calculated PSD functions are applied as inputs for simulation. The simulation results verify the effectiveness of the model and give the same evaluation level. Comparison of acceleration under different traveling velocities shows the significant effects of high velocity to dynamic response. And the responses at different components indicate that the acceleration of wheel is much greater than that of bogie and train body. Therefore the dynamic response of wheel should be considered as the typical parameter for analysis and evaluation.

For future work, the parameter research for suspension system of the train should be carried out. And the contact force between wheel and track along with the acceleration could be studied as well.

References

Chen, X. (2006). "Time-Frequency Analysis and Prediction Study on Track Irregularities." PhD Thesis, China Academy of Rail Sciences.

Chen, X., Yang, F., Wu, W. and Chai, X. (2011). "Study on Evaluation Method of Power Spectrum Density for the Qinhuangdao-Shenyang Dedicated Passenger Railway Line". Journal of the China Railway Society, Vol28(4).

Corbin, J. C. and Kaufman, W. M. (1983). "Classifying Track by Power Spectral Density." Proceedings Mechanics of Transportation and Suspension System, American Society of Mechanical Engineers (ASME), New York, N.Y.

Galvin, P., Romero, A. and Dominguez, J. (2010). "Vibrations induced by HST passage on ballast and non-ballast tracks". Soil Dynamics and Earthquake Engineering, 30(9): 862-873.

Jin, S. and Zeng, Z. (2009). "Analysis of Bogl Slab Track Irregularity of Beijing-Tianjin Intercity High Speed Railway". Journal of Railway Science and Engineering, Vol. 6(1).

Kassa, E. and Nielsen, J. C. (2009). "Dynamic train-turnout interaction in an extended frequency range using a detailed model of track dynamics". Journal of Sound and Vibration, 320(4/5); 893-914.

Lyengar, R. N. and Jaiswa, O. R. (1995). "Random Field Modeling of Railway Track Irregularities." Journal of Transportation Engineering, Vol. 121(4).

Mohammadzadeh, S., Sangtarashha, M. and Molatefi, H. (2011). "A Novel Method to Estimate Derailment Probability Due to Track Geometric Irregularities Using Reliability Techniques and Advanced Simulation Methods", Archive of Applied Mechanics, Vol. 81(11).

Vanmarcke, E. (2010). "Random Fields: Analysis and Synthesis, Revised and Expanded New Edition".

Wang, K. and Liu, P. (2011). "Research on the Nonlinear Hunting Stability of Railway Freight Car on Curved Track". China Rail Science, Vol39(7).

Operational Evaluation of Vehicle Detection Systems at Rural Signalized Intersections

Juan C. Pernia[1] and Yolibeth Mejias[2]

Abstract

Approaches considered to improve safety at rural high speed signalized intersections most likely will adversely affect the operational aspect of the intersection, and vice-versa. Vehicle Detection Systems and Advanced Warning Systems (AWS) have been used to end the green phase for the major road approaches in a safely manner and to warn drivers of an upcoming change of phase, respectively. If phase termination is by max-out, it will eliminate the expected safety benefit by ending the green phase without considering vehicles that may be traveling the dilemma zone. In order to address this concern, an intelligent detection control system (D-CS) was developed by Texas A&M University. The main feature of this system is to identify if trucks are located in the dilemma zone in order to extend the green beyond the maximum limit to allow them to safely cross the intersection. This research evaluates the D-CS and traditional vehicle detection systems in a Canadian environment. For this evaluation, operational and safety performance of both systems were determined and compared at high speed signalized intersections. This paper only presents results for the operational evaluation. Parameters considered for this evaluation include: control delay, percent of vehicles stopping on red, and percent of vehicles in the dilemma zone. For field data collection, video cameras were used to record actual data (traffic volume, signal timing, others) at two signalized intersections. Results indicated that the D-CS has a better operational performance than the traditional vehicle detection system.

Introduction

Rural high speed signalized intersections are locations of great concern to professionals working in the transportation area. Efforts to improve the safety performance, operational performance or both at these locations are complex. Approaches considered to improve safety will adversely affect the operational aspect of the intersection, and vice-versa. Vehicle Detection Systems and Advanced Warning Systems (AWS) have been used to end the green phase for the major road approaches in a safely manner and to warn the drivers of a change of phase in the signal ahead, respectively. These systems will extend

[1] Lakehead University, Department of Civil Engineering, 955 Oliver Road, Thunder Bay, ON P7B 5E1 Canada; PH (807)766-7173; FAX (807) 346-7943; Email: jpernia@lakeheadu.ca

[2] University of South Florida, Department of Civil & Environmental Engineering, 4202 E. Fowler Ave., Tampa, FL 33620 USA; Email: mejiasde@mail.usf.edu

the green phase until a suitable large gap occurs in the traffic stream being served or, at approaches with high volumes, this phase will extend to its maximum limit (max-out). Phase termination by max-out eliminates the expected safety benefit by ending the green phase without considering vehicles that may be traveling the dilemma zone.

In order to address this concern, a new intelligent detection control system (D-CS) was developed by Texas A&M University through a project sponsored by the Texas Department of Transportation and the Federal Highway Administration. This system monitors cars and trucks at rural high speed signalized intersections in order to determine the best time to end the signal phase. The main feature of the D-CS is to identify trucks approaching the intersection and if the system determines that these trucks will be located in the dilemma zone when green reaches its maximum limit, it will extend the green beyond the limit to allow them to safely cross the intersection (Bonneson et al. 2002).

The Ministry of Transportation of Ontario (MTO) decided to install the D-CS in a high speed intersection in a Highway in Thunder Bay, Ontario in order to evaluate the operational and safety performance of this system in a Canadian environment. The research project conducted for this purpose was sponsored by MTO. This paper presents only the results of the operational evaluation of the D-CS and a traditional vehicle detection system at high speed signalized intersections.

Dilemma Zone

The dilemma zone is defined as the area of the approach wherein drivers demonstrate uncertainty about their ability to stop at the onset of the amber indication. When a driver is located in this zone on the onset of amber, he/she is exposed to a potentially hazardous situation in which a rear end collision may occur if he/she stops abruptly during the amber or an angle collision if he/she attempts to cross the intersection at the onset of red.

The dilemma zone boundaries have been established by several researchers (Zegeer et al. 1978, Parsonson et al. 1978 and Middleton et al. 1997). The beginning and ending of the zone have been defined as a distance from the stop line at which 90% of all drivers would stop or 10% of drivers would attempt to stop at the onset of the amber indication, respectively (Table 1). These studies suggest that the beginning and ending of the zone are about 5.0 seconds and 2.0 to 3.0 seconds travel time upstream of the intersection, respectively. For this project the dilemma zone is measured using the Ministry's Dilemma Zone Chart (STC 1997). The boundaries of the zone are adjusted from this chart according to the characteristics of the intersection.

Table 1: Dilemma Zone Boundaries

Approach Speed (mph)	Distance from Intersection in ft.	
	Probability of Stopping	
	10%	90%
35	102	254
40	122	284
45	152	327
50	172	353
55	234	386

Vehicle Detection Systems

Basic Green Extension Systems

These systems use one or more detectors per lane in advance of the intersection to extend the green until there are no vehicles in the dilemma zone or until maximum green limit is reached. MTO uses the Long Distance Detection or Double Long Distance Detection.

Long Distance Detection (LDD) System

For this system, a loop detector is placed upstream of the intersection, just outside the dilemma zone (MTO 2000). This placement is largely dependent of the speed of the vehicles approaching the intersection. When a vehicle passes over the loop, the information collected is used by the signal controller to extend the green interval to allow vehicles to pass through the dilemma zone prior to the onset of the amber. If no vehicles trigger the detector, the green phase end at the minimum time set.

Double Long Distance Detection (DLDD) System

This system uses two detecting loops imbedded in the highway in advance of the intersection (Figure 1). This system works similar to the LDD, information collected by the detectors is sent to a signal controller in order to determine if the green will be extended or not (MTO 2000). The main difference with the LDD system is that vehicle speeds are estimated with the DLDD. In this regard, if vehicles approaching have acceptable speed, the amber indication can be provided with a reasonable assurance of compliance. If the speed of the vehicles is excessive, the green will be extended to allow these vehicles to safely pass the dilemma zone before the onset of the amber indication. If no vehicles trigger the detectors, the green phase ends at the set minimum time, usually 20 seconds.
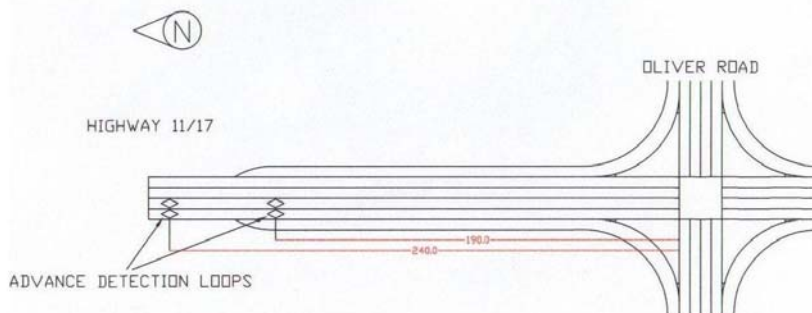

Figure 1: Double Long Distance Detection System (MTO 2000)

These vehicle detection systems are effective in moving the majority of vehicles through the dilemma zone without phase change when traffic volumes are not too high. However, if volumes are high, a maximum green limit will be used when ending the phase. In these cases, drivers caught in the dilemma zone will be prone to indecisive behaviour which may compromise their safety. Another concern with these systems is that when intersections experience high volumes of traffic flow on the major roadway, the maximum green limit will be reached continuously which translates in delays to the minor road approaches.

Green Termination Systems
The Detection Control System (D-CS)
The D-CS (Figure 2) is similar to vehicle detection systems such as the DLDD as it utilizes detectors placed upstream from the intersection to extend the green phase. The difference of the D-CS is that it employs an external computer installed near the intersection to determine the time best suited for ending the green phase on the major approaches by examining the vehicle speed and length characteristics. The best time to end the phase will be based on the fewest number of passenger cars in the dilemma zone, no heavy vehicles in this zone, and the delay to vehicles waiting on the side road (Zimmerman et al. 2002).
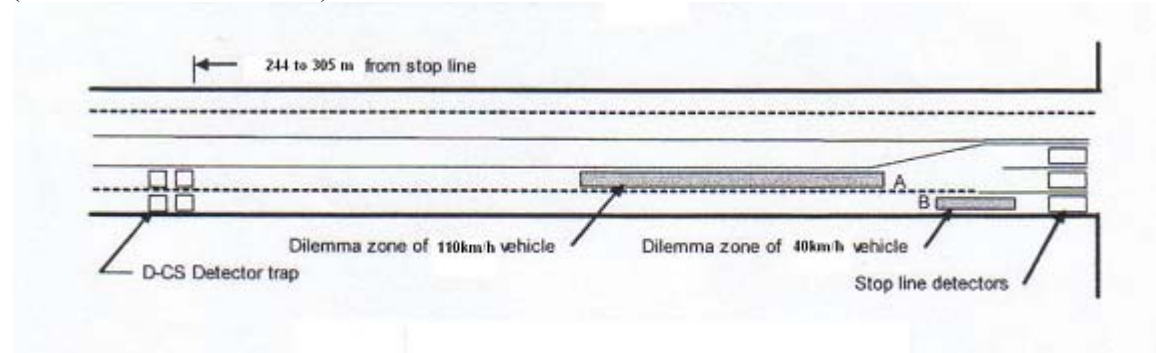

Figure 2: Detection-Control System Detection Design (Zimmerman et al. 2002)

The D-CS objective is to safely and efficiently control the high speed approaches of the intersection. The system identifies, in real-time, when vehicles are entering and leaving the dilemma zone. The computer defines the dilemma zone boundary using travel time to the stop line, usually beginning 5.5 seconds from the stop line and ending 2.5 seconds from the stop line. This system gives priority to heavy vehicles located in the dilemma zone. The system adaptive operation allows it to adjust to the changes in speed that occurs during the day as well as for the type of vehicle approaching the intersection when searching for the best time to end the green phase. This ultimately increases the safety of the intersection by reducing dilemma zone conflicts. Also, efficiency may be improved as delay to all traffic movements could be minimized by ending phases sooner.

Study Sites
Table 2 presents the characteristics of the study sites located in Thunder Bay, Ontario.

Table 2: Study Sites

| Intersection | Major Road Characteristics | | | | |
	Name	Approach	Through Lanes	Speed Limit (km/h)	Detection System
Highway 11/17 & Oliver Road	Highway 11/17	NB	2	90	D-CS (June 06)
		SB	2	90	D-CS (June 06)
Highway 11/17 & John Street	Highway 11/17	NB	2	90	DLDD
		SB	2	90	DLDD

Data Collection
For data collection, traffic and signalization characteristics were measured for the before and after periods for both sites with the D-CS and vehicle detection systems. Data were collected for a total of four hours a day, including morning, noon, and afternoon peak hours and one non-peak hour, during three days per period per major road approach per location. Data were collected during weekdays under good weather conditions.

The data collected included number of vehicles (trucks and cars) in dilemma zone when the signal changes to amber, number of vehicles stopping during red signal, cycle length, and control delay. Heavy vehicles were defined as transport trucks, tractor trailers, and construction vehicles (cement trucks, dump trucks, etc.). The quality of the data collection process was controlled to ensure the accuracy of the data gathered. Timing plans and location of loop detectors were gathered at the MTO office. Safety procedures were followed when collecting data at each site.

Study Site Set Up
The dilemma zone was marked out with spray paint to be consistent each day the data were collected at each site. Cones were placed on the side of the highway at the start, middle and end of the dilemma zone, with one cone lying on its side 20 m before and after the middle cone. The sideways cones were used as visual aids in order to determine a vehicles true location. Full dimensions for the dilemma zone can be seen in Figure 3.
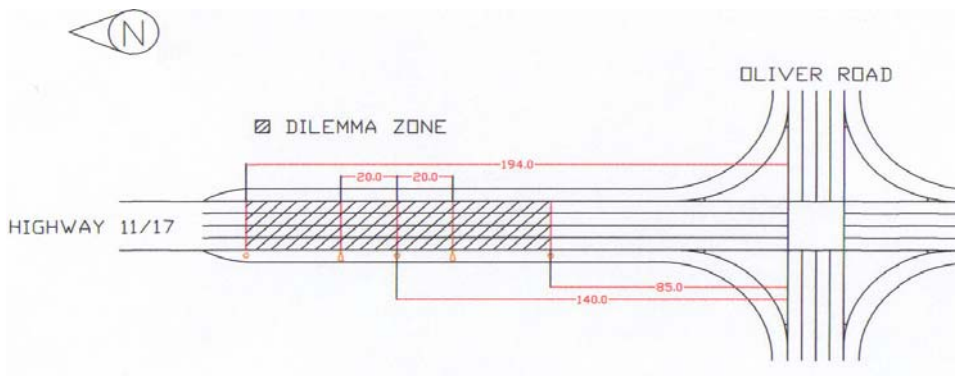

Figure 3: Dilemma Zone and Cone Placement

Two video cameras were used in the field to collect data. Each camera had a purpose, one to record the dilemma zone and the traffic light indications, and the other to record the intersection at close range to detect red light violations. The best location to place the first camera was on the highway shoulder just before the dilemma zone. The proper location for the red light violation camera was determined to be on a traffic island facing the same direction as the first camera. Figure 4 shows the camera set up at the locations.

Data Reduction
Most of the operational performance measures at each intersection were collected directly at the field. The video obtained from the dilemma zone camera was used extensively to review each case of vehicles caught in the dilemma zone and the driver's action. Results obtained on-site were found to be accurate as few changes had to be made

to the compiled data. This process was time-consuming, since some tapes were played more than once to ensure the accuracy of the data reduced.
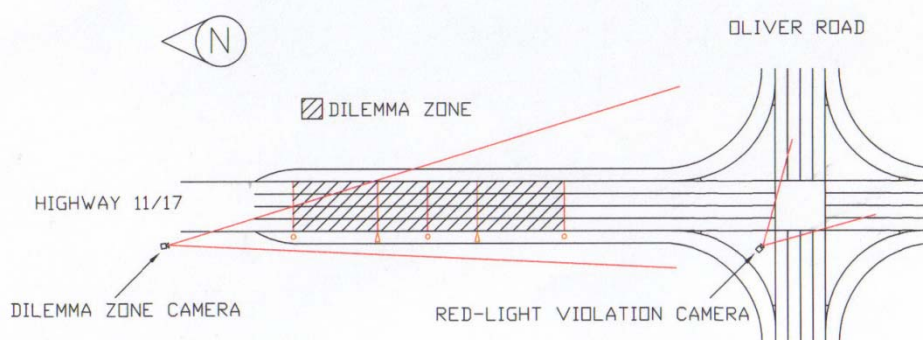

Figure 4: Typical Camera Locations at the Sites

Data Analysis and Results

A before and after study was conducted in order to evaluate the operational performance of the D-CS. This system was also compared to the DLDD of the control location. For this evaluation, the measures of effectiveness considered include: stop frequency, total control delay, and number of vehicles in the dilemma zone on the onset of amber.

Table 3 presents traffic characteristics and hours of data collected at the two intersections. The before and after refer to the period when the D-CS was installed at the intersection of Highway 11/17 and Oliver Road. For the control intersection, the vehicle detection system is DLDD for both periods. The before and after for this intersection is for comparison purposes only. The hours of data collected were four per day for three days for both periods per intersection. If a lower amount of hours is shown, it accounts for issues with the data collected. Average flow rates increased for the after period at both intersections.

Table 3: Traffic Characteristics and Hours of Data Collected

Intersection	Approach	Hours Collected		Flow Rate (veh/h)		
		Before	After	Before	After	Change
Highway 11/17	NB	12	12	524	554	30
& Oliver Road	SB	11	12	560	577	17
Highway 11/17	NB	11	8	382	435	53
& John Street	SB	8	12	491	522	31

Table 4 shows that the average green durations for the intersection where the D-CS was installed are greater for the after period as compared to the before period and basically the same for both periods at the control site. In regard to total control delay, it was estimated using the field survey method describe in Chapter 16 of the HCM (HCM 2000). Tables 4 also presents total control delay per hour for the before and after periods for both intersections. Control delay decreases for all approaches for both intersections even though average flow rates increased for all approaches in the after period.

Table 4: Average Green Duration and Total Control Delay

Intersection	Approach	Average Green Duration (s)		Total Control Delay (per hour)		
		Before	After	Before	After	Relative Change
Highway 11/17	NB	34.8	43.4	3.07	2.73	- 11
& Oliver Road	SB	36.5	42.3	4.13	3.64	- 12
Highway 11/17	NB	35.8	36.3	3.18	2.69	- 16
& John Street	SB	30.8	30.2	3.49	2.89	- 18

The value for total number of vehicles stopping at the approaches was calculated by estimating the average per hour for each approach and then multiplying by 12 hours (to account for difference in hours collected per period). When observing total number of vehicles stopping (Table 5), it increased for light vehicles but decreased for heavy vehicles at the intersection with the DC-S and increased for light and heavy vehicles for the after period at the other site. The relative change shows the direction of the change.

Table 5: Total Vehicles Stopping

Intersection	Approach	Vehicle Type	Total Vehicles Stopping		
			Before	After	Relative Change
Highway 11/17 & Oliver Road	NB	Light	2932	3096	6
		Heavy	164	158	-4
	SB	Light	3261	3426	5
		Heavy	172	143	-17
Highway 11/17 & John Street	NB	Light	2369	2697	14
		Heavy	188	227	21
	SB	Light	3422	3571	4
		Heavy	209	267	28

Table 6 presents information regarding number of light and heavy vehicles in the dilemma zone at the onset of amber and driver's action. This number of vehicles decreased for the intersection with the D-CS in the after period and increased for both types at the intersection without the D-CS. In reference to the driver's action, the proportion of vehicles stopping at the intersection of Oliver Road increased for the after period for light and heavy vehicles and is similar for both periods at the other location.

Conclusions

According to the results obtained on this study, the D-CS operational performance is more efficient that the one for the traditional vehicle detection system. In this sense, total control delay was lower in the after period for the location with the D-CS even though the average rate flows increased as well as the green times for this period. The increased of average green time for the after period for the intersection with D-CS seems to demonstrate adjustments made by the new system to account for heavy vehicles in the dilemma zone. Furthermore, the number of heavy vehicles captured in the dilemma zone as well as the number of vehicles stopping at the signal was lower for the after period for the intersection at Oliver Road. For the control location with the traditional DLDD, these numbers were greater for the after period. It is recommended to evaluate the D-CS at other locations in order to have a better assessment of its operational performance.

Table 6: Dilemma Zone Information

Intersection	Approach	Vehicle type	Vehicles in dilemma zone at onset of amber		Driver Action			
					Stop		Proceed	
			Before	After	Before	After	Before	After
Hwy 11/17 & Oliver Rd	NB	Light	283	112	173	98	110	14
		Heavy	25	5	12	4	13	1
	SB	Light	171	120	129	105	43	15
		Heavy	12	9	9	6	3	3
Hwy 11/17 & John St	NB	Light	120	146	94	126	26	20
		Heavy	3	14	3	11	0	3
	SB	Light	158	146	125	117	36	29
		Heavy	21	16	14	11	7	5

References

Bonneson, J., Middleton, D, Zimmerman, K., Charara, H., and Abbas M., (2022) "Intelligent Detection-Control System for Rural Signalized Intersections", Report No. FHWA/TX-02/4022-2, Texas Department of Transportation, Austin, Texas.

Highway Capacity Manual 2000, 4th Edition, Transportation Research Board, National Research Council, Washington, D.C.

Middleton, D., Nowlin, R.L., Shafer, M., Parham, H., and Jasek D. (1997) "Evaluation of Detector Placement for High-Speed Approaches to Signalized Intersections", Report No. TX-98/3977-1. Texas Department of Transportation, Austin, Texas.

Ministry of Transportation Ontario (2000) "Report on Pilot Project: Advanced Warning System. Highway 11/17 at Balsam Street", Thunder Bay Expressway.

Parsonson, P.S. (1978) "Signalization of High Speed Isolated Intersections", Transportation Research Record 681, Transportation Research Board, Washington D.C.

Synectics Transportation Consultants, Inc. (1997) "A review of Advance Warning and Detection Devices for Traffic Signals on Ontario Highways"

Zegeer, C.V., and Deen, R.C. (1978) "Green-Extension Systems at High Speed Intersections", ITE Journal, Washington D.C., 19-24.

Zimmerman, K., and Bonneson, J. (2002) "In-Service Evaluation of a Detection-Control System for High-Speed Signalized Intersections", Report No. FHWA/TX-05/5- 4022-01-1, Texas Department of Transportation, Austin, Texas.

A Metamodeling Technique for Exploring the Correlation between Mobility and Environmental Factors at Signalized Intersections

Rui Guo[1], Yu Zhang[2]*

ABSTRACT

Given the limitations of built-in emission estimation modules within current traffic simulations and signal optimization tools, this study aims to explore how the environmental impacts of transport are related to mobility measurements at signalized intersections based on high-fidelity simulation. The metamodeling-based method, involving experimental design, high-fidelity simulations, and multivariate regression analysis, is developed in this paper. The high-fidelity simulations, from microscopic traffic modeling and emerging emission estimator, provide the flexibility of utilizing various intersection types, vehicle types, and other characteristics such as drivers' behaviors, fuel types and meteorological factors. The multivariate multiple regression analysis provides large gains in expected prediction accuracy by taking the correlations between the response variables into account. The case studies demonstrate the operability of the proposed methodology and also set up the base for extensive application of simulation optimization to sustainable traffic operations and management.

INTRODUCTION

With the growing concern for the carrying capacity of natural systems and the environment, it has been generally recognized that transportation systems should be sustained in order to continually provide accessibility to the communities they serve (Richardson, 2005). A sustainable transport system is not only about mobility and accessibility; it also includes the aspects of energy efficiency and environmental protection. However in practice, majority of existing traffic control schemes are designed to mitigate traffic congestions, smooth traffic flows, or improve traffic safety, which rarely consider controlling the environmental externality of traffic for sustainable development. To develop eco-friendly control strategies, the ability to adequately measure and quantify fuel consumption and emissions from different traffic operational control strategies is of high importance.

Among many elements of the surface transportation system, the signalized intersections along urban arterials are often "hot spots" for fuel consumption and air pollution. It is because the higher traffic density, the longer vehicle idling time, and the most deceleration and acceleration driving cycles are usually involved at signalized intersections. Existing signal timing optimization tools, including fixed-time, coordinated actuated, traffic responsive and adaptive control(FHA, 2008), mainly focus on capturing an optimal cycle length and green time split to improve the mobility(Lv, 2012). Although some of these tools have the component of fuel consumption and emission when calculating the measurements of effectiveness, they are just imprecisely estimated at a macroscopic level. Given existing literature, it is not clear whether improving overall mobility (i.e., reducing delays and stops) would naturally lead to less energy consumption and result in reductions in all types of engine emissions. Thus, to better understand

[1]Department of Civil and Environmental Engineering, University of South Florida, 4202 E. Fowler Ave, ENB 118, Tampa, FL 33620; PH(813) 974-8906; email: rui@mail.usf.edu
[2]Department of Civil and Environmental Engineering, University of South Florida, 4202 E. Fowler Ave, ENB 118, Tampa, FL 33620; PH(813) 974-5846; email: yuzhang@usf.edu
*Corresponding Author

the environmental factors associated with different traffic conditions and control strategies, this research investigates the comprehensive relationships between mobility and environmental externalities at signalized intersections.

The built-in emission estimation modules within current traffic simulations and signal optimization tools are relatively under-developed with a very limited function. SYNCHRO (Husch and Albeck, 2006) and TRANSYT-7F (Hale, 2008) are two most commonly used macroscopic optimization software for traffic signal timing. Delay and its derivatives are commonly used as objective functions in most optimization software. For example, Synchro optimizes signal settings using a percentile delay, which considers cycle-by-cycle traffic variations. TRANSYT-7F optimizes signal settings using disutility index, which is based on a combination of delay and stops (Hale, 2008). However, mobility-based optimization is usually insufficient to characterize the fuel consumption and emission level of real-world driving behavior because different driving situations with various dynamics can have more or less the same average speed. Estimation of fuel consumption in Synchro and TRANSYT-7F is a linear combination of total travel distance, total delay, and total stops, without explicit considerations such as traffic congestion, vehicle type mix, geometric and environmental factors. Only three types of emissions (CO, NO_x and VOC) in Synchro are roughly estimated based only on fuel consumption with fixed rates. There's no component of emission estimation in TRANSYT-7F. Microscopic simulation modeling (e.g., CORSIM and VISSIM) is a faster, safer, and cheaper way to test actual field implementations. Basic input parameters for microscopic simulation models, such as geometry, number of cars, and traffic signal setting, are easy to be obtained; however, similar to signal optimization tools, the microscopic simulation software cannot adequately estimate environmental measurements of traffic network. Though VISSIM has an add-on module about emissions, the estimation method of emission module is simplified without detailed considerations.

As the air pollution problems attract more and more attentions all over the world, many researchers have attempted to incorporate traffic emission factors into traffic control strategies (Li et al., 2004; Chen and Yu, 2007). The advanced emission estimation models, such as Comprehensive Modal Emission Model (CMEM) (Barth *et al.*, 1999), the VT-Micro model (Ahn *et al.*, 2002) and Motor Vehicle Emission Simulator (MOVES) (EPA, 2012), provide a great opportunity for more accurate estimation. In particular, the emerging model MOVES surpasses previous emission estimation tools. This new emission modeling system is the most sophisticated to date and is being applied at a number of different modeling scales: all the way from the micro-scale (project-level, e.g., parking lot) to the macro-scale, where national-scale inventories are being generated for precursor, criteria, and greenhouse pollutants from on-road mobile sources (EPA, 2012). The embedded database and project level emission analysis in MOVES provide great opportunities for more accurate emission estimations in the traffic performance analysis. Based on the advanced tools, Park *et al.* (2009) proposed an optimization approach by integrating a CORSIM microscopic traffic simulation, the VT-Micro model, and a Genetic Algorithm (GA). Their study demonstrated that the proposed framework is effective in minimizing fuel consumption and emission with moderate trade-offs in delay and stops. Similarly, Stevanovic *et al.* (2009) presented an integration of VISSIM, CMEM, and VISGAOST to optimize signal timings. Findings of these studies show that a formula commonly used to estimate fuel consumption in traffic simulation tools inadequately estimates fuel consumption and cannot be used as a reliable objective function in signal timing optimizations. Kwak, Park and Lee (2012) quantified the impact of direct traffic signal timing

optimization aimed at minimizing fuel consumption based on TRANSIMS, the VT-Micro emission estimator and a GA-based traffic signal optimizer. Although the GA worked well in these studies, the GA-based optimization consumed significant time and computational loads. More efficient computational techniques should be sought and implemented in the direct optimization way. Lately, Lv (2012) investigated the relationship between emissions and control delay to formulate the optimization problem. Although his study demonstrated the air quality benefit by reducing vehicle emissions under different scenarios, the dataset of vehicle trajectories is quite small and he only considered control delay when exploring the relationship between mobility and emissions.

To fill in the gaps of current research, this study focuses mainly on exploring how environmental externalities are related to mobility measurements during the same time period at signalized intersections. Such a study could be integrated into the existing signal timing optimization software to develop a sustainable traffic signal control system that can simultaneously improve mobility and reducing emissions. It will promisingly save time and relief computational loads when comparing to the direct optimization. In addition, from the practical aspect, the findings from this study can provide more accurate estimation when conducting benefit-cost analysis, where benefits usually include reductions from delays and fuel consumptions, in current signal re-timing projects.

PROPOSED FRAMEWORK AND METHODOLOGY

As concluded from introduction, it is not clear how environmental externalities are related to mobility measurements at signalized intersections. Although some of the mobility and environmental measurements (e.g., travel time, emission rates) can be collected in the field, it is hard to collect all factors associated with traffic management operations practically (Golob and Recker, 2004), especially when considering different traffic demand levels with various geometric types and drivers' behaviors. However, the powerful simulation tools and emerging emission estimator provide the flexibility of utilizing various intersection types, vehicle types, and other characteristics such as drivers' behaviors, fuel types and meteorological factors.

Thus, in this study, a framework, based on a metamodeling technique, is build up to analyze the comprehensive relationship between mobility and environmental externalities at signalized intersections. A metamodeling technique is involved with experimental design, simulation modeling, and regression analysis (Kelton and Law, 2000; Wang and Shan, 2007). The experimental design is used for sampling and the regression model is developed from the simulation modeling. In existing literature, some studies applied simulation optimization to simultaneously optimize the mobility and environmental impacts of traffic signal timing at intersections. Nevertheless, due to complicated on-line simulation and tedious computations, the direct optimization method consumes significant time and computational loads. Given the popular coordinated traffic control of corridors and major arterials, methods that can solve multiple intersection problems in an efficient way are urgently needed. The metamodeling-based method proposed in this study will provide a tool to be used in simulation optimization and can reduce the complexity and computation load so that it can be used to solve large scale sustainable traffic management problem. Firstly, traffic signal optimization tool is used to provide optimal signal timing for some basic inputs. With the timing and basic inputs, traffic micro-simulation software is then applied to generate the detailed information needed for MOVES. Finally, given the mobility and emission measurements, econometrics tools are used to unveil the relationship. The same process is applied to different intersection types. The details of each step are discussed as below.

Step1: Traffic Signal Optimization

Traffic signal optimization tool, Synchro**,** used by over 4000 agencies and consultants throughout North America and the world, is selected to develop mobility-based signal timings for different levels of traffic demand. Three types of data are required for optimization and calculation: geometric information, traffic volumes and initial signal timings. Measures of effectiveness that are calculated by Synchro software after the optimization process include vehicle delay, fuel consumption, CO and NO_x emissions. Fuel consumption and emissions estimated by Synchro will be compared with the results from the emission estimator.

Step 2: Traffic Micro Simulation

Micro simulation models generate a significant amount of detail on vehicle performance that is critical for determining emissions and air quality impacts. In this study, VISSIM is used to develop second-by-second resolutions of individual vehicular data (speed/acceleration profiles). The accuracy of a traffic simulation model is mainly dependent on the quality of modeling driver behavior, such as car following and lane change. In contrast to less complex models that use constant speeds and deterministic car-following logic, VISSIM applies the psychophysical driver behavior model developed by Wiedemann (PTV, 2011). Two kinds of data are required for establishing a VISSIM network: 1) static data representing the roadway infrastructure; 2) dynamic data required for traffic simulation applications, which includes: (a) traffic volumes for all links; (b) vehicle routing, departure times and dwell times; (c) priority rules and signal timing plans at intersections. All of these data can be collected from the field. Note that multi-run for each scenario will be conducted in this study to reflect the different drivers' behaviors.

Step 3: Emission Estimation

Emission Estimator, Motor Vehicle Emission Simulator (MOVES**),** is used to model project level emissions. There are three approaches/options for describing vehicle activity in MOVES: (1) link average speed; (2) link drive schedules; and (3) operating mode distribution. The link drive schedules and the operating mode distribution approaches are more accurate and widely used in the project level modeling. One of the most important parameters in MOVES is Vehicle Specific Power (VSP), the primary metric to determine operating modes and to estimate emissions. VSP is an estimation of engine load based on the vehicle type, the vehicle's speed and acceleration, and the road grade:

$$VSP= (A/M)*v+ (B/M)*v^2+(C/M)*v^3+ (a+g*sin\theta)*v \qquad (1)$$

Where: v: velocity; a: acceleration; g: road grade; M: weight; A: rolling resist; B: rotating resist; C: aerodynamic drag. The coefficients *A, B, C,* and *M* vary among vehicle types. For example, for a passenger car, A=0.1565Kw-sec/m, B=2.002*10^{-3} kW-sec^2/m^2, C=4.926*10^{-4}kW-sec^3/m^3, and M=1.479 tons.

The outputs from VISSIM provide necessary details to calculate the operating mode distribution of the simulated traffic volume. Note that one advantage of the emission estimator MOVES is the default data of the contributing factors in the simulator database. MOVES can adjust the default emission rates to represent user specific values of these factors. Therefore, default data will be used for generating the emission rate look-up tables, with the exceptions of link drive schedules, meteorology, vehicle types and emission types.

Step 4: Regression Analysis

Regression analysis is commonly used in the field of air pollution (Vlachogianni et al., 2011). After the complex simulation modeling, correlation and regression analyses were conducted to approximate the environmental responses given high-fidelity simulation databases.

The outcomes of the traffic simulation and the advanced emission estimator are two training sets consisting of Set 2, the evaluations of the environmental response vector $\{y^m; m=1, 2, ..., n\}$ corresponding to Set 1, the mobility measurements $\{x^m; m=1, 2, ..., n\}$ (detailed comments are included later in the illustrative example on forming a database).

Considering the multidimensional characteristics of both sets of variables, a multivariate multiple linear regression (MMLR) was conducted to determine a formula that can describe how elements in a vector of variables respond simultaneously to changes in others. Multivariate statistics encompass the simultaneous observation and analysis of more than one outcome variable. This regression is "multivariate" because there is more than one outcome variable and a "multiple" regression because there is more than one predictor variable (SAS, 2009). Compared to the outcomes from conducting linear regression separately for each response variable on the common set of predictor variable, MMLR can provide large gains in expected prediction accuracy by taking the correlations between the response variables into account (Breiman and Friedman, 1997). The hypothesis being tested by a multivariate regression is that there is a joint linear effect of the set of independent variables on the set of dependent variables. Hence, the null hypothesis is that the slopes of all coefficients are simultaneously zero. Suppose we have p variables in Set 1, $X \in \square^{n*p}$ indicating mobility measurements, and q variables in Set 2, $Y \in \square^{n*q}$ indicating environmental externalities, then the statistical model for MMLR is:

$$\left[y_1 \cdots y_q \right] = \left[x_1 x_2 \cdots x_p \right] \left(\beta_1 \cdots \beta_q \right) + E_{n \times q}$$

$$Y_{n \times p} = X_{n \times q} B_{p \times q} + E_{n \times p}$$

Where **Y** represents n observations of a q-dependent variable, **X** represents the design matrix of rank p with its first column being the vector 1, B is a matrix of parameters to be estimated, and E represents the matrix of residual.

RESULTS AND DISCUSSION

This illustrative example aims to explore the relationship between mobility and environmental externalities at signalized intersections. Based on the proposed framework, two typical intersection types along the sample corridor are examined with different levels of traffic volume. The sample corridor, Bloomingdale Avenue, is a four-lane, divided roadway located in Hillsborough County, Florida. The Average Daily Traffic (ADT) volumes range from 29,100 vehicles per day (vpd) (east end) to 42, 600 vpd (west end) for weekday travel. Figure 1 illustrates the locations of traffic signals (red) and the placement of BlueTOAD™(blue) units along the corridor. The field travel time data is collected by the BlueTOAD™ units, which is very useful in the model validation.
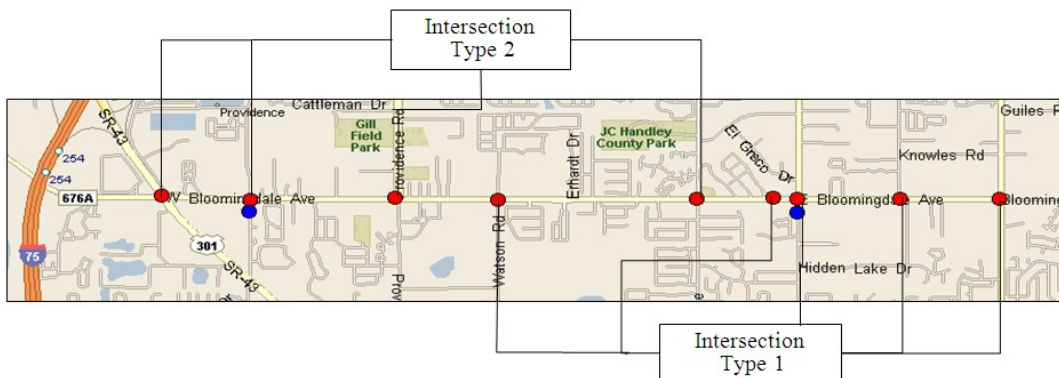

Figure 1. Map of the Sample Corridor-Bloomingdale Ave in Tampa, FL

Sampling for High-fidelity Simulation

The illustrative intersections in traffic simulation models are developed based on the two intersection types along the sample corridor, as shown in Figure 1. They are both the 4-leg intersection with actuated signal control and urban unrestricted access links. The major difference of these two types of intersection is the number of lanes in the minor street, which determines the capacity of the approaches in the minor street. The speed limits are 45mph for major roads and 30mph for minor streets. For turning vehicles, their speeds are reduced to 15 mph for left-turn and 9mph for right-turn movement, respectively.

Thirty scenarios for each type of intersection are designed to input in the traffic simulation models and emission estimator. The high-fidelity outputs are then used for the purpose of multivariate regression analysis. Thirty scenarios for each type are reasonable, given that a sample size of 25 or 30 is generally considered sufficiently large for most situations in statistical analysis (Howell, 2011). To assess the impact of various levels of traffic demand, different scenarios are generated based on 5 groups. The first group with 5 scenarios is based on the collected turning movement traffic data from the field. Group 2, 3 and 4 are developed based on the flow ratios with the consideration of different geometric configurations, with or without exclusive turning lanes. It is assumed that the base saturation flow rate is 1,900 pc/h/ln in this study. The flow ratio of critical lane groups is calculated by v/s, where v is adjusted flow rate in lane group, and s is adjusted saturation flow. The last group is developed to represent various percentages of turning vehicles on major and minor roads.

Quantification of Mobility and Environmental Measurements

Based on the proposed framework and developed scenarios, the traffic signal optimization software, Synchro, is used to develop mobility-based signal timings for different levels of traffic volume. Two vehicle types, a typical passenger car and heavy vehicle are modeled, which corresponds to MOVES vehicle type 21 (passenger car) and type 62 (combination long-haul truck with diesel engine). Based on heavy vehicles percentage in the AADT dataset along the studied area, heavy vehicles are set to be 5% in major road and 2% in minor road in all models. Measures of effectiveness, including mobility, fuel consumption and emissions, are all calculated and exported as the Synchro outputs.

Within the VISSIM model, exclusive turning lanes are coded with appropriate storage lengths obtained from the designed case. All links are modeled with 0% gradient as no nominal grade changes exist at the intersection. In VISSIM, vehicle reports are generated for a specified start and end time. Trajectory files generated in VISSIM are configured to output vehicle speed, acceleration, and location, within the network on a second by second basis. The data is stored in an .FZP file. Note that 10 model runs for each scenario are conducted for this analysis to reflect the stochastic nature of traffic flow and driving behaviors.

The detailed micro simulation outputs enable a direct quantitative linkage with MOVES. Within MOVES, the vehicle operating modes are stored as an operating mode distribution, which is the percent of all vehicle-hours for a specific link, pollutant, and vehicle type that fall within each operating mode. In our study, links are defined by each segment, including links for traffic approaching and departing at the signalized intersections. In addition, the connections for different turning movements in the center of the intersection are designed as small links. The link drive schedule approach, using user-defined drive cycles in MOVES, is adopted in this research. Based on the user-defined input and default data in the MOVES model, the emission rates are generated after running the MOVES.

Multivariate Regression Analysis for Model Fitting

After the complex simulation modeling, statistical analysis is applied to explore the relations between environmental externalities and mobility measurements. The data to be analyzed comes from the quantification of last step with a sample of n=60. Two collections of variables are measured, as listed in Table 1. There are 7 mobility performance variables in the first group and 7 environmental externality variables in the second group. Moreover, a dummy variable is used to test if there's significant difference between two intersection types.

Table 1. Summary of descriptive statistics

Variable	Mean	Standard deviation	Min	Max
Dependent variables(Environmental Measure)				
Y1: CO_2 (kg)	1000.36	577.98	263.1	2923.5
Y2: CO (kg)	9.23	4.35	2.514	22.249
Y3: NO_X (kg)	3.72	5.08	0.422	21.987
Y4: Total_PM10(kg)	0.13	0.09	0.028	0.434
Y5: Total_PM25(kg)	0.12	0.09	0.024	0.426
Y6: SO_2(kg)	0.01	0.01	0.002	0.03
Y7:Total Energy (MetaJoules)	13832.51	7964.44	3643.9	40304.4
Explanatory variables(Mobility Measure)				
X1: Control Delay(*s/veh*)	64.06	73.57	8.9	320.3
X2: Total Delay(hr)	102.87	157.63	4	667
X3: Stops (/veh)	0.68	0.08	0.5	0.8
X4: Total Stops(#)	2798.27	1252.20	698	6072
X5: Average Speed(mph)	14.42	7.59	2	29
X6: Total Travel Time(hr)	121.57	164.81	10	711
X7: Total Distance Traveled(*veh-mi*)	807.55	373.06	245	1985
Type: Dummy variable for intersection type	0.50	0.50	0	1

To avoid the multicollinearity problem, the interrelationship among multiple dependent variables is computed first, as shown in Table 2. Table 2 shows that X3 *(stops/vehicle)* has relatively weak relation to all other mobility measurements. X5 *(average speed)* shows negative relation to other variables and not as strong as others' relation. X2 *(total delay)* and X6 *(total travel time)* are strongly related, which means only one of them will be selected for regression.

Table 2. Correlations for Set 1-Mobility Variables

	X1	X2	X3	X4	X5	X6	X7
X1	1.00						
X2	0.97	1.00					
X3	0.32	0.20	1.00				
X4	0.88	0.87	0.49	1.00			
X5	-0.83	-0.76	-0.48	-0.89	1.00		
X6	0.97	**1.00**	0.21	0.88	-0.77	1.00	
X7	0.83	0.86	0.33	0.95	-0.78	0.87	1.00

The results of multivariate statistics and F approximations for MMLR, shown in Table 3, indicate if all of the equations, taken together, are statistically significant. The F-ratios and p-

values for four multivariate criterions are given, including Wilks' lambda, Pillai's Trace, Hotelling-Lawley Trace, and Roy's Greatest Root ((Breiman and Friedman 1997). The tests for the overall mode for our study indicate that the model is statistically significant, regardless of the type of multivariate criteria that is used (i.e. all of the p-values are less than 0.0001).

Table 3. Multivariate Statistics and F Approximations

S=7 M=-0.5 N=22					
Statistic	Value	F Value	Num DF	Den DF	Pr>F
Wilks' Lambda	0.00004365	30.23	49	237.96	<.0001
Pillai's Trace	3.15511872	6.10	49	364	<.0001
Hotelling-Lawley Trace	228.28867490	207.97	49	139.57	<.0001
Roy's Greatest Root	207.73050599	1543.14	7	52	<.0001
NOTE: F Statistic for Roy's Greatest Root is an upper bound.					

Table 4 summarizes the regression results for MMLR. The adjusted R square values, adopted to test how good the model fit to the sample data, show that all models are appropriate and good fits. The signs of the coefficients show if the mobility measurements have the positive or negative impact on the environmental factors. T values show if the coefficients of independent variables are statistically significant. The regression results and t-values demonstrate that 1) $Y1(CO_2)$ and Y7(Energy) follow the same trend, strongly related to X_2 (Total Delay) and X_4(Total stops) at 99% confidence interval; 2) For Y2(CO), the trend is slightly different from Y1 and Y7, the coefficient of X7(Total distance travelled) is significant at 1%, instead of X_2 (Total Delay); 3) Interestingly, NO_x shows strongly linear relationship with not only X2 (Total Delay) and X7(Total distance travelled), but also X5(average speed), this means NO_x emissions are also related to the vehicle speed; 4) Similar but not the same as NO_x, Particular matter (PM10 and PM25) also show strongly relationship with X5(average speed); 5) For SO_2 pollutant, the dataset is more scattered and other models may be needed to find a better fitting curve (the coefficients are significant at 5%); 6) For dummy variable-intersection type, the coefficients for model Y3(NOx), Y4 (PM10) and Y5(PM25) are significant at 95%, which means nitrogen dioxide and particular matter would be statistically different for different signalized intersection types. On the other hand, the coefficients of Type for other environmental factors are not significant; meaning others' relation with mobility would be statistically the same for different signalized intersection types. Thus, we can conclude that the current practice of mobility-based optimization can simultaneously reduce the fuel consumption and carbon emissions at 99% confidence interval. However, to reduce nitrogen oxide and particular matters, the mobility-based optimization is not good enough, especially for different types of intersections. Moreover, certain pollutants (especially NO_x, PM10 and PM25) statistically show different distribution at different types of signalized intersections since the coefficients of type are significant for these pollutants. Thus, for a corridor-level optimization, it is not trivial to incorporate environmental factors into the formulation of control strategies, since certain pollutants (especially NOx, PM10 and PM25) statistically show different distribution. Eco-driving control strategy is recommended for reducing these pollutants.

Table 4. Results of Multiple Regressions with Coefficients and T values

	Environmental Factors						
	Y1 (CO_2)	Y2 (CO)	Y3 (NO_x)	Y4 (PM10)	Y5 (PM25)	Y6 (SO_2)	Y7 (Fuel)
Adj. R^2	0.9783	0.9790	0.9902	0.9924	0.9922	0.9177	0.9780
Constant	527.305 (1.76)	1.049 (0.47)	-4.773 (-2.70)**	-0.088 (-3.08)**	-0.092 (-3.24)**	0.0097 (1.62)	7404.452 (1.79)
X1(control delay)	-2.544 (-2.13)*	0.006 (0.67)	0.0126 (1.77)	0.0005 (4.33)**	0.0004 (3.86)**	-5.1E-005 (-2.14)*	-35.610 (-2.14)*
X2(total delay)	1.686 (2.78)**	-0.0006 (-0.12)	0.024 (6.64)**	0.0001 (1.74)	0.0001 (2.28)*	8.8E-006 (0.73)	23.180 (2.75)**
X3(stops per vehicle)	-866.606 (-3.01)**	-2.587 (-1.22)	0.775 (0.46)	-0.006 (-0.23)	0.011 (0.41)	-0.011 (-1.94)	-12055 (-3.02)**
X4(total stops)	0.290 (4.05)**	0.0018 (3.38)**	-0.0003 (-0.79)	9.4E-006 (1.37)	8.2E-006 (1.21)	3.8E-006 (2.66)**	4.035 (4.06)**
X5(average speed)	-3.691 (-0.68)	0.016 (0.40)	0.1003 (3.11)**	0.002 (3.88)**	0.002 (3.67)**	0.0002 (-1.52)	-52.847 (-0.70)
X7(total distance travelled)	0.367 (1.38)	0.0054 (2.73)**	0.004 (2.85)**	0.0001 (5.33)**	0.0001 (5.10)**	5.4E-006 (1.02)	5.012 (1.36)
Type(intersection type)	-16.787 (-0.27)	0.036 (0.08)	1.180 (3.23)**	0.026 (4.36)**	0.024 (4.09)**	-0.001 (-0.79)	-254.497 (-0.30)

N-60; **Significant at1%; * Significant at 5%

CONCLUSION

Characterizing the relationship between environmental impacts from transport with mobility is critical for sustainable development. In this study, the authors developed a framework to determine how environmental externalities are related to mobility measurements during the same time period at signalized intersections. A metamodeling-based framework, involving experimental design, high-fidelity simulation (i.e., a traffic signal optimization tool, a microscopic simulation model, and an instantaneous emission estimator), and multivariate regression analysis were developed to explore the environment-mobility relationship at signalized intersections. Given the high-fidelity simulation databases, MMLR analysis was conducted to approximate the environmental responses to the mobility measurements. The results showed good fits for multiple-responses. However, t-values, which indicate if the coefficients of independent variables are statistically significant, showed various conclusions for different response variables (i.e., energy and emissions). The regression outcomes show that, to reduce NO_x, PM and SO_2, the mobility-based optimization is not good enough. Furthermore, the relationships between these emissions and mobility measurements considered in the study are different for various types of intersections, which requires the consideration of trade-offs between different intersections in a coordinated arterial while pursuing eco-friendly traffic control.

In future research, other types of regression models such as radial basis functions (RBF), multivariate adaptive regression spines (MARS), Kriging, and support vector machine (SVM) can be used and compared with MMLR used in this study. We also recommend incorporating NGSIM vehicle trajectory datasets and field travel time data using advanced technologies (i.e., BlueTOAD™ technology) to validate the simulation model. Moreover, emissions data can be collected in the field to validate the estimation results in the future. Another extension of this

study could be metamodeling-based optimization for a sustainable traffic signal control system that can simultaneously improve mobility and reduce emissions. Metamodeling-based optimization will save much time and relieve computational loads when compared to direct optimization.

REFERENCES

Ahn, K., Rakha, H., Trani, A., Van Aerde, M., (2002). "Estimating vehicle fuel consumption and emissions based on instantaneous speed and acceleration levels". Journal of Transportation Engineering, 128(2),182-190.

Barth, M., An, F., Younglove, T., Scora, G. et al.(1999). User's guide: comprehensive modal emissions model, Version 2.0. Research report prepared by the University of California, Riverside, CA.

Breiman L., Friedman J. H., (1997). "Predicting multivariate responses in multiple linear regression". Journal of the Royal Statistical Society, 59(1): 3-54.

Chen, K., Yu, L., (2007). "Microscopic Traffic-Emission Simulation and Case Study for Evaluation of Traffic Control Strategies". Journal of Transportation Systems Engineering and Information Technology, 7(1), 93-100.

Environmental Protection Agency (2012). "Motor Vehicle Emissions Simulator (MOVES) User Guide for MOVES2010b", Assessment and Standards Division, Office of Transportation and Air Quality.

Federal Highway Administration.; Kittelson and Associates, Incorporated.,(2008). "Traffic Signal Timing Manual". U.S. Department of Transportation. Publication Number: FHWA-HOP-08-024.

Golob, T. F., Recker, W.W.,(2004). "A method for relating type of crash to traffic flow characteristics on urban freeways". Transportation Research Part A: Policy and Practice, 38(1), 53-80.

Hale, D.(2008). "Traffic Network Study Tool- TRANSYT-7F User Guide", United States Version. Mc.Trans Center in the University of Florida, Gainesville.

Howell, D.C. (2011). "Statistical methods for psychology". Cengage Learning.

Husch, D., Albeck, J. (2006), "Synchro Studio 7 User Guide". Trafficware Ltd.

Law, A. M., Kelton, W. D. (2000). "Simulation modeling and analysis". Boston, MA.

Kwak, J., Parkand, B., Lee, J., (2012). "Evaluating the impacts of urban corridor traffic signal optimization on vehicle emissions and fuel consumption", Transportation Planning and Technology, 35(2), 145-160.

Li, X. G., G.Q. Li, S.S. Pang, et al.(2004). Signal timing of intersections using integrated optimization of traffic quality, emissions and fuel consumption: a note. Transportation Research Part D, 9, 401-407.

Lv, J.P.,(2012). "Investigating Emission Reduction Benefit from Intersection Signal Optimization". The ITE Daniel B. Fambro Student Paper Award Competition, Texas District.

Park, B., Yun, I., Ahn, K.,(2009). "Stochastic optimization for sustainable traffic signal control". International Journal of Sustainable Transportation, 3(4), 263-284.

PTV AG (2011). "Vissim 5.40-01 user manual". Karlsruhe, Germany.

Richardson, B.C.,(2005). "Sustainable transport: analysis frameworks". Journal of Transport Geography, 13(1), 29-39.

Stevanovic, A., Stevanovic, J., Zhang, K., Batterman, S., (2009). "Optimizing Traffic Control to Reduce Fuel Consumption and Vehicular Emissions". Transportation Research Record: Journal of the Transportation Research Board, No. 2128, 105-113.

Vlachogianni, A., Kassomenos, P., et al. (2011). Evaluation of a multiple regression model for the forecasting of the concentrations of NO_x and PM10 in Athens and Helsinki. Science of the Total Environment, 409, 1559-1571

Wang, G.G., Shan, S., (2007). "Review of metamodeling techniques in support of engineering design optimization". Journal of Mechanical Design, 129(4), 370-380.

An Optimization on Subway Vehicle Maintenance Using Multi-population Genetic Algorithm

Zhang Di[1], Hu Hao[2]*,

Abstract: In the area with subway engineering, maintenance optimization is an important issue for engineers and subway administrations because these actions allow maintenance costs to be reduced with acquired reliability. Aiming to optimize maintenance strategy of subway vehicle, this paper presents a multi-objective maintenance model of cost effectiveness. Moreover, there is no doubt that subway vehicle has more than two statuses, rather than simple linear 0-1 statuses (working, or failure), so this paper develops a multi-status subway vehicle model to reflect the reality. Multi-population genetic algorithm is employed to solve the non-linear model. Additionally, to subsidize the optimized maintenance strategy, this paper studies a case of driven locking mechanism subsystem in subway vehicle. The result shows the advantages of the optimized selective maintenance. The maintenance strategy proposed in this paper reveals a new method of subway maintenance.
Index Terms: Subway vehicle; Maintenance; Universe generating function (UGF); Multi-population genetic algorithm (MPGA)

INTRODUCTION

Considered as an inevitable way to solve modern serious traffic congestions，subway has played an important role in urban transportation. In 2012, subway was responsible for 5,160,000 daily passengers, accounting for approximately 32.25% of all public passenger traffic volume in Shanghai and it is expected that the passenger transportation of subway in Shanghai will continue to increase in at least 10 years. It is obvious that this demand increase cannot be satisfied with only building new subways, the efficiency of existing and new subways should be increased.

Maintenance clearly impacts on component and system reliability: If too little is done, this may result in an excessive number of costly failures and poor system performance and, therefore, reliability is degraded; done too often, reliability may improve but maintenance costs increase. Maintenance strategy is always a hot issue with the aim of finding trade-offs between maintenance expenditure and system risk and profit (Wang 2002).

[1] School of Naval Architecture, Ocean and Civil Engineering, Shanghai Jiao Tong University; e-mail: zhangdifanny@gmail.com
[2] * Corresponding Author, School of Naval Architecture, Ocean and Civil Engineering, Shanghai Jiao Tong University; e-mail: hhu@sjtu.edu.cn

Maintenance problems for subway vehicles have been extensively investigated in the literature. Ref. (Liu 2008) studies on the maintenance mode problem and focuses on the method of maintenance source distribution, without considering imperfect maintenance and maintenance constraints. Aiming to reduce vibration, (Zepfe 2008) studies the influences of targeted maintenance tasks on subway vehicles with a statistical model. Ref. (Pievato 2003) considers the prediction of failures in subway vehicles using Bayesian analysis. Ref. (Shi 2008) analyzes the cycle and the maintenance rank of subway vehicle door system, by applying RCM. Ref. (Yan 2008) proposes to use FMEA and RCM in subway vehicles maintenance. Some researches on demanding for spare parts, an important aspect of system maintenance, have been done, which have been summarized by (Wen 2011).

In the field of multi-status system, some researches have been done. Multi-status system was firstly proposed by (Barton 1974, Barlow 1978). Ref. (Rice 1998) develops a mathematical programming model to optimize the selective maintenance problem for a parallel-series system with identical components. A selective maintenance model on common multi-status system is established, and GA is used to solve the optimized problem in (Liu 2010). Ref. (Wang 2011) develops the model of reliability with maintenance constraints but fails to consider selective maintenance strategy.

The remainder of this paper is organized as follows. Section II firstly gives a brief introduction to imperfect maintenance, as well as some definitions and assumptions during the model formulation. Then multi-objective model of optimized maintenance method is set up. A case study of a driven locking mechanism of subway with related results studies are presented in Section III. Finally, conclusions are followed.

MAINTENANCE OPTIMAZATION MODELING

During researches on maintenance of subway vehicle system, the condition of system after maintenance activity is often treated as maximum repair, which is referred to return to a perfect condition, or minimum repair, which means the system returns to the condition just before failure happens. However, in fact, the vehicle generally recovers to the status between the two extreme conditions mentioned above. As a result, this paper models the imperfect maintenance of the multi-status subway vehicle and describes the dynamic changes of the system performance before and after maintenance.

To focus on key problems, definitions and assumptions have been made as:

1). Vehicle is composed by M two-status elements. The two-status of element i is expressed by $g_i = \{g_{(i,1)}, g_{(i,2)},\}$, where $g_{(i,1)} = 0$ means component i is inactive and $g_{(i,1)} \neq 0$ means active. g_i is the capability of element i in the vehicle system.

2). Vehicle system has k_s types of status, where status i can be described as g_{si} with the possibility of p_{si}.

3). When an element is failure, the poor status can be detected immediately.

4). The reliability function and age of each element can be obtained.

Subway vehicle has characteristics of aging related to operating time period. As a result, Kijima I, a classic model of maintenance performance, is chosen to present the service age (Levitin 2008, Kijima 1988). Service age of components can be used to describe the vehicle's service age after maintenance according to Kijima I (Liu 2010).

$$A_i(k+1) = \alpha_i(k) \cdot A_i(k), \quad \alpha_i(k) = 1 - (\frac{s_i}{N-1})^m, \quad m = \frac{W}{A-W} \tag{1}$$

Where $A_i(k)$ and $A_i(k+1)$ denote the service age of element i before and after task k respectively. $\alpha_i(k)$ is the service age reduction factor of element i. A is the life cycle of subway vehicle, and W is the working time period of subway vehicle. m is a constant that determines the exact relationship between cost and reduction factor. s_i is the chosen maintenance strategy of element i. N is the number of maintenance strategy levels.

Each element of the vehicle has N levels of maintenance strategies to choose. The level of maintenance action and cost corresponding to s_i for elements either in failure or working status is numerated in Table 1 and Table 2 respectively (Liu 2010).

Table 1 Corrective Maintenance Action And Cost Corresponding To s_i For Failure Element i

s_i	Maintenance Action	Corrective Cost $C_r(k)$
0	Minimal maintenance	c_i^0
⋮	⋮	⋮
i	Imperfect Maintenance	$i/(N-1) \cdot C_{r0} + c_i^0$
⋮	⋮	⋮
$N-1$	Corrective Replacement	$C_{r0} + c_i^0$

Table 2 Preventive Maintenance Action And Cost Corresponding To s_i For Working Element i

s_i	Maintenance Action	Preventive Cost $C_p(k)$
0	Do Nothing	0
1	Minimal Maintenance	c_i^0
⋮	⋮	⋮
i	Imperfect PM	$(i-1)/(N-2) \cdot C_{p0} + c_i^0$
⋮	⋮	⋮
$N-1$	Preventive Replacement	$C_{r0} + c_i^0$

The aim of maintenance is to reach the highest reliability $R(k)$ using the lowest cost $C(k)$, during mission k. Therefore, the multi-objective vehicle system maintenance model can be set up.

$$\begin{cases} \max R(k) \\ \min C(k) \end{cases} \quad \text{s.t} \quad R(k) \geq Q(k), \quad C_r(k) + C_p(k) \leq C_0(k) \tag{2}$$

Where Q_k is the minimum status value of the system to accomplish task k. $C_r(k)$ and $C_p(k)$ denote corrective cost and preventive repaired cost respectively. And $C_0(k)$ is the distributed maintenance cost budget of task k.

The system reliability can be counted by classic method, using Universe Generating Function (UGF)—firstly put forward by Ushakov in 1987, which is a concise and efficient tool in discrete random variables combination calculation (Cochran 1003, Levitin 2005, Levitin 2007). Since then, it has been widely applied in reliability evaluation area.

$$u_i(z,t) = R_i z^{g_{i1}} + (1 - R_i) z^{g_{i2}} \tag{3}$$

$$u_s(z,t) = \otimes \{u_1(z, L(k)), u_2(z, L(k)), \cdots, u_m(z, L(k))\} = \sum_{i=1}^{k_s} p_{s_i}(L(k)) \cdot z^{g_{s_i}} \tag{4}$$

The system status g_{si} can be calculated by

$$g_{si} = f(g_1, g_2, \dots g_m) =$$

$$\begin{cases} sum(g_1, g_2, \dots g_m), elements\ 1,2, \dots, m\ are\ connected\ in\ series \\ min(g_1, g_2, \dots g_m), elements\ 1,2, \dots, m\ are\ connected\ in\ parrell \end{cases} \quad (5)$$

Where $\otimes$ indicates the calculation combination operator, which is determined by the way of elements connected. $L(k)$ denotes the time period of task k. g_{si} and $p_{si}(L(k))$ represent value and possibility of system status i during task k respectively (Levitin 2008).

After the system reliability has been made, the possibility of the system accomplishing task k can be described by the following function.

$$R(k,w) = \sum_{i=1}^{k_s}(p_{si}(L(k)) \cdot \mu), \ \mu = \begin{cases} 0, \ g_{si} < Q_k \\ 1, \ g_{si} \geq Q_k \end{cases}, \ Q_k = 1 - \exp\left(-\omega\frac{L(k)}{E(L)} - \beta\right) \ (6)$$

To reflect the vehicle operating, Q_k is a variable, which is mostly related with $L(k)$. The relation between Q_k and $L(k)$ can be described as the function bellow.

Here ω denotes the shape of the function, whereas β determines the minimum reliable possibility of the system. And $E(L)$ is mathematical expectation of L (refers to time period of each task) in one year.

The risk will be very high, if the vehicle, the core of subway, is in poor status. Moreover, the maintenance cost is not only repaired cost pluses preventive cost but also the potential risk cost of vehicle failing to complete the mission. Therefore the cost formula of system maintenance is the sum of corrective maintenance cost, preventive maintenance cost and risk cost.

$$C(k) = C_r(k) + C_p(k) + C_h(k) \tag{7}$$

$$C_r(k) = \sum_{i=1}^{M}\left(\left(\frac{S_i+1}{N} \cdot C_{r0} + c_i^0\right) \cdot [E_k(n_i)]\right) \tag{8}$$

$$C_p(k) = \sum_{i=1}^{M}\left(\frac{S_i}{N-1} \cdot C_{p0} + c_i^0\right) \tag{9}$$

$$C_h(k) = \sum_{i=1}^{M}\left([E_{k+1}(n_i)] \cdot C_{hi}\right) \tag{10}$$

$$\text{s.t}\ \ E_k(n_i) = \int_0^{A_i(k)} h_i(x)dx = \int_0^{A_i(k)} \frac{(1-R_i(x))'}{R_i(x)} dx_i$$

$$E_{k+1}(n_i) = \int_0^{A_i(k+1)} h_i(x)dx = \int_0^{A_i(k+1)} \frac{(1-R_i(x))'}{R_i(x)} dx_i$$

Where c_i^0 denotes fixed cost of element i. C_{r0} and C_{p0} determine cost of perfect corrective maintenance and perfect preventive maintenance respectively. After mission k completed, elements may change the status from good to poor, and because of limited maintenance source, the workers have to pay special attention to the elements, which may play a big role in system reliability. $E_k(n_i)$ is the mathematical expectation of failed number of element i after mission k. And $[E_k(n_i)]$ is the rounded number of $E_k(n_i)$, which is a parameter for judging the status of element i before maintenance. When $[E(n_i)]=0$, element i is assumed to be functioning; if not, element i is treated as failed. $h_i(x)$ is the risk rate function of element i.

CASE STUDY

The proposed model is implemented by using a vehicle on subway line 5 in Shanghai as a case study. As the complexness of subway vehicle, only key issues are emphasized. In all the failure cases caused by subway vehicle during operation, the percentages of different failures are that the door system accounting for 35-40%, the braking system accounting for 35-40%, the air-condition system accounting for 10%-15% and others accounting 29%-30%, according to the failure cases statistics (Yan 2008). As the door system accounts for the largest percentage, it should be firstly analyzed. As a result, the driven locking mechanism is selected during this analysis because of its key role in security of the door system.

Driven locking mechanism is composed of driven silk pole, right nut assemble, left nut assemble and unlock wheel assemble. Although the system is still functioning at the end of the last mission (k mission) without any maintenance action, the probability of accomplishing the next mission is only 0.8666. As a result, decision maker has to optimally allocate the maintenance cost to each element to maximize the probability of successfully completing $(k + 1)$ mission with minimum cost.

The failure rates of all the elements obey Weibull Distribution of two-parameter, based on the data collection in Shanghai subway and relative research (Shi 2008). The duration of the $k + 1$ mission $L(k)$ is supposed to be 500 hours before taking next maintenance action. According to the operating time period of vehicles provided by maintenance engineers of Shanghai subway, $E(L) = 400$ hours is chosen. And using (6), $Q_k = 0.9762$ is achieved. The life cycle of subway vehicle $A = 2 \times 10^5$h (Shi 2008). And the operating time period of the subway vehicle is $W = 4 \times 10^4$h. So the parameter m in (1) is 0.25. Additionally, the system status is $g_{si} = \{0, 0.5, 1\}$. Maintenance budget $C_0(k)$ is assumed to be \$200 and maintenance quality level N is 6. All the values of the others are numerated in Table 3 (Cochran 2003).

Relative Parameter Values

In this case, variable $R_i(k)$ of the model can be described as (11), so $E_i(k)$ is (12).

$$R_i(k) = exp\left[-\left(\frac{L(k+1)+A_i(k)}{\eta_i}\right)^{\beta_i} + \left(\frac{A_i(k)}{\eta_i}\right)^{\beta_i}\right] \tag{11}$$

$$E_i(k) = \left(\frac{L(k+1)+A_i(k)}{\eta_i}\right)^{\beta_i} - \left(\frac{A_i(k)}{\eta_i}\right)^{\beta_i} \tag{12}$$

Table 3 Values Of Relative Parameters

E. No	$g_{(i,2)}$	$\eta_i/10^3$	β_i	c_i^{rp}	c_i^{rf}	c_h	c_i^0	$A_i(k)/10^3$
1	100%	48.734	3.545	200	240	400	20	38
2	50%	29.106	3.011	150	170	160	10	29
3	50%	34.725	2.527	150	170	160	10	25
4	100%	36.578	2.386	170	180	320	20	46

Reliability Chart

To calculate the system reliability, the reliability chart has to be drawn. Among the four elements—driven silk pole, right nut assemble, left nut assemble and unlock wheel assemble, right nut assemble and left nut assemble are connected in parallel, and

then these two elements are connected with the other two in series. Therefore, the reliability chart can be done in Figure 1.
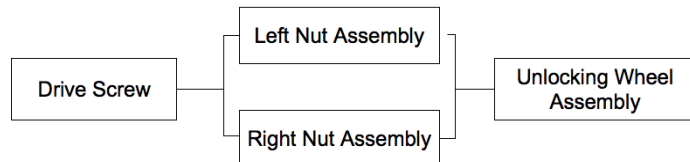
Figure 1 Reliability Chart of Driven Locking Mechanism

Results of Maintenance Model Using MPGA

The selective maintenance optimization is no longer a simple linear 0-1 programming problem. MPGA is used to search the global optimal solution. Because of word limit, only some suitable maintenance strategies are presented in Table 4.The optimal allocations of maintenance cost are listed in column '$C_r(k) + C_p(k)$'.

Table 4. Numeration Of Parato Optima Partly Found

No.	E₁		E₂		E₃		E₄		$C_r(k)$ $+ C_p(k)$	$C(k)$	$R(k)$
	S_1	St_1	S_2	St_2	S_3	St_3	S_4	St_4			
1	0	(0,0)	1	(1,0)	0	(0,0)	1	(1,0)	69	69	0.9355
2	0	(0,0)	2	(1,0)	0	(0,0)	1	(1,0)	88	88	0.9395
...	...	...	...	...	...	...	...	...	...	...	...
25	1	(0,0)	2	(1,0)	2	(0,0)	2	(1,0)	157	157	0.9778
26	0	(0,0)	1	(1,0)	2	(0,0)	5	(1,0)	178	178	0.9630

Notes: Sti is a variable, which describes the status of element i before and after maintenance action. The first value $St_i(1)=[E_k(n_i)]$, and the second value $St_i(2)=[E_{k+1}(n_i)]$.

The available Pareto optima with unlimited maintenance resources versus the probabilities of successfully completing the mission are plotted in Figure 2. Besides, the curve of number of available maintenance strategies versus maintenance cost budget is plotted in Figure 3.
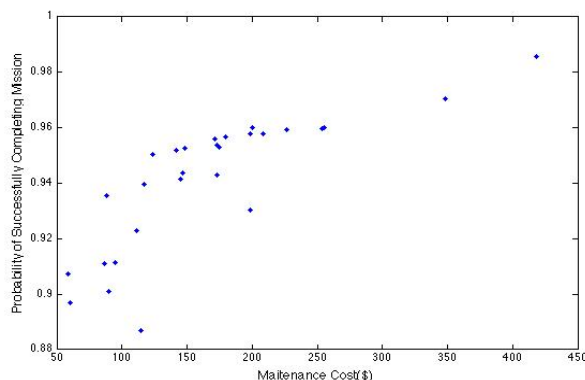
Figure 2. Parato Optima
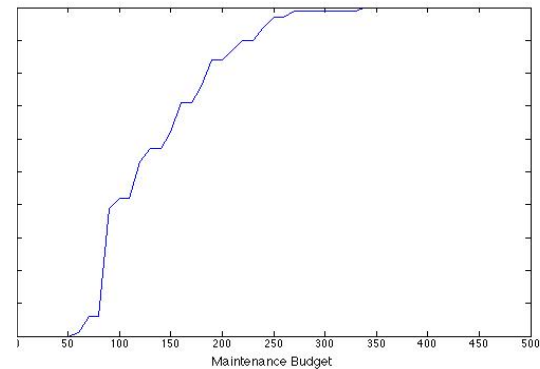
Figure 3. Number Of Available Strategy

Result Discussion

It is observed that, with the same maintenance cost budget and different maintenance strategies, the probabilities of the system successfully completing mission have some differences. As a result, the decision-maker may have the chance to choose the optimal selected maintenance strategy based on available maintenance sources (e.g. spare parts and maintenance time).

Generally, with more maintenance cost, higher probability of successfully completing the mission will be achieved, seeing Figure 2. Additionally, with more maintenance cost, more maintenance strategies are available, easily found in Figure 3.

If resources are unlimited, and either corrective or preventive maintenance is performed on each element before the next mission, the probability of mission success is 0.9999 with a total maintenance cost of $760. Comparing them with limited maintenance resources, two maintenance strategies (1st, 25th) from Table 4 are selected, which has the minimum and the maximum probability respectively. It indicates that the maintenance cost in selected strategies decreases by 57.32%, while the probability of successfully completing the mission decreases by only 4.33%.

CONCLUSION

In this paper, the multi-status and imperfect maintenance of subway vehicles is addressed. The selective maintenance model using system age reduction factor is considered to formulate the improvement after maintenance, and a relationship linking maintenance level with cost is proposed. UGF is employed to facilitate the evaluation of the probability of successfully completing the next mission. The calculation of age reduction factor is presented as well.

Nevertheless, the limitations of this work are that every element is assumed to be binary state, and the reliability function and age of every element can be obtained. To overcome the deficiency, the imperfect maintenance model, considering multi-state elements and the uncertainty of reliability, needs further investigation. The trade-off between the mission success rate and maintenance cost budget, as well as other limited maintenance resources (e.g. repairmen, spare parts and maintenance time) needs addressing through multi-objective optimization.

Additionally, simulating the dynamic probability of accomplishing missions with the optimal allocation of maintenance resources for multiple subsequent missions will be explored in our future work.

REFERENCE

Barton, R. M., Damon, W. W. (1974). Reliability in a multi-state system. The Sixth Annual Southeastern Symposium on Systems Theory, Louisiana, USA.

Barlow, R. E., Wu, A. S. (1978). Coherent systems with multi-state components. Mathematics of Operations Research, 3(4), 275-281.

Cochran, J.K., Horng, S.M, Fowler, J. W. (2003). A multi-population genetic algorithm to solve multi-objective scheduling problems for parallel machines. Computers & Operations Research, 30, 1087–1102.

Kijima, M., Morimura, H. and Suzuki, Y. (1988). Periodical replacement problem without assuming minimal repair. European Journal of Operational Research, 37(2), 194–203.

Kijima, M. (1989). Some results for repairable systems with general repair. Journal of Application Probability, 26(1), 89–102.

Levitin, G. (2005). The universal generating function in reliability analysis and optimization. London: Springer.

Levitin, G. (2007). Block diagram method for analyzing multi-state systems with uncovered failures. Reliability Engineering and System Safety, 27, 727-734.

Levitin, G., Amari, S. V. (2008). Multi-state systems with multi-fault coverage. Reliability Engineering and System Safety, 93(11), 1730-1739.

Li, C.Y., Chen, X., Yi, X.S, et al. (2010). Heterogeneous redundancy optimization for multi-state series-parallel systems subject to common cause failures. Reliability Engineering and System Safety, 95(3), 202–207.

Liu, Y., Huang, H.Z. (2010). Optimal selective maintenance strategy for multi-State systems under imperfect maintenance. IEEE Transactions on Reliability, 59(2), 356-367.

Lv, D.F., Guo, X.C, et al. (2011). Maintenance in section interval of metro vehicle based on availability. Journal of Southeast University (Natural Science Edition), 41(4), 877-881.

Pievato, A., Ruggeri, F., Argiento, R. (2003). Bayesian analysis and prediction of failures in underground Trains. Quality and Reliability Engineering International. 19, 327-336.

Shi, X. (2008). Method of fault diagnosis and maintenance decision on vehicle door system in subway. Beijin Jiao Tong University.

Wang, H. Z. (2002). A survey of maintenance policies of deteriorating systems. European Journal of Operational Research, 39(3), 469–489.

Wang, Q.X. (2011). Optimization of system reliability over multiple periods under constrained maintenance resources, University of Rhode Island.

Wen, W., Syntetos, A. (2011). Spare parts demand: Linking forecasting to equipment maintenance. Transportation Research Part E: Logistics and Transportation Review. 47(6), 1194–1209.

Yan, J. (2008). Failure Analysis and maintenance technology application research of the metro Vehicle. Shanghai Jiao Tong University.

Zepfe, J. A., Ungar, E. (2008). Case study of potential ground-borne vibration reductions from targeted maintenance of subway vehicles. Transportation Research Board, 306, 27-32.

The Failure Criterion for Steel-Concrete Composite Walls

Xiaobing Song[1], Meng Chu[2], Honghui Ge[3], Hailin Wang[4]

ABSTRACT

This paper generates a failure criterion model to analyze the ultimate strength of steel-concrete sandwich composite (SC) wall subject to biaxial membrane forces, which are tension and compression on each side of the wall and in-plane shear. The failure criterion is demonstrated in principal stress space and $\sigma_x - \sigma_y - \tau_{xy}$ space respectively. Test data in literature of steel concrete composite wall is summarized and 7 shear wall tests are conducted to verify the model.

1. Introduction

Steel-concrete (SC) composite structures are examples of an efficient use of systems that involve interactive behavior of thin steel faceplates with thick concrete core section. This structure features good integrity, ductility, and the ability to prevent leakage, impact and explosion. It has been widely used in infrastructure construction, such as that for nuclear power plants, offshore structures, and high-rise buildings, etc. (Sasaki,1995).

In practice, SC walls are mainly loaded by forces equivalent to plane force system in the middle plane of the wall. A number of experimental and theoretical studies have been reported in the past. Three kinds of specimens were loaded. One is flanged shear wall specimens under in-plane lateral loading conditions (Sasaki, 1995), (Varma, 2011), in this case, shear force is mainly carried by the web wall, while bending moment is mainly carried by flanges. Another is rectangular cross section

---

[1] Associate Professor, School of Naval Architecture, Ocean & Civil Engineering, Shanghai Jiao Tong University, Shanghai, China (xbsong@sjtu.edu.cn)

[2] Senior Engineer, Shanghai nuclear engineering research and design institute, Shanghai, China

[3] Chief Engineer, Shanghai nuclear engineering research and design institute, Shanghai, China

4 Master Student, School of Naval Architecture, Ocean & Civil Engineering, Shanghai Jiao Tong University, Shanghai, China

shear specimens under in-plane lateral loading conditions (Takeuchi, 1995), (Varma, 2013), in this case, shear force and bending moment are carried by the shear wall. The third is SC panels under pure shear (Ozaki, 2004), the panels were tested using a specially devised test rig in which load forces were applied along each edge of the panel, attempting to simulate a condition of uniform edge stress. Typical failure procedure include cracking of concrete, followed by pre-yield buckling of the steel faceplates in the compression direction, and concluded with yielding of the faceplates in the tension direction and crushing of the concrete in compression. The pre-yield buckling of the steel faceplates may not happen in special conditions, such as the cases with small stud spacing to plate thickness ratio.

Simple formulae for predicting the fundamental in-plane behavior of SC composite walls has been developed by (Takeuchi, 1995), (Ozaki, 2004) and (Varma, 2011). The in-plane shear behavior of SC composite wall can be estimated as a tri-linear shear force-strain curve. A failure criterion in principal force space was developed based on mechanics based model and finite element models by (Varma, 2011), which is expected to be used for design.

In the past two years, funded by SNERDI, a serious of experimental research works have been conducted by Shanghai Jiaotong University, covering a wide range of mechanical behaviors (Meng Chu, 2013). In the present paper, a failure criterion for steel-concrete composite walls is developed based on theory of plastic limit analysis, the failure criterion is demonstrated in principal stress space and $\sigma_x - \sigma_y - \tau_{xy}$ space respectively for convenience of engineering practice. Comparison is made with the experimental results given by (Ozaki, 2004) and the previous model presented by (Varma, 2011). The new model is more accurate for the cases with high compression force.

2. Solution of In-plan Stress Problem

Stresses of the steel plate are termed σ_{sx}, σ_{sy} and τ_{sxy}, and the stresses of the concrete are termed σ_{cx}, σ_{cy} and τ_{sxy}, as shown in Figure 1(a). The stresses obtained when the total forces in the steel and concrete are considered to be evenly distributed over the thickness of concrete are called the equivalent stress, as shown in Figure 1(b).

2.1 The Concept of Reinforcement Degree

We introduce the term reinforcement degree Φ, defined as being the ratio between the force per unit of length that the steel is able to carry and the force per unit of length that the concrete is capable of carrying in pure compression. For SC Wall, reinforcement degree should be equal in any direction, we have

$$\Phi_x = \Phi_y = t_s f_y / t f_c = \Phi \tag{1}$$

In which t signifies the thickness of concrete, t_s signifies the thickness of steel plate.

(a) Stresses of concrete and steel plate   (b) Equivalent stress
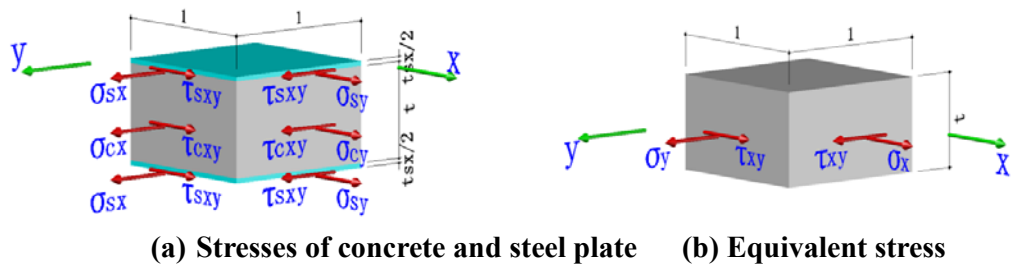
Figure 1. The in-plane stresses in steel-concrete composite Wall

2.2   Tension and Compression
2.2.1   Tension and Compression for Steel Plate

The tensile or compressive strength in the direction of the x-axis of the steel plate is

$$f_{tx} = f_{cx} = \frac{t_{sx} f_y}{t} = \Phi_x f_c = \Phi f_c \tag{2}$$

In which f_{tx} and f_{cx} signifies the equivalent tensile strength and compressive strength of steel plate respectively, f_y signifies the steel plate yield stress. Similarly，in the direction of the y-axis

$$f_{ty} = f_{cy} = \frac{t_{sy} f_y}{t} = \Phi_y f_c = \Phi f_c \tag{3}$$

Figure 2(a) shows the yield envelope for steel plate in principal stress space，in which Tresca criterion is adopted as steel yield criterion.

（a）Steel plate   （b）Concrete
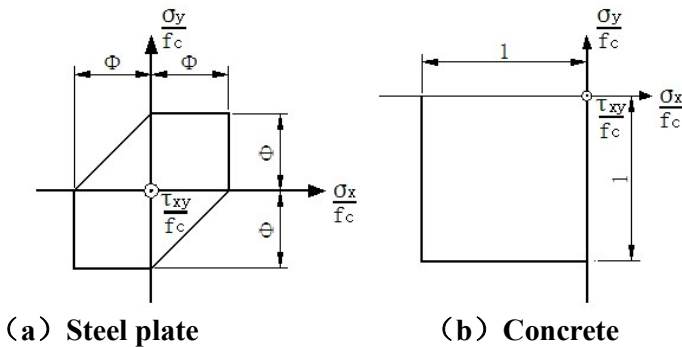
Figure 2. Yield envelope in principal stress plan

2.2.2   Tension and Compression for Concrete

In limit state, concrete will crack in the principal tensile stress direction. For conservative consideration, it can be assumed that concrete have zero tensile strength, and the influence of biaxial compression on the compressive strength can also be ignored. Figure 2(b) shows the yield envelope for concrete in principal stress space.

2.2.3   Tension and Compression for SC Wall

For Q235 and Q345 steel, the yield strain of steel plate is less than 2000 $\mu\varepsilon$, steel will yield before concrete reaches its peak strain in compression. The bearing capacity of steel and concrete can be superimposed, and the equivalent compressive strength for SC wall in the direction of the x-axis and y-axis can be expressed as:

$$f_{cx} = f_{cy} = (1+\Phi)f_c \tag{4}$$

The equivalent tensile strength for SC wall in the direction of the x-axis and y-axis can be expressed as:

$$f_{tx} = f_{ty} = \Phi f_c \tag{5}$$

In combined tension and compression stress state, the yield condition is not that simple. In principal stress space (σ_1, σ_2), the principal stresses of steel plate and concrete can be donated as $(_s\sigma_1, _s\sigma_2)$ and $(_c\sigma_1, _c\sigma_2)$ respectively.

According to the equilibrium condition, we have，

$$t \times \begin{Bmatrix} \sigma_1 \\ \sigma_2 \end{Bmatrix} = t_s \times \begin{Bmatrix} _s\sigma_1 \\ _s\sigma_2 \end{Bmatrix} + t \times \begin{Bmatrix} _c\sigma_1 \\ _c\sigma_2 \end{Bmatrix} \tag{6}$$

Assume $\sigma_1 > 0$, and $\sigma_2 < 0$, the yield condition for steel plate can be discussed as follows:

（1）Where $\sigma_2 > -f_c$, the equivalent principal compressive stress is less than the concrete compressive strength. If we keep the equivalent principal compressive stress σ_2 unchanged and increase the equivalent principal tensile stress σ_1 from 0 gradually. In the beginning, the equivalent principal compressive stress σ_2 is shared by the steel plate and concrete. However, in the process of increasing σ_1, because of Poisson effect, free contraction of steel plate in the direction of principal compressive stress is limited by concrete. As a result, the steel plate principal compressive stress reduces, and the concrete principal compressive stress increases. The failure of the SC wall can be divided into two categories: In the first one, steel will yield in tension by tensile stress reaches fy, and concrete carry the whole compressive stress σ_2; In the second one, in an intermediate state t₁, steel plate may yield in combined compression and tension. Because concrete doesn't reach its compressive strength, we can still increase σ_1, steel plate maintains yield in combined compression and tension by Tresca criterion, and the concrete principal compressive stress increases. In the limit state, concrete will bear all the compressive stress in the direction of σ_2, and steel plate will yield in uniaxial tension. The stress state of concrete will be

$_c\sigma_1 = 0$, $_c\sigma_2 = \sigma_2$. The stress state of steel plate will be $_s\sigma_1 = f_y$, $_s\sigma_2 = 0$, yield condition for steel plate is $\sigma_1 = \Phi f_c$.

（2）Where $\sigma_2 < -f_c$, the equivalent principal compressive stress exceeds concrete compressive strength. In limit state, principal compressive stress is shared by steel plate and concrete, and concrete will reach its compressive strength, the principal compressive stress of steel plate can't be zero, steel plate will yield in combined compression and tension. In this case, the stress state of concrete is: $_c\sigma_1 = 0$, $_c\sigma_2 = -f_c$. The stress state of steel plate is: $_s\sigma_1 = \sigma_1 t/t_s$, $_s\sigma_2 = (\sigma_2 - f_c)t/t_s$, according to Tresca criterion, the yield condition for steel plate is $_s\sigma_1 - _s\sigma_2 = f_y$, and the yield condition for SC wall is: $\sigma_1 - \sigma_2 = (1+\Phi)f_c$.

The yield criterion in in-plan principal stress space SC wall is clear as shown in Figure 3(a).

2.3 Yield Surface

The relationship between principal stresses and element stresses are as follows:

$$\sigma_1 = \frac{1}{2}(\sigma_x + \sigma_y) + \sqrt{\frac{1}{4}(\sigma_x - \sigma_y)^2 + \tau_{xy}^2} \tag{7}$$

$$\sigma_2 = \frac{1}{2}(\sigma_x + \sigma_y) - \sqrt{\frac{1}{4}(\sigma_x - \sigma_y)^2 + \tau_{xy}^2} \tag{8}$$

For the equivalent principal stress state：$\sigma_1 = \Phi f_c$，$-f_c \le \sigma_2 \le \Phi f_c$，By Eq. (7)，we obtain

$$-(\Phi f_c - \sigma_x)(\Phi f_c - \sigma_y) + \tau_{xy}^2 = 0 \tag{9}$$

The yield surface is an elliptic cone, which start from vertex (Φ, Φ). By Eq. (7) and (8), we obtain：

$$(\sigma_x + \sigma_y) \ge (\Phi - 1)\, f_c \tag{10}$$

$$(\sigma_x + \sigma_y) \le 2\Phi f_c \tag{11}$$

For the equivalent principal stress state：$-(1+\Phi)f_c \le \sigma_1 \le 0$，$\sigma_2 = -(1+\Phi)f_c$，By Eq. (8)，we obtain：

$$[(1+\Phi)f_c + \sigma_x][(1+\Phi)f_c + \sigma_y] - \tau_{xy}^2 = 0 \tag{12}$$

The yield surface is an elliptic cone, which start from vertex $(-(1+\Phi), -(1+\Phi))$. By Eq. (7) and (8), we obtain：

$$[(1+\Phi)f_c + \sigma_x][(1+\Phi)f_c + \sigma_y] - \tau_{xy}^2 = 0 \tag{13}$$

$$(\sigma_x + \sigma_y) \le -(\Phi+1)f_c \tag{14}$$

The equivalent principal stress state： $0 \le \sigma_1 \le \Phi f$, $-(1+\Phi)f_c \le \sigma_2 \le -f_c$

For the equivalent principal stress state： $\sigma_1 - \sigma_2 = (1+\Phi)f_c$, By Eq. (7) and (8), we obtain：

$$\sqrt{(\sigma_x - \sigma_y)^2 + 4\tau_{xy}^2} = (1+\Phi)f_c \tag{15}$$

$$(\sigma_x + \sigma_y) \ge -(\Phi+1) f_c \tag{16}$$

$$(\sigma_x + \sigma_y) \le (\Phi-1) f_c \tag{17}$$

The yield surface is an elliptic cylinder. The SC Wall yield surface is shown in Figure 3(b).

(a) Yield envelope
in principal stress space

(b) Yield surface
in element coordinate system
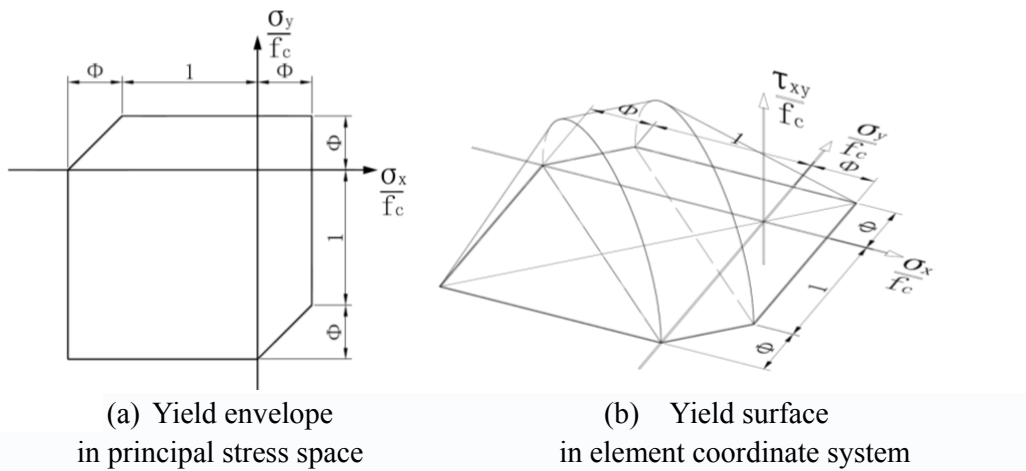
Figure 3. SC wall yield criterion for in plane stress state

2.4 Modification
If further increases the strength of steel, steel plate will yield after the concrete reaches its compressive strength. Under this circumstance, the yield stress of steel plate should be reduced to 400MPa in calculation.

3. Verification
The SC wall yield criterion model can be used to predict the behavior of SC

wall panels subjected to combined axial compression and in-plane shear (Ozaki, 2004). The specimens were $1200\times1200mm$ square panels with 200mm thickness. Table 1 shows the details of the verification for in-plan shear behavior. Comparison with Varma's model is also listed in the Table 1.

As shown in Table 1, both Varma's model and the new yield criterion model coincide well with experiment results. Two analytical models share the same results on the aspect of pure in-plan shear behavior. However, in compression plus in-plane shear stress states, the new model seems to be more accurate. Figure 4 shows the SC wall yield enveloping line in the case of $\sigma_{y=0}$.

Table 1 Experimental result and analytical comparisons

Specimen	Experimental		Varma's Model		Our yield criterion Model	
	Axial	Shear	Shearl	Relative	Shearl	Relative
	(kN)	(kN)	(kN)	error	(kN)	error
S2-00-NN	0	2290	1877	-18.03%	1877	-18.03%
S2-15-NN	-353	2330	1989	-14.64%	2046	-12.19%
S2-30-NN	-705	2490	2088	-16.14%	2201	-11.59%
S3-00-NN	0	3070	2611	-14.95%	2611	-14.95%
S3-15-NN	-353	3130	2707	-13.51%	2782	-11.12%
S3-30-NN	-705	3170	2793	-11.89%	2942	-7.18%
S4-00-NN	0	3510	3672	4.62%	3672	4.62%
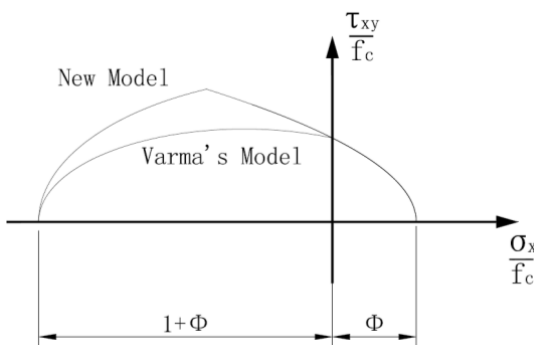
Figure 4. SC wall yield envelope in in-plan stress space ($\sigma_y = 0$)

4.   Conclusion

The model presented in the present paper is effective in analyzing the ultimate strength of steel-concrete sandwich composite walls subjected to biaxial membrane force, compared with the model presented by (Varma, 2011), this model is more accurate under the condition of relatively high compressive stress state.

References

1) Sasaki, N. et al. (1995). "Study on a concrete filled steel structure for nuclear power plants part 3: shear and bending loading tests on wall member." *Proc., SMiRT13, Porto Alegre, Brazil, 27–32.*

2) Amit H. Varma, et al. (2011). "In-Plane Shear Behavior of SC Composite Walls: Theory vs. Experiment." *Proc., SMiRT 21, New Delhi, India, Div-VI: Paper ID# 764*

3) Takeuchi, M. et al. (1995). "Study on a concrete filled structure for nuclear power plants (part 1 4)" *Proc., SMiRT13, Porto Alegre, Brazil, 15–20.*

4) Amit H. Varma, et al. (2013). "An experimental study of the in-plane response of steel-concrete composite walls." *Proc., SMiRT22, San Francisco, California, USA, 15–20.*

5) Ozaki, M., et al. (2004). "Study on steel plate reinforced concrete panels subjected to cyclic in-plane shear." *Nuclear Engineering and Design 228 (13), 225–244.*

6) Amit H. Varma, et al. (2011). "Steel-plate composite (SC) walls for safety related nuclear facilities: design for in-plane and out-of-plane demands." *Proc., SMiRT 21, New Delhi, India, Div-VI: Paper ID# 760*

7) Meng Chu, Xiaobing Song, Honghui Ge, (2013). "Structural performance of steel-concrete-steel sandwich composite beams with channel steel connectors." *Proc., SMiRT 22, San Francisco, California, USA, Division IX Div-IX*

Research of Wave Incoherence Effect of Nuclear Power Plant

on Soft Soil Site

Zhenkun Ding[1], Zufeng Xia[2]

ABSTRACT

Pakistan Chashma (PC) nuclear project was constructed on soft soil site. Research was made to find the effect of wave incoherence on PC Nuclear Island. To find out the inner margin in original design response spectra and as a technical support for further seismic margin evaluation, two kinds of incoherence effects were studied: random spatial variation and wave passage. Compare to the results from coherent analysis, the wave passage effect led to larger margin than the random spatial variation. Considering of the wave incoherence effect will reduce the unnecessary conservative in the seismic analysis of nuclear project.

1. Introduction

According to Section 3.3.1.10 of ASCE 4-98 (ASCE 4, 1998) , when the normial soil structure interaction analysis performed, the shear and compressional waves are assumed to propagate vertically. This assumption can not fully repesent the actual situation. The generated in-structure response spectra will become conservative under this assumption. Incoherence analysis can be introduced to reduce this conservative for regular structure. In general, the reduction will be obvious beyond 10Hz, and increases with the foundation dimension increasing.

Pakistan Chashma (PC) nuclear project was constructed on soft soil site and had operated for over ten years. In the future, a seismic margin evaluation needs to be performed on this project. Wave incoherence effect was researched to find out the inner margin and make a more realistic evaluation of equipments, especially for electronic instruments.

2. Project Descriptions

The depth of soil deposit in PC project is about 150 meter, and the shear wave velocity of soil change from 245 m/s to 640 m/s. The average shear wave velocity of the soil in 30 meters of top layers is about 300 m/s. It reached the lowest requirement

of SRP 3.7.2 for the competent soil. 51 soil layers were developed according to the SSI(Soil Structure Interaction) modeling requirement (ASCE 4, 1998).

The max acceleration value of input SSE was 0.25g in horizontal direction and 0.17g in vertical direction. Time histories were generated match to RG1.60 spectra, the reference time history was EL. Centro wave.

A 3 dimension (3D) shell and stick hybrid model was used for this research, which was developed for 3D analysis in original project. The underground part was developed with shell elements, and the part above ground was developed with beam elements. For most equipments were arranged on the floors of auxiliary building and internal structure, typical nodes represent for main floors of internal structure were chosen for research. Node 746 represent for the floor of elevation 0 meter and node 754 represent for elevation 15 meter. The 3D model and critical locations were shown in Figure 1.
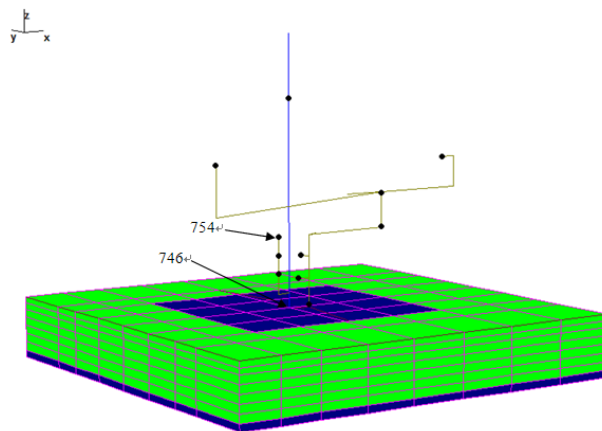
Figure 1 Finite Element Model

3.   Wave Incoherence

The wave incoherence effect has been accepted by nuclear industry for years. The Abrahamson model for hard rock site has been permitted by US NRC（Nuclear Regulatory Commission）. But the model for soft soil site has not been permitted yet. It's hard to use these graphs (figure 3) to deal with the complicated response spectra of nuclear island directly. So the software (ACS SASSI, 2009) with incoherence functions was used for this research. According to the requirement of ASCE4-09(draft) (ASCE 4, 2010), two kinds of incoherence effects should be considered in analysis: 1) Random spatial variation: scattering of waves due to the heterogeneous nature of the soil or rock beneath the foundation and along the propagation paths of the incident wave fields. 2) Wave passage effects: systematic spatial variation due to difference in arrival times of seismic waves across a foundation. The incoherence effects reduce the foundation translational motions and increase the rotational motions.

At present, stochastic and approximate deterministic approaches can be used for performing incoherent SSI analyses.
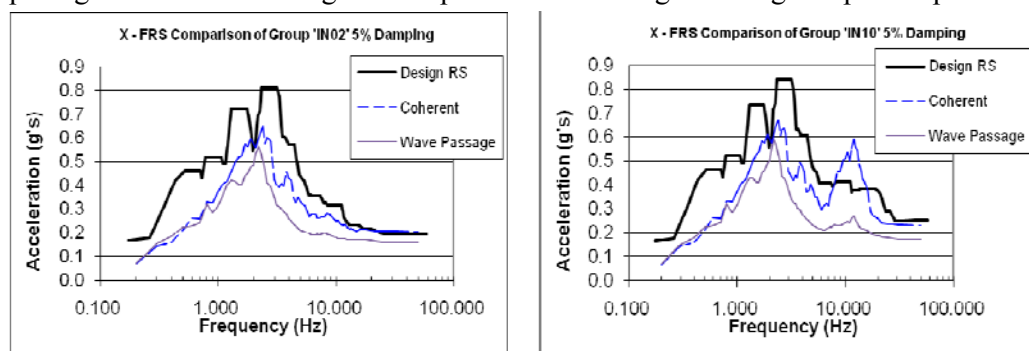
Stochastic simulation approach (similar to Monte Carlo simulation used for probabilistic analyses) is based on performing statistical SSI analyses for a set of random field realizations of the incoherent free field motion input. It respects in all details the SSI physics. It computes the mean of incoherent SSI responses, but also produces information on the scatter of these responses. It is recommended for both simple and complex SSI models with either rigid or flexible foundations by EPRI(Electric Power Research Institute).

Deterministic approaches based on approximate simple rules for combining the incoherency modes or modal SSI responses. These deterministic approaches approximate the mean of incoherent SSI responses, but offer no information on the SSI response variability. They are recommended for simple stick models with rigid basemats as applied in the EPRI incoherent SSI benchmark studies.

4. Results

Stochastic simulation approach was used in this research. Luco-Wong model and 2006 Abrahamson model for all sites and embedded foundations were chosen. The final results were the average value of ten time's random analyses. Five times analyses were performed with Luco-Wong model, and five times were performed with 2006 Abrahamson model.

The response spectra of main floors were generated and compared with original design response spectra.Typical results of the top and bottom of internal structrue were shown in figure 2. "Coherent" represent for the results from coherent analysis. "Wave-Passage" represent for the reults from incoherence analysis including wave passage effect. And "Design RS" represent for the original design response spectra.

(a)Node 746   (b)Node 754
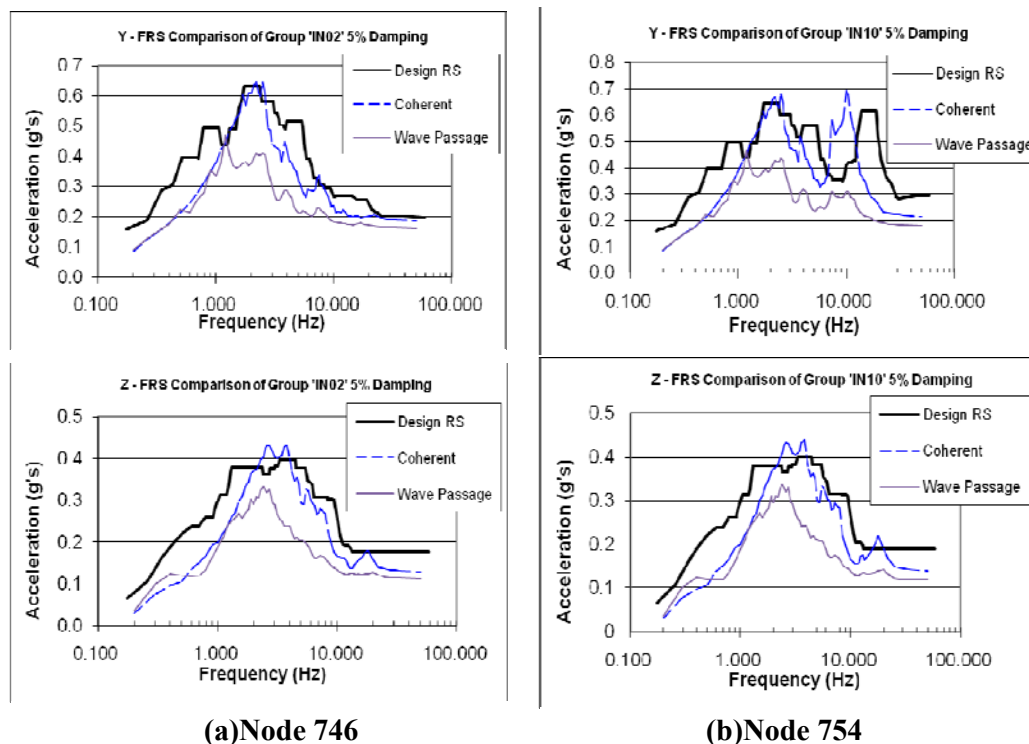
Figure 2 FRS Comparison of Internal Structure

5. Discussion

5.1 Comparison of PC Project Reponse Spectra

Results from coherence analysis and incoherence analysis were compared in figure 2. The dimension of basement for PC project is 85meter x87meter, which belongs to large-size basement. And Chashma site belongs to soft soil site (average shear wave velocity of 30 meter depth is 300m/s). According to the figure C5.1-2 and C5.1-3 of ASCE4-09(draft) (ASCE 4, 2010) the incoherence reduction of repsonse spectra would be obvious for large-size basement. But according to the results, the incoherence reduction was not as obvious as shown in these figures. The reduction was not monotone increasing with the frequency increasing. Due to the complication of actual structure model, the reduction of response was not exactly the same as these theoretical graph. The law seems to be more appropriate for the responses on main frequencies. And the reduction were more obvious for the frequencies beyond 20Hz. Incoherence effect was more obvious for the response spectra in vertical direction than in horizontal. For vertical direction, the incoherence reduction effect were more obvious beyond 2Hz (not limited to 10Hz).
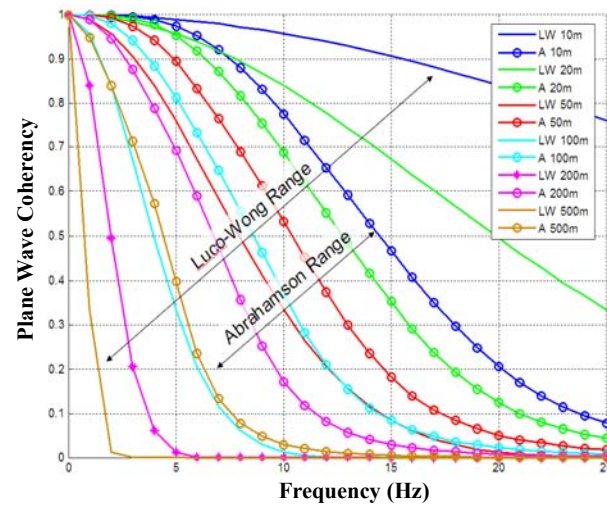
Figure 3 Incoherence Models

In figure 4, a comparison was made among coherent analysis, incoherence analysis with random spatial variation and incoherence analysis with both random spatial variation and wave passage effect. It seems that the wave passage effect had larger effect than the random spatial variation.

The new analysis code ASCE4-09 (ASCE 4, 2010)emphasized, for the incoherence analysis, only 3D model should be used in SASSI or CLASSI.
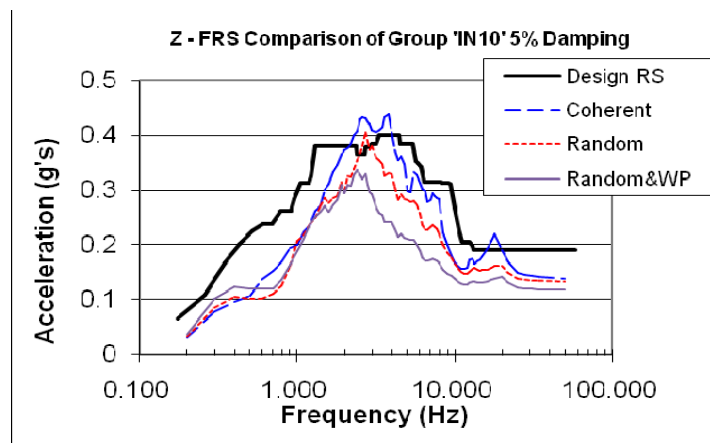
Figure 4 Comparison of Two Incoherence Effects

5.2 Incoherence Effect Research for Seismic Safety Evaluation

The analysis and design for nuclear project are always begun long before the construction start. From design period to FSAR(Final Safety Analysis Report) period or operation period, external factors will change a lot and can be significant different

with orignal design. It's necessary to make a reconciliation for the final situation. The method used for the reconciliation may not the same as used in the orignal design.

In figure 2, the new response spectra considered incoherence effect(including wave passage) could be enveloped by orignal design response spectra. And the exceeding situation was much better than coherence analysis. Except for the response of some special frequencies that were close to the design response spectra, most responses were much lower than design response spectra. And those peaks amplitude were allowed to be reduced by 15% when there were broadened (ASCE4-98 section 3.4.2.3). So consider the wave incoherence effect(including wave passage), the margin in the design response spectras are at least 1.15.

The incoherece analysis can be used for further seismic safety and seismic margin evaluation of Chashma project. From incoherence analysis, most in structure response will be envoloped by orignal design response spectra, and it's not necessary to make additional evaluation in continuation project C3/C4 for some equipments which located in the exceeding areas (response can not be enveloped by DRS(Design Response Spectra)).

6. Conclusions

According to the primary incoherence research, due to the complexity of Nuclear Island, generation of floor response spectra should use 3D model. Random analysis should be performed when incoherence effect need to be consider. The incoherence graph and table cannot be used for quantitative analysis directly, but they can be used for qualitative evaluation.

Incoherence analysis can be used as a supplement of traditional coherence analysis in future nuclear projects. Considering of the wave incoherence effect will reduce the unnecessary conservative in the seismic analysis of nuclear project. It will benefit the further seismic probabilistic safety analysis and seismic margin evaluation.

References

1) American Society of Civil Engineers (1998). ASCE 4-98. *Seismic Analysis of Safety-Related Nuclear Structures and Commentary*, Reston, Virginia

2) Ghiocel Predictive Technologies, Inc. (2009) ACS SASSI Version 2.3.0. "An Advanced Computational Software for 3D Dynamic Analysis Including Soil Structure Interaction"

3) American Society of Civil Engineers (2010). ASCE 4-09 Draft *Seismic Analysis of Safety-Related Nuclear Structures and Commentary*

4) American Society of Civil Engineers (2005). ASCE43-05 *Seismic Design Criteria for Structure, Systems, and Components in Nuclear- Facilities*, Reston, Virginia

ANALYSIS OF A LARGE WIDE-BODY COMMERCIAL PLANE IMPACT ON CAP1400 SHIELD BUILDING

Shujian Cheng[1], Xiaowen Wang[2], Honghui Ge[3], Zufeng Xia[4]

Abstract：

CAP1400 is a new type nuclear plant designed by SNERDI. As a 3rd generation nuclear plant, it should survive after a large commercial plane crash on its shield building. A large wide-body commercial plane is chosen as the impact aircraft and these phenomenons will be modeled by LS-DYNA. This paper will demonstrate the results of these impact simulations and how to check the rationality of these analyses.

1. Introduction

This paper mainly about the research of a large commercial plane impact on the shield building of CAP1400 nuclear power plant. A finite element model of a large wide body commercial plane(LWBCP) which can envelop the target load curve together with the shield building(SB) model are built. And the middle of cylindrical wall, the airinlet zone and the conical roof of the SB are chosen as the impact targets. By analysis the phenomenon during the impacts, the anti-impact capacity of CAP1400 is proved.

Modeling methods by LS-DYNA are benchmarked against the experiments by Tsubota H（1999）as prophase work. Details of benchmark works are not mentioned in this paper.

2. Finite element model of structure

2.1 Modeling of structure

Based on the result of nuclear safety screening, the shield building is chosen as the target and need to build its finite element model. The model of CAP1400 steel-plate composite concrete (SC) shield building is as shown in Fig.1, and it is precisely according to the construction drawing.

Concrete is modeled by Solid elements. Steel plates and steel beams are modeled by Shell elements. Rebar, studs and tie bars are modeled by Beam elements. Some parts of the model is fine meshed as shown in Fig.1 to get balance between accuracy and efficiency.

---

[1] Engineer, Shanghai nuclear engineering research and design institute(SNERDI), Shanghai, China,(chengsj@snerdi.com.cn)

[2] Senior Engineer, SNERDI, Shanghai, China

[3] Chief Engineer, SNERDI, Shanghai, China

[4] Design Master of National Engineering, Professor, SNERDI, Shanghai, China
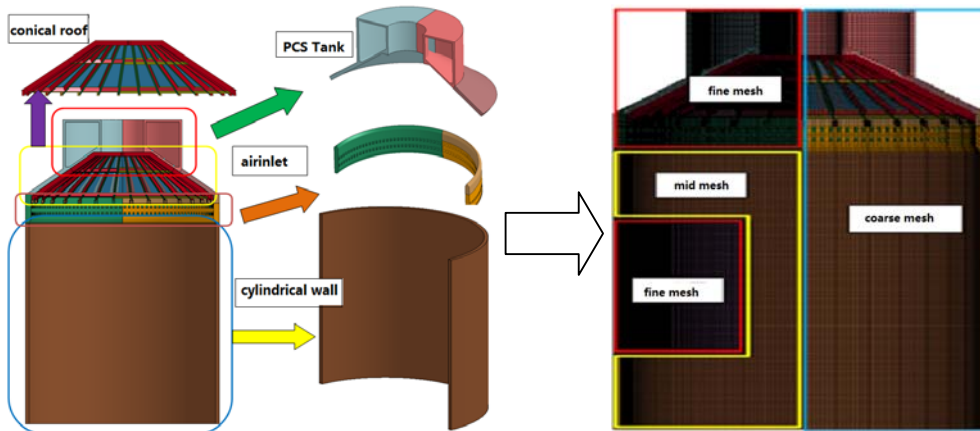
Figure 1. Finite element model and mesh zones of shield building

2.2 Connection, constraint and boundary conditions

Concrete elements with same mesh size are connected by co-nodes. Fine meshed zone, mid meshed zone and coarse meshed zone are connected to each other by LS-DYNA contact "contact_tied" on their contact surfaces.Steel beams and steel plate elements are mainly connected by co-nodes. And shell elements of steel components also are connected to concrete elements by co-nodes. Studs and tie bars are connected to concrete elements by co-nodes, and it's good for their working compatibility.

Rebar elements are connected to each other by co-nodes, and are connected to concrete by LS-DYNA constraint "constrained lagrange in solid" ,which not only can couple the rebar elements' nodes and the concrete elements' nodes, but also can simulate the sliding between concrete and rebar. But most importantly, this constraint is much simpler than the co-nodes connection method.

The bottom of the cylindrical wall (both concrete and steel plate elements) is considered to be completely fixed.

Because the SB model has 2.6 million elements and the analysis cases are symmetric, for calculation efficiency, the 1/2 model with 1.3 million elements is used and the symmetric plane is X-Z (Z is the vertical direction).   In this paper, all whole model pictures are generated by LS-DYNA post processing.

2.3 Material and the constitutive model

Q345 (fy=345MPa) is used for steel plate and steel beams. HRB400 (fy=400MPa) is used for reinforcement, studs and tie bars.

Steel material is simulated by " Mat_Piecewise_Linear_Plastic"mat model （LSTC，2007）. In high speed impact, the strength and stiffness of material will be higher because of the high strain rate, and this phenomenon is taken into account.

Concrete material is simulated by "Winfrith"mat model（LSTC，2007）. Winfrith mat model is a smeared crack, smeared rebar model, and is implement in the 8-node

single integration point continuum element. The crack of Winfrith is an important index of safety for concrete structures. But it can not simulate element erosion, unless "mat_add_erosion" is added to it.

C55(6000psi) concrete is used for shield building. Because of the flying ash added to concrete, the strength of concrete will continue growing in long term. In real construction, the strength of concrete will be a little higher than the testing value. According to NEI07-13（NEI，2011）and ACI 349（ACI　2006），long term strength growing, testing margin should be taken into account to modify the concrete mat model. The strength and stiffness of material will be higher because of the high strain rate, and this phenomenon is taken into account.

2.4 Finite element model of plane

A large wide body commercial plane (LWBCP) with the weight of 204t and velocity of 156m/s is chosen as the impacting aircraft. The finite element model of the plane is shown in Fig.2. "Mat_ Piecewise_ Linear_ Plastic" mat model is used to simulate aluminum alloy.
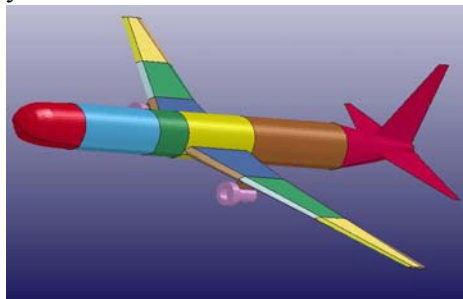
Figure 2.　FE model of aero plane

The finite element model is tested by impacting a rigid wall. As shown in Fig.3, the test load curve can match and envelop the target load curve. So this plane FE model is suitable for impacting analysis.
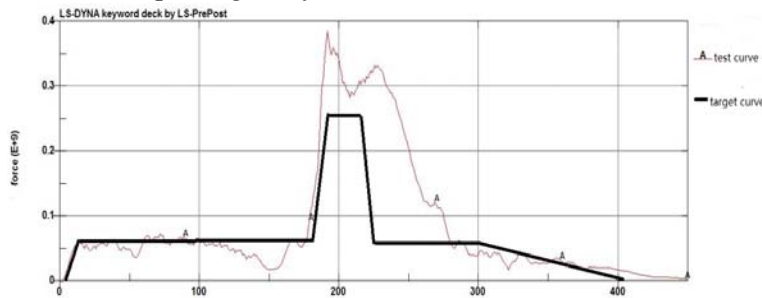
Figure 3.　The test load curve VS the target load curve
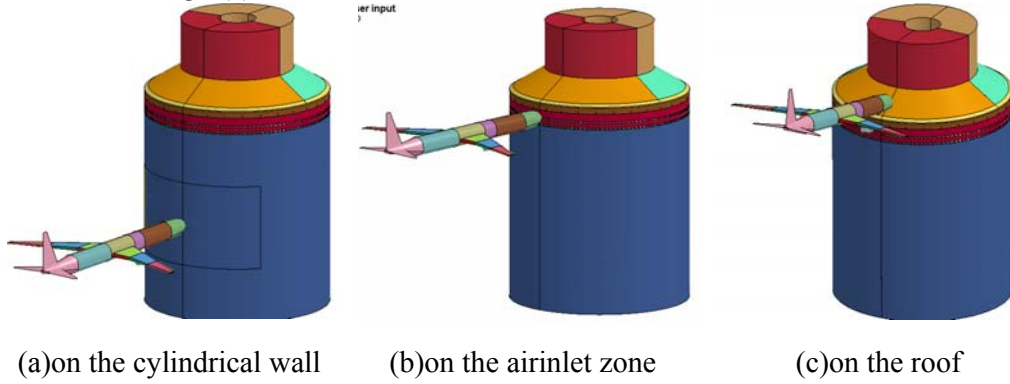
2.5 Dimension

In this paper, the fundamental units are as follow: mass-g, length-mm, time-ms. Based on the fundamental units, other units are as follow: force-N, pressure-MPa, energy-0.001J. If any fig don't indicate the units, the above units are suitable.

3.   Impacting analysis
3.1 Impact on the cylindrical wall
The cylindrical wall will perform with a bending mode in the impact process, so the worst situation will occur on the middle of the cylindrical wall. The height of the CAP1400 shield building cylindrical wall is 50m and the thickness is 1.1m, so the middle of the cylindrical wall (25m above ground) is chosen as the impacting target as shown in Fig.4(a).
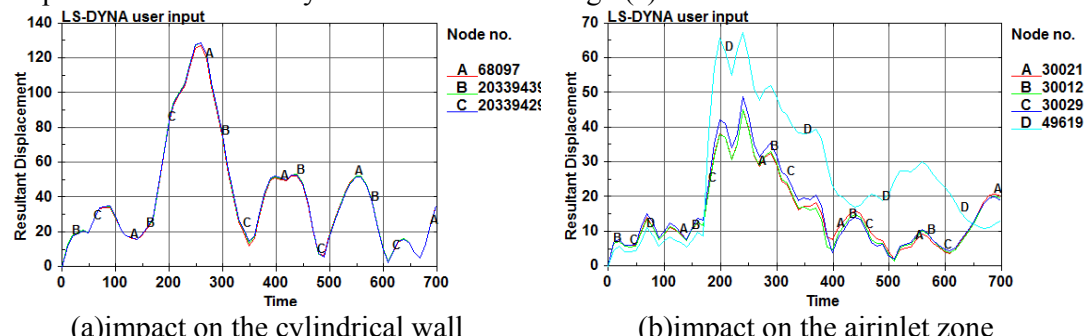
(a)on the cylindrical wall   (b)on the airinlet zone   (c)on the roof
Figure 4.   Impact on different positions of the shield building

Check the deformation animation and find that at the time of 250ms the structural deformation reaches its peak value of 130mm. Find the nodes of maximal deformation both of inner side and out side at 250ms, and get their resultant displacement time history curves as shown in Fig.5(a).

(a)impact on the cylindrical wall   (b)impact on the airinlet zone
Figure 5. The displacement time history curves of the maximum nodes

Via Fig.5(a), the deformation of inner side is almost the same as out side. At 250ms, the deformation reaches its peak of 130mm. Then, because the impacting load goes down, the structure rebounds. From the shock shape, the residual deformation is about 30mm. The peak deformation of SB is 130mm and is much smaller than the gap between the SB and the steel containment vessel which is 1.3m. So, the steel containment vessel is not touched.

In the impact process, a small part of the out steel plate is damaged, as shown in Fig.6.

The cylindrical wall is a SC structure. Only little part of out steel plate is eroded, and only little part of inner steel plate reaches plastic phase, so the concrete is

protected well. The concrete is well constrained and the allowable volume strain can be much higher than common reinforcement concrete, so the anti-impacting capacity is obviously enhanced. In the impacting process, no concrete element is deleted.

Mat84 (Winfrith concrete) can calculate the cracking of concrete. As shown in Fig.7, aircraft impacting on the cylindrical wall will cause a lot of surface cracks and some inner cracks. In general, the inner cracks are few, and the penetration cracks also are few. Because the inner steel plate hasn't been damaged, even if the concrete peel off because of the cracks, it will not affect the steel containment vessel.
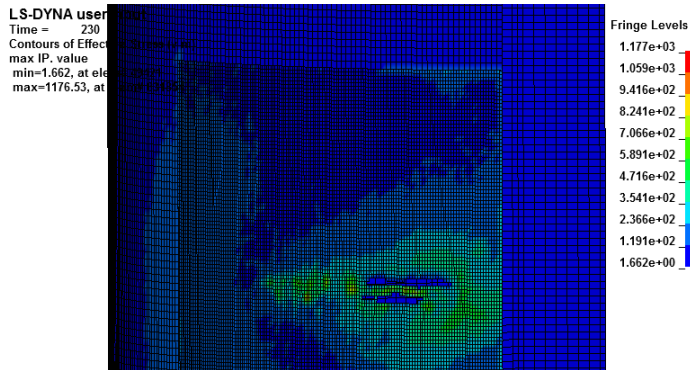

Figure 6.   The contour of effect stress (v-m) of the out side steel plate
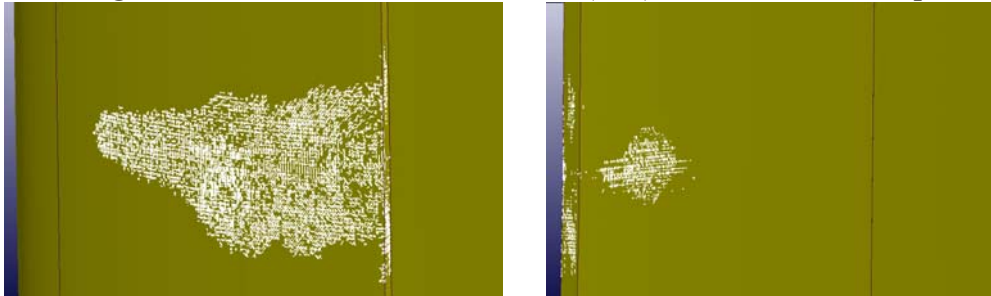
Figure 7.   The cracks at the maximum displacement time point

3.2 Impact on the airinlet zone

The airinlet zone is a cylindrical wall with the thickness of 1.5m and tow row of airinlet tubes. In FE model, the round tube section is simplified to rectangle section to avoid radical element meshing. The impacting position is in the middle of the two tube rows.

Check the deformation animation and find that at the time of 250ms the structural deformation reaches its peak value of 67mm. Find the nodes of maximal deformation at 250ms both of inner side and out side, and get their resultant displacement time history curves as Fig.5(b).（49619 is out side node，others are inner side nodes.)

Via Fig.5(b), the deformation of inner side is 50mm and is 17mm smaller than that of out side, so it can be concluded that local deformation occurred at the max deformation node of out side. At 250ms, the deformation reaches its peak of 50mm. Then, because the impacting load goes down, the structure rebounds. At 400ms, the

impacting is almost ended, but the structure is still vibrating in big range. From the shock shape, the residual deformation is about 10mm.

The peak deformation of SB is 50mm and is much smaller than the gap between the SB and the steel containment vessel. So, the steel containment vessel is not touched.

In the impact progress, a small part of the out steel plate is damaged, as shown in Fig.8.
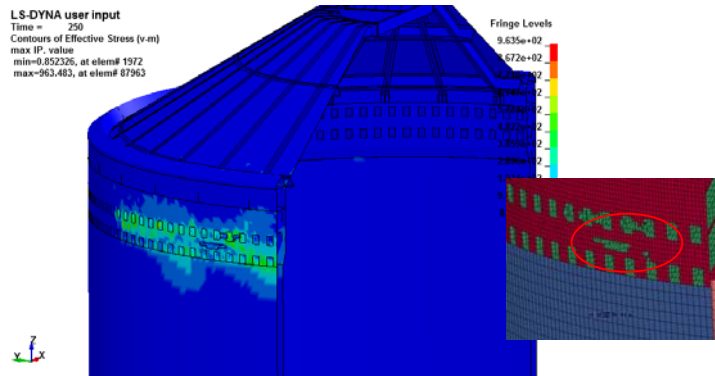
Figure 8.   The contour of effect stress of steel plate and deleted elements

The shield building is a SC structure. Only little part of out steel plate is eroded, and only little part of inner steel plate reaches plastic phase, so concrete is protected well. In the impacting process, no concrete element is deleted.

As shown in Fig.9, aircraft impacting on the air inlet zone will cause a lot of surface cracks and some inner cracks. In general, the inner cracks are few, and the penetration cracks also are few. Because the inner steel plate hasn't been damaged, even if the concrete peel off because of the cracks, it will not affect the steel containment vessel.
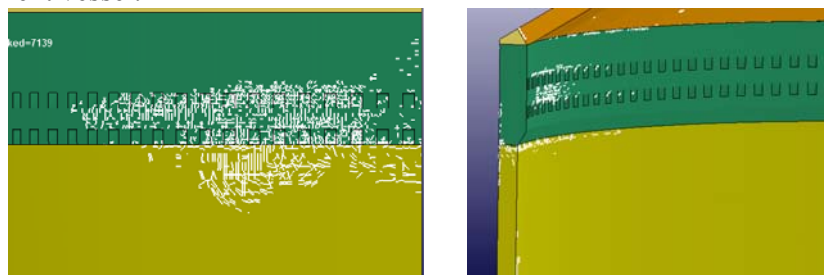
Figure 9.   the cracks of the air inlet zone at the maximum displacement time point

3.3 Impact on the conical roof

The roof includes a conical roof with the gradient of 35°and a PCS tank which contains 3700t water. Usually, a large commercial plane can only impact a structure within the angle of ±10° at a high speed, so the angle of -10°is chosen as the impacting angle as shown in Fig.4(c). The PCS tank is excluded by nuclear safety

screening, so the conical roof is chosen as the impact target. The conical roof is supported by inner steel plate and steel beams, so the position in the middle of conical roof and between two steel beams is chosen as the impact position.

Check the deformation animation and find that at the time of 210ms the structural deformation reaches its peak value of 28mm. Find the nodes of maximal deformation at 210ms both of inner side and out side , and get their resultant displacement time history curves as Fig.3-10.（1074547 is out side node，784267 is inner side node)
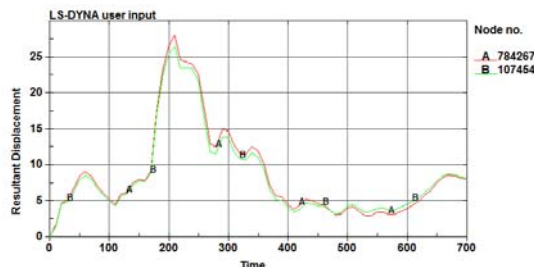
Figure 10.   The displacement time history curves of the maximum nodes

Via Fig.10, the deformation of inner side is almost the same as out side. At 210ms, the deformation reaches its peak of 28mm. Then, because the sliding of the aircraft, the structure rebounds. From the shock shape, the residual deformation is about 5mm. The peak deformation of SB is much smaller than the gap between the SB and the steel containment vessel. So, the steel containment vessel is not touched.

（a）   out side cracks of 210ms   （b）element deletion of 500ms
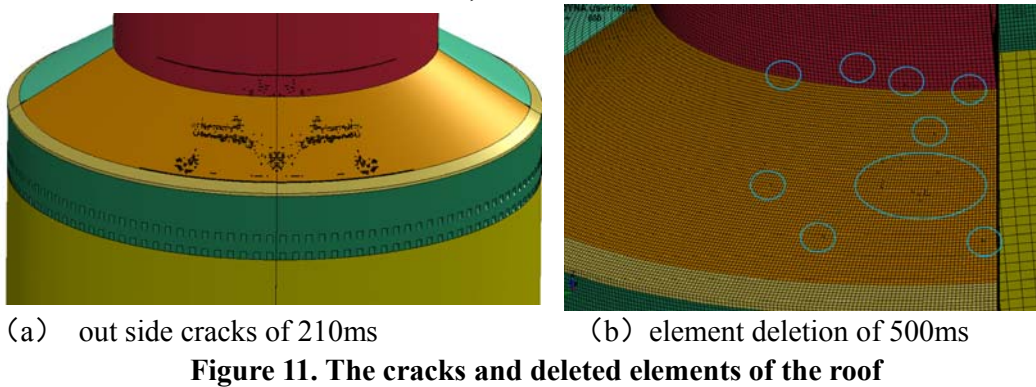
Figure 11. The cracks and deleted elements of the roof

The conical roof is a seimi-SC structure, and only the inner side is protected by steel plate. The concrete's allowable volume strain is conservatively set to be a little higher than RC concrete but much less than SC concrete.

As shown in Fig. 11(a) and (b), aircraft impacting on the conical roof will cause a lot of surface cracks but almost no inner cracks. Because the inner steel plate hasn't been damaged, even if the concrete peel off because of the cracks, it will not affect the steel containment vessel.

In the impacting process, some concrete elements are eroded and deleted. At the time of 500ms when the impacting is almost ended, deleted elements are shown in Fig.3-11(c). The erosion depth is 157mm（one mesh layer）.

4. Rationality demonstration

Fig.2 shows the energy time history curves of the case of impacting on the conical roof. The total energy keeps balance in the whole impacting process, and is generally the same as the initial kinetic energy. The sum of internal energy, kinetic energy, hourglass energy, sliding energy and external works is equal to the total energy at all the time. There is no abnormal phenomenon such as negative sliding energy which usually indicates abnormal elements penetration. It suggests that the analysis is rational to a certain extent.
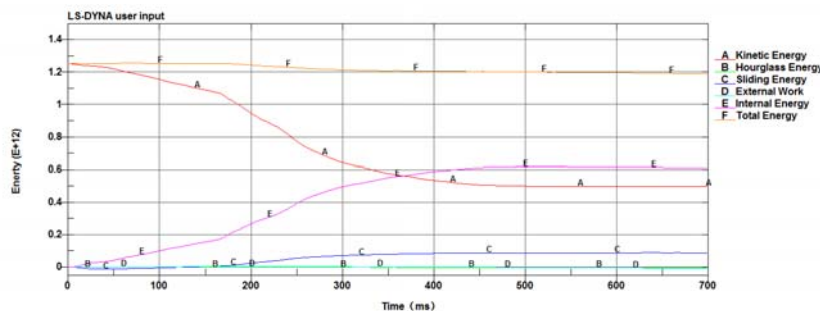
Figure 12.   energy time history curves of the system

5. Conclusion

This paper assesses an aircraft impact on CAP1400 Shield Building's cylindrical wall, airinlet zone and conical roof. The results show that:

1. The shield building is still integrative after impact. In the 3 impacting cases, the deformation is 130m, 50mm and 28mm respectively.

2. When impact on the cylindrical wall or the airinlet zone, a small part of the out steel plate is damaged, but no concrete element or inner steel plate element is deleted. The concrete particles caused by cracks wouldn't affect the steel containment which is protected by the shield building.

3. When impact on the conical roof, a layer (about 157mm) of elements are deleted, but no inner steel plate element is deleted. The concrete particles caused by cracks wouldn't affect the steel containment.

So it can be proved that CAP1400 can continue to provide adequate protection for the public health and safety after a LWBCP impact affair.

References

1) American Concrete Institute.(2006)."Code Requirements for Nuclear Safety-Related Concrete Structures and Commentary". ACI 349-06.
2) The Nuclear Energy Institute (NEI). (2011)."Methodology for Performing Aircraft Impact Assessments for New Plant Designs". NEI 07-13 Rev 8p.
3) Livermore Software Technology Corporation(LSTC).(2007). "LS-DYNA Keyword User's Manual", Revision 971.

4) Tsubota H, Mizuno J, Sanai M, Peterson B, Saito H, Imamura A.(1999)."Scale Model Tests of Multiple Barriers against Aircraft Impact: Part1 Experimental Program and Test Results". Transacations of the 15th International Conference on Structural Mechanics in Reactor Technology, 1999, Vol. J04/2:137-144.

Enclosed circular coal yard: experimental study, numerical modeling, and engineering design

Fan Zhenzhong[1] Zhou Liqiong[2] Zhou Daibiao[3] Ding Weiliang[4]

[1] Professor of Engineering, Central Southern China Electric Power Design Institute, China Power Consulting Group Corporation, Wuhan, Hubei 430071, e-mail: fanzhengzhong@csepdi.com

[2] Professor of Engineering, Central Southern China Electric Power Design Institute, China Power Consulting Group Corporation, Wuhan, Hubei 430071, e-mail: zhouliqiong@csepdi.com

[3] Senior Engineer, Central Southern China Electric Power Design Institute, China Power Consulting Group Corporation, Wuhan, Hubei 430071, e-mail: zhoudaibiao@csepdi.com

[4] Engineer, Central Southern China Electric Power Design Institute, China Power Consulting Group Corporation, Wuhan, Hubei 430071, e-mail: dingweiliang@csepdi.com

Abstract: Enclosed circular coal yard have been widely utilized for environmental protection and land conservation purposes. On the basis of in-situ testing, experimental modeling, and numerical evaluation, this study presents a comprehensive methodology for the determination of the key design parameters and the experimental and analytical modeling of coal stockpile structural systems. Multiple engineering applications show that the proposed approach is reliable and economical.

Key words: Enclosed Circular Coal yard, Lateral Pressure Distribution in Coal Piles, Thermal Effects, Wind Pressure Coefficient, Field Tests and Experiments, Numerical Modeling.

1. Introduction

With the development of economy in China, the electricity demand is on the rise. In order to better protect the environment and save the land, enclosed circular coal yard is widely used in coal-fired power plants. However, due to the lack of many design parameters such as the lateral pressure of the coal pile, the temperature difference in the coal pile, and the wind load profile for spherical roof, the building cost for different cases can be significantly different. To this aim, we propose a computational approach for the analysis and design of enclosed circular coal yard as well as the calculation of the design parameters, which is based on our research experience and engineering practice, including field tests, experimental modeling, and numerical analysis. The proposed approach has been also verified and validated with a number of engineering projects.

2．Analytical and experimental determination of lateral pressure distribution in coal pile

2.1 Theoretical analysis of the lateral pressure coefficient of the coal pile

According to the limit equilibrium theory, consider the friction between the coal pile and the concrete wall, and suppose that the reaction force on the coal retaining wall can be computed by varying the slip surface, the maximum of which is the lateral pressure exerted by the coal pile, further assume that the lateral pressure distribution in the vertical direction is linear, the lateral pressure coefficient can then be determined.

Because the friction angle and the friction coefficient are different for different coal materials, the lateral pressure coefficient of the coal pile can be obtained using the Kuhlmann graphic method. Alternatively, assuming that the sliding wedge of the coal retaining wall has reached the limit equilibrium state, the lateral pressure coefficient can also be determined by the Coulomb earth pressure theory.

The Kuhlman graphic method, which has been widely used in engineering practice, is an effective technique for the computation of the lateral pressure coefficient for different coal pile diameters and heights，refer to figure 1。

	A=90-(1+u)*38	B	Ko=2845*B*2/(10*20.5^2*20.7)
0.000	52.0°	6.6352	0.4340
0.300	40.6°	6.3578	0.4159
0.400	36.8°	6.3249	0.4137
0.468	34.3°	6.3185	0.4133(*)
0.500	33.0°	6.3200	0.4134
0.600	29.2°	6.3429	0.4149
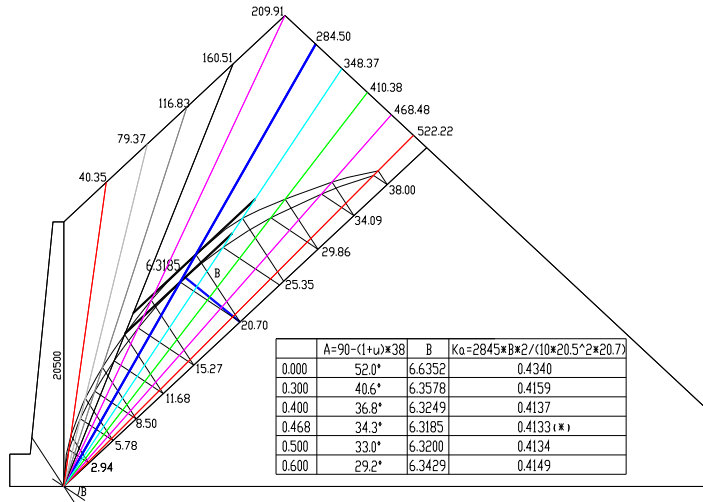
Figure 1   Illustration of the Kuhlmann graphic method

2.2 Field Testing

In this research, we select a representative enclosed coal stockpile in China that is currently in service to conduct the field test. To be more specific, as shown in Figure 2, we deploy pressure sensors on the silo wall for the real-time monitoring of the change of the pressure along the vertical direction of the coal pile. In this way, the

lateral pressure in the coal pile can then be determined. Furthermore, we also compare the field test data with the results predicted by analytical modeling. On the basis of the aforementioned field testing and analytical modeling, we then put forward the recommended value for the lateral pressure coefficient to better serve industrial purposes.
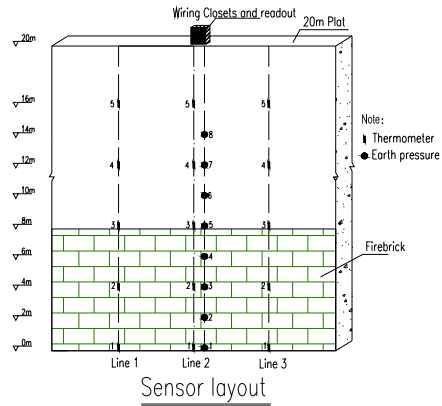

Figure 2   Field measurement sensor layout　　　Figure 3   The lateral pressure variation along the height
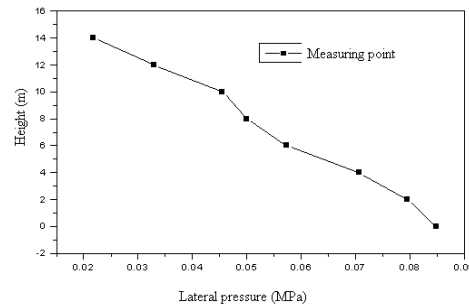
The field test results show a basically linear distribution of the coal pile pressure along the wall, which is in good agreement with those obtained from analytical modeling shown in Figure 3, indicating that the analytical modeling approach can be applied in engineering practice.

It is also noticed that there are slight changes in the lateral pressure coefficient values for different coal pile heights and diameters. Thus, the pressure coefficient value may vary from 0.45 to 0.50, depending on the specific case of the problem.

3. Thermal Effect

To quantify the thermal effect, we carry out field tests on a presently operating coal pile in China to find out the temperature variation of the coal pile. The evaluation reveals that the central region has higher temperature than the sidewall. On the other hand, along the sidewall height direction, the middle region has the highest temperature. The temperature near the top of the coal pile is slightly lower than that in the middle part. The bottom region has the lowest temperature. Based on field test results, the temperature near the sidewall may be taken to be 38℃, as shown in Figure 4 and Figure 5.

According to field observations, spontaneous combustion can occur in bituminous coal in approximately 40 to 45 days after be placed in the field. It is also found that self-combustion is much more likely to take place in the central region. The outer

region has a lower possibility of self-combustion. This observation is also found to be consistent with other actually observed cases.
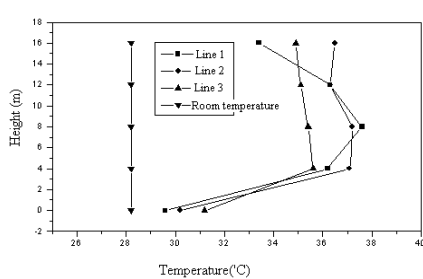

Figure 4   The temperature change of each measuring point

in the first 42 days
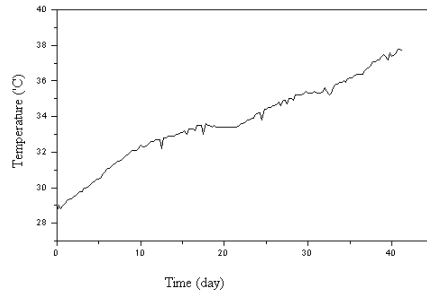
Figure 5   Typical measuring points (column 1

measuring point 3) temperature variation over time

4．Wind load coefficient determination of the spherical shell

For enclosed coal stockpile structures, the determination of the design parameters of the wind load such as the body shape coefficient of wind load, the wind load factors is required. On the other hand, other design parameters, including the basic wind pressure and the pressure variation coefficient can be obtained by relevant provisions, standards, and regulations.

To achieve the goal, we use both physical and numerical models to determine the wind load coefficient and the wind load factor of the enclosed coal yard roof. We then evaluate the physical and numerical modeling results. We also compare the results with those computed by the Chinese codes and the European Codes.

4.1   Wind tunnel test

We carry out experiments using a rigid physical model of 120 m in height at the wind tunnel laboratory in the School of Environmental Science and Engineering at Peking University. The wind tunnel is an open-suction wind tunnel, which has a width, height, and length of 3 m, 2 m, and 32 m, respectively.

The physical model has a 1:129 scale to the prototype. In the test, we focus on the influence of the wind load coefficient at different heights of the coal retaining wall, site classification, and fully and partially enclosed coal yard roof structural configuration，as shown in Figure 6.

4.2   CFD Modeling

With the rapid development of modern computer technology and computational fluid dynamic technology, it is possible to use wind tunnel to simulate the wind field

around structures. Numerical Wind Tunnel is a numerical technique that relies on Computational Fluid Dynamic (CFD) to simulate the wind field around the structure, thus attaining its wind load distribution. The technique was originally proposed during the last decade, and has now evolved into a new discipline, i.e. Computational Wind Engineering (CWE).

In the modeling, we compare he wind tunnel test and CFD modeling results. Based on that, we analyze the many effects such as varying coal stockpile diameters.

4.3 Code specification

4.3.1 According to the Chinese "Design Code for Building Structures" (GB50009-2012), in particular the 36th item in Table 8.3.1, we have

   (a) If f/l>1/4，$\mu_s = 0.5\sin^2\varphi\sin\psi - \cos^2\varphi$；

   (b)If f/l≤1/4，$\mu_s = -\cos^2\varphi$。

   where φ is the elevation angle, ψ is horizontal azimuth angle, f is the top of the vertical rotating shell height loss, and l the bottom diameter rotating shell top in the formula.

4.3.2 The calculations are performed according to the code and specification Appendix 1 provided by the Wind Effect Technical Committee (T12) of European Steel Association (ECCS), as shown in Figure7.

Figure 6   The physical model in the wind
tunnel laboratory
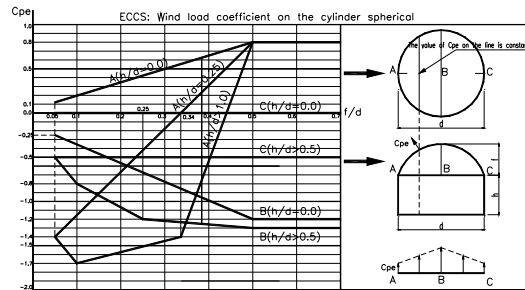
Figure 7   Wind load coefficient from the
European Steel Association (ECCS)

4.3.3 Major conclusions from the analysis of the physical and numerical modeling results can be summarized in the following:

(1) The physical and mathematical modeling results are consistent. Thus, mathematical modeling appears to be effective in determining the shape coefficient of wind load.

(2) From the comparative analyses of the wind tunnel test results and the Chinese code specification "Design Code for Building Structures" (GB50009-2012), both the positive and negative pressure distribution areas are consistent. However, the wind load shape coefficient values obtained by the Chinese code (GB50009-2012) appear

to be higher than those from the wind tunnel test results. Further studies to evaluate if the Chinese code (GB50009-2012) needs modifications are needed.

(3) From the comparative analyses of the wind tunnel test results and the specifications of the European Institute of Steel Construction (ECCS), both the positive and negative pressure distribution areas are consistent. However, the wind load shape coefficient values obtained by the ECCS specification are found to be higher than those from the wind tunnel test results, showing that the ECCS specification is conservative.

(4) Based on the comparative studies of the physical modeling results and the ECCS code provisions and specifications, it appears that the ECCS code has incorporated the effects of the variation of the height of the coal retaining wall height and on the wind load shape coefficient, the computed wind load shape coefficient compares well with the physical and numerical modeling results, demonstrating that it can be used in practical engineering design.

5 Applications

5.1 Loadings

5.1.1 Pressure Distribution of the coal pile (including the lateral pressure acting on the coal retaining wall and the vertical pressure acting on the foundation)

Lateral Pressure of the coal pile: the lateral pressure exhibits a triangular shape distribution along the coal retaining wall height direction, the lateral pressure of retaining walls can be computed by $P_h = k\gamma h$, where k is the lateral pressure coefficient of the coal pile, a typical value of which can be taken as 0.46, γ is the unit weight of the coal materials.

Vertical Pressure of coal pile: the vertical pressure as the linear variation of surface loads is acted on the foundation surface of the coal yard. As shown in Figure 8, the vertical pressure of the coal pile is $P_V = \gamma h_n$, in which h_n is the height of coal pile and γ is the unit weight of the coal materials，as shown in Figure 8.
.
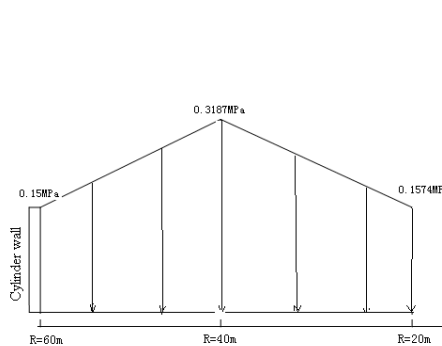
Figure 8   vertical pressure with radius R   Figure 9. Illustration of the temperature difference
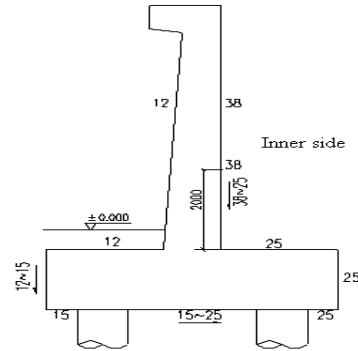
5.1.2 The temperature difference between internal and external coal retaining walls

The external temperature of the coal retaining wall depends on the exterior environment temperature, while the internal temperature depends on the temperature of the coal pile.

In this study, the temperature from the distance higher than 2m above the side coal retaining wall to the top surface is taken as 38   , while the temperature from the elevation lower than 2m to the bottom platform varies from 38   to 25   . According to local meteorological data, the monthly mean minimum temperature is 12.7   . Thus we set 12   as the outer wall temperature. As a result, the temperature difference between the internal and external wall is 26   . The inner temperature of the bottom platform was set to be 25   , whereas the outer surface temperature is taken as 12   ~ 15   . In addition, from the outside to the inside of the bottom platform, the transition temperature ranges from 15   to 25   , as shown in Figure 9.

5.2 Example Applications

5.2.1 Application Examples: Case A

Case A is a power plant project with two 600 MW supercritical coal-fired units, which consists of two circular enclosed coal yard whose diameters and heights are 120 m and 15.5 m, respectively. The coal heap height of coal retaining wall is 15.0m, coal heap inclination 38°, the net shell height 65 m, and the wind pressure 0.3kPa (designed for a return period of 50 years).

Each individual coal stockpile can store 180,000 tons of coal. The project has two coal retaining walls that use unreinforced concrete structures along the circumferential wall. The power plan has been running since 2009 and is currently in good condition，as shown in Figure 10.

5.2.2 Application Examples: Case B

Case C is a power plant project with four   350 MW supercritical coal-fired units, the coal stockpile diameter and height of which are 100 m and 17.2 m. The coal heap height of coal retaining wall is 16.8 m, coal heap inclination is 38 °, the net shell height is 52.8 m, and the wind pressure is 0.8kPa (designed for a return period of 50 years).

Each individual coal stockpile can store 110,000 tons of coal. The project has two continuous retaining walls without seam connection along the circumferential direction, which is made from in-situ poured concrete. The project was completed in 2009 and is currently operating well，   as shown in Figure 11.

Figure 10   Case A   Figure 11   Case B

6. Conclusions

The proposed approach has been applied in numerous coal projects in China that has been operating in good condition after completed. Engineering practice shows that the approach is capable of ensuring structural safety and reliability as well as achieving economic gains. In addition, the Central Southern China Electric Power Design Institute has collaborated with other consulting firms and research institutes to initiate the Chinese code "structural design guidelines for circular coal yard" (Q/DG 1-T009-2012), with the aim of providing recommendation and guidance to the industry for the design of enclosed circular coal yard.

References

1   GB50009-2012   《Load code for the design of building structures》
2 《Housing and Structural Calculation of Wind Effects》, ECCS wind effects technical committee。
3   China Power Engineering Consulting Group Corporation Science and technology projects，The civil parts of   《Enclosed circular coal yard optimization design research》 （DG1-M01-2006）

Tower Destruction Mechanics of Overhead Transmission Lines and Prevention Technologies in Ice Disasters

Fengli Yang[11], Jingbo Yang[2], Junke Han[3] and Zifu Zhang[4]

Abstract：Some advances on tower destruction mechanics of overhead transmission lines and prevention technologies in ice disasters are introduced. Firstly, based on the numerical and experimental study on the tower-line system with ice-shedding and broken of conductors, dynamic responses of the tower-line system were obtained, and the unbalanced tensions as well as the uplift loads were proposed. Secondly, study on the bearing capacity of K type joints with an included angle less than 30 degree was completed. The first ultra high voltage (UHV) steel tubular cup type tower in the world was designed for transmission lines in heavy icing area, and the prototype test was carried out in the UHV tower test station. Thirdly, the bearing capacity and the destruction modes of transmission towers with galloping conductors were studied. A practical calculation method of the galloping loads was obtained. A constructional measure realized by the bolt strengthen technology were proposed for the transmission towers in the galloping area with high intensity. Lastly, the structural reinforcement technologies of the transmission towers after ice disaster were developed, especially for the enhancement of design standards and reinforcement technology for main members of transmission towers.

Keywords: Transmission tower; Accreted ice; Load characteristic; Destruction mechanics; Reinforcement.

1.Introduction

The electrical and mechanical properties of transmission lines will be reduced with heavily accreted ice. In icing area, non-uniform accreted ice, ice-shedding, conductors broken as well as galloping can cause high longitudinal unbalanced tension. The tower will be collapsed and even a major collapse with cascading effect happens. In the serious ice disaster of the power grids in South China in 2008, one hundred twenty-two 220kV and fifty-four 500kV transmission lines were destroyed. The industrial and agricultural production and the people's everyday life were severely affected. The direct economic loss of the State Grid Corporation of

---

[1]1Ph.D, China Electric Power Research Institute, Beijing, 100055, China(corresponding author). E-mail: yangfl1@epri.sgcc.com.cn.
[2]Ph.D, China Electric Power Research Institute, Beijing, 100055, China.
[3]Senior Engineer, China Electric Power Research Institute, Beijing, 100055, China.
[4]Senior Engineer, China Electric Power Research Institute, Beijing, 100055, China

China(SGCC) is up to 10.45 billion Yuan(Yang J.B. et al., 2008). Many cross arms were damaged and even some transmission towers were overall collapsed in this disaster.

From November 9th, 2009 to March 1st, 2010, influenced by the frequent severe weather with strong wind, lower temperature, and frozen rain and snow, conductors galloping of many transmission lines occurred in a wide range of power grids in China(Yang F.L. et al., 2013a). Many towers were damaged in this galloping disaster. Types and distribution of the mechanical damages can be seen in Figure 1. The quantities of the tower damages occupy 82 percent of the total damage quantities in Henan province.
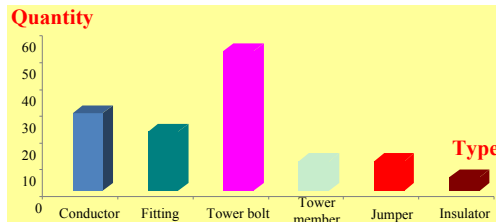
Figure 1. Types and distribution of the mechanical damages

In order to solve the problems in the destruction mechanics and the prevention technology of the transmission towers in icing area, as well as improve the prevention level of transmission towers, research on the tower destruction mechanics and prevention technologies of overhead transmission lines in ice disasters was carried out from 2008 to 2012 by China Electric Power Research Institute(CEPRI). Four parts of the research are mainly introduced in this paper, which include dynamic loads from ice-shedding and broken conductors, the cup-type steel tubular tower in heavy icing area, structural analysis on towers with conductors galloping as well as the reinforcement technology for main members of transmission towers.

2.Loads from Ice-shedding and Broken Conductors

*2.1Load from Ice-shedding Conductors*

A FEA model of seven continuous span conductors and insulators for UHV transmission line in heavy icing area was established for the ice-shedding analysis. Some parameters were considered in the ice-shedding simulating analysis, which include damping ratio, ice-shedding ratio, ice-shedding modes and ice thickness. The dynamic responses of jumping heights, unbalanced tensions and vertical loads at the end of the insulator were obtained. The effects of each of these parameters on the dynamic responses were determined. The values of unbalanced tensions and vertical loads were calculated for the UHV suspension tower in heavy icing area (Yang F.L. et al., 2013b).

In the case of ice-shedding in three continuous span conductors, when the ice thickness is 20mm, the calculated unbalanced tension percent is lower than the regulation value. When the ice thickness is 30mm and the ice-shedding ratio is not less than 70%, the ice thickness is 40mm and the ice-shedding ratio is not less than 50%, as well as the ice thickness is 50mm and the ice-shedding ratio is not less than 50%, the calculated unbalanced tension percent exceed the regulation values. In the case of ice-shedding in one span conductor, the calculated unbalanced tension percent is lower than the value in the regulation. The dynamic amplifying effect of

the vertical load from ice-shedding conductors is very significant and cannot be ignored. The magnification factors of the vertical load are proposed to be valued from 1.06 to 1.11.

According to the Technical Code for Designing of Overhead Transmission Line in Medium & Heavy Icing Area (China Electricity Council, 2009), if the vertical span factor(representing by K_v) of the suspension tower is lower than 0.8, the up-pull load can be valued as 5% to 10% of the maximum working tension of conductors. As shown in Figure 2, a seven continuous spans FEA model was established for the calculation of the up-pulling load. For the ice thickness of 20mm, 30mm, 40mm and 50mm, the basic span length is 450m, 400m, 400m and 350m respectively. The ratio of the span difference to the basic span length is defined as the span difference percent. The fifth span has a span difference with other spans and the span difference ratio is 35%. The fourth suspension tower has an elevation difference with other towers, and the elevation difference ratio is 15%. Only the sixth span conductor happens ice-shedding and the ice-shedding ratio is 100%. Two initial calculating parameters are listed in Table 1, which include the initial tension T_0, the vertical span factor K_v.
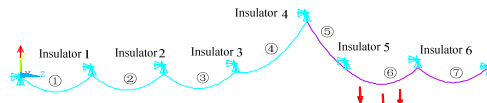
Figure 2. FEA model for the up-pull load calculation

Table 1. Parameters for the calculation of up-pull loads

Ice thickness(mm)	T_0(kN)	K_v
20	23.80	0.524
30	20.08	0.612
40	14.37	0.722
50	10.83	0.761

The up-pull loads at the end of the fifth suspension insulator are listed in Table 2. Time histories of the vertical loads at the fifth suspension insulator are presented in Figure 3. The ratio of the up-pull load to the maximum working tension of conductors is defined as the up-pull load percent. For the same span difference ratio and elevation difference ratio, the vertical span factor increases with the ice thickness, and the up-pull load percent decreases. By considering the importance and the maintenance difficulty of the UHV transmission lines in heavy icing area, as well as only a small amount of members are controlled by the up-pull load, the up-pull load percent for 20mm and 30mm icing area can be valued to 10%, and 5% for 40mm and 50mm icing area.

Table 2. Calculated values of the up-pull loads

| Ice thickness(mm)	Up-pull load(kN)	Up-pull load percent (%)
20	4.90	8.67
30	5.50	8.27
40	2.61	3.93
50	1.98	2.98
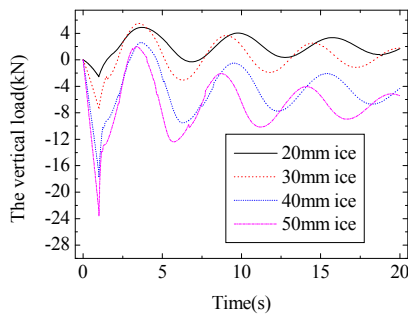
Figure 3. Time histories of the vertical loads

2.2 Load from Broken Conductors

A full scale transmission line section of three continuous spans was established. With the consideration of the equivalent mass and stiffness of the accreted ice, steel cables are used to simulate the iced conductors. For different types of conductors and ice thickness, broken conductor experiments were carried out. Under different broken cases, time histories of the tensions and displacements at the middle of conductor spans were measured. The first order damping coefficients of the line section for different broken cases were calculated. The dynamic impact factors of the conductor tensions were determined. The experimental results show that the impact effect is more significant for the location nearer to the break point. The dynamic impact factors decrease with the increasing of the ice thickness, and the impact factors of conductors without accreted ice are much higher than those of conductors with accreted ice. With the increasing of the ice thickness, the initial tensions before break as well as the ratios of the residual static tensions to the initial tensions increase. Nearly all the first peak tensions are close to the initial tensions for the broken cases with accreted ice. The damping coefficients determined by the experimental identification were applied to the FEA model. The numerical simulations were performed for different broken cases. Both the residual static tensions and the first peak tensions by the numerical simulations are well agreed with the experimental values. The maximum differences are 5.6% and 12.9% respectively (Yang F.L. et al., 2012).


Figure 4. Prototype model of four poles and three span conductors

The broken tests were carried out at the UHV transmission tower test station of CEPRI. A line section with four poles and three span conductors was constructed in south-north direction. The arrangement of the test line section is presented in Figure 4. The span lengths of the three spans are 95m, 100m and 95m in turn.

Time histories of the conductor tensions under A2 test case are presented in Figure 5. The conductor remains in an equilibrium state with the self weight and the initial tension. Immediately at the break time the conductor tension drops to a near zero level and reminds at that value for 0.1 to 0.2 seconds. This is followed by the first

peak due to the recoil of the tension in the conductors. This peak due to the strain energy occurs only once. A second major peak value follows which occurs at a time interval. After about 15 to 30 seconds, the tension reaches a steady value for the effect of the damping properties of conductors.

(a)The second span
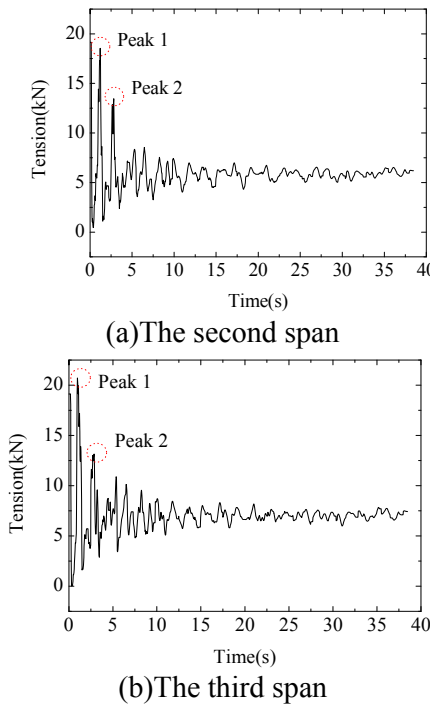
(b)The third span

Figure 5. Time histories for A2 case

The steady value of the tension is called residual static tension expressed by T_r. Peak values of the tensions as well as the residual static tensions in the second span and the third span conductors are shown in Table 3. For all test cases except the cases of A2 and A3 for the third span, the first peak tension is lower than the initial tensions before conductor break.

With the consideration of conductor-ground contact, damping coefficient, bundle numbers and spacers, a seven continuous span FEA model of conductors and insulators was established. Under different load cases, the dynamic responses of the broken conductors were analyzed. The calculated results for the third span conductor are well agreed with the experimental values as shown in Table 4, and the rationality of the FEA model was verified.

Table 3. Peak values of tensions (kN)

Number	The second span			The third span		
	Peak1	Peak2	T_r	Peak1	Peak2	T_r
A1	8.97	5.01	1.90	9.19	5.24	2.20
A2	18.50	13.41	6.20	20.72	13.11	7.43
A3	20.36	14.97	9.88	25.98	17.91	12.20
B1	8.88	9.34	2.68	10.76	9.77	3.29
B2	23.21	15.81	8.19	23.36	18.84	9.98
B3	27.52	21.74	12.17	35.47	25.07	14.65

Table 4. Comparison on the tensions from broken conductors

Number	The residual static tension(kN)			The peak tension(kN)		
	ANSYS value	Test value	Error percent(%)	ANSYS value	Test value	Error percent(%)
A1	2.20	2.20	0.0	9.34	9.19	1.6
A2	7.52	7.43	1.2	22.28	20.72	7.5
A3	11.86	12.20	-2.8	26.08	25.98	0.4

According to the dynamic simulation analysis of broken conductors, some conclusions were obtained. The unbalanced tensions from broken conductors are almost same with and without conductor-ground contact. When all the sub-conductors are not broken simultaneously, the unbalanced tensions calculated by the model with spacers are much lower than those by the model without spacers. For suspension towers in 20mm and 30mm icing area, the tensions calculated by the static analysis method are a little lower than the limit values in the regulation. For other icing area, the calculated values are higher than the regulated values by about 10 percent. Four sub-conductors of the eight bundle conductor are assumed broken in the dynamic analysis. The tensions from broken conductors are lower than the regulated values.

3. New Type UHV Transmission Tower in Heavy Icing Area

3.1 K-type Joint

Experimental and FEA analysis on the K-joints with different included angles between the main tubular member and the side tubular member were completed. The results show that the K-joint designed by the applicable steel structural design standard is not safe when the included angle is less than 18 degree (Li M.H. et al., 2013).

3.2 Prototype Test of a UHV Steel Tubular Tower

In the design process of the ZB1 cup-type steel tubular tower, in order to ensure the strength of the K-type joint, the angle between the main tubular member and the side tubular member at the top bending arm and the bottom bending arm is 23 degree and 20 degree separately. In addition, annual ribbed stiffer is set around the gusset, which can improve the local stress distribution. Arrangement of the K-type joint at the bending arm is presented in Figure 6.

Figure 6. Arrangement of the K-type joint

The ZB1 cup-type steel tubular tower is the first single-circuit tower for UHV transmission line in heavy icing area. Reliability and design method of ZB1 tower is verified by the full-scale test. Full-scale test of ZB1 tower was carried out at UHV transmission tower test station of CEPRI from January 10 to January 14, 2012. The

test tower is shown in Figure 7. Ten types of controlling loads were applied to the test tower. The test tower is not damaged until the load is up to 120% of the design value under 60 degree wind load.

Figure 7. The testing tower

The test values of the stresses and the axial forces were compared with the calculated values by ANSYS in Table 5. It can be seen that the test values of axial forces are well agreed with the FEA analysis values for most of the members except the diagonal member. Especially for the main member of the tower body, the error percent between the test value and the calculated value are only 3%(Zhang Z.F. et al., 2013).

Table 5. Comparison of the stresses and axial forces

Member type	Test values		FEA values	Test values/ FEA values
	Stress (MPa)	Axial forces(kN)	Axial forces (kN)	
Main members at cross arm	-245	-1471	-1449	1.01
	261	1314	1252	1.05
	-245	-922	-739	1.25
Main members at bending arm	-225	-1827	-1743	1.05
	120	452	393	1.15
	-207	-2067	-2046	1.01
Diagonal members	-162	-813	-542	1.50
	106	534	546	0.98
Main members at tower body	-162	-2008	-2063	0.97
	-161	-1999	-2063	0.97
	-162	-2009	-2063	0.97

4.Transmission Towers with Galloping Conductors

4.1 Load from Galloping Conductors

Three calculation methods for the galloping amplitudes of the conductors were compared. The meteorological method is proposed to determine the galloping amplitudes for different vibration orders. Standing sine wave was used to excite the galloping of the conductors. The excitations of standing waves were applied along the axis of the conductor. The galloping displacements at the nodes of the conductor were given as(M.A. Baenzier et al., 1994):

$$y_g(x,t) = a_0 \sin\left(\frac{n\pi}{l}x\right)\sin\omega t \qquad (1)$$

where a_0 is the peak galloping amplitude, which is half of the peak-to-peak value. n is the number of the half waves, l is the conductor span length. ω is the natural circular frequency of the conductor.

Conductor length method, energy equilibrium method and the finite element analysis (FEA) method were applied to compute variation values of the tension forces of galloping conductors. Variation values of the tension forces calculated by FEA method are approximate close to those by conductor length method. Results by energy equilibrium method are lower than those by length method and FEA method. A difference of 40 percent to 50 percent is observed when the number of the semiwaves is odd. Continuous conductor FEA models including one single strengthen section and two strengthen sections were established in general software ANSYS. Unbalanced tension forces between the galloping conductors locating at two sides of the strengthen tower and the suspension tower were analyzed. When the span number is not less than 4, changing of the span numbers has little effect on the tension forces and the unbalanced tension forces between two adjacent conductors. Unbalanced tension force of the tension tower by a FEA model with not less than four spans is 50 percent of the value by two span theoretical model. With the same span numbers, unbalanced tension force of the suspension tower is 12 percent to 25 percent to that of the tension tower. Based on the results of the galloping tension forces, calculating method of the galloping loads for transmission towers is presented. Especially for tension towers, the conductor tensions T_1 and T_2 at two adjacent spans can be calculated by Eq.2 and Eq.3(Yang F.L. et al., 2011).

$$T_1 = \frac{EAa_{10}^2 n_1^2 \pi^2}{4l_1^2}\sin^2(\omega_1 t) - \frac{2EA\gamma a_{10}}{T_0 n_1 \pi}\sin\omega_1 t + T_0 \tag{2}$$

$$T_2 = \frac{EAa_{20}^2 n_2^2 \pi^2}{4l_2^2}\sin^2(\omega_2 t + \Phi) - \frac{2EA\gamma a_{20}}{T_0 n_2 \pi}\sin(\omega_2 t + \Phi) + T_0 \tag{3}$$

where E is the elastic modulus, A is the sectional area, γ is the weight of per unit length, T_0 is the initial tension, Φ is the phase angle.

4.2 Destruction Modes of Transmission Towers

FEA models of the conductor-insulator system and the tower-line system were established for a 500kV line section (Xiangshao line) with galloping disasters. Failure modes of the towers in this line are presented in Figure 8. The FEA model of the tower-line system in ANSYS is shown in Figure 9(Yang F.L. et al., 2013a).

If the first order galloping mode does not occur at the two adjacent spans of a tension tower, the galloping amplitudes are relatively small. The longitudinal unbalanced tension is usually lower than the broken tensions used in the tower design code, and the tension tower will not be destroyed. When the first order galloping mode occurs, the unbalanced tension is higher than the broken tension. Distribution of the tower members at the bottom of the cross arms controlled by the unbalanced tensions is presented in Figure 10.

(a)No.228 tower   (b)No.230+1 tower
Figure 8. Failure modes of the towers
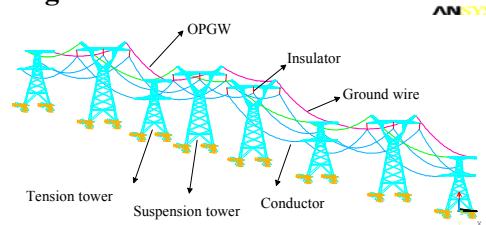
**Figure 9**. FEA model of tower-line system
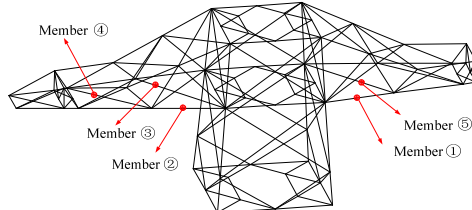
Figure 10. Distribution of the tower members

Two suspension modes were considered in the tower-line system model. The calculated axial forces of the members are close by two modes. According to the real suspension condition, the two suspension points model was proposed. When the conductor of the left phase happens first-order galloping, the axial forces and the stress ratios of the members marked in Figure 10 are shown in Table 6. Time history of the axial force of member ③ is shown in Figure 11. It can be seen that the stresses of the diagonal member ③ and ④ at the bottom of the cross arm exceed the design value by 41 percent and 17 percent. The failure of the cross arm firstly happens at the diagonal member. The cross arm will be broken under the load from the first-order galloping. The broken mode is coincident with the real state in the galloping disaster.

Table 6. Axial forces and stress ratios of the members

Member number	Tower (model 1)		Tower-line system(model 2)		Ratio of the calculated values
	Axial force(kN)	Stress ratio	Axial force(kN)	Stress ratio	
②	-467.42	0.73	-466.59	0.73	0.998
③	-122.38	1.41	-113.34	1.30	0.92
④	-184.14	1.17	-187.78	1.19	1.02
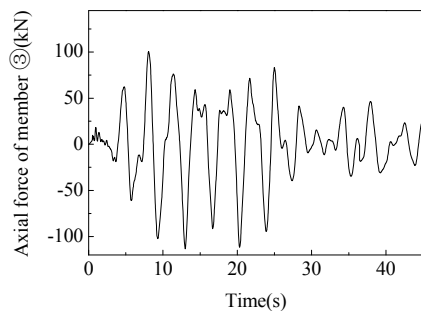
Figure 11. Time histories of the axial forces

   Peak values of the conductor tensions and the unbalanced tensions by the tower-line system model are close to the conductor-insulator model. The axial force of the main member of the cross arm is basically consistent calculated by the tower-line system model with two suspension points and the tower model, and the axial forces of the diagonal members have the differences of 0.2%, 8% and 2% separately.

4.3 Constructional Measures

Loose and slough of the joint connections is one of the main reasons which causes the damage of the cross arms of transmission towers with galloping conductors. The joint connection at the cross arm after the bolts loose and slough is shown in Figure 12.

   In the galloping disaster in Henan province happened in 2010, loose and slough of the bolts can be found in all 28 destroyed towers. In order to solve the problem caused by loosen bolts, some constructional measures have been regulated in the design requirement for the transmission lines in galloping regions. For tension towers and suspension towers adjacent to tension towers, as well as the towers in the important crossing transmission lines, two caps and anti-loosing bolts should be applied in all the bolt joints of the towers.

Figure 12. Loosen bolts at cross arms

5.Tower Reinforcement Technology

5.1 Variation of the Design Standard

After the ice disaster of power grids in 2008, the prevention level in the design of the transmission lines is enhanced. Firstly, based on the ice data from meteorological department as well as the statistical analysis on the ice disasters, a distribution map of the ice thickness for the power grids was completed by SGCC. This map provides important reference to the design and operation of the transmission lines in icing area. Secondly, the broken tension of the ground wires is increased by 100 percent than the original values. In addition, the vertical load from the accreted ice should be

considered in broken cases of the conductor or ground wire. Thirdly, for the transmission lines in serious galloping area, the tower should be checked under galloping load case.

5.2 Typical Reinforcement Technology

In order to improve the bearing capacity of the transmission towers established in heavy icing area, some reinforcement technologies have been developed and used. Two technologies are commonly used for transmission towers in icing area. One is that adding auxiliary member method, which can decrease the calculation length of the main member. The compression stresses main members can be decreased and the bearing capacity can be improved. However, the improving level by this method is limited to some cases with more severe ice load, such as when the ice thickness or the unbalanced tension is much higher than the design values. For these cases, the other technology called adding vice main member method can be used. Connection form of the original and the vice main member is presented in Figure 13. Two main members are connected by a '⸺' shape plate. One bolt is used for every flange of the angle main member. The strengthen process can be carried out with the usual operation of the transmission lines. The temporary staying wires are also not needed in the construction process. The safety and reliability can be ensured in the whole strengthen process.
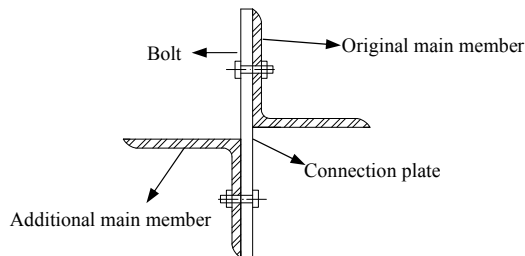
Figure 13. Connection form of the original and the vice main member

The feasibility of this technology has been verified by member test and model tower test (Figure 14). The experimental results shows that the bearing capacity can be increased by about 70 percent(Han J.K. et al., 2010). Based on the experimental and theoretical study on the main member strengthened by the vice member, the bearing capacity under compressed load can be checked by Eq.4.

$$\frac{N}{k_d \varphi A} \le m_N f \qquad (4)$$

where φ is the stability factor of the compressed member, A is the gross sectional area of the original main member, k_d is the co-operation working coefficient valued by 1.50, f is the design strength of the steel. m_N is the reduction factor of the compressed member, which is related to the ratio of the flange length to the thickness.

Figure 14. Model tower in test

6.Conclusions

Research on the tower destruction mechanics and prevention technologies of overhead transmission lines in ice disasters was carried out. Unbalanced tensions and vertical loads from ice-shedding and broken conductors for UHV transmission towers in heavy icing area are proposed. The up-pull load percent for 20mm and 30mm icing area can be valued to 10%, and 5% for 40mm and 50mm icing area. For steel tubular cup type transmission towers in icing area, the K-joint designed by the applicable steel structural design standard is not safe when the included angle is less than 18 degree. Reliability and design method is verified by the full-scale test of a typical UHV tubular tower. A practical calculation model of the galloping loads based on standing waves excitation was established. The bolt strengthen technology is advised and applied for the transmission towers in the galloping area with high intensity. Adding vice main member method is proposed in the reinforcement of the towers. The bearing capacity can be increased by about 70 percent. The co-operation working coefficient of the original main member and the vice main member is valued by 1.50.

References

Yang J.B., Li Z., Yang F.L., and Huang T.Z. (2008). "Analysis of the features of covered ice and collapsed tower of transmission line snow and ice attacked in 2008." *Advances of Power System & Hydroelectric Engineering,* 24(4), 4-8.

Yang F.L., Dang H.X., Yang J.B., and Li Q.H. (2013a). "Analysis on bearing capacities and failure modes of transmission towers with galloping conductors." *Proceedings of the CSEE*, 33(22), 135-141.

Yang F.L. and Yang J.B.(2013b). "Analysis on loads from ice shedding conductors in heavy icing area." *Journal of Vibration and Shock,* 32(5), 10-15.

China Electricity Council(2009). Technical code for designing of overhead transmission line in medium & heavy icing area, *China Electric Power Press*, Beijing, China.

Yang F.L., Yang J.B., Zhang Z.F., and Xing H.J. (2012). "Experiments and numerical simulation on the broken conductors in transmission lines." *Journal of Vibration Engineering,* 25(2), 154-160.

Li M.H., Xing H.J., Hu X.G., and Gao Y. (2013). "Research on load-carrying capacity of smaller K-joints for power transmission steel tubular tower." *Building Structure,* 43(5), 48-53.

Zhang Z.F., Yang J.B., Yang F.L., and Li Q.H. (2013). "Design and full-scale test for cup-type tubular tower of UHV transmission line in heavy icing area." *Electric Power,* 46(5), 45-50.

M.A. Baenzier, W.D. James, B. Wouters, and L. Li (1994). "Dynamic loads on transmission line structures due to galloping conductors." *IEEE Transactions on Power Delivery*, 9(1), 40-49.

Yang F.L., Yang J.B., Fu D.J., and Li Q.H. (2011). "Analysis on the loads from galloping conductors of transmission lines." *Proceedings of the CSEE*, 31(16), 102-107.

Han J.K., Yang J.B., Yang F.L., and Li Z.B. (2010). "Study on bearing capacity of reinforced and strengthened transmission tower." *Industrial Construction,* 40(7), 114-118.

Design and Research for Foundations of Turbine-Generator Sets

Zhou Jianzhang[1]   Shao Xiaoyan[2]

Abstract: This paper reviews and analyzes history and present situation of turbine generator foundation in China for last ten years. It states dynamic analysis, static deflection analysis and model test technology. By analyzing project examples, this paper introduces the development and application of this technology. In order to advance China's technology of turbine-generator foundation designing, this paper provides reference for designing of foundations of turbine generators.
Key words: Balanced quality grade, foundation of turbine-generator sets, dynamic analysis, static deflection analysis, model test

1 Current situation of T-G foundation design

In recent years, China's electric power construction develops rapidly. The construction scale expands day by day. The capacity of full and half speed machines develops from 600MW, 1000MW to 1750MW. There are different kinds of machines from countries like the United States, Japan, Germany and France and those improved by domestic manufactures. Higher demands for the turbine generator foundation design in China (hereinafter referred to as the 'T-G foundation') are put forward. The technology of T-G foundation designing has advanced to a new level.

Manufactures introduce these imported and improved machines and provide T-G foundation design criteria and references of T-G foundation. According to the manufacturer and design criteria in China and abroad and the experience of previous T-G foundations, considering the different design conditions of each power plant, the T-G foundation design engineers carry out a large amount of numerical analysis and model tests for T-G foundation in order to ensure steady and safe operation of the machine. T-G foundations of different machines and capacities are improved and optimized. A lot of low frequency foundations with slender columns appear, which are typical of Siemens 600MW and 1000MW machine foundations.

Zhou Jianzhang[1] and Shao Xiaoyan[2]
[1]EAST CHINA ELECTRIC POWER DESIGN INSTITUTE, Shanghai, E-mail: zjz@ecepdi.com
**[2]QINGDAO CREATE ENVIRONMENT CONTROL TECHNOLOGY CO. LTD, Qingdao Shandong**
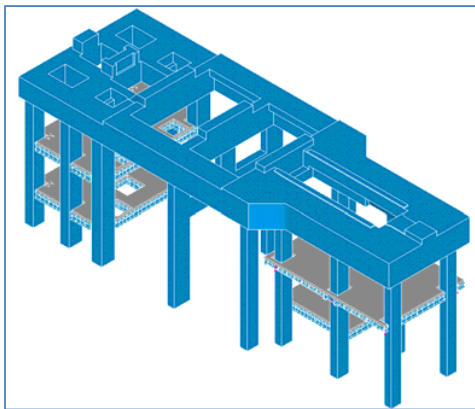
Figure 1 1000MW Siemens T-G foundation in operation
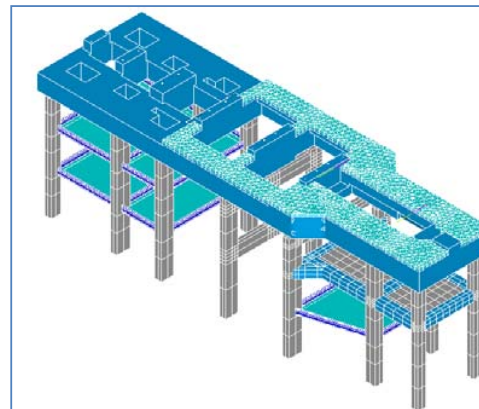
Figure 2 1000MW T-G spring foundation under construction

At the same time, several 600MW full speed and 1000MW half speed machines with spring foundations have been put into operation. Several 1000MW full speed and half speed new machines with spring foundations are under construction. Because the spring foundation has incomparable advantages to conventional T-G foundation, it is designed and analyzed primarily.
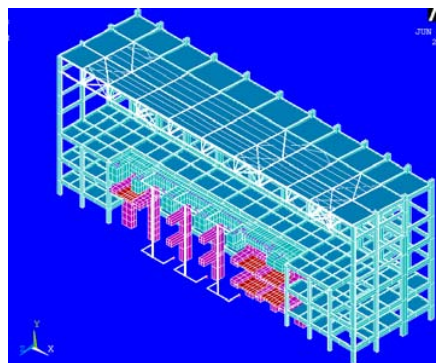

Figure 3 Research on the layout of spring foundation combined with turbine house

2 Vibration analysis of foundation

The unbalanced force is input data for vibration analysis of foundation. Generally the unbalanced force is determined by a constant balanced quality grade. Based on vibration analysis of shaft system by Manufacturer recently, unbalanced forces are resulted from bearing forces under rotor excitation. The following example briefly describes the use of this kind of unbalanced force to calculate forced vibration.

2.1 Set and foundation

1000MW full speed machine has a high pressure turbine, an intermediate pressure turbine, two low-pressure turbines and a generator. The bearing is supported on transverse beam directly. The shaft system is composed by 6 rotors and 7 bearings, which is called single shaft and single support point bearing.

Figure 4 single shaft and single support point bearing set

Table 1 rotor

Rotor	HP	IP	LP1	LP2	GEN	EXC	Total
Weight(g)	16460	35419	91756	93228	90944	2155	329962
Length(mm)	5277	7368	8485	8545	13250	2930	45855
1ST Critical speed (rpm)	2170	1620	1410	1470	660	3650	
2ND Critical speed (rpm)	>3600	>3601	>3602	>3603	1930	>3605	
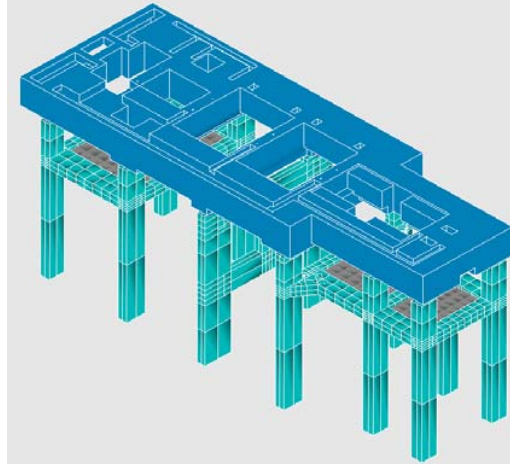
Figure 5 Spring foundation

The foundation is spring foundation. The bottom surface and top surface elevation of the concrete deck are respectively 13.5 and 17(m). The bottom elevation of three transverse beams between intermediate pressure turbine, low pressure turbine 1, 2 and generator are respectively 13, 12.75 and 13(m). The width of turbine and generator are respectively 17.85 and 12(m). The total length of the deck is 51.3(m). The total weight of concrete deck is 46344(kN). The total weight of equipment is 17300(kN). The ratio of total weight between the concrete deck and the equipment is 2.67.

2.2 Unbalanced force

During the vibration analysis of turbine generator shafting, the rotor eccentric loads on the intermediate position or both ends of the rotor are taken as one load case. Each rotor has two or three load cases. The force response of each load case on each bearing in operating speed is the unbalanced force of turbine foundation forced vibration. The under mentioned real example has 14 load cases.

According to the manufacturer's requirements, in each load case of the unbalanced force, when the speed is between ± 10% of the normal operating speed, the vibration response amplitude of turbine foundation could not be more than 40% of the values for zone "A". It is the same when the unbalanced force is multiplied by 2.5, the vibration response amplitude of turbine foundation could not be more than the values

for zone "A".
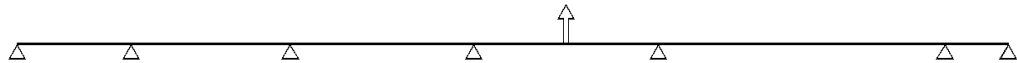
Figure 6 Rotor eccentric load on the intermediate position of the rotor
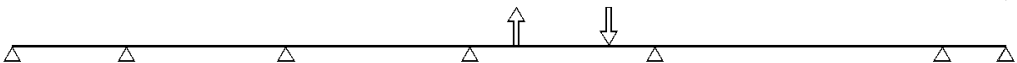

Figure 7 Rotor eccentric loads on both ends of the rotor

The Harmonic method is used in the forced vibration analysis of turbine foundation. The vertical and horizontal unbalanced force on each bearing and their phase should be determined during the analysis, according to the manufacturer's information. The vertical and horizontal vibration amplitude should be acquired in order to check by the criteria in each load case. Turbine foundation forced vibration analysis show that under the unbalanced force of the ninth load case, in the second load position of low pressure rotor 2, the vibration amplitude in bearing Brg_4 between two low pressure turbines is the maximum. The unbalanced force is listed as follows:

Table 2 unbalanced force

Unbalanced force (LP2_2)										
Bearing	Rotor	Fv(kN)	DRG_v	Fh(kN)	DRG_h	Fv/Fh	Fr(kN)	Fv/R	Fh/R	Fr/R
Brg_1	80.71	7.53	252.00	17.55	273.00	0.43	19.10	0.09	0.22	0.24
Brg_2	254.38	19.38	119.00	35.18	105.00	0.55	40.16	0.08	0.14	0.16
Brg_3	623.58	61.83	35.00	38.78	324.00	1.59	72.98	0.10	0.06	0.12
Brg_4	907.04	138.65	249.00	27.20	262.00	5.10	141.29	0.15	0.03	0.16
Brg_5	903.06	88.08	78.00	35.73	111.00	2.47	95.04	0.10	0.04	0.11
Brg_6	456.49	8.70	32.00	15.08	75.00	0.58	17.41	0.02	0.03	0.04
Brg_7	10.57	0.70	310.00	1.23	341.00	0.57	1.41	0.07	0.12	0.13
Max	907.04	138.65	310.00	38.78	341.00	5.10	141.29	0.15	0.22	0.24
Mark	Brg_4	Brg_4	Brg_7	Brg_3	Brg_7	Brg_4	Brg_4	Brg_4	Brg_1	Brg_1
Total/ Average	3235.82	46.41	153.57	24.39	213.00	1.61	55.34	0.09	0.09	0.13

note：

Fv,Fh：Vertical and horizontal unbalanced force multiplied by 2.5；

DRG_v, DRG_h：Phase of the vertical and horizontal unbalanced force；

Fr：SRSS of vertical and horizontal unbalanced force；

Fv/Fh：The ratio of unbalanced force between vertical and horizontal；

Fr/R,Fv/R,Fh/R：The ratio between unbalanced force and weight of rotor；

2.3 Summary and discussion：

(1) The unbalanced force resulted from vibration analysis of shaft system is compared with the unbalanced force resulted determined by a constant balanced quality grade, the differences are listed as follows:

1) The amplitude of vertical and horizontal unbalanced force is not the same；
2) Each bearing unbalanced force is unable to be determined by constant balanced quality grade；
3) When the balanced quality grade is G2.5 and G6.3 for full speed machine, the unbalanced force is 0.08 and 0.2 of weight of the rotor. The Table 2 shows that: during the shafting vibration analysis, the vertical unbalanced force in turbine module is greater than G2.5 and less than G6.3. The horizontal unbalanced force of bearing Brg_1 in turbine module is greater than G6.3.

(2) Under the unbalanced force of the shafting vibration analysis and constant balance quality grade analysis, the differences between maximum vibration amplitude analysis methods are summarized as follows.

Table 3 Analysis methods of maximum vibration amplitude of T-G foundation

Num.	Analysis load case number	Unbalanced force number of each load case	The maximum value method
1	Determined by the total number of rotor and vibration analysis of shafting system	All bearings	Take the maximum
2	The total number of rotor is multiplied by 2	Single bearing	SRSS
3	All unbalanced forces in the same or alternating direction and vertical or horizontal direction, A total of 4 load cases.	All bearings	Take the maximum

Note：
Num. 1：Unbalanced force of shaft vibration analysis；
Num. 2 and 3：Unbalanced force of constant balanced grade；

(3) The shafting vibration analysis of unbalanced force marks the progress of technology. When manufacturers provide unbalanced force of shafting vibration analysis, the forced vibration should be analyzed based on the unbalanced forces provided by the manufacturer.

3 Static Deflection analysis of turbine-generator foundation

Along with the unit capacity becoming larger and the continuous updating of the machine, T-G foundation static deflection analysis is attracting more and more attention from foundation designers. With the updating of the new machines by every manufacturer, strict rules have been made for the deflection limits of the foundation shafting. Various methods for stipulating deflection limits and their advantages and disadvantages are briefly reviewed as fol1ows.

3.1 Radius of Curvature Criteria

The radius of curvature is defined as the circle determined by any three points that lie in one plane. This criterion generally requires that radius of curvature need to be checked at each set of three adjacent transverse girders along both the vertical and transverse directions. The acceptable limits of vertical and transverse radius that describe the shaft curvature caused by static load in operating（hereinafter referred to as the 'operating loads') subsequent to initial alignment vary from one machine to another. One criterion is greater than 40km for a single bearing and 3000-r/min

machine. After calculating, the criterion is met for spring foundation of a 3000-r/min and 1000mw machine.


Center Point coordinates: $Xcenter=\dfrac{Dx}{2\times D}$; $Ycenter=\dfrac{Dy}{2\times D}$;

Radius: $R=\sqrt{(Xcenter-X_1)^2 + (Ycenter-Y_1)^2}$

$$D=\begin{vmatrix}1 & 1 & 1 \\ X_1 & X_2 & X_3 \\ Y_1 & Y_2 & Y_3\end{vmatrix}; \quad Dx=\begin{vmatrix}1 & 1 & 1 \\ X_1^2+Y_1^2 & X_2^2+Y_2^2 & X_3^2+Y_3^2 \\ X_1 & X_2 & X_3\end{vmatrix}; \quad Dy=\begin{vmatrix}1 & 1 & 1 \\ X_1^2+Y_1^2 & X_2^2+Y_2^2 & X_3^2+Y_3^2 \\ Y_1 & Y_2 & Y_3\end{vmatrix};$$
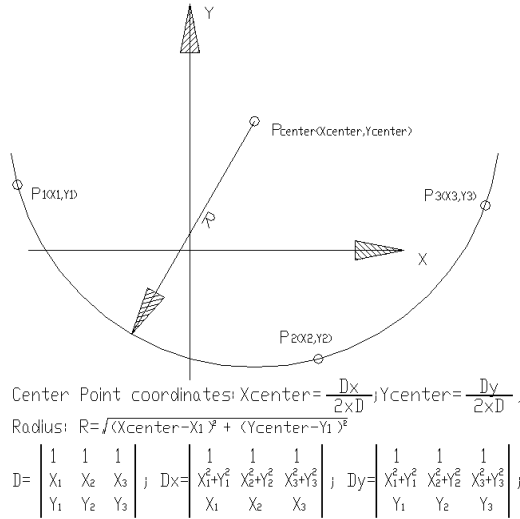
Figure 8 Procedure to calculate the Center point coordinates and the Radius

3.2 Δα' Criteria

Δα' criteria consider the whole shaft-line project onto horizontal plane of the foundation table，with all rotors represented by segments of line. Owing to foundation deflection under operating loads, angles are generated at each coupling between the various successive segments representative of the rotors. The limit of Δα' is less than 5×10^{-5}. After calculating, the criterion is met for spring foundation of a 1500-r/min and 1000mw machine.

According to Figure10，the radius of curvature and Δα' all are based upon the circle determined by any three points. The formula (1) is expressed as relation between the radius of curvature and Δα'. Suppose the distance between the first and third point is 10 (m)，the radius of curvature R is 40 (km) and Δα' is 12.5×10^{-5}, which exceeds the 5×10^{-5} of limit value. Indicating：Δα' criteria are stricter than the radius of curvature criteria. When the distance between the three points is equal, arch height H = 0.313 (mm) which is the displacement difference of the adjacent bearings is more than 0.25 (mm).
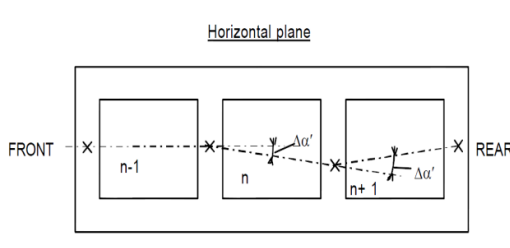
Figure 9 Δα' Criteria   Figure 10 Radius of curvature R and Δα'
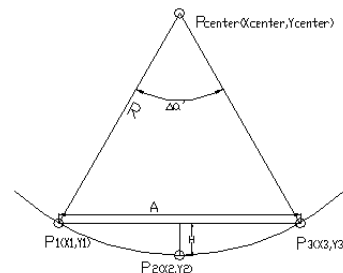
Table 4 Radius of curvature R and Δα'

A(m)	R(km)	Δα'(5.0E-05)	H(mm)
10.000	130.000	3.846	0.096
10.000	120.000	4.167	0.104
10.000	110.000	4.545	0.114
10.000	100.000	5.000	0.125
10.000	90.000	5.556	0.139
10.000	80.000	6.250	0.156
10.000	70.000	7.143	0.179
10.000	60.000	8.333	0.208
10.000	50.000	10.000	0.250
10.000	40.000	12.500	0.313
10.000	30.000	16.667	0.417
10.000	20.000	25.000	0.625

$$A = 2Rsin\left(\Delta\alpha'/2\right) \qquad (1)$$

3.3 Differential radial displacement between adjacent bearings

Under operating loads, one new datum line is established respectively by drawing a line connecting the rotor support points. The new datum lines can be sloped lines which are established based on the condition that the distance between the line and each point W1, W2, … is minimal (best line). In the under mentioned sketch, the label 'Datum Operating Load' is used to identify these new datum lines. The deflection of any rotor support points from the new datum line for operating loads must not exceed ΔR/2＝0.125mm. The differential displacement between adjacent bearings must not exceed ΔR＝0.25mm. After static deflection calculation for two spring foundations of 900mw and 3000-r/min Siemens machine in operating, the deflection of any rotor support point from the new datum line and the differential displacement between adjacent bearings all exceed the limit. Compared with two above-mentioned criteria of three point pattern, the criteria are difficult to meet. This criteria is based upon the best line pattern of each bearing of the shaft system. When this criteria is used to analyze the static deflection, it can be determined by consulting with the manufacturer based on the comparison of the results between the new foundation and the reference foundation.
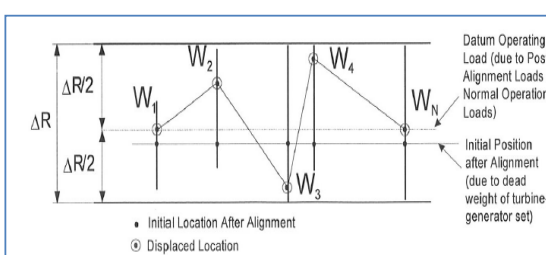
Figure 11 Displacement and differential radial displacement: side view
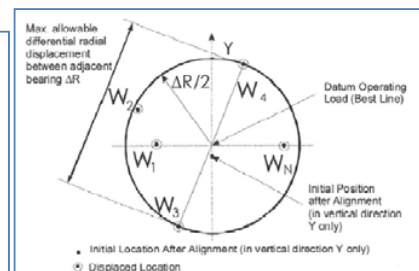
Figure 12 Displacement and differential radial displacement: end view

3.4 Influence Coefficient Approach

In order to more accurately determine the effects of displacement of the foundation under operating loads, these criteria define the amount of misalignment that a turbine-generator rotor system can withstand without imposing unacceptable loads on the rotor bearings in the rotor system.

Based on the static analysis of shaft system by Manufacturer, matrix $[\Delta R/R\ ]_{0.1mm}$ is obtained from a successive, arbitrary lowering 0.1mm of each journal bearing.

Based on the static analysis of foundation by foundation designer, matrix $[\delta]$ is obtained from bearing displacement under normal operating loads.

Under operating loads, the loads on the rotor bearings in the rotor system are calculated by formula follows.

$$\left(\frac{\Delta R}{R}\right) = \left[\frac{\Delta R}{R}\right]_{0.1mm}^{T} . (\delta)$$

The limit of $\Delta R/R$ vary from one machine to another. One limit is less than 10% and 20% in vertical and horizontal respectively for 1000mw and a 1500-r/min machine.

4 Model test

For new kind and the first design of T-G foundation, model test is an effective method to verify and evaluating the foundation design and analysis of reasonable and reliable, and is advanced technology that is different from the numerical analysis of the dynamic characteristics and vibration response of the T-G foundation.

The first vibration and seismic model test of spring foundation has been done based on T-G foundation of the 1000MW and half speed ALSTOM machine, date in 2009. Test according to the proportion of 1:10 established the spring foundation of real model, including the spring vibration isolation system simulation, seismic action considering the deck and the equipment of gravity on the column pressure. The substructure design under spring conclusion is according to the general structure seismic requirements, can be used as the engineering design and technical support.

5 Conclusions

Promoting technological development depend on productivity, T-G foundation design engineers are to make unremitting efforts to explore and master the technique of T-G foundation, expecting to make greater contributions to the T-G foundation design for large capacity and new type of machine.

Reference

[1] "Design of Large Steam Turbine-Generator Foundation." Task Committee on Turbine Foundations of the Fossil Power Committee and the Nuclear Energy Division of ASCE(1987)

Research Program on Design and Construction for 500kV Underground Substation

Z. Chen[1] and Y. Ren[2]

Abstract: This paper presents an overview of Shanghai Expo ultra-deep underground substation project and introduces several critical engineering issues encountered in the design and construction. This paper will provide a better understand of the construction of underground substation and relevant techniques for underground substation construction.

Keywords: substation, design, construction, research program

1. Background

Shanghai 500kV substation is the first underground large-capacity substation in China and one of the major power facilities for 2010 Shanghai World Expo. It is also one of the largest urban underground power substations in the world. The Shanghai Power Company had invested in the project. The project's design and consultation were provided by the ECEPDI. The substation is located at Shanghai downtown, Jinan district, near to the BeiJingxi road and ChengDubei road. The substation is a four story cylindrical structure which is fully embedded in soil mass. The structure is 2.0m below the ground level and has an outer diameter of 130m. A sculpture park has been built right above the substation after the completion of the construction.

Figure 1. Perspective view of Shanghai World Expo 500kV substation

1.1 Brief description of the structure

Reinforced concrete frame-wall structure and pile-raft foundation were adopted in the design of the World Expo 500kV underground substation. The shearing wall is composed of external wall of the main structure and internal blocking wall. The rest structure was

---

[1] East China Electric Power Design Institution, Shanghai, China; e-mail: chz@ecepdi.com

[2] East China Electric Power Design Institution, Shanghai, China; e-mail: renyu@ecepdi.com

frame. The bottom plate is rested 31.0m below the ground level and has a thickness of 2.5m. The excavation has an area of about 13300m^2, a perimeter of 408m and a depth of 33.7m.

1.2 Environment

Shanghai World Expo 500kV substation is located at Shanghai downtown, Jingan district, and around by BeiJingxi road, ChengDubei road, ShanHaiguan road and DaTian road. The project is 30m east away from South-North viaduct and only 10m north away from the ShanHaiguan road. The engineering environment of the project is very complex that many residency, urban power and water supply lines are distributed around the construction site. There are two metro lines around the site and 150m is the nearest distance from the excavation. Therefore, the influence of excavation on surrounding environment should be considered sufficiently in the design and construction to protect underground lines and roads.

1.3 Geology and hydrology

1) Soil properties

The basic engineering properties of each major soil stratums are listed in table 1.

Table 1. Soil properties

NO.	STRATUM	WEIGHTγ kN/m^3	DIRECT SHEAR Cq		PERMEEABILITY COEFFIENCE	
			COHESION c kPa	INTERNAL FRICTION ANGEL φ	VERTICAL k_v cm/s	HORIZONTAL k_h cm/s
②	Silty clay	19.1	21.7	16.8	8.07E-08	2.02E-07
③	Peat with silty clay	17.8	10.1	16.3	1.25E-06	3.87E-06
④	Peat	17.2	6.7	14.2	5.72E-07	5.00E-07
⑤$_{1-1}$	Clay	18.2	12.0	11.0	4.62E-08	4.00E-08
⑤$_{1-2}$	Silty clay	18.2	8.4	19.7	5.63E-07	4.65E-07
⑥$_1$	Silty clay	19.6	43.3	14.4	——	——
⑦$_1$	Sandy silt	19.1	5.0	31.2	1.56E-04	1.92E-04
⑦$_2$	Silty sand	19.3	——	——	——	——
⑧$_1$	Silty clay	18.4	19.1	26.3	8.21E-07	1.04E-05
⑧$_2$	Silty clay	18.5	13.4	26.9	5.34E-05	1.04E-04
⑧$_3$	Silty clay	19.4	——	——	——	——
⑨$_1$	Medium sand	20.1	——	——	——	——
⑨$_2$	Dense sand	20.3	——	——	——	——
	Silt	19.6	——	——	——	——

2) Hydrology

Underground water at the construction site is mainly load bearing water, and the No.6 stratum is the aquiclude layer.

2. **General description of structural design**

According to the design requirement for the structure and protection of surrounding environments, as well as the availability of currently used construction technique and equipment, the main structure and diaphragm wall was built at same time using the reversed construction technique. The whole design scheme can be described as "diaphragm wall used as outside structural wall + structural beam and slab used as horizontal support system + temporary circular brace".

1.   Diaphragm wall

The diaphragm is 1.2m thick and has an inserting depth of 23.8m. Its inserting ratio is 0.71 and the elevation of the bottom of diaphragm wall is -57.5m. Its effective length is 54.0m.

2.   Horizontal bracing system

The underground four-story structural system is a dual dimension beam-slab system. The beams and slabs are used as bracing system to resist the horizontal load.

3.   Temporary brace

Temporary circular bracing system is adopted to reduce the vertical length of the diaphragm wall and to improve the performance of the structure.

4.   Wall inside diaphragm wall

A concrete wall of 800mm thick is placed inside the diaphragm wall with which makes a compound wall structure. This concrete wall has also been built with reversed construction technique.

3. **Major contents of the research**

The excavation of this substation is ultra-deep and its surrounding environment is very complex. Plus, there are very few similar projects have been conducted before. The lack of the experiences and references on both design and construction poses a great challenge. Therefore, to secure the safety of substation design and construction and to explore the techniques to design and build ultra large urban underground substation, the ECEPDI has performed lot of researches on many subjects aiming to solve the issues involved in the design and construction. The major contents of these researches are listed below.

(1)   Distributions of water and earth pressure for excavation engineering in deep soft soil

(2)   Environmental control and protection technique for large ultra-deep excavation

(3)   Analysis of the performance of excavation in complex condition

(4)   Behavior of uplift pile under deep excavation condition

(5)   Application of reversed construction technique in underground substation construction

(6)   Controlling of seepage for underground substation

3.1 Research on distribution of water pressure and earth pressure for excavation engineering in deep soft soil

Proper evaluating the distribution of water and earth pressure is critical for design of underground structure. The distribution of water pressure and later earth pressure are affected by many factors, including excavation depth, soil properties, hydrology,

construction procedures, brace stiffness, external load and seepage action. In the research, experimental studies were carried out to investigate the major factors that affect the pressure distribution. A model for evaluating the distribution of water pressure and earth pressure is also proposed.

3.2 Techniques for environmental controlling and protection for large scale ultra-deep excavation

1) Analysis of seepage field induced by excavation

The Shanghai World Expo substation excavation is circular, and its boundary condition for seepage is complex. Besides, excavation may induce significant excess pore water pressure which will also have effect on the seepage. Therefore, the seepage involving in this project is not a simple one-dimensional steady seepage problem but a complex three-dimensional unsteady seepage problem. In research, the characteristic of seepage are investigated using finite element method.

2) Effect of seepage on the distribution of water and earth pressure

FE models considering the effects of seepage were established to study the procedures for dissipation of excess pore water pressure under excavation. An analytical model in which seepage effects are considered is proposed for predicting the distribution of water and earth pressure. Comparisons are made between the results calculated both by proposed model and currently used regulation. The effects of seepage on the behavior of excavation are also analyzed and discussed.

3) Lateral deformation and settlement of the ground caused by lowering water

Because of the deep excavation, the large gap is found between external and internal excavation surface. Unloading and seepage may induce significant soil uprising at the bottom of the excavation. Besides, large ground settlement may occur when the in . The ground movement caused by the seepage and change in stress state due to excavation is investigated, the effects of the on surrounding environmental condition are also considered.

4) Effects of seepage on soil property

Laboratory tests and analytical studies are carried out to investigate the seepage on soil properties. Methods for predicting the soil stress condition, strain-stress behavior, and soil modulus and strength parameter definition are presented.

5) Seepage prevention and dewatering design

Because the pressure-bearing water table is very close to the excavation surface, cracks are easy to generate on the joint between two diaphragm walls under the very high level water pressure. Canal gush and soil flow may occur to induce large ground deformation which could jeopardize the safety of the buildings and supply lines around the excavation. To address this, techniques for controlling the seepage within the soil inside the pit and dewatering of the deep excavation with the consideration of the limitation in ground settlement were developed.

3.3 Analysis of behavior of retaining structure under complex loading condition

1) Behavior of the retaining wall

The retaining structure of the substation is greatly different from most retaining structure. The currently used method does not provide reasonable prediction of the behavior of retaining structure. Based on the mechanics of circular retaining wall and slab bracing, an approach which takes both soil-structure interaction and time-spacing effect into consideration is proposed.

2) Analysis of the interaction between bracing system and retaining wall during reversed construction

In reversed construction the differential settlement of central column and retaining wall will induce cracks on slabs and beams. Thus settlement problem should be carefully considered in the design and construction of reversed construction. In the study, the interaction between bracing system and retaining wall is analyzed using FE method.

3) Analysis of behavior of foundation bottom slab

The elevation of the bottom slab is -34.0m and the underground water table is very high in Shanghai, therefore the bottom slab is mainly exposed to the action of water buoyancy. Behavior of bottom slab under water buoyancy is analyzed.

4) Temperature effect

The change in temperature and hydration heat due to the cement may cause temperature difference at inside and outside surface of the retaining wall. The influence of temperature difference on the behavior of retaining structure is analyzed.

5) Effects of seismic loading on underground structure

As an unsymmetrical loads, seismic load have a significant impact on retaining structure. Relative few studies have been conducted on this subject. Currently the seismic loads are often simplified as a horizontal static load in the analysis.

3.4 Analysis of behavior of uplift pile under excavation

1) Uplift capacity of pile group

To resist huge uplift force due to water buoyancy, pile group is implemented in the project. Yet, excavation may result in soil rebound and stress redistribution, which will affect the uplift pile capacity. Numerical and experimental investigations of the uplift capacity of pile group are performed. Analysis of characteristic of stress field of the ground is conducted. The characteristic of load distribution at head of corner pile, side pile and center pile is studied. An approach to design pile under uplift load is developed. The proposed approach is based on dual control of displacement and force at pile head.

3.5 Application of reverse construction technique in substation construction

1) Techniques for connecting electricity tunnel with reversed constructed retaining wall

2) Technique for reverse constructed column in underground substation

3) Approach to dewater load-bearing water in underground substation construction

4) Analysis of behavior of reverse constructed structure with pre-cast hole

5) Influence of construction on surrounding environment

3.6 Control of seepage for underground substation

1) Design and construction of high impervious retaining wall

2) Construction of high density concrete

3) Design and construction of key spot of anti-seepage in reverse constructed structure
4) Approach to testing anti-seepage structure
5) Choosing and using of first grade impervious material

4. **Conclusion**

The research studies presented above have been completed at present and its outcomes have been successfully applied to the design and construction of Shanghai 500kV underground substation. The completion of the construction has validated these research achievements. We will detail more aspects of our research outcomes in future to make a reference for future similar projects.

Study on seismic performance of concrete frame-bent structure of power plant main building

LI Hongxing[1], ZHAO Chunlian[2], TANG Liujiu[1], and XUE Min[1]

Abstract: Power plant is a kind of critical infrastructure. The single span concrete frame-bent structure-which is called "single frame structure", is often used in main building because of the equipment layout optimized design. Kobe earthquake, Chi-Chi earthquake and Wenchuan earthquake show that the single span frames are easily damaged. So the "Code for seismic design of buildings" GB50011 and the electric industry codes make strict rules for the use of single frame structure. In order to distinguish the similarities and differences between the "single frame structure" in main power plant and conventional single-frame structure, a dynamic elastic-plastic time-history analysis is carried out based on the characteristics of the main building structure in power plant. The scope of application is given for this kind of structure and the design guide is specifically complied for engineering design.

Keywords: Power plant, main building, single span frame-bent structure, dynamic elastic-plastic time-history analysis, Design Guide

1   Introduction

Power plant is a kind of critical infrastructure. The single concrete span frame-bent structure is often used in main building because of the equipment layout design, as shown in Figure 1. Because the main load of structure and the lateral force resistant component are applied on the frame part and the frame part is always single-span frame, so this kind of structure is often called single frame structure in the power plant main building.

[1]Northwest electric power design institute of China power engineering consulting group, Xi'an, Shaanxi, 710075, P. R. China;
e-mail: lihongxing@nwepdi.com
[2]Electric power planning & engineering institute, Beijing, 100120, P. R. China;
e-mail: clzhao@cpecc.net

The Figure 1 shows a single frame main building structure, AB span is for turbine room, the lower part is frame structure and the upper is bent. Due to setting up turbine generator pedestal, the frame part is actually a large opening; at the same time there is bigger live load on the platform (maximum 40 kN/m^2). The BC span is frame structure, there are six coal buckets located on the high floor. The total weight of coal buckets is close to 5000t. Variety equipments and larger maintenance live loads locate on each storey of platforms.

Kobe earthquake, Chi-chi earthquake and Wenchuan earthquake indicate that the single span frames easily get damaged, see Figure 2. So the "Code for seismic design of buildings" GB50011 and the electric industry codes make strict rules for the use of single frame structure. The "Code for seismic design of buildings" stipulate that the building in class A, class B as well as class C shouldn't adopt single span frame structure while the height is greater than 24 meters; "Structure design technology of the thermal power plant construction" stipulate when single span frame structure is adopted, reliable measures should be carried out to improve the safety of structure.

Actually, the single span frame-bent structure in power plant is different from pure single frame structure. The platform structure in AB span also participates in the overall seismic force, the bent parts and frame constitute as a whole part. So the performance under earthquake is other than pure single frame structure. In order to distinguish the similarities and differences between single frame structure in power plant and the original single frame structure, according to the characteristics of main power plant structure, an elastic-plastic time history analysis is conducted under seismic action. The analysis point out the scope of this kind of structure and a design guideline is compiled specifically to guide engineer design.

2 Dynamic elastic-plastic analyses

2.1 The constitutive relation of concrete

The MARC software is used to analysis structure dynamic elastic-plastic, the compression of concrete constitutive monotonic load envelope curve is selected from Légeron & Paultre Mode (Légeron et al. 2003). The restrain effect of longitudinal and transverse reinforcement in concrete is also considered. In order to reflect the hysteresis behavior of concrete under repeated loading, the quadratic parabola is brought to simulate the main parts of concrete unloading and loading paths, while considering the stiffness and strength degradation in the process of repeated loading 0. In order to simulate the surface effect brought by concrete crack closure, while concrete is intension and compression transition zone, the linear closure function is adopted to simulate the stiffness recovery process of concrete from cracking to compressive (Esmaeily et al. 2005) (Légeron et al. 2005). In tension zone, the Jiang Jianjing Model (Jiang et al. 2005) is introduced to imitate open crack of concrete and softening behavior, for purpose of considering the tensile players effect. See Figure 3.

2.2 Calculation Model

The basic model is shown in Figure 4.

2.3 Classification of calculation

There are eight kinds of circumstances to be considered, including 7, 8 degrees seismic fortification zone, site soil in class I_1, II, III and IV.

2.4 seismic waves selected

The wave selected software is developed by China academy of building research and Chongqing University, it ensure the records generated response spectrum could match with the standardized response spectrum. The Figure 5 shows the seismic wave selection under Class II site (situations are same under other site). The seismic waves are Usa000160, Usa02587 and Usa04430. The dots on the abscissa are structure basic period. It shows that the selected seismic wave response spectrum value is near to standard response spectrum value.

2.5 Top displacement time-history

Due to lots of calculation results, the following list only two kinds of working conditions of top displacement time history. Figure 6 shows top displacement time-history of X directional under site class I_1 in 8 degree seismic fortification zone.

Figure 7 indicates top displacement time-history of X directional under site class III in 8 degree seismic fortification zone.

As shown in Figure 7, when displacement tends to infinity, the actual structure has been collapsed already. While the displacement in Figure 6 doesn't tend to infinity, the maximum elastic-plastic displacement-angle is not beyond the limit 1/50 which is imposed by the "Code for seismic design of buildings" (GB50011 2010). If it exceeds, the structure still cannot meet the requirements.

2.6 Structural deformation and the plastic hinge distribution

Figure 8 indicates the deformation and plastic hinge distribution of structure under Y directional seismic action at 8 degrees.

The following can be seen from the analysis of the results over several conditions:

1. At first, a few beam hinges appear at lower part of the structure, and then, hinges comes on the underlying columns. With the development of the earthquake, the beam-column hinges increase and extend.

2. If calculating by inputting X axis seismic wave, the maximum displacement angles all appear at first floor. The interlayer displacement angles are small at second floor and above. It proves that the first layer is a weak layer of a structure on X direction.

3. When inputting Y axis seismic wave, there are not much differences between the displacements angles of each layer at lower part of the structure. But all of them are bigger than the upper part. This demonstrates, lower part of the structure is the seismic weak position under high axial compression ratio.

4. All of the structure collapse firstly by the damage of beams and columns on middle cross of axis B, which leads the structure to vertical collapse. This is caused by the large opening between AB span. So the middle cross beam and column on Axis B should be strengthened.

2.7 Summary of calculation

For easy viewing, the calculation results of seismic action in unidirectional and bidirectional under 7 and 8 degrees have been tabulated in Table 1. The judging principle of structure applicable or not is if structure collapse under one seismic wave, it means the structure cannot meet the requirement.

Table 1 Situations under different site classification and seismic fortified level

Fortified level	Input on X axis	Input on Y axis	bidirectional	Whole part
Site classification	Whether satisfied fortified requirements	Whether satisfied fortified requirements	Whether satisfied fortified requirements	Whether satisfied fortified requirements
7-I$_1$	√	√	√	√
7-II	√	√	√	√
7-III	√	×	×	×
7-IV	×	√	×	×
8-I$_1$	√	√	×	×
8-II	√	×	×	×
8-III	×	×	×	×
8-IV	×	×	×	×

Note: Numbers on first line means fortified seismic degrees, roman numerals after hyphen means site classification. × means structure will collapse or does not meet requirement.

3   Design criteria

3.1 The definition of single span frame-bent structure system

The platform frame structure on AB span connect with frame structure on BC span, although the frame structure on AB span is weak relatively, in fact the multi span frame still constitute at the lower part. But on the top of the structure, the whole part still belongs to single span frame structure (even though the roof beam of turbine house has certain constraints on single frame structure), and the height is often more than 24m.

So we define this kind of power plant main building structure as single span frame-bent frame structure. It is different from pure single frame structure. We have written guidelines suggesting that in future design work; such a structure should be called single span frame-bent frame structure rather than a single frame structure.

3.2 Scope of application for structure system

According to the results of elastic-plastic analysis, combined with the new version of the "Code for seismic design of buildings" (GB50011 2010), the research results of the thermal power factory workshop early (Li et al. 2011), the "Code for seismic design of structures" (GB50191 2012) and other information, this kind of concrete single span frame-bent frame structure system could be applied in 7 degrees with site class II at most.

3.3 The improvement of structural system

When the site condition is worse than 7 degrees with site class II, the measure of decreasing the axial compression ratio could be adopted if the concrete single span frame-bent frame structure system still needs to be used. Other studies have shown that, decreasing the axial compression ratio can effectively prevent structure collapse. Also, there are some other measures to strengthen the seismic defense of a structure system, for instance, increasing the number of shear wall and steel support. After doing this, the structure is no longer a frame-bent frame structure system, but a frame-shear wall structure or a frame-support structure, the applicable scope of this structure could be expanded.

4 Conclusions

Through the research on this special single span frame-bent frame structure system in power plant, some main conclusions list as below:

1. This kind of structure in power plant is a single span frame-bent frame structure system, not a single frame structure in "Code for seismic design of building".
2. This kind of single span frame-bent frame structure system in power plant could be applied in 7 degrees with site class II at most.
3. Decreasing the axial compression ratio and strengthen the seismic defense are effective measures to expand the applicable scope of this kind of structure.
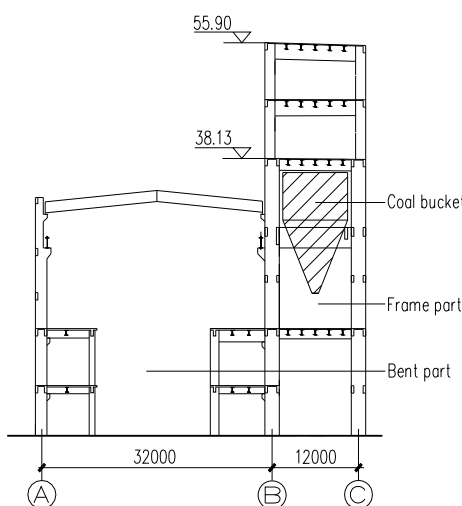
Figure 1 Structure shape

Figure 2 Single span frame structure earthquake damage
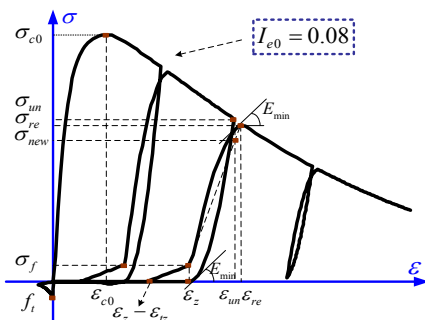
Figure 3 The concrete stress-strain curve
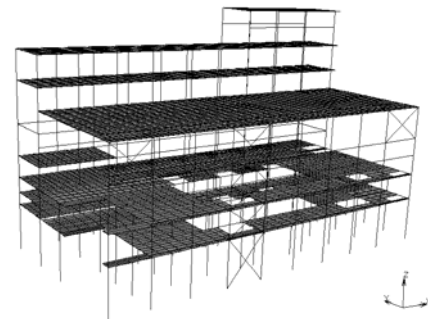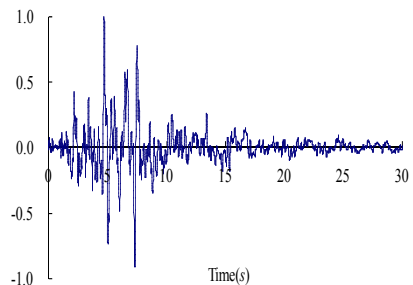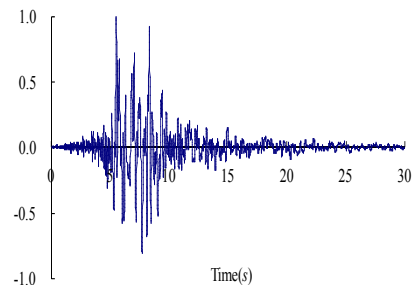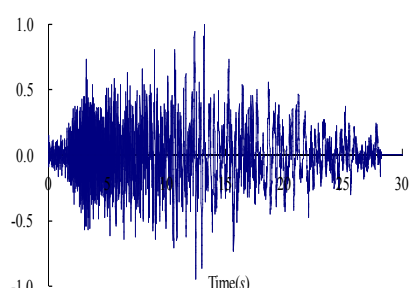
Figure 4 MARC calculation model

Usa000160

Usa02587

Usa04430
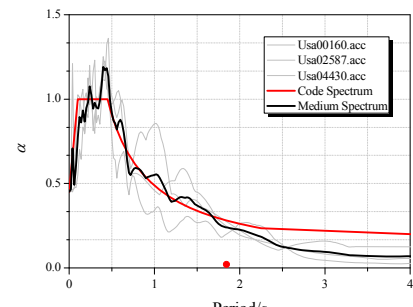
Site classification: II，T_g=0.45s

Figure 5 Seismic wave under site classification II (input on X-axis)
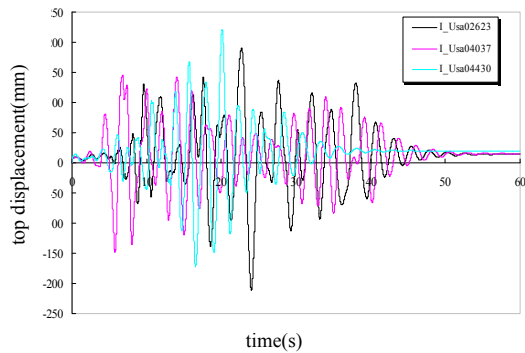
Figure 6 Top displacement time-history of X directional under site class I$_1$
in 8 degree seismic fortification zone
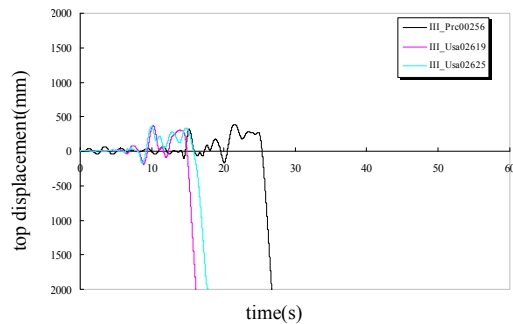
Figure 7 Top displacement time-history of X directional under site class III
in 8 degree seismic fortification zone
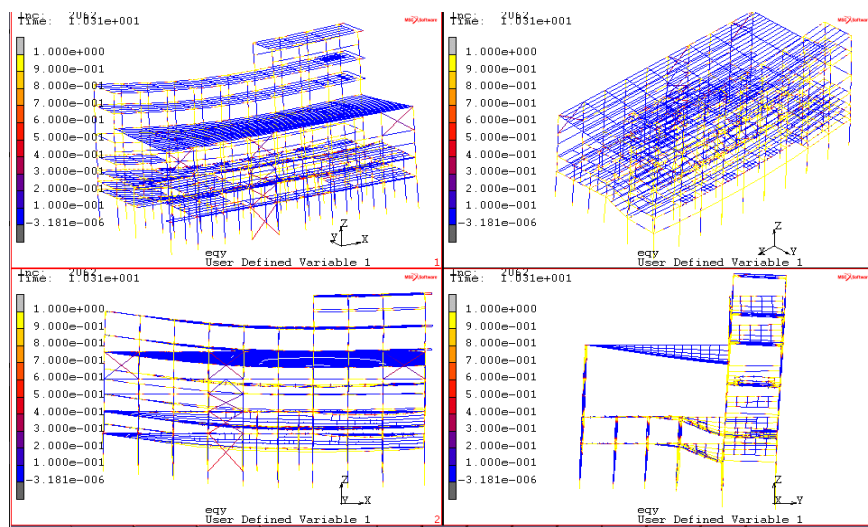
Figure 8 Structure deformation and plastic hinge distribution under Y
directional seismic action at 8 degrees

References

Esmaeily, A. and Xiao, Y. (2005). "Behavior of reinforced concrete columns under variable axial loads: analysis ." ACI Structural Journal., 102(5), 736-744.

GB50011 (2010). "Code for seismic design of buildings." Beijing, China Architecture & Building Press.

GB50191 (2012). "Code for seismic design of special structures." Beijing, China Architecture & Building Press.

Jiang, Jianjing, Lu, Xinzheng, and Ye, Lieping (2005). "Concrete structure finite element analysis ." Beijing, Tsinghua University Publishing Company.

Légeron, F. and Paultre, P. (2003). "Uniaxial confinement model for normal and high-strength concrete columns." Struct. Eng., 129(2), 241–252.

Légeron, F., Paultre, P., and Mazar, J. (2005). "Damage mechanics modeling of nonlinear seismic behavior of concrete structures." Struct. Eng., 131(6), 946-954.

Mander, J. B. Priestley, M. J. N., and Park, R. (1988). "Theoretical stress-strain model for confined concrete." Struct. Eng., 114(8), 1804-1825.

Li, Hongxing Et al. (2011). "Seismic research on single span frame structure." CPECC NWEPDI report.

Design and Research on Braced Frames Steel Structure

Qin Xuedong[1], Liu Chungang[1], Zhang Wenyuan[2]

ABSTRACT：Since lack of design code for braced frame steel structure, one research Project named "Research and Application for Seismic Design of Steel Structure of Main Building in Thermal Power Plant" had been carried out. Systemic experiments and theoretic research for braced frame steel structure had been completed, and some theories about steel structure arrangement, connection and seismic design etc. had been gained. Some construction design for main power buildings of thermal power plants had been completed according to the achievement. Accumulating some experience in design and application. The achievement will conduce to promote the application of braced frames steel structure.
KEYWORDS：steel structure;　braced frames;　seismic design

0　Foreword

In china, steel structure generally be adopted in thermal power plant in the condition of high earthquake intensity area. But frame-brace is the only structure system that can be used according to Chinese seismic code (GB 50011-2010). Furthermore the code is mainly aim at civil construction, that is not applicable to industry construction. the structure style named Special concentrically braced frames (SCBF) had been put forward in the Specification (CECS 160:2004), and SCBF was put forward firstly by UBC[3] code in 1990s. There's one problem whether braced frames system can be adopted in thermal power plant. In order to solve this problem, Northeast Electric Power Design Institute and Harbin Institute of Technology had carried out the research project "Research and Application for Seismic Design of Steel Structure of Main power Building in Thermal Power Plant". The goal of the research is such that, research on the seismic performance of braced frames system based on Chinese code, reference to foreign standards and documents, carry out some necessary structural test, and combined with practical engineering design; finally propose the principle and method of seismic design of multistory steel structure in high earthquake intensity area, lay the foundation for the design of braced frames steel structure.

1 Earthquake pedestal experiment and simulation of braced frames steel structure

1.1 The purpose and content of research

Objective: select one main power building structure of thermal power plant that in seismic precautionary intensity 8 area, verify that whether it can meet the seismic design principle "not damaged in case of frequently earthquake and not collapsed in case of rarely earthquake". In addition, verify the rationality of construction measures, such as the selection of components and construction of joints.

Contents: 1) the seismic performance of braced frames structure; 2) the response of structure under frequently earthquake; 3) the response of structure under rarely earthquake; 4) the seismic performance of bracing and damage sequence; 5) the seismic performance of joint plate and connection.

1.2 Experiment equipment

The experiment equipment used are as follows: 3mx4m sized unidirectional earthquake pedestal, LVDT large range displacement meter, compression type acceleration sensor, charge amplifier, spectrum digital dynamic data acquisition instrument etc. (see Figure1)

Figure1 earthquake pedestal and detection equipment

1.3 Model design and fabrication

Select axis 3 frame of the main power building as the research object. In order to reduce the model size, only the bunker bay was cut out for the model. The size of the model similarity ratio is 1:12, quality similarity ratio is 1:400. (see Figure2)

Figure2 Structure diagram and experiment model

The important members such as beam and column are designed in conformance with the principle of special concentrically braced frames (SCBF) in ANSI/AISC 341-05 (AISC 2005). Limit the width to thickness ratio of braces strictly. Inelastic deformation and energy dissipation capacity are considered in the design of joint plate connections according to the references (Astaneh-Asl 1998).

1.4 Results and analysis of model experiment

1.4.1 Experiment performance

(1) The model remains in elastic state under frequently earthquake in 8 degree seismic intensity. This performance indicates that the structure conforms to the seismic design principle "not damaged in case of frequently earthquake".

(2) The model response is increased under precautionary earthquake in 8 degree seismic intensity. But the phenomenon of inelastic deformation and paint breaking off on members and joints was not observed. The readings of the strain gauge embedded in column is also far less than the yield strength. The frequency and the stiffness of the structure are not obviously reduced. This performance indicates that this structure conforms to the seismic design principle "can be repaired in case of precautionary intensity earthquake".

(3) The model response more intensely under rarely earthquake in 8 degree seismic intensity. Beams and columns are still in good condition. Only individual braces and the gusset plates appeared small deformation out-of-plane. All of the braces do not appear obvious bending deformation in-plane. This performance indicated that this structure has enough earthquake resistance under rarely earthquake. The structure conform to the seismic design principle "not collapsed in case of rarely earthquake", and has some security reserve.

(4) The model responded very intensely under rarely earthquake in 8.5 degree seismic intensity. All of the braces do not appear obvious bending deformation in-plane, except the out-of-plane deformation of some braces is increased, and except that individual gusset plates appear little rotation along the line 2t (Astaneh-Asl 1986). The surface Paint on some gusset plates break off slightly.

But on the whole, the irreversible deformation of the whole structure is not obviously, it can still maintain the capability "not collapsed in case of rarely earthquake".

1.4.2 Natural vibration characteristics of model, acceleration response, displacement response, stress on monitoring point

The relative displacement in two directions at the top of model are only 1/224 and 1/171 under frequently earthquake in 8.5 degree seismic level. These conform to the requirement of Chinese code GB 50011.

Steel column is in elastic state under various working conditions. Under the rarely earthquake of 8.5 degree, the maximum stress is 261.15 MPa, it is still less than the yield strength of Q345 steel.

1.5 Finite element analysis of experiment model

The calculated results of the finite element software ABAQUS (Hibbitt 2001) were compared with the model earthquake pedestal experiment results. Analyzed and verified the reliability of the finite element model.

1.6 Brief summary

Braced frames structure system showed good seismic performance, and meet the seismic design principle perfectly. The structure still has enough bearing capacity suffered several rarely earthquake. Model experiment and finite element analysis show that, Braced frames structure that be designed according to the idea and method obtained from this research can be used in 8 degree seismic area.

Braces showed good ductility in earthquake pedestal experiment, although some braces got into plastic state and had some instability deformation out-of-plane. But no brace show low cycle fatigue failure or other brittle failure, these show that the design method of brace is feasible.

The seismic response of plate connection joints showed the expected seismic yield and deformation mechanism. The plastic rotation around the 2t line is realized successfully, these show that the structure measures in seismic design are reasonable and applicable.

2   Research on performance and design method of plate-type brace connection

2.1 The purpose and content of research

Plate connection is adopt to Brace joint, not only has the advantages of simple structure, but also make the system has good energy dissipation ability by detail design of gusset plate. The content of research is as follow:

(1) Research the rotation of inverted V-type brace and beam connection joint.

(2) Compare the seismic performance of gusset plate in the same structure system when it be designed according to different method. Finally achieve joint design method which is suitable for engineering application.

(3) Study the influence on seismic performance of the structure system by changing the distance between brace joint and the center line of beam.

(4) Study the influence on seismic performance of the structure system by changing gusset plate parameters such as thickness and ribbed plate etc.

2.2 Experiment equipment and result

For experiment equipments see Figure3.

Figure3 Load equipment

All the buckling mode of brace test-piece are out-of-plane buckling, then the plastic rotational deformation began happen on the gusset plate. At the end of the test, there is a phenomenon that the paint on the surface of brace flange breaking off. This phenomenon (see Figure4) showed that most deformation happened on the brace, which provides a basis for analysis of the failure mechanism of joint. The failure sequence of brace is as follow: ①brace buckling; ②rotation bulking out-of-plane of brace; ③low cycle fatigue break of brace. This sequence conforms to the seismic requirements of structure system.

Figure4 Failure mode of gusset plate test-piece

2.3 Analysis of experiment data

The parameters of gusset plate (thickness, size, shape, free edge length and ribbed plate condition) will have great influence on the seismic performance of structures. Through process the test data of brace connection joint, the seismic performance of three kinds of joints under cyclic load is analyzed. Bearing capacity, deformation capacity, energy dissipation capacity, stiffness and failure mechanism of the brace connection joint were studied, through analyzing the load-displacement curve, and achieved relevant conclusions (see Figure5 and Figure6).
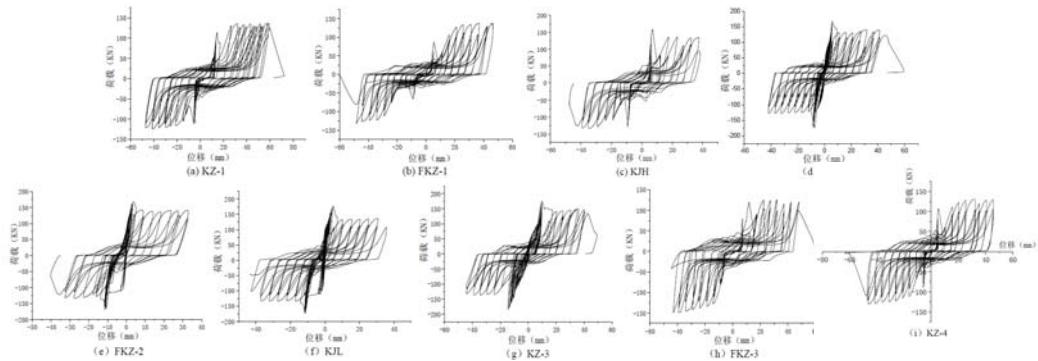
Figure5 Beam load-displacement hysteresis curve
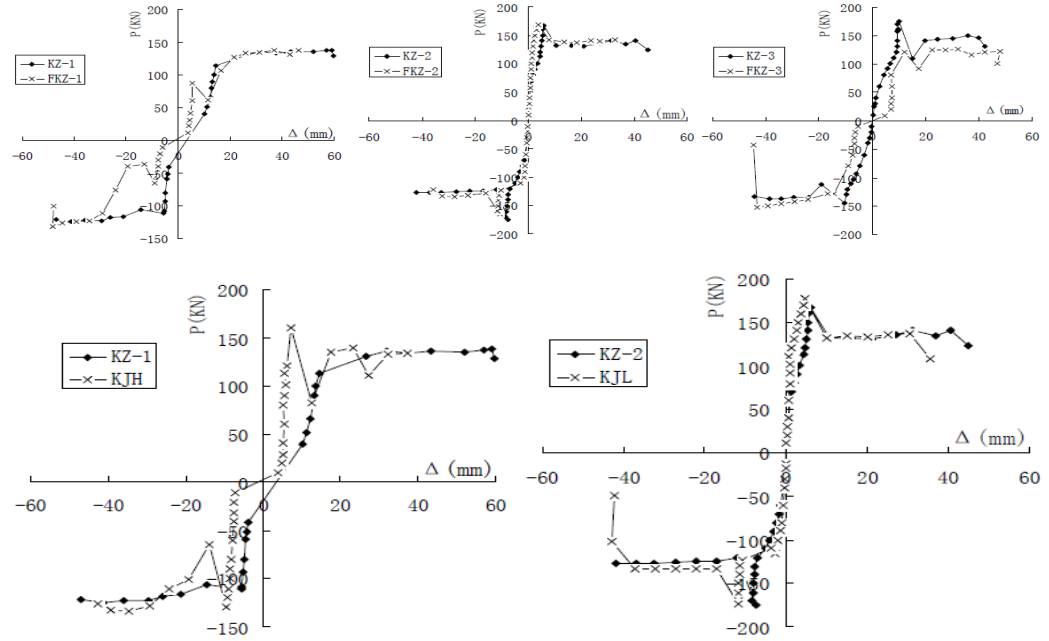
Figure6 Beam load-displacement skeleton curve

2.4 Finite element analysis of experiment model

Take the joint KZ-1 as example, in the elastic stage, high stress region is concentrated in the load action point and the gusset plate at the end of the brace. In the elastic-plastic stage, plastic strain is concentrated in the middle and the gusset plate at the end of the brace, see Figure7.

Elastic stage

Elastic-plastic stage
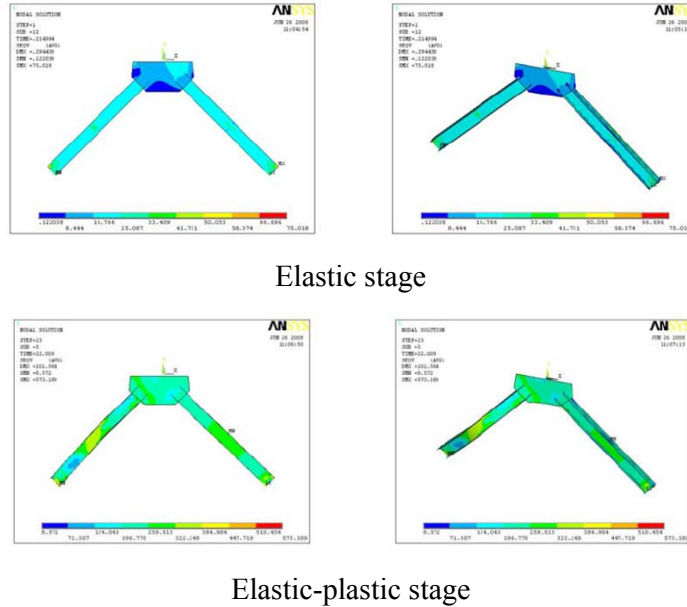
Figure7 stress distribution nephogram in Elastic and elastic-plastic stage

2.5 Research on plastic hinge line of gusset plate

The define of Plastic hinge line (Astaneh-Asl 1984 1985) is a line of maximum plastic strain point. The research found that draw a arc which through the nook point of gusset plate and two points at the end of the brace, the line is just the maximum plastic strain position of gusset plate. It show that the plastic hinge line is an arc, see Figure8.

2.6 Finite element analysis (FEA) of performance of plate connection joint

The stress and strain of gusset plate were studied by ANSYS finite element simulation analysis. The position and shape of plastic hinge line of gusset plate were found. Relevant conclusions about free edge of gusset plate were provided through the research.

2.7 Brief summary

(1) Plate connection joint of brace has enough bearing capacity and the capacity of resistance to low cycle fatigue if it is designed in conformance with the principle "Strong joint and weak member".

KZ-1	FKZ-1	KJH	KZ-2
FKZ-2	KJL	KZ-3	KZ-4
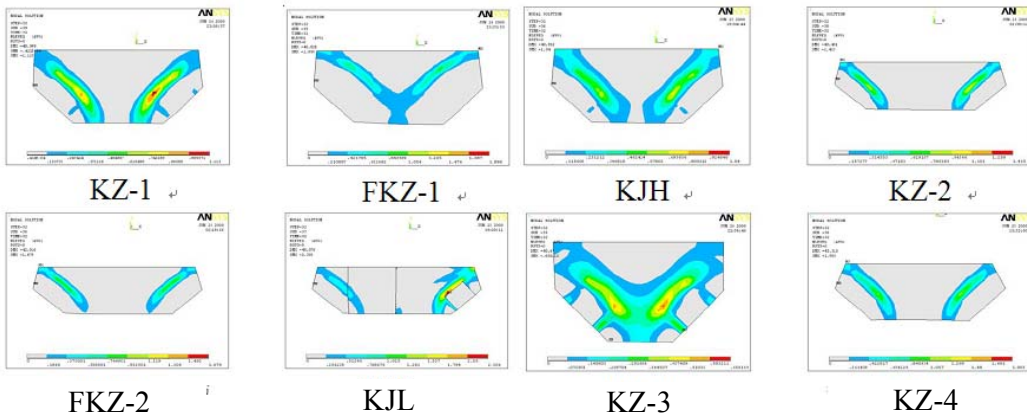
Figure8 distribution diagram of equivalent plastic strain of the test-pieces

(2) Tensile and press members   exist in the inverted V-type brace frame at the same time. Because the material of tensile member has plastic hardening effect, the bearing capacity of structure system did not reduce before the braces broken, and even that of some test-pieces increased slightly. But in the process of unloading and reverse loading, two braces appeared bending deformation out-of-plane at the same time, and the stiffness of system was very low, and the storey drift was considerable.

(3) If the design of gusset plates is in conformance with the requirement of 2t plastic hinge line, the buckling bearing capacity, deformation capacity and energy dissipation performance of system is superior to the gusset plate that is not designed according to the requirements. The experiment also discovered that the braces still have better ability of plastic deformation even if the end of brace does not meet the requirements of 2t plastic hinge line; The plastic hinge line is a curve, the gusset plate can happen plastic rotation when the brace have buckled out-of-plane. But the finite element analysis shows that, when the brace length into the gusset plate is too large, the stress will concentrate in the nook of the gusset plate, The equivalent plastic strain will increase, and the gusset plate is easy to break.

(4) Through analyzing the test data found that the energy dissipation capacity and ductility of the brace is best when the axis of brace and the beam intersect at the bottom flange of beam. But the intersection point position has little effect on the system stiffness in case of the brace buckling. Finite element analysis discovered that the structure system have the highest buckling bearing capacity when the axis of brace and the beam intersect at the bottom flange of beam, in case of the gusset plates having the same thickness

(5) The advantages of Increase the thickness of gusset plate are that, increasing the stiffness of brace connection, improving the buckling bearing capacity, Reducing of the equivalent plastic strain in the corner of the gusset plate, and delaying the weld seam breaking.

(6) For the structure under the story horizontal load action, setting ribbed plate on the gusset plate did not enhance the energy-dissipating capacity and buckling bearing capacity of system significantly.

3   Seismic elasto-plastic analysis of braced frames steel structure
3.1 The necessity of elasto-plastic seismic response analysis

● The shape of main power building is complicated, the Mass distribution is uneven. The structure will turn in case of earthquake. The overall performance of the structure is not be reflected by one frame experiment. For the FEA model, see Figure9.

● The Influence of the joint size effect in a scale model is that the slenderness ratio of brace will be smaller than the reality.

● The load plate used in experiment is very large, the center of gravity moving up cause additional moment. This makes the model is different from the original structure.

● Numerical analysis can accurately track the buckling state and stress level of the brace, make up for the deficiencies in the test.
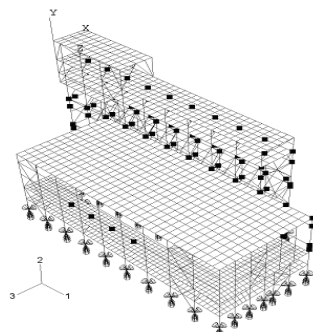
Figure9 FEA model of main power building

3.2 Result of analysis

(1) The first mode of the structure is longitudinal translational mode with a slight torsion. The second mode is lateral translational mode. The natural vibration period of first two modes are very similar. See Figure10.

Elevation of First mode   Planform of First mode   Elevation of second mode
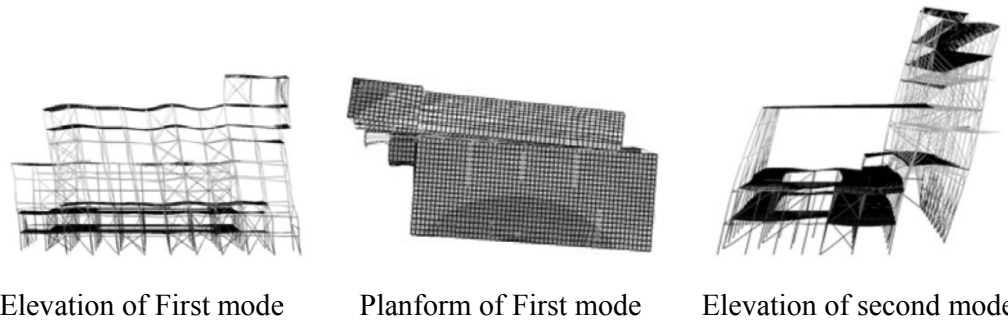
Figure10 First and second mode diagram

(2) For the structure under four frequently earthquakes which intensity are 8, there is only individual floor which lateral shift ratio is more than 1.5 limit value of the code. All the story drift rotations meet the requirements of the code.

(3) Under four frequently earthquakes, no brace buckle out-of-plane, no beam and column enter plastic stage, the transversal story drift rotation distribution along the height are uniform.

(4) For the structure under four rarely earthquakes, there are many braces appeared out-of-plane buckling, and parts of longitudinal beam and column got into plastic state, but the story drift rotations distribution along the height are still uniform, and conform to the requirements of the code. This show that the structure has no obvious weak story.

(5) For the structure under rarely earthquake which intensity are 8, it has great tension at the bottom end of the column of bunker bay.

3.3 brief summary

Through time-history analyzing under four frequently and rarely earthquakes which intensity are 8, the results indicated that the design scheme of the structure is reasonable.

4 Some technical problems in the design of steel structure of main power building
4.1 Structure system

According to the relevant Chinese and foreign documents and the characteristics of the main power building for thermal power plant, some advices on structure vertical arrangement are proposed. The importance of plan layout and space cooperation work shall be paid attention. The main points are as follows:

(1) The design shall pay attention to proper adjusting the number of brace and section size, to make the horizontal stiffness of bunker bay is roughly equal with that of turbine house within the height range of turbine house.

(2) One question shall be noted, the horizontal stiffness of the floor is affected by opening big holes opened for the turbine pedestal and other equipments.

(3) Because the bracing force is very large, so hot rolled section steel shall be selected to be brace.

(4) For the braces locate above the coal bunker girder shall not use too small section. The column section shall be designed to shrink reasonably.

(5) For the upper two stories of bunker bay, the vertical load and seismic action are small, so knee-bracing can be used to constrain the beam-to-column hinged joint.

(6) The vertical non-balanced force can be reduced by adopt X-type and V-type brace in the structure.

(7) The group number of longitudinal braces shall not be less than 3.

(8) Brace shall be arranged between the columns which bearing larger load, and the braces shall be continued in one column space.

(9) Through the research, the principals for floor and horizontal brace arrangement are proposed.

(10) Through the research, the measures for controlling structure torsion are proposed.

4.2 design of component

(1) For the beams that are intersected by V-type or inverted V-type braces, the non-balanced force shall be considered, and the lateral braces shall be set at the joints. The width-to-thickness ratio of steel element shall be limited.

(2) Through the research, proposed the limit value for the column slenderness ratio, the width-to-thickness ratio and the axial-force-ratio of column. One table for calculating length of variable section column was proposed.

(3) The limit value for the slenderness ratio of brace and the calculating formula for brace were proposed.

(4) The principals for horizontal brace design are proposed.

4.3 seismic design for joint

Base on the seismic design principal "strengthen the joint and weaken the element", the requirements for seismic design and measures were proposed.

On the basis of American specifications and documents, provided the complete calculating methods of joint, including that: block shear calculation, limit value of free edge, ribbed plate calculation, strength calculation of gusset plate (strength

calculation of effective width section (Whitmore 1952), strength calculation of gusset plate of beam-to-column connection, calculation of the connection weld between gusset plate and beam or column), stability calculation of gusset plate, etc.

For the column splice joints, proposed the force transmission principle for calculation of high strength bolts. Provided the joint calculation method according to the principal of 50% bending strength .

For beam-to-column connection, proposed five advices for seismic design in principal.

For column footing joints, because the footings appear uplift force under rarely earthquake, the calculation principals were proposed based on the domestic and abroad documents about column footing calculation.

5   Comparative analysis of economic of steel structure of main power building

The main power building was designed one time again conform to frame-brace structure system. The weights of structural steel of two different systems are compared. The weight of braced frames is 465t less than that of frame-brace. The weight of braced frames is about 17% of frame-brace weight.

In addition, the braced frames have other advantages, such as: simple fabrication, no welding, convenient transportation and easy installation, the comprehensive benefit is remarkable.

6   Summary

(1) The research is based on the Chinese code, and the theories of braced frames, experiment and practical achievements of America is referenced. For the seismic performance of main power building braced frames structure system of thermal power plant, integrated model earthquake pedestal experiment and plate connection performance test were carried out, and with the finite element analysis was carried out. Through the experiments and analysis, it is proved that the main power building of thermal power plant in tn may use braced frames structural type, the scheme is reasonable and secure.

(2) Through the research on the principal of structure arrangement and analysis method, component selection, joint calculation, details of seismic design requirement, etc. a series of regulations, calculating methods and formulas for seismic design of braced frames structure were proposed.

(3) Through the integrated economic comparison of braced frames and frame-brace structure system, the results indicated that The braced frame system not only has the advantages of simple fabrication and convenient installation, but also can save on steel material effectively. Therefore, promoting the application of braced frames system will bring obvious economic and social benefits.

REFERENCES

ANSI/AISC 341-05 Seismic Provisions for Structural Steel Buildings. *American Institute of Steel Construction Inc.* Chicago, 2005.

Astaneh-Asl,, A., Cyclic In-Plane Buckling of Double Angle Bracing. *Journal of Structural Engineering*, 110(9): 2036-2055, 1984.

Astaneh-Asl, A.,. Cyclic Out-of-Plane Buckling of Double Angle Bracing. *Journal of Structural Engineering*, 111(5):1135-1153, 1985.

Astaneh-Asl, A., Geol,S.C., and Hanson, R.D., Earthquake-Resistant Design of Double Angle Bracing. *Engineering Journal*, Vol.23, No.4, 4th Quarter, AISC, Chicago, IL., 1986.

Astaneh-Asl, A., Seismic Behavior and Design of Gusset Plates for Braced Frames. *Steel Tips*, Structural Steel Education Council, Moraga, CA., 1998.

CECS 160:2004 *General Rule for Performance-Based Seismic Design of Buildings*, China Planning Press, Beijing, 2004.

GB50011-2010 *Code For Seismic Design Of Buildings*, China Building Industry Press, Beijing, 2010.

Hibbitt, Karlsson, Sorensen. *ABAQUS Standard User's Manual Version 6.6.* University of Pennsylvania, Philadelphia, 2001.

UBC(1997), *Uniform Building Code*. California: International Conference of Building Officials, 1997.

Whitmore R.E., Experimental Investigation of Stresses in Gusset Plates. Bulletin No.16, Engineering Experiment Station, University of Tennessee, Knoxville, 1952.

Design and Construction of Large-scale Floating
Precast Pump House

WU Caihong,[1] HU Die,[1] and ZHANG Xionghui[2]

Abstract: The pump house of a coastal power plant, adopting direct current water intake system, locates near sea, with features of bulky volume, large embedded depth, complex design loads and difficult construction, etc. Pump houses of Shenzhen Eastern power plant were constructed by floating the caisson. Each caisson weighs 5000 tons is 30.1 meters long, 19.2 meters wide, and 10.6 meters high. After caissons were prefabricated at a specialized dock, one of them was towed to a semi-submerged barge using airbags, and then transported to a designated place for diving. It was fitted in position after floating. Shipping such a large-scale caisson from a dock to a semi-submersible barge is rarely in China, moreover，which may broaden design thought and provide a new construction method for other large pump houses of coastal power plants.

Key Words: Coastal power plant, Pump house, Caisson, Floating construction method, Semi-submersible barge

Introduction

Coastal power plant uses seawater as cooling water, and coastal pump house adopting direct cooling system to supply water. To meet the requirements of water quantity and quality, the design of the pump house should consider various natural conditions, such as water levels, waves, sediments, ice, floating blocks, topography, and engineering geology conditions. Besides these, marine lives and marine corrosion are required to be taken into account.

Coastal pump house has characteristics of variational marine hydrology condition，complex engineering geological condition, deep embedment depth, bulky volume, difficult construction, etc. It is according to specific project features to choose appropriate pump house structural form and construction method.

The structural form of costal pump house needs to be considered in conjunction with construction method and region natural conditions. There are 4 common types of the pump house structure: Boxing structure using open excavation method, caisson structure with caisson method, the diaphragm wall structure with the corresponding diaphragm-wall method, and caisson structure with floating method.

The floating-caisson pump house method has several applicable conditions:The intake water area formed by coastal reclamation, the pump house situated in the front of the protection embankment, or using harbor basin to supply water for the pump

---

house；A suitable water depth at pump house frontier, enable to floating ship the precast caisson to the designed location; The pump house region has good geologic condition，or with condition to improve ground with excavation and filling or the blasting toe-shooting method; Construction yard capable to precast large caisson is in near, and having a clear shipping channel from the yard to the pump house area; Equipped with professional construction team and modern construction equipment.

Project Profile of Shenzhen Eastern Power Plant

Natural Conditions

The water intake area of Shenzhen Eastern power plant is about 1km to the northwest of the power plant, which is filled with hill stones. The filled sea area formed a coastline, where locates the pump station (includs 3 pump houses), caisson revetment and slopping embankment revetment. Figure 1 shows the layout of coastline in water intake area.The submarine contour of the sea area where the coastal pump house locates is nominally -9.0m, and the natural water depth condition is suitable. For easy to build, and take up less coastline, The pump houses of Shenzhen Eastern power plant，should have been built in three stages, positioned intensively and constructed simultaneously.

The stratums where the pump station locates from top to bottom are silt (mixed with slush), gravelly sand, clay(granite residual soil),completely weathered granite, intensely weathered granite, and moderately weathered granite. As surface subsoil bearing capacity is too weak to meet design requirements, the clay layer is chosen as bearing stratum, with the characteristic value of subsoil bearing capacity 220KPa and the native elastic modulus 8MPa. Superficial soft soil was replaced about 6 meters, and excavation part was dump-filled with rubbles up to the designed bottom elevation of the pump house. It is demand to explode and fine leveling the rubble bed under water to decrease settlements after fixing pump caisson in place.

Structural Design Scheme Comparison

Caisson structure, diaphragm-wall structure and floating-caisson structure solutions have been compared before designing the structure of pump houses in Eastern Shenzhen power plant.In both caisson structure and diaphragm-wall structure plans, it is required to build a temporary cofferdam around the coastal pump house region, and backfill medium coarse sand to form a sand island before build a caisson or a diaphragm wall. As the pump-house area submarine contour is deep, about -9.00m, in this project, cofferdam height above 11m affords to build the caisson or the diaphragm wall on land. Because sea water is deep and waves are big in this area, the ocean side of the temporary cofferdam should take some face protective measures to resist the wave forces during construction, which makes build a temporary cofferdam cost more. Besides these, it pays plenty of people and machine-shift expenses to demolish the cofferdam after pump houses built, which not only increase project cost, but also it hard to dismantle the ocean dam. Modern construction devices, such as large semi-submersible barge, the floating crane, etc., are utilized in

floating-caisson structure solution, although high equipment rental and site use fees, water depth condition in water intake area is beneficial to float and dive. In this solution backfilling water intake area and building revetment while precasting floating the caissons, which saves construction time.

Through economic and technical comparisons and considering construction condition, construction period and other factors, the pump houses adopt caisson structure with floating method in Eastern Shenzhen power plant.

Pump House Structure Design

Design Condition

Tide level:Design high-tide level with a hundred-year return period is 3.42 m ; Design low-tide level with 97% probability is -1.23 m; Check low-tide level with 99% probability is -1.32m; Construction high-tide level with accumulated frequency 10% is 1.32m.Design wave height: it is 5.26m, and the wave has 50 year recurrence interval and accumulated frequency is H1%.

Maintenance condition: it is permitted to empty one hole in design high-tide level in application period, while prohibited to empty two or three holes in the same time.

Floating period: there is no water in precast caisson while outside is full of water. Construction period: One hole in the pump house is empty, and the water level is construction high-tide level.

Structural Design for the Precast Caisson

Each pump house has three flow channels, the plane size of the underground structure is 30.10mx19.20m, and total height is 15.10m(from -9.10m to 6.00m in elevation).To guarantee cast-in-situ above water after the caisson installed in place，the top elevation of the prefabricated part is higher than the construction tide level. Owing to construction high-tide level is 1.32m and constantly construction tide level is 1.00m，it is suitable set the top elevation of precast part 1.50m. The total height of the caisson is 10.60m (from -9.10m to 1.50m) and cast-in-situ part is from elevation 1.50m to 6.00m.The outer wall is 1.1m thick and the partition wall is 1.0m thick，and the base plate is 1.1m in thickness. Figure 2 shows the geometry of the precast caisson unit of the pump house.

For facilitate to transport, it is needed to lighten the weight of pump house as more as possible when designing, so the precast part of the caisson, including the bottom plate and outer walls has only 0.5m in thick when primary concreting, less than design thickness 1.1m. Due to powerful hydrostatic pressure and buoyancy in floating and construction periods, it is necessary to take 4 structural measures to satisfy pump house structure and shipping requirements: Wall depth reaches design thickness 1.1m in force nodes; In weak parts（where the wall thickness is 0.5m），increase the rebar amount; In the traverse of the pump house install 2 temporary steel braces; Three steel shields are used to block the inlet conduits to satisfy floating and cast in-place requests. After devices installed in the pump house，depart these shields from the pump house to form flow channels.

Floating Stability Calculation

The related hydrostatic properties of the caisson, namely, volume (V), Vertical volume moment (M), gravity (G), vertical center of gravity (Y_G), volume of displacement (V_D), draught depth (T),vertical center of buoyancy(Y_W) , the distance from vertical center of gravity to vertical center of buoyancy(a) , the metacentric radius (ρ), the metacentric height (m) , and freeboard height (F)are provided for a caisson are provided in Table 1.

Table 1. Related properties in floating stability calculation

V (m^3)	M (m^4)	G (kN)	Y_G (m)	V_D (m^3)	T (m)	Y_W (m)	a (m)	P (m)	m (m)	F (m)
1949.6	8328.88	48740	4.27	4923	8.52	4.26	0.01	3.61	3.60	2.08

As the dive site is near the installation place, belonging to short range floating, the metacentric height is no less than 0.2m (CCCC4 Harbor, 2009). It is easy to know the metacentric height 3.60m meeting floating stability. Freeboard height (F) should meet $F \geqslant B/2tan\ \theta +2h/3+S$(CCCC4 Harbor, 2009).Where h is the wave height on floating, valuing 1.0m;S is the rich freeboard height,valuing 0.7m; B is the width of the caisson, valuing 19.2m; θ is the obliquity of the caisson on floating, valuing 7°. As the value of F is 2.08m, less than 2.55m, the calculated value of the right part of above formula, it stands for freeboard height are not capable to float stability, so a floating crane is needed to assist floating.

Pump House Construction

General Construction Plan

Floating caissons in Shenzhen Eastern power plant were prefabricated in a special construction yard. On concrete obtaining design strength，high pressure airbags were used to jack-up and tow the caisson onto a 16000-t semi-submersible barge.After the caisson was shipped to the scheduled diving area that near the water intake area, the barge dove and unloaded at high tide level as the caisson rising. With the help of a 300-t floating crane and tugs, the caisson was transported to the installation place, filled with water and be fixed on the leveled rubble-bedding. Then consequently pump water from the caisson cabins, finish second-time pouring under water and cast-in-situ above water.

Land Disposal and the Caisson Precast

Construction yard is a gravity dock with huge back storage yard, more than 100kpa yard capacity load, appropriate water depth in the dock frontier and broad basin water. To facilitate the airbag shipping, the place where produced the caisson should be handled specially, and three pedestals are required to precast in the dock,the pedestal respectively 1.5m longer and broader than the pump house base in a plane view. Precast pedestals in the dock is shown in figure 3, in which   -stage caisson is the closest to the dock apron.

The sequence to produce a caisson is as follows: making the pedestals, assembling base plate steels, assembling wall steels，installing inner and outer steel moulds，pouring the concrete，stripping moulds and curing.

Moving and Boarding of the Caisson

Moving a floating caisson unit from the dock to the semi-submerged barge is a difficult task and the critical step in the whole construction procedure. Towing devices mainly are divided into two categories: traction system and air compressor system. Traction system serves to tow the caisson, including winches, wire ropes, tackle blocks, etc, and air compressor system is used to aerate the airbags. Airbag arrangement, number, steady height when moving, and corresponding work pressure are key factors whether caisson launching successfully. Airbags were to jack-up and move the caissons，in this shipping process，40 φ1x100 （the diameter is 1m and length is 10m）airbags were used. 32 moving-forward airbags were used to move the caisson(including 2 lifting airbags for jacking caisson up)；and 8 moving-forward supplied airbags supplies the moving-forward caisson，also used as moving-forward airbags in next phase. In this project 32 airbags were placed in 2 columns and 16 rows ,airbag moving height is 50cm,and work pressure is 0.27MPa (larger than actual pressure 0.258 MPa)in moving-forward process. Calculated airbag interval is 0.63m, greater than the safety distance 0.5m to avoid collision when shipping.

Boarding procedure is described as follows：Setting out high pressure jack-up airbags，jacking-up the caisson and removing I-steels away; Putting up sleepers，putting moving-forward airbags on，inflating airbags, removing sleepers; caissons moving forward until winches finished their ropes; Removing some tractive ropes to backstay; Dragging caissons to the designated parking place in the barge; Setting out high pressure jack-up airbags; Jacking caissons and removing sleepers, and the caisson staying smoothly in the sleepers-finishing caissons

Lengthways moving. The   -stage caisson moved the longest, from the prefabricated pedestals to the wharf apron, roughly 120m.And then the caissons moved averagely 70m in the barge (ZHONG REN 1601).

Launch and brake ：Two winches pulled in front of caisson in moving direction, and two pinned in the rear. Adjust moving-forward airbag pressure to decrease traction when the caisson launch or brake. By reducing the pressure of front airbags，caisson leaned forward and traction decreased，and vice verse. Decreasing pressure in the process of moving, consequently increase rolling resistance to lower velocity.

Connecting with supply airbags：Before the caisson reached the supply airbags, adjust connecting distance. When the caisson was moved to place above half of the airbag body, aerate the airbags to work pressure. At this time launch the pulling winches and continue to move forward.

When winches were out of ropes, it is needed to move and re-install the hauling system. Re-placing brace sleepers, and then deflating the airbags slowly. After the caisson smoothly landed on the sleepers, re-install the hauling system and move

forward. Repeat these work, until the caisson was moved to the designated place, and the caisson moved 30m forward in every installation.

Boarding. Caisson boarding the barge stably is the most important step in the whole towing and moving process. This process was carried out in high-tide level, and the caisson was towed to the barge before tide ebbed.

Caisson boarding working conditions are listed : Water depth in harbor basin is no more than 8m, wind velocity is less than 4 degree, and wave height is less than 1m ; Prohibiting vessels shipping in and out of the harbor in high speed; Boarding process is in high-tide level ,when caisson launch to board ,the tide is more than 0.5m and the tide duration exceeds 4 hours; Before pulling the caisson onto the barge, move the caisson to place that is 1 meters away from the dock .

When the semi-submersible barge was docked at Pier, the barge was roughly 40cm away from the wharf. For successively boarding, a 3cm-thick, 4m-wide steel plate was used to connect the dock and the barge, and the plate should be longer than the airbag. Also the connecting plate is used to decrease the impact of barge bobbing on the caisson at the moment of boarding.

The method caisson lengthways moving from the wharf to semi-submergible barge is the same with that in the wharf. Whenever an airbag boarded, ballast water was back-pumped immediately to adjust barge height. It is safer to boarding faster and pump earlier

The ballast pump has a 2400 m^3/h displacement, and it takes 3 hours to displace 3800m^3 from launch boarding to all boarding. When the caisson moving to the parking place, adjust airbag pressure for modify the caisson height and brace sleepers. After sleepers placed in place, airbags were deflated and shifted out. The caisson was successfully moved onto the barge until all wire ropes released. Figure 4 shows that the caisson boarding the barge.

Transportation, Diving and Unloading

After the caisson was towed to a semi-submergible barge (ZHONG REN 1601), a auxiliary tug(GANG WU tug), cooperating with a main tug(QING GANG tug) transported the barge to a scheduled dive area(the best water depth is 15.5m),where beginning to fill water into barge tank, caisson buoyed along with the barge submergence. After the caisson floating, towed by QingGang tug , trailed by GangWu tug, and assisted by a 300-ton floating crane .the caisson was floating-towed in place, when towing, it is obliged to select suitable climate and appropriate sea condition to ensure floating caisson safety. The transportation process is showed in Figure 5.

Installation in Place

Before fitting the precast caisson in place, check the formed rubble bed, clear the back silting content at the top of the bed, re-riprap and tamp parts that do not meet the design requirement, and level the whole rubber bed. In order to improve the accuracy of installation, use a 300-t floating crane to assist installation. Finally fill
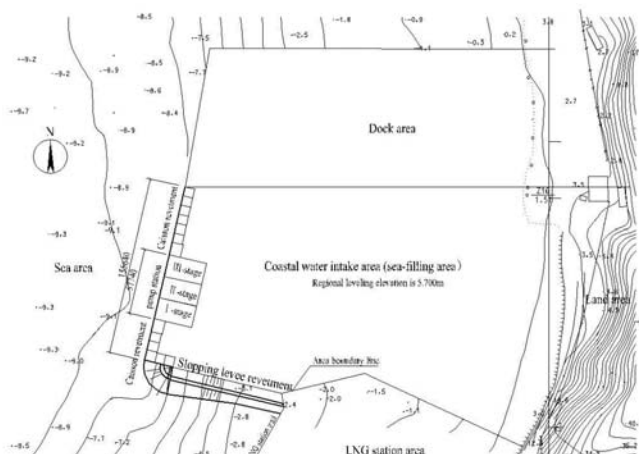
water into the caisson cabins to sink the caisson on the foundation bed. Figure 6 shows the floating crane aid to fit the caisson in place.

Conclusion

Shenzhen Eastern pump house locates at the forefront of the protecting embankment in water intake area, with well water depth and geological condition, suited dock capable to cast huge caissons and professional construction team in near place. These natural conditions and regional conditions are suitable for boxing-structure pump house using floating methods. Employing high-pressure airbags to jack-up a 5000t caisson and move it from the wharf to the barge is not common in China power industry. This successful experience broadens design ideas and develops construction methods for other large-scale coastal pump houses in power plants. Moreover, this project provides a successful example for"Transportation of Major Components Using High Pressure Airbags" research project, which is sponsored by Guangzhou government.

References

JTS 167-2-2009. (2009). "Design and Construction Code for Gravity Quay." Beijing: China Communications Press.

Figure 1. Coastline layout of water intake area
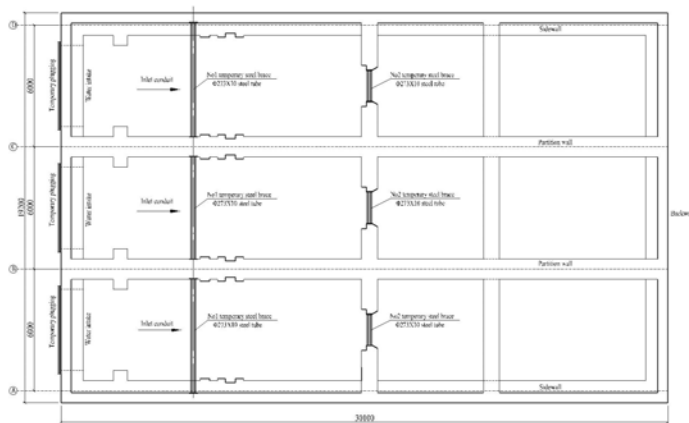
Figure 2(a). Plane geometry of a precast caisson unit
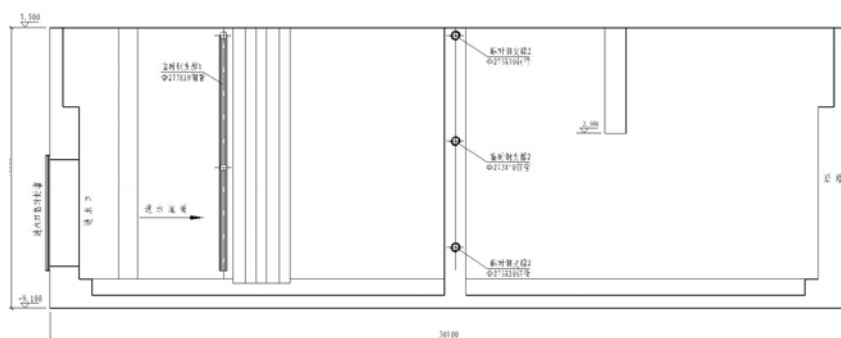
Figure 2(b). Profile drawing of a precast caisson unit
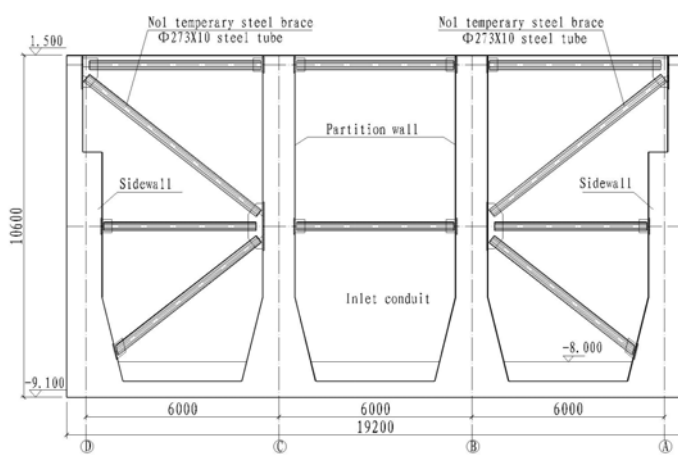
Figure 2(c). Cross sectional drawing of a precast caisson unit
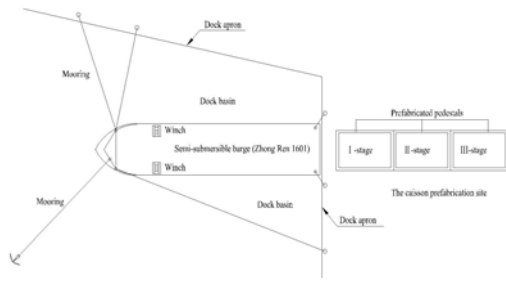
Figure 3. Operation of the barge towing the caisson   Figure 4. Boarding the barge

Figure 5. Transportation   Figure 6. Fitting the caisson in place

Bearing Capacity of the High-Rise Pile Cap Foundation for Offshore Wind Turbines

Wen-Gang QI[1], Jing-Kui TIAN[2], Hong-You ZHENG[2], Hai-Yan WANG[2], Jing YANG[2], Guang-Ling HE[2], Fu-Ping GAO[1]

Abstract: A proper foundation design is crucial for the structural stability of offshore wind turbines (OWT) in the severe ocean environments. As one of the typical foundation type for OWT, the high-rise pile cap foundation has been utilized in wind farm of China. In this study, a 3-dimensional finite element model for simulating the pile-soil interaction subjected to multi-axis complex loads is proposed and verified with existing experimental data. The bearing capacity of the high-rise pile cap foundation under various ultimate limit state (ULS) conditions is investigated. Local scour usually occurs around the pile and significantly reduces the bearing capacity of the foundation. Numerical simulation shows that scour could amplify the lateral displacement and tilt of the foundation.

Key words: high-rise pile cap foundation; pile-soil interaction; bearing capacity; scour effect

Introduction

In recent decades, quite a few pile foundations have been utilized in the prosperously developing OWT. Large-diameter monopile foundation is a common choice for most offshore wind farms in Europe, while the high-rise pile cap foundation is currently employed in East China Sea area, due to different soil properties and pile driving ability between Europe and China. The height of the wind turbine hub can reach approximately 100 meters for a 3 MW turbine, producing huge lateral force in the order of 5 MN and bending moment in the order of 1×10^8 N.m. These huge loads pose significant challenge in the design and construction of the foundation.

Many different calculation methods have been developed and employed by various researchers to assess the bearing capacity of monopile and pile groups. Poulus (1980) put forward a state-of-art review on the elasticity method of pile foundation design. Poulos and Hull (1989) found that the selection of the soil parameters and their distribution with depth have significant influence on the prediction accuracy. However, the method is only valid for small strains as soil is more likely to behave elasto-plastically while the soil is assumed to be elastic in this method.

In current design of laterally loaded offshore monopiles, the *p-y* curves are typically used to characterize the interaction between pile and soil. The *p-y* approach is adopted in the offshore design codes of American Petroleum Institute (API, 2007) and Det Norske Veritas (DNV, 2010). This method assumes that the pile acts as a beam supported by a series of uncoupled springs, which represent the soil reaction. The non-linear behavior of the springs is specified by the assi[1]gned *p-y* curves. At a given depth, the *p-y* curve relates the soil reaction *p* at a given depth to the corresponding pile lateral deflection *y*. Details on the *p-y* methodology for analysis of laterally loaded piles can be found in Reese et al. (1974) and Reese and Van Impe (2001). The

---

[1] *Institute of Mechanics, Chinese Academy of Sciences, Beijing, China*

[2] *North China Power Engineering CO., LTD of China Power Engineering Consulting Group, Beijing, China*

diameters of the monopiles utilized in offshore wind farms could be up to 5~7.5 m (Achmus et al., 2009) and outside the scope of existing experience, which is particularly evident when comparing the database used by Murchinson and O'Neill (1984) to develop the existing API approach (D<1.5 m) with the monopile diameters being installed today. Paul and Kenneth (2011) presented main limitations and differences between the API (2007) design code and industry practice, including the different failure modes, diameter effects, ignoring pile properties, et al. According to the results of the numerical calculations carried out for monopiles of large diameter, Abdel-Rahman and Achmus (2005) concluded that the p-y curve method given in API (2007) underestimates pile deformations for large-diameter monopiles.

Much effort has been devoted to the 3-dimensional numerical simulation of large-diameter monopiles under either monotonic or cyclic loading, e.g. Abdel-Rahman and Achmus (2005), Leblanc et al. (2010), Achmus et al. (2009), and Bourgeois et al. (2010). These fully 3-dimensional numerical simulations often propose empirical modifications of the p-y curves to account for the diameter effect, group effect and interactions with neighbouring structures, providing a way to overcome the aforementioned limitations of the classical p-y curve method.

The existing studies focus on the bearing characteristic of large-diameter monopile foundation rather than high-rise pile cap foundation, which is at present the most popular foundation type for OWT in East China Sea area. In this study, a 3-dimensional finite element model of high-rise pile cap foundation is established to shed some light on its bearing behavior.

Local scour will occur around the pile foundations due to the action of waves and current. The scour depth could significantly reduce the bearing capacity of the foundation. This scour effect is also investigated in the present study.

Numerical model
Finite element mesh and constitutive models of materials
The bearing process of high-rise pile cap foundation under an axial or vertical load can be considered as a plane-symmetric problem. A three-dimensional plane-symmetric finite element model is thereby proposed for simulating the pile-soil interaction using the finite element code ABAQUS.

Fig. 1 illustrates the geometry of the finite element model, which is mainly consisted of the foundation and the surrounding soil. The foundation is composed of four vertical open-ended steel piles and a circular concrete cap fixed upon their upper surfaces. The cap and piles are connected with a "tie-type" constraint provided by ABAQUS software. There exist soil-plugs inside the pile interior surfaces. Both the foundation and soil are composed with three-dimensional 8-node reduced-integration solid elements (C3D8R). The computational grids get denser in the closer proximity to the pile for high computation efficiency. A total of approximately 20000 elements are utilized. The interfacial behavior is a key issue to efficiently simulate the complex pile-soil interaction. A contact-pair algorithm was adopted to characterize the interfacial constitutive relationships between pile exterior surfaces and surrounding soil, pile interior surfaces and soil-plugs, respectively.

Since the failure of the pile structure usually does not occur during the loading process in the field, the piles and the cap are assumed to be linear elastic with different mechanical parameters (see Table 1). The Mohr-Coulomb plasticity constitutive model (M-C model) is used to simulate the elasto-plastic behavior of the soil.
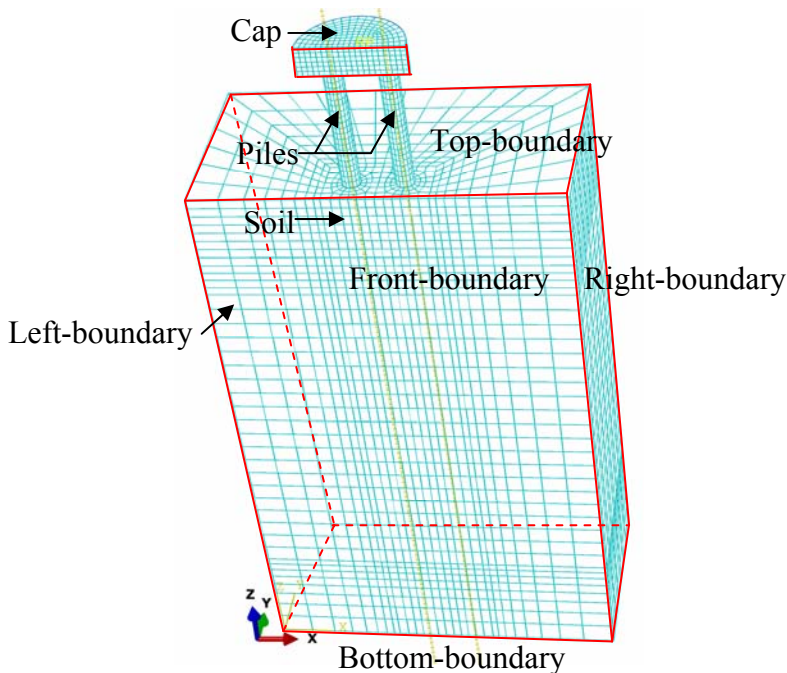
Fig.1 Three-dimensional finite element meshes of foundation and surrounding soil

Boundary conditions and loading conditions

As illustrated in Fig. 1, the top-side of the soil is treated as a free boundary. The front-side of the model is a plane-symmetric boundary, i.e. both the rotational degrees of freedom in x and z directions and translational degree of freedom in y direction are constrained to zero. At the left, right and back-sides of the soil, the translational degree of freedom in x and y directions are constrained. At the bottom of the model, the translational degrees of freedom in both x, y and z directions are fixed.

Following design codes of DNV (2010), characteristic combined load effect can be obtained by combining the individual characteristic load effects due to the respective individual environmental load types (see Table 1). Each load case is defined as the combination of two or more environmental load types. For each load type in the load combination of a particular load case, the table specifies the characteristic value of the corresponding, separately determined load effect. The characteristic value is specified in terms of the return period. The final results of the loads for 5 different ULS cases are given in Table 1. The sketch of static loads exerted on the foundation is illustrated in Fig 2.

Table 1. Load combinations and corresponding results of load calculations

| Limit state | NO. | Environmental load type and return period to define characteristic value of corresponding load effect | | | | | Loads | | | |
		Wind	Waves	Current	Ice	Water level	F_x (kN)	F_y (kN)	F_z (kN)	M_y (kN.m)
Ultimate limit state (ULS)	1	50 years	5 years	5 years		50 years	2402	0	3140	93458
	2	5 years	50 years	5 years		50 years	2057	0	3941	59631
	3	5 years	5 years	50 years		50 years	2003	0	3140	60070
	4	5 years		5 years	50 years	Mean water level	3225	0	0	57245
	5	50 years		5 years	50 years	Mean water level	3673	0	0	89986
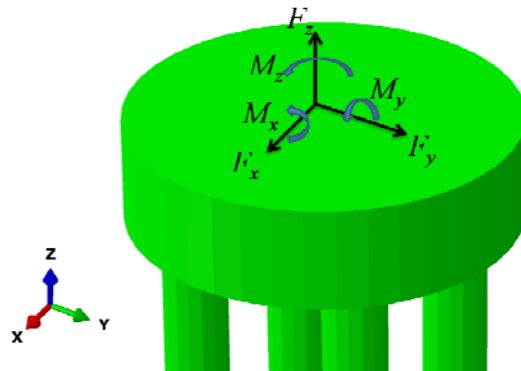
Fig.2 Sketch of static loads

Model parameters

As a case study, the parameters for the examined foundation are listed in Table 2, considering the practical condition of the water depth and the design parameters of similar preceding projects. According to the geotechnical investigation result, the soil can be approximately divided into three layers, as listed in Table 3. The pile-soil frictional coefficient (μ) is calculated with following formula proposed by Randolph and Wroth (1981)

$$\mu = \tan\left[\frac{\sin\phi \times \cos\phi}{(1+\sin^2\phi)}\right] \tag{1}$$

where ϕ is the angle of soil internal friction.

Table 2. The parameters for piles and cap of the foundation

	Wall thickness (m)	Embedded pile length (m)	Length/Height L/D (m)	Pile/Cap diameter D(m)	Mass density ρ (kg/m^3)	Young's modulus E (GPa)	Poisson's ratio υ
Piles	0.05	65	83.5	2.5	6900	210	0.3
Cap	/	/	4.0	15.0	2300	28	0.17

Table 3. Properties of the layered soil

Stratum No.	Stratum Name	Stratum Thickness	Mass density ρ (kg/m^3)	Cohesion strength c(kPa)	Angle of internal friction ϕ(°)	Young's modulus E (MPa)	Poisson's ratio υ
1	Silt	10.55	1700	5.0	20	5.0	0.32
2	Silt	4.8	1960	15.0	20	9.0	0.30
3	Silty clay	56.45	1900	15.0	25	10.0	0.30

Verification with experimental results

To verify the proposed finite element model, comparisons are made between the present numerical results and two series of existing experimental results, i.e. the laterally-loaded pile tests by Rao & Prasad (1993) (see Fig.3 (a)); and the tests of vertically-loaded pile groups with a cap by McCabe & Lehane (2006) (see Fig.3 (b)) The calculated result is in good agreement with the experimental data, which indicates that the present finite element model is capable of simulating the bearing process of monopile and pile groups.

(a)   (b)
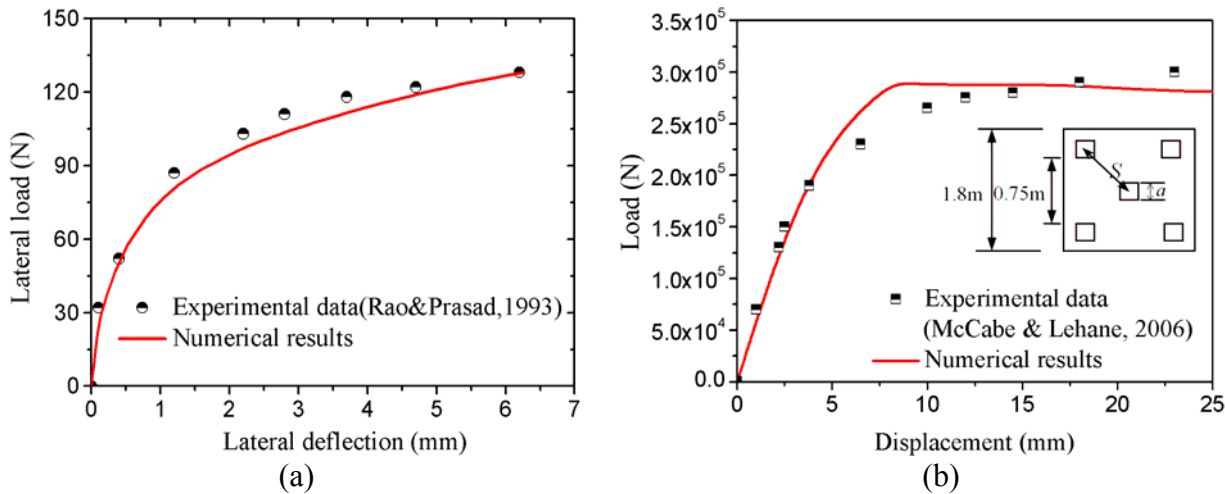
Fig. 3. Comparisons between the present numerical results and the existing experimental results of (a) tests of monopile by Rao & Prasad(1993) (D=18.0 mm, L=270.0 mm, γ=18620N/m3, c_s=10.0 kPa, φ=25°); and (b) tests of pile groups with a cap by McCabe & Lehane (2006) (a=0.25 m, L=6.00 m, γ=18130 N/m3, c_s=22 kPa, ϕ=35°)

Numerical results and discussions

Displacements under ULS conditions

For an onshore wind turbine, the maximum allowable tilt at pile head after installation is typically between 0.003 to 0.008 radian (0.2 degrees to 0.45 degrees). A somewhat larger tilt 0.009 (0.5 degrees) may be allowed for offshore wind turbines (Malhotra, 2011).

The displacement contour of foundation and soil under different ULS conditions are given in Fig 4. It can be seen that for ULS-5 (Fig. 4(e)), the pile experiences the most serious deformation. For ULS-1 (Fig. 4(a)) and ULS-4 (Fig. 4(d)), the deformation of the model is still great, but not so much compared with ULS-5. For ULS-2 (Fig. 4(b)) and ULS-3 (Fig. 4(c)), deformation is obviously more limited than other cases. Analyzing Fig. 4 along with Table 3, it can be concluded that the wind load component and ice load component play a key role in the deformation of the pile. This could be owed to the great arm of wind force exerted on the blades and the huge value of ice force due to large contact area between the cap and surrounding ice. Taking the aforementioned allowable tilt at pile head as tan(α)=0.008 (α is the rotating angle of the cap top-side), the current design of the foundation can satisfy the bearing requirements for all the ULS conditions.

The tilt of the cap top-side (e.g. in Fig.4 (e), tan(α)=0.0062) is approximately the same as that of the piles section at the mudline (tan(β)=0.0056, β is the rotating angle of piles section at the mudline), which implies that the upper part of the foundation outside the soil generally rotates as a whole rigid body. Comparing the soil deformation inside the pile (soil-plug) and outside the pile, it can be seen that the deformation of the soil-plug is consistent with the soil outside the pile. And the soil-plug acts as a deformation core along with the piles. The soil-plug is favorable for piles to resist the vertical force and bending moment.
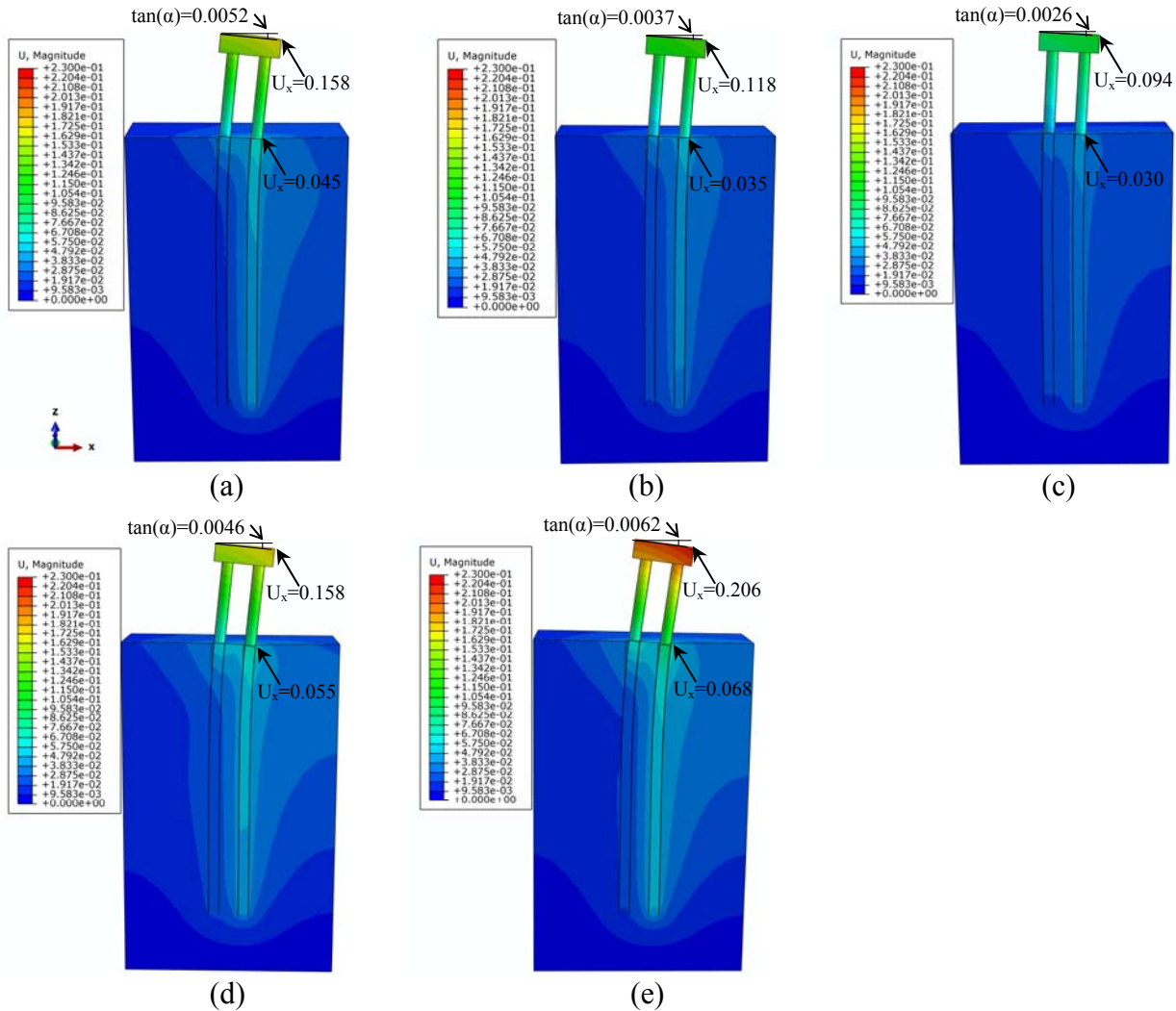
Fig.4 Displacement contour of foundation and soil under different ULS conditions: (a) ULS-1; (b) ULS-2; (c) ULS-3; (d) ULS-4; (e) ULS-5; (Deformation scale factor = 20; cut on x-z plane; unit: m)

Scour effect

Sumer et al. (1992) determined the mean value (*S/D*=1.3) and the standard deviation ($\sigma_{S/D}$=0.7) of the equilibrium scour depth in waves based on experiment result. In the severe shallow water environments where OWT locate, ocean waves and current are usually coexisting. Qi and Gao (2014) investigated scour around piles in combined waves and current through experimental modeling. They concluded that the superimposition of the waves on a current has much effect on the time-development of local scour and the resulting equilibrium scour depth. To ensure the safety of the OWT, a relatively conservative scour depth value of 5.0 m (2*D*) is assumed.

Li et al. (2013) demonstrated that assuming the removal of the whole soil layer above the scour depth is a conservative method considering the scour effect. Besides, judging from the load-deflection curves under various slope angles of the scour hole, the influence of the slope angle is not so much obvious. Therefore, in the present study, the removal of whole soil layer above the scour depth is adopted as a conservative approach to investigate the scour effect.

The scour effect on the deformation of the foundation under ULS-5 condition is shown in Fig.5. The vertical displacement at the center of the upper cap surface increases from 0.204m to 0.285 m as scour occurs. And the tilt increases about 20% from 0.0062 to 0.0075. Coincidentally,

the momentum exerted on the foundation at the mudline also increases 20% (see Table 1). Thus the increased momentum resulted from the lowering mudline should be responsible for the increasing of the tilt. As shown in Fig 5, the deformation of the upper part of the foundation is obviously amplified while the lower part of the foundation has hardly any difference. This indicates that the length of the exposed pile considerably affect the stiffness and deformation, and therefore the bearing capacity of the foundation.
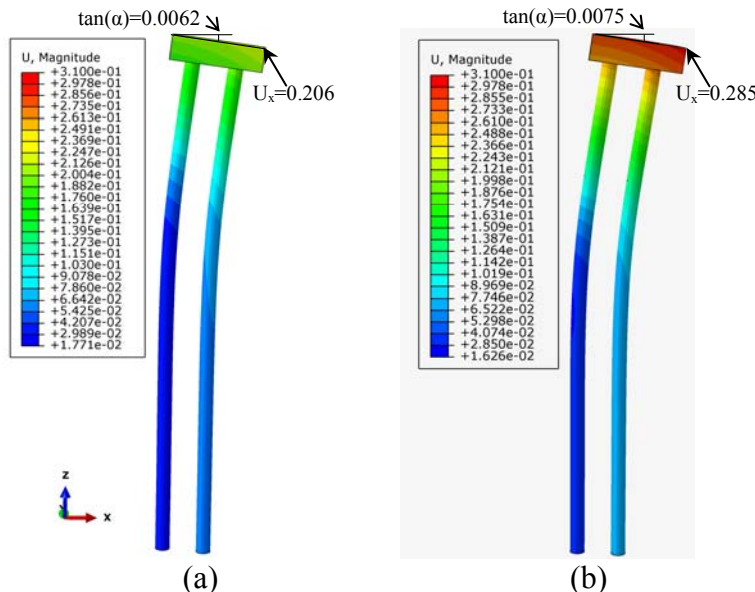
Fig.5 Displacement contour of foundation under ULS-5: (a) No scour; (b) Scour depth=5 m. (Deformation scale factor = 20)

Conclusions

A 3-D plane-symmetric finite element model to simulate the interaction between a high-rise cap foundation and the neighboring soil is proposed and verified with the existing experiments. As a case study, the total load values applied on the foundation under different ULS conditions are obtained. The deformation in various ULS conditions is examined with the proposed numerical model. The present designed foundation can satisfy the tilt criterion of OWT. Scour could obviously amplify the displacements of the foundation and decrease its bearing capacity. The increased momentum resulted from the lowering mudline should be responsible for the increasing of the tilt.

Acknowledgements

References

Abdel-Rahman K, and Achmus M. (2005). "Finite element modelling of horizontally loaded monopile foundations for offshore wind energy converters in Germany" In: Proc., Int. Symp. on frontiers in offshore geotechnics, ISFOG, Perth, Australia. 391-396.

Achmus M, Kuo YS, and Abdel-Rahman K. (2009). "Behavior of monopile foundations under cyclic lateral load" Comput. Geotech., 36: 725-735.

API (American Petroleum Institute) (2007) API RP2A: "Recommended practice for planning, designing and constructing fixed offshore platforms" Working stress design, 22nd edition. API, Washington, DC.

Bourgeois E, Rakotonindriana MHJ, Le Kouby A, Mestat P, and Serratrice J.F. (2010). "Three-dimensional numerical modelling of the behaviour of a pile subjected to cyclic lateral loading" Comput. Geotech., 37: 999-1007.

DNV (Det Norske Veritas) (2010) DNV-OS-J101: "Design of offshore wind turbine structures" DNV, Oslo.

Doherty P, and Gavin K. (2011). "Laterally loaded monopile design for offshore wind farms" Proce., ICE - Energy, 165(1): 7-17.

Leblanc C, Houlsby GT, and Byrne BW. (2010). "Response of stiff piles to long-term cyclic Lateral load" Géotechnique, 60(2): 79-90.

Li F, Han J, and Lin C. (2013). "Effect of scour on the behavior of laterally loaded single piles in marine clay" Mar. Georesour. and Geotec., 31: 271-289.

Malhotra S. (2011). Selection, design and construction of offshore wind turbine foundations, wind turbines" Dr. Ibrahim Al-Bahadly (Ed.), InTech.

McCabe BA, and Lehane BM, (2006). "Behavior of axially loaded pile Groups driven in clayey silt" J. Geotech. Geoenviron., 132(3): 401-410.

Murchinson JM, and O'Neill MW. (1984). "Evaluation of p-y relationships in cohesionless soil: analysis and design of pile foundations" Proce., Symp. in Conjunction with the ASCE National Convention, San Francisco, CA. ASCE Technical Council on Codes and Standards, New York, 174-191.

Poulos HG, and Davis EH. "Pile foundation analysis and design" 1980.

Poulos HG, and Hulls T. (1989). "The role of analytical geomechanics in foundation engineering" In Foundation engineering: Current principles and practices, 1578-1606. Reston, VA: ASCE.

Qi WG, and Gao FP. (2014). "Physical modeling of local scour development around a large-diameter monopile in combined waves and current" Coast. Eng., 83: 72-81.

Randolph MF, and Wroth CP. (1981). "Application of the failure state in undrained simple shear to the shaft capacity of driven piles" Géotechnique, 31(1): 143-157.

Reese LC, and Van Impe WF. 2001. "Single piles and pile group under lateral loading" A. A. Balkema, Rotterdam.

Reese LC, Cox WR, and Koop FD. (1974). "Analysis of laterally loaded piles in sand" Offshore Technology Conf., Houston, Texas.

Sowa VA. (1970). "Pulling capacity of concrete cast in situ bored piles" Can. Geotech. J., 7: 482-493.

Sumer BM, Fredsøe J, and Christiansen N. (1992). "Scour around vertical pile in waves" J. Waterw. Port C., 118: 15-31.

Damage detection from continuous long-term static response using Cointegration and MEWMA Control chart

Gang Liu[a,b], Jianxin Zhang[a], xuan Yao[a], Ping Qin[a]

Abstract: The operational and environmental variability (OEV) will mask subtle changes caused by damage for in-situ civil infrastructures, thus it is one of the obstacles that significantly hinder the application of structure health monitoring. An approach based on cointegration and control chart technique is proposed for identifying damage from continuous long-term static response with the presence of varying OEV. Cointegration theory is used as a data normalization technique to remove the stochastic common trend, which is induced by OEV, in the measured static response observed from several locations on the structure. The multivariate exponentially weighted moving average control chart is employed as a statistic metric to detect the presence of damage and then the drop-one-out strategy is implemented to localize damage. The proposed method is validated by a numerical simulation and monitoring response from a large-span bridge. Results demonstrate that this method can successfully identify damage despite of the operational and environmental variations.

Keyword: Structural health monitoring, damage detection, static response, cointegration, control chart

[a]School of Civil Engineering, Chongqing University, Chongqing, 400045, China;

[b]Key Laboratory of New Technology for Construction of Cities in Mountain Area (Chongqing University), Ministry of Education, Chongqing, 400030, China;

1. Introduction

An abundance of structural health monitoring (SHM) and damage detection methods have been developed and applied to numerical simulations and lab-scaled structures. However, the application of SHM on in-situ civil infrastructures has been rather slow since the existence of OEV.

Several methodologies, such as singular value decomposition and auto-associative neural network, have been exploited to extract OEV-free damage feature in recent years [1,2]. Actually, the aforementioned methods belong to an overall concept of cointegration, which remove the non-stationary common trend caused by OEV. Thus, the residuals obtained from cointegration analysis are only sensitive to damage.

This study further explores the SHM application of cointegration for detecting damage from the continuous long-term static monitoring of civil infrastructures, which vary with environmental and operational conditions obviously. Moreover, the drop-one-out strategy and the multivariate exponentially weighted moving average (MEWMA) control chart are used to localize damage, which is very important in large-size civil structures for further diagnose.

2. Cointegration theory and MEWMA Control chart

2.1 Cointegration theory

The original ideas of cointegration (CI) are to remove the stochastic common trend of multivariate time series in economics field, thus CI is very suited to the OEV problem since the structural responses caused by OEV at different locations will have similar stochastic trend.

Two or more nonstationary time series are said to be cointegrated if a linear combination of the variables is stationary [2], that is, the nonstationary multivariate time series $\{y\}$ will form a new stationary univariate time series z by $z=\{\beta\}^T\{y\}$, where $\{\beta\}$ is referred to as a cointegrating vector [3]. It is clear that a single variable of environmental and operational variations will induce common trends (nonstationary) in the measured multivariate response series from the structure. The common trends are insulted by the linear combination, thus the result time series (residuals) are only sensitive to damage.

Johansen has developed an approach to determine the appropriate cointegrating dimension and find $\{\beta\}$ using maximum likelihood estimation. More detailed discussions about the theory of Cointegration and Johansen approach can be found in references [4, 5].

2.2 MEWMA Control chart

In control charts, the quality characteristic is plotted as a function of the sampling sequence. The system is out-of-control (or damage in SHM) when the quality characteristic is beyond the specified control limit (UCL). Since results of the cointegration analysis for several sensors is dependent and in order to improve the sensitivity of detection, the MEWMA control chart is adopted in this paper.

The MEWMA control chart uses a scalar value r between 0 and 1 to obtain a new multivariate time series Z from observed multivariate time series X by $Z_i = rX_i + (1-r)Z_{i-1}$, where i is the ith time step. And then the statistical data charted T_i^2 is defined as $T_i^2 = Z_i' \Sigma_Z Z_i$, where Σ_Z is the covariance matrix of Z and is asymptotically r/(2-r) times of covariance matrix of X. The UCL and in-control average run length (ARL) for different variable dimensions can be obtained through Monte Carlo simulation and are listed in table in reference [6].

2.3 Damage detection procedure

The measured static responses at different sensor locations are need for identifying the presence and location of damage. The damage-detection approach is summarized in the following steps:

1.Under health condition, the Johansen approach is implemented to achieve the CI model (parameters) and residuals using the measured responses from several sensors;

2.Calculate the mean vector and covariance matrix of the residuals;

3.For unknown condition, the residuals are computed using the CI model (parameters) obtained from health condition;

4.Compute the statistical dataT2 using the residuals obtained in steps 3 and the mean vector and covariance matrix acquired from step 2;

5. Plot the MEWMA control chart to detect the presence of damage;

6. Drop the response from one sensor out and replicate step 1 to 5. If the statistical data T2 is under the UCL, the damage occurs at the drop-out sensor location.

3. Numerical simulation

Assuming the continuous measured static response can be taken as linear superposition of the following effects:

$$D(t) = D_T(t) + D_L(t) + D_D(t) + D_E(t) \quad (1)$$

where t describes time; $D_T(t)$ is the temperature effect (TE); $D_L(t)$ is the loading effect; $D_D(t)$ is the structural damage effect and $D_E(t)$ is the testing error effect.

There are tow types of TE, namely the day temperature effect (DTE) and the year temperature effect (DTE). Both of them are periodic process. If the sampling interval is one hour and one year includes 365 days, the TE can be reasonably simulated as $D_T(t) = a\sin(2\pi t / 24) + b\sin(2\pi t / 8760)$, where a and b are coefficient of DTE and YTE respectively. For the sake of brevity, the loading effect is defined as stochastic process with zero mean. The damage effect is set as monotonic function when damage severity develops. The testing error effect is simulated with white Gaussian noise.

It is assumed that there are four displacement sensors and the monitoring period is tow years with one hour sampling interval. Damage is introduced in the sensor 2 from 10,000 hours to 10,500 hours. The loading effect and testing error effect are considered simultaneously as Gaussian process with boundary [-10,10]. The simulated data is plotted in Figure 1.

(a)   (b)
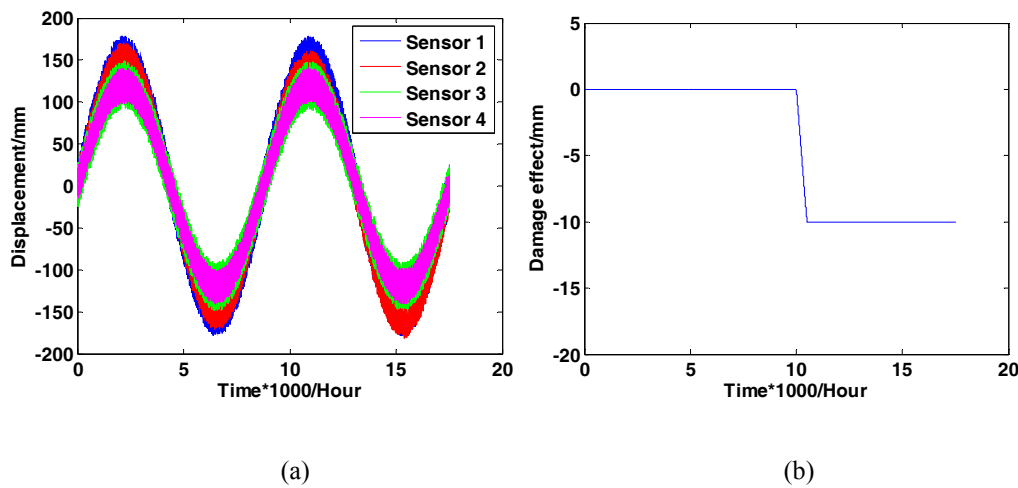
Figure 1. Simulated data for (a) four sensors in two years and (b) the damage effect of the sensor 2

In order to evaluate the type I (false positive) and type II detection error, the simulated data is divided into three sections: baseline section from beginning to 4,380 hours (half a year), reference section from 4,381 to 9,999 hours and damaged section including the rest. The system is health both at baseline and reference condition.

The parameters of the CI model are estimated by the Johansen approach using all baseline section data. The prediction errors (residuals) calculated with the estimated parameters from the data in reference section between 7,001 and 7,500 hours are shown in Figure 2. It's obvious that the fluctuation amplitude of residuals is equal to the level of noise in Figure 2(b), indicating that the TE induced trend has been removed successfully.
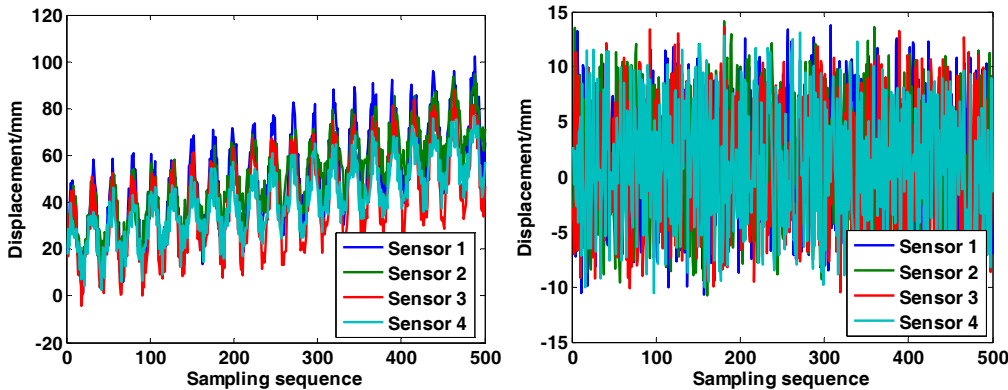
Figure 2. Displacement for (a) testing data (b) residuals after CI analysis

When the in-control ARL and the control chart parameter r are set to be 200 and 0.1 respectively, the MEWMA control chart for reference and damaged section are plotted in Figure 3. Evidently, all the data points in reference condition is under UCL. However, some of the data points which are marked with red star in damaged section is beyond the UCL, especially after the 150 sampling sequence, meaning that the damage can be identified perfectly by MEWMA control chart.
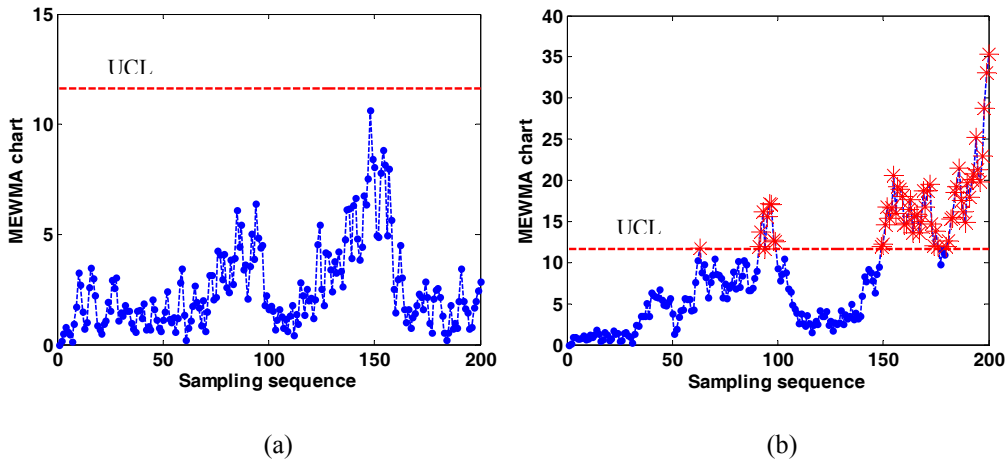
Figure 3. MEWMA control chart for (a) reference condition (b) damaged condition

Since the damage only occurs at sensor 2, the drop-one-out strategy is implemented to localize damage. When sensor 1 to 4 are dropped out successively, the corresponding MEWMA control charts are plotted in Figure 4. It is evidently observed that the statistical data is only in control when sensor 2 is removed since there is no damage in the other sensors, indicating that the damage can be localized satisfactorily. It should be noted that the residuals from each sensor can not be used to localize damage by univariate EWMA control chart because the four residual series do not have physical location information according to theory of the Johansen approach, for example, the first residual does not correspond to the response from sensor 1.
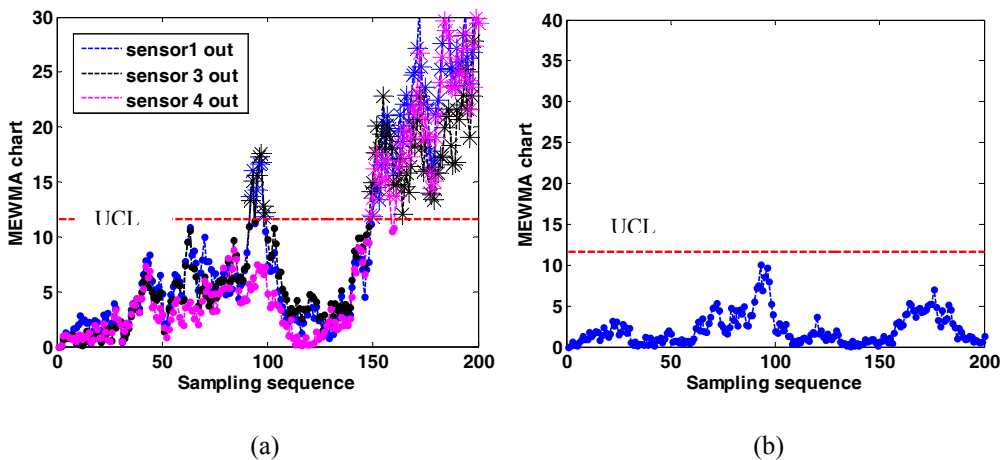
Figure 4. MEWMA control chart when one sensor is dropped out (a) sensor 1,3 and 4 (b) sensor 2

If the number of data points in baseline condition is reduced to 2,190 for training, the MEWMA control chart under reference condition is plotted in Figure 5(a). It is observed that the process is out of control even there is no damage, which implies type I detection error. Therefore, if the number of training data is small, performance of the CI method will decrease.

When the boundary of the noise is increase from [-10,10] to [-30,30], the MEWMA control chart under damaged condition is plotted in Figure 5(b). All the statistical qualities T^2 are in control even though the actual condition is damaged. If the noise level is too high, the CI method would possibly lead to type II detection error.

（a）   （b）
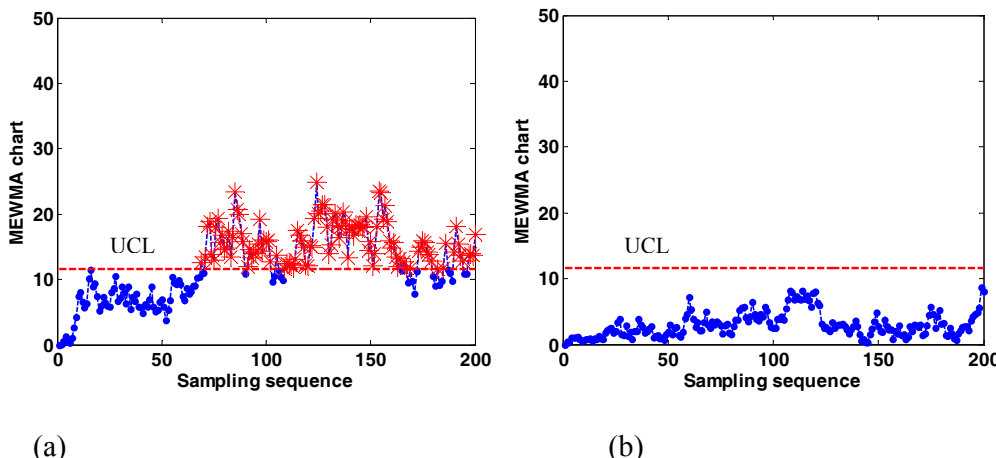
Figure 5. MEWMA control chart considering parameter influence (a) less training data points (b) higher noise amplitude

Although the displacement is used in the above example, this procedure can be easily extended to any long-term measured static variable, such as strain and inclination.

4. Test description

A health monitoring system is installed in a continues rigid frame bridge, whose main span is 330m meters long. To lighten the dead load of concrete, a steel box beam with 108-meter length is adopted in the middle of the main span. The disposal of the bridge is shown in figure 6. Although strain sensors have been mounted to fifteen sections of the box beam, only four sensors from two sections (two per section) are randomly selected to validate the proposed method. These two sections are marked with S1 and S2 in figure 6.
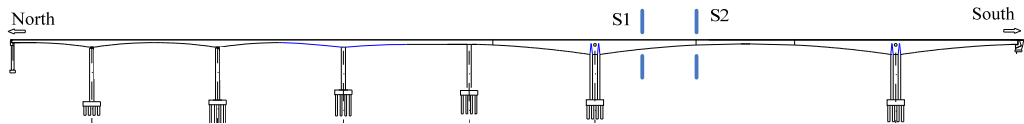
Figure 6. The elevation view and part sensor location of the monitored bridge

The measured data for one year monitoring period is investigated in this paper as shown in Figure 7 (a). The sampling interval is 2 hours. Using the data from beginning to 4000 hours as train sets, the Johansen approach is used to obtain the CI model parameters and the mean vector and covariance matrix.

(a)   (b)
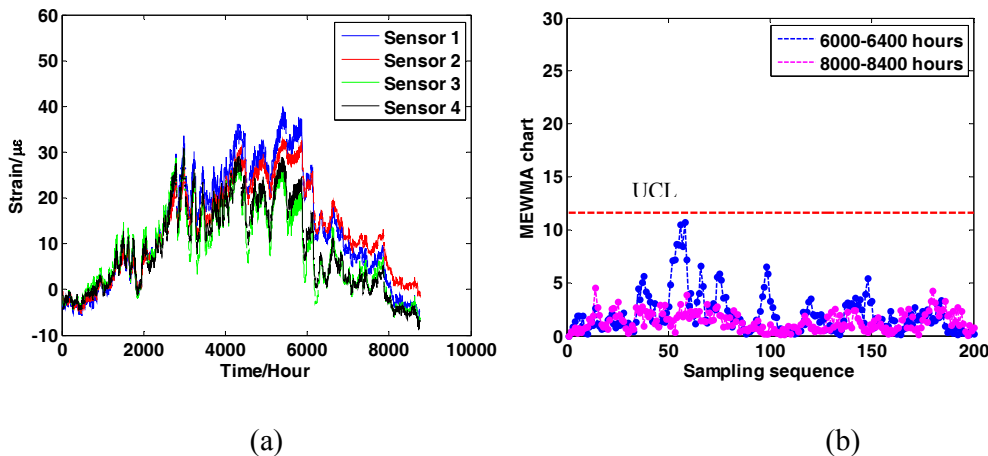
Figure 7. Monitored data and result for a bridge (a) data (b) MEWMA control chart

Then two time periods are exploited to detection the damage using MEWMA control chart as shown in Figure 7 (b). As can be seen in this graph, all the data points are under the ULC. Thus the bridge is health according to results of control chart. This conclusion fits well with the one from human inspection and other types of sensor in these periods, such as accelerometer.

5. Conclusion

In this study, a method is proposed to apply cointegration theory and MEWMA control chart to identify damage from continues long-term static responses. Performance of the proposed method is demonstrated by numerical simulation study and in-situ monitoring responses from a large-span bridge. Results obtained from the numerical simulation demonstrate that the presence and location of damage can be

identified satisfactorily. The performance will decrease if the training data is insufficient and the noise level is high. Only the presence of damage is validated in the monitored bridge since there is no damage in this bridge at present. It should be mentioned that the factor of OEV considered in this paper is linear temperature effect, and further study will be focused upon nonlinear OEV factors, such as the creep and shrinkage effect of concrete.

Acknowledgments

Reference:

[1] F Lanata , A Del Grosso. Damage detection and localization for continuous static monitoring of structures

using a proper orthogonal decomposition of signals.Smart Mater. Struct. 15 (2006) 1811–1829

[2]Sohn H, Worden K, Farrar C R. Statistical damage classification under changing environmental and operational conditions[J]. Journal of Intelligent Material Systems and Structures, 2002, 13(9): 561-574.

[3] Harveya D Y, Todda M D. Cointegration as a data normalization tool for structural health monitoring applications[C]. Proc. of SPIE Vol. 2012, 8348: 834810-1.

[4] Cross E J, Manson G, Worden K, et al. Features for damage detection with insensitivity to environmental and operational variations[J]. Proceedings of the Royal Society A: Mathematical, Physical and Engineering Science, 2012, 468(2148): 4098-4122.

[5] Johansen S. Likelihood-based Inference in Cointegrated Vector Autoregressive Models. (1995) Oxford: Oxford University Press

[6] Lowry C A, Woodall W H, Champ C W, et al. A multivariate exponentially weighted moving average control chart[J]. Technometrics, 1992, 34(1): 46-53.

Displacement monitoring of expansion joints of long-span steel bridges with viscous dampers

Tong Guo[1], Jie Liu[2] and Shenjun Pan[3]

ABSTRACT

This paper presents the displacement monitoring of expansion joints of long-span steel bridges, with emphasis laid on the effect of viscous dampers. Monitored data from the Sutong Bridge and the Jiangyin Bridge were analyzed and compared with those of the Runyang Suspension Bridge. Decomposition of displacement signals in various frequency bands shows that the temperature-induced movements are only a very small portion of the total cumulative displacements; while due to the small but fast movements caused by vehicle/wind loads, the cumulative displacements of long-span steel bridges may be very considerable. The viscous dampers can reduce the vehicle/wind-induced displacements but have no significant influence on the temperature-induced movements. In addition, the measured temperature-displacement relationships of the Sutong Bridge are not linear ones, as reported previously, but are hysteretic, which is due to the time delay between temperature and displacement signals.

Keywords: Expansion joint; Displacement monitoring; Steel bridge; Viscous damper

Introduction

Expansion joints are typically situated above the bridge piers or abutments, connecting two bridge decks. These joints accommodate different types of necessary movements of bridge decks, including the temperature-induced, earthquake-induced and vehicle/wind-induced displacements. However, it is known in the bridge community that expansion joints are maintenance headaches and often the cause of premature failure (Chang and Lee 2002; Lima and Brito 2009; Fu and Zhang 2011). For long-span steel bridges, which are flexible and vibration-sensitive, expansion joints are even more vulnerable than those in short or medium-span concrete bridges.

---

[1]Professor, Key Laboratory of Concrete and Prestressed Concrete Structures of the Ministry of Education, Southeast University, Nanjing, 210096, P. R. China (corresponding author). E-mail: guotong@seu.edu.cn

[2] Postgraduate Researcher, School of Civil Engineering, Southeast University, Nanjing, 210096, P. R. China. E-mail: 641492251@qq.com

[3] Postgraduate Researcher, School of Civil Engineering, Southeast University, Nanjing, 210096, P. R. China. E-mail: 496183759@qq.com

With the recent development of structural health monitoring techniques (Mufti 2002; Ko and Ni 2003), it has become possible to give more insights to the authentic and long-term performance of these expansion joints. For example, based on the monitored displacement and temperature data of the Ting Kau Bridge, a procedure was proposed by Ni *et al.* (2007). Regression analysis showed that the displacement of expansion joints had a linear relationship with bridge temperature, and the fitted relationship was thus used to estimate the maximum displacement of expansion joints. In previous studies (Ni *et al.* 2007; Deng *et al.* 2009), extreme displacement rather than the cumulative displacement was the emphasis.

In the past decades, an increasing use of various dampers has been seen in many long-span steel bridges (Seim and Ingham 2000; Moroni *et al.* 2005; Vader and McDaniel 2007), so as to mitigate the seismic responses of girders or towers in earthquakes. However, the influence of these dampers on the displacements of bridge expansion joints requires further investigation. In this study, monitored longitudinal displacements of expansion joint and temperature of three long-span steel bridges were taken for analysis. Emphases were laid on the constitution of displacement data, the displacement-temperature relationship and the influence of dampers on the cumulative displacements.

Bridges under investigation
Monitored data from three bridges were presented in this study. The Sutong Bridge (referred as the STB hereafter), with a main span of 1,088 m, was the cable-stayed bridge with the longest main span in the world when it was open to traffic in 2008, as shown in Fig.1(a). At two pylons and two ends of approach spans, there are four DS 2600 swivel-joist expansion joints. Each piece has a length of 17.72 m, a width of 5.78 m and a maximum extension amount of 2.6 m. To control the seismic displacements of the girder, a viscous damper system with a displacement stopper was installed on the cross-beam of the bridge pylons. Eight nonlinear viscous dampers, each with a maximum damping force of 3,025kN, were placed longitudinally at the cross beam of pylons. This system was designed to limit dynamic movement and load caused by turbulent wind, braking, and seismic loading by dissipating energy; at the same time, it was expected that these dampers provide no significant restriction to the movements caused by temperature, traffic and wind.

The Jiangyin Bridge (referred as the JYB hereafter), open to traffic in 1999, was the first suspension bridge in China with a main span over 1,000 m (i.e., 1,385 m), as shown in Fig.1(b). DS 2000 swivel-joist expansion joints with the maximum extension amount of 2.0 m were used on the bridge. However, damage to the bearings of the swivels and excessive wear of the support steel boxes were observed after three years of service, resulting in frequent maintenance and interruption of traffic. In 2007, these expansion joints were completely replaced. To limit the dynamic displacements of steel girders, four viscous dampers, each with a maximum

damping force of 1,000 kN and a maximum displacement of ±1,000 mm, were installed at two bridge pylons in April, 2006.
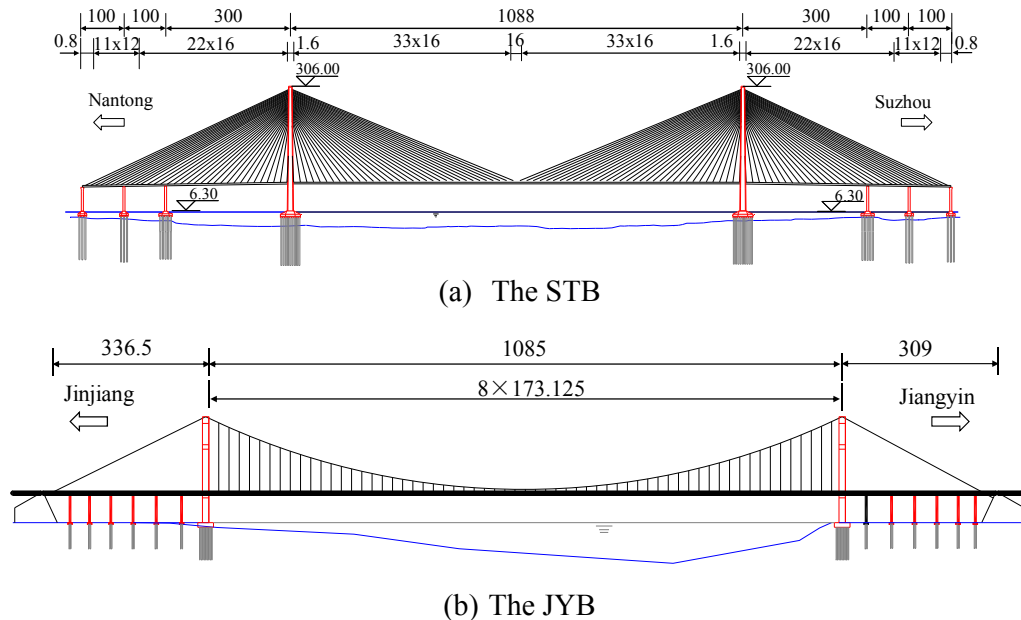
(a) The STB

(b) The JYB

**Figure 1** Profiles of the STB and the JYB (dimensions in meter)
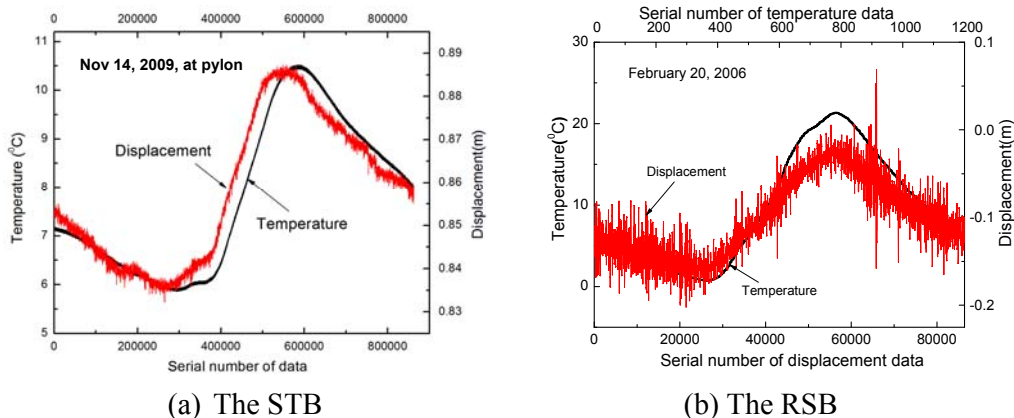
The Runyang Suspension Bridge (referred as the RSB hereafter), was open to traffic in 2005, and has a similar geometry to the JYB but a longer main span (i.e., 1,490 m). Four LR27 expansion joints, with the total weight of 2,400 kN and the maximum expansion amount of 2,160 mm were used. Unexpectedly large movements of the joints, however, were observed which resulted in excessive wear on bearings and expansion joints. Especially the sliding materials and the elastomeric control springs of the bridge's expansion joints showed clear signs of accelerated wear. In 2008, more durable sliding material was used for the bearings and the damaged springs were replaced during the retrofit.

Monitored Data and Correlation Analysis
Monitored temperature and displacement data
The aforementioned three bridges were all installed with long-term structural health monitoring systems. First, one-year (i.e., 2009) monitored data of the STB were selected for analysis, in which the temperature data were taken from the thermometer underneath the top plate of the steel box-girder at the mid-span, and the displacements were taken from the displacement gauges at the end of the approach span and at the pylon, respectively. Fig. 2(a) plots a typical daily temperature time-history, where it is observed that the temperatures go up and down during the day. Such a pattern is similar to that of the daily displacement time-history, showing that the displacements of expansion joints have a close relationship with

temperatures. For comparison, monitored data from the RSB are also analyzed. As shown in Fig.2 (b), an S-shaped displacement time-history that is similar to those in Fig.2(a) is observed; however, larger burrs could be observed in Fig.2(b) than those in Fig.2(a). Another difference between Figs.2(a) and (b) is that there is a time delay between displacement and temperature signals in Fig.2(a), whereas the time delay in Fig.2(b) is insignificant. Taking the peaks and valleys of time-histories in Fig.2(a) for example, the time delay is estimated as about 45 min.

(a) The STB (b) The RSB

Figure 2 Comparison between daily temperature and displacement time-histories

Displacement decomposition in various frequency bands

It is known that the measured displacement signals are influenced by ambient temperature, vehicle/wind loads and even the electromagnetic noises, and thus have different frequency components. To obtain a better understanding on the constitution of cumulative displacements, decomposition of displacements in various frequency bands was conducted using the Butterworth filter. Considering that a full cycle of temperature fluctuation is completed in one day (i.e., 86,400 sec), the frequency of temperature fluctuation is approximately 1.157×10^{-5} Hz (i.e., 1/86,400), though temperature fluctuation could be faster or slower in particular parts of a day. In this study, 5.785×10^{-5} Hz was taken as the upper bond of temperature-induced displacements (five times of 1.157×10^{-5} Hz). The electromagnetic noises, however, are usually much higher in frequency (i.e. higher than 5 Hz). On the other hand, signals between 1.157×10^{-5} Hz and 5 Hz are basically caused by vehicle/wind loads.

Taking the signals in Nov 14, 2009 for example, the decomposed data are illustrated in Fig.3. It is observed that the temperature-induced displacement fluctuation is about 0.06 m, as shown in Fig.3(a). The vehicle/wind-induced displacements are in general from -0.005 m to 0.004 m, as shown in Fig.3(b). The artificial displacements due to electromagnetic noises are very small, being about -3.5×10^{-5} m to 3.5×10^{-5} m, as shown in Fig.3(c). The cumulative displacements, calculated using the decomposed signals in the three frequency bands, are 0.19 m, 48.63 m and 7.96 m, respectively. Therefore, the cumulative displacement due to temperature fluctuation is only a small part of the total cumulative displacement (i.e.,

56.79 m). The influence of electromagnetic noises on cumulative displacement has a limited contribution (i.e., about 14 percent) and should be excluded, whereas the vehicle-induced displacements are the major part.


(a) Lower than 5.785×10^{-5} Hz

(b) From 5.785×10^{-5} Hz to 5Hz

(c) Higher than 5 Hz
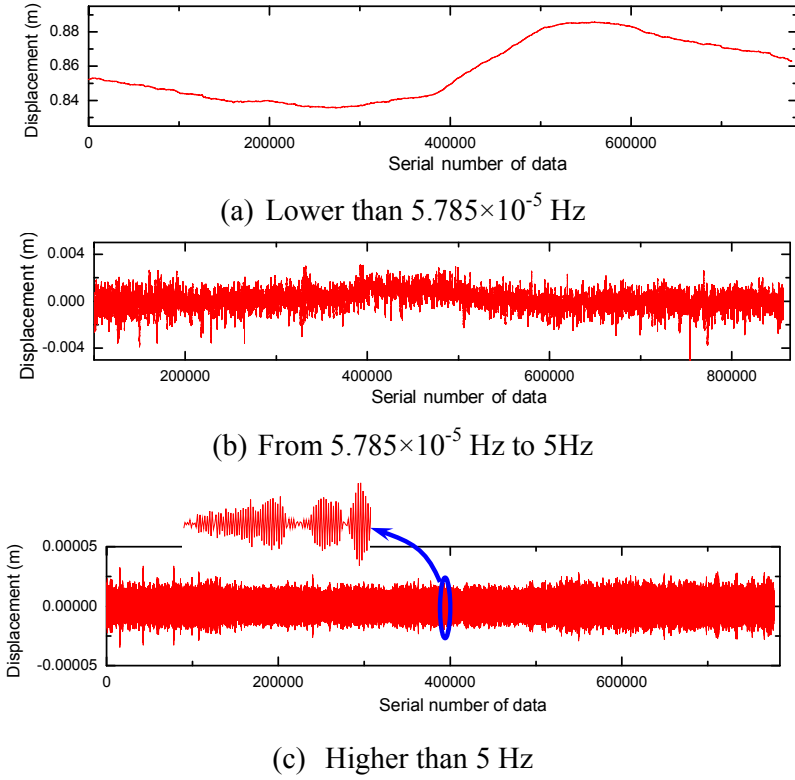
Figure 3 Displacement time-histories in various frequency bands

(a) The STB

(b) The JYB
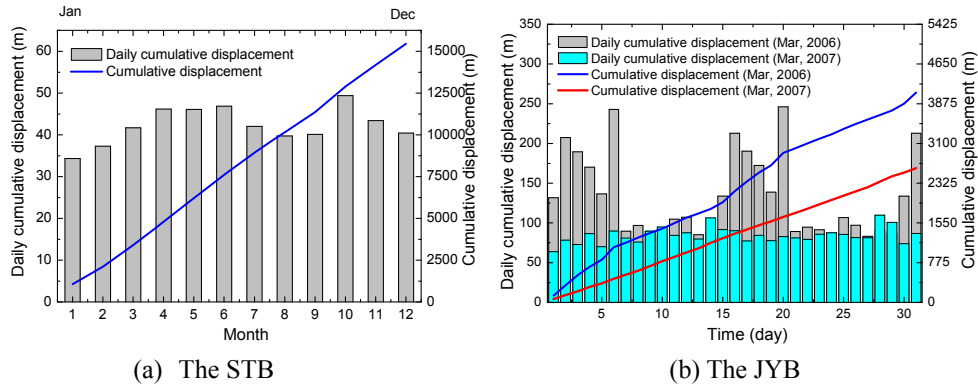
Figure 4 Comparison between cumulative displacements of expansion joints

Fig.4(a) shows the average daily cumulative displacements of the STB in each month of 2009, where it is observed that the values are similar to each other, and the mean value is around 42 m per day. Accordingly, the cumulative displacements in 2009 increase in a linear pattern and the total amount is as large as 15,447 m, which is rather considerable. Fig.4(b) further shows the comparison between cumulative

displacements in March, 2006 and March, 2007, where significant reduction could be observed after the dampers were installed. When the cumulative displacements in Fig.4(a) and in Fig.4(b) are compared, the latter are significantly larger. There are several possible reasons for the difference. First, the JYB is a suspension bridge while the STB is a cable-stayed bridge; second, the main-span of the JYB (i.e., 1,385 m) is much longer than that of the STB (i.e., 1,088 m), making the JYB more flexible than the STB; in addition, the number of dampers on the JYB are less and the maximum damping forces are also much smaller than those of the STB.

Displacement-temperature relationship

According to the monitored displacement and temperature data, the displacement-temperature relationships of the STB were obtained, as shown in Fig.5. It is observed that the relationships are not linear ones, as reported previously (Ni *et al.* 2007; Deng *et al.* 2009), but are hysteretic. At the same temperature, there are two different displacements in the displacement-temperature relationships. If the temperature at 24:00 is close to that at 0:00 of the day, a closed circle can be obtained, as shown in Fig. 5(a); otherwise, an open circle is observed, as shown in Fig. 5(b).

| (a) | (b) |
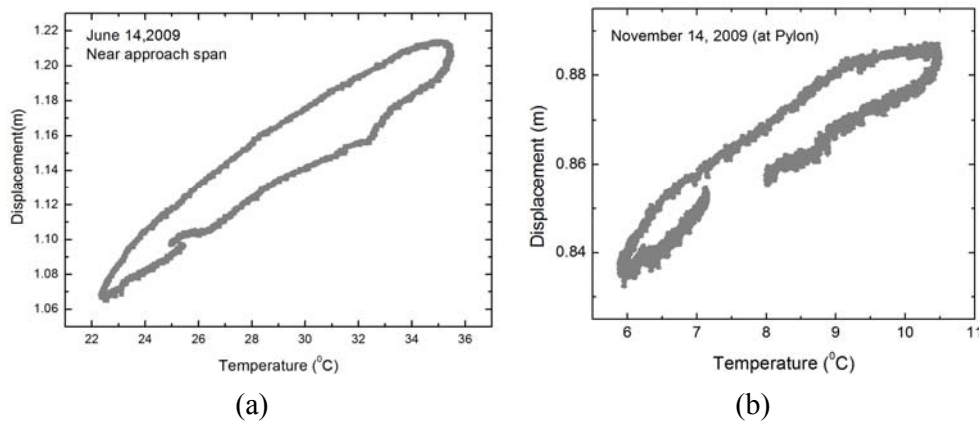
Figure 5 Displacement-temperature relationships (the STB)

For comparison, a typical displacement-temperature relationship of the RSB is also given, as shown in Fig.6(a), where approximately linear relationship is observed. Taking the JYB for another example, it can be observed from Fig.6(b) that the displacement-temperature relationship is basically linear, which is similar to that in Fig.6(a). Therefore, it seems that the dampers, though their damping forces are not as large as those of the STB, did not significantly influence the pattern of displacement-temperature relationships. Accordingly, the hysteretic loops in Fig.5 are not likely due to the existence of large viscous dampers. Besides, the daily temperature fluctuation is slow and therefore may not generate significant damping forces in these velocity-dependent dampers. Instead, the hysteretic relationships are mainly due to the time delay of temperature signals. Taking the displacement-temperature relationships in Figs.5(a) and (b) for example, the time

delays are approximately 45 min and 50 min respectively. By putting the temperature data 45 min and 50 min behind the displacement data, the updated displacement-temperature relationships were obtained, where they became linear ones, as shown in Fig.7.

(a) The RSB   (b) The JYB
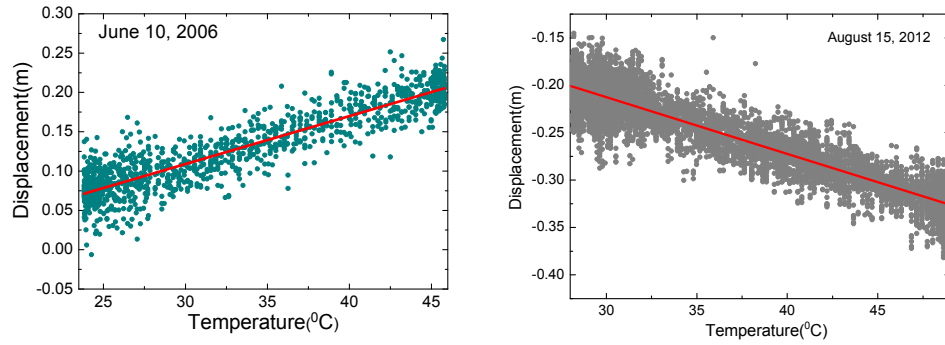
Figure 6 Displacement-temperature relationships (the RSB and the JYB)

(a)   (b)
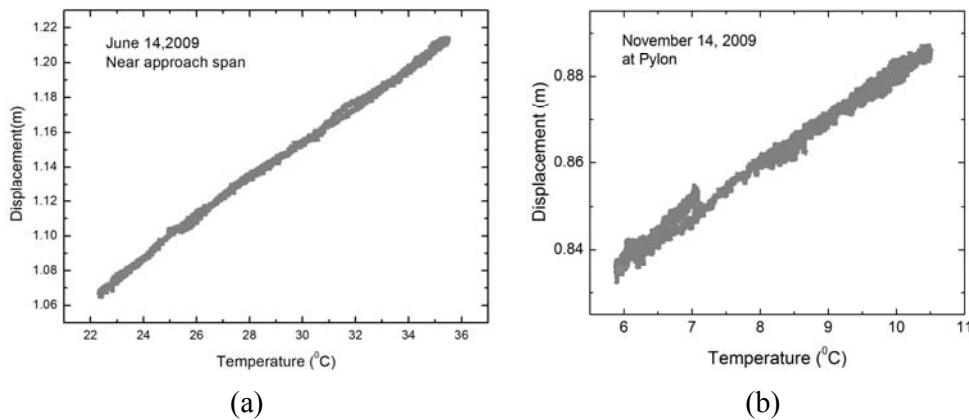
Figure 7 Temperature-displacement relationships of the STB (without time delay)

Conclusions

In spite of the increasing use of dampers to mitigate seismic response of long-span steel bridges, their influence on the displacements of expansion joints has seldom been monitored and reported in-depth. According to the field monitored data, the cumulative displacements of expansion joints on long-span bridges may exceed the design or expected value by a considerable margin, which would result in excessive wear on bearings and fatigue problem of expansion joints. Decomposition of displacements in various frequency bands reveals that the temperature-induced cumulative displacements are very small, whereas vehicle/wind loads may be the dominating factor affecting the cumulative displacements.

Besides, the temperature-displacement relationships of the STB are hysteretic, which are different from the linear ones reported previously. However, it is not due to the existence of hysteretic dampers, because that ambient temperature always

changes in a very slow mode and won't cause significant damping forces, but due to the time delay between temperature and displacement signals.

According to the comparison of cumulative displacements of the JYB before and after damper installation, the dampers significantly reduced the displacements of expansion joints. Due to the existence of large dampers, the displacements of expansion joints of the STB are also much less than those of the RSB.

Acknowledgments

References

Chang, L.M. and Lee, Y.J. (2002)."Evaluation of Performance of Bridge Deck Expansion Joints."*Journal of Performance of Constructed Facilities*, 16(1), 3-9.

Deng, Y., Li, A.Q., Ding Y.L. (2009). "Research and application of correlation between beam end displacement and temperature of long-span suspension bridge." *Journal of Highway and Transportation Research and Developmen*, 26(5), 54-58.

Fu, C.C. and Zhang, N. (2011). "Investigation of bridge expansion joint failure using field strain measurement." *Journal of Performance of Constructed Facilities*, 25(4), 309-316.

Ko, J.M. and Ni, Y. Q.(2003). "Structural health monitoring and intelligent vibration control of cable-supported bridges: research and application". *KSCE Journal of Civil Engineering*. 7(6), 701-716.

Lima, J.M., Brito, J.D.(2009). "Inspection survey of 150 expansion joints in road bridges." *Engineering Structures*. 31(5), 1077-1084.

Moroni, M., Boroschek, R., and Sarrazin, M. (2005). "Dynamic characteristics of Chilean Bridges with seismic protection." *Journal of Bridge Engineering*, 10(2), 124-132.

Mufti, A. A. (2002). "Structural health monitoring of innovative Canadian civil engineering structures." *Structural Health Monitoring*, 1(1), 89-103.

Ni, Y. Q., Hua, X.G., Wong, K.Y. and Ko, J. M. (2007). "Assessment of bridge expansion joints using long-term displacement and temperature measurement." *Journal of Performance of Constructed Facilities*, 21(2), 143-151.

Seim, C. and Ingham, T. (2000). "Innovative seismic retrofit of steel bridges: some examples." *Advanced Technology in Structural Engineering*, pp. 1-8.

Vader, T.S., and McDaniel, C. C. (2007). "Influence of dampers on seismic response of cable-supported bridge towers."*Journal of Bridge Engineering*, 12(3), 373-379.

Beam Damage Localization Method Considering Random

Uncertainty Using Mid-span Displacement Data

Y.L. Wang,[1] and X.L. Liu[2]

ABSTRACT

Random uncertainty is recognized as one of the main barriers against the application of existing damage detection techniques on actual structures. This paper investigates the damage localization of simply supported beams with original random uncertainty. A new index DIILMSD, which is based on the idea of 'Second Order Difference of Displacement Influence Line', has been presented. The damage localization method based on DIILMSD has been theoretically discussed and its application to the random uncertain case is studied as a highlight. Numerical example has been conducted to examine the suitability of the method. It is proved that this method can work in the presence of random uncertainty in geometric and material properties, which means that it is suitable for real-world beams. Another significant attraction of this method is that only mid-span displacement measurements are required during the application process of this method.

Key word: Damage; Localization; Uncertainty; Displacement; Influence line

Introduction

Simply supported beams are used widely. Reliable and efficient damage localization techniques for existing beams are essential to safe operation and failure prevention. Finding and testing a proper index should prioritize over other work. During the past years, several damage localization indices have been proposed.

One category of indices are vibration-based indices, such as natural frequencies (Morassi, 2007), modal shapes (Huth et al., 2005), damping (Curadelli et al., 2008), modal-shape curvatures (Reynders et al., 2007), frequency response function (Liu et al., 2009), etc. Another significant index category is based on static displacement under prescribed loads. For example, 'Partial Eigenstructure Assigned Method' was presented to identify the parameters of damaged structures by treating the damage detection problem as an optimization task (Feng, 2002). Jang et al. (2002) introduced nonlinear regularization and adaptive substructure techniques to modify the structure model to detect damage.

---

[1] School of Civil Engineering, Shandong Jianzhu University, Fengming Road, Jinan, Shandong province, 250101, China. e-mail: xgwang_wang@163.com

[2] Department of Civil Engineering, Shanghai Jiao Tong University, 800 Dongchuan Road, Shanghai, 200240, China. e-mail: xilaliu@tsinghua.edu.cn

However, it should be noted that the original uncertainty in geometric and material properties for the real-world beams usually was ignored in existing methods. In fact, it is particularly important to address the random uncertainties in Young's modulus and geometry from a practical point of view, because the presence of damage is usually expressed by the reduction of flexural stiffness in present studies (Perera et al., 2008). Therefore, it is difficult to determine whether the changes of the damage detection index are caused by actual damage or random uncertainty.

The existing knowledge cannot be expected to reduce random uncertainty although it may be useful in quantifying the uncertainty. At present, statistical strategy (Zhang, 2007), fuzzy logic (Chandrashekhar et al., 2009) are usually suggested for the effort to account for this kind of uncertainty. However, statistical strategy can account for only distinct damage features for which data can have a crisp point-wise quantification. Fuzzy logic approaches are mainly suitable for detecting damage occurrence and classifying progressive levels of damage. Therefore, the problem of finding a new index that can deal with the original random uncertainty of in-service beams properly still remains a challenge.

This paper attempts to provide a new damage localization method for simply supported beams which can work in the presence of random uncertainty. An index termed as 'Difference Index of Influence Line for Mid-span Displacement, DIILMSD' will be proposed.

Methodology

The whole length of a beam can be discretized into several regions with the same length as m firstly. x' is used to denote the distance between damage region and the beam end. To denote the damage extent, z is used: the flexural stiffness EI of the damage region becomes $z'EI$ upon the occurrence of damage.

Case analysis of original random uncertainty

A concentrated load F is employed to travel on the beam. Attention is paid to the corresponding mid-span displacement change induced by F when it occurs on each node of the regions. x_1 denotes the distance between F and the left end of beam.

For clarity, it is assumed that only one region has local flexural stiffness value EI' while all the rest regions have the same local stiffness value EI to consider original random uncertainty of a simply supported beam (Figure 1).
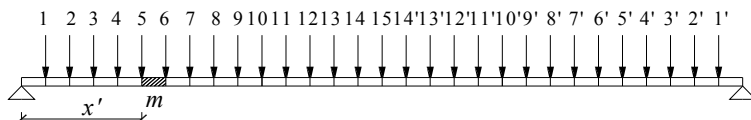

Figure 1 Analytical model of the original beam

(1) When F occurs at $x_1=x'$, the corresponding mid-span displacement incremental value is denoted by $\Delta\omega_{x'}$. Eq.1 can be obtained based on Virtual Work Principle:

$$EI\Delta\omega_{x'} = \left[\frac{Fl^2x'}{16} - \frac{Fx'(m+x')^2}{4} + \frac{Fx'(m+x')^3 + Fx'^3(l-x')}{6l}\right] - \frac{Fmx'(2m^2 + 6mx' - 3lm + 6x'^2 - 6lx')}{12lz'} \tag{1}$$

Where l is the whole length of beam.

Because commonly used single-span beams are not deep beams, shear deformation is negligible in the whole paper. When F occurs at $x_1 = l - x'$, the corresponding mid-span displacement incremental value is denoted by $\overline{\Delta}\omega_{x'}$ and solved. The difference between $\Delta\omega_{x'}$ and $\overline{\Delta}\omega_{x'}$, is then represented as $\dot{\Delta}\omega_{x'}$ and solved. When F occurs at $x_1 = x' - m$, $x_1 = x' - 2m$, $x_1 = x' - 3m$ and the corresponding symmetrical positions, $\dot{\Delta}\omega_{x'-m}$, $\dot{\Delta}\omega_{x'-2m}$, $\dot{\Delta}\omega_{x'-3m}$ can be obtained similarly.

Then worthy of attention is the fact that

$$\dot{\Delta}\omega_{x'} - \dot{\Delta}\omega_{x'-m} = \dot{\Delta}\omega_{x'-m} - \dot{\Delta}\omega_{x'-2m} = \dot{\Delta}\omega_{x'-2m} - \dot{\Delta}\omega_{x'-3m} = \frac{Fm^2(z'-1)(4m^2 + 12mx' - 3lm + 12x'^2 - 6lx')}{12EIz'l} \tag{2}$$

Subsequently, the right side of the damage region is considered. When F occurs at $x_1 = x' + m$, $x_1 = x' + 2m$, $x_1 = x' + 3m$ and the corresponding symmetrical positions, $\dot{\Delta}\omega_{x'+m}$, $\dot{\Delta}\omega_{x'+2m}$, $\dot{\Delta}\omega_{x'+3m}$ can be obtained. According to the above results, a new index can be defined as $\overline{\Delta}_{x_1} = \dot{\Delta}\omega_{x_1} - \dot{\Delta}\omega_{x_1-m}$. When F gets across the damaged region, value of $\overline{\Delta}_{x_1}$ will suffer a sudden jump. Accordingly, the position of damage can be detected. This new index can be termed as 'Difference Index of Influence Line for Mid-span Displacement, DIILMSD'.

In conclusion, DIILMSD value of two points ($x_1 = x'+m$ and the corresponding symmetrical point) will be different from the nearby ones when original random uncertainty occurs within the region [x', $x'+m$] or [$l-x'-m$, $l-x'$].

Subsequently, the influence of damage occurrence on DIILMSD will be studied.

***Damage case* 1**
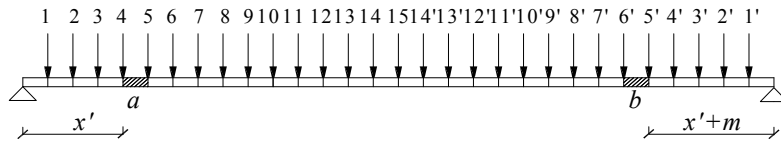
Figure 2 Damage case 1

Damage scenario is shown in Figure 2. The position of damage b and original random uncertainty a will be adjacent if one of them is displaced symmetrically. Flexural stiffness of the suppositional partition which has original random

uncertainty and damage are denoted by $z_1'EI$ and $z_2'EI$, respectively. In this case, it is found that DIILMSD values of two groups of symmetrical points ($x_1=x'+m$, $x_1=l-x'-m$ and $x_1=x'+2m$, $x_1=l-x'-2m$) will be different from the nearby ones.
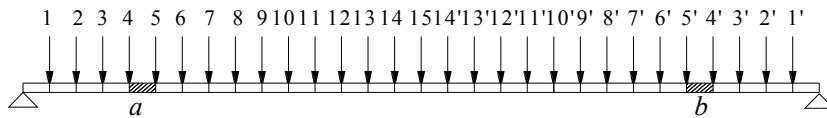
Damage case 2

Figure 3 Damage case 2

Damage scenario is shown in Figure 3. Damage b and original random uncertainty a occur in the symmetrical suppositional partition. Similarly, the flexural stiffness of the suppositional partition which has original random uncertainty and damage are denoted by $z_1'EI$ and $z_2'EI$. Procedures same as above are carried out. According to the results, it is found that DIILMSD values of two points ($x_1=x'+m$ and the corresponding symmetrical point) will also be different from the nearby ones.

Method establishment

Damage localization method then can be established. Positions on a beam can be mapped to the points on a coordinate axis where the left side of the beam is the origin and the distance from the origin to the section under study is denoted by variable x_2.

In practice, the DIILMSD values of each suppositional partition node can be obtained and then plotted. A beam under intact and unknown condition should be tested. A set of two DIILMSD graphs are then generated. Close attention should be paid to the slopes of attachment lines between each point and its two adjacent points.
(1) When the beam with original random uncertainty is intact, DIILMSD values of each suppositional partition change from $\dfrac{Fm^2(z'-1)(4m^2+12mx'-3lm+12x'^2-6lx')}{12EIz'l}$ (when $x_2<x'+m$) to $\dfrac{Fm^2(z'-1)(4m^2+12mx'-2lm+12x'^2-3lx')}{12EIz'l}$ (when $x_2=x'+m$) to $\dfrac{Fm^2(z'-1)(m^2+3mx'+3x'^2)}{3EIz'l}$ (when $x_2>x'+m$).

If attention is paid to the slope of attachment line between each point and its two adjacent points, it can be found that: when $x_2<x'$, the slopes of two attachment lines between each point and its two adjacent points are zero; when $x_2=x'$, the slope of attachment line between this point and its left adjacent point is zero while the slope of attachment line between this point and its right adjacent point is $\dfrac{Fm(z'-1)(m+3x')}{12EIz'}$; when $x_2=x'+m$, the slope of attachment line between this point and its left adjacent point is $\dfrac{Fm(z'-1)(m+3x')}{12EIz'}$ while the slope of attachment line between this point and its right adjacent point is $\dfrac{Fm(z'-1)(2m+3x')}{12EIz'}$; when $x_2=x'+2m$, the slope of attachment

line between this point and its left adjacent point is $\dfrac{Fm(z'-1)(2m+3x')}{12EIz'}$ while the slope

of attachment line between this point and its right adjacent point is zero; when $x_2 > x'+2m$, the slopes of two attachment lines between each point and its two adjacent points are renewed to be zero.

It is shown that the slopes of two attachment lines between one point ($x_2 = x'+m$) and its two adjacent points are different with zero. This point can be defined as a 'special point'. It is noted that this point can indicate the suppositional partitions which have original random uncertainty ([x', $x'+m$] or [$l-x'-m$, $l-x'$]).

(2) When damage case 1 occurs, DIILMSD values of each suppositional partition

change from $\dfrac{-Fm^2\left[4m^2z_2'-28m^2z_1'-12x'^2\left(z_1'-z_2'\right)+9mlz_1'-3mlz_2'\right]}{12EIlz_1'z_2'}+$ (when $x_2 < x'+m$) to

$$\dfrac{-Fm^2\left[-36mx'z_1'+12mx'z'+6lx'\left(z_1'-z_2'\right)+24m^2z_1'z_2'-6mlz_1'z_2'+24mx'z_1'z_2'\right]}{12EIlz_1'z_2'}$$

$\dfrac{Fm^2\left[28m^2z_1'-4m^2z_2'+12x'^2\left(z_1'-z_2'\right)-9mlz_1'+2mlz_2'+36mx'z_1'\right]}{12EIlz_1'z_2'}+$ (when $x_2 = x'+m$) to

$\dfrac{Fm^2\left[-12mx'z_2'-6lx'z_1'+3lx'z_2'-24m^2z_1'z_2'+7mlz_2'-24mx'z_1'z_2'+3lx'z_1'z'\right]}{12EIlz_1'z'}$

$\dfrac{-Fm^2\left[4m^2z_2'-28m^2z_1'-12x'^2\left(z_1'-z_2'\right)+5mlz_1'\left(1-z_2'\right)\right]}{12EIlz_1'z_2'}+$ (when $x_2 = x'+2m$) to

$\dfrac{-Fm^2\left[-36mx'z_1'+12mx'z_2'+3lx'z_1'\left(1-z_2'\right)+24mz_1'z_2'\left(m+x'\right)\right]}{12EIlz_1'z'}$

$\dfrac{-Fm^2\left[m^2z_2'-7m^2z_1'-3x'^2\left(z_1'-z_2'\right)-9mx'z_1'+3mx'z_2'+6mz_1'z_2'\left(m+x'\right)\right]}{3EIlz_1'z_2'}$ (when $x_2 > x'+2m$).

If attention is paid to the slope of attachment line between each point and its two adjacent points, it can be found that: when $x_2 < x'$, the slopes of two attachment lines between each point and its two adjacent points are zero; when $x_2 = x'$, the slope of attachment line between this point and its left adjacent point is zero while the slope of attachment line between this point and its right adjacent point is $\dfrac{Fm(m+3x')(z_1'-1)}{12EIz_1'}$;

when $x_2 = x'+m$, the slope of attachment line between this point and its left adjacent point is $\dfrac{Fm(m+3x')(z_1'-1)}{12EIz_1'}$ while the slope of attachment line between this point and its

right adjacent point is $\dfrac{-Fm(2mz_2'-4mz_1'-3x'z_1'+3x'z_2'+2mz_1'z_2')}{12EIz_1'z_2'}$; when $x_2 = x'+2m$, the slope

of attachment line between this point and its left adjacent point is

$\dfrac{-Fm(2mz_2'-4mz_1'-3x'z_1'+3x'z_2'+2mz_1'z_2')}{12EIz_1'z_2'}$ while the slope of attachment line between this

point and its right adjacent point is $\dfrac{Fm\left[5mlz_1'\left(1-z_2'\right)+12mx'z_2'+3lx'z_1'\left(1-z_2'\right)\right]}{12EIlz_1'z_2'}$; when

$x_2 = x'+3m$, the slope of attachment line between this point and its left adjacent point

is $\dfrac{Fm\left[5mlz_1'(1-z_2')+12mx'z_2'+3lx'z_1'(1-z_2')\right]}{12EIlz_1'z_2'}$ while the slope of attachment line between this

point and its right adjacent point is zero; when $x_2>x'+3m$, the slopes of two
attachment lines between each point and its two adjacent points are renewed to be
zero.

It is shown that two special points (the slopes of two attachment lines between
them and their two adjacent points are different with zero) will occur. The new added
one can indicate the suppositional partitions which have damage while the foregoing
one indicates the suppositional partitions which have original random uncertainty.

In addition, when damage case 2 occurs, DIILMSD values of each suppositional

partition change from $\dfrac{Fm^2\left(z_1'-z_2'\right)\left(4m^2+12mx'-3lm+12x'^2-6lx'\right)}{12EIlz_1'z_2'}$ (when $x_2<x'+m$) to

$\dfrac{Fm^2\left(z_1'-z_2'\right)\left(4m^2+12mx'-2lm+12x'^2-3lx'\right)}{12EIlz_1'z_2'}$ (when $x_2=x'+m$) to $\dfrac{Fm^2\left(z_1'-z_2'\right)\left(m^2+3mx'+3x'^2\right)}{3EIlz_1'z_2'}$

(when $x_2>x'+m$).

It is shown that the special point under this damage case is the same with the intact
beam. However, it can be found that: when $x_2=x'$, the slope of attachment line

between this point and its right adjacent point is $\dfrac{Fm\left(m+3x'\right)\left(z_1'-z_2'\right)}{12EIz_1'z_2'}$; when $x_2=x'+m$,

the slope of attachment line between this point and its left adjacent point is

$\dfrac{Fm\left(m+3x'\right)\left(z_1'-z_2'\right)}{12EIz_1'z_2'}$ while the slope of attachment line between this point and its right

adjacent point is $\dfrac{Fm\left(z_1'-z_2'\right)\left(2m+3x'\right)}{12EIz_1'z_2'}$; when $x_2=x'+2m$, the slope of attachment line

between this point and its left adjacent point is $\dfrac{Fm\left(z_1'-z_2'\right)\left(2m+3x'\right)}{12EIz_1'z_2'}$.

That is to say, the special point still can be differentiated because the slopes of two
attachment lines will change because of the occurrence of damage. In conclusion,
damage position can be detected by comparing two DIILMSD graphs before and
after damage. If the slopes of two attachment lines between one point ($x_2=x'+m$) and
its two adjacent points in the second graph are different with the slopes in the first
graph, it means that damage occurs within the region [x', $x'+m$] or [$l-x'-m$, $l-x'$].

When multiple regions of beam have original random uncertainty or damage
scenarios, example will be given to validate that the above method is still applicable.
Example
A simply supported beam has span of 10m. The height and width of girder section
are 0.5m and 9m. The modal is built using ANSYS. E=34500MPa, I=0.09375m^4 are
used as benchmark of E, I values. m is selected as 0.2m. A concentrated load F
equals 100kN. Mid-span displacement values are solved by finite element analysis.

Considering random uncertainty, the assumed values of equivalent *EI'* of each partitioned interval are listed in Table 1. (For clarity, only two symmetrical parts of beam, $x_2 \in [2m, 4m] \cup [6m, 8m]$, are studied)

Table 1 Equivalent *EI'* of each partitioned interval

Interval	*EI'*	Interval	*EI'*	Interval	*EI'*	Interval	*EI'*
[2.0m, 2.2m]	0.99*EI*	[3.0m, 3.2m]	1.02*EI*	[6.0m, 6.2m]	1.01*EI*	[7.0m, 7.2m]	0.98*EI*
[2.2m, 2.4m]	0.98*EI*	[3.2m, 3.4m]	0.99*EI*	[6.2m, 6.4m]	0.99*EI*	[7.2m, 7.4m]	0.99*EI*
[2.4m, 2.6m]	1.01*EI*	[3.4m, 3.6m]	0.98*EI*	[6.4m, 6.6m]	0.98*EI*	[7.4m, 7.6m]	1.01*EI*
[2.6m, 2.8m]	0.98*EI*	[3.6m, 3.8m]	0.99*EI*	[6.6m, 6.8m]	1.02*EI*	[7.6m, 7.8m]	0.99*EI*
[2.8m, 3.0m]	0.99*EI*	[3.8m, 4.0m]	0.98*EI*	[6.8m, 7.0m]	0.99*EI*	[7.8m, 8.0m]	0.98*EI*

Damage scenario: the distance between damage region and the beam end is 6.8m; the length of damage region is 0.1m; the beam width of damage region is 8.8m. DIILMSD graphs of the intact state and damaged state are shown in Figure 4.
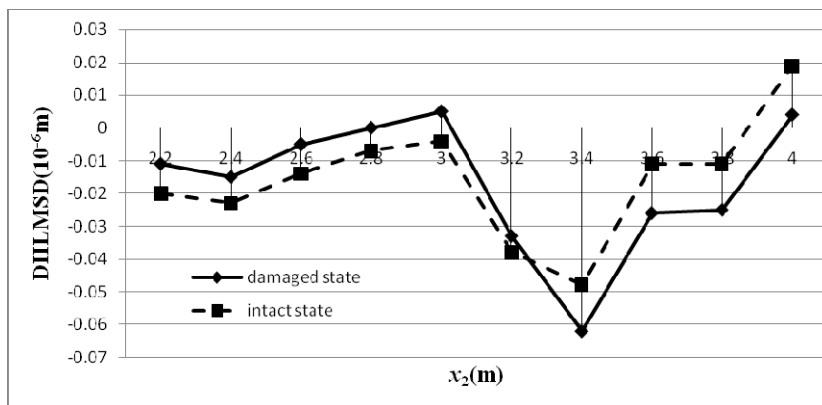
Figure 4 Data under intact state and damaged state

Figure 4 shows that due to uncertainty in geometric and material properties, the curve shape seems to be irregular. By comparing the two graphs, it can be observed that the slope of attachment line between point (x_2=3.2m) and its two adjacent points changes in the set of graphs, which means that damage occurs within the region [3m, 3.2m] or [6.8m, 7m]. This result coincides with the damage scenario.

Application process

1. Just before the tests, a proper value of *m* is chosen for the beam.

The way to choose *m* is to start with a large value and then depending upon the experience and the result of preliminary inspection, reduce the value of *m*.

2. When the beam is intact, let load *F* travel on it at a constant speed. When *F* occurs on the positions of each suppositional partition node, the corresponding incremental values of mid-span displacement are recorded.

3. Values of DIILMSD can be calculated according to the rule presented in the above section and graph can then be plotted.

4. When the beam is damaged, another same test is employed. New DIILMSD graph can be obtained. By comparing these two graphs, damage regions can be detected.

5. True damage location can be determined from the two results with the cooperation of inspection means.

Conclusions

This study presents a new method for multiple damage localization of simply supported beams with original random uncertainty. A novel index termed as 'Difference Index of Influence Line for Mid-span Displacement, DIILMSD' is proposed. Values of mid-span displacement constitute the only information required for the analysis. It is also characterized by a negligible computational effort. It involves much less computation steps than the traditional methods.

Acknowledgements

References

Chandrashekhar, M. and Ganguli, R. (2009). "Damage assessment of structures with uncertainty by using mode-shape curvatures and fuzzy logic." *J.Sound Vib.*, 326(3-5), 939-957.

Feng, X., Zhou, J. and Chen, J.Y., et al. (2002). "Identification of structural parameters based on measured flexibility." *World Earthquake Eng.*, 18(1), 51-55. (in Chinese)

Huth, O., Feltrin, G. and Maeck, J., et al. (2005). "Damage identification using modal data: experiences on a prestressed concrete beam." *J. Struct. Eng.*, 131(12), 1898-1919.

Jang, J.H., Yeo, I. and Chang, S.P. (2002). "Experimental investigation of system-identification-based damage assessment on structures." *J. Struct. Eng.*, 128(5), 673-682.

Liu, X., Lieven, N.A.J. and Escamilla-Ambrosio, P.G. (2009). "Frequency response function shape-based methods for structural damage localization." *Mech.Syst. Signal Pr.*, 23(4), 1243-1259.

Morassi, A. (2007), "Damage detection and generalized Fourier coefficients." *J. Sound Vib.*, 302(1-2), 229-259.

Perera, R., Huerta, C. and Orquı′n, J.M. (2008). "Identification of damage in RC beams using indexes based on local modal stiffness." *Constr. Build. Mater.*, 22(8), 1656–1667.

Reynders,E., Roeck, G.D. and Bakir, P.G., et al. (2007). "Damage identification on the Tilff Beam by vibration monitoring using optical fiber strain sensors." *J.Eng. Mech.*, 133(2), 185-193.

Zhang, Q.W. (2007). "Statistical damage identification for beams using ambient vibration data." *Comput. Struct.*, 85(7-8), 476-485.

Damage Localization Method Using Vertical Support Reaction Data

for Real-world Continuous Bridge

Y.L. Wang,[1] and X.L. Liu[2]

ABSTRACT

Damage localization of real-world continuous bridges with original random uncertainty is studied in this paper. By employing influence line analysis, an index termed as 'Difference Index of Influence Line for Vertical support reaction, DIILSR' has been presented. A damage localization method based on DIILSR then has been established. Significant attraction of this method is that comparatively small quantity of measurements is required because the number of bridge bearing is usually small. Damage position can be detected by comparing two DIILSR graphs before and after damage. If the slopes of two attachment lines between one point ($x_2=x'+m$) and its two adjacent points change, it can be known that damage occurs within the region [x', $x'+m$] or [$l-x'-m$, $l-x'$]. The effectiveness of the proposed method is demonstrated by a numerical simulation performed on a bridge with multiple damages.

Key word: Damage; Localization; Uncertainty; Support reaction; Influence line

Introduction

Most continuous bridges are exposed to internal and external defects. Efficient damage localization techniques are essential to meet the need of failure prevention.

A lot of work has been done to localize the damage. One category of indices are vibration-based indices, such as natural frequencies, modal shapes, damping (Curadelli et al. 2008), modal-shape curvatures (Reynders et al. 2007), strain modal, frequency response function (Liu et al. 2009), etc. In practical cases, there are some kinds of limitations: (1) It is very difficult to accurately measure the needed values using current available sensors; (2) Information from small even medium levels of damage is usually masked by the noise embedded in measured signals (Trentadue et al. 2007); (3) Environmental effects (temperature, etc) may induce changes in the measured data that make damage detection very difficult (Kim et al. 2007).

Another significant index category is based on static displacement. For example, Jang et al. (2002) introduced nonlinear regularization and adaptive substructure techniques to detect damage. However, while values for static displacement are

---

[1] School of Civil Engineering, Shandong Jianzhu University, Fengming Road, Jinan, Shandong province, 250101, China. e-mail: xgwang_wang@163.com

[2] Department of Civil Engineering, Shanghai Jiao Tong University, 800 Dongchuan Road, Shanghai, 200240, China. e-mail: xilaliu@tsinghua.edu.cn

available at every node in numerical simulations, the number of instrumented points is limited in situ and then the effect of these methods is significantly reduced.

Moreover, the original uncertainty in geometric and material properties for the real-world bridges usually was ignored. However, it is particularly important to address the effect of random uncertainties because the damage is usually expressed by the reduction of flexural stiffness. It is difficult to determine whether the changes of index value are caused by actual damage or by random uncertainty.

Therefore, the problem of finding a new index that can deal with the original random uncertainty properly still remains a challenge. Aiming at two-span continuous bridges, this paper attempts to provide a new damage localization method based on influence line concept which can work in the presence of random uncertainty. It is noted that influence line concept has been used and demonstrated as a promising method for damage detection. For example, the synchronized image and sensing data have been analyzed to obtain unit influence line as an index for monitoring bridge behavior and detecting damage (Zaurin et al. 2010). In this paper, a new index termed as 'Difference Index of Influence Line for Vertical support reaction, DIILSR', will be developed.

Methodology

To show the localization of damage, two parameters are needed: x denotes the distance between damage region and the bridge end; y denotes the length of damage region. In fact, y can be considered as a constant m. Other part of bridge can also be divided by the length m. Accordingly, x will then be modified as x'. Only one unknown parameter, x', is needed for damage localization.

To denote the damage extent, z is used: the flexural stiffness EI of the damage region becomes $z'EI$ upon the occurrence of damage.

Case analysis of original random uncertainty

A two-span continuous bridge with equal spans is employed. Firstly, the whole length of main girder can be divided into several regions with the same length as m. A concentrated load F travels on this bridge. When F occurs on each position of suppositional partition nodes, the corresponding vertical support reaction change induced by F is studied.

To consider the original random uncertainty, it is assumed that one partitioned interval has local flexural stiffness value EI' while all the rest intervals have the same local stiffness value EI for clarity (Figure 1). The distance between F and the left end of bridge is denoted by x_1.
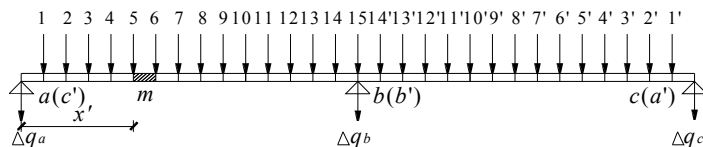

Figure 1 Analytical model of the original girder

(1) When F occurs at $x_1=x'$ and the corresponding symmetrical position:

When F occurs at $x_1=x'$, $\Delta q_2^{x'}$ (the vertical support reaction incremental value of the middle bearing b) can be solved by the Force Method for statically indeterminate structures.

$$\Delta q_2^{x'} = \frac{z'\left[\dfrac{Fl^2x'}{16} - \dfrac{Fx'(m+x')^2}{4} + \dfrac{Fx'(m+x')^3 + Fx'^3(l-x')}{6l}\right] - \dfrac{Fmx'(2m^2+6mx'-3lm+6x'^2-6lx')}{12l}}{z'\left[\dfrac{x'^3}{12} + \dfrac{l^3}{48} - \dfrac{(x'+m)^3}{12}\right] + \dfrac{(x'+m)^3 - x'^3}{12}} \tag{1}$$

Where l is the whole length of bridge.

Because commonly used continuous bridges are not deep bridges, shear deformation is negligible in the whole paper.

When F occurs at the corresponding symmetrical position $x_1=l-x'$, the vertical support reaction incremental value denoted by $\overline{\Delta q}_2^{x'}$ is solved. The difference between $\Delta q_2^{x'}$ and $\overline{\Delta q}_2^{x'}$ is then represented as $\dot{\Delta} q_2^{x'}$ and solved. When F occurs at $x_1=x'-m$, $x_1=x'-2m$, $x_1=x'-3m$ and the corresponding symmetrical positions, $\dot{\Delta} q_2^{x'-m}$, $\dot{\Delta} q_2^{x'-2m}$, $\dot{\Delta} q_2^{x'-3m}$ can be obtained similarly.

Then worthy of attention is the fact that

$$\dot{\Delta} q_2^{x'} - \dot{\Delta} q_2^{x'-m} = \dot{\Delta} q_2^{x'-m} - \dot{\Delta} q_2^{x'-2m} = \dot{\Delta} q_2^{x'-2m} - \dot{\Delta} q_2^{x'-3m} = \frac{Fm^2(z'-1)(4m^2+12mx'-3lm+12x'^2-6lx')}{12lz'EI\delta_{11}} \tag{2}$$

Subsequently, the right side of the damage region is considered. When F occurs at $x_1=x'+m$, $x_1=x'+2m$, $x_1=x'+3m$ and the corresponding symmetrical positions, $\dot{\Delta} q_2^{x'+m}$, $\dot{\Delta} q_2^{x'+2m}$, $\dot{\Delta} q_2^{x'+3m}$ can be obtained. According to the above results, a new index can be defined as $\Delta_{x_1} = \dot{\Delta} q_2^{x_1} - \dot{\Delta} q_2^{x_1-m}$. When F gets across the damaged region, value of Δ_{x_1} will suffer a sudden jump. Accordingly, the position of damage can be detected.

This new index can be termed as 'Difference Index of Influence Lines for Support Reaction, DIILSR'. DIILSR values of two points ($x_1=x'+m$ and the corresponding symmetrical point) will be different from the nearby ones when original random uncertainty occurs within the region $[x', x'+m]$ or $[l-x'-m, l-x']$.

Subsequently, the influence of damage occurrence on this new index will be studied.

Damage case 1

Damage scenario is shown in Figure 2.
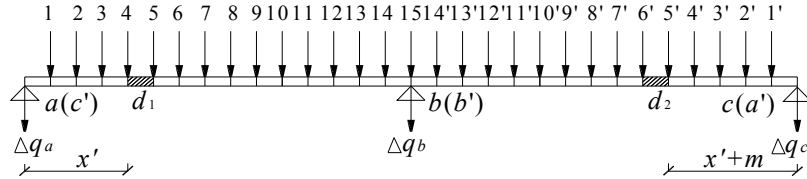
Figure 2 Damage case 1

The position of damage d_2 and original random uncertainty d_1 will be adjacent if one of them is displaced symmetrically. Flexural stiffness of the suppositional partition which has original random uncertainty and damage are denoted by $z_1'EI$ and $z_2'EI$, respectively.

In this case, it is found that DIILSR values of two groups of symmetrical points ($x_1=x'+m$, $x_1=l-x'-m$ and $x_1=x'+2m$, $x_1=l-x'-2m$) will be different from the nearby ones.

Damage case 2

In this case, damage d_2 and original random uncertainty d_1 occur in the symmetrical suppositional partition. Similarly, flexural stiffness of the suppositional partition which has original random uncertainty and damage are denoted by $z_1'EI$ and $z_2'EI$, respectively.

It can be found that DIILSR values of two points ($x_1=x'+m$ and the corresponding symmetrical point) will be different from the nearby ones.

Method establishment

New damage localization method can then be established according to the above character of DIILSR values in different cases. Positions on a bridge can be mapped to the points on a coordinate axis where the left side of the bridge is the origin and the distance from the origin to the section under study is denoted by variable x_2.

In practice, the DIILSR values of each suppositional partition node can be obtained and then plotted. A bridge under intact and unknown condition should be tested. A set of two DIILSR graphs are then generated. Close attention should be paid to the slopes of attachment lines between each point and its two adjacent points.

(1) When the bridge with original random uncertainty is intact

DIILSR values of each suppositional partition change from $A(B-3lm)$ (when

$x_2<x'+m$) to $A(B-2lm)$ (when $x_2=x'+m$) to $A(B+6lx')$ (when $x_2>x'+m$).

In which, $A = \dfrac{Fm^2(z'-1)}{12lz'\left[\dfrac{x'^3}{12}+\dfrac{l^3}{48}-\dfrac{(x'+m)^3}{12}\right]+\dfrac{(x'+m)^3-x'^3}{12z'}}$, $B=4m^2+12mx'+12x'^2-6lx'$.

If attention is paid to the slope of attachment line between each point and its two

adjacent points, it can be found that: when $x_2<x'$, the slopes of two attachment lines between each point and its two adjacent points are zero; when $x_2=x'$, the slope of attachment line between this point and its left adjacent point is zero while the slope of attachment line between this point and its right adjacent point is $C(m+3x')$; when $x_2=x'+m$, the slope of attachment line between this point and its left adjacent point is $C(m+3x')$ while the slope of attachment line between this point and its right adjacent point is $C(2m+3x')$; when $x_2=x'+2m$, the slope of attachment line between this point and its left adjacent point is $C(2m+3x')$ while the slope of attachment line between this point and its right adjacent point is zero; when $x_2>x'+2m$, the slopes of two attachment lines between each point and its two adjacent points are renewed to be zero.

In which, $C = \dfrac{Fm(z'-1)}{z'\left[x'^3+\dfrac{l^3}{4}-(x'+m)^3\right]+(x'+m)^3-x'^3}$.

It is shown that the slopes of two attachment lines between one point ($x_2=x'+m$) and its two adjacent points are different with zero. This point can be defined as a 'special point'. It is noted that this point can indicate the suppositional partitions which have original random uncertainty ($[x', x'+m]$ or $[l- x'- m, l- x']$).

(2) When damage case 1 occurs

DIILSR values of each suppositional partition change from

$D\left[E-3mlz_2'-6lx'z_2'-6mlz_1'z_2'\right]$ (when $x_2<x'+m$) to $-D\left[E-2mlz'-3lx'z_2'-7mlz_1'z_2'-3lx'z_1'z_2'\right]$

(when $x_2=x'+m$) to $D\left[E-4mlz_1'-5mlz_1'z_2'-3lx'z_1'-3lx'z_1'z_2'\right]$ (when $x_2=x'+2m$) to

$D\left[E-9mlz_1'-6lx'z_1'\right]$ (when $x_2>x'+2m$).

In which, $D = \dfrac{-Fm^2}{12lz_1'z_2'\left[\dfrac{l^3}{48}-\dfrac{2m^2x'+mx'^2}{2}-\dfrac{2m^3}{3}+\dfrac{m^3+3m^2x'+3mx'^2}{12z_1'}+\dfrac{7m^3+9m^2x'+3mx'^2}{12z_2'}\right]}$,

$E = \left[4m^2z_2'-28m^2z_1'-12x'^2\left(z_1'-z_2'\right)+9mlz_1'-36mx'z_1'+12mx'z_2'+6lx'z_1'+24m^2z_1'z_2'+24mx'z_1'z_2'\right]$.

If attention is paid to the slope of attachment line between each point and its two adjacent points, it can be found that: when $x_2<x'$, the slopes of two attachment lines between each point and its two adjacent points are zero; when $x_2=x'$, the slope of attachment line between this point and its left adjacent point is zero while the slope of attachment line between this point and its right adjacent point is $H(m+3x')(z_1'-1)$;

when $x_2 = x' + m$, the slope of attachment line between this point and its left adjacent point is $H(m + 3x')(z_1' - 1)$ while the slope of attachment line between this point and its right adjacent point is $\dfrac{-H(2mz_2' - 4mz_1' - 3x'z_1' + 3x'z_2' + 2mz_1'z_2')}{z_2'}$; when $x_2 = x' + 2m$, the slope of attachment line between this point and its left adjacent point is

$\dfrac{-H(2mz_2' - 4mz_1' - 3x'z_1' + 3x'z_2' + 2mz_1'z_2')}{z_2'}$ while the slope of attachment line between this point and its right adjacent point is $\dfrac{H(5m + 3x')z_1'(1 - z_2')}{z_2'}$; when $x_2 = x' + 3m$, the slope of attachment line between this point and its left adjacent point is $\dfrac{H(5m + 3x')z_1'(1 - z_2')}{z_2'}$

while the slope of attachment line between this point and its right adjacent point is zero; when $x_2 > x' + 3m$, the slopes of two attachment lines between each point and its two adjacent points are renewed to be zero.

In which, $H = \dfrac{Fm}{12z_1'\left(\dfrac{l^3}{48} - \dfrac{2m^2x' + mx'^2}{2} - \dfrac{2m^3}{3} + \dfrac{m^3 + 3m^2x' + 3mx'^2}{12z_1'} + \dfrac{7m^3 + 9m^2x' + 3mx'^2}{12z_2'}\right)}$.

It is shown that two special points (the slopes of two attachment lines between them and their two adjacent points are different with zero) will occur. The new added one can indicate the suppositional partitions which have damage while the foregoing one indicates the suppositional partitions which have original random uncertainty.

In addition, when damage case 2 occurs, DIILSR values of each suppositional partition change from $J(B - 3lm)$ (when $x_2 < x' + m$) to $J(B - 2lm)$ (when $x_2 = x' + m$) to

$J(B + 6lx')$ (when $x_2 > x' + m$).

In which, $J = \dfrac{Fm^2(z_1' - z_2')}{12lz_1'z_2'\left[\dfrac{l^3}{48} - \dfrac{m^2x' + mx'^2}{2} - \dfrac{m^3}{6} + \dfrac{m^3 + 3m^2x' + 3mx'^2}{12z_1'} + \dfrac{m^3 + 3m^2x' + 3mx'^2}{12z_2'}\right]}$.

It is shown that the special point under this damage case is the same with the intact bridge. However, it can be found that: when $x_2 = x'$, the slope of attachment line between this point and its right adjacent point is $K(m + 3x')$; when $x_2 = x' + m$, the slope of attachment line between this point and its left adjacent point is $K(m + 3x')$ while the slope of attachment line between this point and its right adjacent point is $K(2m + 3x')$; when $x_2 = x' + 2m$, the slope of attachment line between this point and its left adjacent point is $K(2m + 3x')$.

In which, $K = \dfrac{Fm(z_1' - z_2')}{12z_1'z_2'\left(\dfrac{l^3}{48} - \dfrac{m^2x' + mx'^2}{2} - \dfrac{m^3}{6} + \dfrac{m^3 + 3m^2x' + 3mx'^2}{12z_1'} + \dfrac{m^3 + 3m^2x' + 3mx'^2}{12z_2'}\right)}$.

That is to say, the special point still can be differentiated because of the change of the slopes of two attachment lines.

In conclusion, damage position can be detected by comparing two DIILSR graphs before and after damage. If the slopes of two attachment lines between one point ($x_2=x'+m$) and its two adjacent points are different in these two graphs, it means that damage occurs within the region [x', $x'+ m$] or [$l- x'- m$, $l- x'$].

When more than one partition have original random uncertainty or damage scenarios, the above method will be shown to be still applicable by the following example.

Example

A continuous bridge with box section has span of 2×50m. The height, width, and wall thickness of girder section are 3m, 6m, and 0.4m, respectively. The theoretical modal is built using ANSYS. E=32500MPa is used as benchmark of E value. m is selected as 1m. A concentrated load F equals 100kN.

Considering random uncertainty, the assumed values of equivalent EI' of each partitioned interval are listed in Table 1. (For clarity, only two symmetrical parts of bridge, $x_2\in$[6m, 14m]$\cup$[86m, 94m], are studied)

Table 1 Equivalent EI' of each partitioned interval

Interval	EI'	Interval	EI'	Interval	EI'	Interval	EI'
[6m,7m]	0.99EI	[10m,11m]	0.99EI	[86m,87m]	0.98EI	[90m,91m]	0.98EI
[7m,8m]	0.98EI	[11m,12m]	1.02EI	[87m,88m]	0.99EI	[91m,92m]	1.02EI
[8m,9m]	1.01EI	[12m,13m]	0.99EI	[88m,89m]	1.01EI	[92m,93m]	0.99EI
[9m,10m]	0.98EI	[13m,14m]	0.98EI	[89m,90m]	0.99EI	[93m,94m]	0.98EI

Damage scenario: the distance between damage region and the girder end is 90m; the length of damage region is 0.1m; the girder height of damage region is reduced to he=2.9m. For clarity, only bearing $b(b')$ is employed for illustration here. DIILSR graphs of the intact state and damaged state are shown in Figure 3.
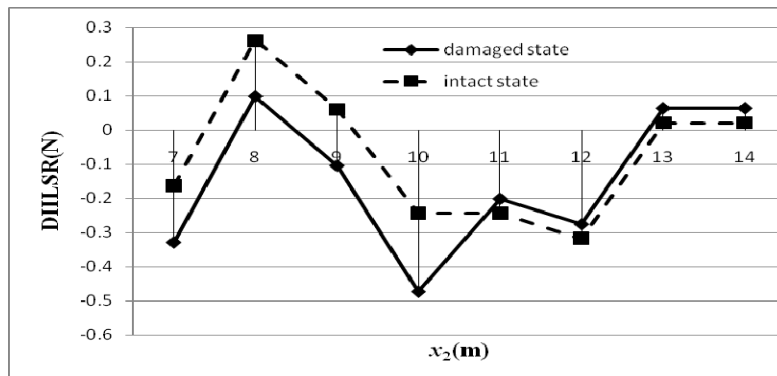
Figure 3 Data under intact state and damaged state

Figure 3 shows that due to uncertainty in geometric and material properties, the curve shape seems to be irregular. By comparing the two graphs, it can be observed that the slope of attachment line between point (x_2=10m) and its two adjacent points changes in the set of graphs, which means that damage occurs within the region [9m, 10m] or [90m, 91m]. This result coincides with the damage scenario.

Conclusions

DIILSR method has been demonstrated as an efficient tool for damage localization of two-span symmetrical continuous bridges. Though DIILSR always locates the damage with two symmetrical indications, it is easy to determine the true damage situation with the cooperation of inspection means.

In addition, according to the above analysis, one effective way to improve robustness is increasing the value of F. The magnitude of relative change in graphs will enlarge with the increase of F. Thus the damage is more discernible. The negative effect of resolution limitation and noise pollution can be decreased.

In future, for other kinds of bridges, similar index should be developed. The effect of measurement error should also be studied in detail. In addition, the practical way to load a bridge is with a 3-axle truck. When the bridge is to be loaded with a truck, how to modify the DIILSR method is needed to be studied.

Acknowledgement

References

Jang, J.H, Yeo, I, Chang, S.P. (2002). "Experimental investigation of system-identification-based damage assessment on structures." *J. Str. Eng.*, 128 (5), 673-682.

Kim, J.T, Park, J.H, Lee, B.J. (2007). "Vibration-based damage monitoring in model plate-girder bridges under uncertain temperature conditions." *Eng. Str.*, 29, 1354-1365.

Liu, X, Lieven, N.A.J, Escamilla-Ambrosio, P.G. (2009). "Frequency response function shape-based methods for structural damage localization." *Mech. Syst. Signal Proc.*, 23(4), 1243-1259.

Reynders, E, Roeck, G.D, Bakir, P.G, Sauvage C. (2007). "Damage identification on the Tilff Bridge by vibration monitoring using optical fiber strain sensors." *J. Eng. Mech.*, 2, 185-193.

Trentadue, B, Messina, A, Giannoccaro, N.I. (2007). "Detecting damage through the processing of dynamic shapes measured by a PSD-triangular laser sensor." *Inter. J. Solids Str.*, 44, 5554–5575.

Zaurin, R, Catba F.N. (2010). "Integration of computer imaging and sensor data for structural health monitoring of bridges." *Smart Mater. Str.*, 19, 1-15.

Numerical Simulation of PZT Bonded Reinforcement for Heath Monitoring of Reinforced Concrete Structure

Juan Yi[1], Wanjun Li[1], Fan Wu[1]

ABSTRACT

An active sensing diagnostic system using PZT for Structural Health Monitor of reinforced concrete has been currently under the investigation. As an embedded system, it is good for structural health monitoring of the locations that can't be easily accessed, such as bridge footing areas or piles. To fundamentally understand the damage algorithm, an accurate Finite Element Analysis (FEA) for the system has been performed. In the simulation model, the rebar with PZT and epoxy layers is built using 2D axisymmetric type. The analysis uses the direct coupled-field module. And material properties such as the Raleigh damping coefficients are discussed. The numerical model has been validated with the experimental testing. The good consistency between simulation and test shows that the model is reasonably accurate, which provides a base for further system optimization. A potential signal improvement method is explored. By changing PZT layout into different configuration, the output signal is increased four times larger than the original one. Further simulation analysis is made for concrete structure with debonding damage. The results from simulation are consistent with test ones. It shows that the output sensor's amplitude increases potentially with the debonding size.

KEYWORDS：Steel rebar, PZT, structural health monitoring, numerical modeling.

INTRODUCTION

The guided stress wave method uses time of arrival and amplitude change of signals to detect defects of a structure (Wu and Chang 2006, Song, Huang et al. 2008, Ha and Chang 2010). Although surface guided wave methods have been successfully applied for crack detection in concrete structures (Popovics, Song et al. 2000, Shin, Yun et al. 2007), less studies have been conducted for PZT-based guided waves on such structures. In fact, PZT elements are very suitable for integration into the concrete structures as an in-situ actuator/sensor because of the low cost and the stable properties. Recently, an active sensing diagnostic system using PZT for SHM of concrete structures has been under investigation (Wu and Chang 2006) .

The experimental tests have been conducted on scale down concrete beams (20in.

[1] Department of Civil Engineering, School of Naval Architecture, Ocean & Civil Engineering, Shanghai Jiao Tong University; Email: fanwu@sjtu.edu.cn; Tel: 13916926727

x4in. x4in.) with one #6 (0.75in.) steel reinforcement bar in the middle(Figure 1). PZT disks, as actuators and sensors, were bonded symmetrically onto the bar with silver epoxy. Actuators and sensors were placed on the bar with 16 in. (406.4mm) separation. A 90 kHz five-peak burst ultrasonic wave with a peak value of 200V was applied to the actuators.
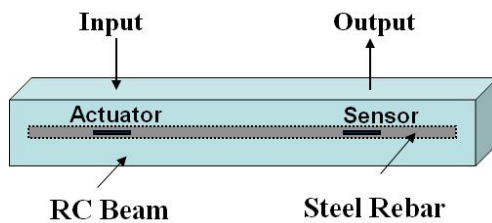

Figure 1. Reinforced concrete beam with PZT

The amplitudes and time of arrival of the first wave peak from sensors were recorded and analyzed(Bond 1982), and signal changes between the data of baseline and after the damage were evaluated (Figure 2). The narrow band five peak burst wave gets most energy of frequency concentrated at the center frequency. It controls well the wave dispersion while it propagates. Besides, changes in the waveform could be observed easily. Since the waveform is very sensitive to any anomalies in the wave propagating medium, this wave type has been frequently used in structural health evaluations (Bond 1982, Crawley and Anderson 1990, Berthelot, Ben et al. 1993).

Test results show that the crack /debonding damage in RC structures could be detected using such a PZT based active sensing diagnostic system. The amplitude of the sensor output increases as the extent of crack/debond increases (Wu and Chang 2006). And it is further found that signal's amplitude is exponentially increased with the damage size (Wu and Chang 2006). In this paper, numerical analysis and simulation for PZT bonded steel reinforcement bar has been investigated using ANSYS with accurate modeling. The ultimate goal is to find effective ways to improve the output signals, which is found too small to be used in the real application (Wu and Chang 2006).
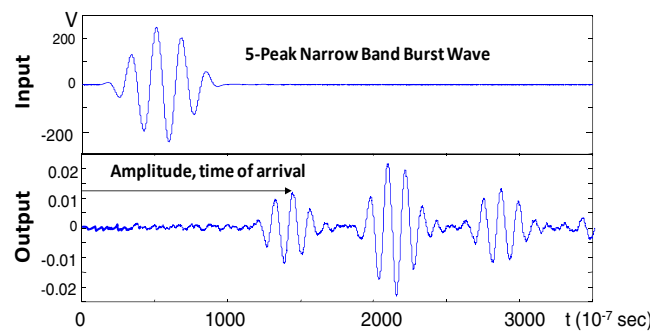
Figure 2. Test Wave and the Principle of SHM

REBAR NUMERICAL SIMULATION

Due to the complexity of concrete microstructure and PZT's coupling effect of structural and electrical fields, numerical simulation turns to be a good approach for providing theoretical guidance for such an SHM system. The commercial finite element software, ANSYS 14.0, is used for our work. During the simulation, the electromechanical coupled field module is selected, so that the actuating/sensing elements are directly loaded with electrical voltage signals. The analysis type used is the full transient dynamic analysis.

A partial mesh figure for the FE model of a steel reinforcement bar with PZT is shown in Figure 3. Using 2 dimensional (2*D*) axi-symmetric model type, the mesh consists 3 layers in vertical, i.e., steel bar, silver-epoxy and PZT. And the void between steel bar and PZT is also simulated. For this 2*D* axi-symmetric model, PZT is used PLANE223 coupled-field solid element. The steel bar and epoxy layer are used 2*D* PLANE82 element which is a structural solid element.

It is suggested that at least 20 elements exist for each wavelength along the direction of wave propagation (Bathe 1996, Wu and Chang 2006), in order to get converge of simulation results. In our model, a finer mesh has been used, and different mesh size on and around the PZT are applied for simulating the electric window effect (Fig. 3) (Wojcik, Vaughan et al. 1993). Input signal is added as voltage on the top nodes of the PZT actuator, and 0 voltage is applied on the bottom nodes of PZT actuators and sensors to simulate the grounding operation as in real application.

Rayleigh damping is selected in the simulation. Since the transient analysis uses ultrasonic waves with a central frequency of 90 kHz, the coefficient β is more related to the stiffness damping ratio ζ, which works more directly with high frequency. The stiffness matrix β cannot be given directly, it can be calculated through damping coefficient ζ_t using following equation(Eq.1) (Chopra 2005). Here ω_t is the *i*th model frequency of the structure.

$$\zeta_i = \frac{\alpha}{2\omega_i} + \frac{\beta\omega_i}{2} \qquad (1)$$

The coefficient ζ is initially defined as 0.0001, based on the reference(Cremer and Heckl 1988). The corresponding stiffness damping ratio β is 3.54 x 10^{-10}. Because of
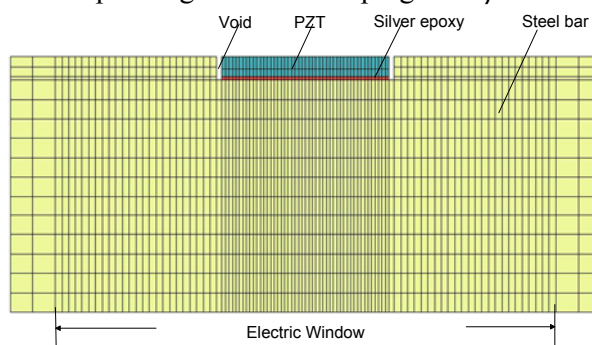

Figure 3. Mesh design of a steel rebar with PZTs (partial)

the numerical noise caused by the simulation, extra value is needed to depress the noise. The coefficient ζ used in the model is 0.003, and the corresponding β is 1x 10^{-8}.

VALIDATON

Validation for numerical model has been performed by adding 200V 90kHz 5-peak burst transient waves onto PZT actuators as the input load. The properties for PZT material are based on PZT-850 from American Piezo Corporation. The distance between sensors and actuators is 16in (406.4mm).

By analyzing the output results, it is found that the voltages on different nodes of PZT elements are different at one time moment. It shows a parabolic type of shape, with the middle point having a maximum value (Figure 4). This can be explained by the configuration of FE elements on PZT. Since there is a void between PZT and rebar (Figure 3), and PZT has been simulated with multiple elements, this leads to the voltage changes from boundary element to middle element to meet the boundary conditions and continuity. There is only one voltage value as sensor output in the test results. Therefore the upper surface voltage degree of PZT has to be coupled. The value has been taken as the output voltage of the sensors after coupling nodal degrees.

In the simulation, the extra damping has been added to depress the numerical noise. This causes the sensor's output from simulation being smaller than the real one. To compensate it, a parametric study between the sensor's output amplitude and the stiffness damping ratio β has been carried out. Because the signal amplitude is decayed exponentially with the distance(Gaydecki, Burdekin et al. 1992, Wu and Chang 2006), the relationship of amplitude and damping is curve-mapped using an exponential formula (Eq.2).

$$V = 0.0411e^{-7.511\times10^8 \times \beta} + 0.1196e^{-1.704\times10^7 \times \beta} \qquad (2)$$

The voltage got from the Eq. 2 is the value using the β without considering numerical noise.
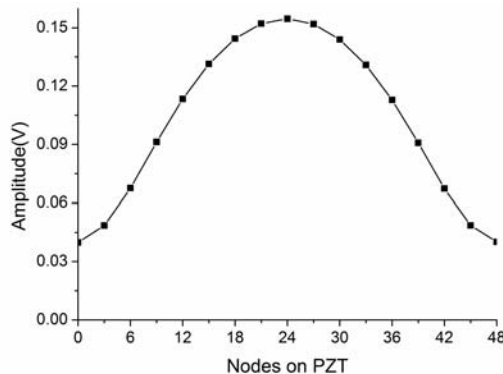
Figure 4 Voltage distributions on the nodes of PZT

The ratio of output from Eq. 2 and the numerical simulation is the amplification factor to be compensated. In the case here, the ratio is 1.6. By multiplying it with the numerical result and comparing it with the test result, it shows almost perfect match (Figure 5). This validates the FE model for a steel rebar with PZT is precise enough. Further parameter studies for signal improvement can be carried out on the model. From the time of arrival of the signals, the wave speed is about 4461m/s, which shows that it is longitudinal wave who dominates the propagation of waves in the rebar case.

MODEL OPTIMIZAION FOR SIGNAL IMPROVEMENT

The biggest problem found from the experimental test is the output from PZT sensors being too small. How to improve the strength of the signals becomes critical for this PZT based active diagnostic system. By analyzing the forces in the model simulated above, we've found that the waves arriving to PZT are carried out by the shear forces on the bottom of PZT surface, i.e., shear forces are transferred from rebar to epoxy layer then to the PZT. This is because PZT is bonded through silver epoxy on the surface of the rebar, and there are voids between PZT and the rebar.

One improvement of the model is to fill in the voids between PZT and rebar with solid material. The purpose is to let both normal stresses and shear stresses along the bar surface to carry out the waves to the PZT. By filling voids with silver epoxy, the simulation shows signal from sensors increased 4 times, as shown in Figure 6.

By analyzing the forces acting on the PZT, it shows that both normal stresses on the PZT thickness side and shear stresses at the PZT bottom have significant values, which proves that both type of forces contributing to the conversion of sensor output voltage. The wave speed is about 4470m/s, which is still longitudinal wave who dominates the propagation of waves in the rebar case. With preliminary optimization of the model, the output voltage from PZT increases significantly.
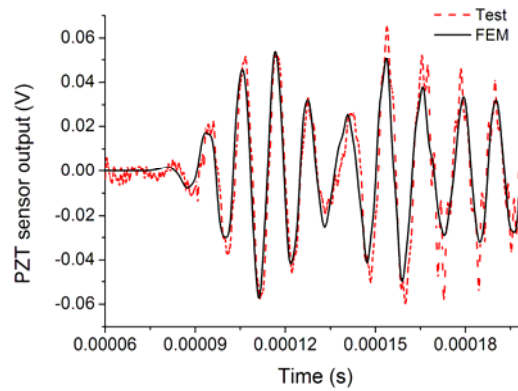
Figure 5 Signal comparisons of numerical simulation and the experimental test
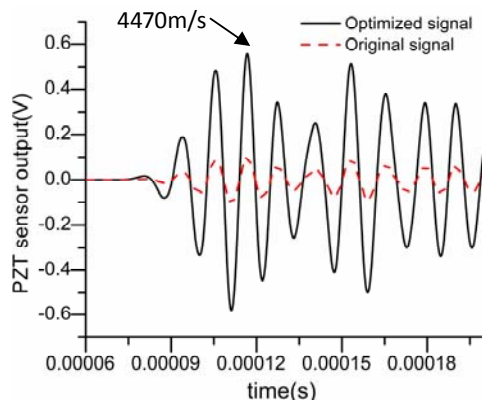
Figure 6 Signal comparisons of optimized and original signal

NUMERICAL SIMULATION FOR REINFORCED CONCRETE BEAM

Simulation of concrete with debonding damage has been performed, and debond was simulated as one layer of a void in concrete on the boundary of the steel bar. The debond size was changed from 1inch to 8inch, respectively, to simulate different debonding damage situation. As mentioned in previous rebar model, the concrete analysis also uses axis-symmetric modeling and full transient dynamics type. In order to simplify the model, concrete material was modeled as isotropic material. Due to complexity of concrete microstructure, a large amount of energy was dissipated during wave propagation. Hence, damping was applied to equivalent these energy loss. In the numerical simulation, material properties of concrete are explored. By referring to the published papers (Wu and Chang 2006, Song, Huang et al. 2008), the final properties used in the simulation are listed in the following table (Table1).

By comparing simulation with test results, it can be seen that the two sets are matched very well (Figure 7). It shows from simulation the stress waves disperse serious while they propagate on the rebar, and the propagation velocity become slower with the concrete surrounded on the rebar. This reflects that a large portion of energy is dissipated into concrete structure. From the simulation, it also shows that the amplitude increases exponentially with the debond size.

Table 1 Concrete Material Properties using in Simulation

Property constant (unit)	Value
Young's Modulus for Concrete E_c	2.8×10^{10}
Material Density for Concrete ρ_c (kg/m³)	2400
Poisson Ratio for Concrete ν_χ	0.2
Damping Ratio for Concrete β	1.5×10^{-7}
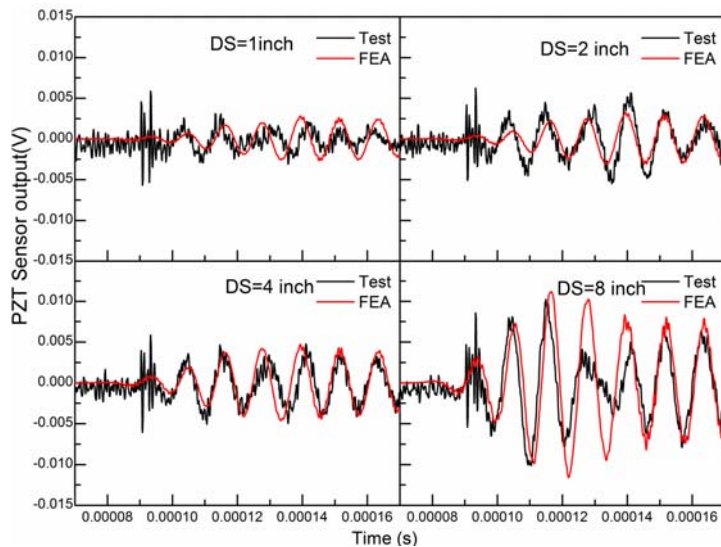
Figure 7 Signal comparisons of numerical simulation and the experimental test

CONCLUSIONS

In this paper, we've demonstrated the numerical simulation of a PZT bonded rebar, which is a key part of the active sensing diagnostic system for SHM of concrete structure currently under investigation. The simulation uses ANSYS software, and all of the material layers including steel rebar, silver epoxy and PZT have been simulated. The 2*D* axi-symmetric model with electromechanical coupled-field, full transient dynamic analysis type is applied for modeling and calculation.

The very good agreement between simulation and experimental tests shows that the wave propagation on the steel rebar can be precisely simulated. With preliminary optimization of the model, the output voltage from PZT increases significantly. Reinforced concrete structure with different debonding sizes is further modeled. The results show that sensor signals are increased exponentially with the debond size.

ACKNOWLEDGEMENT

REFERENCES

Bathe, K. J. (1996). *Finite Element Procedures.* 2nd edition, Prentice-Hall.
Berthelot, J.-M., S. M. Ben and J. L. Robert (1993). "Study of wave attenuation in concrete." *Journal of Materials Research.* 8(9): 2344-2353.
Bond, L. (1982). "Methods for the Computer Modeling of Ultrasonic Waves in Solids." *Research Techniques in Nondestructive Testing.* 6: 107 – 150.

Chopra, A. K. (2011). *Dynamics of Structures : Theory and Applications to Earthquake Engineering.*4th Edition Prentice Hall.

Crawley, E. F. and E. H. Anderson (1990). "Detailed Models of Piezoceramic Actuation of Beams." *Journal of Intelligent Material Systems and Structures.* 1(1): 14-25.

Cremer, L. and M. Heckl (1988). "Structure-Borne Sound."

Gaydecki, P. A., F. M. Burdekin, W. Damaj and D. G. John (1992). "The propagation and attenuation of medium-frequency ultrasonic waves in concrete: a signal analytical approach " *Measurement Science and Technology.* 3(1): 126-135.

Ha, S. and F. K. Chang (2010). "Optimizing a spectral element for modeling PZT-induced Lamb wave propagation in thin plates." *Smart Mater. Struct.* 19(1): 1-11.

Moharana, S. and S. Bhalla (2012). "Numerical investigations of shear lag effect on PZT-structure interaction: review and application." *Current Science.* 103(6): 685-696.

Popovics, J. S., W.-J. Song, M. Ghandehari, K. V. Subramaniam, J. D. Achenbach and S. P. Shah (2000). "Application of Surface Wave Transmission Measurements for Crack Depth Determination in Concrete." *Materials Journal.* 97(2): 127-135.

Shin, S. W., C. B. Yun, J. S. Popovics and J. H. Kim (2007). "Improved Rayleigh Wave Velocity Measurement for Nondestructive Early-Age Concrete Monitoring." *Research in Nondestructive Evaluation.* 18(1): 45-68.

Song, F., G. L. Huang, J. Kim and S. Haran (2008). "On the study of surface wave propagation in concrete structures using a piezoelectric actuator/sensor system." *Smart Mater. Struct.* 17(5): 1-8.

Wojcik, G. L., D. K. Vaughan, N. Abboud and J. Mould, Jr. (1993). "Electromechanical Modeling Using Explicit Time-Domain Finite Elements." *IEEE Ultrasonics Symposium Proceeding.* 2: 1107-1112.

Wu, F. and F.-K. Chang (2006). "Debond detection using embedded piezoelectric elements in reinforced concrete structures-part I: experiment." *Structural Health Monitoring.*5(1): 5-15.

Wu, F. and F. K. Chang (2006). "Debond detection using embedded piezoelectric elements for reinforced concrete structures-Part II: Analysis and algorithm." *Structural Health Monitoring.* 5(1): 17-28.

Reliability-based Safety assessment of Bridge Members on Monitored Live Load Effects

Zhijie Yuan[1], Congqi Fang*[2], Xila Liu, Shuai Yang

Abstract: In the decades, monitoring concepts for structural systems have been subjected to a rapid development process. They have become more and more important in the intervention planning (e.g., maintenance, repair) on new and existing structures. Nevertheless, there is still a strong need for the efficient use of structural monitoring data in the reliability assessment. In an extended sense, structural monitoring can be considered similar to quality assurance and acceptance sampling, since it is not practically possible to continuously monitor all performance indicators in all critical sections of an entire structural system. The aim of this paper is two folds: (a) The probability density of strain of sensors locations based on the monitoring data was researched; and (b) to shift the reliability index to the differentiation value. An illustration of the proposed approach is provided on Hongdao Bay Bridge located in Qingdao, China. The monitoring system has been working since 2011.

Keywords: Structural safety; Monitoring; Bridge Member; Reliability score

1. Introduction

Structural reliability analysis can be employed to calculate the probability of the limit state failure of structural members or structures at any time during their service life. Improvements of current structural safety evaluation practices that primarily rely on visual inspection are anticipated. Therefore, structural health monitoring (SHM) will be applied to more and more new and existing structures and infrastructures. There is a gap between SHM and bridge inspection and management methods so far (Frangopol, 2011; Glaser et al. 2007). In addition, SHM is focused primarily on damage detection, and bridge managers are focused on answers to serviceability and safety issues (Frangopol, 2008; Strauss et al. 2008; Catbas et al. 2008). As a result, evaluating the failure probability for main components based on long-term monitoring data becomes a key and urgent scientific research subject. The popular method to complete this task is using the reliability index.

This paper complements the previous study on the reliability estimation of long-span bridges (Frangopol, 2008), which aims to estimate the reliability for

[1] Department of Civil Engineering, Shanghai Jiao Tong University, Shanghai 200240, China, e-mail: yuanzhijiexue@126.com.
[2] Corresponding author. Department of Civil Engineering, Shanghai Jiao Tong University, Shanghai 200240, China, Tel: 021-34206727, e-mail: cqfang@sjtu.edu.cn.

stiffening girders of long-span cable stayed bridges using the monitoring data collected by SHM system. The variations of the monitored structural responses and component conditions from SHM data are also explicitly considered, and can be verified by statistical and probabilistic methods theories. Furthermore, compared to the hundred percentage point system, reliability index which is often used to reflect the degree of structure safety is more difficult to understand for bridge managers. A method for converting reliability index to a 100-point scale is proposed, which is validated in an actual bridge-Hongdao Bay bridge, in eastern China's Jiao zhou Bay.

2. Bridge Description

Hongdao Bay Bridge is a single pylon cable stayed bridge located in the Shandong province of China. It is a steel-box girder bridge with two-span of 240m. For safety assurance, a sophisticated long-term structural health monitoring system has been designed and implemented since June, 2011. Figure 1 gives the locations of strain sensors and temperature sensors in different girder segments. Each cross section consists 6 strain gauges and 6 temperature sensors.
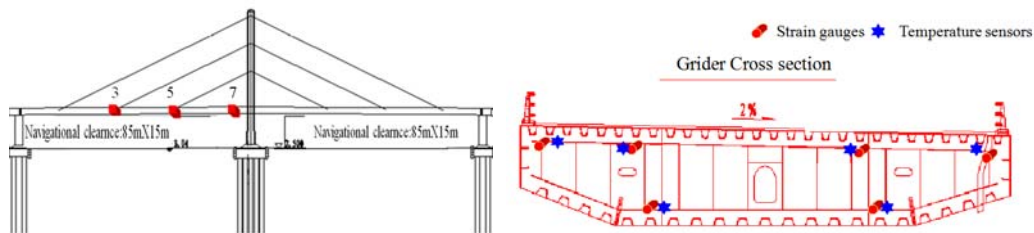
Figure 1. Location of sensors and strain gage layout of cross section

The sensors were designated as Sx-y and Tx-y, in which S stands for strain sensors, T stands for temperature sensors, x stands for the number of main girder cross section, and y stands for the number of sensor i.e. from left to right and top to bottom number the strain sensors sequentially from 1-6. For example, S3-2 stands for the second strain sensor on the upper plate of the third cross section of girder.

3. Reliability Analysis

3.1 Reliability Method

In general, two basic methods (FORM and SORM) are used to estimate the structural reliability. FORM was used for reliability analysis in this paper. The reliability index is defined as Eq. 1.

$$\beta = \frac{\left(\mu_R - \mu_Q\right)}{\left(\sigma_R^2 + \sigma_Q^2\right)^{1/2}} \qquad (1)$$

In Eq. 1 μ_R and μ_Q is mean resistance and mean load effect respectively, and σ_R

and σ_Q is standard deviation of the resistance and the standard deviation of the load effect, respectively. The resistance and load effects are not necessarily normally distributed, so the equivalent normal method is employed to transform the non-normal random variables into normal random variables. According to Unified Standard for Reliability Design of Highway Engineering Structures (GB/T50283-1999) (Ministry of Communications of the People's Republic of China 1999), the reliability index β was shown as Eq. 2.

$$
\begin{cases}
\beta = \dfrac{\sum_{i=1}^{n} \frac{\partial g}{\partial x_i}\big|_{P^*} \left(\mu_{x_i} - x_i^*\right)}{\left[\sum_{i=1}^{n} \left(\frac{\partial g}{\partial x_i}\big|_{P^*} \sigma_{x_i}\right)^2\right]^{1/2}} \\[4mm]
x_i^* = \mu_{x_i} + \beta \sigma_{x_i} \cos\theta_{x_i} \\[2mm]
\cos\theta_{x_i} = -\dfrac{\sum_{i=1}^{n} \frac{\partial g}{\partial x_i}\big|_{P^*} \sigma_{x_i}}{\left[\sum_{i=1}^{n} \left(\frac{\partial g}{\partial x_i}\big|_{P^*} \sigma_{x_i}\right)^2\right]^{1/2}} \\[4mm]
\mu_{x_i'} = x_i^* - \phi^{-1}\left[F_i(x_i^*)\right]\sigma_{x_i'} \\[2mm]
\sigma_{x_i'} = \dfrac{\varphi\left\{\phi^{-1}\left[F_i(x_i^*)\right]\right\}}{f_i(x_i^*)}
\end{cases}
\tag{2}
$$

x_i, x_i' are the non-normal random variable and equivalent normal random variables respectively; the mean value and standard deviation of x_i, x_i' are $(\mu_{x_i}, \sigma_{x_i})$ and $(\mu_{x_i'}, \sigma_{x_i'})$; $F_i(x_i^*)$, $f_i(x_i^*)$ represent the cumulative distribution function and probability density function of variable x_i at checking point x_i^*; $\phi^{-1}[.]$, $\varphi(.)$ indicate the inverse cumulative standard normal distribution function and standard normal.

3.2 Integration of SHM Data into Structural Safety Evaluation

For bridges installed structural health monitoring system, the strain responses of certain girder segments can be measured directly by the strain sensors. Supposing that the section plane remains a plane surface after bending, the moment of the i-th girder segment can be approximately calculated by the following Eq. 3 (Li, 2012):

$$
M = \frac{E_L I_{ni}\left(\varepsilon_{ui} - \varepsilon_{li}\right)}{y_{ui} + y_{li}}
\tag{3}
$$

where M indicates moment of the *i*-th girder segment; E_L represents the elastic

modulus ; I_{ni} represent the area and moment of inertia; ε_{ui} and ε_{li} demonstrate

the strain measurement of lower and upper flange; y_{ui} and y_{li} are the distances

from locations of upper, lower flange strain sensors to the inertia axis;

$E_L I_{ni} / \left(y_{ui} + y_{li} \right)$ indicates the coefficient associated with the *i*-th girder segment.

The moment calculated from measured strain is mainly caused by vehicle load. In this paper the bridge is supposed to be in an elastic stage, the coefficient remains a constant.

3.3 Convert Reliability index into Reliability scores

Compared to the hundred percentage point system, reliability index which is often used to reflect the degree of structure safety is more difficult to understand for bridge managers. A method for converting reliability index to a 100-point scale is proposed, shown as Eq. 4. According to the Code GB/T 50283-1999 (Ministry of Communications of the People's Republic of China 1999), the reliability index of highway bridges should be larger than 3.7. The bridge cannot meet the demand when the reliability index is lower than 3.7. Therefore, supposing that when reliability index equals 3.7, G equals to 60. In addition, supposing that when reliability index

equals β_i, which is the reliability index of the project that is just completed， G

equals to 100. For Hongdao Bay bridge was just completed, β_i was 7.7 when the

bridge was in perfect circumstances.

$$G = \begin{cases} (\beta-3.7)\times 15+60 & (0\leq\beta<3.7) \\ (\beta-3.7)\times 10+60 & (3.7\leq\beta\leq\beta_i)(\beta_i=7.7) \\ 100 & (\beta>\beta_i) \end{cases} \qquad (4)$$

Where G represents the Reliability scores, a scale of 0 to 100, the specific

classification of G is shown as table 1, β indicates reliability index, β_i is the

initial reliability index.

Table 1 the specific classification of G

score range of G	the health of the bridge	the appropriate action to take
[0,50]	dangerous	heavy repair, reinforce or rebuild
(50,60)	below standard	medium repair
[60,75]	qualified	minor repair and maintain after special testing
(75,90)	in good condition	minor repair and maintain
[90,100]	in perfect circumstances	maintain

4. Case study

The steel used in the main girders of Hongdao Bay Bridge is Q345D, with a mean value of 376 MPa and a standard deviation of 27 MPa. The nominal yield strength of this steel is 345 MPa. The sensors of the Hongdao Bay Bridge provided the strain ($\mu m / m$) level. In addition, the strain provided by strain sensors concluded the temperature strain. Therefore, the temperature strain should be subtracted.
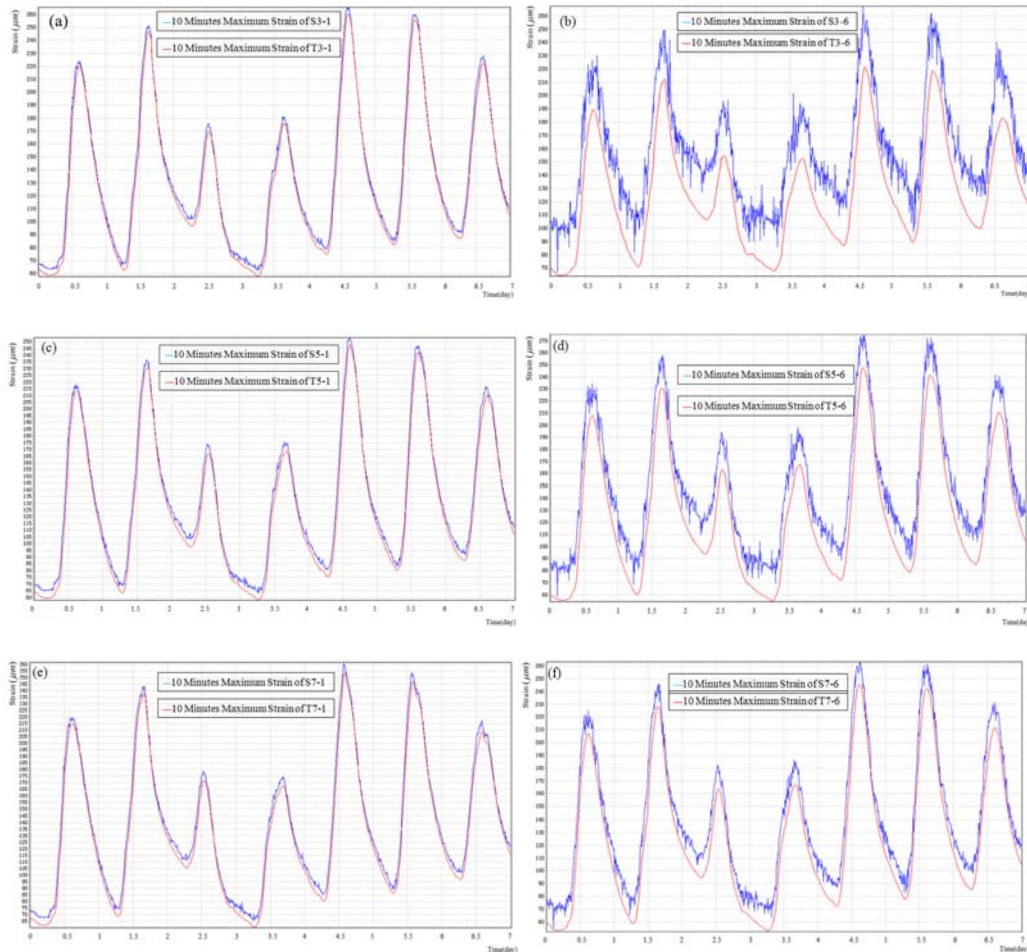
Figure 2. The 10 minutes maximum strain of strain sensors and temperature sensors

The 10 minutes maximum of the measured strains at different sensors of the 3, 5 and 7 cross section of main girder from 10th Sept 2013 to 17th Sept 2013 are shown in Fig. 2. Fig. 2 (a) (b), Fig. 2 (c) (d) and Fig. 2 (e) (f) is the strain of upper and bottom plate of cross section 3, 5 and 7 respectively. The strain of Sx-y not only concludes the strain of vehicle load, but also the strain of temperature load and wind load. In this study, temperature load and vehicle load are considered to be the two significant factors. Therefore, the strain of vehicle load was the difference between of Sx-y and Tx-y. In figure 2, the strain of upper plate of cross section 3, 5 and 7 was less than the bottom plate of cross section 3, 5 and 7.

The stress of vehicle load at different cross section was shown as figure 3 and table 2. It was observed that maximum stress of bottom plate at section 3 was 0.82 times larger than section 5 and 1.19 times larger than section 7. However, the maximum stress of upper plate at section 7 was largest. Besides, deviation of stress at section 5 was smallest, which may be caused for section 5 was located between mid-span section and tower.
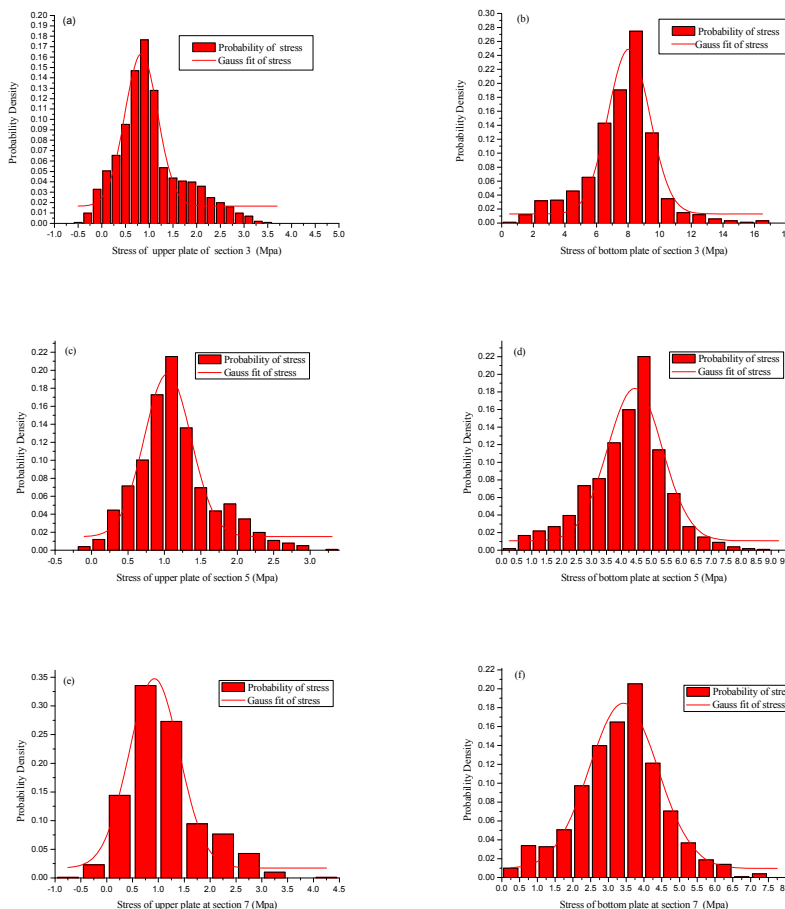
Figure 3. Stress of upper plate and bottom plate at different cross section

Table 2 Stress of different cross section

Section	Average stress of upper plate	Maximum stress of upper plate	Average stress of bottom plate	Maximum stress of bottom plate	Deviation of stress of upper plate	Deviation of stress of bottom plate
3	0.83298	3.4075	8.04534	16.3212	0.34596	1.31378
5	1.04455	3.33585	4.44839	8.9480	0.32065	0.91629
7	0.9201	4.095	3.42404	7.4634	0.48901	0.96326

According to the Hooke's law and Eq. 3, vehicle load-induced moment of cross sections was calculated, as shown in figure 4 and table 3. Vehicle load-induced moment of section 3 was 2.15 times of that of section 5, and 2.95 times of section 7.
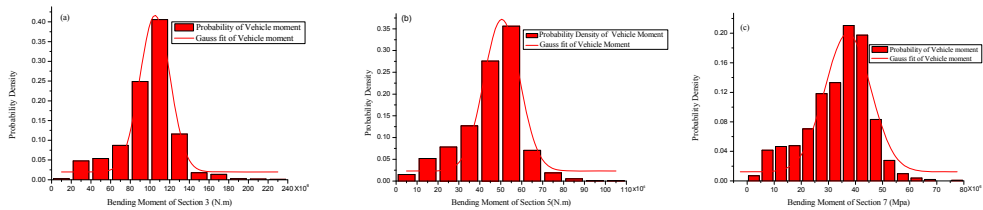
Figure 4. Vehicle load-induced moment of different section

Table 3 Vehicle load-induced moment of different cross section (10^6 N. m)

Section	Maximum Bending Moment	Average Bending Moment	Deviation of Bending Moment
3	230.59	105.13894	15.30298
5	107.36	50.51123	8.54214
7	78.12	37.18049	8.32895

Based on the Eq. 2 and Eq. 4, reliability index and score of different sections from 10th Sept 2013 to 17th Sept 2013 were calculated, as shown in figure 5. Most of reliability index of section was larger than 8.0, for the bridge was completed not long before. Minority of reliability index at section 3 was lower than 7.0, which was caused by section 3 was the mid-span section. In figure 5, reliability score reach 100 mostly, the smallest score of section 3 was more than 87.
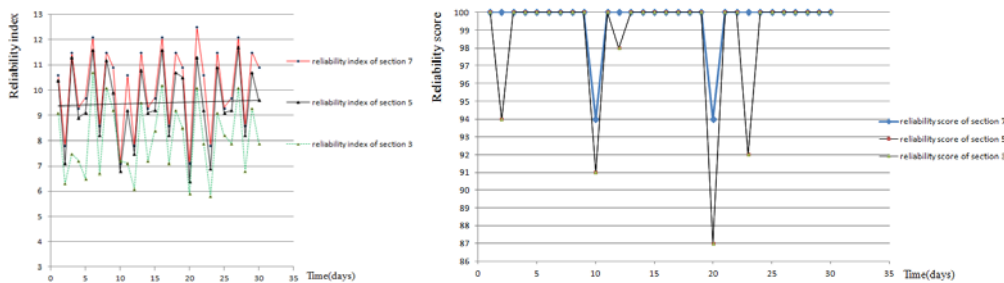
Figure 5. Reliability index and reliability score of different cross section

5. Conclusions

This paper integrated achievable SHM data into structural safety evaluation, and presented a novel approach to shift the reliability index to reliability score. An illustration of the proposed approach is provided on Hongdao Bay Bridge in Shandong, the reliability indices of the critical components (i.e. main girder) of the bridge are investigated. The following conclusions can be drawn from this study.

(1)For the structural responses of the structure, the vehicle loads and temperature loads can be collected by the SHM system. The measured strain can be approximately described as the Gauss process. The distribution of strain generated from the monitoring system would be helpful for reduction uncertainties related to the assumptions, which is necessary for the accurate reliability estimation of real and complicated cable-stayed bridges.

(2) The measured strain can be used to calculate moments at segments with sensors. The vehicle load-induced moments can be fitted by the Gauss process. Vehicle load-induced moment of section 3 was 2.15 times of that of section 5, and 2.95 times of section 7, which was for that section 3 was at the mid-span of bridge.

(3) The approach can effectively shift the reliability index to reliability score, which was easier to understand for bridge managers. Based on the method, reliability score of the main girder of Hongdao Bay Bridge reaches 100 mostly, the smallest score of section 3 was more than 87, which is consistent with facts.

6. Acknowledgements

References

Catbas F N, Susoy M, Frangopol Dan M. (2008). "Structural health monitoring and reliability estimation: long span truss bridge application with environmental monitoring data." *Engineering Structures*, 30(9): 2347-59.

Frangopol Dan M. (2011). "Life-cycle performance, management, and optimization of structural systems under uncertainty: accomplishments and challenges. Structure and Infrastructure Engineering." *Taylor and Francis*, 7(6): 389-413.

Frangopol Dan M, Strauss A, Kim S. (2008). "Bridge reliability assessment based on monitoring. " *Journal of Bridge Engineering*, ASCE, 13(3): 258-70.

Frangopol Dan M, Strauss A, Kim S. (2008). "Use of monitoring extreme data for the performance prediction of structures: general approach." *Engineering Structures,* Elsevier, 30(12): 3644-53.

Glaser SD, Li H, Wang ML, Ou J, Lynch J. (2007). "Sensor technology innovation for the advancement of structural health monitoring: a strategic program of US-

China research for the next decade." *Smart Structures and Systems,* 3(2): 221-44.

Li Hui, Li Shunlong, Ou Jinping, and Li Hongwei. (2012). "Reliability assessment of cable-stayed bridges based on structural health monitoring techniques." *Structure and Infrastructure Engineering.* 8(9), 829-845.

Strauss A, Frangopol Dan M, Kim S. (2008). "Use of monitoring extreme data for the performance prediction of structures: Bayesian updating." *Engineering Structures,* 30(12):3654-66.

Progressive Collapse Resistance of Braced Steel Frames Exposed to Fire

Jian Jiang,[1] Guo-Qiang Li,[2] and Asif Usmani[3]

ABSTRACT

OpenSees is an open-source object-oriented software framework developed at UC Berekeley. The OpenSees framework has been recently extended to deal with structural behaviour under fire conditions. This paper summaries the key work done for this extension and focuses on the application of the developed OpenSees to study the influence of fire scenarios and bracing system on the resistance of steel frames against fire-induced progressive collapse. Single and multi-compartment fire scenarios are applied. Additional horizontal and vertical restraints are applied to the frame to simulate the braced steel frame. A parametric study is carried out to find the fire-induced progressive collapse mechanisms of steel frames under various fire scenarios and restraining conditions. The collapse mode of frames is in the form of lateral drift and downward collapse of frames. It is proved that these two collapse nodes can be resisted by applying lateral and vertical restraint on the frame, respectively. The combination of two restraints has a better resistance effect.

KEYWORDS: progressive collapse; fire-induced; fire scenario; bracing system; OpenSees

1. INTRODUCTION

Since the Broadgate Phase 8 fire in London and the subsequent Cardington fire tests, researchers have began to investigate and understand the behaviour of whole composite steel-framed concrete structures in fire. Especially since the collapse of the Word Trade Tower (WTC) under terrorist attack on September 11, 2001, there has been considerable interest in understanding the collapse of tall buildings in fire. Quintiere et al. (2002) proposes the compression buckling of the truss rod as the main trigger to further collapse of the WTC towers. Usmani et al. (2003,2005) carried out a 2D numerical modelling of the WTC tower subjected to fire alone regardless of the damage caused by the terrorist attack. Ali et al. (2004) studied the collapse mode and lateral displacement of single-storey steel-framed buildings exposed to fire. Usmani (2005) proposed a possible progressive collapse mechanism for tall frames such as the WTC twin towers in fire. Fang et al. (2011) proposed multi-level system models for structures exposed to fire and two robustness assessment approaches namely temperature-dependent and temperature-independent approaches, respectively. Quiel and Marjanishvili (2012) used a multi-hazard approach to evaluate the performance a

---

[1] College of Civil Engineering, Tongji University, Shanghai 200092, China.
e-mail: jiangjian_0131@163.com
[2] State Key Laboratory for Disaster Reduction in Civil Enginering, Tongji University, Shanghai 200092, China. e-mail: gqli@tongji.edu.cn
[3] School of Engineering, the University of Edinburgh, Edinburgh EH9 3JF, United Kingdom. e-mail: asif.usmani@ed.ac.uk

damaged structure subjected to a subsequent fire. Fang et al. (2012) conducted a realistic modeling of a multi-storey car park under a vehicle fire scenario. Lange et al. (2012) proposed two collapse mechanisms of tall buildings subjected to fire on multiple floors. Sun et al. (2012a) carried out static-dynamic analyses of progressive collapse of steel structures under fire conditions using Vulcan. The same procedure was then used to study the collapse mechanisms of bracing steel frames under fire conditions (Sun et al. 2012b).
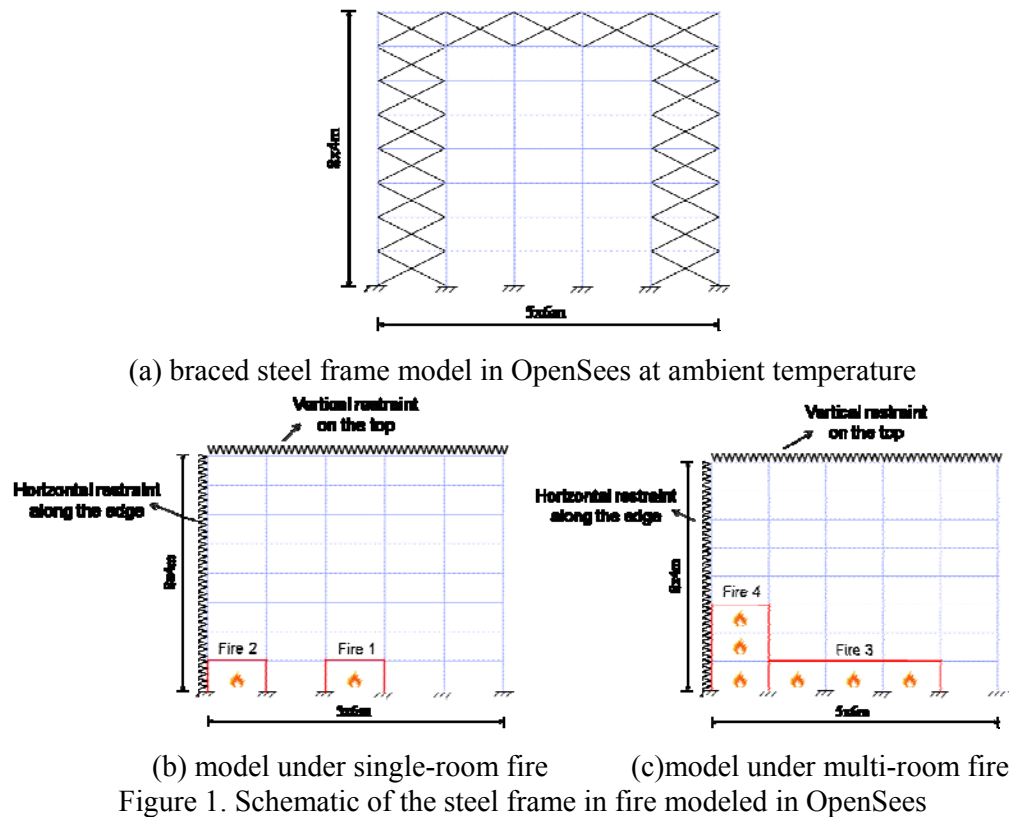
Many finite element program codes have been written to simulate the structural behaviour at elevated temperature and the results are compared well with the test data from Cardington test. These include specialist programs such as ADAPTIC, SAFIR, VULCAN and commercial package such as ABAQUS and DIANA. The specialist programs are cost-effective but lack generality and versatility because they are always developed to focus on some special feature of structural behaviour in fire. OpenSees is an open-source object-oriented software framework developed at UC Berekeley (McKenna 1997). OpenSees has so far been focussed on providing an advanced computational tool for analysing the non-linear response of structural frames subjected to seismic excitations. Given that OpenSees is open source and has been available for best part of this decade it has spawned a rapidly growing community of users as well as developers.

The framework OpenSees has been recently developed for thermomechanical analysis of structures and the class hierarchy and validation of the extended OpenSees can be found in references by the authors (Jiang 2012; Jiang et al. 2013). This paper presents its utilization to investigate the progressive collapse mechanism of steel frames under various fire scenarios and bracing system. Parametric studies are carried out by performing dynamic analysis in OpenSees to investigate the influence of the lateral and vertical restraints on the resistance of structures against progressive collapse.

2. DETAILS OF STEEL FRAMES STUDIED

The main objective of this paper is to investigate the progressive collapse mechanism of steel-framed structures under different fire scenarios and restraints conditions. Hence, considering both computational efficiency and structural representation, a 2D steel frame of five bays and eight storeys as shown in Figure 1 is modeled. Sun et al. (2012a) studied the mechanism of progressive collapse of a steel frame due to the failure of columns alone. Since a fire is usually initiated and developed in a compartment, both the beams and columns are heated together. Therefore, in this study, the authors decided to perform the analysis on the steel frame subjected to fire which thermal expansion effects of beams are considered. Uniform temperature distributions were assumed in all the heated columns and beams. The Newmark dynamic analysis method in OpenSees was carried out to study the behaviour of the steel frame under fire conditions. The Newmark parameters γ and β were taken as 0.8 and 0.45, respectively. Corotational geometrical transformation in OpenSees was used to consider the geometric nonlinearity. A series of cases have been conducted to deeply understand the collapse mechanisms of frames under multi-compartment fire and horizontal/vertical restraint conditons. A uniformly distributed load (UDL) of 40 kN/m were applied. The beams and columns comprising the frame is UB 305x165x40 and UC 254x254x89.

Eight and twelve elements were employed for beams and columns, respectively. Temperature dependent bilinear plastic material was used. The strain hardening is assumed to facilitate the convergence of the analysis. The modulus of elasticity and yield strength at ambient temperature are taken as 200 GPa and 280MPa, respectively. The properties of the steel material at elevated temperature were taken from Eurocode 3 (ENV 2005).


(a) braced steel frame model in OpenSees at ambient temperature

(b) model under single-room fire   (c) model under multi-room fire
Figure 1. Schematic of the steel frame in fire modeled in OpenSees

3. SINGLE-COMPARTMENT FIRE

A single-compartment fire is used in this case and it is located at the central bay and edge bay on the ground floor, respectively. Figure 2 shows the collapse mode of steel frames under these two fire conditions. For single-compartment fire, the failure mode is in the form of local downward collapse and global lateral drift of frames. The collapse is caused by the buckling of the heated columns but confined in a limited scope. The sway phenomenon of frames above the heated floors is driven by the tensile force generated in the heated beam under large deflection. The lateral drift of steel frames is expected to be resisted by adding lateral restraints along one sides of the frame and the failure modes are shown in Figure 3. Unfortunately, the lateral sway of frames is resisted at the expense of global collapse. The loads previously retained by the buckled heated columns are redistributed to the adjacent columns which cause their sequential buckling. In this way, the local damage on the heated column is spread to the surrounding parts of the frame and the structure fails in the form of global downward collapse mechanism.

For central bay fire, when there is vertical restraints on the top of the frame, the local damage is retained by the surrounding frames and no collapse happen as shown in

Figure 4a. In contrast, for edge bay fire as shown in Figure 4b, the whole frame sways away and cause buckling of all the columns on the ground floor.

Figure 5 shows the collapse mode of frames laterally and vertically restrained subject to the edge bay fire and no collapse occurs.
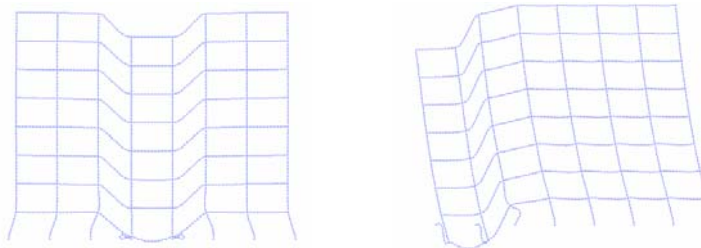
(a) Central by fire-Fire 1   (b) Edge bay fire - Fire 2
Figure 2. Collapse mode of frame without restraint under single-compartment fire
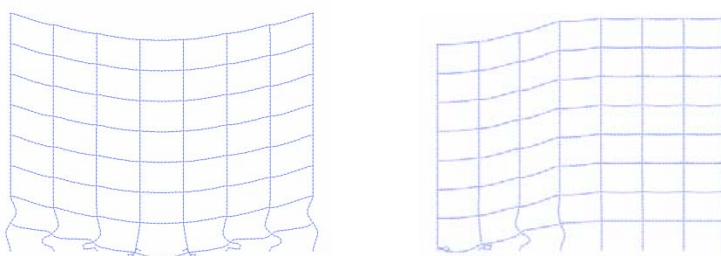
(a) Central by fire-Fire 1   (b) Edge bay fire - Fire 2
Figure 3. Collapse mode of frame laterally restrained alone under single-compartment fire
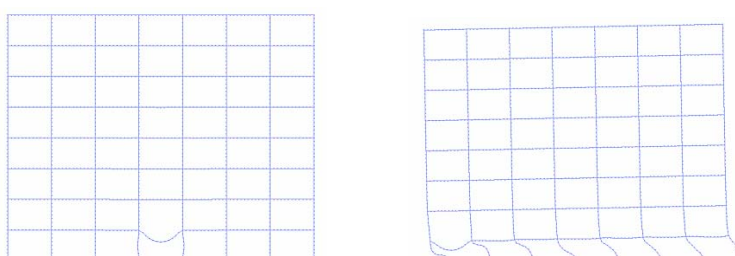
(a) Central by fire-Fire 1   (b) Edge bay fire - Fire 2
Figure 4. Collapse mode of frame vertically restrained alone under single-compartment fire
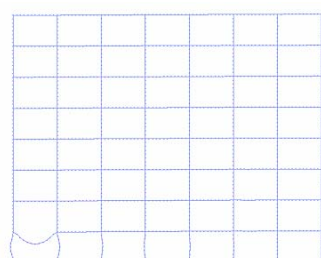
Figure 5. Collapse mode of frame laterally and vertically restrained under single-compartment fire at the edge bay

4. HORIZONTAL MULTI-COMPARTMENT FIRE

For a frame exposed to a single-compartment fire, the application of lateral and vertical restraints are of importance to resist its progressive collapse. In this section, the collapse mode of steel frames subject to multi-compartment fires is studied. In this case, a typical three-compartment fire is used and distributed horizontally. Figure 6 shows the collapse mode of steel frames under the three-compartment fire at the central bay and edge bay, respectively. Similar to the single-compartment fire, the local collapse of the frame is caused by the buckling of the heated columns. The lateral restraints added on the frame can resist the sway of the frame but cause a more severe failure model of global downward collapse (see Figure 7). On the other hand, it is interesting to note that the vertical restraint applied on the top of the frame under central by fire cause a drift of the heated floor which leads to the buckling of the columns on the ground floor as shown in Figure 8. The drift of the heated floor is driven by the tensile force formed in the heated beams due to its the catenary effect. Figure 9 shows the global downward collapse mode of frames with both lateral and vertical restraints.

(a) Fire 3 at central bay   (b) Fire 3 at edge bay
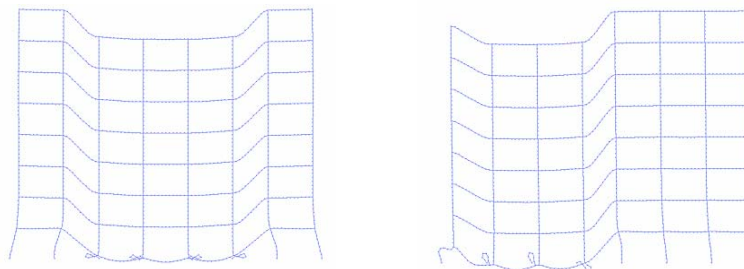
Figure 6. Collapse mode of frame without restraints under multi-compartment fire

(a) Fire 3 at central bay   (b) Fire 3 at edge bay
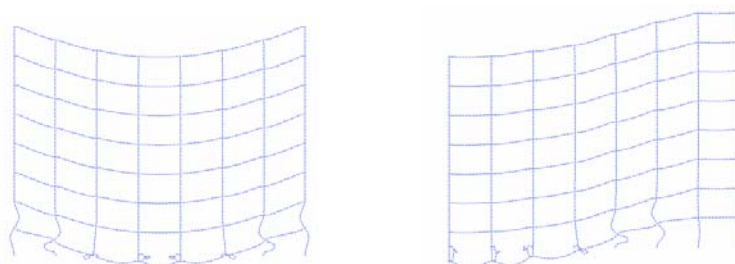
Figure 7. Collapse mode of frame laterally restrained alone under multi-compartment fire

(a) Fire 3 at central bay   (b) Fire 3 at edge bay
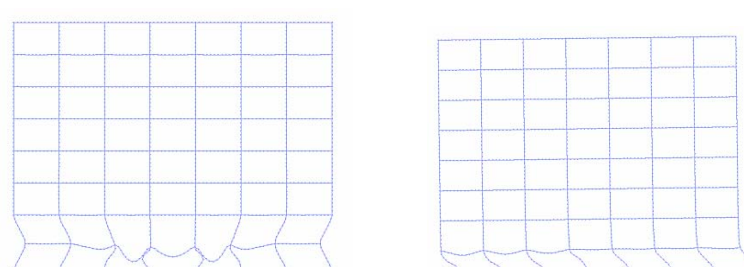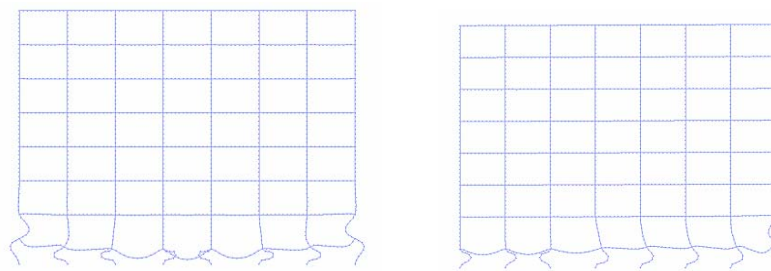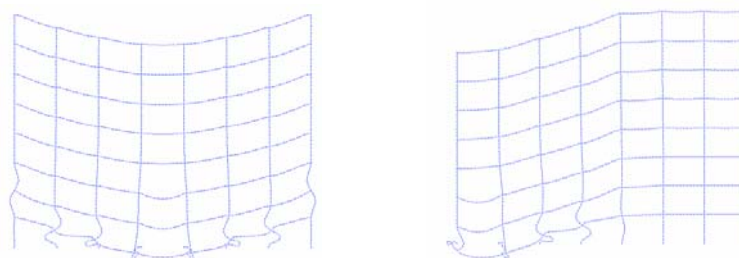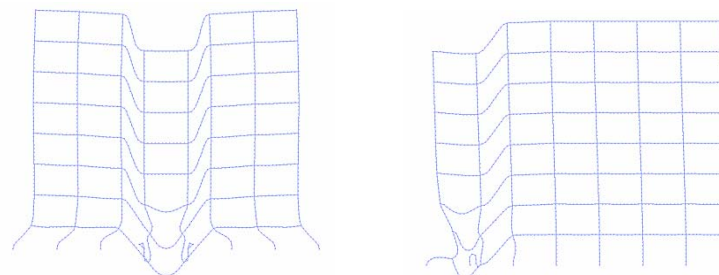
Figure 8. Collapse mode of frame vertically restrained alone under multi-compartment fire

(a) Fire 3 at central bay   (b) Fire 3 at edge bay
Figure 9. Collapse mode of frame laterally and vertically restrained under horizontal multi-compartment fire

5. VERTICAL MULTI-COMPARTMENT FIRE

This section presents the collapse mode of steel frames subject to vertical multi-compartment fires. Figure 10 shows the collapse mode of steel frames subjected to central bay fire and edge bay fire, respectively. Similar to the single-compartment and horizontal multi-compartment fire discussed above, the buckling of the heated columns leads to a downward collapse of the heated bay. The collapse of frames is unable to be resisted by either lateral restraints or vertical restraints applied alone as shown in Figure 11 and 12. The combination of the lateral and vertical restraints are helpful for resisting the progressive collapse of structures as shown in Figure 13.


(a) Fire 4 at central bay   (b) Fire 4 at edge bay
Figure 10. Collapse mode of frame without restraints under vertical multi-compartment fire


(a) Fire 4 at central bay   (b) Fire 4 at edge bay
Figure 11. Collapse mode of frame laterally restrained alone under vertical multi-compartment fire

(a) Fire 4 at central bay   (b) Fire 4 at edge bay
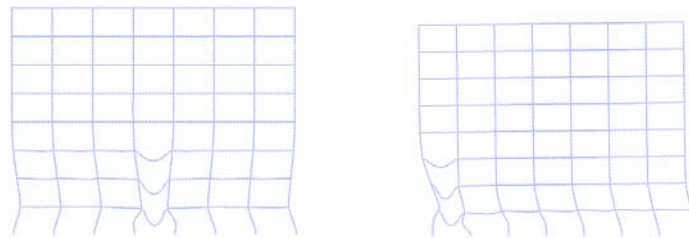
Figure 12. Collapse mode of frame vertically restrained alone under vertical multi-compartment fire

(a) Fire 4 at central bay   (b) Fire 4 at edge bay
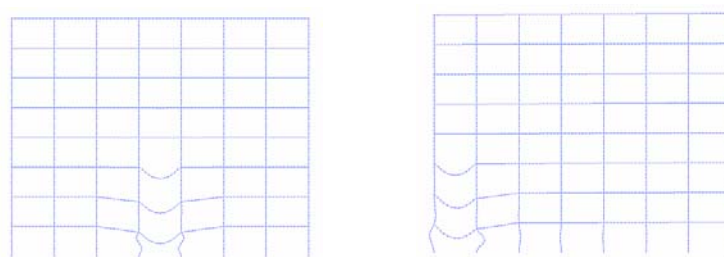
Figure 13. Collapse mode of frame laterally and vertically restrained under vertical multi-compartment fire

6. CONCLUSIONS

This paper presents the collapse mechanisms of steel frames exposed to single and multi-compartment fires. The influence of the lateral and vertical bracing on the resistance of structures against progressive collapse is studied. The conclusions can be drawn as follows:

1. The collapse of steel frames in fire is triggered by the buckling of the heated columns followed by sequent buckling of the columns at the same storey of the heated column or below.
2. The collapse mechanism of frames is in the form of lateral drift of the frame above heated floors and downward collapse of frames along the heated bay. The sway of frames is driven by the tensile force generated in the heated floor due to the catenary action of beams under large deflection.
3. The resistance of steel frames against progressive collapse can be enhanced by applying lateral and vertical restraint and the combination of these two restraints shows a better resistance than that of application alone.

ACKNOWLEDGEMENTS

REFERENCES

Ali, H.M., Senseny P.E., and Alpert R.L. (2004). "Lateral displacement and collapse of single-storey steel frames in uncontrolled fires." Engineering Structures, 26: 593-607.

ENV 1993-1-2. (2005). "Design of steel structures, Part 1.2: General Rules —— Structural Fire Design." Eurocode 3 Part 1.2.

Fang, C., Izzuddin, B.A., Elghazouli, A.Y. and D.A. Nethercot. (2011). "Robustness of steel-composite building structures subject to localized fire." Fire Safety Journal, 46: 348-363.

Fang, C., Izzuddin, B.A., Obiala R., Elghazouli, A.Y. and Nethercot D.A. (2012). "Robustness of Multi-storey Car Parks under Vehicle Fire." Journal of Constructional Steel Research, 75: 72-84.

Jiang Jian. (2012). "Nonlinear Thermomechanical Analysis of Structures using OpenSees." PhD Dissertation, University of Edinburgh, Edinburgh, UK.

Jiang, J., Jiang L.M., Kotsovinos P., Zhang, Jian., Usmani A.S., McKenna, F. and Li G.Q. (2013a). "OpenSees Software Architecture for the Analysis of Structures in Fire." Journal of Computing in Civil Engineering, (accepted).

Jiang J. and Usmani A.S. (2013b). "Modelling of Steel Frame Structures in Fire using OpenSees." Computers & Structures, 118: 90-99.

Lange D., Roben, C. and Usmani, A.S. (2012). "Tall Building Collapse Mechanisms Initiated by Fire: Mechanisms and Design Methodology." Engineering Structures, 36: 90-103.

McKenna, F. T. (1997). "Object-Oriented Finite Element Programming: Frameworks for Analysis, Algorithms and Parallel Computing." PhD thesis, University of California, Berkeley.

Quiel, S.E. and Marjanishvili S.M. (2012). "Fire Resistance of a Damaged Steel Building Frame Designed to Resist Progressive Collapse." Journal of Performance of Constructed Facilities, 26(4): 402-409.

Quintiere, J.G., Marzo, M.di, and Becher R. (2002). "A Suggested Cause of the Fire-induced Collapse of the Word Trade Towers." Fire Safety Journal, 37: 707-716.

Sun R.R., Huang Z.H. and Burgess I., (2012a). "Progressive Collapse Analysis of Steel Structures under Fire Conditions." Engineering Structures, 34: 400-413.

Sun R.R., Huang Z.H. and Burgess I. (2012b). "The Collapse behaviour of Braced Steel Frames Exposed to Fire." Journal of Constructional Steel Research, 72: 130-142.

Usmani, A.S., Chung Y.C., and Torero J.L. (2003). "How did the WTC Towers Collapse: A New Theory." Fire Safety Journal, 38:501-533.

Usmani, A.S., Flint, G.R., Jowsey A., Lamont S., Lane B., and Torero J. (2005). "Modelling of the collapse of large multi-storey Steel Frame Structures in Fire." Proceedings of the 4th International Conference on Advances in Steel Structures, pp. 991-998.

Usmani, A.S. (2005). "Stability of the Word Trade Center Twin Towers Structural Frame in Multiple Floor Fires." Journal of Engineering Mechanics, 131(6) : 654-657.

Performance Spectra-based Methodology for the Implementation of Supplemental Dampers in Buildings subjected to Earthquakes

Jack Wen Wei Guo[1] and Constantin Christopoulos[2]

Abstract

An overview of the performance spectra method is first provided. Using this method a 3-storey special moment resisting frame is then retrofitted with 4 different types of supplemental dampers to meet two different performance targets. The results of the nonlinear time-history analyses show that the trial damping designs obtained by the method were close to the initial performance targets without any design iterations. The performance spectra can underestimate the reduction in base shear due to higher mode effects. However, this can be corrected using the supplemental damping properties computed from the method. This design example demonstrates the effectiveness of the performance spectra procedure for producing trial performance-based designs using different types of supplemental damping devices.

Introduction

Seismic upgrade of low to medium-rise structures using supplemental damping has recently gained increased attention as reflected by its inclusion in the new design standards such as the ASCE-7 and ASCE-41. However, these standards focus on the analysis of damped structures rather than helping engineers select the optimum damping solution for a given performance target. To breach this gap, the Performance Spectra-based methodology (Guo and Christopoulos 2012a) utilizes damped nonlinear SDOF response curves called Performance Spectra to help engineers navigate through different damping systems to directly identify potential solutions or trial designs that meet or are close to meeting the performance targets at the onset of the design process. This paper uses design examples to illustrate how performance spectra can be used to compare and select the most suitable supplemental damping system for meeting different performance requirements.

---

[1]PhD Candidate, Department of Civil Engineering, University of Toronto, M5S 1A4, 35 St. George St, Toronto, Canada; PH (416) 978-6067; email: wen.guo@mail.utoronto.ca

[2] Professor, Department of Civil Engineering, University of Toronto, M5S 1A4, 35 St. George St, Toronto, Canada; PH (416) 978-6238; email: c.christopoulos@ utoronto.ca

Overview of performance spectra-based design methodology

Performance spectra (P-Spectra) are response curves of SDOF system equipped with supplemental dampers at different period and strength levels. Each individual P-Spectrum contains parametric plots of the system normalized base shear/acceleration, $R_a = A_D/A_E$ and normalized residual drift, $R_s = D_R/D_D$ against the normalized displacement, $R_d = D_D/D_E$ with respect to damping parameters that characterize a particular damping system. Here, D_D, A_D and D_R are the peak displacement, peak acceleration and residual displacement of the damped SDOF system, D_E and A_E are the peak displacement and peak acceleration of the undamped elastic SDOF system. Since the SDOF system acceleration is proportional to the base shear, R_a also represents the normalized base shear. However, except for viscous-viscoelastic dampers, the normalized restoring force $R_V = F_{RD}/F_{RE}$ is often a more useful for quantifying the base shear as it excludes the somewhat arbitrary inherent viscous damping force. Here, F_{RD} and F_{RE} are the system restoring force calculated by adding the restoring force from the base frame to the force generated by the dampers. P-Spectra are classified by the type of dampers considered. Besides the conventional hysteretic and viscous-viscoelastic dampers, P-Spectra can be extended to more advanced damping devices such as self-centering energy dissipating braces (SCED) (Christopoulos et al. 2008), and viscoelastic-plastic dampers (VEP), which were first studied by Kasai et al. (2007). P-Spectra can be generated either from nonlinear time-history analyses (NLTHA) or from an equivalent linearization procedure (Guo and Christopoulos 2012b). Figure 1 shows sample NLTHA P-Spectrum for each of the four types of damping systems.
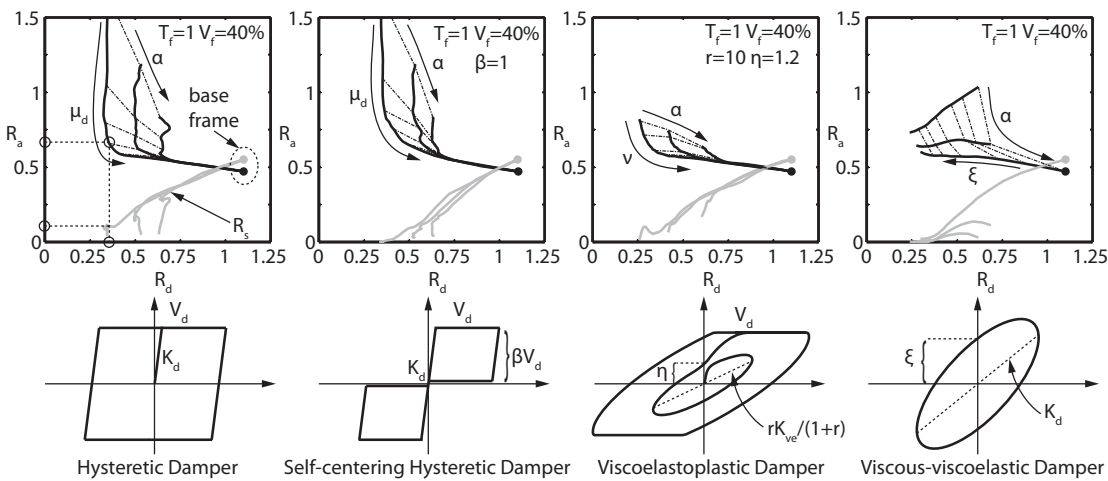
Figure 1: Sample P-Spectra for different types of supplemental damping systems

Each P-Spectrum in Figure 1 corresponds to a base frame fundamental period T_f and a normalized strength V_f as a percentage of the first mode contribution to the elastic base shear, V_E. The point in the dotted circle represents the inelastic response of the bare base frame. The arrows indicate how the damped response is influenced by increasing the

damping parameters, which are described below. The stiffness ratio α applies to all four different types of dampers and it is defined as $\alpha = K_f/(K_f + K_d)$, where K_f and K_d are the base frame stiffness and the stiffness of the damping system. The other damping parameter depends on the type of damping system considered: the damper ductility $\mu_d = K_d u/V_d$ is used for both hysteretic and SCED dampers; the viscous damping factor $\xi = T_f c/m\pi$ is used for viscous-viscoelastic dampers; the activation ratio $v = K_{ve}u/V_d$ is used for VEP dampers. Here, u is the system displacement, V_d is the damper activation load, c is the viscous constant, m is the system mass and K_{ve} is the stiffness of the viscoelastic component in VEP dampers. Figure 1 also defines the additional damping parameters that influence the response such as the SCED energy dissipation coefficient β, as well as the brace stiffness ratio r and the VE loss factor η for VEP dampers. Typical values of β, r and η are used for the SCED and VEP P-Spectra in Figure 1.

To use the P-Spectra for damper design, target first mode drift θ_t, base shear V_t and acceleration A_t need to be converted into first mode normalized targets R_d^1 and R_a^1:

$$R_d^1 = H_{eff}\theta_t/S_d(T_f); R_a^1 = \min\left(V_t/M_{eff}S_a(T_f), A_t/\Gamma_f\phi_n^1 S_a(T_f)\right) \tag{1}$$

Here, H_{eff} and M_{eff} are the first mode effective height and modal seismic mass; S_d and S_a are the spectral displacement and acceleration; Γ_f and ϕ_n^1 are the first mode participation factor and first mode shape roof ordinate. Next, modal combination is used to correct for higher mode effects in local drift and acceleration responses. The normalized targets $R_d^t = f_{hd}R_d^1$ and $R_a^t = f_{ha}R_a^1$ are used for design where

$$f_{hd} = \min\left(\frac{\theta_t}{\sqrt{(R_d^1\theta_i)^2 + \sum R_d^m\theta_{m,i}^2}}\right); f_{ha} = \min\left(\frac{A_t}{\sqrt{(R_a^1 A_i)^2 + \sum R_a^m A_{m,i}^2}}\right) \tag{2}$$

The higher mode drift and acceleration reduction factors R_d^m and R_a^m are assumed to be 0.6 and 0.63 for viscous type dampers based on 15% added damping and 1.0 for other types of dampers. Once the desired damping parameters are selected from the P-Spectra, a direct transformation procedure is applied (Guo and Christopoulos 2012b) to transforms the equivalent damped SDOF system into a damped MDOF system that achieves or is close to achieving the targeted normalized responses. For brevity, the readers are referred to the references for details of this procedure.

Design example

A 3-storey MRF designed only for strength (Ramirez et al. 2000) is retrofitted using different damping systems to illustrate the P-Spectra method. Design 1 uses hysteretic, linear viscous and SCED dampers to meet the 2% drift code requirement

under the design based earthquake (DBE) and 3.5% drift under the maximum considered earthquake (MCE) for collapse prevention. Design 2 targets a base frame with very minor yielding at DBE (1.5% drift) and is done using hysteretic, viscous and VEP dampers. Seven scaled records selected from the SAC steel project suite (Somerville et al. 1997) for 10% /50 years in Los Angeles were selected for time-history analysis. The records are scaled up by 1.5 to represent the MCE level seismic hazard. Figure 2 shows the 3-storey structural model and the ground motion suite.
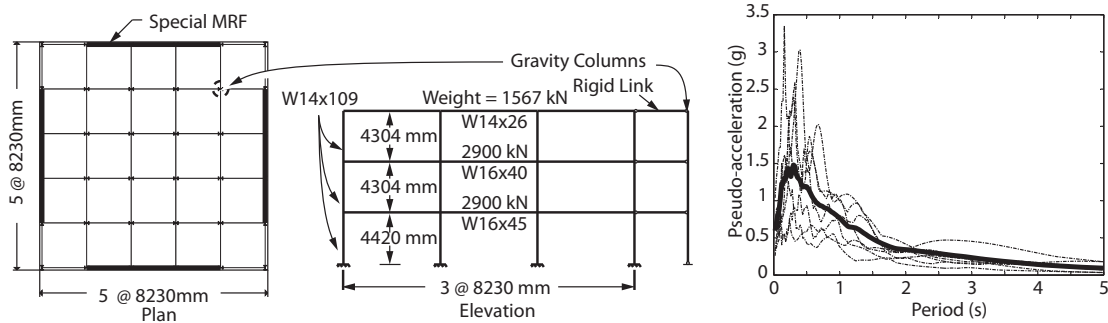

Figure 2: 3-storey MRF and DBE ground motions

Figure 3 and 4 show the NLTHA P-Spectra for Design 1 (Hysteretic, SCED with $\beta = 1$ and Viscous-viscoelastic dampers) and for Design 2 (Hysteretic, VEP with $r = 10$; $\eta = 1.2$ and viscous-viscoelastic dampers). The P-Spectra were generated for a period $T_f = 1.7sec$ and normalized strength $V_f = 50\%$ and 33%, which correspond to the fundamental period and the strength of the MRF at DBE and MCE, respectively. These values were obtained by an eigenvalue and a pushover analysis using the first mode shape.
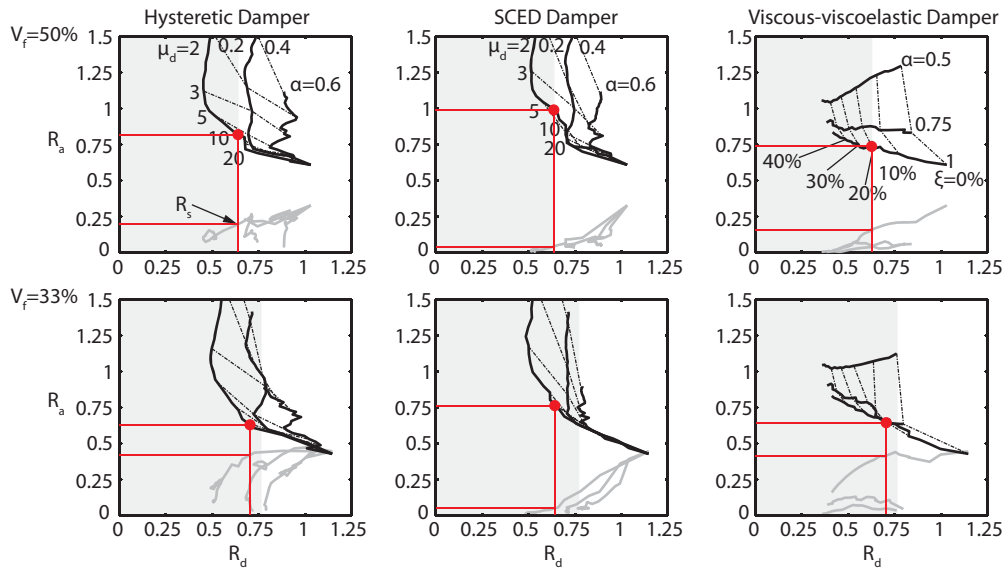

Figure 3: P-Spectra solutions for Design 1 at DBE and MCE

For Design 1, the normalized drift targets R_d^t computed using (1) and (2) are 0.65 at DBE and 0.76 at MCE. Figure 3 shows that all solutions are able to meet the drift

targets at DBE and MCE indicated by the shaded regions in the P-Spectra, although the SCED system requires somewhat larger supplemental force to do so due to reduced energy dissipation of the flag-shape hysteresis. However, the clear advantage of the SCED systems is the suppressed residual drift at both hazard levels.
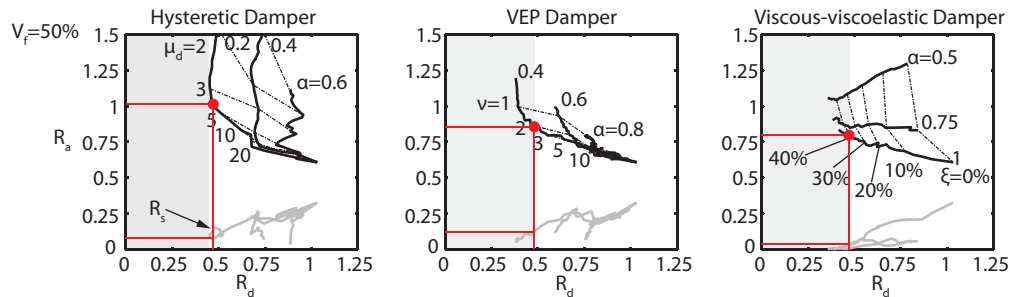
Figure 4: P-Spectra solutions for Design 2 at DBE

For Design 2, the required drift target for hysteretic dampers is $R_{d-t} = 0.43$. The target for VEP and viscous dampers is $R_{d-t} = 0.49$ because the higher mode contributions are smaller for supplemental viscous damping. From the P-Spectra in Figure 4, the hysteretic solution is actually slightly greater than the 1.5% drift target. Furthermore, since the solution lies in a region where R_a rapidly increases with decreasing R_d, the base shear required for the hysteretic system is very large. On the other hand, the R_a for the viscous solution is much smaller for the same R_d since the force in the damper is out-of-phase with the restoring force in the frame. However, the viscous solution requires $\xi = 40\%$, which can lead to large forces in the damper and connecting elements. Finally, the base shear/acceleration for VEP systems lie between the previous two solutions, and is closer to the viscous solution. The difference between VEP and the viscous system is that the former has a fuse mechanism which caps off the forces in the damper which may lead to more economical designs. The corresponding damping parameters that satisfies the drift targets for Design 1 and Design 2 are summarized in Table 1.

Table 1: Summary of solutions that meet DBE drift targets

Damping System	Design 1			Design 2		
	Hysteretic	SCED	Viscous	Hysteretic	VEP	Viscous
	$\alpha = 0.2$	$\alpha = 0.2$	$\alpha = 1.0$	$\alpha = 0.2$	$\alpha = 0.4$	$\alpha = 1.0$
	$\mu_d = 13$	$\mu_d = 7$	$\xi = 20\%$	$\mu_d = 3.5$	$\nu = 2$	$\xi = 40\%$

The Design 1 solutions in Table 1 were also verified for the MCE drift targets using the P-Spectra for MCE. For this example, the DBE is the governing scenario and the design is carried out based on the P-Spectra with $V_f = 50\%$. Table 2 summarizes the lateral supplemental damping properties obtained from the SDOF to MDOF transformation procedure in the reference.

Using OpenSees (McKenna et al. 2000), the frame in Figure 2 is analyzed for each earthquake in the suite and the normalized roof displacement, base shear, storey

acceleration and roof residual drift are compared to the P-Spectra targets in Table 3. Table 3 shows that the normalized displacement responses agree very well with the target for all solutions. The normalized base shear and accelerations are generally overestimated by the P-Spectra by about 15%. The main reason for this result is (in contrast to the elastic response of the base frame) that the higher mode contributions to the base shear in the damped systems are suppressed due either to the cap-off of the shear forces (Hysteretic, SCED and VEP) or to added damping in higher modes (Viscous and VEP). Instead of using R_a and R_V which are influenced by the higher modes of the elastic structure, an accurate base shear can be obtained using the damper properties in Table 2. Figure 5 and 6 summarize the average displacement, base shear, acceleration and residual responses for Designs 1 and 2.

Table 2: Summary of damper distribution for Designs 1 and 2

Storey	Design 1					Design 2				
	Hysteretic		SCED		Viscous	Hysteretic		VEP		Viscous
	K_d*	V_d**	K_d	V_d	C_d***	K_d	V_d	K_{VE}	V_d	C_d
3	25.8	141	25.8	257	0.73	25.8	373	9.5	253	1.46
2	60.6	331	60.6	605	1.32	60.6	878	24.6	642	2.64
1	69.1	389	69.1	712	2.32	69.1	1032	24.0	655	4.64
	*stiffness in kN/mm **activation loads in kN ***viscous constants in kNs/mm									

Table 3: Comparison of global performance for Design 1 and Design 2

	Design 1 (DBE targets)						Design 2 (DBE targets)					
	Hysteretic		SCED		Viscous		Hysteretic		VEP		Viscous	
	Tar.	Act.	Tar.	Act.	Tar.	Act.	Tar.	Act.	Tar.	Act.	Tar.	Act.
R_d	0.64	0.60	0.64	0.62	0.63	0.68	0.46	0.49	0.48	0.50	0.49	0.52
R_a	0.82	0.68	0.99	0.84	0.72	0.59	1.05	0.79	0.86	0.63	0.78	0.66
R_V	0.73	0.65	0.89	0.77	-	-	0.99	0.87	0.82	0.71	-	-
R_s	0.20	0.09	0.04	0.03	0.16	0.10	0.08	0.09	0.13	0.12	0.04	0.05
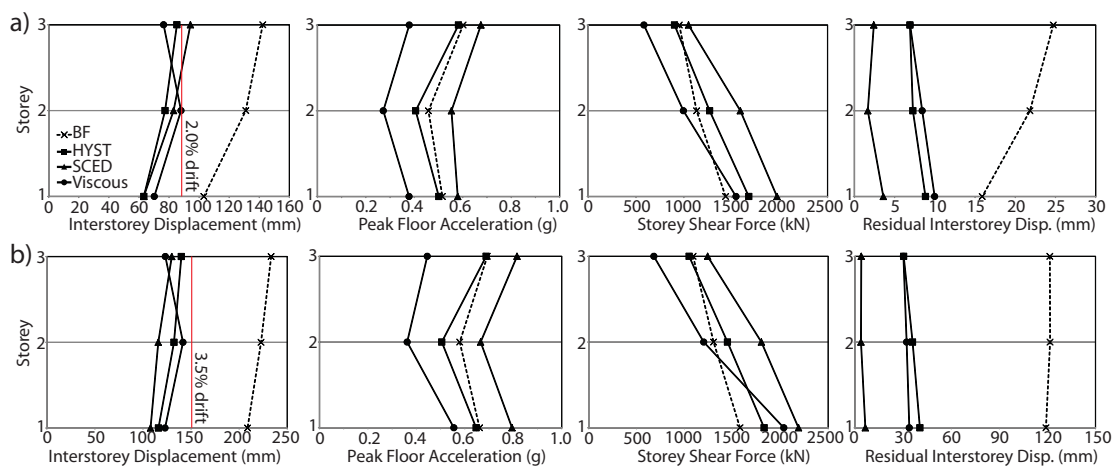
Figure 5: Summary of Design 1 response at a) DBE and b) MCE

Figure 5 shows that all three damping systems in Design 1 achieve the 2% drift at DBE and 3.5% at MCE, as they were designed to do. This illustrates that different kinds

of supplemental dampers are able to provide similar drift reduction. The viscous system has the smallest base shear and acceleration due to the phase lag in damper forces and large higher mode damping. On the other hand, since the flag-shape SCED hysteresis dissipates less energy than hysteretic dampers with the same activation load, it requires a larger damper force to achieve the same displacement reduction, which lead to higher base shear and acceleration response. However, the biggest advantage for the SCED system is its ability to suppress residual drifts even at MCE level hazard. In fact, the SCED system is the only solution that has less than 0.5% residual drift at the MCE, which according to previous studies (McCormick et al. 2008, Erochko et al. 2010) is the limit for post-disaster reparability.
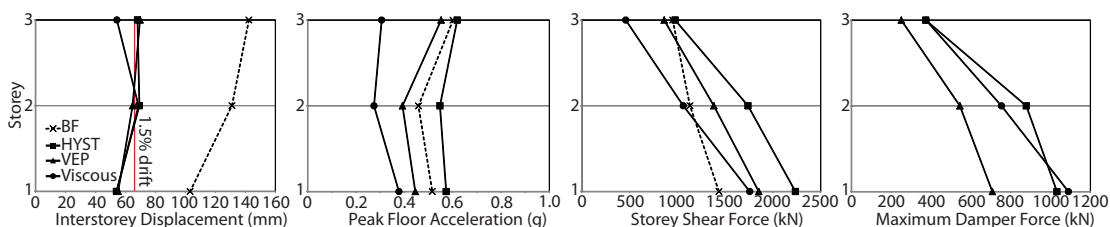

Figure 6: Summary of Design 2 at DBE

Figure 6 shows that the drift performances are very similar amongst the three systems in Design 2. The viscous solution has the smallest peak floor acceleration, followed by the VEP system and then the hysteretic system. A similar trend is observed for the base shear. The advantage of the VEP system however, is most clearly demonstrated by the peak damper force plot in Figure 6. Both hysteretic and viscous dampers require significantly larger design forces, though for different reasons: the hysteretic solution requires a large damper force because the P-Spectrum lies on a branch where R_a increases rapidly with decreasing R_d, where as the viscous solution requires a large damper force because of a large viscous constant. Although in this case, using multiple viscous dampers in the same storey can reduce the force, but for taller frame structures the peak damper force increases quickly and can easily approach the physical limits for supporting elements. In contrast, since VEP dampers have much larger damping than hysteretic dampers at low v due viscoelastic energy dissipation, it can achieve the same displacement reduction with a lower activation load. Under large excitations, the fuses activate and limit the peak damper force.

Conclusion

Using the P-Spectra method, a 3-storey special moment frame is retrofitted using 4 different types of damping systems to meet the code drift requirements and an enhanced performance requirement. Time-history analyses demonstrate that all dampers achieve similar peak drift responses with distinctly different force, acceleration and residual drift responses, as predicted by the P-Spectra at the onset of the design process. The examples demonstrate how P-Spectra can be used to select designs tailored to a specific set of

performance requirements. Due to higher mode influence, the P-Spectra can overestimate the normalized reduction in the base shear and accelerations, in this case, by 15%-20%. However, the correct base shear of the damped structures can be directly calculated using the supplemental damping properties obtained using the design procedure without running time-history analysis. Finally, the limitation of the P-Spectra predictions to global responses indicates that there is a need for further investigation on more accurate prediction of local responses.

References

Somerville, P., Smith, N., Punyamurthula, S., Sun, J. (1997). *Development of Ground Motion Time Histories for Phase 2 of the FEMA/SAC Steel Project*. SAC Joint Venture, Richmond, California.

Ramirez, O.M., Constantinou, M.C., Kircher, C.A., Whittaker, A.S., Johnson, M.W., Gomez, J.D. (2000). *MCEER-00-00: Development and Evaluation of Simplified Procedure for Analysis and Design of Buildings with Passive Energy Dissipation Systems*. Buffalo, New York.

McKenna, F., Fenves, G. L., Scott, M. H., and Jeremic, B., (2000). Open System for Earthquake Engineering Simulation (OpenSees). Pacific Earthquake Engineering Research Center, University of California, Berkeley, CA

Kasai, K. Minato, N., Sakurai, K. (2007). "Passive control design method based on tuning of equivalent stiffness of visco-elasto-plastic dampers." *AIJ J. Struct. Constr. Eng.* 618, 23-31. (In Japanese)

Christopoulos, C., Tremblay, R., Kim, H., and Lacerte, M. (2008). "Self-Centering Energy Dissipative Bracing System for the Seismic Resistance of Structures: Development and Validation." *J. Struct. Eng.* 134, SPECIAL ISSUE: Design and Analysis of Structures with Seismic Damping Systems, 96–107.

McCormick, J., Aburano, H., Ikenaga, M., Nakashima, M. (2008). "Permissible residual deformation levels for buildings structures considering both safety and human elements." *Proc. 14th World Conference on Earthquake Engineering*. Beijing, China.

Erochko, J., Christopoulos, C., Tremblay, R., and Choi, H. (2011). "Residual Drift Response of SMRFs and BRB Frames in Steel Buildings Designed according to ASCE 7-05." *J. Struct. Eng.*, 137(5), 589–599.

Guo, J.W.W., Christopoulos, C. (2012). "Performance spectra based method for the seismic design of structures equipped with passive supplemental damping systems." *Earthquake Engineering and Structural Dynamics*. 42(6), 935-952.

Guo, J.W.W., Christopoulos, C. (2012). "A procedure for generating performance spectra for structures equipped with passive supplemental dampers." *Earthquake Engineering and Structural Dynamics*. 42(9), 1321-1338.

Self-Centering Energy-Dissipative (SCED) Brace:
Overview of Recent Developments and Potential Applications for Tall
Buildings

J. Erochko[1] and C. Christopoulos[2]

Abstract

The self-centering energy-dissipative (SCED) brace is an innovative cross-bracing system that eliminates residual building deformations after an earthquake while simultaneously dissipating energy to reduce drifts. Several recent studies are summarized which have confirmed and extended the capabilities of SCED braces. These include a multi-storey SCED frame shake table test, a high axial-capacity SCED brace prototype and a telescoping configuration called the T-SCED brace which greatly increases axial elongation capacity. These recent advancements have improved the desirability of SCED braces for use in high-rise structures because the braces can now better accommodate the larger forces and elongations prevalent in tall buildings. SCED braces may also provide an increased level of performance compared to other damping systems for tall buildings because they are designed to return a structure to its original undeformed position after an earthquake. This paper reviews several potential configurations for the use of SCED braces in tall buildings including the use of SCED braces in tall braced frames, coupled with shear walls and with vertical outriggers.

Introduction

The self-centering energy-dissipative (SCED) brace is a high-performance cross-brace for structures (Christopoulos et al., 2008). It combines energy-dissipation through the use of friction, hysteretic or viscous damping, with post-tensioning tendons that provide a restoring force that self-centers the brace (Christopoulos et al. 2008). This restoring force eliminates residual drifts in the building, making it more likely that the building will be useable after an earthquake. Recently, this brace concept has been extended and verified through a number of related projects. The first part of this paper will summarize these projects which extend the state-of-the-art in self-centering braces.

---

[1] Assistant Professor, Department of Civil and Environmental Engineering, Carleton University, 1125 Colonel By Drive, Ottawa ON, Canada, K1S 5B6. E-mail: jeffrey.erochko@carleton.ca
[2] Professor, Department of Civil Engineering, University of Toronto, 35 St. George Street, Toronto, ON, Canada, M5S 1A4. E-mail: c.christopoulos@utoronto.ca

The second part of this paper will discuss potential applications of this newly improved brace technology for the design of tall building structures. In particular, the newly increased axial load and axial deformation capacity of the braces makes them better able to accommodate the demands of tall buildings. Although SCED braces are naturally well-suited to use within tall braced-frame structures, they may also be used as in other configurations to provide the restoring force capacity to self-center a structure. Proposed tall building configurations that utilize SCED braces in different ways will be discussed towards the end of the paper.

The Self-Centering Energy-Dissipative (SCED) Brace Concept

The mechanics of the SCED brace are fully described by Christopoulos et al. (2008) and are summarized briefly here. The SCED brace consists of four main elements as shown in Figure 1. The inner and outer members are axial elements that are connected at opposite ends of the brace. In the figure, the inner is connected to the left side only and the outer is connected at the right side only. Via a pair of floating end plates, the tendons abut the inner and outer member ends on each side. These tendons are pretensioned and provide a positive restoring force to the system. As shown in the figure, when a tension or compression force is added to the brace, the tendons always experience an increase in strain over and above the strain that was caused by the initial pretension force. In addition to the inner and outer members and the tendons, an energy dissipating device is also included in the brace, This device provides energy dissipation using either a hysteretic (yielding/friction), viscous, or shape memory alloy mechanism that is activated based on the relative movement of the inner and outer members.

The resulting hysteretic response of the SCED brace is shown on the right side of Figure 1. This type of hysteretic response is common for self-centering systems and is generally called a 'flag-shaped' hysteresis.

Recent Extensions of the SCED Brace Concept

Four related projects have recently been carried out to extend the SCED brace concept. First, a shake table test of a three storey braced frame with SCED braces showed that the multi-story frame behaved as expected and could be accurately modelled (Erochko et al., 2013). Then, a high-capacity brace prototype was constructed to confirm that the SCED brace concept could be scaled up for use in taller buildings. Last, the elongation capacity of the SCED brace was improved through the development of an innovative telescoping brace configuration called the T-SCED (Erochko et al., 2012).

Confirmed Dynamic Multi-story Behaviour (Erochko et al. 2013)

A shake table test of a three story, one-third scale SCED braced frame was recently conducted in the structural laboratory at the Ecole Polytechnique in Montreal, Canada. The goal of this test was to confirm the behavior of SCED braces within a multi-story frame context. The laboratory setup for this test is shown in Figure 2.

The shake table test frame was subjected to a suite of twelve ground motions, including both design basis earthquake (DBE) and maximum-considered earthquake (MCE) excitations. In parallel with the dynamic testing, dynamic nonlinear models of the tests were built using OpenSees (McKenna et al., 2000) and SAP2000 (Computers and Structures Inc., 2009). Examples of the hysteretic response of the first story SCED brace

for two of the shake table tests is shown in Figure 3, with the model results also shown for comparison. As this figure shows, both models were able to replicate the test results well.
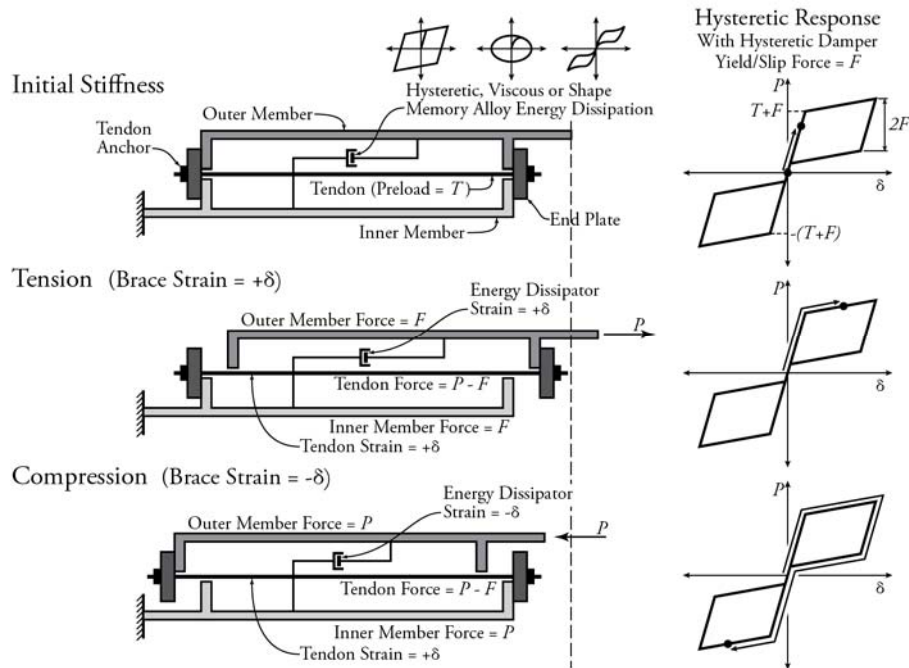

Figure 1: SCED Brace Mechanics

The shake table tests successfully demonstrated that SCED braces behave as intended within the context of a multi-story braced frame. They also showed that the braces were able to reliably eliminate residual drifts in the structure and that the SCED braces did not exhibit any significant degradation in their response even though they were subjected to a large number of earthquakes. These results are relevant for tall building structures because they provide verification that existing models of SCED braces can predict the dynamic response of buildings equipped with SCED braces.

Increased Axial Capacity

Previous SCED brace prototypes had a maximum axial load capacity of approximately 800 kN (Christopoulos et al., 2008). To improve the range of possible SCED braces that can be available for use in real structures, a high capacity SCED brace (HC-SCED) was recently designed and tested with a target axial load capacity of 3800 kN. This prototype HC-SCED brace design is shown in Figure 4.

This brace had an elongation capacity of approximately 70 mm. This was based on the elongation capacity of the aramid tendons that provided the restoring force. This was equivalent to approximately 2% story drift in the assumed design building. To increase the overall drift capacity of the system to accommodate extreme earthquakes, a prototype high-capacity friction fuse mechanism was also designed and fabricated in series with the main brace (shown on the left side of the brace in Figure 4). This fuse doubled the total axial deformation capacity to 140 mm (or approximately 4% drift).
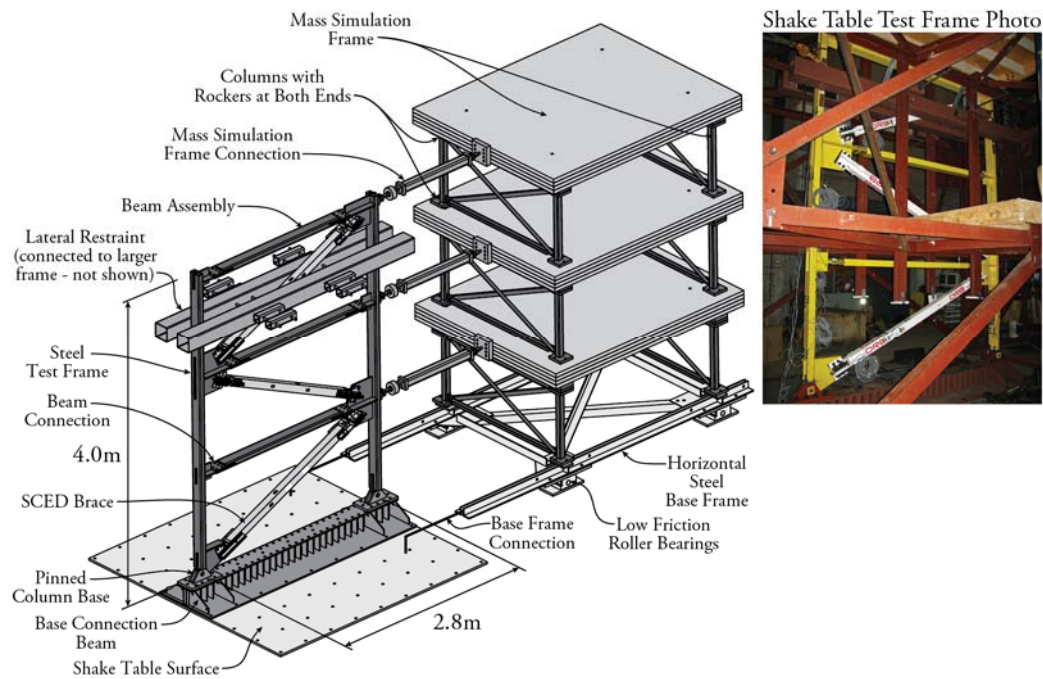
Figure 2: SCED Braced-Frame Shake Table Test Setup
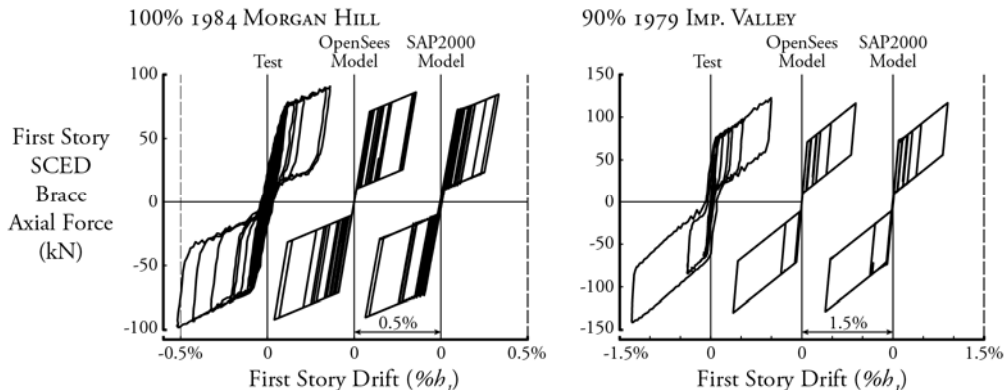
Figure 3: Sample Hystereses for First Story SCED Brace

The HC-SCED brace was tested in a 12 MN axial load frame at the Ecole Polytechnique in Montreal, Canada. It was subjected to simulated wind loading, test protocol loading, and dynamic earthquake time history loading. The test protocols were designed to satisfy the AISC 341-05 buckling-restrained brace protocol from Appendix T (AISC, 2005).

Example hysteretic responses of this brace for both a dynamic earthquake time history and a full AISC buckling restrained brace protocol are shown in Figure 5. In these figures, fuse slip (the horizontal parts of the hysteresis) are shown to result in residual drifts for extreme earthquake scenarios. The prototype high capacity friction fuse exhibited some stick-slip behavior at high loading velocities; however, its response was shown to be adequate for the purposes of limiting the force in the HC-SCED under extreme earthquake conditions. The HC-SCED also fully satisfied the AISC 341-05

buckling-restrained brace protocol (AISC, 2005). These HC-SCED prototype tests show that SCED braces can be successfully built and operated to withstand the high force demands that are expected in tall building design.
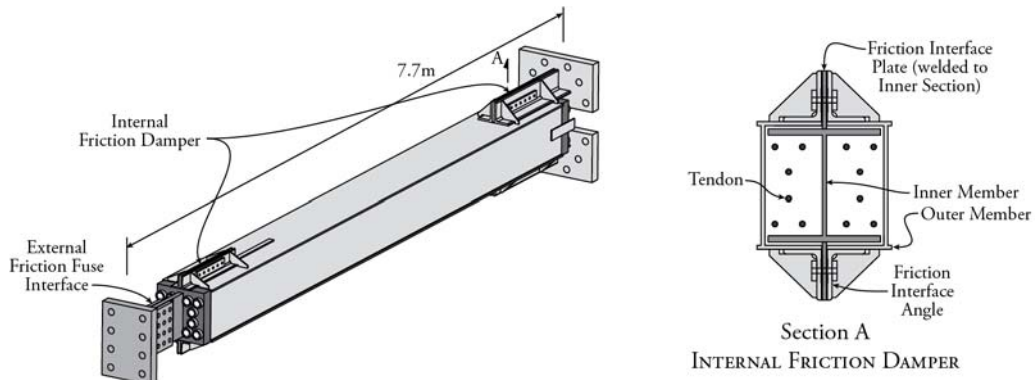

Figure 4: High-Capacity SCED (HC-SCED) Design
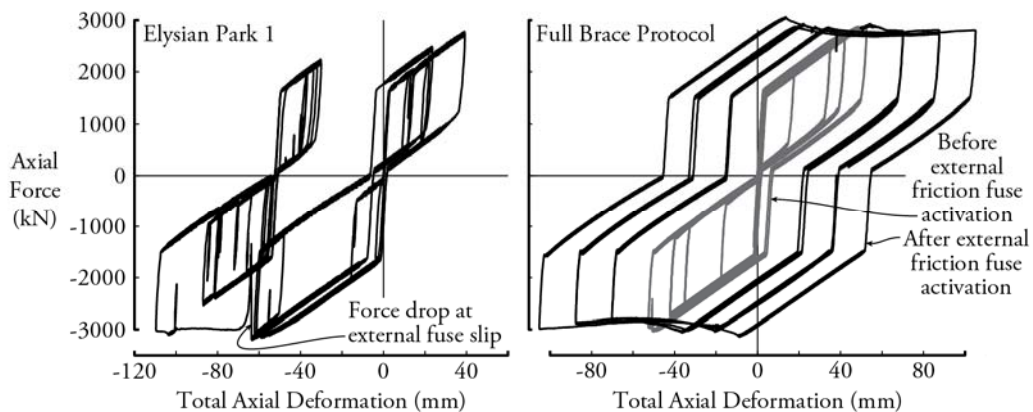
Figure 5: HC-SCED Sample Hysteresis Results

Increased Elongation Capacity (Erochko et al., 2012)

To avoid the need for a friction slip fuse at the end of a SCED brace to accommodate extreme earthquake loads, an innovative telescoping SCED brace (T-SCED brace) has been recently designed and tested at the University of Toronto. This T-SCED brace has double the elongation capacity of a comparable original SCED brace because it uses an extra axial member (in addition to the inner and outer members shown in Figure 1) and an additional set of tendons to share the total brace deformation across the two sets of tendons. The resulting mechanics for the T-SCED brace with these additional elements (for tension only) are shown in Figure 6.

This T-SCED brace was tested in a full-scale single-story steel building frame. Similarly to the HC-SCED, it was subjected to both dynamic earthquake loadings and test protocol loadings. Two example earthquake response hystereses are shown in Figure 7. The earthquake response for the Elysian Park record applied to the HC-SCED is also included for comparison. This Elysian Park test represents a maximum considered earthquake excitation. As this figure shows, the T-SCED brace provides full self-centering even under this extreme earthquake loading. This is in contrast to the HC-

SCED, which showed satisfactory results but had some residual drift at the end of the earthquake due to the slipping of the external friction fuse. The T-SCED brace easily satisfied the AISC 341-05 buckling-restrained brace protocol (AISC, 2005) and was able to accommodate up to 4.0% drift in the steel test frame. This was equivalent to 104 mm of axial brace deformation.

The development of the T-SCED brace is relevant to the design of tall buildings with SCED braces because it increase the range of use of the SCED brace by doubling its elongation capacity for a given set of tendons.
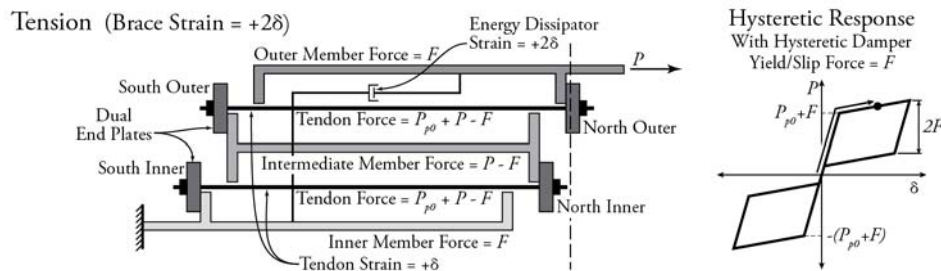
Figure 6: Telescoping SCED (T-SCED) Brace Mechanics
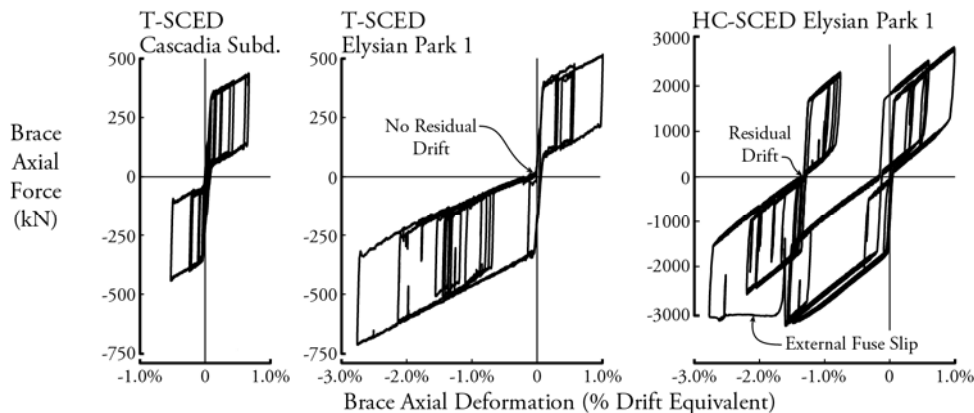
Figure 7: T-SCED Sample Hysteresis Results

Potential Applications to Tall Building Design

Recently there has been significant research into the incorporation of damping elements into tall buildings to improve seismic performance. Tuned mass dampers (TMDs) and tuned liquid column dampers (TLCDs) have been used for wind effect mitigation for some time, including relatively recent studies that investigated the use of semi-active control to improve performance (Yalla & Kareem, 2003; Nagarajaiah & Sonmez, 2007); however, these systems are therefore sensitive to building mode periods, and it is not generally practical to use them for mitigation of extreme seismic effects (Smith & Willford, 2007). Therefore, there has been significant recent research into the use damping elements in tall buildings. Damping elements are independent of building periods, and are able to mitigate both wind and earthquake effects. For example, the damped outrigger concept, proposed by Smith and Willford (2007) uses viscous dampers that act between an outrigger from a shear wall or braced frame and axial columns on the

outside of the building. Christopoulos and Montgomery (2013) developed a viscoelastic damping system that acts in shear between two parallel shear walls in the place of conventional shear wall coupling beams.

It is anticipated that the use of SCED braces in place of viscous dampers or viscoelastic dampers in tall structures could provide benefits in addition to energy dissipation. The self-centering behaviour of the braces can provide a restoring force to mitigate any potential residual drifts in the structure.
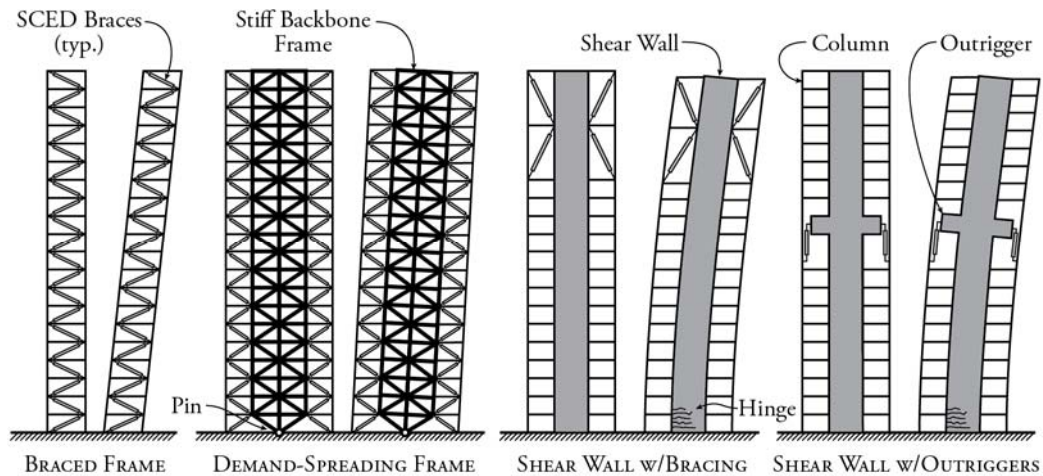

Figure 8: Potential Tall Building Configurations using SCED Braces

Some potential tall building structural configurations that may utilize SCED braces are shown in Figure 8. The 'Braced Frame' configuration on the left is a typical multi-storey braced frame. Due to their self-centering mechanism and relatively high post-activation stiffness, SCED braced frames tend to spread the drift demand across the height of the structure well (Tremblay et al. 2008), making them particularly effective for use in tall braced frames. The drift demand can be even more effectively spread by using a 'Demand-Spreading Frame', which consists of a backbone frame that rotates at the base and is designed to remain linear and relatively stiff (Merzouq & Tremblay, 2006). SCED braces could also be used in conjunction with a traditional shear wall, shown in the figure as 'Shear Wall w/Bracing' (Tremblay et al., 2010). The last configuration shown in the figure adapts the Smith and Willford (2007) damped outrigger concept for use with SCED braces. This configuration utilized SCED braces as vertical axial elements between a shear wall outrigger and an exterior column. The SCED braces in this configuration could be fabricated to be arbitrarily long, thereby allowing them to accommodate any level of axial deformation that is anticipated.

Conclusions

Recent advances in the development of self-centering energy-dissipative damping systems, including increased axial load capacity and increased elongation capacity, have made them more desirable for use in tall buildings. Four different tall building structural configurations have been proposed to take advantage of SCED braces. Future numerical modeling work needs to be conducted to fully assess the potential of the proposed structures.

References

American Institute of Steel Construction [AISC] (2005). *Seismic Provisions for Structural Steel Buildings, ANSI/AISC 341s1-05 Including Supplement No.1.* Chicago: American Institute of Steel Construction, Inc.

Christopoulos, C., Tremblay, R., Kim, H.-J., & Lacerte, M. (2008). Self-Centering Energy Dissipative Bracing System for the Seismic Resistance of Structure: Development and Validation. *J. Struct. Eng.*, 134:96-107.

Christopoulos C., Montgomery, M. (2013), Viscoelastic coupling dampers (VCDs) for enhanced wind and seismic performance of high-rise buildings. *Earthquake Engng. Struct. Dyn.* doi: 10.1002/eqe.2321

Computers and Structures Inc. (2009) SAP 2000 [Software]. Computers and Structures, Inc.: Berkeley, CA.

Erochko, J., Christopoulos, C., Tremblay, R. (2012) Design and Testing of an Enhanced Elongation Telescoping Self-Centering Energy-Dissipative (T-SCED) Brace. *15th World Conference on Earthquake Engineering*, Lisbon, Portugal.

Erochko, J., Christopoulos, C., Tremblay, R., Kim, H-J. (2013) Shake table testing and numerical simulation of a self-centering energy dissipative braced frame. *Earthquake Engineering and Structural Dynamics*. 42:1617-1635.

Merzouq, S., Tremblay, R. (2006). Seismic Design of Dual Concentrically Braced Steel Frames for Stable Seismic Performance for Multi-Storey Buildings. *Proc. 8th U.S. Nat. Conf. on Earthquake Eng.,* San Francisco, CA, Paper 1909.

McKenna F, Fenves GL, Scott MH, Jeremic B. (2000) Open System for Earthquake Engineering Simulation (OpenSees) [Software]. Pacific Earthquake Engineering Research Center, University of California: Berkeley, CA.

Nagarajaiah, S., Sonmez, E. (2007) Structures with Semiactive Variable Stiffness Single/Multiple Tuned Mass Dampers. *J. Struct. Eng.* 129:960-971.

Smith, R.J., Willford, M.R. (2007) The Damped Outrigger Concept for Tall Buildings. *Struct. Design Tall Spec. Build.* 16:501-517.

Tremblay, R., Lacerte, M., & Christopoulos, C. (2008). Seismic Response of Multistory Buildings with Self-Centering Energy Dissipative Steel Braces. *J. Struct. Eng.*, 134(1), 108-120.

Tremblay, R., Christopoulos, C., Erochko, J., Kim, H-J. (2010) Experimental Validations and Design of Self- Centering Energy Dissipative (SCED) Braced Structures. *Proc. 9th U.S. National & 10th Canadian Conference on Earthquake Eng.* Toronto, Canada.

Yalla, S.K., Kareem, A. (2003) Semiactive Tuned Liquid Column Dampers: Experimental Study. *J. Struct. Eng.* 133:67-77.

Controlled Rocking Systems for Enhanced Seismic Resilience: State of the Art

L. Wiebe[1] and C. Christopoulos[2]

ABSTRACT

Sustainable development requires attention not only to initial costs, but also to long-term performance. Although common structural systems can be designed economically to protect the lives of users during an earthquake, most cannot easily be designed to be usable after an earthquake. As an alternative, controlled rocking systems are being developed to economically provide not only life safety, but also seismic resilience. This paper gives an overview of the research that has demonstrated the seismic performance of controlled rocking systems in concrete, steel, timber, and masonry. Although most practical implementations have been in low- to mid-rise buildings, recent research has shown that multiple mechanisms could make controlled rocking systems competitive for taller structures.

1. Introduction

Although modern structures are likely to be safe during design-level earthquakes, they may require expensive and time-consuming repairs, or even demolition. Because this has been demonstrated in recent earthquakes, there is an increasing awareness that structures should be designed for seismic resilience, which is defined in this paper as the ability to return rapidly to normal use following a major earthquake. One way to promote seismic resilience is to use self-centering systems, which have a nonlinear response that controls peak seismic

[1]Department of Civil Engineering, McMaster University, 1280 Main Street West, Hamilton, ON; PH (905) 525-9140 x24620; e-mail: wiebel@mcmaster.ca
[2]Department of Civil Engineering, University of Toronto, 35 St. George Street, Toronto, ON; PH (416) 978-6238; e-mail: c.christopoulos@utoronto.ca
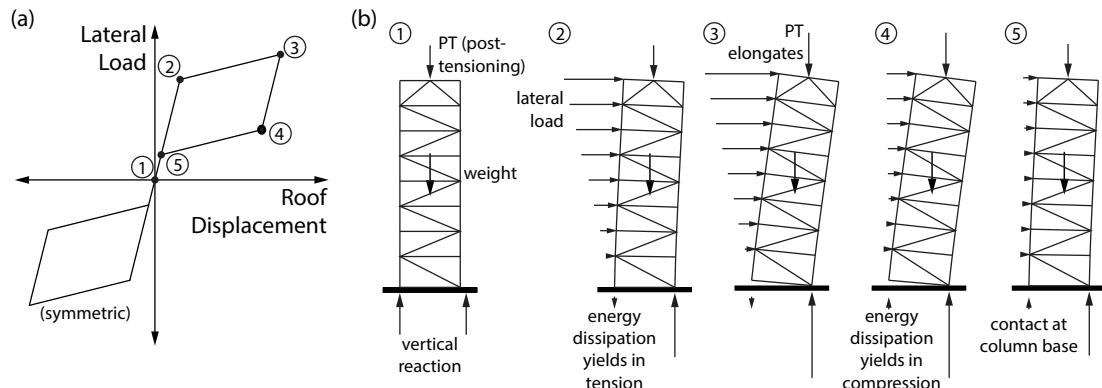
Figure 1   (a) Flag-shaped hysteresis; (b) Behaviour of controlled rocking system

forces without residual deformations. These systems are characterized by the flag-shaped hysteresis shown in Figure 1a.

Housner [1] showed that the reason many structures survived the 1960 Chile earthquake, despite appearing unstable, was that these structures had rocked on their foundations or on the underlying soil. Since that time, rocking has emerged as a potential design objective for new or retrofitted structures. Many studies have considered *pure rocking systems*, which rely only on their own weight to resist overturning moments. Although rocking can enable ancient structures to survive earthquakes [e.g. 2], new design generally uses *controlled rocking systems*, which are designed with post-tensioning and/or supplemental energy dissipation to control the rocking response. Figure 1b summarizes the response of a controlled rocking system to reversed cyclic loading.

2. Early Studies of Controlled Rocking Systems

The first large-scale implementation of controlled rocking as a design method was for the South Rangitikei rail bridge, which was designed in the 1970s [3]. Around the same time, shake table studies were conducted at Berkeley on steel frames where the columns were permitted to uplift [4]. Some of these tests used supplemental energy dissipation to control the peak response [5-6]. The seismic forces were generally lower when uplift was permitted, while the displacements were not consistently larger or smaller for the uplifting frames relative to the fixed-base frames. Despite the potential of controlled rocking, these systems received little attention from the structural engineering community until the Precast Seismic Structural Systems (PRESSS) program of the 1990s.

3. Concrete Controlled Rocking Systems

The PRESSS program was a research effort across many institutions, which sought to develop precast seismic force resisting systems that would reduce initial construction costs relative to traditional systems while maintaining or improving seismic performance [7]. In particular, the PRESSS program developed *connections* that would have a nonlinear seismic response, rather than confining the nonlinear response to precast concrete *members* by attempting to make them behave as though the connections were monolithic. The PRESSS project was the first to use unbonded post-tensioning to increase the lateral load capacity

of rocking systems. Several structural systems were developed to provide cost-effective ways of improving seismic resilience, but this paper focuses on controlled rocking systems.

As part of the PRESSS program, Kurama et al. [8] completed a numerical study using fibre element models of unbonded post-tensioned precast concrete walls. Later studies considered alternative configurations with supplemental viscous damping [9], friction dampers [10], or yielding steel that replaced some of the post-tensioning [11]. These studies identified the limit states of controlled rocking concrete walls and provided insight into their seismic response.

The PRESSS program culminated with testing of a 60%-scale five-storey building that included a precast concrete rocking wall system [12]. Two adjacent walls were coupled using U-shaped steel devices that yielded in flexure due to the relative displacement between the two wall units. The wall systems withstood pseudo-dynamic tests up to 50% greater than the design-level event with only cosmetic damage. Other tests of concrete rocking walls have also shown an ability to reach large drifts with little or no damage or residual drifts [13-16].

Following this research, several groups have developed design guidance for practicing engineers [17-19]. Figure 2 shows one example of a building that uses coupled controlled rocking concrete walls with U-shaped flexural plates as the seismic force resisting system in one direction. Controlled rocking concrete walls have been used in numerous other buildings around the world, some of which are described in [19].

4. Steel Controlled Rocking Systems

Following the success of the PRESSS project, several research groups have studied controlled rocking *steel* systems. Researchers in Japan have studied frames in which the column base plates are designed to yield, allowing the column to uplift [e.g. 20]. Numerical and shake table studies showed reduced base shears when this occurs, al-though the peak displacements have sometimes been larger than in fixed-base systems.

In other shake table testing, Tremblay et al. [21] used viscous dampers at the base of a 50%-scale two-storey controlled rocking steel braced frame that had no post-tensioning. The recorded behaviour was adequately captured by a numerical model.


Figure 2   Endoscopy Consultants Building, Christchurch, New Zealand: (left) view of building; (right) rocking walls with U-shaped flexural plates [photos by first author, May 2013]

Pollino and Bruneau [22] proposed retrofitting steel bridge truss piers by allowing them to rock and adding supplemental energy dissipation without post-tensioning. Bidirectional shake table testing of a 20%-scale model of a four-legged pier showed that it self-centered after peak lateral displacements of 3.9%.

Several recent large-scale tests have validated *post-tensioned* controlled rocking steel braced frames. At Lehigh University, a 60%-scale model of a four-storey frame was designed to fit between two non-uplifting gravity columns [23]. The lateral loads were transferred to the rocking system using bearings that also dissipated energy through friction. During hybrid testing to a roof displacement of 1.9%, the structure was self-centering and undamaged except for minor yielding of the post-tensioning.

Tests at the University of Illinois at Urbana-Champaign dissipated energy using replaceable steel plates with water-jet cutouts [24]. After quasi-static cyclic testing of a 43%-scale model to more than 3% roof displacement, the model had no significant residual displacements. However, early failure of some post-tensioning wires was reported at strains as low as 0.85%. In subsequent shake table tests of a 68%-scale three-storey frame, no residual deformations were observed after a test at the Maximum Considered Earthquake (MCE) level [25]. Moreover, early post-tensioning failure was avoided by preloading the tendons before reducing the prestress to the target value [26].

Researchers from the University of Toronto and École Polytechnique de Montréal reported the results from 56 large-amplitude shake table tests of a 30%-scale model of an eight-storey controlled rocking steel brace frame [27]. No significant damage or residual deformations were observed, but the peak forces were shown to be strongly influenced by higher mode effects (see Section 6).

Figure 3 shows a building that uses controlled rocking steel braced frames as the lateral force resisting system in both directions [28]. Several other buildings have also been built with controlled rocking steel braced frames [e.g. 29-31].

5. Timber and Masonry Controlled Rocking Systems

Controlled rocking has also been applied to other materials. Toranzo et al. [32] successfully tested a 40%-scale three-storey confined masonry wall, in which external yielding bars provided supplemental energy dissipation and helped to transfer the base shear. Palermo et

Figure 3   Kilmore Street Medical Centre, Christchurch, New Zealand: (left) view of building; (right) bottom corner of controlled rocking frame [photos by first author, May 2013]

al. [33] reported good behavior of a 1.7 m tall laminated veneer lumber post-tensioned rocking wall that dissipated energy using yielding steel bars.

6. Controlled Rocking Systems for Tall Buildings

Like any seismic force resisting system, controlled rocking systems should be capacity designed to ensure that nonlinear response occurs only in the ductile mechanism that is specified by the designer. This requires designing all frame members to remain elastic under the largest forces that can occur when the base rocking joint reaches its maximum deformation. The maximum expected base overturning moment can easily be calculated from the geometry of the frame, together with the weight that acts on the frame and the properties of the post-tensioning and supplemental energy dissipation. However, the member force demands may be grossly underestimated if an inverted triangular lateral force distribution is used to calculate the demands that correspond to the maximum base overturning moment [34]. Figure 4a-b show schematically how the overturning moments above the base, and the storey shears throughout the structure, are likely to increase due to higher mode effects. These effects are similar to what has been observed in reinforced concrete walls, and they are known to become more significant as the building height increases [35].

Although the members of controlled rocking steel braced frames can be designed to resist the maximum expected forces, this may be uneconomical if higher mode effects are significant, as is likely for structures that are more than about 10 storeys tall. As an alternative, higher mode effects can be mitigated by using multiple mechanisms. Figure 4c shows an upper rocking joint, which can be designed to limit the overturning moment at that location (see Figure 4a), and a nonlinear brace at the first storey, which can be designed to limit the base shear (see Figure 4b). Because of the relationship between moment and shear, both mechanisms reduce both the overturning moment and the shear force envelopes.

Both of these higher mode mitigation mechanisms were validated by shake table testing of a 30%-scale model of an eight-storey frame. The same frame was tested rocking only at the base and with an additional upper rocking joint (1M and 2M, respectively), as well as with a conventional first-storey brace and with a nonlinear self-centering first-storey brace (0V and 1V, respectively). Figure 5 demonstrates the reduction in the overturning moment
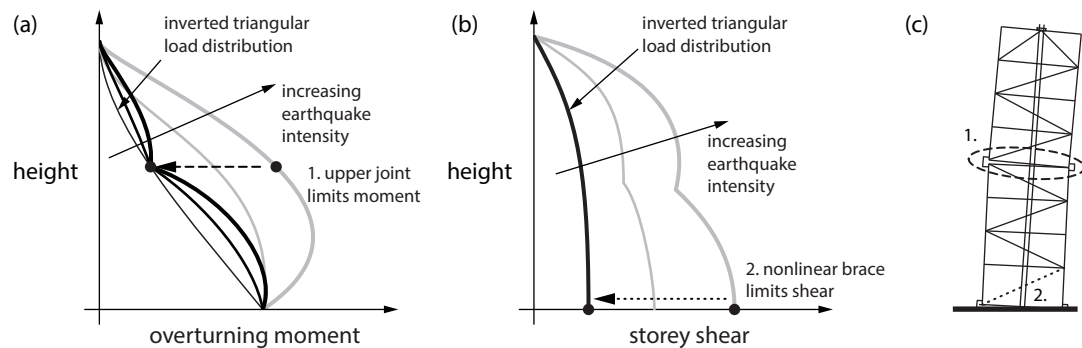

Figure 4   Schematic of controlled rocking steel braced frame: (a) overturning moment envelopes; (b) storey shear envelopes; (c) frame with multiple mechanisms
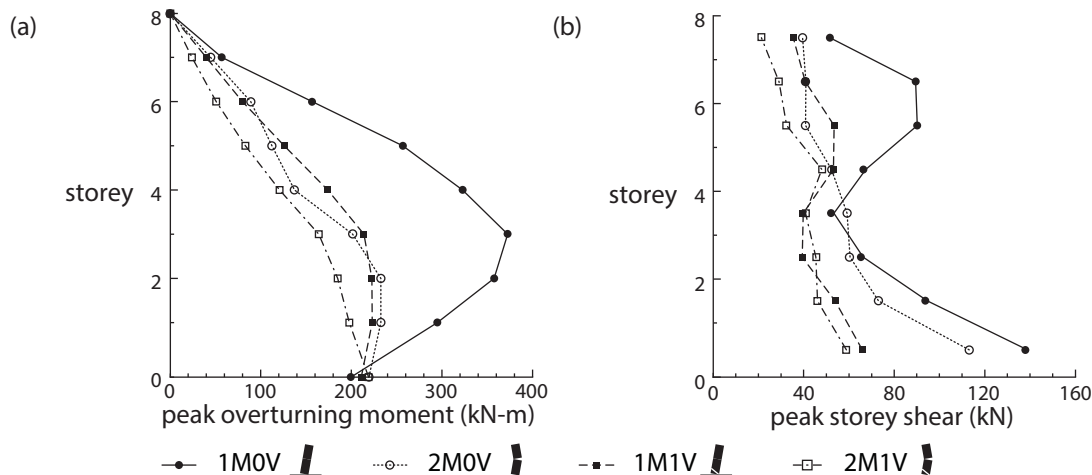
Figure 5   Measured response during shake table testing of 30%-scale model under record ENA-1: (a) overturning moment envelope; (b) storey shear envelope

and storey shear envelopes that were measured when multiple mechanisms were implemented. In more extensive testing, both concepts were demonstrated to reduce the peak column and brace forces with little or no increase in peak displacements [27]. This work suggests that multiple mechanisms could greatly improve the economy of medium- to high-rise controlled rocking steel braced frames.

7. Conclusions

Controlled rocking systems rely on uplift, rather than material yielding, to limit the peak seismic forces. Research over the last forty years has demonstrated that this is an attractive way of enhancing seismic resilience at a competitive initial cost. Extensive numerical and experimental testing has validated controlled rocking systems in concrete, steel, masonry, and timber, and these systems have also been implemented in practice. Although the design forces for tall controlled rocking systems may be strongly influenced by higher mode effects, these effects can be mitigated by using multiple mechanisms, thereby making controlled rocking systems viable for tall structures.

References

1. Housner, G. (1963). "The behavior of inverted pendulum structures during earthquakes." *Bull. Seism. Soc. Am.,* 53(2), 403-417.
2. Makris, N., and Vassiliou, M. F. (2013). "Planar rocking response and stability analysis of an array of free-standing columns capped with a freely supported rigid beam." *Earthq. Eng. Struct. Dyn.*, 42(3), 431-449.
3. Beck, J., and Skinner, R. (1974). "The seismic response of a reinforced concrete bridge pier designed to step." *Earthq. Eng. Struct. Dyn.*, 2(4), 343-358.

4. Clough, R. W., and Huckelbridge, A. A. (1977). "Preliminary experimental study of seismic uplift of a steel frame." *Report UCB/EERC-77/22*, Earthquake Engineering Research Center, Berkeley, CA.

5. Kelly, J., and Tsztoo, D. "Earthquake simulation testing of a stepping frame with energy-absorbing devices." *Report UCB/EERC-77/17*, Earthquake Engineering Research Center, Berkeley, CA.

6. Huckelbridge, A. A. (1977). "Earthquake simulation tests of a nine story steel frame with columns allowed to uplift." *Report UCB/EERC-77/23*, Earthquake Engineering Research Center, Berkeley, CA.

7. Priestley, M. J. N. (1991). "Overview of PRESSS research program." *PCI J.*, 36(4), 50-57.

8. Kurama, Y., Pessiki, S., Sause, R., and Lu, L.-W. (1999). "Seismic behavior and design of unbonded post-tensioned precast concrete walls." *PCI J.*, 44(3), 72-89.

9. Kurama, Y. C. (2000). "Seismic design of unbonded post-tensioned precast concrete walls with supplemental viscous damping." *ACI Struct. J.*, 97(4), 648-658.

10. Kurama, Y. C. (2001). "Simplified seismic design approach for friction-damped unbonded post-tensioned precast concrete walls." *ACI Struct. J.*, 98(5), 705-716.

11. Kurama, Y. C. (2002). "Hybrid post-tensioned precast concrete walls for use in seismic regions." *PCI J.*, 47(5), 36-59.

12. Priestley, M. J. N., Sritharan, S., Conley, J. R., and Pampanin, S. (1999). "Preliminary results and conclusions from the PRESSS five-story precast concrete test building." *PCI J.*, 44(6), 42-67.

13. Holden, T., Restrepo, J., and Mander, J. B. (2003). "Seismic performance of precast reinforced and prestressed concrete walls." *J. Struct. Eng.*, 129(3), 286-296.

14. Perez, F. J., Sause, R., and Pessiki, S. (2007). "Analytical and experimental lateral load behavior of unbonded posttensioned precast concrete walls." *J. Struct. Eng.*, 133(11), 1531-1540.

15. Restrepo, J. I., and Rahman, A. (2007). "Seismic performance of self-centering structural walls incorporating energy dissipators." *J. Struct. Eng.*, 133(11), 1560-1570.

16. Marriott, D., Pampanin, S., Bull, D., and Palermo, A. (2008). "Dynamic testing of precast, post-tensioned rocking wall systems with alternative dissipating solutions." *Bull. NZ Soc. Earthq. Eng.*, 41(2), 90-103.

17. Federation Internationale du Beton. (2003). "Modelling and analytical methods." Chapter 9 in *fib Bulletin 27: Seismic design of precast concrete building structures*. fib, Lausanne, Switzerland.

18. American Concrete Institute. (2009). "Requirements for design of a special unbonded post-tensioned precast shear wall satisfying ACI ITG-5.1 (ACI ITG-5.2-09) and commentary." *ACI ITG-5.2-09*, ACI, Farmington Hills, MI.

19. New Zealand Concrete Society. (2010). *PRESSS Design Handbook*. NZCS, Auckland, NZ.

20. Midorikawa, M., Azuhata, T., Ishihara, T., and Wada, A. (2006). "Shaking table tests on seismic response of steel braced frames with column uplift." *Earthq. Eng. Struct. Dyn.*, 35(14), 1767-1785.

21. Tremblay, R., Poirier, L.-P., Bouaanani, N., Leclerc, M., Rene, V., Fronteddu, L., and Rivest, S. (2008). "Innovative viscously damped rocking braced frames." *Proc., 14th World Conf. Earthq. Eng.*, Beijing, China.

22. Pollino, M., and Bruneau, M. (2010). "Seismic testing of a bridge steel truss pier designed for controlled rocking." *J. Struct. Eng.*, 136(12), 1523-1532.

23. Sause, R., Ricles, J. M., Roke, D. A., Chancellor, N. B., and Gonner, N. P. (2010). "Seismic performance of a self-centering rocking concentrically-braced frame." *Proc., 9th US and 10th Cdn. Conf. Earthq. Eng.*, Toronto, ON.

24. Eatherton, M., Hajjar, J., Ma, X., Krawinkler, H., and Deierlein, G. (2010). "Seismic design and behavior of steel frames with controlled rocking – Part I: Concepts and quasi-static subassembly testing." *Proc., ASCE Struct. Congress 2010*, Orlando, FL.

25. Ma, X., Eatherton, M., Hajjar, J.,Krawinkler, H., and Deierlein, G. (2010). "Seismic design and behavior of steel frames with controlled rocking – Part II: Large scale shake table testing and system collapse analysis." *Proc., ASCE Struct. Congress 2010*, Orlando, FL.

26. Ma, X. (2010). "Seismic design and behavior of self-centering braced frame with controlled rocking and energy-dissipating fuses." *PhD Dissertation*, Stanford University, Stanford, CA.

27. Wiebe, L., Christopoulos, C., Tremblay, R., and Leclerc, M. (2013). "Mechanisms to limit higher mode effects in a controlled rocking steel frame. 2: Large-amplitude shake table testing." *Earthq. Eng. Struct. Dyn.*, 42(7), 1069-1086.

28. Latham, D. A., Reay, A. M., and Pampanin, S. (20130). "Kilmore Street Medical Centre: application of a post-tensioned steel rocking system." *Proc., Steel Innovations Conf. 2013*, Christchurch, NZ.

29. Gledhill, S. M., Sidwell, G. K., Bell, D. K. (2008). "The damage avoidance design of tall steel frame buildings – Fairlie terrace student accommodation project, Victoria University of Wellington." *Proc., 2008 NZSEE Conf.*, Wellington, NZ.

30. Mar, D. (2010). "Design examples using mode shaping spines for frame and wall buildings." *Proc., 9th US and 10th Cdn. Conf. Earthq. Eng.*, Toronto, ON.

31. Tait, J., Finnegan, J., and Sidwell, G. (2013). "A low damage design solution for a 15 storey steel framed building." *Proc., 2013 NZSEE Conf.*, Wellington, NZ.

32. Toranzo, L.A., Restrepo, J. I., Mander, J. B., and Carr, A. J. (2009). "Shake-table tests of confined-masonry rocking walls with supplementary hysteretic damping." *J. Earthq. Eng.*, 13(6), 882-898.

33. Palermo, A., Pampanin, S. and Buchanan, A. (2006). "Experimental investigations on LVL seismic resistant wall and frame subassemblies." *Proc., 1st Euro. Conf. Earthq. Eng. Seism.*, Geneva, Switzerland.

34. Eatherton, M., and Hajjar, J. (2010). "Large-scale cyclic and hybrid simulation testing and development of a controlled-rocking steel building system with replaceable fuses." *NSEL Report NSEL-025*, Dept. Civ. Env. Eng., UIUC, Urbana, IL.

35. Paulay, T., and Priestley, M. J. N. P. (1992). *Reinforced concrete structures*. John Wiley & Sons, Inc., New York, NY.

Viscoelastic Coupling Dampers (VCDs) and Viscoelastic-Plastic Coupling Dampers (VPCDs) for enhanced efficiency and resilience of high-rise buildings

Michael Montgomery[1] and Constantin Christopoulos[2]

ABSTRACT

New damping systems, the viscoelastic (VE) Coupling Damper (VCD) and Viscoelastic-Plastic Coupling Damper (VPCD) has been developed to improve the performance of tall reinforced concrete (RC) buildings subject to both wind and earthquake loads. VCDs are introduced in lieu of RC coupling beams to take advantage of differential shear deformations between adjacent walls during lateral loading of the structure. The VCDs utilize multiple VE material layers that are bonded to alternating steel plates with each consecutive steel layer extending out to the opposite side and anchored into the walls using a number of alternate connection details.

When the building is subject to frequent or design level wind storms or low level earthquakes, the damper exhibits both a displacement-dependent elastic restoring force providing coupling to the walls and a velocity dependent viscous force, providing supplemental damping to the building.

In regions of severe seismicity, a ductile "fuse" element can also be included in the damper to enhance its performance. The "fuse" is capacity designed such that if predefined load levels are reached in the damper during extreme seismic loading, connection elements act as force limiting members and prevent damage from occurring in adjacent structural elements. The response during severe earthquakes is viscoelastic at small amplitudes and becomes plastic once the connections start yielding resulting in what is termed a Viscoelastic-Plastic (VEP) hysteresis. Replaceable connections are utilized to allow for repair or replacement after an earthquake.

This paper describes the Viscoelastic and Viscoelastic-Plastic response of this new damping system and provides some examples of the design concept and applications of this technology.

[1] Principal, Ph.D., Kinetica, 203 College Street, Suite 301A. Toronto, ON Canada M5T 1P9, www.kineticadynamics.com. E-mail: m.montgomery@kineticadynamics.com
[2] Professor, Department of Civil Engineering, University of Toronto, 35 St. George Street, Toronto, ON, Canada, M5S 1A4. E-mail: c.christopoulos@utoronto.ca

Introduction

Challenges in Designing Tall

Tall and slender high-rise buildings are extremely sensitive to both wind and earthquake vibrations. Frequent wind storms can cause vibrations that can be as severe as to cause motion sickness to the building's occupants while less frequent wind storms can cause a very large dynamic response of the structure which can lead to large lateral loads that must be designed for. Frequent earthquakes can cause damage to non-structural members and extreme earthquakes can cause distributed damage to structural members, which, even without any risk of collapse, can lead to the building being decommissioned if the repairs are too costly.

The current state-of-the-art for mitigating wind loads consists of stiffening the building laterally. Stiffening the building is typically done by increasing the size of structural members or by using a stiffer structural system, which increases the material costs, adds to the construction time and reduces the architectural space. If stiffening of the building is insufficient, a vibration absorber (typically Tuned Mass or Tuned Sloshing Dampers) is introduced. A vibration absorber is a large mass located at the top of the building which, if tuned and calibrated properly to a mode of vibration, can transfer vibrational energy from the primary structure to the vibration absorber and thereby reduce the dynamic response of the primary structure. Vibration absorbers are complicated to design and require continual monitoring and maintenance to ensure performance, but most importantly they typically occupy the most valuable architectural space at the top stories of the building. Furthermore because most tall buildings are now constructed with reinforced concrete (RC), whose properties change with time, it is difficult to ensure that vibration absorbers are calibrated to the correct in-situ properties over the life of the building and therefore they are not relied on to reduce ultimate wind loads or earthquake loads.

In seismic zones, walls are often coupled by deep coupling beams with two sets of diagonally intersecting steel reinforcing bars. Under severe earthquakes the coupling beams are designed to respond nonlinearly through yielding of the diagonally reinforced coupling beams throughout the building as well as yielding of the concrete walls at the base, while all other structural members are capacity designed to remain essentially linear elastic. Under frequent earthquakes all structural members are designed to remain essentially linear elastic. The coupling beams used in this construction are typically very labor intensive and costly to construct and after a large earthquake, as expected, buildings designed in this manner can sustain significant damage, which can result in decommissioning, as observed in New Zealand (Kam and Pampanin 2011).

It has been shown that the inherent damping of tall buildings is lower than typically used in design practice and decreases with increasing height (CTBUH 2008). In fact, recent measurements have reported that the majority of buildings over 250 meters in height have had less than 1% inherent damping, regardless of building typology (composite, steel or reinforced concrete). This is a main reason why tall RC buildings are so sensitive to wind and earthquake vibrations.

The most efficient way to control wind and seismic dynamic vibrations in tall buildings is through added distributed viscous damping. A new damping system, the Viscoelastic Coupling Damper (VCD, US Patent #7,987,639, Chinese Patent #200680040409.X and Canadian Patent #2,634,641 and 11 international patents pending) (see Figure 1), has been developed to achieve this. VCDs add distributed

viscous damping to all lateral and torsional modes of vibration, enhancing both the wind performance and the seismic resilience of tall buildings. VCDs are configured in-place of coupling beams or outriggers and therefore there is no loss of architectural space when they are implemented in a building.
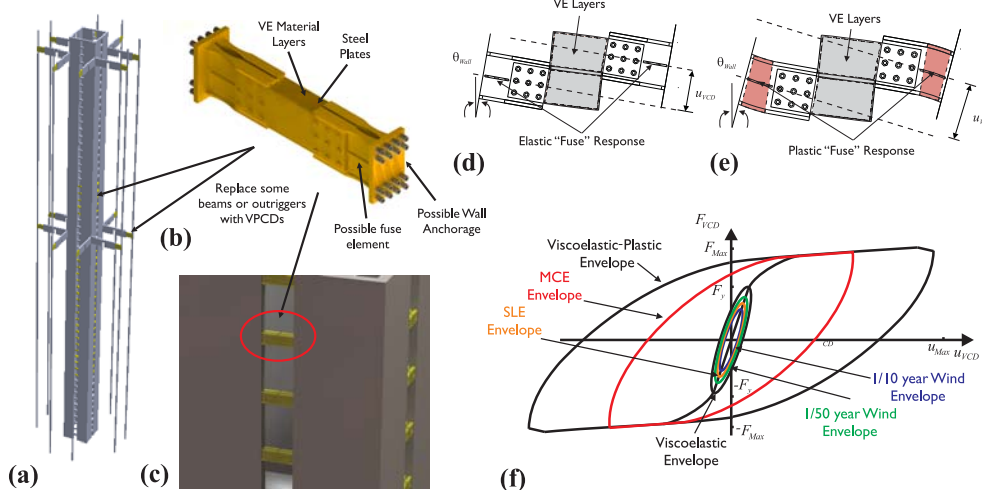

Figure 1: (a) lateral structural model; (b) VCD; (c) VCD-wall configuration; (d) VE response; (e) VEP response; (f) VCD hysteretic response

This paper describes the Viscoelastic and Viscoelastic-Plastic response regimes of the VCD when subjected to dynamic loads of various amplitudes. When the dampers are efficiently configured in the buildings, the dual response characteristics of the VCD allows for performance improvements over a spectrum of loadings, including frequent wind loads, blast loads and extreme earthquakes.

Viscoelastic Coupling Dampers (VCDs)

VCDs consist of multiple layers of viscoelastic (VE) material layers bonded in-between multiple steel plates which are anchored into vertically extending structural members on the opposite sides with a number of different possible connection details (see Figures 1(a), 1(b) and 1(c)). Vibrations due to lateral or torsional loads induce vertical differential motion in adjacent walls causing the VE material to be deformed in shear (See Figures 1(d) and 1(e)).

For tall buildings in regions of high seismic demand, a ductile force limiting structural "fuse" is introduced (see Figure 1(b)). The "fuse" is capacity designed such that if a predefined load level is reached, connecting members built into the damper activate and prevent damage from occurring in the walls and the VE material layers from tearing. If the fuse has been activated it can easily be inspected and replaced, if required, if a replaceable connection detail is used.

Design Concept

The VCD achieves a similar function as conventional structural coupling members (coupling beams and outriggers) with the added benefits of providing supplemental damping. For frequent wind storms (service level 1 in 10 year wind loads), rare wind storms (ultimate level 1 in 50 year wind loads), frequent earthquakes (service level 1 in 43 year earthquake loads) VCDs are intended to

respond as a viscoelastic damping element where connecting elements behave essentially elastically and where most of the deformations occur primarily in the VE layers (Figures 1(d) and 1(f)).

For extreme earthquakes (maximum credible level 1 in 2500 earthquake loads) the VCD "fuse" activates and limits the forces that are transferred to the walls (Figures 1(e) and 1(f)). Through different "fuse" details it is possible to achieve large shear deformations as a combination of the VE material deformations and the "fuse" plastic deformations.

Modeling Viscoelastic Response

A simple and effective mechanical model for VE material in shear is the Kelvin-Voigt solid model (see Figures 2(a) and 2(b)), which has been described in numerous other references (Soong and Dargush, 1997 and Christopoulos and Filiatrault, 2006). The force-displacement of the VE material can be expressed in terms of force, F_{VE}, displacement, u_{VE}, and velocity, $\dot{u}_{VE}$, as:

$$F_{VE}(t) = k_{VE}u_{VE}(t) + c_{VE}\dot{u}_{VE}(t) \tag{1}$$

where k_{VE} and c_{VE} are the stiffness and damping coefficients, respectively, and are expressed as a function of the total VE material area, A, and VE material height, h and the VE material damping and stiffness properties, which are functions of the frequency, strain and temperature. The response of the VE material can be modeled using more advanced models to take into account these effects (Fan 1998).

The viscoelastic behavior of the VCD can be effectively modeled in shear by extending a rigid offset from the wall to the center of the VE material using a spring element representing the stiffness of the steel connection elements and the "fuse", k_{Fuse}, in series with the Kelvin-Voigt VE model (see Figures 2(c)). As the stiffness of the fuse element is increased, the VCD behaviour approaches a purely viscoelastic element. When the stiffness of the fuse element is reduced it reduces the effectiveness (both stiffness and damping) of the overall VCD as more of the deformation occurs in the connections instead of the VE material.

This behaviour can also be simplified and modeled as an "equivalent" Kelvin-Voigt model in shear (Figure 2(d)). The equivalent viscous damping coefficient, c_{VCD}, and the equivalent stiffness coefficients, k_{VCD}, of the VCD are obtained by combining the shear stiffness of the steel connection elements and the "fuse", k_{Fuse}, and the VE Kelvin-Voigt model (Kasai et al. 1997 and Montgomery 2011). The hysteretic response of the VCD beam element in shear at time t (see Figure 2(e)) is expressed as:

$$F_{VCD}(t) = k_{VCD}u_{VCD}(t) + c_{VCD}\dot{u}_{VCD}(t) \tag{2}$$

where $F_{VCD}(t)$, $u_{VCD}(t)$ and $\dot{u}_{VCD}(t)$ are the VCD shear force, displacement and velocity, respectively. This model can be implemented in commercial software such as ETABS, SAP2000 and Perform-3D (Montgomery 2011) and can also be modeled using more advanced analytical models (Montgomery 2011).
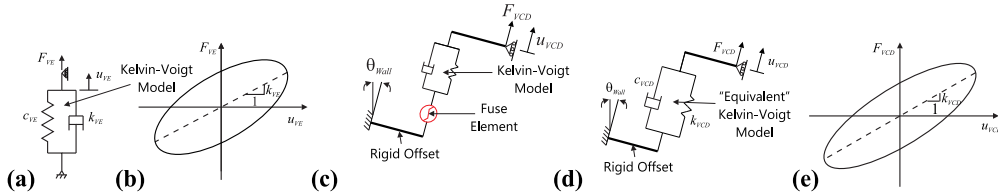
Figure 2: (a) Kelvin-Voigt solid model of VE material; (b) force-displacement hysteresis of VE material; (c) VPCD model; (d) "equivalent" Kelvin-Voigt model of VCD; (e) force-displacement hysteresis of VCD

Viscoelastic-Plastic Response

Beyond a certain load level, the VCD response transitions from a viscoelastic (VE) response to a viscoelastic-plastic (VEP) response. The degree of overstrength is directly related to the type of structural fuse used in series with the VE material. This can consist of a steel reduced beam section (RBS), shear critical link or a nearly perfect elasto-plastic friction critical bolted link. The (VEP) model for this is the same as the model shown in Figure 2(c).

To demonstrate the nonlinear behaviour, a harmonic displacement signal is applied to the model in Figure 3(a), where the cyclic VCD displacement amplitude is increased every cycle by $0.25\,u_{Max}$ until u_{Max} is reached with a plastic force of the fuse of F_{Max}. In the first cycle, the response of the fuse is elastic, as $F_{Max} > F_{VE}$ and the VCD response is completely viscoelastic in nature and the deformation is mainly accommodated in the VE material. This could be modeled as the "equivalent" Kelvin-Voigt model as described previously. During the second cycle the fuse is activated when the plastic force is reached, i.e. $F_{Max} = F_{VE}$, and the majority of the VCD response is concentrated in the plastic fuse while the deformation in the VE material is limited. When the fuse is a perfectly elasto-plastic with for example a friction critical link, the maximum VE displacement, u_{VEMax}, can be calculated as:

$$u_{VEMax} = F_{Max} / k_{VE} \tag{3}$$

In the remainder of the cycles of increasing amplitude the VE material displacement and the maximum force in the VCD can be effectively limited with the fuse element (see Figures 3(b), 3(c) and 3(d)). If the elasto-plastic fuse element has significant ductility capacity, large deformations can be achieved in the VCD. If the fuse has a higher post-yield stiffness, after yielding takes place the force and strain in the VE layers can continue to increase, which could potentially lead to tearing of the VE material. To prevent tearing in such cases, the activation fuse force can be decreased or a strain limiting mechanism could be introduced to the VCD. Examples of some simple strain limiting mechanism could be a slotted bolted connection or extending the flanges of the connection elements above and below the VE material.
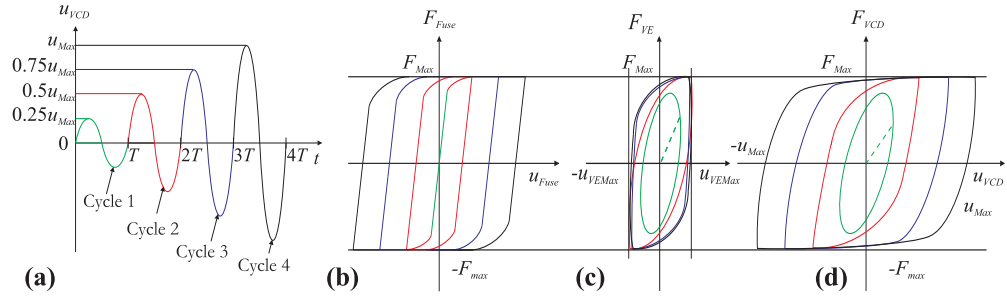
Figure 3: (a) displacement time-history; (b) force-displacement hysteresis of fuse; (c) force-displacement hysteresis of VE material; (d) force-displacement hysteresis of VPCD

Example of Viscoelastic-Plastic Response

Figure 4 shows a full-scale VCD test on a VCD specimen of 2,100 *mm* length, with two RBS fuses built into the damper (see Figure 4(a) and 4(b)). The full-scale racking test and test setup has been described elsewhere (Montgomery 2011). An exaggerated deformed shape of the test setup when the fuse element is responding elastically is shown in Figure 4(c).

The specimen was cycled dynamically at a constant frequency of $f_0 = 0.2$ *Hz* for 3 cycles and for each subsequent test the displacement amplitude was increased. For the first tests, the RBS fuses did not yield and the total damper response was characterized by the VE response. As the displacement was increased however, the RBS fuses began to yield at a shear displacement of 20 *mm* (over the total damper length), corresponding to a VCD chord rotation of 0.01 radians (shown in Figure 4(d)). As can be seen, the specimen exhibited a VEP hysteretic response beyond this deformation. Yielding was concentrated in the RBS regions, which provided a ductile response, however there was a large overstrength in the RBS fuses and therefore once the fuses yielded the response in the VE material still continued to increase slightly Figure 4(e). Note that this could be completely eliminated if a strain limiting mechanism was introduced as described earlier.
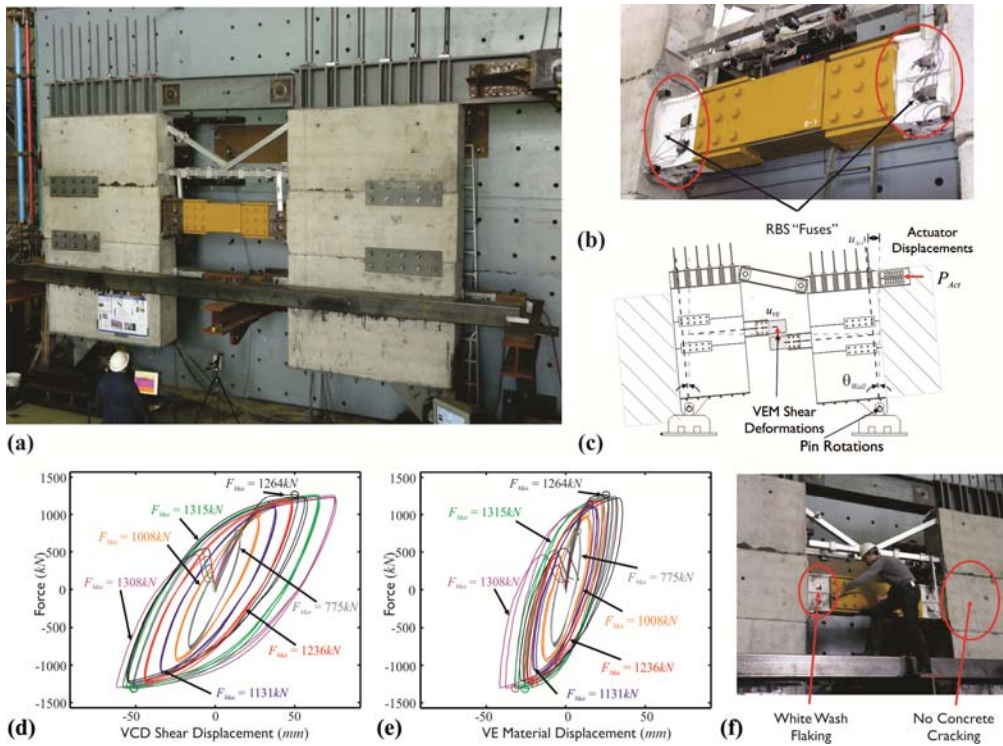
Figure 4: (a) photo of test setup; (b) close up photo of the VCD with RBS fuses;
(c) exaggerated deformed shape; (d) overall VCD response; (e) VE material
response; (f) VCD after dynamic tests

A clamping device was used to lock the VE material layers in place to test the steel
fuses to complete failure using an incremental quasi-static cyclic loading regime. The
maximum force achieved in the quasi-static tests was 1,330 *kN* and the inelastic response
was concentrated in the RBS locations without any cracking in the concrete walls.
Although the damper strain was able to achieve more than 600% strain
(Montgomery 2011), it was estimated that if the VE material deformation was
conservatively limited to only 400% strain (corresponding to 0.012 radians) the
total deformation prior to buckling of the RBS would correspond to about 154 *mm*
or 0.072 radians. This would be greater than the deformation capacity of a
diagonally reinforced coupling beam of the same length, calculated using
ASCE/SEI-41 (ASCE 2006), of 72 *mm* of shear displacement or 0.035 radians.

VCDs and VPCDs for Seismic Resilient Tall Buildings
A comparative study was conducted on the seismic of the performance of two tall
reinforced concrete core wall structures, one with diagonally reinforced coupling
beams, termed the base structure, and one with VCDs, termed the VCD structure,
(MacKay-Lyons 2013). The case study building was designed as a case study for
the Pacific Engineering Research Center (PEER) Tall Buildings Initiative (TBI)
designed by Magnusson Klemencic Associates (PEER/ATC 2011).
For this building MacKay-Lyons (2013) found that the most effective strategy was
to replace stiff RC beams with less stiff VCDs, such that the lateral stiffness of the
structure was reduced allowing the natural period to elongate while relying on the
damping added by the inclusion of the VCDs to dissipate the seismic energy and
control drifts. The results showed that the interstory drifts, peak floor
accelerations and core wall shears could be reduced for all hazard levels, however

these improvements were most pronounced at the SLEs, for the VCD structure compared to the base structure (where it was on average 35% for the drifts, accelerations and forces). This is because at this loading level, the VCDs dissipate energy, unlike the structural members of the base structure which do not dissipate any energy, because they are designed to respond elastically at this level of seismic loading. For both the DBE and the MCE level loading the VCD structure still had performance improvements compared to the base structure (on average 15% for the drifts, accelerations and forces). However there was significant distributed structural damage to the coupling beams for both the DBEs and MCEs in the base structure that required repair (for example, on average 85% of the coupling beams were damaged requiring repair for the MCEs), because at this level of loading the coupling beams were designed to yield. Meanwhile the VCDs had considerably less damage that required repairs, less than 10% of the VCDs required repair after the MCEs and none after the DBEs in the VCD structure.

Resilience
As discussed in the previous section at lower level earthquakes the VCD structure has significantly more capacity to absorb dynamic vibrations with a VE response in the VCD members compared to a linear elastic response of the diagonally reinforced members in a traditionally designed building. As the amplitude of loading increases, the coupling beams begin to yield and start to dissipate energy, and as a result sustain damage and may require repair. Finally for MCE level ground motions the energy dissipated in the VCDs and diagonally reinforced coupling beams is comparable, however significantly more damage is expected in the traditional RC structure. This distributed damage that is expected in a state-of-the-art tall reinforced concrete building may be extremely expensive to repair and therefore could actually result in decommissioning of the entire structure. Meanwhile if there is damage observed in the VCDs, due to their modular and replaceable nature, they could be easily inspected and repaired or replaced if required.

Conclusion
In this paper, some of the main challenges facing engineers designing tall, slender buildings are first discussed, followed by the introduction of a newly developed concept for a more effective and resilient design of tall buildings, the Viscoelastic Coupling Dampers (VCD). The VCD responds as a viscoelastic damper prior to activation of the fuses and once a preselected load is reached, the fuses activate transitioning the damper response into a Viscoelastic-Plastic regime. When the fuses activate, it limits the forces transferred to the structural walls and the shear deformation in the VE material and increases the energy dissipation capacity of the damper. It is suggested that the VCDs be designed to respond as VE dampers for wind loads and low level seismic vibrations and respond as a VEP dampers for severe seismic vibrations. The possibility of increased structural resilience of tall buildings designed with this system is also discussed, with improved performance (drifts, accelerations and core wall shears) for low to moderate seismic loads and significantly less structural damage for extreme Maximum Credible Earthquakes.

References

Christopoulos C, and Filiatrault A. (2006) "Principles of passive supplemental damping and seismic isolation." *IUSS Press,* Pavia, IT.

Christopoulos, C., Montgomery, M., Kokai, T., Smith, S., Hasan, A., Bentz, E., and Collins, M. (2005). "Fork configuration dampers and method of using the same." *United States Patent No. 7.987,639* October 26.

Christopoulos, C., Montgomery, M., Kokai, T., Smith, S., Hasan, A., Bentz, E., and Collins, M. (2005). "Fork configuration dampers and method of using the same." *Chinese Patent No. 101316973A* October 26.

Christopoulos, C., and Montgomery, M. (2011). "Coupling member for damping vibrations in building structures." *Provisional Patent Application US 61/432,631* January 14.

Christopoulos, C., and Montgomery, M. (2013). "Viscoelastic Coupling Damper (VCD) for enhanced dynamic performance of high-rise buildings." *Earthquake Engineering and Structural Dynamics.* DOI: 10.1002/eqe.2321.

CTBUH. (2008) "Recommendations for the seismic design of high-rise buildings." *Council of Tall Buildings and Urban Habitat.*

Fan, C. P. (1998). "Seismic analysis, behavior, and retrofit of non-ductile reinforced concrete frame buildings with viscoelastic dampers." *Ph.D. Dissertation,* Department of Civil and Environmental Engineering, Lehigh University, Bethlehem, PA.

Kasai, K., Minato, N., and Kawanabe, Y. (2006) "Passive control design method based on tuning equivalent stiffness of visco-elastic damper." *Journal of Construction Engineering, AIJ.* 610(12):75-83.

Kam, W.Y. and Pampanin S. (2011) "General building performance in the Chirstchurch CBD: A contextual report." *University of Cantebury Report, Prepared for the Department of Building and Housing (DBH)*, Christchurch, NZ.

Montgomery, M. S. (2011). "Fork configuration dampers (FCDs) for enhanced dynamic performance of high-rise buildings." *Ph.D. Dissertation,* University of Toronto, Department of Civil Engineering, Toronto, ON.

Soong, T. T., and Dargush, G. F. (1997) "Passive energy dissipation systems in structural engineering." *John Wiley and Sons*, New York, NY.